Coupling stochastic and numerical approaches for investigating the dynamics of coastal extreme events : Case of the English Channel and the ormandy coasts

Carlos Lopez Solano

Normandie Université

UNIVERSITÉ DE ROUEN NORMANDIE

THÈSE

Pour obtenir le diplôme de doctorat

Spécialité **SCIENCES DE L'UNIVERS**

Préparée au sein de l'**Université de Rouen Normandie**

Coupling stochastic and numerical approaches for investigating the dynamics of coastal extreme events : Case of the English Channel and the Normandy coasts

Présentée et soutenue par

CARLOS LOPEZ SOLANO

Thèse soutenue le 15/10/2024

devant le jury composé de :

MME EMMA TURKI	Maître de Conférences HDR - Université de Rouen Normandie (URN)	Directeur de thèse
M. ROBERT LAFITE	Professeur des Universités - Université de Rouen Normandie (URN)	Co-directeur de thèse
M. JULIEN REVEILLON	Professeur des Universités - Université de Rouen Normandie (URN)	Président du jury
M. XAVIER BERTIN	Directeur de Recherche - Centre Nat Rech Scientifique	Membre du jury
M. GABRIEL DIAZ-HERNANDEZ	Chargé de Recherche - Université de Cantabria (ESPAGNE)	Membre du jury
M. YASSER HAMDI	Professeur Associé - INRS de QUEBEC	Membre du jury
MME NADIA SENECHAL	Professeur des Universités - Universite de Bordeaux	Rapporteur du jury
MME MARISSA YATES	Chargé de recherche HDR - Ecole des Ponts Paristech	Rapporteur du jury

Thèse dirigée par **EMMA TURKI** (MORPHODYNAMIQUE CONTINENTALE ET COTIERE) et **ROBERT LAFITE** (Université de Rouen Normandie)

ED 497 NBISE
Normande de Biologie Intégrative, Santé, Environnement

M2C

Normandie Université

UNIVERSITÉ DE ROUEN NORMANDIE

THÈSE

Pour obtenir le diplôme de doctorat

Spécialité **SCIENCES DE L'UNIVERS**

Préparée au sein de l'**Université de Rouen Normandie**

Coupling stochastic and numerical approaches for investigating the dynamics of coastal extreme events : Case of the English Channel and the Normandy coasts

Présentée et soutenue par

CARLOS LOPEZ SOLANO

Thèse soutenue le 15/10/2024

devant le jury composé de :

MME. E. IMEN TURKI	Maître de Conférences HDR - Université de Rouen Normandie	Directrice de thèse
M. ROBERT LAFITE	Professeur des Universités émérite - Université de Rouen Normandie	Co-directeur de thèse
M. XAVIER BERTIN	Directeur de Recherche - Centre Nat Rech Scientifique	Membre du jury
M. GABRIEL DIAZ-HERNANDEZ	Enseignant-chercheur - Institute of Environmental Hydraulics (Espagne)	Membre du jury
M. YASSER HAMDI	Professeur Associé - INRS de Quebec	Membre du jury
M. JULIEN REVEILLON	Professeur des Universités - Université de Rouen Normandie	Membre du jury
MME. NADIA SENECHAL	Professeur des Universités - Université de Bordeaux	Rapporteur du jury
MME. MARISSA YATES	Chargée de recherche HDR - Ecole des Ponts	Rapporteur du jury
M. ANTONIN MIGAUD	Ingénieur-Chercheur - Institut de Radioprotection et de Sureté Nucléaire	Invité
MME. DELPHINE JACONO	Agence de l'Eau Seine Normandie - Rouen	Invitée

Thèse dirigée par **E. IMEN TURKI** (MORPHODYNAMIQUE CONTINENTAL ET COTIERE) et **ROBERT LAFITE** (Université de Rouen Normandie) et co-encadrée par **YASSER HAMDI** (IRSN)

ED 497 NBISE
Normande de Biologie Intégrative, Santé, Environnement

M2C

ACKNOWLEDGEMENTS

This thesis has been the work of 4 years, probably the most tough and challenging time of my life. But I have not been alone through this journey, so I want to dedicate some words to all the people who supported me and carried me to the end.

First of all, I would like to thank my thesis directors Imen Turki and Robert Lafite, who have been the most comprehensive and, at the same time, the most demanding people with me, and without who not even a small part of all the objectives and great results that we accomplished could have been reached. Imen, you believed in me from the beginning because of my background and trusted me to continue a very important part of your research, introducing me to scientific and professional aspects that I have never known before. I am aware of how difficult it was for you to obtain the fulfillment of this project, so I will always be grateful to you for choosing me. You have taught me, you have worked with me, and you have taken care of me, being my professor, my mother or my supervisor and changing from one to another when I have needed it. Robert, I cannot describe how supportive you have been for me. I arrived in Rouen in a difficult time, and I quickly felt totally lost, without any idea about the administrative system, about how to behave in a research atmosphere and interact with the closer and more distant colleagues, or even without knowing a single word of French! And you guided me to make me feel comfortable and self-confident with every step I took in every environment in which I found myself. Et maintenant je m'exprime facilement en français, en grande part grâce à toi. I want to finish by apologizing to both of you for those moments of doubt or absence in which I did not believe in myself, and I did not think I could finish the thesis, but you were there waiting for me after that and helped me to finish the work.

I also want to thank the Normandy Region, the IRSN (*Institut de Radioprotection et de Sureté Nucléaire*) and the AESN (*Agence de l'Eau Seine Normandie*) for the funding of this project. In particular, I would like to thank Yasser Hamdi in the framework of the collaboration with the IRSN. You have given me the opportunity to work with other colleagues in a totally different environment, providing useful and very interesting experiences, and sharing with me your scientific and research knowledge. In the same way, I want to thank Antonin Migaud and Lise Bardet, who took over the situation in a tricky moment and understood how complicated it was at that point, and with who working was an absolute pleasure, letting me focus on the work and being by my side until the culmination of the thesis.

An especial thanks to the members of the defense committee: Nadia Senechal and Marissa Yates, your comments, suggestions and propositions are of the most interest, you helped a lot in

the improvement of this manuscript and the presentation. Xavier Bertin, who was also in my CSI and suggested different points of view throughout the project. Julien Reveillon, the president of the jury who made me feel comfortable during my defense. And Gabriel Díaz Hernández, my master's professor and now friend, who came to Rouen to support me and who has proposed me thinking from a different perspective. I also want to thank the other members of the CSI, María Maza Fernández, my master's professor too, Pascal Fevriel and Markus Neupert.

I wish to express my gratitude to my colleagues in the M2C (*Morphodynamique Continentale et Côtière*) laboratory. The head of the laboratory, Nicolas Massei, who was supportive and understanding, the other researchers, Nicolas Lecoq, who took me to field campaigns when I had just arrived, Sophie Le Bot, Luminita Danaila and Manuel Fossa, who involved me in informational and educational activities, and Valérie Mesnage, Julien Deloffre, Benoit Laignel and all the other colleagues who frequently asked me and encouraged me to go on. I thank also the permanent staff of the laboratory, Maria Decaux and Cécile Tremege, with who the communication at my arrival was impossible but we managed to succeed. I especially thank my fellow PhDs, the ones who explained everything at the beginning, Antoine Soloy and Nazih Al-lababidi, the ones who suffered with me during the developments of our respective theses, Sivarama Krishna Reddy Chidepudi, Claire Da Costa, Imad Janbain and Romain Gilbert, and the one who saw with me Verstappen smashing Hamilton, Edward Salameh. And thank you to Pierre Chauris, Antoine Chapon and the other interns who helped me with my thesis.

The most difficult parts of the project would have been impossible to solve without the priceless help of Ángel David Gutiérrez Barceló and Ernesto Tonatiuh Mendoza. David, you helped me no matter the time, the day, the country or even the continent. A huge part of this work exists thanks to you.

But outside the scientific atmosphere, on my personal side, I have a long list of people whose support was fundamental to achieving this goal. Every time I had to run away to Madrid, I realized how important the people I have there are. My friends, Elena, Natalia, Gabriela, Esther, Dani B, Marisa, Carol, who asked me to meet no matter how every time they knew I was there, and also all the others who were happy to see me. Time is the most valuable thing we have, and you chose to share it with me. But outside Madrid too, Eric, Iris, Rubén, Akane, you are my shelter from Barcelona. My civil engineering friends, who are crazy to go abroad as me, Julen, Dani L. My master's friends, who I met in Santander and still in contact, Cris, Fran, Isa, sorry for not going to your weddings, you can see I was busy, Laura, always so heartwarming, and all the others. Especially thanks to Paula, vaca, I could not understand life without you, my personal,

professional and most difficult to understand friend, no matter the thousands of kilometers or if we see each other one time every 4 years.

My family too, my aunts and uncles, Grace, Tere, Javi, Ama, Janita, Jose, Diana, Paquito, my cousins, Andrea, Irene, Mario, Dánae, Roberto, María, with Emma and Alejandro. You joked and complained with me and made me forget for some moments to return with more energy and motivation. I had an amazing time with you these years everywhere we met and everywhere we went, in Spain, France or any other place. I know you believed in me all the time, but that does not count if you always do it. But especially thanks to my parents and siblings, mamá, papá, Laura, Alfonso, you had made this journey much easier, and it would have been impossible if you were not there. You even came to Rouen a lot when I was not going to Madrid enough times, and I still expect you to come more. Gracias a todos de corazón.

And my friends in Rouen. The first ones I met, Esteban, Melissa, Tatiana. You stayed by my side when we did not know what was going to happen and supported me, listened to me and counted on me when I did not know anyone else. The ones who arrived later, Julián, Josepha, we have had so much fun. You made me spend the most amazing time out of the hardest moments. All the others who have been really important through these years, Nath, Diego, Pipe, María, Jorge, Sara, Salima, Jose, Christian, you make life shine.

My French friends, Marie, Antoine, Titia, Lola, Félix, Sarah D, Aloïs, the ones who took the patience to listen to me and got to know me surpassing every cultural or language barrier we could have. The last ones I met, Sarah H, Flo, Louis, Johanna, Inès, Léa, Louise, Clara, and all the others, thank you for always inviting me and following up with my life. And of course, you, Victor, thank you for your support, your time and your dedication. I know it was not easy, but here we are, you have made me learn a lot about myself, and I hope I did you too. Merci à toutes et tous, on a encore beaucoup à faire.

And thank you to all the people I did not mention above but who also feel part of this journey.

RESUME

Les zones côtières sont de plus en plus vulnérables en raison du changement climatique, ce qui entraîne des risques tels que les submersions côtières ou l'érosion des plages, exacerbés par les activités anthropiques et le réchauffement climatique. Une gestion côtière efficace et des stratégies d'adaptation sont cruciales. Les modèles numériques avancés et la surveillance des tempêtes extrêmes sont essentiels pour une évaluation précise des risques et des systèmes d'alerte précoce. Cette thèse examine les houles extrêmes et les surcotes en Manche, mer située entre la France et l'Angleterre), en intégrant les oscillations climatiques globales et les facteurs hydrodynamiques locaux. Les plages de Normandie, avec leurs morphologies diverses, sont étudiées en utilisant des modèles numériques et des systèmes de surveillance pour comprendre les hydrodynamiques et les risques côtiers.

Les facteurs stochastiques de l'hydrodynamique marin sont explorés en se concentrant sur les variations de la hauteur des houles et du niveau de la mer, analysées à travers des méthodes statistiques et spectrales. Une variabilité significative des surcotes a été identifiée, alimentée par les tendances à long terme du niveau de la mer et les interactions marée-surcote, les hauteurs des houles étant influencées par les interactions océan-atmosphère, révélant des dépendances à la température de surface de la mer, à la pression atmosphérique et aux indices climatiques. Une classification des événements extrêmes typiques dans la Manche est récemment réalisée.

Une simulation de 40 ans de données avec une validation par rapport aux mesures de bouées et de marégraphes en Angleterre et en France a été réalisée. L'étude classe les tempêtes, en évaluant leur impact sur la côte de Normandie, montrant des variations significatives de la hauteur des houles, principalement en fonction de leur origine et de leur direction de propagation, principalement l'océan Atlantique. Les simulations détaillées soulignent le rôle de la morphologie côtière dans la dissipation de l'énergie et le comportement des houles.

La modélisation numérique pour simuler les dynamiques des houles de tempête sur trois sites côtiers normands, est détaillée et validée en comparant les simulations avec les mesures des bouées, les formulations théoriques et les données de run-up de houles mesurées par les Systèmes de Surveillance Vidéo (VMS). Les résultats montrent que la hauteur de run-up est influencée par les niveaux d'eau et la hauteur des houles, avec des variations spécifiques pour chaque site en raison des caractéristiques des plages, principalement la porosité des différents sédiments.

Les méthodologies stochastiques et numériques ainsi que les bases de données des études précédentes sont enfin appliquées pour lier l'hydrodynamisme avec la morphodynamique des plages dans des conditions extrêmes, en étudiant les composantes d'inondation sur la baie de Seine et l'impact des structures côtières et de la perméabilité sur l'érosion des plages.

ABSTRACT

Coastal zones face increasing vulnerability due to climate change, leading to hazards like coastal flooding or beach erosion, exacerbated by anthropogenic activities and global warming. Effective coastal management and adaptation strategies are crucial. Advanced numerical models and monitoring of extreme storms are essential for accurate risk assessment and early warning systems. This thesis aims to enhance understanding of storm dynamics, focusing on coastal flooding to improve risk assessment and mitigation efforts. This dissertation examines extreme waves and storm surges along the English Channel, integrating global climate oscillations and local hydrodynamic factors. Normandy's beaches, with diverse morphologies, are studied using numerical modelling and monitoring systems to understand hydrodynamics and coastal risks.

The stochastic drivers of maritime hydrodynamics are explored, focusing on wave height and sea level variations, analyzed through statistical and spectral methods. The research identifies significant variability in surges driven by long-term sea level trends and tide-surge interactions, with wave heights influenced by ocean-atmosphere interactions, and revealing dependencies on sea surface temperature, sea level pressure, and climate indexes. A classification of typical extreme events on the English Channel is lastly performed.

A simulation of 40 years of data, with validation against buoy and tide gauge measurements in England and France has been carried out. The study classifies storms, assessing their impact on Normandy's coast, showing significant wave height variations, dependent mostly on their origin and direction of propagation, primarily the Atlantic Ocean. Detailed simulations emphasize coastal morphology's role in energy dissipation and wave behavior.

The numerical modeling to simulate storm wave dynamics at three Norman coastal sites is detailed, validated by comparing simulations with buoy measurements, theoretical formulations, and wave run-up data measured by Video Monitoring Systems. Results show that run-up height is influenced by water levels and wave height, with site-specific variations due to beach characteristics, mainly the porosity of gravels and pebbles.

The stochastic and the numerical methodologies and databases from previous studies are finally applied to link hydrodynamics with beach morphodynamics under extreme conditions, studying compound flooding on the Seine Bay and the impact of coastal structures and beach permeability on beach erosion.

LIST OF CONTENTS

LIST OF CONTENTS 1

LIST OF FIGURES 10

LIST OF TABLES 16

LIST OF ABBREVIATIONS 20

RÉSUMÉ SUBSTANTIEL 25

CHAPTER 1. INTRODUCTION 40

1.1. GENERAL CONTEXT 41

1.2. OBJECTIVES OF THE DYNSEEC PROJECT 44

1.3. THE INVOLVEMENT OF THIRD PARTIES IN THE DYNSEEC PROJECT: AESN AND IRSN 46

CHAPTER 2. SCIENTIFIC INSIGHTS INTO THE EXTREME HYDRODYNAMICS IN THE ENGLISH CHANNEL AND ALONG THE NORMANDY COASTS 49

2.1. MARINE AND COASTAL HYDRODYNAMICS 50

2.1.1. Short waves: sea and swell 51

2.1.2. Water level variations: tides and surges 54

2.2. COASTAL STORMS 56

2.3. OVERVIEW OF THE METHODOLOGICAL APPROACHES USED FOR INVESTIGATING COASTAL HYDRODYNAMICS 57

2.3.1. From global atmospheric circulation to coastal hydrodynamics: stochastic downscaling 57

2.3.2. Dynamics of extreme events with climate teleconnections 59

2.3.3. Numerical approaches for investigating coastal hydrodynamics 61

2.3.4. On the investigation of coastal risks: flooding 63

2.4. STUDY SITES 65

2.4.1. The English Channel 65

2.4.2. The Normandy coasts 68

2.4.2.1. Etretat 69

2.4.2.2. Hautot-sur-Mer 70

2.4.2.3. Villers-sur-Mer 71

2.5. CONCLUSIONS: RESEARCH QUESTIONS AND ORGANISATION OF THE DISSERTATION 72

CHAPTER 3. ON THE USE OF STOCHASTIC APPROACHES TO INVESTIGATE THE MULTI-SCALE DYNAMICS OF EXTREME STORMS IN THE ENGLISH CHANNEL 75

3.1. INTRODUCTION 76

3.2. STUDY AREA AND DATA 78

3.2.1. Stochastic drivers 78

3.2.2. Description of the databases 80
3.2.2.1. Databases of surges 80
3.2.2.2. Wind and wave databases 82
3.3. SPECTRAL ANALYSIS OF TIME SERIES AND EXTREME VALUES 86
3.3.1. Wavelet spectral analysis 86
3.3.2. Multi-timescale variability of time series and extreme values 87
3.3.3. Relationship between extreme values and atmospheric oscillations 96
3.4. NON-STATIONARY ANALYTICAL EXTREME VALUE APPROACH 99
3.4.1. Non-stationary extreme value analysis 104
3.4.2. Dependence structure of wave height and surge extreme values 105
3.4.3. Results of the non-stationary extreme value approach of significant wave height and surges 106
3.4.4. Results of the dependence structure between significant wave height and surges 108
3.4.5. Dynamic copula between frequencies obtained from the spectral analysis 111
3.5. HOW IS AN EXTREME EVENT DEFINED? 113
3.5.1. Definition from a threshold 113
3.5.1.1. Extreme events of significant wave height 115
3.5.1.2. Extreme events of surges 117
3.5.2. Characterization from wave energy 119
3.6. TYPICAL EXTREME EVENTS IN THE ENGLISH CHANNEL 124
3.6.1. Classification of individual and compound extreme events 124
3.6.2. Clustering of extreme events 129
3.7. DISCUSSION AND CONCLUSIONS 136
3.8. CONCLUSIONS OF THE CHAPTER 139

CHAPTER 4. INTEGRATED MODELING FRAMEWORK FOR MONITORING EXTREME EVENTS FROM THE ENGLISH CHANNEL TO THE NORMANDY COASTS 140

4.1. EVOLUTION AND CLASSIFICATION OF EXTREME EVENTS OF WAVES AND SEA LEVELS FROM THE ENGLISH CHANNEL TO THE NORMANDY COASTS 141
4.1.1. Introduction 141
4.1.2. The English Channel and the Normandy coasts 143
4.1.3. Data and methods 145
4.1.3.1. Description of the databases: in-situ measurements and model forcings 145
4.1.3.2. Numerical approach 147
4.1.3.3. Study of bottom roughness in Delft3D 150
4.1.3.3.1. Formulations of bottom roughness in Delft3D 150
4.1.3.3.2. Sensitivity of modelling results to roughness 152
4.1.3.4. Storm characterization 154
4.1.4. Results 155

4.1.4.1. Validation of results: sea level and waves 156
4.1.4.2. Classification and evolution of storms 157
4.1.4.3. Storms tracked throughout the English Channel 161
4.1.5. Discussion 163
4.1.6. Conclusions 167
4.2. DYNAMICS OF NEARSHORE WAVES ALONG THE NORMANDY COASTS 168
4.2.1. Introduction 168
4.2.2. Data 171
4.2.2.1. Study sites: The English Channel and Normandy Coasts 171
4.2.2.2. Wind and wave field measurements 173
4.2.2.3. Storm events identification 175
4.2.3. Methodology 176
4.2.3.1. Wave model 176
4.2.3.2. Model set-up 176
4.2.3.1. Wave statistics 179
4.2.4. Results 180
4.2.4.1. Model validation 180
4.2.4.2. Changes in directional wave spectrum 181
4.2.4.1. Storms Evolution within the English Channel 185
4.2.4.2. Storm Evolution in Normandy Coasts: Case of Etretat and Hautot-sur-Mer 188
4.2.5. Discussion 192
4.2.6. Conclusions 195
4.3. CONCLUSIONS OF THE CHAPTER 196

CHAPTER 5. ASSESSING THE IMPACTS OF EXTREME STORMS ON THE COASTS OF NORMANDY 198

5.1. INTRODUCTION 199
5.2. METHODOLOGY 201
5.2.1. Description of the model 201
5.2.2. Forcings and set-ups of the model 202
5.2.2.1. Villers-sur-Mer 204
5.2.2.2. Hautot-sur-Mer 205
5.2.2.3. Etretat 210
5.3. VALIDATION OF THE MODEL 213
5.3.1. Validation of the forcing inputs 213
5.3.2. Validation with theoretical formulations 215
5.3.3. Validation with timestacks from VMS 219
5.4. IMPACTS OF PHYSICAL DRIVERS: DIFFERENT EVENTS IN ONE SITE 224
5.4.1. Villers-sur-Mer 224
5.4.2. Hautot-sur-Mer 232
5.4.3. Etretat 241

5.5. VARIATION IN DIFFERENT SYSTEMS: FROM SANDY TO MIXED AND GRAVEL BEACHES 249
5.6. STUDY OF WAVE BREAKING IN SWASH 250
5.7. DISCUSSION AND CONCLUSIONS 253
5.8. CONCLUSIONS OF THE CHAPTER 257

CHAPTER 6. APPLICATIONS ODF THE METHODOLOGIES TO COASTAL RISK ASSESSMENT: FROM FLOODING TO BEACH EROSION 258

6.1. COMPOUND FLOODING 259
6.1.1. Introduction 259
6.1.2. Materials and methods 261
6.1.2.1. Datasets 261
6.1.2.1.1. Study site: The English Channel and the Seine Estuary 261
6.1.2.1.2. Model forcings and measurements 262
6.1.2.2. Methodology 263
6.1.2.2.1. Description of the model 263
6.1.2.2.2. Set-ups and forcings of the model 264
6.1.2.2.3. Extreme value analysis 268
6.1.3. Results 271
6.1.3.1. Validation of the results in the coarse grid 271
6.1.3.2. Validation of the results in the Seine grid 271
6.1.3.3. Analysis of compound events 272
6.1.4. Discussion 277
6.1.5. Conclusions 278
6.2. MORPHODYNAMIC RESPONSE OF BEACHES TO EXTREME HYDRODYNAMICS 279
6.2.1. Variability of the morpho-sedimentary dynamics on two gravel beaches in response to hydrodynamics 279
6.2.1.1. Introduction 280
6.2.1.2. Methodological approach 280
6.2.1.3. Results and discussions 281
6.2.1.4. Conclusion 284
6.2.2. Numerical investigation into storm-driven pebble beach morphodynamics 285
6.2.2.1. Introduction 285
6.2.2.2. Methodological approach 286
6.2.2.3. Results 287
6.2.2.4. Discussion 288
6.2.2.5. Conclusions 289
6.3. CONCLUSIONS OF THE CHAPTER 290

CHAPTER 7. CONCLUSIONS AND PERSPECTIVES OF THE DISSERTATION 292

7.1. MAIN CONCLUSIONS OF THE DISSERTATION 293
7.2. RESEARCH PERSPECTIVES 296

REFERENCES.....299

APPENDICES.....321

APPENDIX A. NON-STATIONARY DYNAMICS OF EXTREME MONTHLY WAVES AND SURGES.....322

APPENDIX B. RESULTS OF NON-STATIONARY FITTINGS AND DEPENDENCE STRUCTURES OF Hs AND S 325

APPENDIX C. RESULTS OF CLUSTERING OF EXTREME EVENTS 340

APPENDIX D. FORMULATIONS AND NUMERICAL SOLUTIONS OF DELFT3D 355

APPENDIX E. STUDY OF WAVE BREAKING SIMULATION WITH SWASH.....361

List of Figures

Figure 1. General overview of the DYNSEEC context (modified from original figure from Sixth Assessment Report (AR6) of IPCC (2023)) 45

Figure 2. Pierson-Moskowitz and JONSWAP frequency spectra with the peak frequency fp (adapted from Pierson & Moskowitz (1964) and Hasselmann et al. (1973)) 52

Figure 3. Idealized wave transformation zones (adapted from Horikawa (1988)) 53

Figure 4. A schematic overview of processes contributing to sea level variability at the coast indicating the space and the timescale involved, (adapted from Woodworth et al., (2019)) 55

Figure 5. Overview of the different levels of potential flooding depending on coastal topography, with the components of extreme water level produced during stormy events, extracted from Almar et al. (2021) 57

Figure 6. a) January SLP climatologies for the period 1982-2011 of the NCAR index, b) annual trends in SST of the HadSST4 dataset of NCAR, c) Hurrell's NAO index time series of one of the PCs of the EOF analysis of SLP, d) NOAA's NAO index time series and e) observed AMO index by the NCAR 60

Figure 7. Visual conceptualization of some numerical models available taken as example of each type of model, including the equations solved and the assumptions, and the hydrodynamic processes that could be simulated (in SWASH, k is referred to the number of vertical layers). In red, the numerical models that will be used throughout the dissertation 64

Figure 8. Global to regional and local scales, with the main features relevant for the different studies, including the English Channel and, in red, the Normandy region and coasts 66

Figure 9. Wind (direction to) roses and wave (direction from) roses in the English Channel and the eastern and western open boundaries, the North Sea and the Atlantic Ocean, respectively. Main cities are marked in white, the nuclear power plants of the area in blue, and the study sites of the Normandy coasts in red 67

Figure 10. Example of VMS cameras installed in Etretat (picture of Y. Soufflet 2018) 69

Figure 11. Panoramic composition of the 3 camera views in Hautot-sur-Mer (top), Villers-sur-Mer (center) and Etretat (bottom) (modified after Soloy et al., 2021) 69

Figure 12. Etretat beach from a satellite view with the length (~1 km) and the slope (~12%) in the pebble beach 70

Figure 13. Hautot-sur-Mer beach from a satellite view with the length (~1.1 km) and the slope (~10%) in the composite beach 71

Figure 14. Villers-sur-Mer beach from a satellite view with the length (>2.5km) and the slope (<1%) in the sandy beach 72

Figure 15. English Channel between France and the UK, and the open boundaries in the Atlantic Ocean and the North Sea, with the locations of the tide gauges used for the analysis of surges 80

Figure 16. Calculation of the skew surges S from the measurements of sea level of the tide gauges. Adapted from the website of SHOM (refmar.shom.fr) 82

Figure 17. Wave height (m) map in the English Channel, obtained from the NWSHELF database, taken as an example for 10/02/2020 at 6 am (storm Ciara) 83
Figure 18. Wave period (s) map in the English Channel, obtained from the NWSHELF database, taken as an example for 10/02/2020 at 6 am (storm Ciara) 84
Figure 19. Wave direction (°) map in the English Channel, obtained from the NWSHELF database, taken as an example for 10/02/2020 at 6 am (storm Ciara) 84
Figure 20. Wind speed (m/s) map in the English Channel, obtained from the ERA5 database, taken as an example for 10/02/2020 at 6 am (storm Ciara) 85
Figure 21. Wind direction (°) map in the English Channel, obtained from the ERA5 database, taken as an example for 10/02/2020 at 6 am (storm Ciara) 85
Figure 22. Atmospheric pressure (Pa) map in the English Channel, obtained from the ERA5 database, taken as an example for 10/02/2020 at 6 am (storm Ciara) 86
Figure 23. Time series of a), c), e), g), i), k), and m) extreme values of surges measured by the tide gauges, and b), d), f), h), j), l) and n) extreme values of significant wave height from reanalysis for Brest, Cherbourg, Weymouth, Le Havre, Newhaven, Dover and Dunkirk, respectively 88
Figure 24. Continuous wavelet diagrams of monthly maxima of significant wave height and surges for Weymouth, Newhaven and Dover, from top to bottom 89
Figure 25. Continuous wavelet diagrams of monthly maxima of significant wave height and surges for Brest, Cherbourg, Le Havre and Dunkirk, from top to bottom 90
Figure 26. Wavelet details (spectral components) resulting from the MODWT multiresolution analysis of monthly maxima of surges S at the intermonthly (~3 months and ~6 months), annual (~1 year) and interannual (~2 years, 3-5 years, 6-8 years) time scales for Brest, Cherbourg, Weymouth, Le Havre, Newhaven, Dover and Dunkirk 93
Figure 27. Wavelet details (spectral components) resulting from the MODWT multiresolution analysis of monthly maxima of waves Hs at the intermonthly (~3 months and ~6 months), annual (~1 year) and interannual (~2 years, 3-5 years, 6-8 years) time scales for Brest, Cherbourg, Weymouth, Le Havre, Newhaven, Dover and Dunkirk 94
Figure 28. Time-dependent PDF of monthly extreme surges during the period 1981 – 2018 at the semi-annual and interannual scales in Brest, Cherbourg and Weymouth 97
Figure 29. Time-dependent PDF of monthly extreme waves during the period 1980 – 2022 at the semi-annual and interannual scales in Brest, Cherbourg and Weymouth 98
Figure 30. Correlation of spectral components resulting from the MODWT of normalized variables (in black waves and in red surges) and normalized NAO in blue at the intermonthly (~6 months) and interannual (~1 year, ~2 years, ~3-5 years and ~6-8 years) timescales for the 7 stations 100
Figure 31. Correlation of spectral components resulting from the MODWT of normalized variables (in black waves and in red surges) and normalized SLP in blue at the intermonthly (~6 months) and interannual (~1 year, ~2 years, ~3-5 years and ~6-8 years) timescales for the 7 stations 101

Figure 32. Correlation of spectral components resulting from the MODWT of normalized variables (in black waves and in red surges) and normalized SST in blue at the intermonthly (~6 months) and interannual (~1 year, ~2 years, ~3-5 years and ~6-8 years) timescales for the 7 stations 102
Figure 33. Correlation of spectral components resulting from the MODWT of normalized variables (in black waves and in red surges) and normalized AMO in blue at the intermonthly (~6 months) and interannual (~1 year, ~2 years, ~3-5 years and ~6-8 years) timescales for the 7 stations 103
Figure 34. Bivariate density of monthly maxima of significant wave height from reanalysis and measured surge with effective joint return levels for several return periods for a) Brest, b) Cherbourg, c) Weymouth, d) Le Havre, e) Newhaven, f) Dover and g) Dunkirk 110
Figure 35. Bivariate density of spectral components of significant wave height from and surge in Le Havre with effective joint return levels for several return periods for the time scales of a) 2-3 months, b) 5-6.5 months, c) ~1 year, d) 1.5-2 years, e) 3-5 years, and f) 6-9 years 114
Figure 36. Storm energy for all the storms identified sorted by accumulated wave energy on a) Cherbourg, b) Dover, c) Newhaven, d) Dunkirk, e) Le Havre, f) Brest, and g) Weymouth 120
Figure 37. Percentage of occurrence of compound and individual extreme events at Brest, Cherbourg, Weymouth, Le Havre, Newhaven, Dover, and Dunkirk 126
Figure 38. Classes repartition percentages varying T_p and direction of compound and individual extreme events on the French locations: Brest, Cherbourg, Le Havre and Dunkirk. Purple, blue, green and yellow lines represent respectively the classes 0, 1, 2 and 3 128
Figure 39. Classes repartition percentages varying T_p and direction of compound and individual extreme events on the British locations: Weymouth, Newhaven and Dover. Purple, blue, green and yellow lines represent respectively the classes 0, 1, 2 and 3 129
Figure 40. Gaussian Mixture Model for a one-dimensional problem of 2 classes, with the separate and total PDF and the cluster allocation 130
Figure 41. Model for the selection of the number of clusters with AIC criterion. Example for Newhaven 131
Figure 42. H_s vs Duration and H_s vs Energy with ellipsoids representing the 95% confidence region of a cluster for the classes obtained from the clustering of extreme events on Newhaven 131
Figure 43. Class-averaged values of extreme events on a) Brest, b) Cherbourg, c) Weymouth, d) Le Havre, e) Newhaven, f) Dover, and g) Dunkirk for the complete dataset of identified storms 135
Figure 44. Bathymetry map of the English Channel with the observation points used in the study, five in deep waters, located along the basin (Brest - Land's End, Cherbourg - Weymouth, Buoy 62305, Buoy - Calais and Calais - Dover), and two nearshore in two representative sites on the Normandy coasts (Etretat and Hautot-sur-Mer). Buoy 62103 was used for validation and the three sectors considered for the study. Extracted from López Solano et al. (2024) 144
Figure 45. QQplots of significant wave height (Hs) comparison of reanalysis or results of modelling versus observations measured by buoy 62305: a) reanalysis of ERA5, b) reanalysis of NWSHELF, c) results of the simulations from the Delft3D model forced with the original values of wind, and d) results with the calibrated values of wind speed. Extracted from López Solano et al. (2024) 150

Figure 46. Bottom roughness in the model set-up as a constant value over the whole study area. Heterogeneous bottom roughness length-scale k_N in m 151

Figure 47. Bottom roughness in the model set-up as varying values according to the maps of sediment distribution of Guillou (2013). Heterogeneous bottom roughness length-scale k_N in m 153

Figure 48. Bottom roughness in the model set-up as varying values according to the maps of sediment distribution of Guillou (2013), simplified. Heterogeneous bottom roughness length-scale k_N in m... 154

Figure 49. Time-series of wave height in the Brest – Land's End observation point during the 40 years analyzed with the 262 storms identified over the threshold equivalent to the quantile 95. Storms selected as examples are indicated: Storm Sector I (Joachim), storm Sector II (Andrea) and storm Sector III (designated as Storm 19). Extracted from López Solano et al. (2024)..... 155

Figure 50.(a) Water level measured by the tide gauge of Cherbourg in black and the output of the numerical simulations in the closest location in red for the period 21-08-2010 to 04-09-2010; (b) water level measured by the tide gauge of Dieppe in black and the output of the numerical simulations in the closest location in red for the period 22-04-2009 to 04-05-2009; and (c) water level measured by the tide gauge of Le Havre in black and the output of the numerical simulations in the closest location in red for the period 17-07-2009 to 31-07-2009. Extracted from López Solano et al. (2024)..... 157

Figure 51. Significant wave height (Hs) comparison of results of simulations from the Delft3D model versus observations measured by buoy 62103 and buoy 62305. Extracted from López Solano et al. (2024) 158

Figure 52. Energy content versus wave height at the peak of the storms and every content versus duration of the storms for the three sectors used in the study: I, II and III. Extracted from López Solano et al. (2024) 160

Figure 53. Time-series of wave height for the three storms selected as example (Joachim, Andrea and Storm 19) in the Brest - Land's End, Cherbourg - Weymouth and Buoy observation points, and in the two nodes located nearshore. Extracted from López Solano et al. (2024) 162

Figure 54. Significant wave height contour map of Hs = 3 m and Hs = 6 m of three storms in consecutive instants propagating in the English Channel. The three storms (Joachim, Andrea and "Storm 19") correspond to each one of the three sectors in which the coming waves have been classified according to the direction of origin. Extracted from López Solano et al. (2024)..... 164

Figure 55. Maximum significant wave height of the three selected storms, Joachim, Andrea and "Storm 19", tracked throughout the English Channel. Extracted from López Solano et al. (2024)..... 165

Figure 56. Bathymetry map of the English Channel with the locations of the study sites (Etretat and Hautot-sur-Mer) the two buoys used for validation (in blue), the two points located in deep waters (North Sea and Atlantic Ocean) and the Reference point in intermediate waters. The latter three were used for studying the transformation of waves when getting inside the Channel and when approaching the study sites. Main geographical features are highlighted in yellow. Extracted from López Solano et al. (2022) 172

Figure 57. Time series of significant wave height (Hs) from June 2018 to September 2020. The red dotted line represents the quantile 95, used as threshold for the identification of extreme events. The vertical red still lines locate in the time series the 10 storms used for the analysis of transformation of waves in this study. Extracted from López Solano et al. (2022) 175

Figure 58. Coarse and nested grids, in white and red colors, respectively, for (a) Etretat and (b) Hautot-sur-Mer. DEMs of coarse grids in (c) Etretat and (d) Hautot-sur-Mer, and DEMs of nested grids in (e) Etretat and (f) Hautot-sur-Mer. Bathymetry data obtained from a merged DEM of EMODnet dataset and LiDAR campaign datasets. Satellite images from Google Earth. Extracted from López Solano et al. (2022) 178

Figure 59. Significant wave height (Hs) comparison of results of simulations from the SWAN model versus observations measured by (a) SCENES buoy for Etretat and (b) campaign 07608 for Hautot- sur-Mer. Extracted from López Solano et al. (2022) 181

Figure 60. Probability Density Functions (PDF) of Hs (a) and of Θ (b) and wave roses (c) at deep waters in the North Sea (depth = 44 m), the Atlantic Ocean (depth = 116 m), the Reference point (depth = 28 m), close to Etretat (depth = 13.4 m) and to Hautot-sur-Mer (depth = 13 m). Extracted from López Solano et al. (2022) 183

Figure 61. Continuous Wavelet Transform (CWT) of Hs (a) and Θ (b) at deep waters in the North Sea, the Atlantic Ocean, the Reference point (depth = 28 m), close to Etretat (depth = 13.4 m) and Hautot-sur-Mer (depth = 13 m). Extracted from López Solano et al. (2022) 184

Figure 62. Distribution maps at the peak of the storm of Hs and Θ in the coarse grid (a,c,e,g) and nested grid (b,d,f,h) in Hautot-sur-Mer for Ciara (February 2020) (a,b), Amelie (November 2019) (c,d), Deirdre (December 2018) (e,f) and Gabriel (January 2019) (g,h) storms. White arrows show the refraction of waves when approaching to coast. Extracted from López Solano et al. (2022) 189

Figure 63. Distribution maps at the peak of the storm of Hs and Θ in the coarse grid (a,c,e,g) and nested grid (b,d,f,h) in Etretat for Ciara (February 2020) (a,b), Amelie (November 2019) (c,d), Deirdre (December 2018) (e,f) and Gabriel (January 2019) (g,h) storms. White arrows show the refraction of waves when approaching to coast. Extracted from López Solano et al. (2022) 190

Figure 64. Time series of water level with the output of the English Channel model in Villers-sur-Mer during the 3 days of simulation of Ciara storm and time series of water level corrected according to the corrections in amplitude obtained from SCENES buoy 203

Figure 65. Bathymetry from the LiDAR campaign used for the set-up of the numerical model, and profiles selected for the simulations in Villers-sur-Mer 204

Figure 66. Geometry of the 7 profiles used for the simulations in Villers-sur-Mer relative to the MSL..... 206

Figure 67. Bathymetry from the LiDAR campaign used for the set-up of the numerical model, and profiles selected for the simulations in Hautot-sur-Mer 208

Figure 68. Geometry of the 8 profiles used for the simulations in Hautot-sur-Mer relative to the MSL 209

Figure 69. Bathymetry from the LiDAR campaign used for the set-up of the numerical model, and profiles selected for the simulations in Etretat 211

Figure 70. Geometry of the 8 profiles used for the simulations in Etretat relative to the MSL 212

Figure 71. Time series comparing the outputs of the numerical simulations in the English Channel with the measurements of the buoy SCENES of (a) significant wave height (Hs) and (b) peak period (Tp), and with the measurements of the buoy of Penly of (c) Hs and (d) Tp during the 3 days simulated of storm Ciara 214

Figure 72. Results of Run-Up 2% from the numerical simulations and for the formulations of EurOtop and Stockdon for the four simulated storms in Villers-sur-Mer 218

Figure 73. Snapshot of the GUI timestack processing software used (Vousdoukas et al., 2012). Red lines indicate the swash front motions, and yellow dots the discrete maxima considered for the estimation of 2% exceedance values. The timestack corresponds to 11/02/2020 10:20 221

Figure 74. Results of Run-Up 2% from the numerical simulations for storm Ciara for all the profiles in Villers-sur-Mer. Black dotted line on the left y-axis corresponds to the water level set for each simulation and red dotted line on the right y-axis corresponds to the significant wave height of every sea state 225

Figure 75. Results of Run-Up 2% from the numerical simulations for storm Joachim for all the profiles in Villers-sur-Mer. Black dotted line on the left y-axis corresponds to the water level set for each simulation and red dotted line on the right y-axis corresponds to the significant wave height of every sea state 227

Figure 76. Results of Run-Up 2% from the numerical simulations for storm Andrea for all the profiles in Villers-sur-Mer. Black dotted line on the left y-axis corresponds to the water level set for each simulation and red dotted line on the right y-axis corresponds to the significant wave height of every sea state 229

Figure 77. Results of Run-Up 2% from the numerical simulations for "Storm 19" for all the profiles in Villers-sur-Mer. Black dotted line on the left y-axis corresponds to the water level set for each simulation and red dotted line on the right y-axis corresponds to the significant wave height of every sea state 231

Figure 78. Results of Run-Up 2% from the numerical simulations for storm Ciara for all the profiles in Hautot-sur-Mer. Black dotted line on the left y-axis corresponds to the water level set for each simulation and red dotted line on the right y-axis corresponds to the significant wave height of every sea state 234

Figure 79. Results of Run-Up 2% from the numerical simulations for storm Joachim for all the profiles in Hautot-sur-Mer. Black dotted line on the left y-axis corresponds to the water level set for each simulation and red dotted line on the right y-axis corresponds to the significant wave height of every sea state 236

Figure 80. Results of Run-Up 2% from the numerical simulations for storm Andrea for all the profiles in Hautot-sur-Mer. Black dotted line on the left y-axis corresponds to the water level set for each simulation and red dotted line on the right y-axis corresponds to the significant wave height of every sea state 238

Figure 81. Results of Run-Up 2% from the numerical simulations for "Storm 19" for all the profiles in Hautot-sur-Mer. Black dotted line on the left y-axis corresponds to the water level set for each simulation and red dotted line on the right y-axis corresponds to the significant wave height of every sea state 240

Figure 82. Results of Run-Up 2% from the numerical simulations for storm Ciara for all the profiles in Etretat. Black dotted line on the left y-axis corresponds to the water level set for each simulation and red dotted line on the right y-axis corresponds to the significant wave height of every sea state..... 242

Figure 83. Results of Run-Up 2% from the numerical simulations for storm Joachim for all the profiles in Etretat. Black dotted line on the left y-axis corresponds to the water level set for each simulation and red dotted line on the right y-axis corresponds to the significant wave height of every sea state..... 244

Figure 84. Results of Run-Up 2% from the numerical simulations for storm Andrea for all the profiles in Etretat. Black dotted line on the left y-axis corresponds to the water level set for each simulation and red dotted line on the right y-axis corresponds to the significant wave height of every sea state..... 246

Figure 85. Results of Run-Up 2% from the numerical simulations for "Storm 19" for all the profiles in Etretat. Black dotted line on the left y-axis corresponds to the water level set for each simulation and red dotted line on the right y-axis corresponds to the significant wave height of every sea state..... 248

Figure 86. Sensitivity of the breaking area to a and b for a fixed number of layers (k = 3): a) Influence of a with b constant, and b) Influence of b with a constant. Internship of Pierre Chauris (2024) 251

Figure 87. Estimated breaking position across the timestack. Internship of Pierre Chauris (2024)..... 252

Figure 88. Comparison between the wave height at breaking simulated with SWASH and extracted from timestacks. Internship of Pierre Chauris (2024) 252

Figure 89. Comparison between simulation and image extraction of wave breaking repartition: a) Binary map and associated distribution over a 10-minute duration from SWASH and b) Binary map and associated repartition over a 10-minute duration from timestack. Internship of Pierre Chauris (2024) 253

Figure 90. Comparison of the breaking repartition obtained from SWASH and from timestack images. Plots with a colored background correspond to days during a storm. Internship of Pierre Chauris (2024) 254

Figure 91. Study sites: (a) English Channel between the coasts of France and the United Kingdom, and the locations of the tide gauges of Cherbourg and Dieppe; and (b) the Seine Estuary with the locations of the tide gauges of Le Havre and Tancarville. Extracted from López Solano et al. (2024)..... 261

Figure 92. Computational grids used for the numerical model set-ups in the English Channel and in the Seine Estuary. Waves, sea level and river discharge forcings on the open boundaries are marked for each computational grid in red color. Color scale represents the topobathymetry interpolated in each cell. Extracted from López Solano et al. (2024) 264

Figure 93. Histograms with the relative frequency of the (a) significant wave height Hs; (b) peak period Tp; (c) mean direction; (d) storm surge and (e) river discharge. Extracted from López Solano et al. (2024).. 267

Figure 94. (a) Joint return period of the storm surge and the wave height in the Seine mouth; and (b) Generalized Extreme Value distribution function fitted to the annual maxima for the 62 years timeseries of river discharge. Extracted from López Solano et al. (2024) 269

Figure 95. Synthesis of the methodological approach used to study the compound scenarios of flooding produced by extremes of storm surge, wave height and river discharge on the Seine Bay. Extracted from López Solano et al. (2024) 270

Figure 96. (a) Timeseries of water level measured by the tide gauge of Tancarville in black and the output of the numerical simulations in the closest location in red for the period from 16-06-2011 at 04:00 to 18-06-2011 at 20:00; and (b) timeseries of water level measured by the tide gauge of Le Havre in black and the output of the numerical simulations in the closest location in red for the period from 16-06-2011 at 04:00 to 18-06-2011 at 20:00. Extracted from López Solano et al. (2024) 272

Figure 97. Distribution of the control areas where the outputs of the simulation have been extracted to evaluate the flooding of the compound events. Main features of the study area are also specified. Extracted from López Solano et al. (2024) 273

Figure 98. Hazard curves showing the maximum depth reached in representative cells produced by compound events of flooding. Left panel represents the forcing of storm surge calculated with a high value of wave height and a low value of storm surge and right panel the forcing with a high value of storm surge and a low value of wave height. Each hazard curve represents one return period fixed associated with river discharge and the storm surge varying for 5, 10, 20, 50, 100 and 200 years. Extracted from López Solano et al. (2024) 274

Figure 99. Hazard curves showing the maximum depth reached in representative cells produced by compound events of flooding. Left panel represents the forcing of storm surge calculated with a high value of wave height and a low value of storm surge and right panel the forcing with a high value of storm surge and a low value of wave height. Each hazard curve represents one return period fixed associated with storm surge and the river discharge varying for 5, 10, 20, 50, 100 and 200 years. Extracted from López Solano et al. (2024) 275

Figure 100. Planform evolution of the +2 m elevation shoreline position in Etretat (a) and Hautot-sur-Mer (b), from July 2018 to November 2020. Time series of average beach width between elevations −2 m and + 3 m in Etretat (c), and from +1 and + 3 m in Hautot-sur-Mer (d), with 1 m of span. Average planform shape of the shoreline at the same elevations in Etretat (e) and Hautot-sur-Mer (f). The position of groin structures is indicated with black dashed lines. Extracted from Soloy et al. (2022) 281

Figure 101. Conceptual model of the isolated mechanisms of beach morphological variability in Etretat (left) and Hautot-sur-Mer (right), associated with their corresponding principal component (PC). Extracted from Soloy et al. (2022) 282

Figure 102. Correlation matrix between morphodynamical parameters including Beach Width (BW), Beach Orientation Angle (BOA) and Beach Slope (BS) and the temporal eigenfunction of the principal components (PC) resulting from the EOF analysis applied to Etretat's shoreline position from elevations −2 m to +3 m (a), and to Hautot-sur-Mer from elevations +1 m to +3 m (b). c and d present the

same operation calculated with hydrodynamic parameters including wave energy, current velocity and tidal range. Extracted from Soloy et al. (2022) 284
Figure 103. Digital elevation model (DEM) of the subtidal along the offshore to nearshore transect from SHOM and ROL (a) and of the intertidal area observed using coastal Video Monitoring Systems (VMS, b). All datasets were merged, and elevations were extracted along the transect in order to provide profiles for each modeled day. Extracted from Soloy et al. (2024) 286
Figure 104. Storm energy of the 30 most intense storms sorted by cumulated wave energy. Extracted from Soloy et al. (2024) 287
Figure 105. Energy conditions associated to the different storm event, A (a), B (b) and C (c). Time series of wave energy flux during the three storms modeled using XBeach-G by intervals of 24 h. Vertical red lines (both dashed and solid) indicate the dates at which VMS-derived intertidal DEMs were available, the dashed ones specifically correspond to model starting dates while the solid lines indicate the last date with data available for model performance assessment. Extracted from Soloy et al. (2024) 288
Figure 106. Time-dependent PDF of monthly extreme surges during the period 1981 – 2018 at the semi-annual and interannual scales in Le Havre, Newhaven, Dover and Dunkirk 323
Figure 107. Time-dependent PDF of monthly extreme waves during the period 1980 – 2022 at the semi-annual and interannual scales in Le Havre, Newhaven, Dover and Dunkirk 324
Figure 108. Bivariate density of spectral components of significant wave height from and surge in Brest with effective joint return levels for several return periods for the time scales of a) 2-3 months, b) 5-6.5 months, c) ~1 year, d) 1.5-2 years, e) 3-5 years, and f) 6-9 years 334
Figure 109. Bivariate density of spectral components of significant wave height from and surge in Cherbourg with effective joint return levels for several return periods for the time scales of a) 2-3 months, b) 5-6.5 months, c) ~1 year, d) 1.5-2 years, e) 3-5 years, and f) 6-9 years 335
Figure 110. Bivariate density of spectral components of significant wave height from and surge in Weymouth with effective joint return levels for several return periods for the time scales of a) 2-3 months, b) 5-6.5 months, c) ~1 year, d) 1.5-2 years, e) 3-5 years, and f) 6-9 years 336
Figure 111. Bivariate density of spectral components of significant wave height from and surge in Newhaven with effective joint return levels for several return periods for the time scales of a) 2-3 months, b) 5-6.5 months, c) ~1 year, d) 1.5-2 years, e) 3-5 years, and f) 6-9 years 337
Figure 112. Bivariate density of spectral components of significant wave height from and surge in Dover with effective joint return levels for several return periods for the time scales of a) 2-3 months, b) 5-6.5 months, c) ~1 year, d) 1.5-2 years, e) 3-5 years, and f) 6-9 years 338
Figure 113. Bivariate density of spectral components of significant wave height from and surge in Dunkirk with effective joint return levels for several return periods for the time scales of a) 2-3 months, b) 5-6.5 months, c) ~1 year, d) 1.5-2 years, e) 3-5 years, and f) 6-9 years 339
Figure 114. H_s vs Duration for the classes obtained from the clustering of extreme events on a) Brest, b) Cherbourg, c) Weymouth, d) Le Havre, e) Newhaven, f) Dover, and g) Dunkirk for the complete dataset of identified storms 341

Figure 115. H_s vs Energy for the classes obtained from the clustering of extreme events on a) Brest, b) Cherbourg, c) Weymouth, d) Le Havre, e) Newhaven, f) Dover, and g) Dunkirk for the complete dataset of identified storms 342
Figure 116. Class-averaged values of extreme events on a) Brest, b) Cherbourg, c) Weymouth, d) Le Havre, e) Newhaven, f) Dover, and g) Dunkirk for the complete dataset of identified storms 346
Figure 117. H_s vs Duration for the classes obtained from the clustering of extreme events on a) Brest, b) Cherbourg, c) Weymouth, d) Le Havre, e) Newhaven, f) Dover, and g) Dunkirk for the complete dataset of identified storms 347
Figure 118. H_s vs Energy for the classes obtained from the clustering of extreme events on a) Brest, b) Cherbourg, c) Weymouth, d) Le Havre, e) Newhaven, f) Dover, and g) Dunkirk for the complete dataset of identified storms 348
Figure 119. Class-averaged values of extreme events on a) Brest, b) Cherbourg, c) Weymouth, d) Le Havre, e) Newhaven, f) Dover, and g) Dunkirk for the complete dataset of identified storms 352
Figure 120. H_s vs Duration for the classes obtained from the clustering of extreme events on a) Brest, b) Cherbourg, c) Weymouth, d) Le Havre, e) Newhaven, f) Dover, and g) Dunkirk for the complete dataset of identified storms 353
Figure 121. H_s vs Energy for the classes obtained from the clustering of extreme events on a) Brest, b) Cherbourg, c) Weymouth, d) Le Havre, e) Newhaven, f) Dover, and g) Dunkirk for the complete dataset of identified storms 354
Figure 122. Mapping of physical space to computational space. Extracted from the User Manual of Delft3D-FLOW 358
Figure 123. Breaking zone estimation method: a) Boolean mask over the cross-shore profile between instants 400s and 1200s of simulation, and b) At each time step, the breaking zone is in dark red, and the averaged breaking zone in light red. Internship of Pierre Chauris (2024) 362
Figure 124. Schematic of the principal method. The camera view angle is b and a_B is the wavefront face slope. The roller appears as a dashed oval. L is the wave roller horizontal projection, Cor a correction taking into account a_B and H_B is the actual breaker height. Extracted from Almar et al. (2012). Internship of Pierre Chauris (2024) 364
Figure 125. Step-by-step extraction of the breaking positions in a timestack. Internship of Pierre Chauris (2024) 364
Figure 126. Breaker height extraction methodology: a) timestack intensity around a breaking event at 3 consecutive time steps; b) intensity standard deviation over the 2dt period; and c) horizontal projection of the wave face covered by the roller. Internship of Pierre Chauris (2024) 365
Figure 127. Daily maximal values of wave height and period measured during February 2020 used for the SWASH simulations. The colored sections represent the duration of energetic storm events, with Ciara storm in red. Internship of Pierre Chauris (2024) 366

List of Tables

Table 1. Estimated explained variance of energy expressed as percentage of total monthly maxima of surges in the 7 study sites, with the percentages resulting from the MODWT multiresolution analysis.....91

Table 2. Estimated explained variance of energy expressed as percentage of total monthly maxima of significant wave height in the 7 study sites, with the percentages resulting from the MODWT multiresolution analysis.....91

Table 3. Estimated explained variance of energy expressed as percentage of the climate indexes, with the percentages resulting from the MODWT multiresolution analysis 99

Table 4. Results of the fitting of the GEV with the non-stationary parameters dependent the climate and time indexes for significant wave height and surge in the 7 studied locations.....107

Table 5. Results of the fitting of the copulas between significant wave height and surge with the non-stationary time-dependent parameter in the 7 studied locations.....109

Table 6. Results of the fitting of the GEV with the non-stationary parameters dependent the climate and time indexes for the spectral components of significant wave height and surge in Le Havre 112

Table 7. Results of the fitting of the copulas between spectral components of significant wave height and surge with the non-stationary time-dependent parameters in Le Havre with the 6 timescales 113

Table 8. Statistics of the main characteristics of the extreme events identified over a threshold in the time series of significant wave height 116

Table 9. Statistics of the main characteristics of the extreme events identified over a threshold in the time series of measured surges 118

Table 10. Characteristics of the selected storms sorted by the highest cumulated wave energy in Cherbourg, Dover and Newhaven, the sites with the highest energy.....122

Table 11. Characteristics of the selected storms sorted by the highest cumulated wave energy in Dunkirk, Le Havre and Brest.....123

Table 12. Statistical characteristics (mean and the range min/max) of the classes of the extreme events identified in the clustering in Brest 132

Table 13. Statistical characteristics (mean and the range min/max) of the classes of the extreme events identified in the clustering in Cherbourg.....132

Table 14. Statistical characteristics (mean and the range min/max) of the classes of the extreme events identified in the clustering in Weymouth 133

Table 15. Statistical characteristics (mean and the range min/max) of the classes of the extreme events identified in the clustering in Le Havre.....133

Table 16. Statistical characteristics (mean and the range min/max) of the classes of the extreme events identified in the clustering in Newhaven.....133

Table 17. Statistical characteristics (mean and the range min/max) of the classes of the extreme events identified in the clustering in Dover 134

Table 18. Statistical characteristics (mean and the range min/max) of the classes of the extreme events identified in the clustering in Dunkirk 134

Table 19. Main characteristics in terms of wave height at the peak of the storms (Hs), direction at the peak, duration of the storms and random wave energy density of the storms identified divided in the three sectors used in the study: I (271° to 296°), II (246° to 271°) and III (221° to 246°). Extracted from López Solano et al. (2024) 158

Table 20. Wave height at the peak (Hs), direction at the peak, duration and random wave energy density of the storms selected as example for the three sectors used in the study: Joachim for the I, Andrea for the II and the storm 19, identified from the III, in the Brest - Land's End observation point and the two points nearshore, Etretat and Hautot-sur-Mer. Extracted from López Solano et al. (2024) 161

Table 21. Summary of characteristics of the 10 storms in the Reference point selected from June 2018 to September 2020 with the duration, the wave height $H_{s,max}$, the mean direction $\Theta_{Hs,peak}$, the occurrences of $H_{s,max}$ and $\Theta_{Hs,peak}$, and the standard deviation of $H_{s,storm}$ and Θ_{storm}. Extracted from López Solano et al. (2022) 186

Table 22. Forcings of significant wave height (Hs), peak period (Tp) and water level (WL) for the set-up of the numerical model of every 3-hour sea state of the 4 storms in Villers-sur-Mer 207

Table 23. Forcings of significant wave height (Hs), peak period (Tp) and water level (WL) for the set-up of the numerical model of every 3-hour sea state of the 4 storms in Hautot-sur-Mer 210

Table 24. Forcings of significant wave height (Hs), peak period (Tp) and water level (WL) for the set-up of the numerical model of every 3-hour sea state of the 4 storms in Etretat 213

Table 25. Results of Run-Up 2% (m) from the numerical simulations in P11 and P15 in Villers-sur-Mer and results obtained from the theoretical formulations of the EurOtop manual (EurOtop, 2018) and Stockdon et al. (2006). Scale of colors are conditioned by the results of the simulations of both profiles and for both formulations independently for each storm (with color scales corresponding to range of values) 217

Table 26. Results of RMSE (m) calculated with the Run-Up 2% from the numerical simulations in P11 and P15 in Villers-sur-Mer and results obtained from the theoretical formulations of the EurOtop manual (EurOtop, 2018) and Stockdon et al. (2006) 219

Table 27. Summary of characteristics of the 6 sea states of Villers-sur-Mer for which the validation of run-up 2% with timestacks obtained from VMS has been performed 222

Table 28. Summary of characteristics of the 6 sea states of Etretat for which the validation of overtopping (OT) with timestacks obtained from VMS has been performed 223

Table 29. Summary of characteristics of the 9 sea states of Hautot-sur-Mer for which the validation of overtopping (OT) with timestacks obtained from VMS has been performed 223

Table 30. Results of Run-Up 2% (m) from the numerical simulations for storm Ciara for all the profiles in Villers-sur-Mer. Scale of colors are conditioned by the results of the simulations on all the profiles 224

Table 31. Results of Run-Up 2% (m) from the numerical simulations for storm Joachim for all the profiles in Villers-sur-Mer. Scale of colors are conditioned by the results of the simulations on all the profiles 226

Table 32. Results of Run-Up 2% (m) from the numerical simulations for storm Andrea for all the profiles in Villers-sur-Mer. Scale of colors are conditioned by the results of the simulations on all the profiles 228

Table 33. Results of Run-Up 2% (m) from the numerical simulations for "Storm 19" for all the profiles in Villers-sur-Mer. Scale of colors are conditioned by the results of the simulations on all the profiles 230

Table 34. Results of Run-Up 2% (m) from the numerical simulations for storm Ciara for all the profiles in Hautot-sur-Mer. Scale of colors are conditioned by the results of the simulations on all the profiles 233

Table 35. Results of Run-Up 2% (m) from the numerical simulations for storm Joachim for all the profiles in Hautot-sur-Mer. Scale of colors are conditioned by the results of the simulations on all the profiles 235

Table 36. Results of Run-Up 2% (m) from the numerical simulations for storm Andrea for all the profiles in Hautot-sur-Mer. Scale of colors are conditioned by the results of the simulations on all the profiles 237

Table 37. Results of Run-Up 2% (m) from the numerical simulations for "Storm 19" for all the profiles in Hautot-sur-Mer. Scale of colors are conditioned by the results of the simulations on all the profiles 239

Table 38. Results of Run-Up 2% (m) from the numerical simulations for storm Ciara for all the profiles in Etretat. Scale of colors are conditioned by the results of the simulations on all the profiles 241

Table 39. Results of Run-Up 2% (m) from the numerical simulations for storm Joachim for all the profiles in Etretat. Scale of colors are conditioned by the results of the simulations on all the profiles 243

Table 40. Results of Run-Up 2% (m) from the numerical simulations for storm Andrea for all the profiles in Etretat. Scale of colors are conditioned by the results of the simulations on all the profiles 245

Table 41. Results of Run-Up 2% (m) from the numerical simulations for "Storm 19" for all the profiles in Etretat. Scale of colors are conditioned by the results of the simulations on all the profiles 247

Table 42. Extreme values of river discharge, storm surge and wave height obtained from the distribution functions adjusted to the extreme data of the three variables and associated with the return periods of 5, 10, 20, 50, 100 and 200 years. Extracted from López Solano et al. (2024) 270

Table 43. Results of the fitting of the GEV with the non-stationary parameters dependent the climate and time indexes for the spectral components of significant wave height and surge in Brest 326

Table 44. Results of the fitting of the GEV with the non-stationary parameters dependent the climate and time indexes for the spectral components of significant wave height and surge in Cherbourg 327

Table 45. Results of the fitting of the GEV with the non-stationary parameters dependent the climate and time indexes for the spectral components of significant wave height and surge in Weymouth 328

Table 46. Results of the fitting of the GEV with the non-stationary parameters dependent the climate and time indexes for the spectral components of significant wave height and surge in Newhaven 329
Table 47. Results of the fitting of the GEV with the non-stationary parameters dependent the climate and time indexes for the spectral components of significant wave height and surge in Dover 330
Table 48. Results of the fitting of the GEV with the non-stationary parameters dependent the climate and time indexes for the spectral components of significant wave height and surge in Dunkirk 331
Table 49. Results of the fitting of the copulas between spectral components of significant wave height and surge with the non-stationary time-dependent parameters in Brest with the 6 timescales 332
Table 50. Results of the fitting of the copulas between spectral components of significant wave height and surge with the non-stationary time-dependent parameters in Cherbourg with the 6 timescales 332
Table 51. Results of the fitting of the copulas between spectral components of significant wave height and surge with the non-stationary time-dependent parameters in Weymouth with the 6 timescales 332
Table 52. Results of the fitting of the copulas between spectral components of significant wave height and surge with the non-stationary time-dependent parameters in Newhaven with the 6 timescales 333
Table 53. Results of the fitting of the copulas between spectral components of significant wave height and surge with the non-stationary time-dependent parameters in Dover with the 6 timescales 333
Table 54. Results of the fitting of the copulas between spectral components of significant wave height and surge with the non-stationary time-dependent parameters in Dunkirk with the 6 timescales 333
Table 55. Statistics of the classes of the extreme events identified in the clustering in Brest 343
Table 56. Statistics of the classes of the extreme events identified in the clustering in Cherbourg 343
Table 57. Statistics of the classes of the extreme events identified in the clustering in Weymouth 344
Table 58. Statistics of the classes of the extreme events identified in the clustering in Le Havre 344
Table 59. Statistics of the classes of the extreme events identified in the clustering in Newhaven 344
Table 60. Statistics of the classes of the extreme events identified in the clustering in Dover 345
Table 61. Statistics of the classes of the extreme events identified in the clustering in Dunkirk 345
Table 62. Statistics of the classes of the extreme events identified in the clustering in Brest 349
Table 63. Statistics of the classes of the extreme events identified in the clustering in Cherbourg 349
Table 64. Statistics of the classes of the extreme events identified in the clustering in Weymouth 350
Table 65. Statistics of the classes of the extreme events identified in the clustering in Le Havre 350
Table 66. Statistics of the classes of the extreme events identified in the clustering in Newhaven 351
Table 67. Statistics of the classes of the extreme events identified in the clustering in Dover 351
Table 68. Statistics of the classes of the extreme events identified in the clustering in Dunkirk 351

LIST OF ABBREVIATIONS

Variables are presented in italic and abbreviations in capital letters.

A	Amplitude (m)
AIC	Akaike Information Criterion
ADP	Acoustic Doppler Current Profiler
AEP	Annual Exceedance Probability
AESN	Water Agency of Seine Normandy
AI	Artificial Intelligence
AMO	Atlantic Multidecadal Oscillation index
BOA	Beach Orientation Angle
BS	Beach Slope
BW	Beach Width
C	Copula
C	Chézy friction coefficient ($m^{1/2}/s$)
CDF	Cumulative Distribution Function
CDF	Computational Fluid Dynamics
CMEMS	E.U. Copernicus Marine Service Information
CNES	National Centre of Space Studies
CWT	Continuous Wavelet Transform
d_{50}	Sediment size (m)
DEM	Digital Elevation Model
DHYSED	Hydro-Sedimentary Dynamics
DTM	Digital Terrain Model
DYNECO	Dynamics of Coastal Ecosystems Department
E_{flux}	Energy flux (J/ms^2)
E_{storm}	Cumulated wave energy (W/m)
ECMWF	European Centre for Medium-Range Weather Forecasts
EDF	France Electricity Company
EMODnet	European Marine Observation and Data Network
EOF	Empirical Orthogonal Function
EVA	Extreme Value Analysis
EVT	Extreme Value Theory
f	Frequency (s^{-1})

f_p	Peak frequency (s^{-1})
$F_{X,Y}(x,y)$	Bivariate distribution
$F_X(x), F_Y(y)$	Margins of the distribution
FES	Finite Element Solution
g	Gravity acceleration (m^2/s)
GEV	Generalized Extreme Value
GMM	Gaussian Mixture Model
GP	Generalized Pareto
GS	Gulf Stream
H	Wave height (m)
h	Depth (m)
$H_s, H_{1/3}, H_{m0}$	Significant wave height (m)
H_b	Significant wave height at breaking (m)
IB	Inverse Barometer
IGW	Infragravity waves
IPCC	International Panel on Climate Change
IRSN	Radiological Protection and Nuclear Safety Institute
JONSWAP	Joint North Sea Wave Project
JRP	Joint Return Period (years)
k	Permeability (-)
k_n	Heterogeneous bottom roughness length-scale (m)
k_s	Equivalent geometrical roughness of Nikuradse (m)
L	Wavelength (m)
$L_{m-1,0}$	Wavelength in deep waters (m)
LAT	Lowest Astronomical Tide
m	Monthly maxima
M_t	Months of the year (1 to 12)
M2C	Coastal and Continental Morphodynamics
MARC	Modelling and Analysis for Coastal Research
MARS3D	Model for Applications at Regional Scales
MODWT	Maximum Overlap Discrete Wavelet Transform
MSL	Mean Sea Level (m)
MWL	Mean Water Level (m)
n	Manning coefficient ($s/m^{1/3}$)

NAO	North Atlantic Oscillation index
NASA	National Aeronautics and Space Administration
$NBIAS$	Normalized bias
NCAR	National Center for Atmospheric Research
NCEP	National Centers for Environmental Prediction
NLSW	Non-Linear Shallow Water equations
NHPP	Non-Homogeneous Poisson Process
NOAA	National Oceanic and Atmospheric Administration
NPP	Nuclear Power Plants
NS	Navier-Stokes equations
NWS	Near-surface Wind Speed
p	Porosity
p'_m	Initial porosity of sediment deposit
PC	Principal Component
PDF	Probability Density Function
POT	Peaks Over Threshold
R	Pearson's correlation coefficient
$R_{u2\%}$	2% wave run-up height (m)
RANS	Reynolds Averaged Navier-Stokes
$RMSE$	Root Mean Square Error
ROL	Observation Network of the Coast of Normandy and Hauts-de-France
$S(f,\theta)$	Directional spectrum
$S_f(f)$	Wave spectrum
S	Swash (m)
S_{inc}	Swash uprush related to incident waves (m)
S_{IG}	Additional uprush related to infragravity waves (m)
s_t	Season or sine covariate
SCENES	Coastal Station for the Observation and the Environment in the Seine Estuary
SHOM	Naval Hydrographic and Oceanographic Service of France
S	Skew surges (m)
SI	Scatter Index
SLA	Sea Level Anomaly
SLP	Sea Level Pressure (Pa)

SST	Sea Surface Temperature (K)
SWAN	Simulating WAves till Nearshore
SWASH	Simulating WAves till SHore
SWL	Still Water Level (m)
SWOT	Surface Water and Ocean Topography
t	Time covariate
T	Period / Wave period (s)
T_m, T_{m01}	Mean wave period (s)
$T_{m-1,0}$	Spectral wave period (s)
T_p	Peak period (s)
$\tan\alpha$	Slope of the beach
u_{10}	Wind speed eastward component at 10 m above surface (m/s)
UTM	Universal Transverse Mercator
v_{10}	Wind speed northward component at 10 m above surface (m/s)
VMS	Video Monitoring Systems
w	Width of the breaking zone (m)
$W_{direction}$	Wind direction (°)
W_{speed}	Wind speed (m/s)
WAM	WAve Modelling
WL	Water Level (m)
WMO	World Meteorological Organization
WRD	Wave Reanalysis Databases
WW3	WAVEWATCH III
XB-NH	XBeach Nonhydrostatic
XB-SB	XBeach Surfbeat
θ	Direction of propagation (°)
θ_m	Mean direction (°)
θ_p	Peak direction (°)
$\xi_{m-1,0}$	Breaker parameter, surf similarity parameter or Iribarren number
ξ	Shape parameter of the GEV
γ	Peak enhancement factor
γ_b	Breaking parameter
γ_b	Influence factor for a berm
γ_f	Influence factor for roughness elements on a slope

γ_β	Influence factor for oblique wave attack
ζ	Free surface elevation (m)
$< \eta >$	Setup of the surface of water due to the presence of waves (m)
τ	Kendall's parameter for the copulas
$\Lambda(\mathrm{x})$	Logistic transformation of the copulas
μ	Location parameter of the GEV
σ	Scale parameter of the GEV
ϱ	Sea water density (kg/m^3)

RESUME SUBSTANTIEL

Chapitre 1 : Introduction

Les zones côtières sont de plus en plus vulnérables aux risques liés au changement climatique, comme les inondations, l'érosion et la dégradation des écosystèmes (Vitousek et al., 2017, Ranasinghe & Stive, 2009, Ranjan et al., 2009, Schuerch et al., 2018). Les activités anthropiques et le réchauffement climatique ont déjà modifié les aléas climatiques, comme les houles ou le niveau de la mer, entraînant une augmentation de la fréquence des inondations maritimes et du recul du littoral, une tendance qui devrait se poursuivre (IPCC, 2022). Des plans efficaces de gestion côtière et d'adaptation sont cruciaux pour faire face à ces risques (Wong et al., 2014). Les inondations côtières, causées par l'élévation du niveau de la mer et intensifiées dans certaines zones par de la subsidence, restent l'une des catastrophes naturelles les plus destructrices (Muis et al., 2016, Karpytchev et al., 2018, Rahman et al., 2019, Letetrel et al., 2015). Une augmentation significative de la population vivant dans des zones côtières basses est attendue, ce qui renforce encore la nécessité de communautés côtières résilientes.

Les événements côtiers extrêmes, tels que les tempêtes, deviennent plus fréquents et destructeurs en raison du changement climatique (IPCC, 2022, Switzer et al., 2015). Ces événements provoquent des risques comme l'érosion et les inondations, surtout lorsque les surcotes se combinent avec les houles et la montée du niveau de la mer (Zscheischler et al., 2018, Arns et al., 2017, Church et al., 2013, Wahl et al., 2017). Comprendre et examiner ces dynamiques est crucial pour prédire et gérer les risques côtiers. La surveillance de l'hydrodynamisme côtier implique l'intégration de données multi-capteurs et de diverses approches de modélisation. Le *downscaling* numérique, des échelles régionales aux échelles locales, aide à simuler avec précision la propagation des houles et l'hydrodynamisme côtier, en particulier où les mesures directes sont indisponibles (Camus et al., 2011a, Hegermiller et al., 2017). Les modèles utilisés varient de modèles linéaires aux modèles non linéaires haute résolution tels que SWAN, XBeach et SWASH. Ces modèles sont essentiels pour l'évaluation des risques et les systèmes d'alerte précoce, car ils simulent avec une grande précision les caractéristiques et transformations des houles et des niveaux d'eau.

L'analyse des risques côtiers nécessite l'évaluation de leur probabilité et de leurs conséquences. La gestion des risques côtiers est vitale pour élaborer des stratégies d'adaptation afin de faire face aux menaces en évolution et d'intégrer des solutions durables en tenant compte des impacts du changement climatique et des facteurs socio-économiques. Les approches

stochastiques et numériques aident à déterminer la probabilité et les conséquences des risques en définissant les caractéristiques et les impacts des événements côtiers extrêmes, ce qui est crucial pour comprendre les hydrodynamiques côtières (Stewart & Melchers, 1997, Turki et al., 2023a). Comprendre les diverses conditions climatiques côtières devient essentiel à mesure que les inondations liées aux tempêtes extrêmes augmentent en raison du changement climatique (Liu et al., 2021).

Ce contexte introduit le projet de ce doctorat DYNSEEC (DYNamique multi-échelle des Evénements Extrêmes Côtiers), financé par l'IRSN, l'AESN et la Région Normandie. L'étude se concentre sur les hydrodynamiques de l'échelle régionale de la Manche à celle des côtes de Normandie en réponse aux événements de tempête extrême. Les recherches récentes utilisant des modèles numériques haute résolution ont amélioré la compréhension des dynamiques des tempêtes, des ondes de tempête et de l'érosion côtière dans la Manche (Anthony, 2013, Soloy et al., 2021, 2022, 2023).

Les côtes de Normandie, essentielles pour la faune, le tourisme, et sensibles à l'érosion et aux submersions, sont particulièrement vulnérables aux risques climatiques et anthropiques. L'étude vise à développer une vision intégrative des dangers côtiers en combinant des approches stochastiques et numériques à travers diverses échelles temporelles et spatiales, en mettant particulièrement l'accent sur les submersions dans des environnements complexes comme la Baie de Seine (Turki et al., 2019, 2023). Les résultats seront cruciaux pour une évaluation précise des risques côtiers et pour atténuer les impacts des événements d'inondation composés, avec une collaboration active des organisations publiques telles que l'AESN et l'IRSN.

Chapitre 2 : Compréhension scientifique de l’hydrodynamisme extrême en Manche et sur les côtes normandes

Ce chapitre décrit l'état de l'art ainsi que les sites d'étude.

Les houles sont caractérisées par leur hauteur, leur période et leur direction, qui se combinent pour former des houles irrégulières pouvant être analysées soit par analyse individuelle des houles, soit par analyse spectrale. Cette dernière implique le calcul de la répartition de l'énergie d'un nombre infini de houles composantes. Les houles de vent, irrégulières en hauteur et en période, peuvent se transformer en houles avec des périodes plus longues et des lignes de crête pendant leur propagation. Près de la côte, les houles subissent des processus de transformation sur les hauts-fonds, qui les déforment, ou la réfraction. Dans la zone de

déferlement, les houles perdent de la hauteur en raison du frottement avec le fond et finissent par se briser, entraînant des interactions complexes dans la zone de balancement où les houles rencontrent la côte. Les niveaux d'eau côtiers sont influencés par des facteurs astronomiques, météorologiques, océanographiques et tectoniques, avec les marées qui sont une composante principale. Les tempêtes peuvent élever significativement les niveaux d'eau par les surcotes. Le niveau de la mer total comprend le niveau moyen de la mer, le mouvement vertical local, les marées astronomiques et les surcotes résiduelles.

Comprendre les changements du niveau de la mer à différentes échelles temporelles est crucial pour l'évaluation des submersions. Les événements extrêmes, y compris les tempêtes côtières caractérisées par des vents forts, des houles importantes et des surcotes, augmentent en fréquence en raison du changement climatique. L'analyse des valeurs extrêmes et la modélisation numérique aident à prédire la récurrence et l'impact, les inondations côtières posant des risques importants. Les inondations côtières résultent d'une combinaison de facteurs, notamment les anomalies régionales du niveau de la mer, les marées, les surcotes et le déferlement des houles. Dans le contexte du changement climatique, les changements hydrodynamiques incluent les cycles saisonniers, les tendances à long terme et la variabilité stochastique dictée par les modèles climatiques globaux (Pasquini et al., 2008). Les recherches récentes se sont intensifiées sur les hydrodynamiques extrêmes, en se concentrant sur les modèles statistiques pour capturer la variabilité saisonnière et interannuelle (Lavers et al., 2010, Turki et al., 2019, 2020a, 2020b). L'examen de la relation entre la variabilité du niveau de la mer et les téléconnexions climatiques, telles que les oscillations atmosphériques, est devenu essentiel pour comprendre les impacts climatiques sur les processus hydrodynamiques (Dangendorf et al., 2012 ; Zampieri et al., 2017). Des études ont établi des corrélations entre les houles extrêmes et les modèles atmosphériques comme l'Oscillation Nord-Atlantique (NAO) et l'Oscillation Multi-décennale Atlantique (AMO). Ces modèles influencent la pression au niveau de la mer (SLP) et la température de la surface de la mer (SST), qui à leur tour affectent les extrêmes hydrodynamiques (Hurrell & Phillips, 2023, Trenberth & Zhang, 2023).

Cette recherche examine la Manche et les côtes de Normandie en intégrant les oscillations climatiques globales avec les facteurs hydrodynamiques régionaux et locaux. L'étude couvre l'échelle du climat global jusqu'aux caractéristiques côtières spécifiques de Normandie, influencées par l'océan Atlantique et la mer du Nord. La Manche présente une géomorphologie côtière complexe, caractérisée par des profondeurs variées et des impacts de tempêtes importants. Les eaux peu profondes de la Manche, allant de 100 mètres à l'ouest à moins de 30 mètres à l'est, présentent des modèles de houles dynamiques. Les houles venant de l'océan

Atlantique, principalement des secteurs SW-NW, peuvent atteindre des hauteurs de plus de 12 mètres mais diminuent généralement en taille et en hauteur en se déplaçant vers l'est. Les vents dans l'océan Atlantique et la mer du Nord influencent également les motifs de houles, avec des directions prédominantes est et NE-ESE.

Les régions côtières de Normandie, y compris l'estuaire de la Seine, sont très dynamiques et vulnérables aux changements climatiques et aux activités humaines. Ces zones, avec des morphologies de plages variées (de galets, de sable ou mixte) sont observées à l'aide de systèmes de surveillance vidéo (VMS) pour analyser l'hydrodynamisme et la morphodynamique. Les plages étudiées, Étretat, Hautot-sur-Mer et Villers-sur-Mer, présentent des caractéristiques distinctes : Étretat possède une plage de galets escarpée avec des falaises de craie, Hautot-sur-Mer a un profil mixte de galets et de sable avec des épis, et Villers-sur-Mer est une plage sableuse plate s'étendant significativement dans des eaux peu profondes. Ces conditions diverses contribuent à une dissipation variable de l'énergie des houles et à des niveaux de risque côtier différents.

Basée sur l'état de l'art, une série de questions de recherche ont été abordées pour enquêter sur l'hydrodynamisme de l'échelle de la Manche à l'échelle des côtes de Normandie en réponse aux événements extrêmes en combinant différentes approches stochastiques et numériques :

- Comment caractériser les connexions non stationnaires entre les oscillations climatiques globales et les hydrodynamiques extrêmes à plusieurs échelles temporelles dans la Manche ? Comment cette non-stationnarité est-elle prise en compte pour développer le redimensionnement stochastique et estimer les extrêmes ? Quelles sont les principales classes de tempêtes représentatives des hydrodynamiques extrêmes à plusieurs échelles temporelles dans la Manche au cours des dernières décennies ?

- Comment caractériser l'évolution hydrodynamique des tempêtes depuis la Manche vers les côtes de Normandie au cours des 40 dernières années, et dans quelle mesure la précision de la modélisation numérique pourrait-elle reproduire les hydrodynamiques extrêmes ? Quelles sont les principales transformations physiques des scénarios énergétiques extrêmes dans le bassin et près de la côte ? Comment la gravité des tempêtes extrêmes (ampleur, durée) contrôle-t-elle l'évolution des tempêtes dans la Manche ?

- En intégrant les échelles du bassin régional aux plages locales de Normandie, comment caractériser et modéliser les inondations côtières en réponse à des scénarios extrêmes à cette échelle proche du littoral ? Dans quelle mesure les modèles résolus dans le temps intégrant la sous-résolution de la profondeur peuvent-ils être précis pour reproduire l'étendue des eaux

inondées ? Comment les inondations côtières varient-elles dans différents contextes côtiers normands, des plages sableuses aux plages mixtes et aux plages de galets ?

- Quelles sont les applications côtières hydro-macrodynamiques potentielles qui pourraient être développées en explorant les différentes découvertes de cette recherche thésarde ?

Chapitre 3 : Sur l'utilisation d'approches stochastiques pour l'étude de la dynamique multi-échelle des tempêtes extrêmes en Manche

Ce chapitre examine les facteurs stochastiques influençant l'hydrodynamique maritime, en mettant l'accent sur les variations de la hauteur des houles et du niveau de la mer. La hauteur significative des houlesH_s est centrale dans l'analyse des événements extrêmes, dérivée soit statistiquement comme la moyenne du tiers supérieur des hauteurs de houles, soit spectralement à partir du spectre des houles. La période est généralement mesurée comme la période de pic T_p, représentant la période avec le plus d'énergie. Les variations du niveau de la mer comprennent la marée astronomique prévisible, paramétrée par jusqu'à 37 constituants harmoniques, et la surcote de tempête S, qui est l'élévation anormale au-dessus de la marée prévue. Pour l'analyse des valeurs extrêmes, l'étude se concentre sur la hauteur significative des houles et la surcote de tempête. Les données historiques de surcote provenant des marégraphes à travers la Manche, y compris des sites français comme Brest et Le Havre et des sites anglais tels que Weymouth et Dover, ainsi que les données de hauteur des houles du service marin Copernicus sont utilisées.

L'analyse spectrale utilise des techniques de haute résolution telles que l'analyse par ondelettes multi-résolutions pour décomposer et examiner ces variables à travers différentes échelles temporelles. En suivant les méthodologies établies par Turki et al. (2019, 2020a, 2020b, 2023), les transformations continues par ondelettes (CWT) de S et H_s sont calculées pour cartographier la distribution de l'énergie à travers les échelles temporelles. Une analyse de l'ondelette discrète à chevauchement maximum (MODWT) a ensuite décomposé ces signaux en composants spectraux allant des échelles inter-mensuelles aux échelles inter-décennales. Cette analyse a montré que S est principalement influencée par les cycles inter-mensuels (~3 à ~6 mois) et annuels (~14-20% de variance), avec une variabilité significative des valeurs de surcote due aux tendances de niveau de la mer à long terme et aux interactions marée-surcote. Pour H_s, l'analyse a identifié des motifs annuels (~40%-65%) et semi-annuels (~30%-50%). La variabilité

annuelle est liée aux interactions océan-atmosphère, H_s culminant généralement en hiver et déclinant en été. Les effets locaux du vent ont également un impact sur H_s. L'analyse des composantes spectrales souligne que les extrêmes de S et H_s présentent de fortes corrélations avec les oscillations climatiques. Pour les échelles semi-annuelles et annuelles, la SST et la SLP sont significatives, ainsi que le NAO et l'AMO jouent un rôle plus prononcé aux échelles interannuelles. La recherche révèle que l'AMO affecte notablement la variabilité à des échelles plus grandes que ~6 ans.

L'analyse probabiliste qui suit vise à évaluer les séries chronologiques des maxima mensuels pour H_s et S à différents endroits en utilisant une approche bivariée non stationnaire. L'analyse utilise les fonctions de distribution des valeurs extrêmes généralisées (GEV) combinées avec des copules pour modéliser les valeurs extrêmes, en ajustant pour la non-stationnarité avec des indices climatiques et temporels. Cette méthodologie implique l'ajustement des distributions GEV et des copules aux données, en incorporant des variables telles que la SST de la mer, la SLP, les indices NAO et l'AMO, ainsi que des covariables temporelles linéaires et quadratiques. Les paramètres du modèle GEV sont calculés en fonction de ces covariables, et une gamme de copules bivariées (Clayton, Gumbel, Frank, Joe et Gaussienne) est testée pour déterminer le meilleur ajustement pour la distribution conjointe de H_s et S. L'étude révèle que la copule de Frank fournit le meilleur ajustement pour les sites, bien que les copules dynamiques soient préférables pour la plupart des sites, indiquant des niveaux de risque variables pour les événements extrêmes composés. Les résultats montrent que pour la plupart des sites, H_s dépend fortement de la SST et de la SLP, et souvent des indices NAO, ainsi que les dépendances de S sont plus variables. Les niveaux de retour effectifs sont calculés, démontrant que les niveaux de retour à haute densité pour les événements extrêmes sont plus probables dans la partie centrale de la courbe et diminuent pour les queues extrêmes, reflétant la dépendance décroissante capturée par la copule de Frank.

Cette étude étend l'analyse des extrêmes de H_s et S en appliquant des méthodologies au-delà des analyses stochastiques et spectrales des maxima mensuels. Au lieu de cela, elle explore les événements extrêmes en utilisant des critères de persistance et d'intensité, en incorporant des caractéristiques des houles comme T_p et la direction moyenne θ_m. La définition d'un événement extrême implique à la fois la durée et l'intensité des tempêtes, en utilisant une approche par seuil où H_s et S doivent dépasser une valeur spécifique pendant au moins 24 heures. Les méthodes récentes de Mendoza et al. (2006, 2011, 2013) et des études ultérieures (Molina et al., 2019; Soloy et al., 2024) définissent une tempête marine sur la base de ces critères. Les événements extrêmes sont caractérisés par leur durée, leur H_s de pic, et les caractéristiques

associées T_p et θ_m. Pour S, des seuils et critères similaires sont appliqués, mais la durée des surcotes dépasse souvent celle des tempêtes de hauteur de houles. Les données de H_s et S révèlent des nombres variés de tempêtes par an, avec Brest, Cherbourg, Weymouth, Le Havre, Newhaven, Douvres et Dunkerque montrant chacun des modèles uniques de fréquence et d'intensité des tempêtes. Notamment, Cherbourg, Newhaven et Douvres connaissent les énergies de tempête les plus élevées. L'énergie des houles cumulée fournit une mesure complète de la sévérité des tempêtes, mettant en évidence Cherbourg et Newhaven comme des sites avec les valeurs d'énergie de tempête les plus élevées. L'analyse des événements extrêmes identifie également des tempêtes significatives, telles que la tempête Ciara en février 2020, qui a touché plusieurs sites.

Un processus de classification et de *clustering* des données sur les tempêtes est ensuite appliqué pour comprendre les événements extrêmes de houles et de surcotes. Initialement, les mesures des marégraphes sont alignées avec les données de houles de réanalyse pour garantir la cohérence entre les différentes stations, les données étant normalisées à un intervalle de 3 heures. Les événements de tempête sont catégorisés en quatre classes : Classe 0 pour l'absence d'occurrence, Classe 1 pour les événements extrêmes de houles individuels, Classe 2 pour les événements extrêmes de surcote individuels, et Classe 3 pour les événements extrêmes simultanés de houles et de surcote. Un modèle de réseau neuronal à deux couches est utilisé pour la classification. Le modèle prédit les types d'événements de tempête en fonction des variations de la hauteur des houles et des données de surcote, avec des résultats visualisés pour montrer la distribution des événements et les probabilités de classe pour différents endroits.

Une analyse supplémentaire considère les probabilités de distribution gaussienne pour le *clustering* des données sur les tempêtes en groupes distincts basés sur la similarité, déterminant également le nombre optimal de clusters. Les résultats du regroupement révèlent que les tempêtes les plus fortes sont catégorisées dans des classes d'énergie plus élevées, avec des distributions variées à travers les sites. L'étude compare les fréquences des tempêtes à travers les différentes classes, notant que les classes plus faibles ont souvent des probabilités plus élevées que prévu. Enfin, les périodes de retour pour les classes de tempêtes sont calculées, montrant des similitudes entre les sites voisins malgré des structures de classes différentes. Dans l'ensemble, cette analyse approfondie fournit des informations sur les caractéristiques et les distributions des événements de tempête extrêmes à plusieurs endroits dans la Manche.

Chapitre 4 : Cadre de la modélisation intégrée pour la surveillance des évènements extrêmes de la Manche aux côtes normandes.

Dans ce chapitre, l'objectif principal est d'utiliser diverses bases de données pour réaliser une modélisation numérique et valider les résultats. Les ensembles de données clés comprennent la réanalyse NWSHELF de Copernicus, qui fournit des paramètres de houles depuis janvier 1980, les données de marées astronomiques provenant de la base de données FES2014, offrant des élévations des marées pour de nombreux constituants de marée, et les données de vent et de pression atmosphérique, issues de l'ensemble de données ERA5, qui inclut les composants du vent à 10 m et la pression de surface. La bathymétrie est obtenue à partir du *EMODnet Bathymetry Portal*. La précision du modèle est évaluée à l'aide du RMSE et du coefficient de corrélation de Pearson, tandis que la validation des houles implique des données provenant de bouées, et le niveau de la mer est validé par rapport aux mesures des marégraphes situés en Angleterre et en France, notamment en Normandie. La suite logicielle Delft3D est utilisée pour les simulations, avec un modèle hydrodynamique bidimensionnel fonctionnant sur une grille curvilinéaire variant de 4 km en eaux profondes à 1200 m près de la côte. Un calibrage est nécessaire pour remédier aux surestimations de la hauteur des houles dues à une transmission excessive de l'énergie éolienne, surtout pour les houles plus petites.

L'étude simule 40 ans de données (1983-2022), en évaluant les événements de tempête en définissant des seuils pour la hauteur des houles et leur durée. Les résultats sont analysés à divers points le long de la Manche, montrant que le calibrage a amélioré la précision, en particulier pour les événements de houles extrêmes. Les comparaisons révèlent un RMSE allant de 32 à 50 cm, attribué aux limitations de la résolution spatiale du modèle. Les coefficients de corrélation sont élevés, reflétant une bonne concordance entre les simulations et les mesures. L'étude classe 262 événements de tempête, détaillant leur évolution des échelles régionales aux échelles locales. Les tempêtes sont catégorisées selon leur origine, celles venant de la mer du Nord étant relativement rares et moins impactantes comparées aux tempêtes plus fréquentes et intenses venant de l'océan Atlantique. Ensuite, l'impact de ces tempêtes énergétiques sur les côtes normandes est évalué. La propagation et la modulation des tempêtes à travers le bassin de la Manche sont étudiées, notant des variations significatives de la hauteur des houles et de la durée à mesure que les tempêtes se rapprochent de la côte. Par exemple, les tempêtes venant de l'Atlantique montrent des densités d'énergie et des hauteurs de houles variables selon leur secteur d'origine et leur propagation. Les tempêtes sont suivies depuis leur origine à travers le bassin jusqu'aux zones côtières, montrant comment les hauteurs de houles et l'énergie se

dissipent. Les cartes de contours et les analyses des séries temporelles illustrent l'interaction complexe des tempêtes avec la géométrie de la Manche et la topographie côtière, affectant le comportement des houles et la répartition de l'énergie.

Dans l'ensemble, la recherche souligne l'importance des simulations détaillées et du suivi des tempêtes pour comprendre et gérer les impacts côtiers. Les résultats sont en accord avec la littérature existante, validant la précision du modèle pour l'analyse des tempêtes et les recherches futures. Les tempêtes ont été définies en fonction de la hauteur des houles, de la durée et de l'énergie, en utilisant des seuils et des approches statistiques adaptées aux impacts côtiers. Par rapport à d'autres études, cette recherche identifie un nombre similaire de tempêtes annuelles mais adapte les méthodes aux conditions locales. Cette étude approfondie offre des aperçus cruciaux sur la dynamique des tempêtes et les risques d'inondation côtière, soulignant la nécessité de poursuivre les recherches sur la variabilité hydrodynamique à long terme et les impacts climatiques.

Pour analyser les transformations des houles à une échelle plus locale, la propagation et l'évolution des houles sont simulées à l'aide du modèle SWAN, qui prend en compte la transformation des houles, la dissipation d'énergie et les processus non linéaires. Les simulations utilisent des grilles grossières et imbriquées pour garantir la précision, la dernière fournissant des données de haute résolution près de la côte. Les données sont validées en utilisant les mesures des houles de deux bouées : la bouée SCENES à l'estuaire de la Seine et une autre près de Hautot-sur-Mer, fournissant toutes deux des données H_s. Les résultats indiquent une haute précision dans la reproduction des houles, avec des coefficients de corrélation supérieurs à 90 %. Une méthode *Peak Over Threshold* (POT) identifie les événements de houles extrêmes à partir d'une série temporelle de 26 mois. Ces événements sont analysés en fonction de leurs caractéristiques telles que la magnitude et la direction des houles, avec dix tempêtes notables sélectionnées pour une étude détaillée.

Les caractéristiques des houles sont analysées des eaux profondes aux zones côtières, mettant en évidence une diminution de H_s à mesure que les houles passent des eaux profondes aux eaux peu profondes. Les *swells* dominantes diminuent de 10 m dans l'océan Atlantique à 5 m dans la mer du Nord, et se réduisent encore à 3-4 m près de la côte. θ_m change également en raison de la réfraction et de la dissipation d'énergie, avec des variations notables à Hautot-sur-Mer et Etretat influencées par les caractéristiques bathymétriques et la géométrie côtière. La recherche révèle que les tempêtes en hiver-printemps ont un impact plus fort comparé à celles en été-automne. Des tempêtes spécifiques comme Deirdre et Ciara montrent des pics H_s élevés

et des occurrences associées, soulignant leur potentiel de danger. La dissipation d'énergie est plus prononcée à Etretat en raison de sa configuration côtière, tandis que Hautot-sur-Mer subit des changements plus importants dans le gradient des houles. Cette recherche souligne l'importance de la morphologie côtière dans le comportement des houles et la dissipation d'énergie.

Chapitre 5 : Evaluation des impacts des tempêtes extrêmes sur les côtes de Normandie.

Ce chapitre décrit l'approche de modélisation numérique utilisée pour les trois sites d'étude, en employant le modèle SWASH pour simuler la dynamique des houles de tempête. SWASH, un modèle de flux d'ondes non hydrostatique, prédit la transformation des houles depuis le large jusqu'à la plage, en intégrant des phénomènes tels que la propagation des houles, la réfraction et la diffraction. Les simulations utilisent des données issues d'une base de données précédemment générée, en se concentrant sur les événements de tempête, notamment la Tempête Ciara, choisie pour son intensité. Le modèle fonctionne par intervalles de 3 heures en raison des contraintes de sortie du jeu de données de la Manche, chaque tempête étant simulée sur trois jours pour générer 25 simulations par tempête à chaque site. H_s et T_p sont utilisés comme entrées, avec un niveau d'eau constant fixé au maximum enregistré pendant chaque période de 3 heures pour simuler les pires scénarios. Afin de remédier aux écarts d'amplitude de marée dans le jeu de données de la Manche, les données de la bouée SCENES sont utilisées pour la calibration, en appliquant des facteurs d'amplification pour corriger les amplitudes de marée, garantissant des niveaux d'eau précis pour la simulation. Les configurations du modèle pour Villers-sur-Mer, Hautot-sur-Mer et Etretat impliquent la définition des profils de plage et de bathymétrie basés sur des données LiDAR à haute résolution. Pour chaque site, les profils sont simulés en incluant des couches pour la porosité des sédiments et la taille des grains pour les deux derniers sites. Les simulations génèrent des paramètres de houles, y compris la hauteur de déferlement $R_{u2\%}$, cruciale pour comprendre les impacts côtiers lors des tempêtes.

La validation des simulations pour $R_{u2\%}$ et le niveau d'eau se fait à travers trois aspects principaux. Le premier aspect implique la validation des entrées utilisées dans les simulations SWASH en les comparant aux mesures des bouées dans la zone d'étude, y compris la bouée SCENES et la bouée de la campagne de Penly. Pour l'événement extrême de la Tempête Ciara, la comparaison montre un bon accord, indiquant que les entrées de simulation sont correctement

représentées. La seconde validation compare les résultats de simulation de $R_{u2\%}$ de SWASH avec les formulations théoriques du Manuel EurOtop et de Stockdon et al. (2006). L'ERME moyen pour la Tempête Ciara est de 0,213 m et 0,277 m pour les formulations EurOtop et Stockdon, respectivement, avec des résultats similaires pour d'autres tempêtes. Les plus grandes disparités se produisent lorsque les niveaux d'eau diffèrent du niveau moyen de la mer, bien qu'un bon accord soit généralement observé lorsque les pentes sont cohérentes.

La validation finale utilise des systèmes de surveillance vidéo (VMS) pour comparer les résultats de simulation avec les données réelles de déferlement des houles. Pour Villers-sur-Mer, où des données VMS étaient disponibles pour la tempête Ciara, une bonne correspondance est trouvée avec seulement des différences mineures (jusqu'à 5 cm). Pour Etretat et Hautot-sur-Mer, où la présence de murs verticaux en bout de plage complique la comparaison directe, la validation se concentre sur les événements de dépassement. Les résultats sont généralement satisfaisants mais mettent en évidence des limitations telles que la porosité des sédiments et les changements morphodynamiques affectant la précision du modèle. Globalement, bien que le processus de validation montre des résultats prometteurs, il souligne également les limitations et incertitudes qui doivent être abordées dans les futures améliorations du modèle.

L'étude analyse les statistiques de $R_{u2\%}$ pour quatre grandes tempêtes à travers trois sites côtiers : chaque site ayant des caractéristiques distinctes qui influencent la manière dont les houles de tempête se transforment en déferlement sur les profils de plage. À Villers-sur-Mer, les résultats montrent que le niveau d'eau a un impact plus significatif sur $R_{u2\%}$ que la hauteur significative des houles H_s. Pour la tempête Ciara, le déferlement le plus élevé est associé au niveau d'eau de pointe combiné avec une H_s élevée, avec des valeurs dépassant 1,65 m sur certains profils. La tempête Andrea produit les valeurs de déferlement les plus élevées, jusqu'à 1,7 m, en particulier lorsque les H_s et les niveaux d'eau sont élevés. À Hautot-sur-Mer, deux principaux types de plages, entre les digues et sur les côtés de la plage, montrent des comportements différents. Pour la tempête Ciara, le déferlement est plus élevé sur les profils des côtés de plage comparés à ceux entre les digues, en raison des barrières naturelles créées par les digues. Des schémas similaires sont observés pour la tempête Joachim. La tempête Andrea a souligné une forte corrélation entre $R_{u2\%}$ et H_s, les profils entre les digues montrant un déferlement plus bas en raison de niveaux d'eau plus élevés. À Etretat, les résultats démontrent que $R_{u2\%}$ est plus étroitement aligné avec les tendances du niveau d'eau, notamment pour la tempête Ciara. Les tempêtes Joachim et Andrea montrent également que les valeurs plus élevées de $R_{u2\%}$ ont été influencées par H_s et les niveaux d'eau, avec des variations significatives entre les profils.

Dans l'ensemble, l'étude conclut que bien que des valeurs élevées de H_s et des niveaux d'eau conduisent généralement à un déferlement plus élevé, les caractéristiques locales de la plage et les facteurs spécifiques à la tempête jouent un rôle critique dans la détermination de l'impact du déferlement. À Villers-sur-Mer, une plage de sable, $R_{u2\%}$ varie modérément avec les changements de niveau d'eau, tandis que Hautot-sur-Mer et Etretat, avec des plages de gravier, présentent une relation inverse claire : $R_{u2\%}$ augmente à mesure que les niveaux d'eau diminuent. La Tempête Andrea dévie de ce modèle, avec $R_{u2\%}$ s'alignant plus étroitement avec H_s en raison d'une plage plus petite de niveaux d'eau par rapport aux autres tempêtes. Les faibles valeurs de H_s et de la période de pointe T_p dans certains états de la mer entraînent un $R_{u2\%}$ minimal. Les différences dans les profils de plage et la bathymétrie contribuent à des valeurs variables de $R_{u2\%}$ entre les sites, Etretat connaissant les valeurs les plus élevées en raison de son inclinaison abrupte et de son exposition. Les défis de la modélisation numérique pour simuler les plages de gravier et l'importance d'une paramétrisation précise sont soulignés.

Chapitre 6 : Applications à l'évaluation des risques côtiers : de la submersion à l'érosion des plages.

Ce chapitre examine les applications pratiques des méthodologies et des bases de données développées dans les chapitres précédents, en reliant les études hydrodynamiques aux morphodynamiques des plages dans des scénarios extrêmes.

L'application initiale intègre une approche stochastique non stationnaire pour identifier les scénarios extrêmes de houles et de niveaux marins avec une base de données numérique de la Manche, et étudie l'hydrodynamique de l'estuaire de la Seine en Normandie. L'estuaire, qui s'étend sur 170 kilomètres, se caractérise par des niveaux d'énergie fluviale et marémotrice variables, avec un débit moyen de la rivière de 435 m^3/s, atteignant plus de 1000 m^3/s lors des crues. Pour modéliser ce système, une approche numérique complète utilisant le logiciel Delft3D est employée. L'étude utilise la base de données simulée à l'échelle de la Manche comme un modèle de grille grossière pour des simulations à grande échelle et superpose une grille détaillée pour l'embouchure de l'estuaire de la Seine. Le modèle détaillé se concentre sur les processus d'inondation causés par les effets combinés du niveau marin et du débit fluvial. L'analyse des valeurs extrêmes est appliquée à la surcote, à la hauteur des houles et au débit fluvial pour évaluer les risques d'inondation. L'analyse considère à la fois la magnitude et les périodes de retour de ces variables. Les simulations intègrent 40 ans de données et évaluent 72 scénarios,

combinant différentes périodes de retour du débit fluvial avec des variables maritimes pour comprendre les risques d'inondation dans diverses conditions. L'approche suppose une indépendance entre la surcote et le débit fluvial, en accord avec les résultats des recherches précédentes.

Deux zones témoins sont choisies pour analyser la sensibilité aux inondations : une plaine inondable intertidale vulnérable au nord de la Seine, et une région côtière au sud de Villerville. Pour les 72 cas simulés, des courbes de danger sont dérivées pour diverses périodes de retour (5, 10, 20, 50, 100 et 200 ans) afin d'évaluer la profondeur maximale des inondations causées par la surcote et le débit fluvial. L'analyse indique que la profondeur maximale des inondations est directement proportionnelle aux valeurs extrêmes de la surcote et du débit fluvial. Des hauteurs de houles plus élevées entraînent des profondeurs d'inondation plus importantes par rapport aux scénarios avec des hauteurs de houles plus faibles. Plus précisément, les profondeurs maximales sont jusqu'à 50 cm plus élevées avec des hauteurs de houles plus élevées pour des niveaux de retour plus élevés. L'impact de la surcote est plus important que celui du débit fluvial, surtout dans les zones côtières plus exposées. Le scénario de pire cas combine une période de retour de 200 ans pour la hauteur des houles et le débit fluvial, atteignant près de 4,8 m de profondeur maximale. En revanche, les inondations dans la seconde zone sont moins influencées par le débit fluvial, ce qui est en accord avec les résultats des zones côtières et souligne le rôle principal de la surcote dans les événements de submersion côtière.

Les applications suivantes se concentrent sur la morphodynamique des plages de galets dans des conditions extrêmes. La première examine les changements morphologiques à Etretat et à Hautot-sur-Mer en utilisant les données de la ligne de rivage, révélant les mécanismes clés du changement de la ligne de rivage et l'influence des structures de digues. L'étude finale combine les données côtières avec les VMS pour simuler les tempêtes avec XBeach-G, mettant en évidence comment la perméabilité de la plage affecte l'érosion et la formation de bermes, et soulignant la nature dynamique des plages de galets dans la dissipation de l'énergie des houles.

Chapitre 7 : Conclusions

La recherche de cette thèse examine les dynamiques des événements extrêmes dans les systèmes côtiers, en se concentrant sur la Normandie des échelles régionales à locales et en intégrant les mécanismes climatiques dans l'étude des hydrodynamiques extrêmes. Elle combine de manière innovante des méthodologies stochastiques et numériques pour examiner

les dynamiques de la hauteur des houles et de la surcote, ainsi que leur impact sur le littoral de Normandie.

La recherche aborde les complexités côtières influencées par diverses forçages tels que les houles, les marées, les surcotes et les débits fluviaux. Elle met en évidence l'intégration des différentes échelles temporelles et spatiales, des événements individuels aux impacts plus larges du changement climatique. Le premier ensemble de questions explore les connexions non stationnaires entre les oscillations climatiques mondiales et les hydrodynamiques extrêmes, en utilisant des analyses spectrales et probabilistes pour identifier et caractériser les événements extrêmes dans la Manche. Cela inclut l'évaluation de l'influence des motifs atmosphériques et le développement de niveaux de retour conjoints pour les houles et les surcotes. L'approche stochastique définit également les événements extrêmes par leur durée et leur énergie, en regroupant les tempêtes pour identifier les scénarios hydroclimatiques typiques.

Le second ensemble de questions s'étend aux échelles régionales, en modélisant la dynamique des tempêtes de la Manche à la Normandie. Les simulations numériques sur 40 ans, intégrant des composants de marée harmonique, des paramètres de houles et des données atmosphériques, révèlent que l'océan Atlantique est la principale source d'événements extrêmes, avec des impacts variables en fonction de la direction des tempêtes. L'analyse locale des tempêtes près d'Etretat et de Hautot-sur-Mer montre que les tempêtes se propageant longitudinalement à travers la Manche ont des impacts plus significatifs en raison d'une diffraction minimale et d'une approche perpendiculaire des houles.

Les recherches modélisent également les inondations côtières en réponse à des scénarios extrêmes, en se concentrant sur les morphologies de plage variables en Normandie. L'étude évalue les impacts des inondations sur les plages de gravier et les plages de sable, en utilisant à la fois des simulations numériques et des données VMS. Les résultats indiquent que les plages de gravier dissipent efficacement l'énergie des houles, réduisant le risque d'inondation, tandis que les plages de sable subissent un impact moins significatif en raison de la dissipation de l'énergie des houles.

En fusionnant des approches stochastiques et numériques, l'étude modélise les conditions côtières et fluviales extrêmes dans l'estuaire de la Seine. Les résultats montrent que la surcote a un impact plus substantiel sur les inondations composées que le débit fluvial, particulièrement dans les zones proches de la mer. Les résultats soulignent également l'importance d'incorporer les morphodynamiques dans la gestion côtière et les applications potentielles pour d'autres études.

Dans l'ensemble, la recherche de thèse offre des perspectives précieuses pour les gestionnaires côtiers et les parties prenantes, abordant les questions sociétales et environnementales liées aux événements côtiers extrêmes et à leurs impacts.

Les recherches en cours traitent de la vulnérabilité des systèmes côtiers et estuariens face aux événements extrêmes tels que les tempêtes et les crues fluviales, en se concentrant sur l'intégration des approches multi-capteurs, numériques et physiques. L'intégration des techniques d'apprentissage profond vise à améliorer le couplage entre les modèles numériques et les ensembles de données de télédétection, y compris l'assimilation des données. Les données sur les niveaux d'eau de la mission SWOT seront utilisées pour améliorer la couverture des processus côtiers et estuariens et assimiler les niveaux d'eau dans les modèles hydrodynamiques.

Les défis scientifiques incluent la variabilité du niveau de la mer près du rivage, l'incorporation de la compréhension des interactions non linéaires entre houles, marées et surcotes, l'impact des forçages atmosphériques et des propriétés du plateau continental sur le niveau de la mer ; les changements côtiers et les processus de houles, combinant l'étude des effets des houles à haute fréquence sur les inondations et la variabilité du niveau de la mer, avec un accent sur la déformation des marées et le ruissellement fluvial, soutenu par des expériences en laboratoire pour la validation des modèles ; et la réponse hydro-morphodynamique, évaluant l'impact des événements extrêmes sur les systèmes côtiers, y compris la montée des houles, le débordement et les seiches, pour évaluer la vulnérabilité côtière.

CHAPTER 1

INTRODUCTION

1.1. GENERAL CONTEXT

Nowadays and with the global context of climate change, coastal zones suffer from severe risks at the global scale which is driven by increased exposure of ecosystems and population to coastal hazards, including coastal flooding (Vitousek et al., 2017), erosion (Ranasinghe & Stive, 2009), saltwater intrusion (Ranjan et al., 2009) and ecosystem deterioration (Schuerch et al., 2018). Nearly 70% of beaches may completely erode by 2100 (Vitousek et al., 2017)

Anthropogenic activities and human-induced global warming have already caused observed changes in climate drivers, including waves and water levels, leading to increases in marine flooding and shoreline retreat, and future climate change is expected to increase the magnitude and frequency of these events (IPCC, 2023). Combined with increasing socio-economic pressure in the coastal zone, understanding the behavior and predicting the evolution of coastal environments is essential for the development of suitable management and reliable adaptation plans (Wong et al., 2014). Public policymakers now actively seek the input of the scientific community to assist in providing simple, efficient, and robust tools to project future shoreline changes, which reinforces the need to continue developing and improving empirical shoreline change models.

Coastal flooding, one of the most destructive natural catastrophes, is the result of the combined effects of demographic growth and economic development of coastal zones with the ongoing sea level rise (Muis et al., 2016). This risk can be locally aggravated by land subsidence in some regions such as the Ganges-Brahmaputra Delta in Bangladesh (Karpytchev et al., 2018, Rahman et al., 2019) or along the Mississippi Delta in the Gulf of Mexico (Letetrel et al., 2015). To assess future population changes in low-lying coastal zones, Neumann et al. (2015) conducted a global analysis combining socio-economic and sea level rise scenarios. These authors suggested that the number of people living in low-lying coastal zones in 2000 (~625 million) will increase by 50% by 2030 and will double by 2060, which stresses the need to improve future coastal communities' resilience in response to extreme events.

Extreme events, from a climatic perspective, are the most intense and severe scenarios possible in a given location, sustained by strong conditions over an extended period. Coastal storms, a significant type of extreme event, influenced by atmospheric and oceanic circulations, pose significant challenges in their definition and prediction (Harley, 2017). These dynamic events encompass a spectrum from tropical storms to hurricanes, impacting coastal environments globally through erosion, infrastructure damage, and flooding (Jiménez et al., 2012, Rouhaud & Vanderlinden, 2022). Coastal storms feature characteristics like strong winds, large waves, and

storm surges. With climate change and increased coastal human activities, these impacts are expected to worsen (IPCC, 2022, Switzer et al., 2015), becoming more common and destructive, and presenting significant challenges, necessitating adaptive coastal measures.

These events can cause hazards in coastal systems, where key risks include severe structural damage, coastal erosion, overtopping, and coastal flooding. Overtopping affects breakwaters and vertical walls, flooding impacts low-lying environments and heavily structured coastal areas, and coastal erosion concerns beaches. The combination of extreme storm surges and waves, closely linked to complex interactions between atmospheric, fluvial, and oceanographic phenomena that magnify their impacts (Zscheischler et al., 2018), can exacerbate inland flooding, including estuaries and deltas, especially with rising sea levels contributing to more frequent and intense coastal erosion and inundation events over recent decades (Arns et al., 2017, Church et al., 2013, IPCC, 2022, Wahl et al., 2017). These climate patterns and indexes are crucial for studying extreme coastal events, providing a framework for understanding and predicting the behavior of waves and surges. They increase flood extent, depth, and duration, posing significant social, economic, and infrastructural challenges (Leonard et al., 2014, Zscheischler et al., 2018).

Monitoring coastal hydrodynamics requires accurate and efficient datasets integrating several multi-sensor sources (in-situ measurements, altimetry, ...) and different approaches (numerical modelling, stochastic methods,...) with extensive historical data and expanding technical and scientific efforts, which is crucial for wide variety of applications such as evaluating and managing coastal risks, and designing and maintaining coastal and offshore structures, as well as marine renewable energy devices.

The use of this expanded technology and the combination of the different approaches to investigate nearshore and coastal hydrodynamics should be explored for integrating the time- and spatial- scales, from the scale of the storm to the scale of climate oscillations and from regional to local scales. The connection of the local and regional hydrodynamics with the global climate mechanisms (the so-called downscaling) should be considered to enhance our understanding of the multi-timescale evolution of the physical processes, induced by the meteorological forcing, including during storms. This downscaling has been developed in previous works using statistical combined with spectral approaches, and has proven to be the one of the most accurate ways for predicting the hydrodynamic scenarios (Camus, et al., 2011a, 2014, Hegermiller et al., 2017, Ricondo et al., 2024) in response to extreme energy conditions and the induced coastal flooding

as well as compound flooding in coastal environments controlled by fluvial discharges (Turki et al., 2023)

The numerical downscaling from regional to local scales has been developed in several works for different coastal systems (Antolínez et al., 2019, Camus et al., 2011b). In the last decades, several numerical models for waves and flows have been developed for improving the knowledge of hydrodynamics from deep to shallow waters, especially at locations where instrumental data are not available. The numerical downscaling is considered as a dynamical approach where the wave directional spectra are propagated from deep ocean to shallow water by nesting a wave model for coastal areas used for the wave transformation in the nearshore. Regarding the wave propagation, the used models can be classified into different families ranging from linear models based on the Mild Slope Equation, frequently used in coastal and port engineering applications, to Computational Fluid Dynamics (CDF) models that resolve the Reynolds Averaged Navier-Stokes (RANS) equations for simulating local scale processes (several spatial wavelengths and temporal scales from minutes to hours). The linear models were used in wave engineering because of the computational costs associated with studying wave propagation in large scale domains with non-linear propagation models. The growing interest in providing more physical information related to the nearshore waves was the main reason behind the development of the non-linear models representing more accurately wave propagation at spatial and temporal scales. The spatial and the temporal scales of interest in the coastal zone suggest the use of phase-resolving models, opposed to phase-averaging models, those that introduce approximations to resolve the phase in the RANS equations.

In the nearshore zone, it is important to simulate accurately the non-linear and dispersive characteristics of waves such as the steepness, the relative wave height and the relative water depth. The first and second characteristics increase in shallow water as waves shoal while the third characteristics increase in intermediate and deep water where waves are dispersive. These effects are largely considered to classify the wave propagation models from the family of linear models, models with non-linear and dispersive properties than those based on the RANS equations. With the objective of fulfilling the need for highly accurate, nonlinear models capable of simulating wave propagation and transformation, a series of non-linear models for wave propagation have been implemented from the phase-averaged (SWAN, XBeach) models to the phase-resolving (SWASH) ones. Most of the numerical models applied to coastal regions can be implemented in 2DH/V or 3D configurations. 2DH simulations simplify the computational requirements by solving the shallow water equations. It has been demonstrated that these kinds of models can accurately reproduce current velocity, flood extent, and water levels, being useful

to complement risk assessment tools and early warning systems, because less computational resources are required, and the numerical solutions are much faster obtained.

1.2. OBJECTIVES OF THE DYNSEEC PROJECT

Analyzing coastal risks involves assessing both probability and consequences. Effective risk management aims to reduce the probability and consequences, necessitating precise resilient infrastructure criteria (Neumann et al., 2015). Managing coastal risks is crucial for the development of adaptation strategies, required to reduce the evolving threats (Vousdoukas et al., 2016; Wadey et al., 2015) and sustainable solutions integrating climate change impacts and socio-economic factors. Stochastic and numerical approaches can determine the probability and consequences of risks by defining the characteristics and impacts of extreme coastal events, essential to understand hydrodynamics in coastal environments (Stewart & Melchers, 1997; Turki et al., 2023a). When on-site measurements are lacking, numerical models provide crucial insights into wave behavior and storm impacts (Dee et al., 2011; Ozsoy et al., 2016). Overall, understanding the diverse impacts and behaviors of coastal climate conditions becomes essential as extreme storm-related coastal inundations escalate in urgency due to climate change (Liu et al., 2021). The cascading effects of extreme waves and storm surges combined with the long-term effects of sea level rise are increasing to sharpen coastal instabilities and the heavy population pressure, especially the 40% residing in low-lying coastal areas (Neumann et al., 2015).

This general context introduces this PhD project: the DYNSEEC (*DYNamique multi-échelle des Evénements Extrêmes Côtiers*, Multi-scale dynamics of coastal extreme events) project, funding it in partnership with the IRSN (*Institut de Radioprotection et de Sureté Nucléaire*, the Radiologic protection and Nuclear Safety Institute) and the AESN (*Agence de l'Eau Seine Normandie*, Water Agency of Seine Normandy) as well as 50% support from the Normandy Region.

This study focuses on the hydrodynamics from the regional scale of the English Channel to the local scales of Normandy coasts in response to extreme storm events. The transformation of waves in semi-enclosed environments like the English Channel involves complex dynamics influenced by water depth variability and coastal topography (Komen et al., 1994). In the English Channel, studies have focused on understanding storm dynamics and their effects, including storm surges and coastal erosion (Anthony, 2013; N. Wells et al., 2001). Recent research has

utilized high-resolution numerical models to simulate nearshore hydrodynamics, enhancing accuracy and resolution compared to reanalysis models (Caires et al., 2004; Cavaleri & Sclavo, 2006) and has also explored the morphodynamic impacts of storms on French coastlines, highlighting the role of storm characteristics (Soloy et al., 2021, 2022, 2023).

The coasts of Normandy, vital for wildlife, tourism, and protection against erosion and flooding, are notably vulnerable to climate and human-induced risks. The morphology of the coasts varies from pebble and gravel beaches in the north of the Seine Estuary, produced by the erosion of the chalk cliffs, to rocks and sandy beaches in the south of the Estuary. In terms of protection against flooding, up to 4 French Nuclear Power Plants (NPP) can be found in the English Channel, with 1 located in the Cotentin Peninsula, 2 along the Normandy coasts and 1 in the northern coast.

The objective of this PhD aims at developing an integrative vision of coastal hazards by combining stochastic and numerical approaches and connecting different time- (from storms to interannual or interdecadal) and spatial- (from regional to local and considering the global atmospheric circulation) scales in order to investigate the multi-timescale dynamics of extreme coastal storms, from the regional scale of the English Channel to the local scale of Normandy coasts, and their effects close to the shoreline (**Figure 1**).

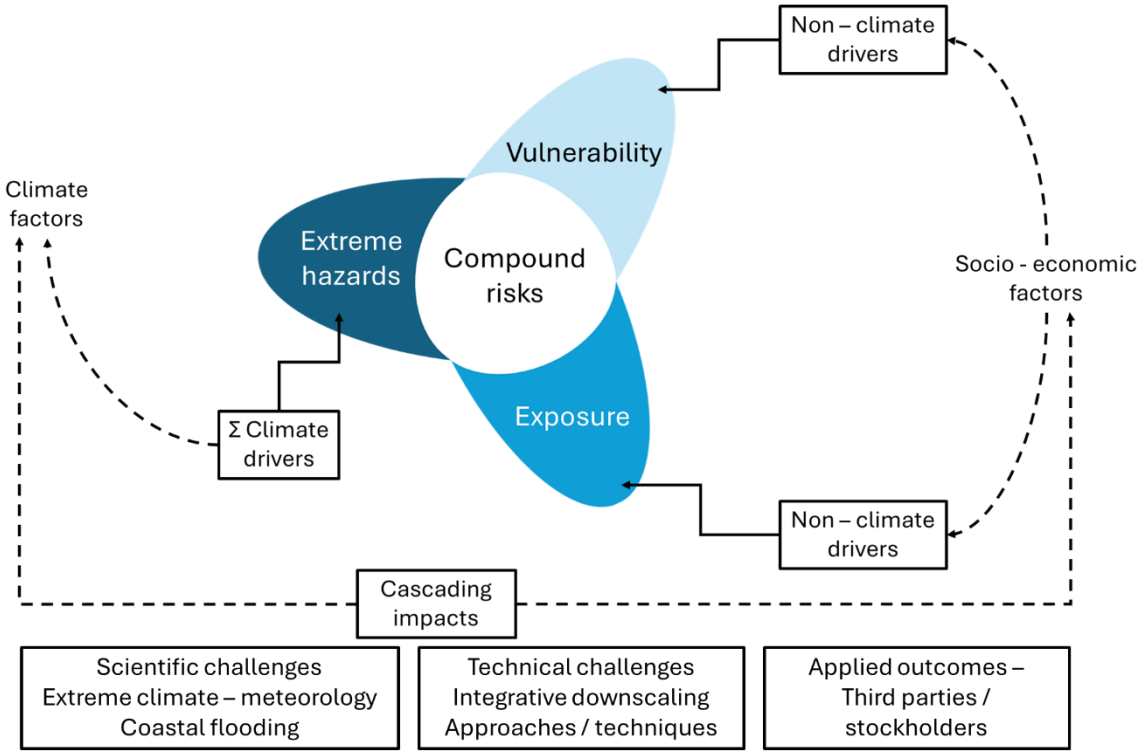

Figure 1. *General overview of the DYNSEEC context (modified from original figure from Sixth Assessment Report (AR6) of IPCC (2023))*

A special focus has been given to coastal flooding in complex environments, case of coastal systems connected with fluvial component as Seine Bay (Turki et al., 2019, 2023). The outcomes of this study will be crucial for an accurate assessment of coastal risks and mitigate the impacts of compound flood events induced by marine and coastal storms, in mutual interaction with the public organisms, as are AESN and IRSN.

Normandy coasts are of special interest because of their particular morphologies. North of the Seine River, they are exclusively composed of high limestone and chalk cliffs, softly anthropized, although some punctual human structures are located at the mouth of less important rivers, that sometimes can be found channelized or drained. In northern Normandy, chalk is dissolved in the sea, and the fragments of flints roll and get rounded under the action of waves becoming the pebbles that compose the beaches. The accumulation of these pebbles has the advantage of protecting coastal structures and anthropogenic activities, since, during a storm, much of the wave energy is dissipated by the movements of pebbles. The coastal structures aim to protect human facilities against the impact of extreme events maximizing the space available.

Generally, anthropogenic activities are concentrated in estuaries closed by a seawall parallel to the coastline, and usually drained or channelized to allow the river flow through. Perpendicular groins are a common addition to limiting longshore sediment transport and to accumulate material, which improves the protection capability of the beaches.

South of the Seine River, the composition of the coastline alternates between high and low rocky coasts, with some accumulation of sediment, mostly sand, in some specific locations, coincident with human settlements. These sandy beaches also have the presence of groins to retain the sediment, and a vertical seawall, acting as coastal protection.

1.3. THE INVOLVEMENT OF THIRD PARTIES IN THE DYNSEEC PROJECT: AESN AND IRSN

The scientific approach includes the study of the non-stationary relationship of the multi-scale dynamics of extreme events, in which the IRSN was notably interested and strongly involved. An analysis of the time series of waves and surges has been carried out along the Channel coasts based on stochastic approaches (probabilistic and spectral). The data has been made available by various French scientific organizations (SHOM, IRSN and Météo-France, either as producers or providers). During the first phase, a deeper understanding of the storm climate

(water levels and waves) of the French coasts is carried out based on previous work (Idier et al., 2012; Turki et al., 2015, 2019, 2020a) and the technical and scientific support provided by SHOM and Météo-France. A fairly dense database of historical storms, developed by IRSN, is used to understand the characteristics of historical extreme events in terms of frequency, succession and return period (https://bddtsh.irsn.fr/).

With the aim to protect the NPP against flooding risks and following the Guide n°13 from the French Nuclear Safety Authority, each flooding scenario must consider a target return period of 10,000 years. For coastal power plants, this return period includes a static sea level scenario (formed by the highest astronomical tide, a skew surge associated with a return period of 1000 years, and the mean sea level evolution) and an ocean waves scenario (100-year return period of offshore waves propagated on the static sea level). Improving the quality of the estimation of the flooding scenarios for coastal sites is one of the objectives of the IRSN during the development of this PhD project.

The characterization of the evolution of typical extreme scenarios from the English Channel basin towards coastal systems and the classification of their hydrodynamic impacts on the Normandy coasts (Etretat, Hautot-sur-Mer and Villers-sur-Mer) is of great interest to the AESN. Indeed, the AESN is interested in questions of submersion and erosion of coastal zones, seeking the best way to predict these phenomena to achieve better management of the coastline. These coastal systems have intrinsic (geometry, sedimentary texture, grain size, beach slope) and extrinsic (energy, interaction of hydrodynamic forcing) characteristics that are fairly representative of Norman coastal systems, in particular those of the Seine Maritime department. These sites are already equipped with Video Monitoring Systems since 2018 by *Syndicat Mixte de la Seine Maritime* (manager: Loïck Le Louargant) and Rouen Normandy University - M2C laboratory (manager: Emma Imen Turki). The different activities, carried out during this work, were supported by a series of research programs hold by Rouen Normandy University - M2C and other institutions.

The DYNSEEC PhD has been developed in the framework of the satellite mission Surface Water and Ocean Topography (SWOT), launched in December 2022. Several investigations have been carried out in relation to the potential use of this new wide-swath satellite altimetry mission to measure the water level in rivers, estuaries and coastal zones. These works have been performed during different TOSCA (*Terre Solide, Ocean, Surfaces Continentales et Atmosphere*, Solid Earth, Ocean, Continental Surfaces and Atmosphere) research programs of CNES-NASA, in collaboration with international researchers from different academic and research centers. This

work is basically supported by the international program SWOT 3MC (Benoit Laignel and Emma Imen Turki, 2020 - 2024).

CHAPTER 2

SCIENTIFIC INSIGHTS INTO THE EXTREME HYDRODYNAMICS IN THE ENGLISH CHANNEL AND ALONG THE NORMANDY COASTS

This chapter introduces the state of the art related to coastal hydrodynamics and the multi-timescale evolution in response to climate drivers. A special focus has been given to the extreme storms and their connections with the physical mechanisms of climate oscillations. The second part presents an overview of the different approaches used for investigating the dynamics of extreme events and the associated risks, including the stochastic downscaling and the numerical modelling, based on the previous works. Then, the study sites are introduced: the English Channel and the Normandy coasts, particularly on Etretat, Hautot-sur-Mer and Villers-sur-Mer as representative systems. To conclude, the strategy of study presents the division of the different topics of interest into the chapters that follow. Finally, a detailed description of the structure of the manuscript and the objective of the different chapters has been highlighted.

2.1. MARINE AND COASTAL HYDRODYNAMICS

Hydrodynamics are defined as the processes occurring on the water due to the influence of external forces and the internal transmission of energy. These dynamics are manifested as the oscillation of the surface of the water, like waves or tides, and the motion of the water under the surface, like currents or rivers (Horikawa, 1988). Among all the global waters that are part of the hydrosphere, this study is centered on the hydrodynamics of the seas, where a distinction can be made between the dynamics of the open sea waters and the coastal waters. The difference between the deep ocean and the coastal waters is that, in the latter ones, the bottom of the sea and the shoreline play an important role (Horikawa, 1988).

Reducing the scale to regional seas, a main focus is given to the oscillatory motion of the water surface, although including other processes like river discharges is also considered, when necessary, since all hydrodynamic conditions interact between them, acting at the same time as drivers that generate new processes.

The oscillations of the surface of water follow the traditional physical description and characteristics of waves, primarily defined by their amplitude (A) and frequency (f). The inverse of the frequency, the period (T), is typically the fundamental variable to differentiate every kind of wave present in the sea.

According to the classification offered in Toffoli & Bitner-Gregersen (2017), waves with shorter periods, approximately below 25 seconds, are gravity waves, making a distinction if the periods are shorter than 1 second. These waves are generated by the action of wind on the water surface, where the restoring force is gravity, and they are often referred to as wind waves and swell. Wind waves, also called sea or short-crested waves, are generated locally and propagate to the shore. Swells were wind waves that propagated outside their generation area and that are transformed in the process. These short waves, sea and swell, are one of the most important parameters in hydrodynamics because they are the most frequent and destructive parameters and represent the main focus of this study (Chau, 2010).

Among the longer waves, those whose periods are more than 1 hour are called water-level variation and can be classified according to their generating forces. If these waves are produced by the gravitational attraction of the Sun and the Moon, and they are sustained by the gravity and the Coriolis force, they are the ordinary tidal waves, with periods ranging between 12 and 24 hours, usually denoted just as the astronomical tide.

If they are produced by the combined effects of the action of wind stress on the water surface, the reduction of the atmospheric pressure, shallow water depths and the horizontal boundaries of adjacent waters (Mangor et al., 2017), they are the storm surges, or only surges, being able to have periods from just a few hours up to a few days (Holthuijsen, 2007). These periods share the same order of magnitude of the meteorological disturbance that produces the surges (Nielsen, 2009; Massel, 1996).

2.1.1. Short waves: sea and swell

Short, or gravity waves can be described as a group of single waves defined individually by three main characteristics, namely the wave height (H), equivalent to the amplitude of the linear wave theory, the wave period (T), and the direction of propagation (θ). Additionally, the wavelength L can also be obtained from the other variables. The addition of all the single waves with their own characteristics form the irregular waves that are just referred to as “waves”.

The irregular waves can be statistically described by the individual wave analysis, in which the distributions of wave heights and wave periods are measured wave by wave using the zero-crossing method. The propagation direction has to be also measured for each wave. This methodology could only be applied to linear non-dispersive waves, only suitable for shallower waters on the nearshore in which the waves propagate uniformly following a common direction so that the analysis can be performed in one dimension. That is not usually the case, the reason why the spectral analysis is introduced, more appropriate for nonlinear waves.

In the spectral analysis the irregular waves consist of an infinite number of component regular waves with their characteristics described based on an energy distribution of the waves themselves. A typical wave spectrum $S_f(f)$ is expressed as the summation of the wave energy of all the range of directions, i.e., a one-dimensional frequency spectrum calculated as the energy density only in terms of frequency. The derivative of the frequency spectrum is the directional spectrum $S(f,\theta)$, the expected energy density or wave energy in terms of frequency f and direction θ. The frequency spectrum $S_f(f)$ of a given set of irregular waves can be calculated generally just from a time series of water surface elevation, but there are multiple theoretical formulations to obtain it with limited information of waves, like the Pierson-Moskowitz spectrum (Pierson & Moskowitz, 1964), the Goda spectrum (Goda, 1985) or the most extended Joint North Sea Wave Project (JONSWAP) spectrum (Hasselmann et al., 1973). An example of the comparison between the Pierson-Moskowitz and the JONSWAP frequency spectra in shown in **Figure 2**.

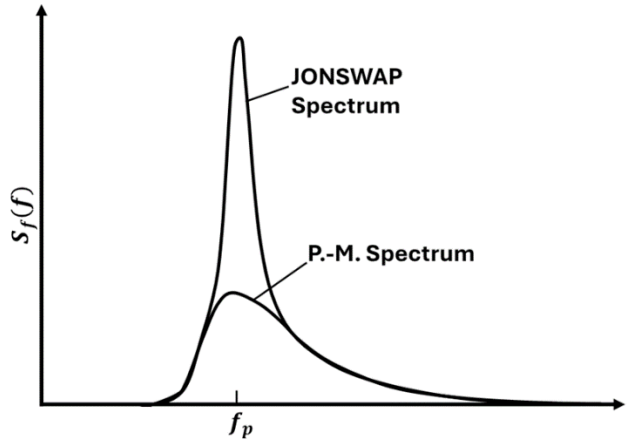

Figure 2. *Pierson-Moskowitz and JONSWAP frequency spectra with the peak frequency f_p (adapted from Pierson & Moskowitz (1964) and Hasselmann et al. (1973))*

As previously stated, wind waves are generated by wind blowing locally in the area, making them irregular in wave height H and period T and three-dimensional in direction θ. It is necessary to have a wind field with a velocity higher than a critical value acting on the water surface with a duration long enough and an almost constant direction to develop the waves on this surface (Chau, 2010). In this generation area it is important too the available fetch, defined as the length in a straight line over which the wind is providing energy to the water, both for the wind field and the water area, called as the meteorological and the geographical fetches, respectively.

The waves already developed can leave the wind field and propagate through the ocean, sometimes approaching toward a coast. In that case, they are usually transformed into swells that tend to gain a similar longer period (smaller frequency) and uniform long crest-lines, acquiring a two-dimensional shape. It is the combination of both types of short waves in a sea surface during a specific delimited time what defines a sea state.

When waves approach the coast they are not just influenced only by the wind, but also by the bottom of the sea and nearshore morphology. This means that the waves have left the offshore zone and entered the nearshore zone (**Figure 3**; Horikawa, 1988). In the nearshore zone, several processes of transformation can occur over the waves. The main processes are the shoaling and the refraction, which, depending on the shoreline contours and the changes in depth, can take place before or after shoaling zone in **Figure 3**. The shoaling is the deformation of waves due to a change in the propagation velocity, producing a shortening and steepening of the waves. This process usually happens when the water depth is about half of the wavelength. The refraction is a change in the direction of propagation because the crest-lines tend to become parallel to the sea bottom contours, and, consequently, to the shorelines, since they are usually aligned too.

As waves continue to propagate, entering the surf zone (**Figure 3**), they are affected by the bottom friction, which is a loss of energy that affects the wave height, reducing it when the water depth become shallower, being more important in large shallow areas located over the continental shelf. At certain location, when the wave height is larger than a specific fraction of the water depth, the shoaling wave finally breaks. This point is called the breaking point (**Figure 3**) and marks the end of the shoaling zone and the beginning of the surf zone, but since waves are irregular, not all of them break at the same location, so that the breaking point is actually a breaker zone.

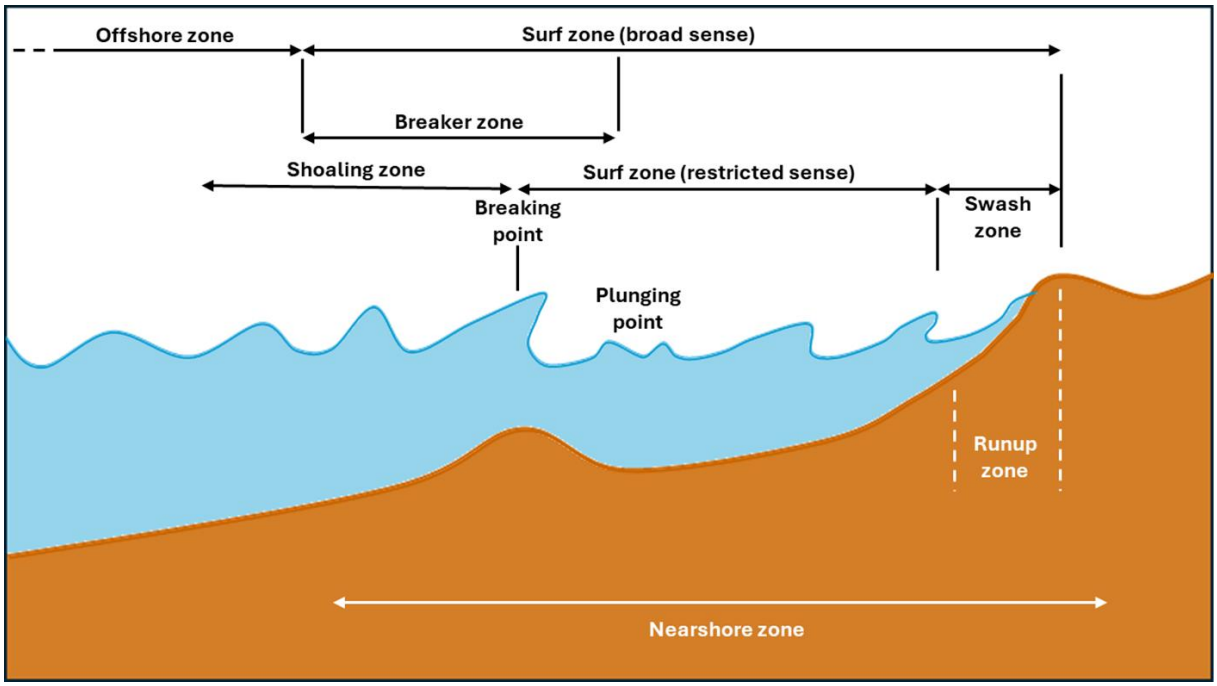

Figure 3. *Idealized wave transformation zones (adapted from Horikawa (1988))*

Beyond this area, the hydrodynamics become more complex, with more interaction between the different processes until waves finally reach the coast. This last part of the sea is called the swash zone (**Figure 3**), delimited by the last wet point of the coast, and it is there where the hydrodynamics meet the morphodynamics, with an added interaction with the coast and the beaches or structures that can be present there. The portion of the swash zone where the waves rush up on the beach face is called the run-up zone (**Figure 3**), and it is the limit of propagation of waves onto the beach slope, marking the end of the transformation too. If there is a structure, a potential wave overtopping could occur, with waves passing over the structure due to an unexpected abnormally large wave height.

2.1.2. Water level variations: tides and surges

Coastal water levels are influenced by a variety of astronomical, meteorological, oceanographical, and tectonic factors, the most readily apparent being the tides, combination of the Earth's rotation and the attraction gravitational forces of the Sun and the Moon (Pugh, 2004; Nielsen, 2009), among other forces. With respect to the amplitude, the difference between the low and the high tide is called tidal range and defines the four classes of astronomical tides worldwide (Levoy et al., 2000): microtides when the tidal range is below 2 meters, mesotides if the tides range between 2 and 4 meters, macrotides from 4 up to 8 meters, and megatides if they exceed 8 meters. The megatidal range usually appears on shores located on the continental shelf.

At times, the factors mentioned interact in a complex way to elevate water levels significantly above the normal tide level. Storms, that develop low atmospheric pressure, are the most common cause of elevated water levels. Strong winds and large waves contribute also to the sea surface perturbations in oceans and coastal zones. These abnormal elevations of the water surface are called storm surges, including atmospheric and meteorological surges, and are obtained as the residual of the total signal, since they can only be predicted stochastically.

Therefore, the total sea level is constituted of different components: (1) the mean sea level, (2) the vertical local movement described by the vertical reference datum for water level and related to the subsidence and tectonic deformations of land, (3) the astronomical tide, and (4) the residual surges (Turki et al., 2015).

The sea level changes occur at all timescales, with processes operating at:

- Higher frequencies (<6 hours) tend to be produced at larger magnitude close to coastal areas due to several dynamics, such as tropical storm surges (short scales of hours to days), seiche resonance (also edge waves and coastal trapped waves; even shorter scales of minutes to hours) and infragravity waves (scales of seconds).
- Higher-lower frequencies (inter-daily scales) due to changes in air pressure (inverse barometer or IB), the wind stress and their combination responsible for storm surges. Other processes spanning at different timescales as wave setup (water level rise due to breaking and wave dissipation in the surf zone) and freshwater runoff from rivers which influence the MSL variability and then the extreme sea levels. Such processes will inevitably contribute to MSL variability on seasonal and even interannual timescales.
- Lower frequencies (seasonal to interannual and decadal scales) should be produced as those related to the rise in MSL which have direct effects on the total water levels as well

as indirect effects on tides and storm surges. At such lower frequencies, the sea level variability is also directly dependent on large-scale teleconnections of climate patterns.

The changes in sea level, resulting from different multi-timescale mechanisms, can be considered negligible in deep water, however, may become significant in shallow-water areas where non-linear interaction processes are generated. This interaction increases during extreme events and induces the mechanisms of extreme river run-off in rivers and coastal wave set-up which contributes to the mean sea level changes and should be used in large-scale climate research.

Understanding such changes at the coast is critical for flooding assessment. The mechanism interactions exhibit a strong spatiotemporal variability, and their manifestation depends on the type of environment (e.g., morphology and hydrometeorological conditions). The consideration of these interactions is required for the assessment of nearshore water levels and induced coastal flooding, which is useful for a full investigation of the future coastal hydrodynamics and inundation through the probabilistic projections (a schematic overview adapted from Woodworth et al. (2019) is presented in **Figure 4**). The effects of climate circulation should be also considered since the coastal wave-driven processes are related to such large oscillations with remote responses of wave set-up and runup through the propagation of swell waves.

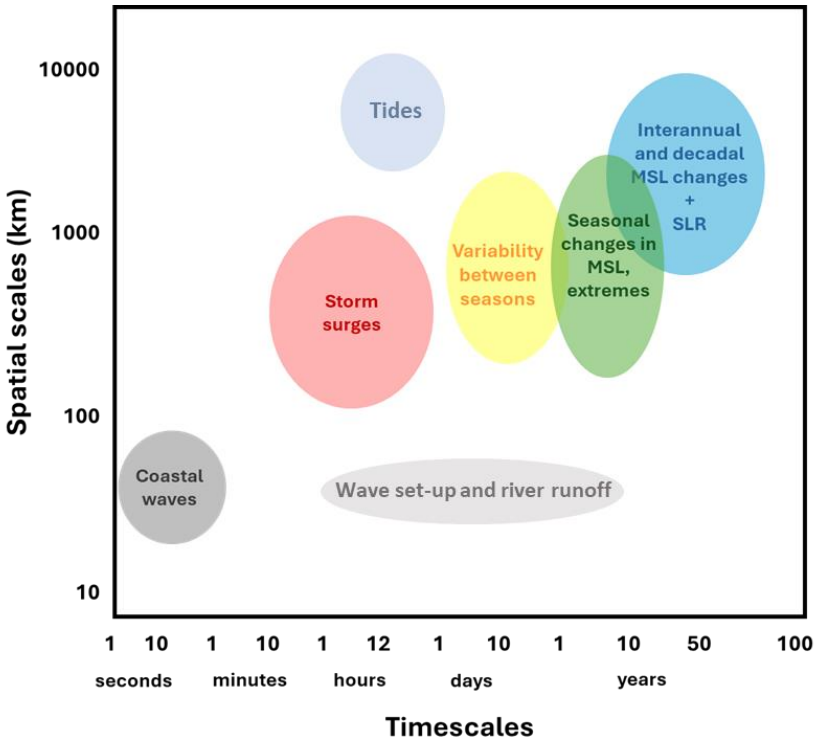

Figure 4. *A schematic overview of processes contributing to sea level variability at the coast indicating the space and the timescale involved (adapted from Woodworth et al., (2019))*

The storm surges are the other main focus of the present PhD research, since, if the high tides are overlapped with large storm surges, they can cause major oscillations, perceiving it from the shore as an elevation of the water level that can generate overtopping on coastal structures and flooding.

2.2. COASTAL STORMS

Extreme events are defined, from a climatic point of view, as the most intense and severe scenarios that can occur in a given location, with strong enough conditions and for a long enough period of time. When these hazardous situations take place on the oceans and, especially, on the shore, they are referred to as coastal storms. Since the conditions of generation are constantly changing, each storm is unique, but some common characteristics can be outlined (U.S. Geological Survey (USGS), 2024):

- Strong winds blowing on the surface of the ocean. They can directly generate structural damage if they are occurring on the shore, but they can also generate extreme waves and surges even if they are just present offshore.
- Large waves, that can travel long distances on the ocean or can be developed nearshore. They can cause catastrophic consequences on the environment like cliff failure or beach erosion, but also inundation and the destruction of coastal properties.
- Storm surges also produced either in deep oceans or on the shore. Because of their longer periods, they can submerge beaches and produce flooding on coastal areas.

A combination of these characteristics is also possible, with the increase of the water level due to storm surges allowing waves to propagate deeper landwards to places that normally will stay far from the shoreline, and winds contributing to worsening both processes. These natural hazards, although not common, have been increasing in number in the recent years, especially when it comes to coastal erosion and inundation. They are among the most destructive natural disasters and are considered a highly challenging issue in the global context of climate change that requires coastal adaptation measures that should be fitted to the changing climates (Liu et al., 2021). The inundation phenomenon can be observed arising concomitantly with an ongoing sea-level rise component (IPCC, 2022) that enhances the frequency of generation and exacerbates the impacts of these extreme events on the coast.

There are multiple ways to analyze extreme events and predict their recurrence, defining then their return periods or return levels, the estimated time that will pass between the occurrence of

events with the same characteristics. If it is calculated as the inverse of the frequency of occurrence, the probability of one event of being exceeded in one year is the inverse of the return period. The Extreme Value Analysis (EVA) and the models developed for the Extreme Value Theory (EVT) allow to define probabilistically the extreme events, but they can be also found by the analysis of the energy spectrum or by the use of numerical modelling, in the case of coastal storms.

Coastal inundation and flooding are considered as one of the most hazardous scenarios in response to extreme hydrodynamics or extreme levels, controlled by a combination of extreme surges and waves, that induce other coastal impacts as overwash close to the shoreline and overtopping in the vicinity of maritime structures. An overview of coastal flooding is shown in **Figure 5**, extracted from Almar et al. (2021). The extreme coastal water level results from the combination of regional sea level anomaly (SLA) due to the steric effect, ocean circulation and transfer of mass from the continents (ice sheets, glaciers, land water) to the ocean, astronomical tide, storm surge due to atmospheric pressure and winds, and wave runup, decomposed into a time-averaged component (setup) and an oscillatory component (swash).

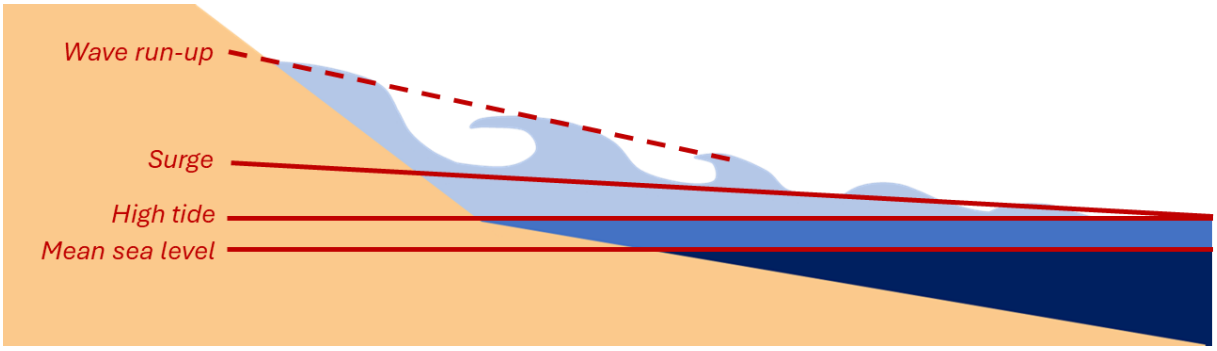

Figure 5. *Overview of the different levels of potential flooding depending on coastal topography, with the components of extreme water level produced during stormy events (adapted from Almar et al. (2021))*

2.3. OVERVIEW OF THE METHODOLOGICAL APPROACHES USED FOR INVESTIGATING COASTAL HYDRODYNAMICS

2.3.1. From global atmospheric circulation to coastal hydrodynamics: stochastic downscaling

With the global context of climate change, most researchers claim that the water level variability and the increase of extreme events are considered significant hazards for several low-

lying coastal and estuarine communities (Hanson et al., 2011; Nicholls et al., 2011). Hence, many efforts have been devoted to better understanding the natural processes driving the multi-scale variability of the hydrodynamics with the aim for producing a more accurate estimation of their fluctuations and ensuring reliable coastal risk assessments.

This challenge serves as the basis for implementing an appropriate adaptation strategy to reduce the disastrous risks of the flooding in the different context of coasts, estuaries and rivers. Changes in hydrodynamics encompass cyclical seasonal components superimposed on long-term trends and stochastic variability. These changes are due to the frequent temporal shifts linked to the nonlinear and stochastic effects of external factors such as the global climate patterns (Pasquini et al., 2008).

During the last decades, the study of the extreme hydrodynamics has increased significantly, including the statistical modeling to reproduce the seasonal and the interannual variability (Lavers et al., 2010; Turki et al., 2019, 2020a, 2020b; Unnikrishnan et al., 2012). Moreover, studying the links of the sea-level variability with the climate teleconnections, related to prominent atmospheric modes as proxies, is necessary to fully understand the interplay between the climate oscillations and the hydrodynamic processes (Dangendorf et al., 2012; Zampieri et al., 2017).

Several works have analyzed the variability in the state of the atmosphere and investigated to what extent the complex relationships of the global atmospheric circulation with the local hydrodynamic forcing can be useful to understand their effect on the interannual variability of the extremes. Other works have been implemented to understand and extract the signature of internal climate variability from the observed water-level patterns with the aim of contributing to the multi-scale predictions that emerge as urgent priorities in the state-of-the-art climate research. However, there was not a clear conclusion about the atmospheric situations that cause the interannual fluctuations on extreme hydrodynamics.

In the early 70's, a synoptic climatology was established as a climatological subfield with the publication of "*Synoptic climatology: methods and applications*" (Barry & Perry, 1973). After that seminar, a lot of techniques have been applied to explore and analyze the climatology in order to understand and simplify data of geophysical variables. Several statistical methods have been developed to relate synoptic-scale atmospheric circulation to local environmental responses (analyzing variables like temperature, precipitation or pressure fields). The main advantage of the statistical techniques is that a large amount of complex data fields (with spatial and temporal

dimensions) can be processed automatically to output a simple and readable synthesis, minimizing the human factors.

2.3.2. Dynamics of extreme events with climate teleconnections

Extreme events, focusing on waves and surges, are highly correlated to atmospheric circulation, and the analysis of climate patterns can help in the understanding of these storms. Several studies (Masina et al., 2015; Turki et al., 2020a, 2020b, 2023) have proved the correlation between extreme waves and surges to some of the most common atmospheric patterns and indexes. The sea level pressure (SLP) and the sea surface temperature (SST) are well known global climate patterns, and, typically from the North Atlantic area, two indexes are extensively studied, the North Atlantic Oscillation (NAO) and the Atlantic Multi-decadal Oscillation (AMO).

Sea Level Pressure (SLP) is a measure of the weight of all the air in a column vertically above a point on the sea surface (Hersbach et al., 2023). In mid to high latitudes of the Northern Hemisphere of the National Center for Atmospheric Research (NCAR), SLP is a long-term continuous gridded analysis based on land station reports (**Figure 6**a). Analyzed fields take into account observed winds, clouds, and other weather variables. Daily data are available, but the monthly mean values are more widely used (Hurrell & Trenberth, 2022), because they have been corrected by Trenberth & Paolino (1980).

Sea Surface Temperature (SST) is the temperature of sea water near the surface. The NCAR provides monthly SST anomalies, derived from a 30-year climatology spanning 1961-90, on a global ocean grid from the year 1850 to the present, based on quality-controlled *in situ* measurements made by ships, drifting buoys and moored buoys with no interpolations in the dataset (**Figure 6**b). The anomalies are derived from a 30-year climatology spanning from 1961 to 1990.

There is no universally accepted index to describe the temporal evolution of the North Atlantic Oscillation (NAO), since there is no unique way to define the spatial structure of this phenomenon (Hurrell & Phillips, 2023). For the NOAA (National Oceanic and Atmospheric Administration), the NAO index is based on the surface sea-level pressure difference between the Subtropical (Azores) High and the Subpolar Low (**Figure 6**d). The positive phase of the NAO reflects below-normal heights (500 millibar height) and pressure across the high latitudes of the North Atlantic and above-normal heights and pressure over the central North Atlantic, the eastern United States and western Europe. The negative phase reflects an opposite pattern of height and pressure

anomalies over these regions (NOAA, 2021). According to Hurrell & Phillips (2024), it can either be measured from instrumental records from individual stations near the NAO centers of action or obtain it from the principal component (PC) time series of the leading Empirical Orthogonal Function (EOF) of SLP anomalies over the Atlantic sector (**Figure 6**c). A major advantage of most of these indices is their extension back to the mid-19th century or earlier.

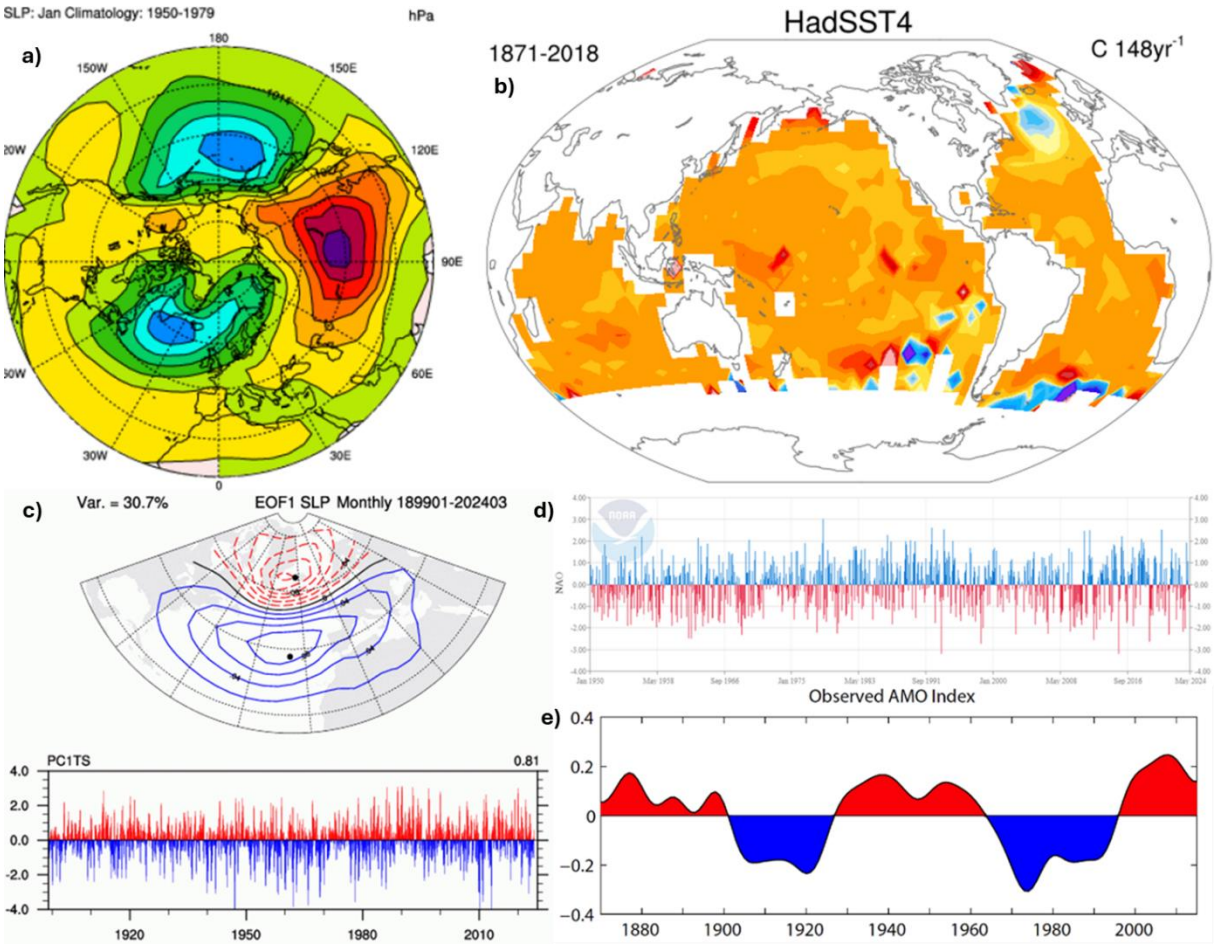

Figure 6. *a) January SLP climatologies for the period 1982-2011 of the NCAR index, b) annual trends in SST of the HadSST4 dataset of NCAR, c) Hurrell's NAO index time series of one of the PCs of the EOF analysis of SLP, d) NOAA's NAO index time series and e) observed AMO index by the NCAR*

The Atlantic Multi-Decadal Oscillation (AMO) has been identified as a coherent mode of natural variability occurring in the North Atlantic Ocean with an estimated period of 60-80 years (**Figure 6**e). It is based upon the average anomalies of sea surface temperatures (SST) in the North Atlantic basin (Trenberth & Zhang, 2023). The AMO is associated with important climate impacts, such as the multidecadal variability of Atlantic Hurricane activity, North American and European summer climate, northern hemispheric mean surface temperature, and Arctic Sea ice anomalies.

These climate patterns and indexes are extensively used in the study of extreme events, specifically in coastal storms, where the behavior of these processes can be explained by the

correlation with the atmospheric oscillations. In the present study, the atmospheric patterns and climate indexes presented will be used.

2.3.3. Numerical approaches for investigating coastal hydrodynamics

Besides stochastic downscaling and spectral analysis of extreme events, the evolution of storms reducing the scale can be performed by numerical modelling, alongside the complete marine and coastal hydrodynamics, including water level and wave simulations.

Computing technology is providing an increasing number of numerical models that are becoming more mature and that are capable of solving engineering and environmental problems in the domain of marine and coastal hydrodynamics (Chau, 2010). The numerical modelling techniques behind them can be based on the finite element, the finite difference, the boundary element, the finite volume, or Eulerian-Lagrangian methods. The modelling can be simplified into different spatial dimensions according to the necessities of each case or study: a one-dimensional model, a two-dimensional lateral-integrated model, a two-dimensional layered model, a three-dimensional model, or other combinations. However, the accuracy of the prediction is majorly dependent on the open boundary conditions of the model, the set-up parameters, and the numerical scheme (Martin et al., 1999).

For each practical coastal problem, the adoption of the most proper numerical model is essential, considering that the use of these predictive tools inevitably involve certain assumptions and/or limitations.

Modelling the hydrodynamics of an incompressible fluid is done by resolving the conservation of mass and the conservation of momentum equations, which, through the introduction of some additional expressions and the combination of both conservation assumptions, become the Navier-Stokes equations.

In the case of simulating non-steady flow and wave hydrodynamics, among the most extended models, the version of these equations that are solved are the nonlinear time-averaged Navier-Stokes equations (NS). At this point, a coarse classification for the numerical models would be between the phase-resolving and the phase-averaging models. By not making approximations, the phase-resolving models give the most accurate results, but the computational cost of them is sometimes too high.

Phase-averaging models can be applied to larger areas to resolve the motion of waves, since they are constructed based on the directional spectrum $S(f,\theta)$, where the elevation of the surface of water is a function of the frequency and the direction of propagation of the set of irregular waves. In these models, the wave energy transfer between wave components in the range of directions and frequencies balances the rate of change of wave energy flux, also including the dissipation and the energy input. They do not resolve the individual linear waves, so, for some processes on the shore they have to be combined with some empirical formulations. That is the reason why they are generally applied out of the shallow water area, like SWAN (Booij et al., 1999), the most commonly used spectral model in deep waters and nearshore applications.

Among the phase-resolving models, an additional distinction could be made between the models that fully resolve the NS equations, called depth-resolving models, and those that do not. As an example, OpenFOAM (Jasak et al., 2007) is a phase-resolving depth-resolving model, able to simulate complex processes such as breaking and nonbreaking waves, and the interaction with currents or structures, including overtopping. Considering these models are too expensive in terms of computational effort, their application should be limited to shallow waters in local intricate problems.

Then, these models can turn into depth-averaging models if the depth is not solved. Nevertheless, the depth can be parametrized to resolve some processes, able to accurately simulate the amplitude and phase variation of sea-swell waves. And two additional types of models can be distinguished, those that resolve the Non-Linear Shallow Water equations (NLSW) and the Boussinesq-type models.

The difference between these two kinds of models is that the NLSW models assume a non-dispersive property of waves, while the Boussinesq-type models account for the dispersive properties, being able to apply them in deeper waters, although still shallow, than the other type. A commonly Boussinesq-type model is BOSZ (Roeber & Cheung, 2012), but its computational cost remains in a really demanding level. To try to reduce the computational effort, but still include some dispersive properties of waves in the NLSW models, one solution is to average just the high-frequency waves to have motion, but at the scale of wave groups. This is what models like XBeach Surfbeat (Roelvink et al., 2009; Roelvink & Costas, 2019) are based on.

Another solution is incorporating the dispersion of waves as a result of the decomposition of the pressure into hydrostatic and non-hydrostatic pressure components. They are more demanding than the other solution since they do not neglect the high-frequency wave motions. Models like XBeach Non-Hydrostatic (Smit et al., 2010) allow to divide the depth into up to 2

vertical layers to increase the accuracy. SWASH (Zijlema et al., 2011), being a NLSW model, i.e., phase-resolving but depth-averaging, allows a higher number of vertical layers, approximating it to a depth-resolving model, increasing in comparison the computational cost, but still far from the totally resolving models, making this non-hydrostatic model a trustful choice in shallow waters.

For resolving a non-steady flow, the three-dimensional NLSW equations for incompressible free surface fluid are solved, including the Boussinesq assumption, i.e., the effect of variable density is only taken into account in the pressure term. That is the case of Delft3D-FLOW (Deltares, 2020), which can simulate the hydrodynamics of tides, wind-driven flows (surges) or river flows among others, either in 2D (being then a depth-averaged model) or in 3D with the so-called sigma coordinates (σ-model) introduced by Phillips (1957). In 3D models the vertical velocities are computed from the continuity equation. Globally, The Delft3D suite is composed of several modules capable of interacting between them. For solving the motion of waves, SWAN is included in the Delft3D suite through the module Delft3D-WAVE.

In **Figure 7** a visual conceptualization of all these equations solved and assumptions is illustrated, including all the possible classes mentioned above, and the numerical models taken as examples. In red, the numerical models that will be used later in the different studies that follow, with Delft3D-FLOW for non-steady flow, SWAN for deep water waves (including the module Delft3D-WAVE when coupled with Delft3D-FLOW), and SWASH and XBeach for shallow water processes in the interaction with the coast, resolving the depth and averaging it, respectively.

2.3.4. On the investigation of coastal risks: flooding

A risk is measured in terms of the hazard probability of an abnormal event occurring and the vulnerability analysis carried out in the economic, social and/or environmental aspects of a system. Gouldby & Samuels (2005) defined a risk as:

$$risk = probability\ (hazard)\ x\ consequences\ (vulnerability) \quad (1)$$

With a hazard defined as "*a physical event, phenomenon, or human activity with the potential to result in harm*", specifying that "*a hazard does not necessarily lead to harm*", and the vulnerability as the "*characteristic of a system that describes its potential to be harmed, which can be considered as a combination of susceptibility and value*", after a revision of the literature.

According to the type of coastal system, three are the main risks associated with extreme events arriving to the shore: overtopping, flooding, and coastal erosion. Overtopping can occur on breakwaters protecting harbors or vertical walls located as the last structural defense of the

shoreline against the sea. Flooding is happening on any coastal system exposed to the sea where a single or a compound event of extreme waves or surges can take place, especially worrying in those which vulnerability is higher because they are low lying environments or with several structures or properties located there. Coastal erosion is particularly concerning in beaches, with different affections according to the different possible morphologies, generally gravel and sandy, but also mixed beaches in the context of Normandy.

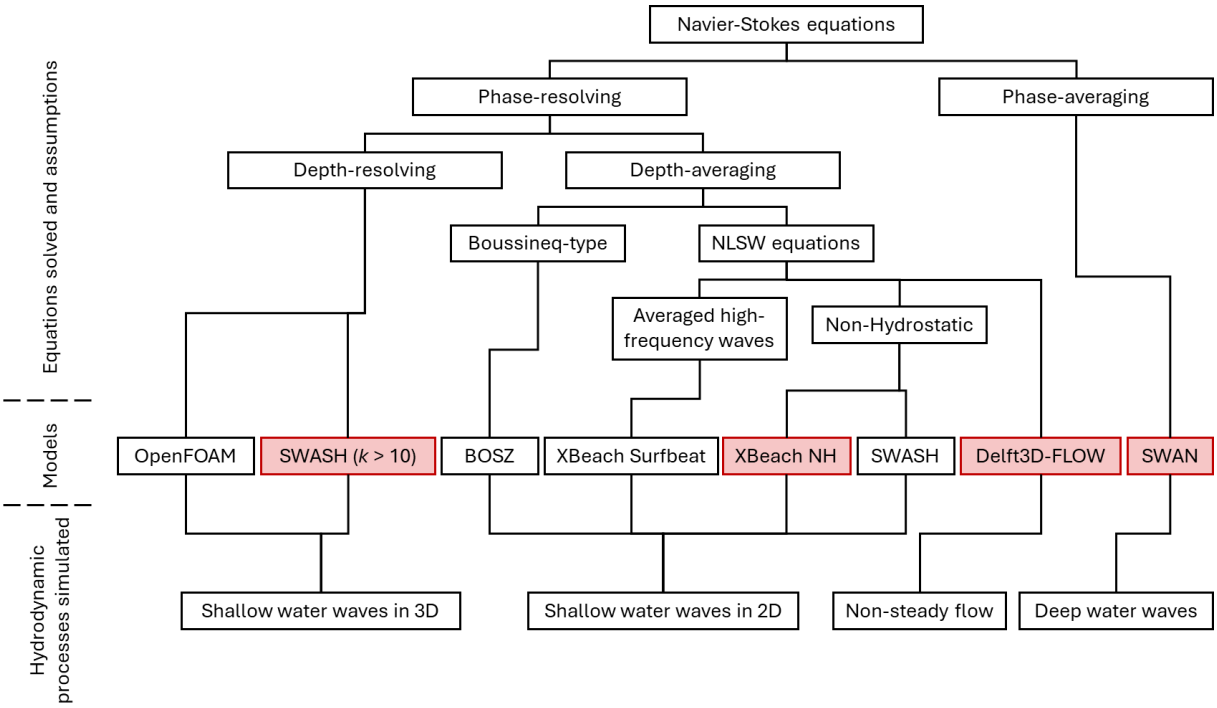

Figure 7. *Visual conceptualization of some numerical models available taken as example of each type of model, including the equations solved and the assumptions, and the hydrodynamic processes that could be simulated (in SWASH,* k *is referred to the number of vertical layers). In red, the numerical models that will be used throughout the dissertation*

In consequence, to study these risks, an analysis of the probabilities in combination with the consequences has to be performed. The methodology developed during this process can determine a risk objectively. Hence, risk management is aimed to elaborate a methodology either to reduce the probability of a risk, to reduce its consequences or a combination of both.

For the overtopping, flooding or coastal erosion, the determination of the probability of the risk and the consequences can be done by stochastic or by numerical approaches, defining the main characteristics of the extreme events arriving to the coast and their impacts.

2.4. STUDY SITES

This PhD research focuses on the English Channel and the Normandy coasts, integrating different scales from the global scale of the climate oscillations to the regional scale of the basin, where the hydrodynamics are controlled by the Atlantic Ocean and the North Sea, and then the local scale of the Normandy coasts, where the interaction between the coastal hydrodynamics and the morphology of beaches (slope, sediment grain size) play a major role (**Figure 8**). The timescales integrating the interdecadal – interannual variability to the scale of the extreme event have been also investigated in the DYNSEEC project.

2.4.1. The English Channel

The English Channel is a sea basin located in Northwest Europe between the coasts of France and England, connecting the Atlantic Ocean and the North Sea. The Channel is one of the most impacted marine areas by human activities worldwide (Halpern et al., 2008). On the eastern boundary, it is connected to the North Sea through the Strait of Dover, and in the western limit, it is open to the Atlantic Ocean (**Figure 8**).

A complex system of capes and bays, alongside multiple islands, characterizes the coastal morphology from the Peninsula of Brittany at the western end of the French coast, to the Cotentin Peninsula (also known as Cherbourg Peninsula) in the middle of the Channel (**Figure 8**). The Channel Islands lie on the West side of this Peninsula. From that area till the Strait of Dover, the coastline gets smoother, with some notable spots such as the Seine Estuary. Likewise, the British coastline is smoother in the eastern part and more intricate in the western part, defined mainly by the presence of the Isle of Wight (**Figure 8**) in the central part of the British coast.

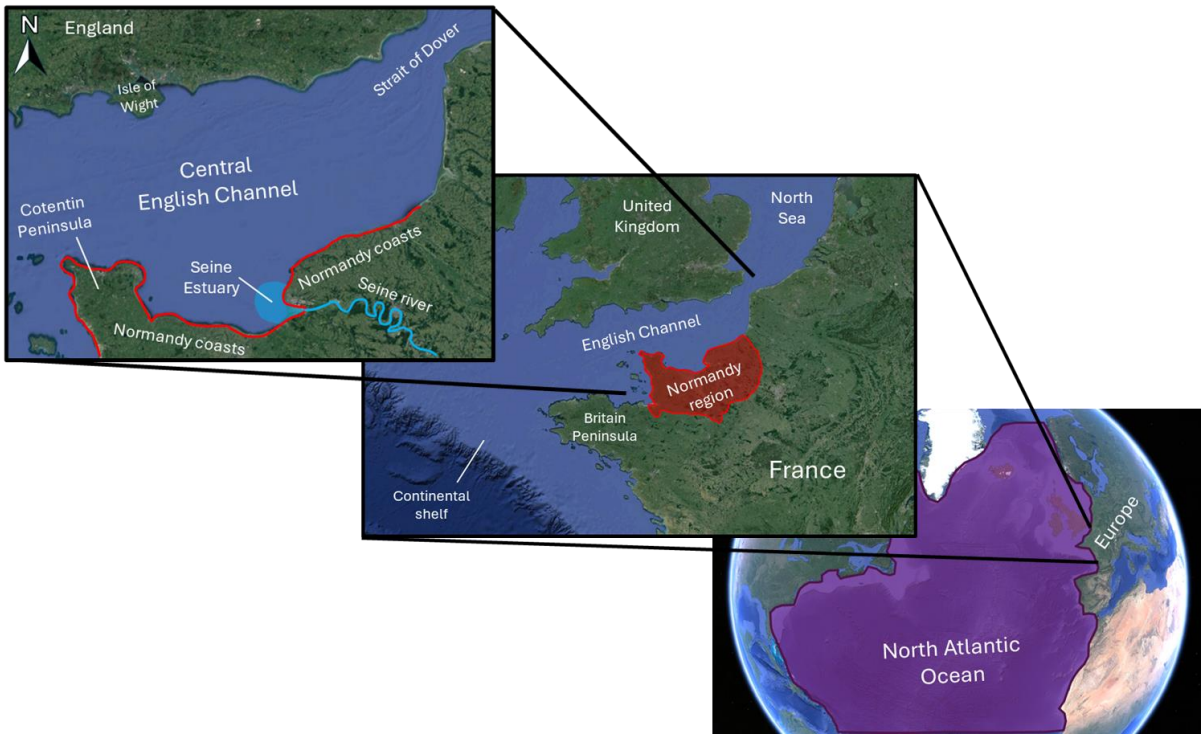

Figure 8. *Global to regional and local scales, with the main features relevant for the different studies, including the English Channel and, in red, the Normandy region and coasts*

The English Channel lies far from the continental slope, considered as a shallow area with a decreasing depth from around 100 m on the West side to less than 30 m on the East (bathymetry is presented in **Figure 9**). The Channel, stretching approximately 560 km in length, boasts a varying width that gives rise to captivating hydrodynamic phenomena unique to this region. In the Strait of Dover, the French and English coasts stand a mere 20 km apart, gradually parting ways until reaching a separation of around 240 km near the Atlantic Ocean.

The high exposure to storms and extreme events is aggravated by the surrounding areas due to the long fetches presented in the North Sea and, especially, in the Atlantic Ocean. In the Atlantic Ocean, the waves come typically from the range SW-NW, with 60% of the waves from the sector W and WNW (wave roses are shown in **Figure 9** for three representative points located in a central point of the English Channel and two points in the open boundaries of the basin, the Atlantic Ocean in the West and the North Sea in the East). More than 78% of the waves in the open boundary of the Atlantic Ocean are within the range 1-4 m, but more than 3% of the waves exceed the 6 m reaching a maximum of 12 m.

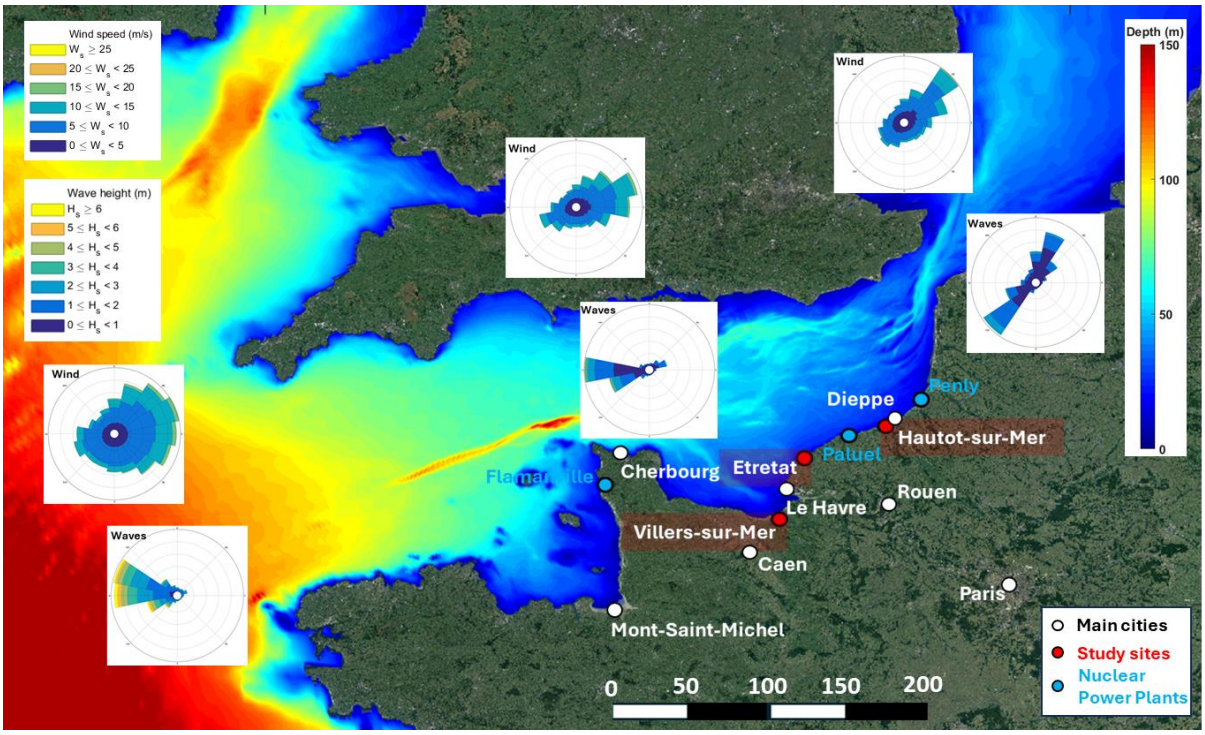

Figure 9. *Bathymetry, wind (direction to) roses and wave (direction from) roses in the English Channel and the eastern and western open boundaries, the North Sea and the Atlantic Ocean, respectively. Main cities are marked in white, the nuclear power plants of the area in blue, and the study sites of the Normandy coasts in red*

These waves acquire the direction of the orientation of the Channel, of about 70 degrees to the North refracting to reduce the range, with more than 60% of the waves propagating from the W and WSW sectors. But some waves arrive also from the North Sea, with more than 15% from the NE and ENE sectors. Waves also suffer from energy dissipation, reducing the height until more than 80% falls into the range of 0-2 m.

In the other open boundary of the English Channel, the North Sea, waves are already lower in origin, more than 90% are below 2 m. Regarding the directions, the range is weighted to NNW-NE, more than 50% comes from those sectors, although waves arrive from the Atlantic Ocean and the sectors SW and WSW represent around 35% of the total.

With respect to winds, they blow mostly to the East in the open boundary of the Atlantic Ocean, with a range of directions covering all the sectors, but mainly concentrating from NNE to SE, presenting a maximum wind speed up to 25 m/s (wind roses are shown in **Figure 9** for the same three representative points as for waves). In the central English Channel, in comparison with the Atlantic Ocean, winds mostly acquire a NE-ESE component. The wind speed is lower in the North Sea, but still blows to a NE sector, following the orientation of the Channel.

2.4.2. The Normandy coasts

The Normandy coastal areas are very dynamic environments offering different services including wildlife habitat, erosion and flooding protection, tourism, economic and recreational activities. In the last decade, these areas have received additional interest for their high vulnerability to extreme climate drivers and anthropogenic activities inducing risks of flooding and erosion. Among the main features, the Seine Estuary is located in the middle part of the Normandy region (**Figure 8**), a river-tide system with high spatial variations of fluvial and tidal energy.

The coasts of Normandy, considered as the one of the most hazardous regions, historically exposed to marine submersion (Turki et al., 2020a; 2020b; Soloy et al., 2021), constitute an area strongly influenced by tides which are semidiurnal and have macro to mega tidal ranges (Levoy et al., 2000), from around 3 m at the neap tides up to 10 m at the spring tides. An accurate estimation of flooding scenarios is essential to protect against those risks the 3 NPP that can be found on the coasts of Normandy (shown in blue in **Figure 9**).

In the North of the Seine Estuary, the coasts are part of a region characterized by their pebble and gravel beaches, where the chalk cliffs that get eroded by the action of water contribute to this configuration. In the South of the Seine River the beaches are mainly sandy beaches, with grain sizes notably smaller than in the North. Three sites are chosen as representative of these morphologies for the subsequent studies, with a pure gravel, a mixed and a sandy beach, and with previous works already developed in them due to the installation of video monitoring systems (VMS) to record and analyze the hydro- and the morphodynamics of the beaches. The three VMS installed are composed of three cameras (**Figure 10**) with different fields of view. The selected sites are Etretat, Hautot-sur-Mer and Villers-sur-Mer, whose locations can be seen in **Figure 9**.

The VMS installed at the three locations (**Figure 11**) provide different products useful for the analysis of hydrodynamics. Three cameras are installed at each of the three beaches, and each camera records 6 images per hour only during daylight, with every image recorded with an exposure time of 10 minutes. On these average images, called timex, some results can be extrapolated, such as the range of run-up/run-down or the breaking area of waves during the 10 minutes of exposure. The var images correspond to the variance images during the 10 minutes. The expected data set for one year includes about 78000 images per VMS, with a resolution of 1936x1216 pixels in Hautot-sur-Mer, 3264x1856 pixels at Villers-sur-Mer and 3840x2160 pixels in Etretat. Other possibility are the so-called “timestacks”, which register the evolution in time of the shoreline on one specific profile of the beach, recording the motion of the sea wave by wave during the 10 minutes.

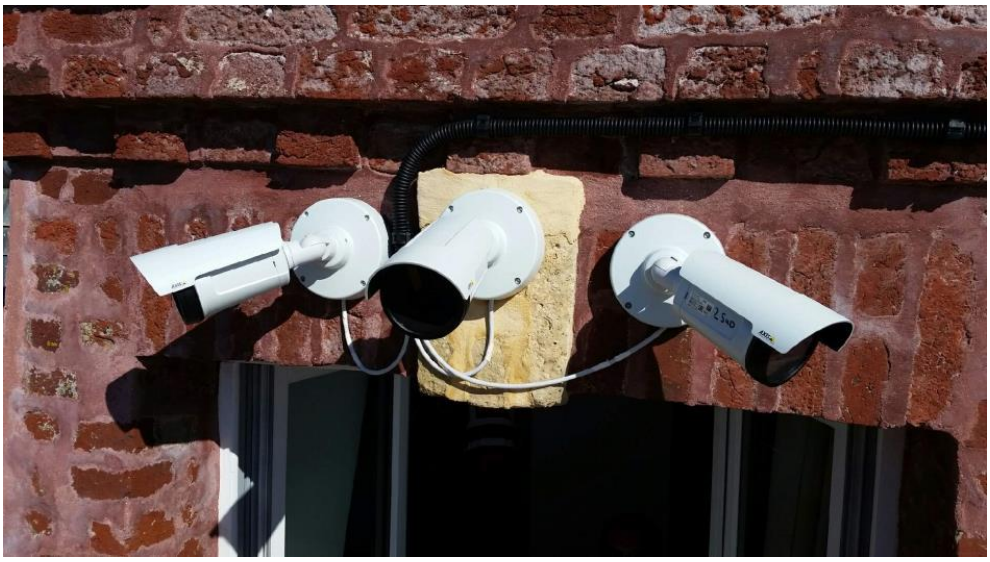

Figure 10. *Example of VMS cameras installed in Etretat (picture of Y. Soufflet 2018)*

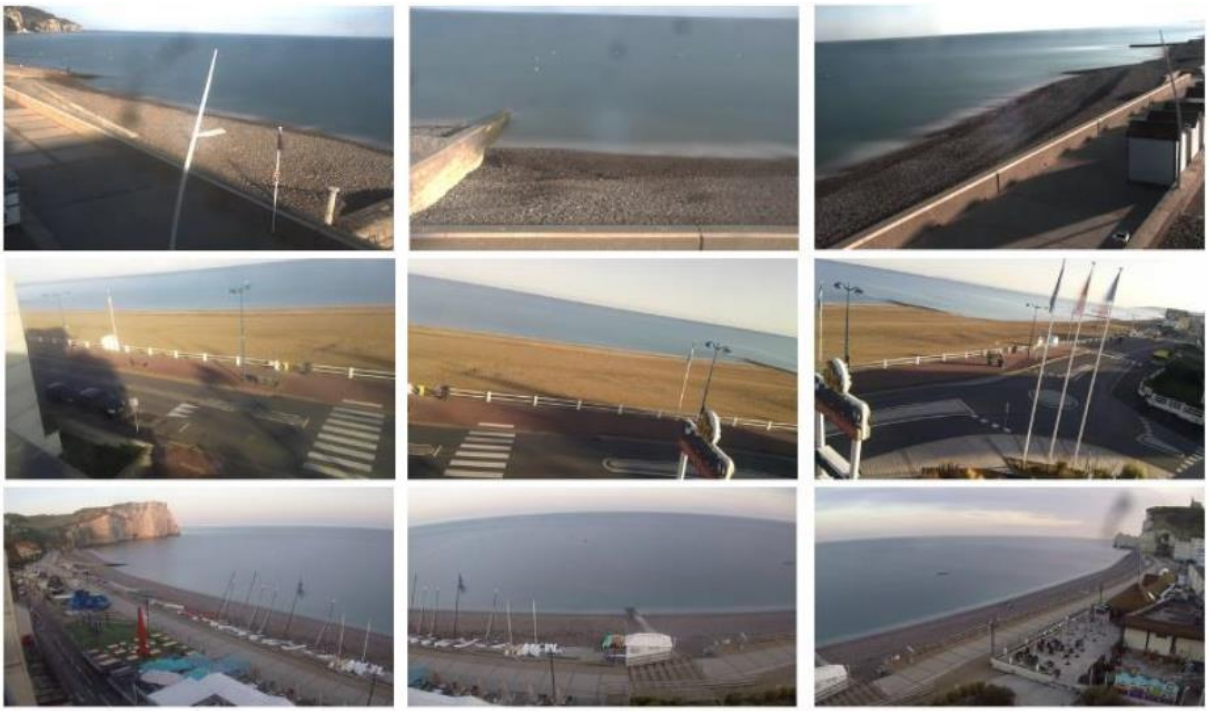

Figure 11. *Panoramic composition of the 3 camera views in Hautot-sur-Mer (top), Villers-sur-Mer (center) and Etretat (bottom) (modified after Soloy et al., 2021)*

2.4.2.1. Etretat

The beach of Etretat is located between two of these cliff systems, the *Falaise d'Aval* is in the West, and the *Falaise d'Amont* is in the East. It is about 1 km long with the width varying with the tidal range. The shoreline is oriented to the Northeast with an inclination of North 47°. The beach

has a steep slope of up to 12% and can be described as a pure pebble beach according to Jennings & Shulmeister (2002), although below the pebbles there is a sandy layer (**Figure 12**). The profile of the beach presents a vertical concrete wall that continues the morphology of the cliffs in the part of the populated area.

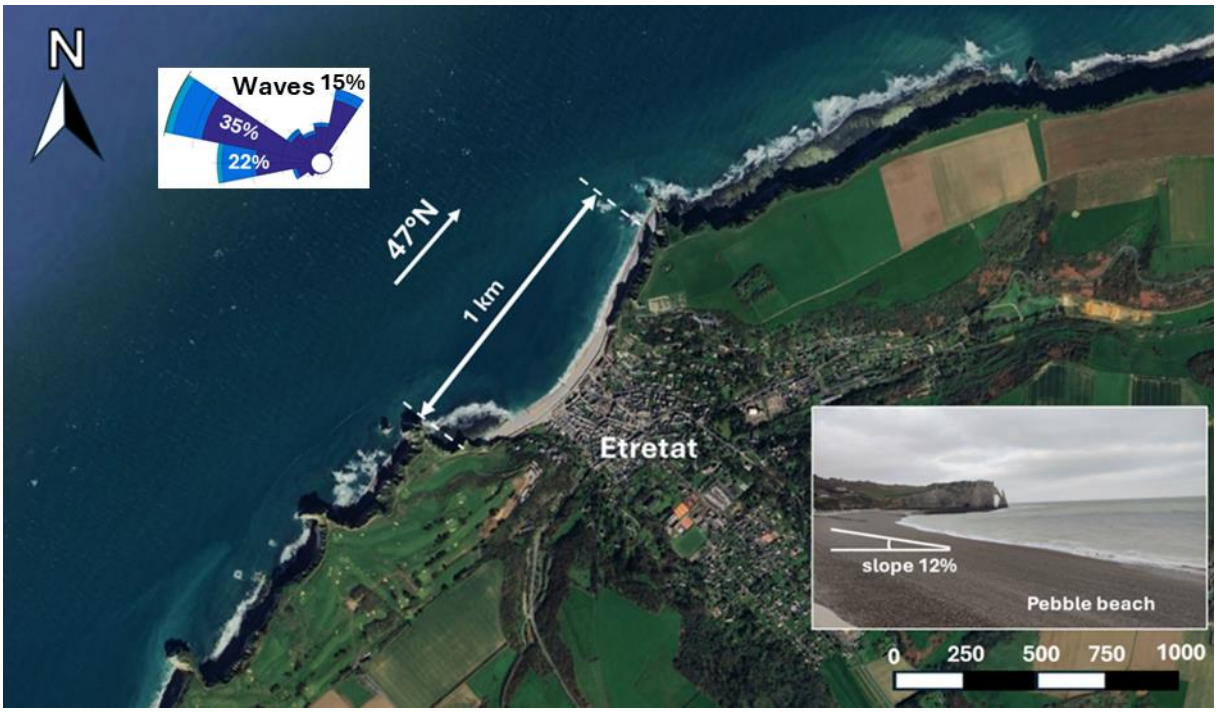

Figure 12. *Etretat beach from a satellite view with the length (~1 km) and the slope (~12%) in the pebble beach*

2.4.2.2. Hautot-sur-Mer

The Hautot-sur-Mer beach is located in the West of the city of Dieppe, being semi-enclosed by chalk cliffs. This beach is 1.1 km long, with width varying with the tidal range, being a composite beach (Jennings & Shulmeister, 2002), which includes a sandy low tide terrace and a pebble ridge, with a slope of 10% for the latter. The shoreline of Hautot-sur-Mer is oriented to the ENE, with an inclination of North 71° (**Figure 13**). It is remarkable that there are several cross-shore groins along the beach that sustain the transit of pebbles, and it also presents a seawall at the end of the profile in the part of the population.

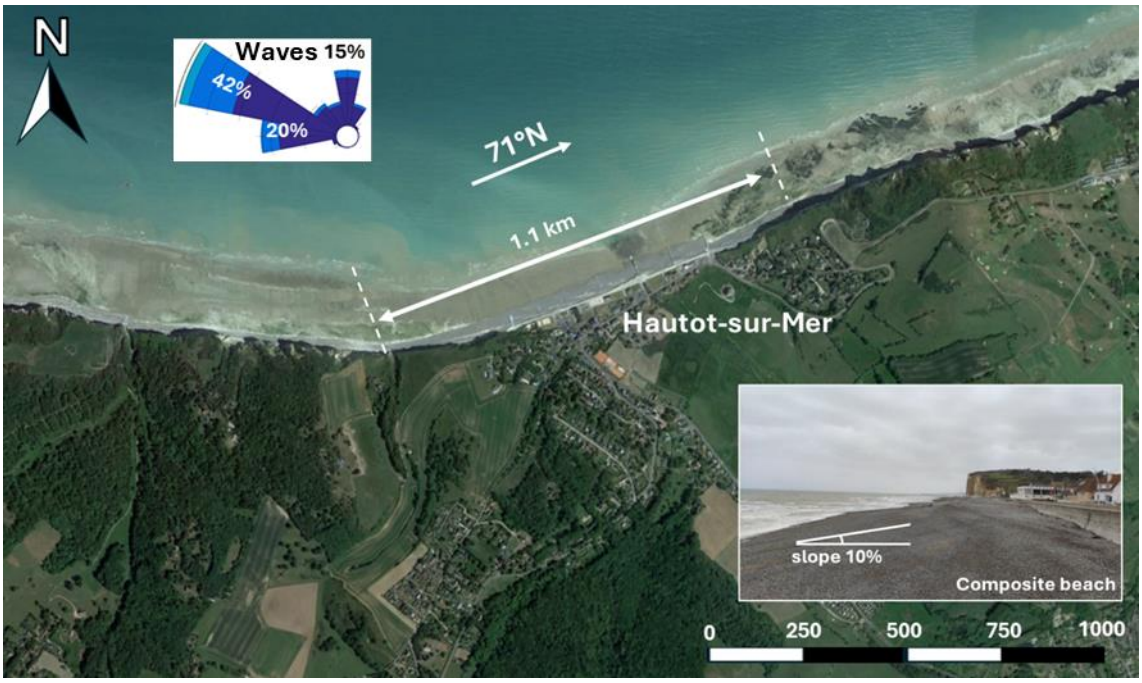

Figure 13. *Hautot-sur-Mer beach from a satellite view with the length (~1.1 km) and the slope (~10%) in the composite beach*

2.4.2.3. Villers-sur-Mer

The beach of Villers-sur-Mer is located in the Southwest of the Seine Estuary, it is an open sandy beach that occasionally can present some pebbles but considered just constituted by sand. This beach is more than 2.5 km long, also with a width varying with the tidal range that can expand up to 300 m wide. This beach is much flatter, with less than 1% of slope (**Figure 14**). The shoreline of Villers-sur-Mer is also oriented to the ENE, with an inclination of North 62°.

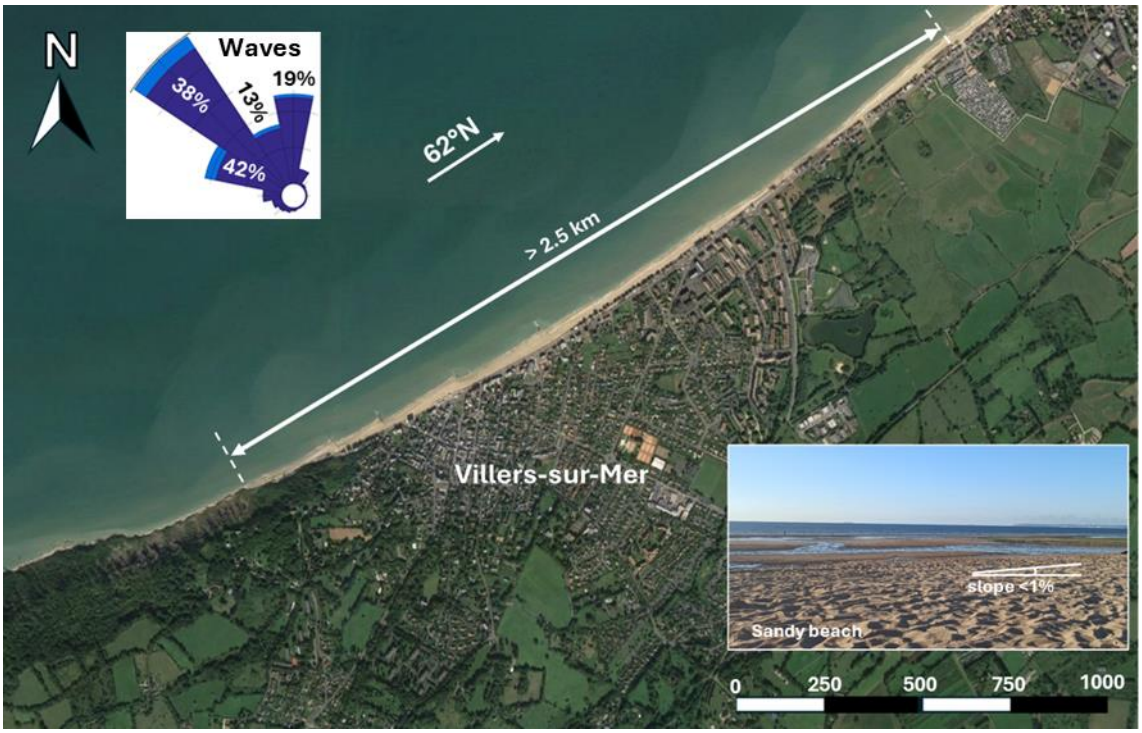

Figure 14. *Villers-sur-Mer beach from a satellite view with the length (>2.5km) and the slope (<1%) in the sandy beach*

In contrast to Etretat and Hautot-sur-Mer, where the 10 m of depth are reached in just 600 m and 2.3 km, respectively, and the 20 m of depth in 4.1 km and 7 km, the gentle slope in Villers-sur-Mer continues seawards due to the deposit of sediments of the Seine River. That makes that the 10 m of depth are reached in 7.1 km and the 20 m of depth in more than 14 km, producing a large shallow area that contributes to the dissipation of energy in the waves.

2.5. CONCLUSIONS: RESEARCH QUESTIONS AND ORGANISATION OF THE DISSERTATION

Based on the state of the art, developed in this chapter, a series of research questions have been addressed to investigate the hydrodynamics from the scale of the English Channel to the scale of Normandy coasts in response to extreme events by combining different stochastic and numerical approaches:

- *How can we characterize the non-stationary connections between the global climate oscillations and the multi-timescale extreme hydrodynamics in the English Channel? How is this non-stationarity considered for developing the stochastical downscaling and*

estimating extremes? What are the main storm classes, representative of multi-timescale extreme hydrodynamics in the English Channel during the last decades?

- *How can we characterize the hydrodynamic evolution of storms from the English Channel towards the Normandy coasts during the last 40 years, and to what extent can numerical modelling accurately reproduce the extreme event hydrodynamics? What are the main physical transformations of extreme energy scenarios within the basin and close to the coast? How is the severity of extreme storms (magnitude, duration) controlling the evolution of storms within the Channel?*
- *By integrating the scales from the regional basin to the local Normandy beaches, how can we characterize and model the coastal flooding, in response to extreme scenarios at this scale close to the coastline? To what extent can phase-resolving models integrating the sub-resolution of depth accurately reproduce the flooded water extent? How varies coastal flooding in different Norman coastal contexts, from sandy to mixed and gravel beaches?*
- *What are the potential hydro-macrodynamic coastal applications that could be developed exploring the different findings of this PhD research?*

Then, the different set of research motivations, addressed above, to fulfill the main objectives of this PhD, "Coupling stochastic and numerical approaches for investigating the dynamics of coastal extreme events: case of the English Channel and the Normandy coasts", the structure of the manuscript has been developed based on the overall questions though 7 chapters.

The first and the last chapters present the general context with the main PhD objectives and the concluding findings, respectively.

After Chapter 2, describing the state of the art and the study sites, the results of this research have been organized following 4 chapters according to the different scientific publications developed during this work:

- Chapter 3 follows the stochastic study of extreme events in 7 locations in the English Channel, by firstly approximating the concept of an extreme value in the coastal hydrodynamics field. Following, a spectral analysis and non-stationary extreme value analysis are performed, correlating the results with the main atmospheric patterns and climate indexes. Finally, an extreme event is defined, and a classification and clustering applied over the dataset of storms obtained in the same locations.
- Chapter 4 gathers up the numerical study of extreme events from the regional scale of the English Channel to the local scale in the coasts of Normandy. A database of 40 years is

generated covering the surface of all the basin. This numerical downscaling allows following and characterizing the behavior of storms when they are propagating through the Channel and approaching the Normandy coasts, already focusing on some of the locations mentioned above.

- Chapter 5 is centered on the study of extreme events when they arrive to the coasts of Normandy, describing their behavior and their impact to assess the risks of this type of events on the three types of morphologies of the sites presented. Run-up and overtopping are the main focus of research to describe the interaction of the coast.
- Chapter 6 exhibits some applications of the data generated throughout the dissertation with the already learnt dynamics of extreme events, combining the different stochastic and numerical approaches, with the aim to, overall, contribute to coastal risk management.

CHAPTER 3

ON THE USE OF STOCHASTIC APPROACHES TO INVESTIGATE THE MULTI-SCALE DYNAMICS OF EXTREME STORMS IN THE ENGLISH CHANNEL

Coastal hazards like flooding and beach erosion are caused by storms impacting shoreline communities and environments. These extreme oceanic events are characterized by their wave height and storm surge. Atmospheric patterns and climate indexes, such as the North Atlantic Oscillation (NAO), play a crucial role in their understanding. Through spectral and non-stationary probabilistic analyses, it is possible to reveal low-frequency variability influenced by meteorological factors and correlations between these indexes and coastal extreme values. Classifying typical extreme events helps understand their intensity and potential impacts. This chapter details the methodologies and spectral and non-stationary probabilistic analyses, with atmospheric indices correlated to extreme values of waves and surges. Additionally, storm duration is defined to enhance understanding of storm characteristics, allowing the calculation of wave energy and ranking the most energetic storms. At last, a classification of typical extreme events in the English Channel is performed, identifying and categorizing storms, providing insights into compound events and clustering similar extreme wave events.

Part of this chapter is the subject of a new publication in preparation for a submission to the journal Oceanologia before December 2024: C. López Solano, P. Chauris, E. I. Turki et al., Non-stationary analyses of extreme waves and surges for investigating the multi-scale dynamics of coastal storms in the English Channel (provisional title).

3.1. INTRODUCTION

Coastal hazards like flooding or beach erosion are produced by storms arriving to the shoreline communities, facilities, and environments. These storms are extreme events generated in the ocean or the open seas that can be identified by the main variables extensively used to characterize the hydrodynamics of the sea, like waves and the variations in the water level. Within these processes, wave height and storm surge are the variables that define the extreme values that are used to study oceanic and coastal hazards, and these extremes, generally induced by atmospheric patterns, are among the main causes of threats like coastal flooding (Vousdoukas et al., 2012). Researchers employ various approaches to investigate extreme waves and extreme sea level dynamics (Rueda et al., 2016), including the impact of global climate oscillations (Massei et al., 2017; Turki et al., 2019). In the present work, these two stochastic drivers are analyzed, the significant wave height and the storm surge, obtained from measurements of tide gauges located on the French and British coasts of the English Channel, and from a wave reanalysis database of the Copernicus Marine Data Service generated by the MetOffice in the same locations.

In recent decades, one of the most common approaches are the spectral analyses and the non-stationary probabilistic approaches (Coles, 2001; Mínguez et al., 2012), and, alongside climate indexes, they have shown that atmospheric patterns like the North Atlantic Oscillation (NAO) significantly influence sea level dynamics and their associated extreme events (Turki et al., 2020a; 2020b). For instance, changes in the NAO have been linked to variations in sea levels and storminess in the Mediterranean (Masina et al., 2015) and along European coasts (Menéndez & Woodworth, 2010). Then, the selection of atmospheric patterns and their link and influence on local extreme values has been proven fundamental to understand and investigate the occurrence and the severity of these events. Following this, a spectral analysis is applied to the time series of extreme values of waves and surges and their demodulated variables obtained in the current study, as well as a non-stationary probabilistic analysis of these extreme values.

The spectral analysis aims to find low-frequency variabilities by decomposing the signal of extreme waves and surges that can be explained by a combination of meteorological, oceanographic, and hydrological factors.

The extreme value analysis can be performed with different methodologies. In this case, the extreme values have been obtained as the monthly maxima of the two variables, fitting a Generalized Extreme Value (GEV) distribution to them, widely used for modelling maxima, but improving it as with non-stationarity approach with the consideration of certain climate indexes. These indexes have been the already mentioned NAO, the Atlantic Multidecadal Oscillation

(AMO), the Sea Level Pressure (SLP) and the Sea Surface Temperature (SST), with which previous works have already demonstrated the link with extreme surge dynamics in the same studied location, the English Channel (Turki et al., 2020a).

Moreover, the probability of a compound event of extreme wave height and extreme surge also intervenes in this approach, since coastal flooding is often produced by more than one single factor (Rueda et al., 2017), needing, then, a joint analysis of these variables to determine realistic hazards that are actually occurring (Chebana & Ouarda, 2011). A copula is chosen to model this dependance structure, carrying out a bivariate analysis, in which the non-stationarity is included one more time to accurately represent these phenomena. The results generate a bivariate distribution for each study site with the different joint return levels that can be used for risk assessment.

Nevertheless, extreme values of increased wave height and storm surges are not enough to explain the whole development of a storm, reason why a threshold must be defined in the time series of these variables to obtain the complete evolution in time of an extreme event, providing the duration of a storm as a fundamental characteristic. By including the duration, multiple outcomes can be acquired like the wave energy or the storm energy content, which, subsequently, allows a classification of these extreme events in terms of intensity (Mendoza et al., 2011). It is important to identify and categorize the coastal storms because it has been already proven that high-energy storms can accelerate shoreline erosion (Morton & Sallenger, 2003), amongst other derived morphodynamic responses of the shore like overwash on beaches, overtopping on protection structures, or the already mentioned coastal flooding.

Throughout the present study the extreme events over a predefined threshold in the time series of significant wave height and surges are calculated to later obtain the wave energy, which, first separately and then jointly, allows to characterize and categorize the different storms on the studied locations. A classification is performed on the database of wave and surge storms, by training a model that is able to identify the occurrence of compound events or an extreme event of just one of the variables. A clustering is also applied to the dataset of extreme waves, including the wave energy, to obtain different classes that can be grouped according to their similarity.

The chapter is structured as follows: In Section 3.2 a definition of the stochastic drivers is presented, including a description of the databases. The spectral analysis is presented in Section 3.3 with the methodology and the results. In Section 3.4 the non-stationary probabilistic approach is described. The definition of an extreme event and the analysis of these storms is included in

Section 3.5, and Section 3.6 is for the classification of the typical extreme events in the English Channel. Finally, in Section 3.7 the results and discussed and some conclusions are outlined.

3.2. STUDY AREA AND DATA

3.2.1. Stochastic drivers

The typical stochastic drivers of hydrodynamics from a maritime perspective are waves, sea level variation, and currents. This study focuses on changes in the free surface of the water, so currents are not of great relevance, primarily focusing on the analysis of waves and sea level. Waves are defined by their amplitude, or wave height, their period, and their direction, fundamental to later proceed to the analysis of extreme events. The wave height as a stochastic variable is usually taken as the significant wave height (H_s), that can be defined from a statistical or a spectral point of view. From a statistical perspective, it is the average of the highest third of a wave height record during some specific time $H_{1/3}$, frequently a sea state of 1 or 3 hours in the most commonly used databases (Hersbach et al., 2023. E.U. Copernicus Marine Service Information (CMEMS) 2024a). From a spectral approach, it can be calculated as:

$$\mathrm{H}_{m0} = 4\sqrt{\int S(f)df} \tag{2}$$

where $S(f)$ is the density spectrum and f is the frequency (Elsevier Ocean Engineering Series, 1999). For non-breaking waves, significant wave height H_s can be obtained from any of them, since $H_{1/3} \approx H_{m0}$, and both are used indistinctly across the present study.

The period, inverse of the frequency, is either defined by the peak period T_p or by the mean wave period T_m. The peak period (T_p) is the wave period at which the variance density spectrum is maximum, i.e., the period with the highest energy of the spectrum. The energy density spectrum of a sea state can be formulated empirically for fully developed wave fields under constant wind stress (**Figure 2**). Typically, the Pierson-Moskowitz spectrum for deep water without fetch restriction or the JONSWAP spectrum for fetch-limited seas where the spectrum is more peaked around the peak frequency f_p, are used for the parametrization of the energy through the peak enhancement factor γ, that takes values between 1 and 7, usually $\gamma = 3.3$. The mean wave period T_m is statistically defined as the average value of all the individual periods of waves during a specific time, and can also be obtained from the spectrum as:

$$T_{m01} = \frac{\int S(f)df}{\int fS(f)df} \quad (3)$$

The peak period is more frequently used in the present study, but for some analyses the mean period is used too, with either the spectral or the statistical definition of it.

Finally, the direction is identified by the mean direction (θ_m), average of the directions of all the waves of a sea state. Sometimes the peak direction θ_p, the direction associated with the highest energy of the spectrum, can be used too.

Therefore, a sea state is defined by the significant wave height (H_s), the peak period (T_p) and the mean direction (θ_m), and those are, especially the wave height, the stochastic drivers used to perform the analysis of extreme values that mark a storm from a wave point of view.

The sea level is formed by different modulations of the water surface that are added to obtain the total water level. The main component in terms of amplitude is the astronomical tide, that can be parametrized by the harmonic constituents, mathematically obtained from the effect of the cyclical motion of the Earth, Moon and Sun on the tides. Up to 37 harmonic components have the greatest effect on tides and can be used to predict the astronomical tide. Large available databases allow obtaining the tidal constituents globally on specific locations, like FES2014 (Carrere et al., 2016) or TPXO (Egbert & Erofeeva, 2002), making the astronomical tide a predictable variable that does not evolve in time, keeping the same coefficients. That is the reason why the second largest component of sea level is the stochastic driver that is used to carry out extreme value analysis. This component is the storm surge, defined as the abnormal rise of the surface of water in respect to the water level predicted by the astronomical tide.

There are some other minor components of the total water level, like a modulation produced by the non-linear interaction between the astronomical tide and the storm surge, and, particularly when waves approach to the coast, a set-up of the surface of water due to the presence of waves propagating or the interaction with the bottom of the sea. In any case, the surge is the stochastic variable used in the extreme value analysis to study a storm from a sea level perspective.

At this point, the significant wave height and the surge are set as the main variables to be examined, looking carefully at their behaviors by the investigation of their time series at different locations. In this study, this analysis is centered on the English Channel and the Normandy coasts, obtaining the records of surge from a number of tide gauges located on the French and the English sides of the Channel, and wave height from a reanalysis database on the same locations.

Other variables can be included in the search of the sources of flooding, like river discharge. Fluvial flooding potentially plays an important role in compound events, contributing to coastal flooding in estuarine systems. In the English Channel, and especially on the Normandy coasts, some important estuarine systems can be found, like the Mont-Saint-Michel Bay, the Bay of Veys and the Seine Bay. This study is focused on extreme waves and surges, but future Sections explore the contribution of river discharge.

3.2.2. Description of the databases

A total number of 7 locations have been investigated across the English Channel, 4 on the French coast and 3 on the English coast, by applying the described methodology on the time series of surges recorded by tide gauges and their equivalent wave heights obtained from reanalysis (the exact locations are shown in **Figure 15**).

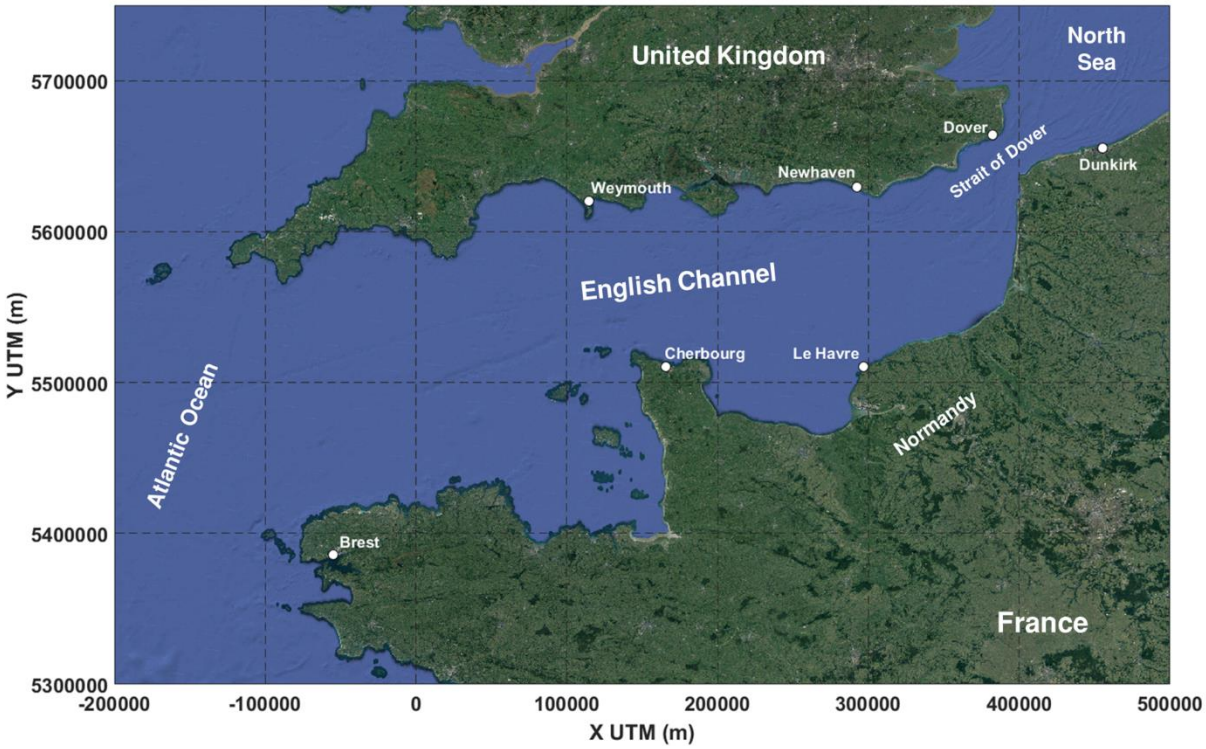

Figure 15. *English Channel between France and the UK, and the open boundaries in the Atlantic Ocean and the North Sea, with the locations of the tide gauges used for the analysis of surges*

3.2.2.1. Databases of surges

The most external location on the Atlantic Ocean is the Brest tide gauge, operated by SHOM (*Service hydrographique et océanographique de la Marine*, the Naval Hydrographic and Oceanographic Service). It is located on the left bank of the mouth of Penfeld River, near the castle of Brest (48.3829°N, 4.49504°W). The first automatic recording device (tide gauge) dates from 1846, covering nearly 300 years and making Brest the longest series of sea level measurements

in France, if not in the world. The time series of surges is available with semi diurnal frequency, from 1846 to 2017.

In the middle West English Channel, the tide gauge of Cherbourg is located in the coast of France and the tide gauge of Weymouth in the English coast. For the tide gauge of Cherbourg, the observatory is managed by the SHOM in partnership with the *Marine Nationale* and the Port of Cherbourg. It is located on the *Quai Sané* in the Cherbourg military port (49.651447°N, 1.635508°W), with semi diurnal frequency series of surges measurements from 1943 to 2017.

The tide gauge of Weymouth is located in the Weymouth Harbor on The Quay, managed under the local authority of Weymouth and Portland (50.608500°N, 2.447944°W). Hourly data of sea level and surges for the years 1991 and 1992, and data with a frequency of every 15 minutes from 1993 on are provided.

In the mouth of the Seine on the coast of Normandy, the tide gauge of Le Havre is also operated by SHOM, but in partnership with the state agency *Grand Port Maritime du Havre* (GPM or Great Port of Le Havre). The RONIM tide gauge unit is installed on the *Quai Meunier* in the port (49.481892°N, 0.10598°E) and provides an hourly time series of surges from 1938.

Facing Normandy in the coast on the UK of the English Channel, a pressure system gauge was installed in May 1982 in the west bank mouth of the Ouse River, in the Newhaven Harbor (50.781778°N, 0.057028°E), although there had been a series of installations from at least 1890. Hourly data of sea level and surges are provided from 1982 to 1992 and every 15 minutes from 1993.

In the Strait of Dover, on the eastern boundary of the English Channel, the Dover Harbor on the British coast has a tide gauge on the northern breakwater of the Inner Harbor (51.114395°N, 1.322550°E), with records from 1958 to 1990 every hour and every 15 minutes from 1994, with several gaps because of records unreliable or erratic readings due to blocking of the stilling well gauge.

In the North Sea, the port of Dunkirk is located on the French coast, it is equipped with a RONIM tide gauge since September 1996, but the first records date from 1956 inside the port (51.048091°N, 2.366698°E). The observatory is managed by SHOM in partnership with the *Grand Port maritime de Dunkerque*. The sensor measures the sea level inside the stilling well providing semi diurnal frequencies for surges from 1956 to 2016.

The component of surges S has been provided by IRSN. S was extracted from the total signal of sea level, measured by the tide gauge. S corresponds to the skew surge, defined as the

difference between the maximal observed sea level and the predicted astronomical high tide, resulting in an approximately 12 h and 25 min time step. Once the Mean Sea Level (MSL) was removed, surges have been separated from the stationary tidal signal and estimated by subtracting the maximum of the theoretical tide predicted from the maximum observation (**Figure 16**). Surges of high tides are estimated as the difference between the maximum water level and the predicted high tide during a tidal cycle. The two levels can be shifted by a few minutes or hours.

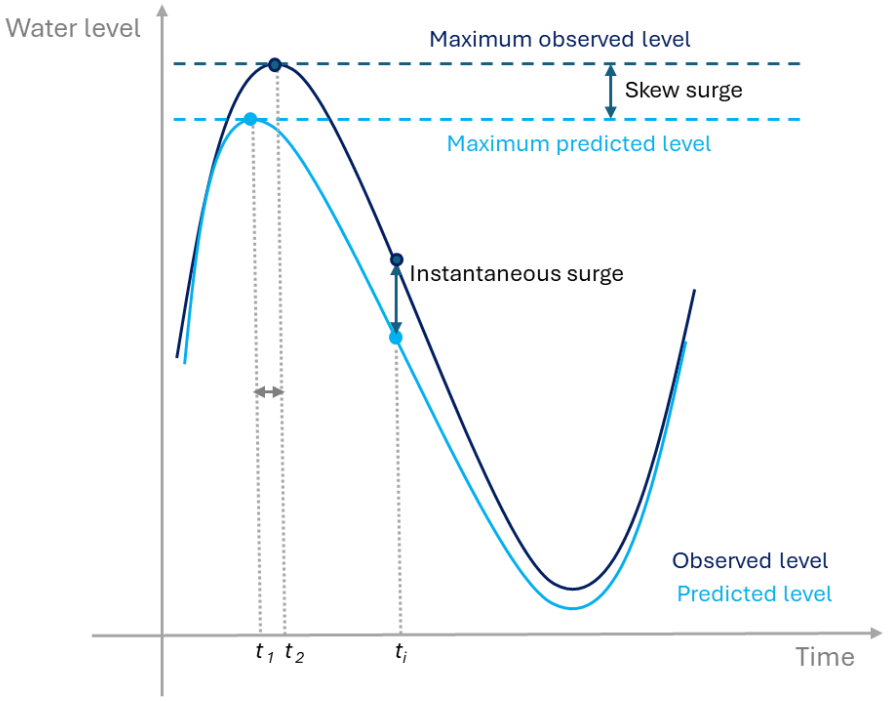

Figure 16. *Calculation of the skew surges S from the measurements of sea level of the tide gauges. Adapted from the website of SHOM (refmar.shom.fr)*

Since this S time series has significant gaps in measurements, regional information from neighboring tide gauges can be used for imputation of data, i.e., filing in the gaps, through the development of statistical approaches (e.g., use of the spatial extremogram in Hamdi et al. (2019)).

3.2.2.2. Wind and wave databases

Significant wave height H_s has been obtained from a particular database of the Copernicus Marine Service, the Atlantic-European North-West Shelf – Wave Physics Reanalysis (E.U. Copernicus Marine Service Information (CMEMS) 2024b). This product provides 3-hourly hindcast outputs from a wave model for the North-West European Shelf, with a temporal extent since January 1980. The wave model used for the simulations is WAVEWATCH III and the North-West Shelf configuration is based on a spherical cell grid mesh with a spatial extent from 46°N to 62.75°N of latitude and from 16°W to 13°E of longitude covering the sea surface. The model is

forced by lateral boundary conditions from a Met Office Global wave hindcast, and the atmospheric forcing is given by the ECMWF ERA-5 Numerical Weather Prediction reanalysis (O'Dea et al., 2012, 2017; King et al., 2018). The product is updated biannually providing a six-month extension of the time series. Example maps of wave height, wave period and wave direction are presented in **Figure 17**, **Figure 18** and **Figure 19**, for 10/02/2020 at 6 am, corresponding to the peak of storm Ciara when it arrived to the coasts of Normandy.

The chosen database has been the NWSHELF instead of the most commonly known ERA5 database because of its highest resolution. The ECMWF ERA-5 Numerical Weather Prediction reanalysis (King et al., 2018; O'Dea et al., 2012, 2017) has two main databases: the single levels, more related to hydroclimatic variables, and the pressure levels, more related to atmospheric variables. ERA5 is the fifth generation ECMWF reanalysis for the global climate and weather. This product provides hourly estimates for a large number of atmospheric, ocean-wave, and land-surface variables, available from 1959 onwards. Data is presented in a regular spherical grid of 0.25 degrees for the atmospheric reanalysis and a regular grid of 0.5 degrees for oceanic variables (Hersbach et al., 2020). The atmospheric variables cover not just sea surface, but also the land, and will be used in following sections in this research. As an example, wind speed, wind direction and atmospheric pressure maps are presented in **Figure 20**, **Figure 21** and **Figure 22**, again for 10/02/2020 at 6 am, the peak of Ciara storm on the Normandy coasts.

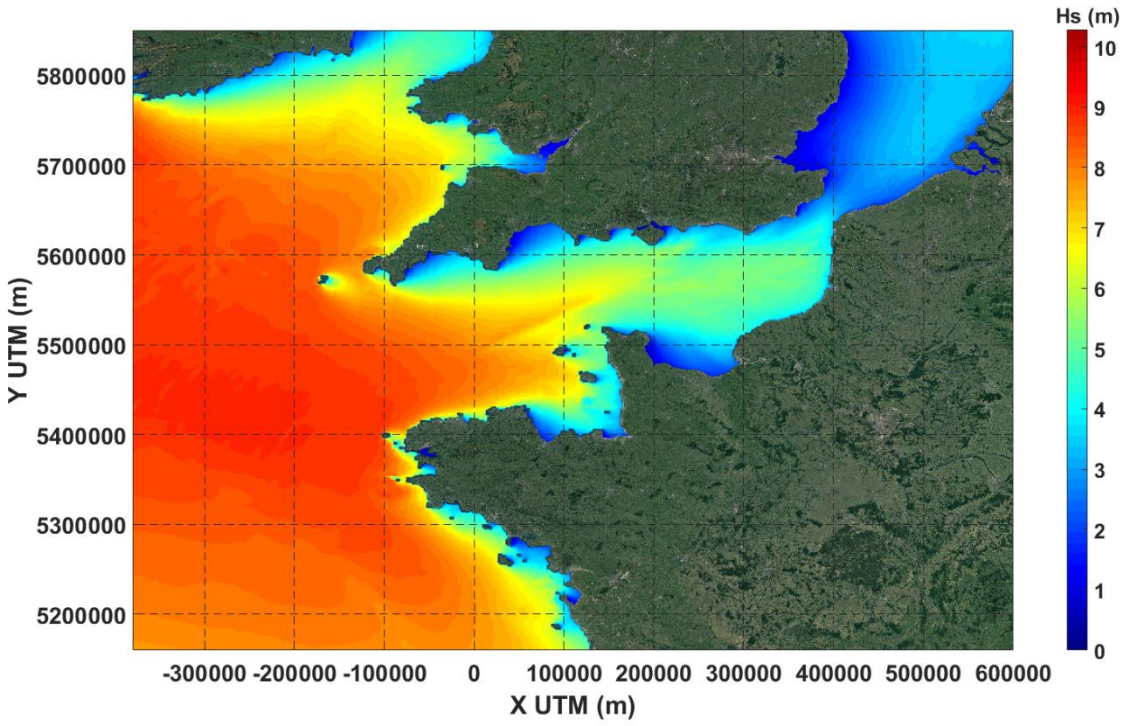

Figure 17. *Wave height (m) map in the English Channel, obtained from the NWSHELF database, taken as an example for 10/02/2020 at 6 am (storm Ciara)*

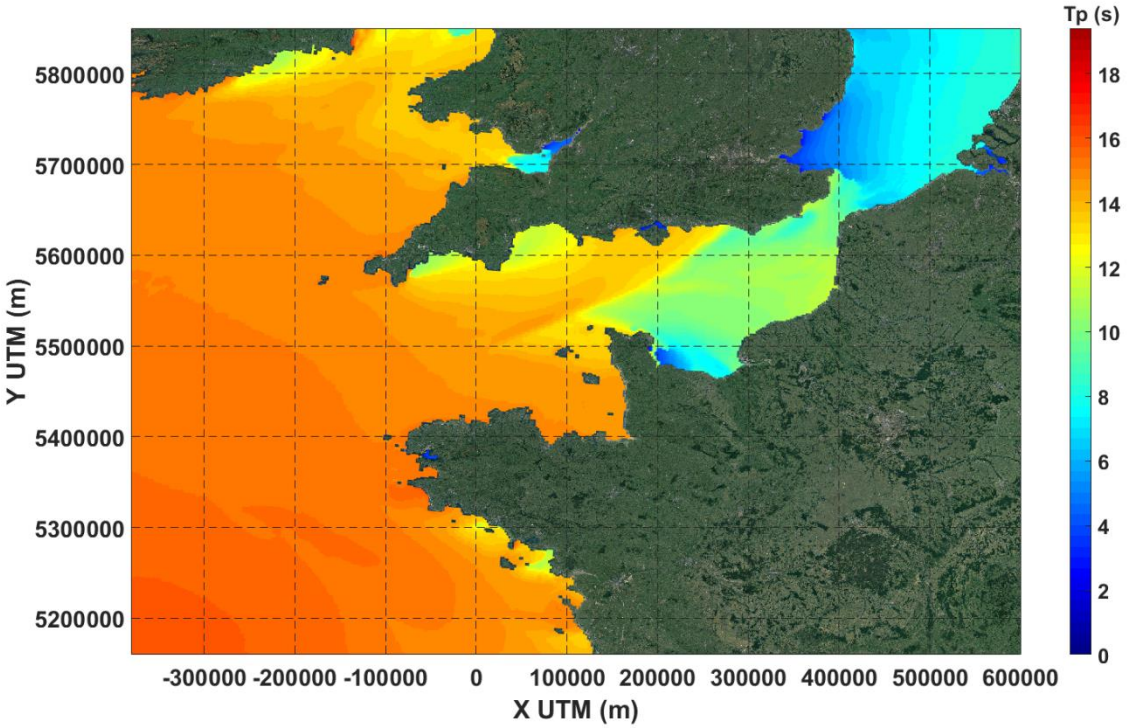

Figure 18. *Wave period (s) map in the English Channel, obtained from the NWSHELF database, taken as an example for 10/02/2020 at 6 am (storm Ciara)*

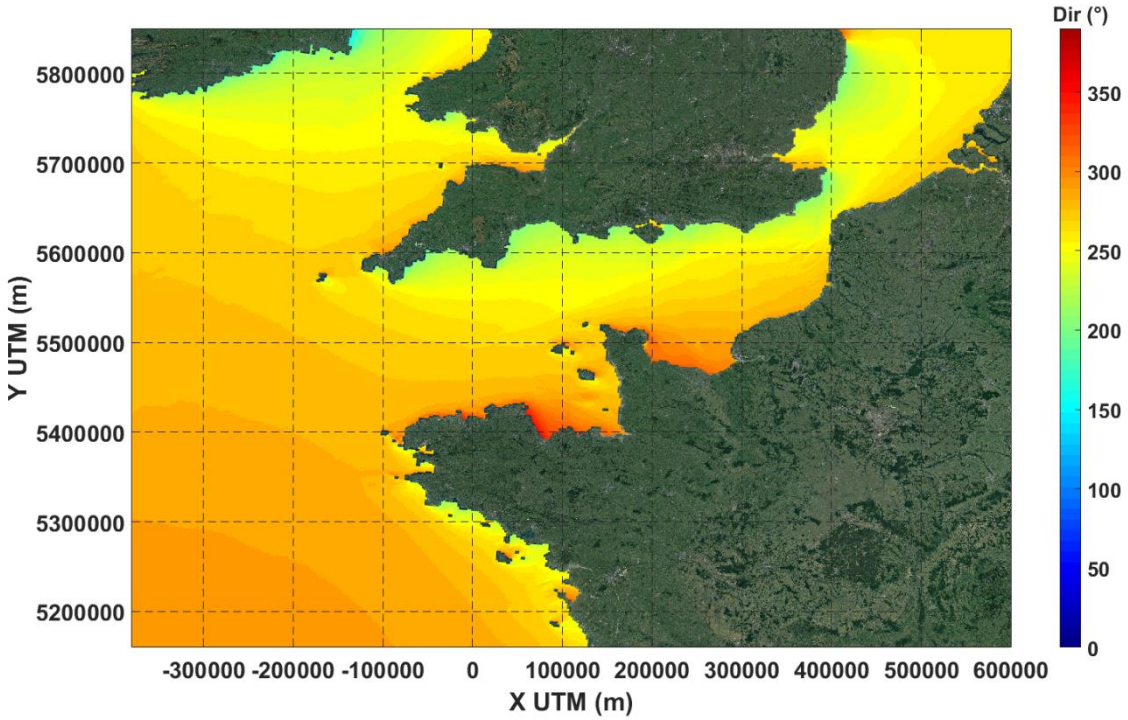

Figure 19. *Wave direction (°) map in the English Channel, obtained from the NWSHELF database, taken as an example for 10/02/2020 at 6 am (storm Ciara)*

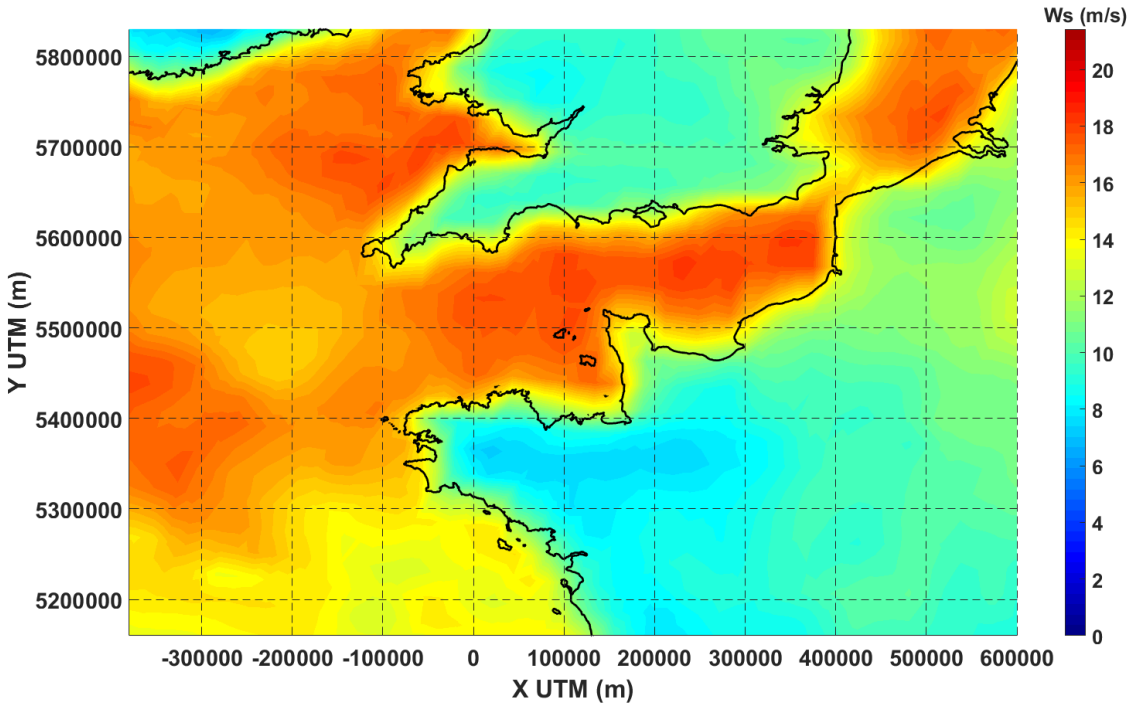

Figure 20. *Wind speed (m/s) map in the English Channel, obtained from the ERA5 database, taken as an example for 10/02/2020 at 6 am (storm Ciara)*

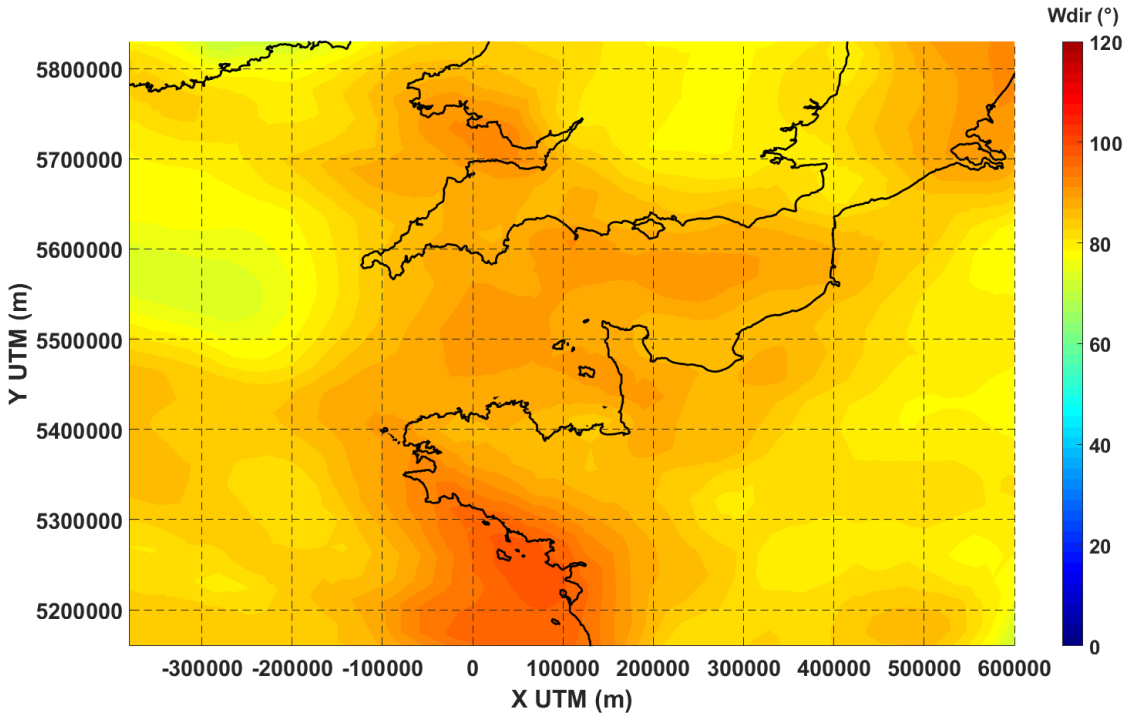

Figure 21. *Wind direction (°) map in the English Channel, obtained from the ERA5 database, taken as an example for 10/02/2020 at 6 am (storm Ciara)*

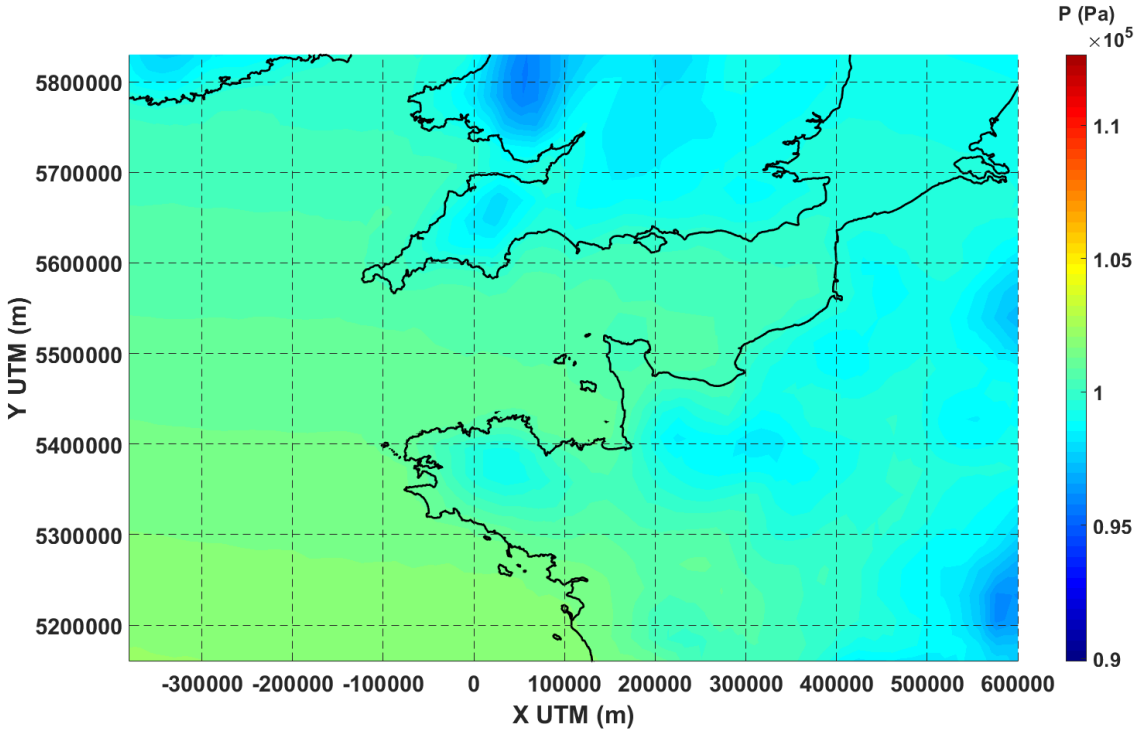

Figure 22. *Atmospheric pressure (Pa) map in the English Channel, obtained from the ERA5 database, taken as an example for 10/02/2020 at 6 am (storm Ciara)*

3.3. SPECTRAL ANALYSIS OF TIME SERIES AND EXTREME VALUES

3.3.1. Wavelet spectral analysis

The spectral analysis of the time series can lead to finding the multi-time-scale variability of the analyzed variables, also finding the time-scale correlations with global climate patterns that explain their behavior, as demonstrated by previous studies (Massei et al., 2017; Turki et al., 2019). High-resolution spectral techniques like the multi-resolution wavelet allows performing the frequency decomposition that facilitates finding the correlations between the global patterns and the different frequencies obtained, with a special focus on the connection between stormy events and the atmospheric circulation.

Reproducing the methodology presented by Turki et al. (2019, 2020a, 2020b, 2023), the non-stationary dynamics of surges S and significant wave height H_s have been investigated using the wavelet spectral analysis. First, the continuous wavelet transforms (CWT) of S and H_s were calculated to identify the distribution of energy between the different timescales. Then, a Maximum Overlap Discrete Wavelet (MODWT) multiresolution analysis was applied with the aim

to extract the internal components and their assigned variances explaining the different timescales of the total variability. This decomposition consists of applying a series of iterative filtering to the signal by the use of low-pass and high-pass filters able to produce the spectral components. The total signal is separated into a relatively small numbers of wavelet, also called spectral, components from high to low frequencies that together explain the total variability of the signal. For each spectral component, the percentage of energy representing the importance of the detail in the total variability is estimated. The components or wavelets obtained can be associated with different timescales, from intermonthly to interdecadal, and with peaks of energy of the continuous wavelet spectra.

3.3.2. Multi-timescale variability of time series and extreme values

Firstly, the extreme values of the studied variables are obtained as the monthly maxima. When available, the analyzed time series cover the period from 1980 to recent years, limited by the availability of wave data in the date of start. The only exception is Weymouth, with a date of start in 1991. The date of end is variable, with the time series of Le Havre in 2020, Weymouth, Newhaven and Dover finishing in 2018, Cherbourg and Brest in 2017, and Dunkirk in 2016.

The time series of extreme surges measured by the 7 tide gauges and the extreme significant wave height from reanalysis on the same locations are shown in **Figure 23**.

In order to later study jointly the monthly maxima of significant wave height and surges in the 7 locations, the common data have been extracted for each site, with Brest presenting the most complete time series and Dunkirk the biggest number of gaps. It is also remarkable that Newhaven and Dover also present a high number of gaps.

For surges, the widest range of extreme values is measured in Le Havre, which also has the highest value among all stations, with 1.97 and 1.96 m, respectively. The second site with the highest value is Dover, with 1.84 m, but the second widest range is obtained in Newhaven, with 1.74 m. In the opposite side there is Cherbourg, which has the lowest absolute maximum with 0.93 m and a range of 0.96 m. Weymouth, Dunkirk and Brest present similar maxima of ~1.3 m and ranges of extreme values of ~1.4 m.

In the case of waves, it is totally conditioned by the configurations and morphologies of the shoreline, since, in some of the locations, waves arrive more dissipated than in others much more exposed. Cherbourg, Dover, and Newhaven have the highest waves with more than 4.5 m in their highest maxima and the two first with the lowest maxima over 1 m. In Dunkirk and Le Havre, waves

arrive with heights up to 2.5 m, with the smallest waves in Brest and Weymouth, barely reaching a maximum of 2.0 m.

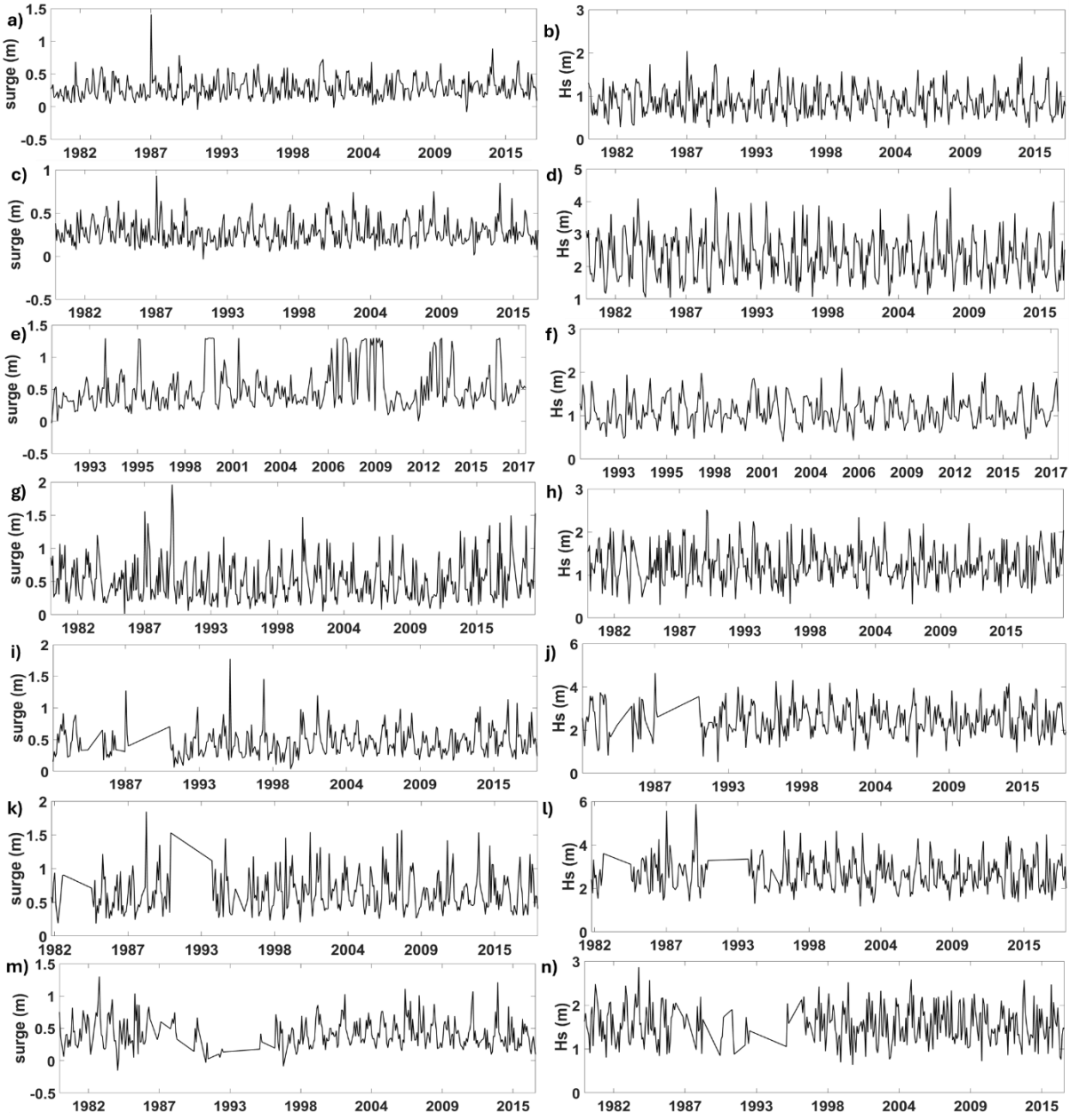

Figure 23. *Time series of a), c), e), g), i), k), and m) extreme values of surges measured by the tide gauges, and b), d), f), h), j), l) and n) extreme values of significant wave height from reanalysis for Brest, Cherbourg, Weymouth, Le Havre, Newhaven, Dover and Dunkirk, respectively*

The next step is proceeding to the spectral analysis. The continuous wavelet diagrams CWT of the monthly maxima of surges and significant wave height are calculated to visually detect the most significant frequencies of each energy spectrum.

In **Figure 24** the continuous wavelet diagrams of the British stations are presented, and in **Figure 25** the same for the French stations.

The variability of the monthly extreme surges and waves along the English Channel coasts has been investigated using the continuous wavelet transform (CWT). In the spectrum of **Figure 24** and **Figure 25** the color scale represents an increasing power (variance) from blue to yellow and red. The CWT diagrams highlight the existence of several scales for all sites with different ranges of frequencies: the interannual scales of ~1, ~ 2–4 and ~ 6-8 years for both physical variables, surges and waves. The CWT energy spectrum is absorbed by the: (1) ~ 1-year frequency, well-structured for H_S and S clearly observed for the signal of waves, (2) lower frequencies > ~ 2 years, well-illustrated for surges.

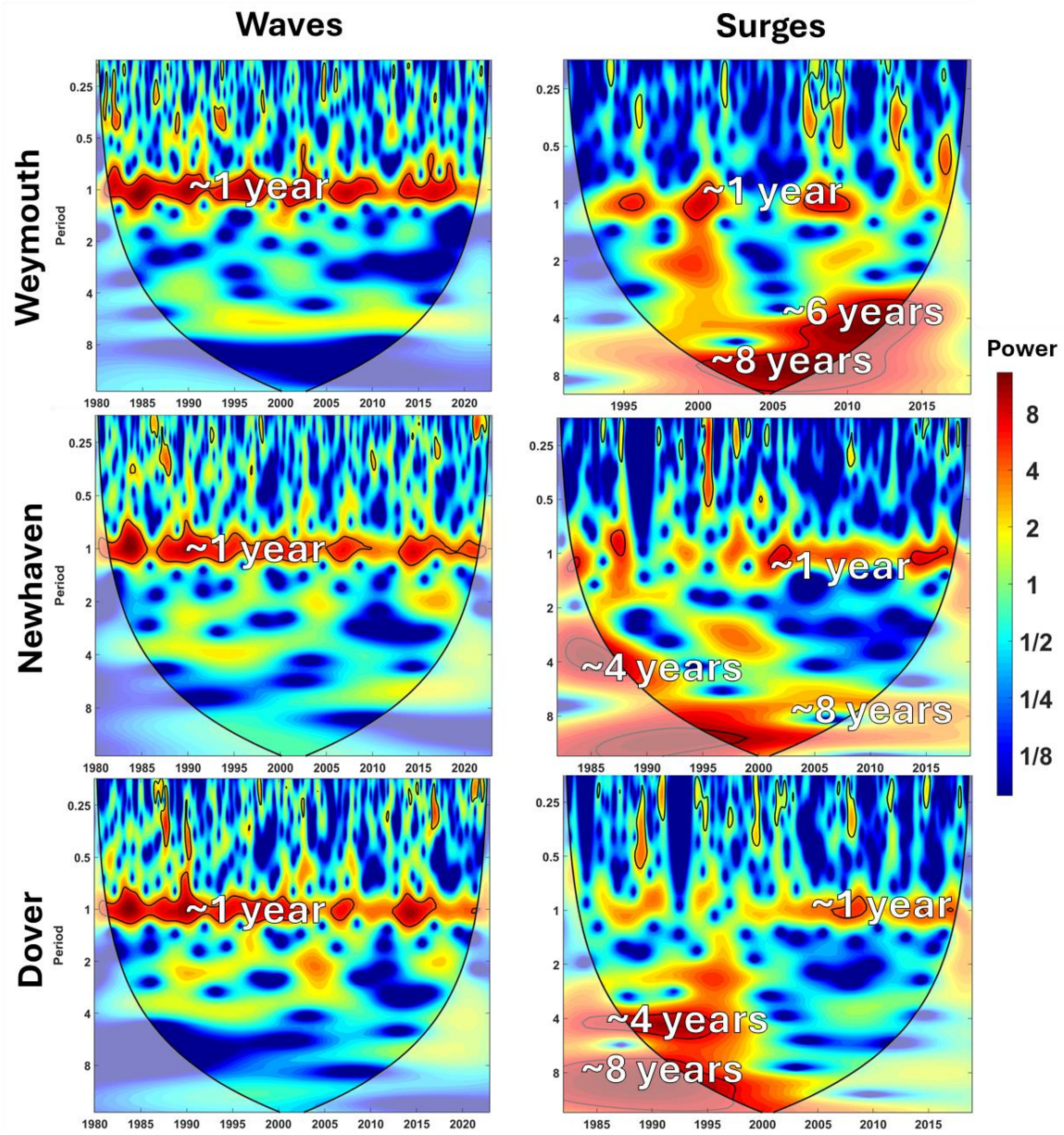

Figure 24. *Continuous wavelet diagrams of monthly maxima of significant wave height and surges for Weymouth, Newhaven and Dover, from top to bottom*

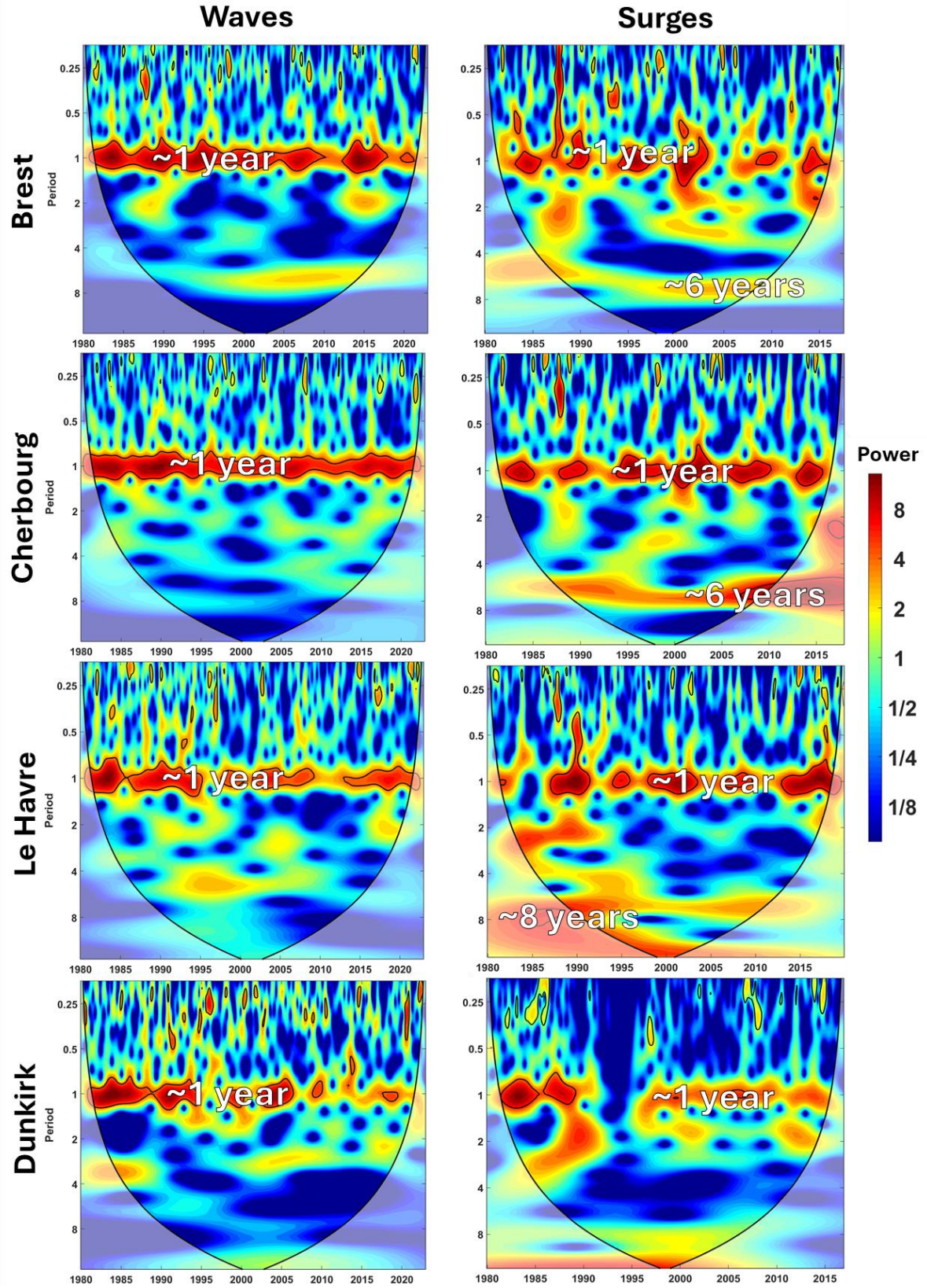

Figure 25. *Continuous wavelet diagrams of monthly maxima of significant wave height and surges for Brest, Cherbourg, Le Havre and Dunkirk, from top to bottom*

The multiresolution analysis has been applied to local surges with the aim of achieving the full timescale decomposition of the signal.

The spectral components obtained from the MODWT multiresolution analysis for significant wave height and surges in the different stations are obtained subsequently. The detailed spectral components of the monthly maxima of both variables with significant explained variance (standard deviation and energy of wavelet details) are shown in **Table 1** for S and in **Table 2** for H_s.

	~ 3 months	~ 6 months	~ 1 year	~ 2 years	~ 3 - 5 years	~ 6 - 8 years
Brest	35.1%	18.0%	19.0%	12.1%	8.1%	3.6%
Cherbourg	36.1%	19.3%	21.7%	10.3%	6.9%	4.5%
Weymouth	20.9%	16.7%	14.8%	12.0%	16.8%	13.4%
Le Havre	31.0%	17.4%	28.4%	8.8%	6.5%	4.4%
Newhaven	33.2%	16.8%	11.5%	9.8%	12.4%	5.9%
Dover	34.3%	17.7%	15.6%	9.3%	13.1%	6.5%
Dunkirk	30.3%	14.6%	18.6%	12.3%	12.8%	6.6%

Table 1. *Estimated explained variance of energy expressed as percentage of total monthly maxima of surges in the 7 study sites, with the percentages resulting from the MODWT multiresolution analysis*

	~ 3 months	~ 6 months	~ 1 year	~ 2 years	~ 3 - 5 years	~ 6 - 8 years
Brest	32.1%	16.0%	45.5%	4.0%	0.9%	1.2%
Cherbourg	27.1%	13.8%	51.7%	4.4%	1.7%	0.8%
Weymouth	30.0%	20.8%	41.7%	4.0%	1.6%	1.5%
Le Havre	37.8%	17.9%	36.1%	4.7%	2.3%	0.8%
Newhaven	33.2%	16.8%	41.5%	4.8%	2.4%	0.9%
Dover	33.4%	17.8%	39.2%	5.6%	2.5%	0.8%
Dunkirk	43.9%	18.8%	28.5%	5.2%	2.2%	0.3%

Table 2. *Estimated explained variance of energy expressed as percentage of total monthly maxima of significant wave height in the 7 study sites, with the percentages resulting from the MODWT multiresolution analysis*

The process results in separation of different components or wavelet details for each signal to quantify the variance of each component in the total signal. The oscillatory components can be associated with different timescales, from monthly to interannual scales.

Most of S variability is controlled by the intermonthly (~3 and ~6 months) and annual modes with an explained variance of ~ 37% - 53% (linear sum between both frequencies) and ~14 - 20%, respectively. This variability should be explained by a combination of different physical processes, including the effects of i) the long-term trends in the mean sea level, ii) the non-stationary tides modulating the sea level, iii) the interactions between tides and surges. This annual mode is stronger in Le Havre, which is influenced by the Seine River with a variance of 28% of the total variability, which is explained by the hydrological signature, induced by the fluvial activity of Seine River (Massei et al., 2017; Turki et al., 2019, 2020a, 2020b).

The annual and semi-annual variability are also dominant for waves with a variance range of 40% - 65% and 30% - 50%. This energy is homogenously distributed during the full study period in Brest, Cherbourg, Weymouth and then Newhaven and Le Havre; it is relatively dissipated and discontinuous in Dunkirk and Dover (**Figure 24** and **Figure 25**). At these scales, waves are controlled by the ocean-atmosphere interaction and storm waves, known as "swell waves" and accounting for most of the global ocean's surface waves. They vary annually, with large waves in the winter and small waves in the summer, due to seasonal changes of storm systems. In some coastal areas, including the coast of English Channel (Normandy and UK coasts), local wind effects cause exceptionally high wind speeds and 'Sea Waves' during the late autumn, winter and early spring, which is different from the global-scale winter maximum in swell waves. The seasonal and annual cycle of wave variability is determined by the exposure to swell and characteristics of the wave field within the region, case of Cherbourg (close to Raz Blanchard) and Brest, controlled by the Atlantic regime. Local winds, operating at the scale of months, have a more identifiable impact in Dunkirk and Dover where coasts are protected from Swell waves and exposed to the effects to North Sea wind field. The ~2-year variability is relatively significant for S with a mean range of 10% and decreases to a mean range of 5% for waves.

Lower frequencies > ~2 years exhibit high variances between 11,5% and 30% for S, compared to waves with a variance less than 5%. The dynamics of surges along UK coasts reveals the significant contribution of ~ 3-5 years and ~ 5-8 years into the total signal of surges with a variance ranging between 23% and 30%.

Here, the signal of S has been extracted from the total sea level, provided by tide gauges, by the use of the classical harmonic analysis and thanks to the assumption that the water level is the sum of the mean sea level, tides and surges. This assumption approximates the quantification of both components in the English Channel where the significant tide–surge interactions (Tomassin and Pirazzoli, 2008) and the effects of the sea level rise on tides and surges are important (e.g. Idier et al., 2017). Neglecting this non-linear interaction between the surges, tides and sea level rise suggests some uncertainties in the estimation of the high frequencies of the spectral components for daily scales, which is not the focus of the present work where the interannual scales are investigated.

Figure 26 and **Figure 27** display a series of oscillatory components, not easily quantified by a simple visual inspection of the signal, resulting from surges and waves, respectively: semi-annual, annual and interannual scales. Time axis in S go up to the limit of available records of each station, being Dunkirk the first to finish in 2016 and Le Havre having records till 2020.

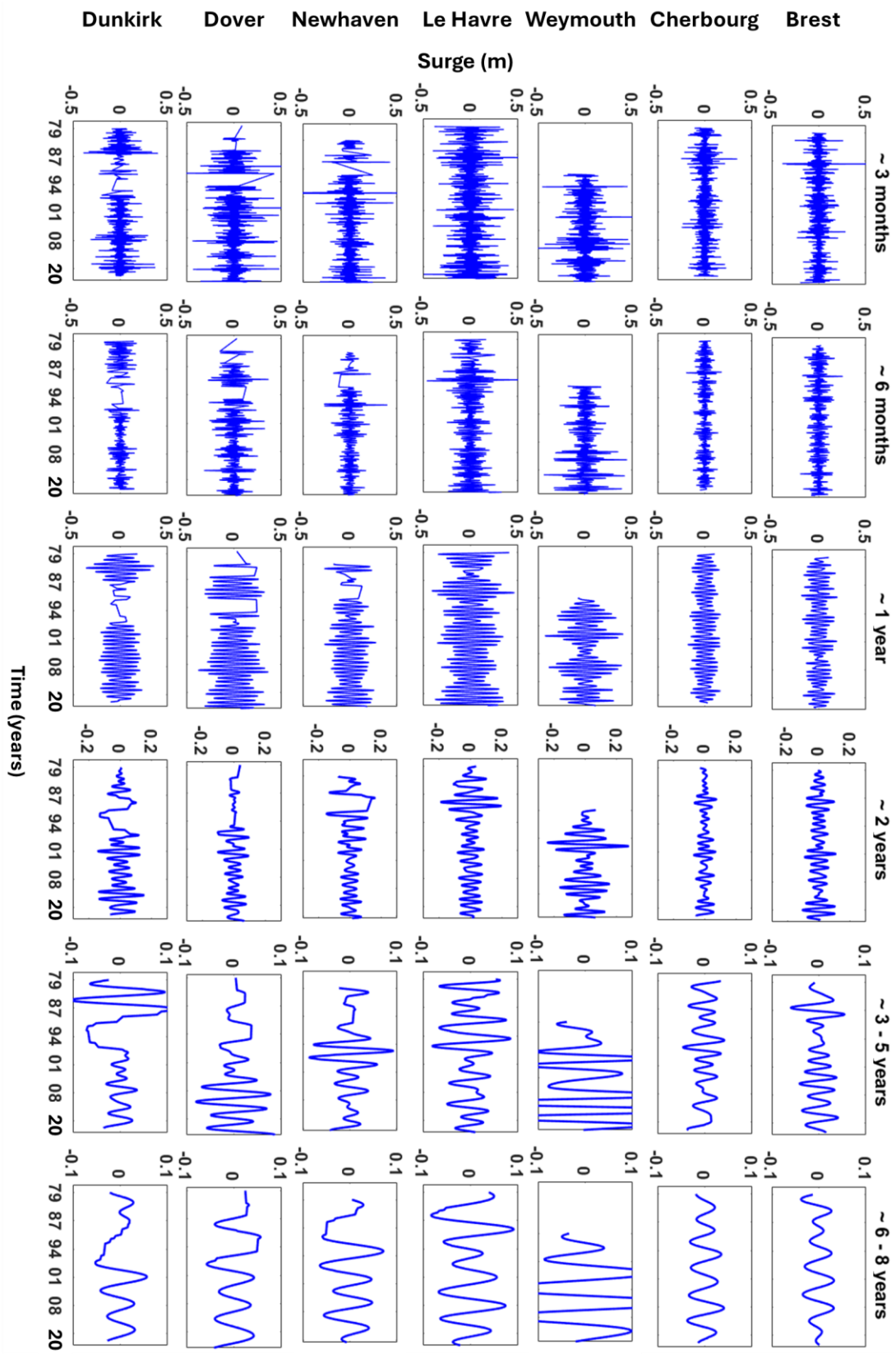

Figure 26. *Wavelet details (spectral components) resulting from the MODWT multiresolution analysis of monthly maxima of surges S at the intermonthly (~3 months and ~6 months), annual (~1 year) and interannual (~2 years, 3-5 years, 6-8 years) time scales for Brest, Cherbourg, Weymouth, Le Havre, Newhaven, Dover and Dunkirk*

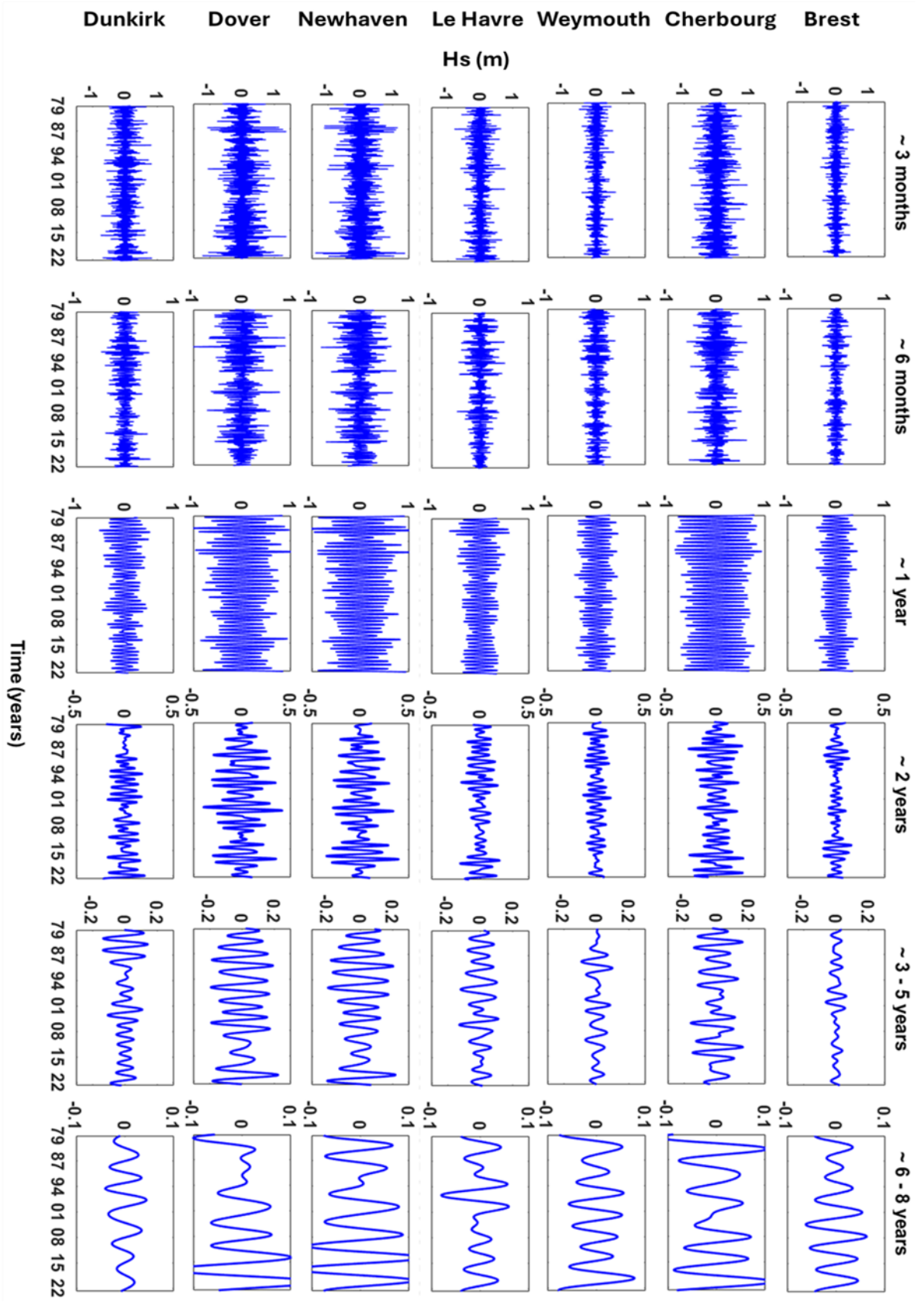

Figure 27. *Wavelet details (spectral components) resulting from the MODWT multiresolution analysis of monthly maxima of waves Hs at the intermonthly (~3 months and ~6 months), annual (~1 year) and interannual (~2 years, 3-5 years, 6-8 years) time scales for Brest, Cherbourg, Weymouth, Le Havre, Newhaven, Dover and Dunkirk*

Changes in extreme surges are around +/- 0.5 m for the semi-annual and annual, +/- 0.3 m for ~2 years and limited to +/- 0.1 m for ~3-5 years and 6-8 years variability, respectively.

At scales larger than 2 years, the variability of surges and waves exhibits high similarities between the different sites with a symmetric behavior between French and UK (Cherbourg - Weymouth, Le Havre - Newhaven and Dover – Dunkirk), while the amplitude of the components is relatively higher in UK stations (Newhaven, Dover, Weymouth). These similarities are less pronounced at the annual and semi-annual scales.

At these short scales, the differences in the extreme surges can be explained by local physical drivers mainly induced by the combining effects of meteorological and oceanographic forces including changes in atmospheric pressures and wind velocities in shallow-water areas.

Such large variability reveals the physical effects of a global contribution related to climate oscillations. The extent of the large-scale oscillations is not strictly similar and changes according to the timescale variability since the dynamics of surges are not necessarily related to the same type of atmospheric circulation process. This relationship will be addressed in the next part of this chapter.

The multi-timescale spectral components have been used to calculate the time-dependent PDF of the monthly maxima of S and H_s, as shown respectively in **Figure 28** and **Figure 29** where the density function has been represented during the period of study using a window of 6 months, for the locations of Brest, Weymouth and Cherbourg. The PDFs of the monthly maxima of S and H_s for Le Havre, Newhaven, Dover and Dunkirk are shown in **Appendix A**.

During a long period, larger than 35 years, the PDF displays changes of the mean values in time which are clearly observed for the semi-annual, annual variability with a wavelength of ~ 6 months and ~12 months, respectively. At such scales, changes in the probability density are more significant in **Figure 29**, exhibiting a strong nonstationary behavior of waves.

These changes are smoothed and less structured for the low frequencies, ~3-5 years and 6-8 years, with some local variations observed particularly at the end of the study period, case of Brest.

Then, the nonstationary dynamics of extreme values control the stochastic signal of extreme surges and waves at small scales; it's dissipated for scales greater than ~1 year.

The previous works of Turki et al. (2020a, 2020b) have demonstrated that the interannual variability (timescales higher than 1 year) of surges is highly represented in the monthly extreme,

which is not the case for the monthly mean surges where most of the power spectrum is concentrated around the annual cycle with an explained variance higher than 50%. The PDF of the spectral component ~1-year contains most of surge variability for monthly mean records with a series of short oscillations showing changes in their amplitude and wavelength each n years (where n > 1). This variability is distributed at the interannual scales of ~2 and ~4 years for monthly extreme records.

This result exhibits that the interannual frequencies of ~2 and ~4 years are inherently expressed within the ~1-year component and seem to be modulated at this scale for monthly mean surges; they are explicitly manifested in the extreme monthly components higher than 1 year.

Accordingly, the multi-scale variability of extreme S exhibits a nonstationary behavior modulated by a nonlinear interaction between the different interannual timescales. Then, assessing the effect of the nonstationary behavior at different timescales is important for improving the estimation of extreme values and the forecast of storms.

3.3.3. Relationship between extreme values and atmospheric oscillations

This section uses spectral components to investigate the correlations between the extreme values and climate oscillations at each timescale: ~ 6 months, ~1 year, ~2 years, ~3-5 years, ~6-8 years. The large-scale climate oscillations are represented by four different climate indices: the North Atlantic Oscillation (NAO), the Sea Level Pressure (SLP), the Sea Surface Temperature (SST) component and the Atlantic Multi-decadal Oscillation (AMO).

These patterns were considered to be fundamental drivers in the Atlantic regions (Massei et al., 2017; Turki et al., 2019, 2020a, 2020b). Monthly time series of climate indices have been provided by the NCEP-NCAR Reanalysis fields until the year 2018 (http://www.esrl.noaa.gov/psd/data/gridded/data.ncep.reanalysis.derived.html).

The overall results are displayed below. **Table 3** presents the significant explained variance of the spectral components obtained from the MODWT multiresolution analysis of the atmospheric patterns. The details of spectral components for both signals of oceanographic variables (S and H_s) and climate oscillations (NAO, the SLP, the SST and the AMO) have been normalized and presented respectively in **Figure 30**, **Figure 31, Figure 32** and **Figure 33**.

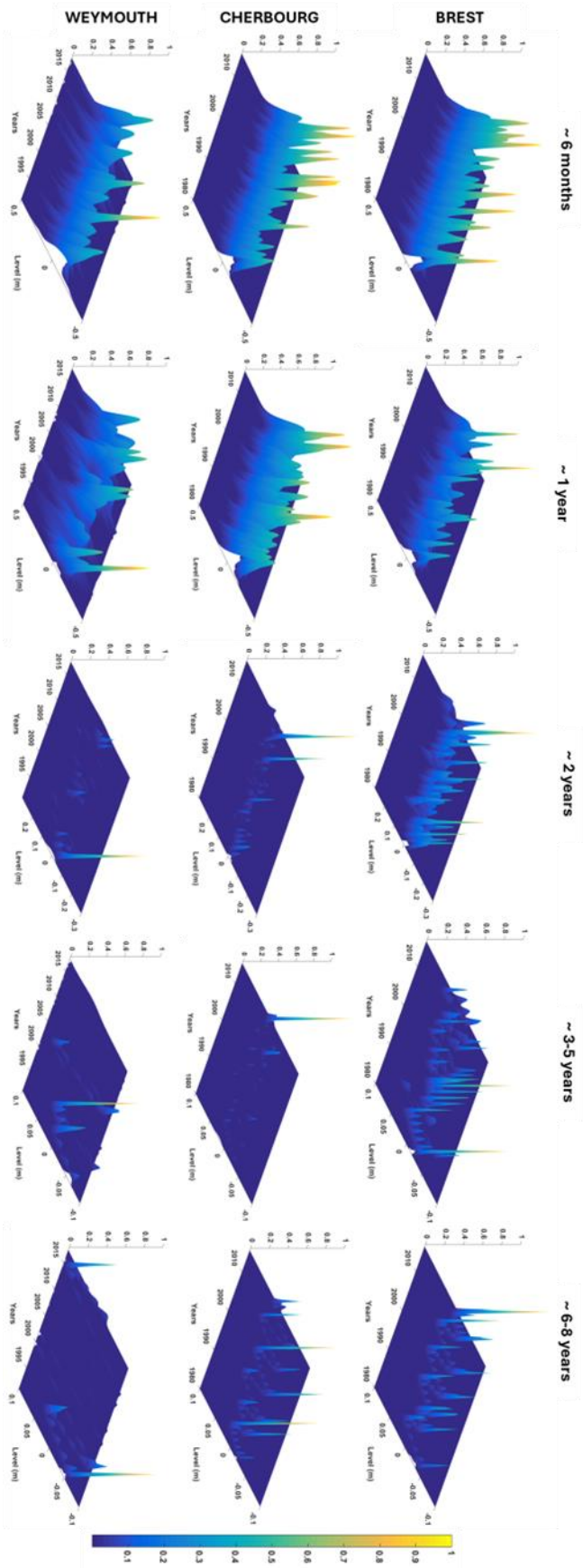

Figure 28. *Time-dependent PDF of monthly extreme surges during the period 1981 – 2018 at the semi-annual and interannual scales in Brest, Cherbourg and Weymouth*

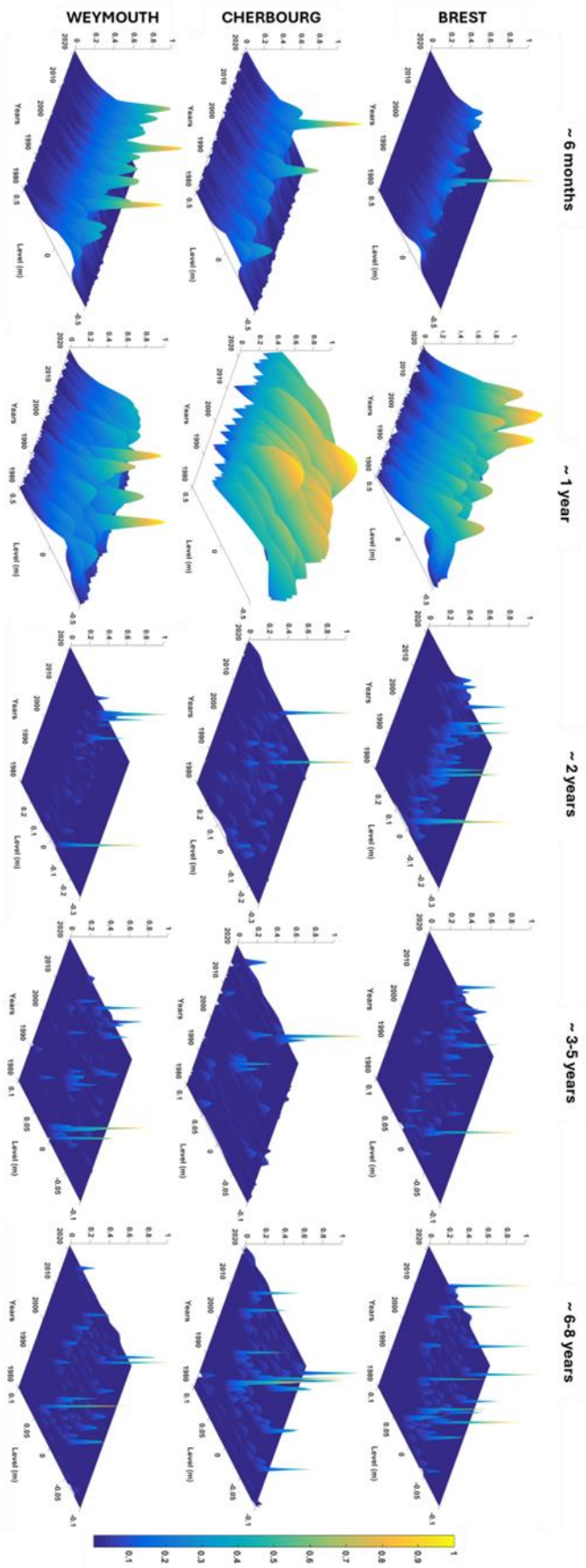

Figure 29. *Time-dependent PDF of monthly extreme waves during the period 1980 – 2022 at the semi-annual and interannual scales in Brest, Cherbourg and Weymouth*

	~3 months	~ 6 months	~ 1 year	~ 2 years	~ 3 - 5 years	~ 6 - 8 years	Lower frequencies
SST	8.2%	6.9%	80.0%	2.1%	0.7%	0.5%	1.6%
SLP	4.6%	4.9%	86.3%	1.9%	0.5%	0.2%	1.6%
NAO	43.4%	25.9%	15.3%	6.7%	3.8%	2.9%	2%
AMO	7.2%	9.6%	11.5%	9.9%	6.3%	8.0%	47.8%

Table 3. *Estimated explained variance of energy expressed as percentage of the climate indexes, with the percentages resulting from the MODWT multiresolution analysis*

Based on these figures, the contribution of climate oscillations varies according to the timescale and the site for S and H_s. At the semi-annual scales, the variability of S and H_s seems to be related to the different climate oscillations; S shows relatively high correlations with SST with a mean variance of ~20% while H_s is better connected with SLP. The effects of NAO and AMO are less pronounced with a mean variance of ~ 10%. The annual scale is mainly controlled by the combined effects of SST and SLP fields with a variance higher than 65%. The effects of SLP are also observed in the variability of ~2 years, combined with NAO. This climate index takes more significant effects at scales higher than ~2 years where the contribution of the interdecadal oscillations of AMO seems to be more pronounced for the ~6-8 year of surges.

These results reveal the complex behavior of the multi-timescale dynamics of extreme values; such dynamics involves the multimodal climate drivers with a dominance of i) SST from the semi-annual and the annual scales and ii) SLP and NAO at the interannual scales. The effects of AMO is more observed at scales larger than ~6 years.

3.4. NON-STATIONARY ANALYTICAL EXTREME VALUE APPROACH

The objective of this study is to analyze the time series of monthly maxima of significant wave height and storm surge of each location with a bivariate and non-stationary approach. The extreme values are modelled with a Generalized Extreme Value (GEV) distribution function and copulas, incorporating as covariates climate and temporal indexes to account for the non-stationarity. Then, the joint return period of both variables is obtained, incorporating the non-stationary GEV and copula previously fitted. The first insights of this approach have been developed in the framework of the master internship of Antoine Chapon (supervision: Yasser Hamdi and Imen Turki, 2022).

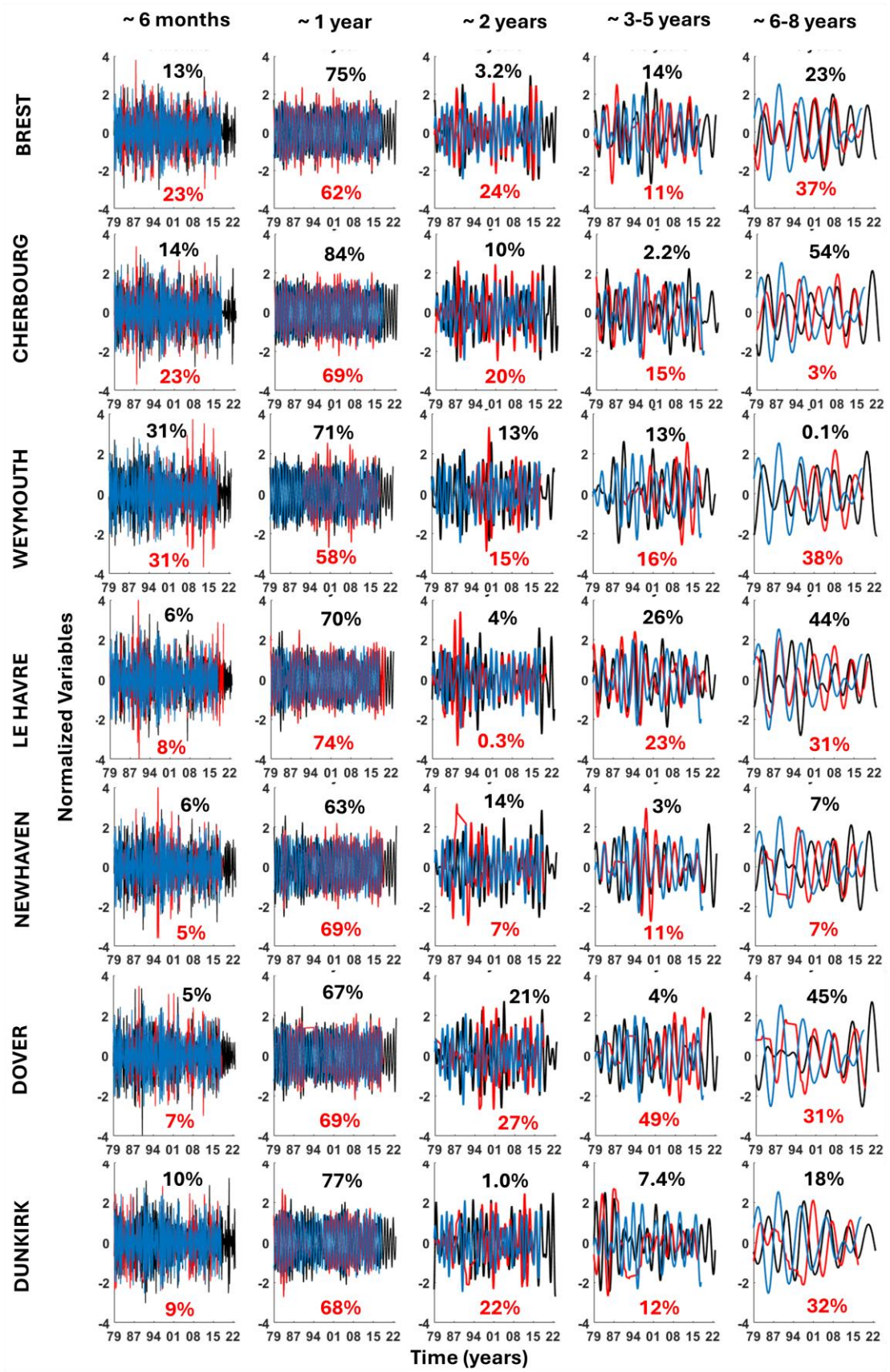

Figure 30. *Correlation of spectral components resulting from the MODWT of normalized variables (in black waves and in red surges) and normalized NAO in blue at the intermonthly (~6 months) and interannual (~1 year, ~2 years, ~3-5 years and ~6-8 years) timescales for the 7 stations*

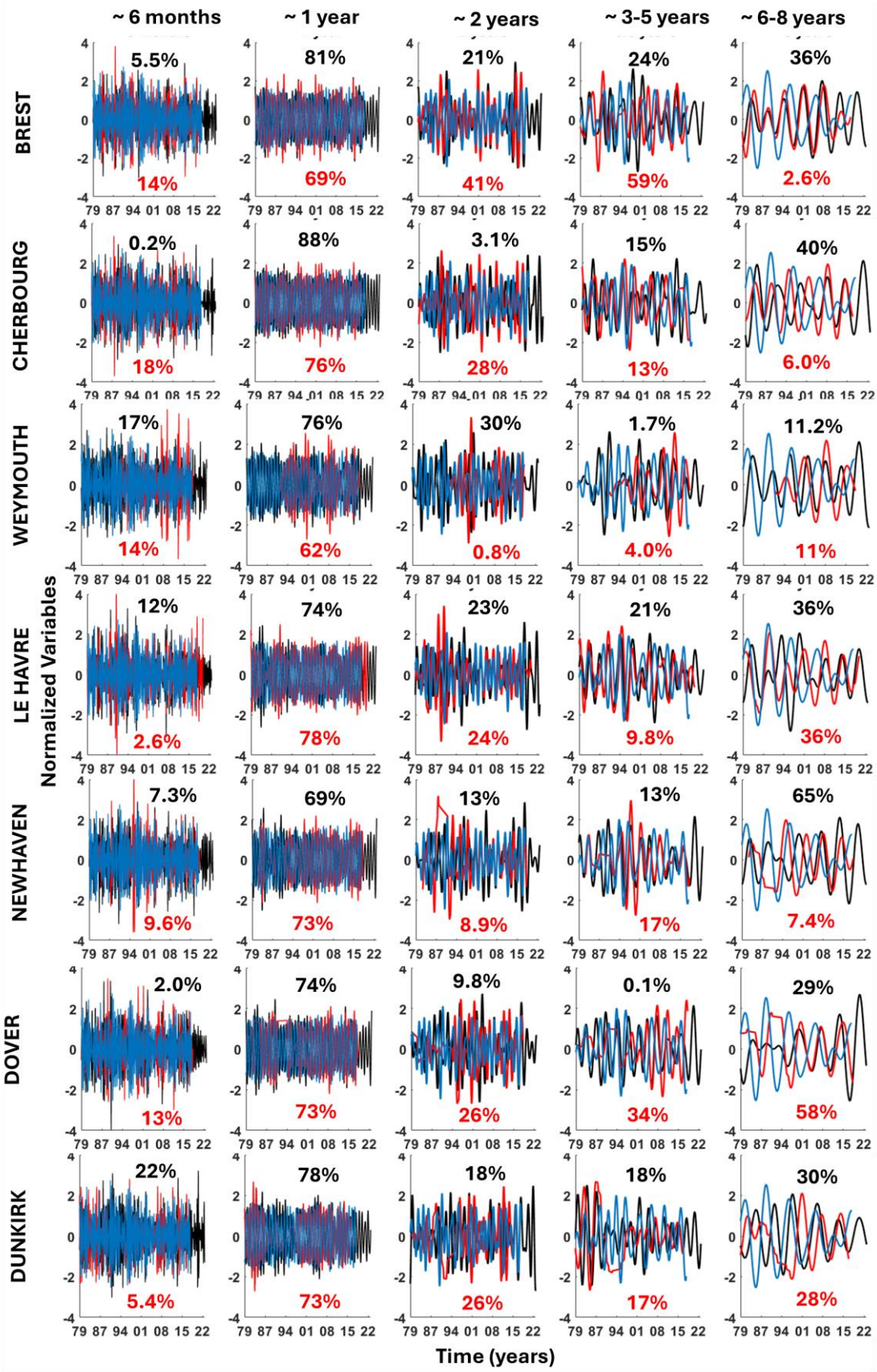

Figure 31. *Correlation of spectral components resulting from the MODWT of normalized variables (in black waves and in red surges) and normalized SLP in blue at the intermonthly (~6 months) and interannual (~1 year, ~2 years, ~3-5 years and ~6-8 years) timescales for the 7 stations*

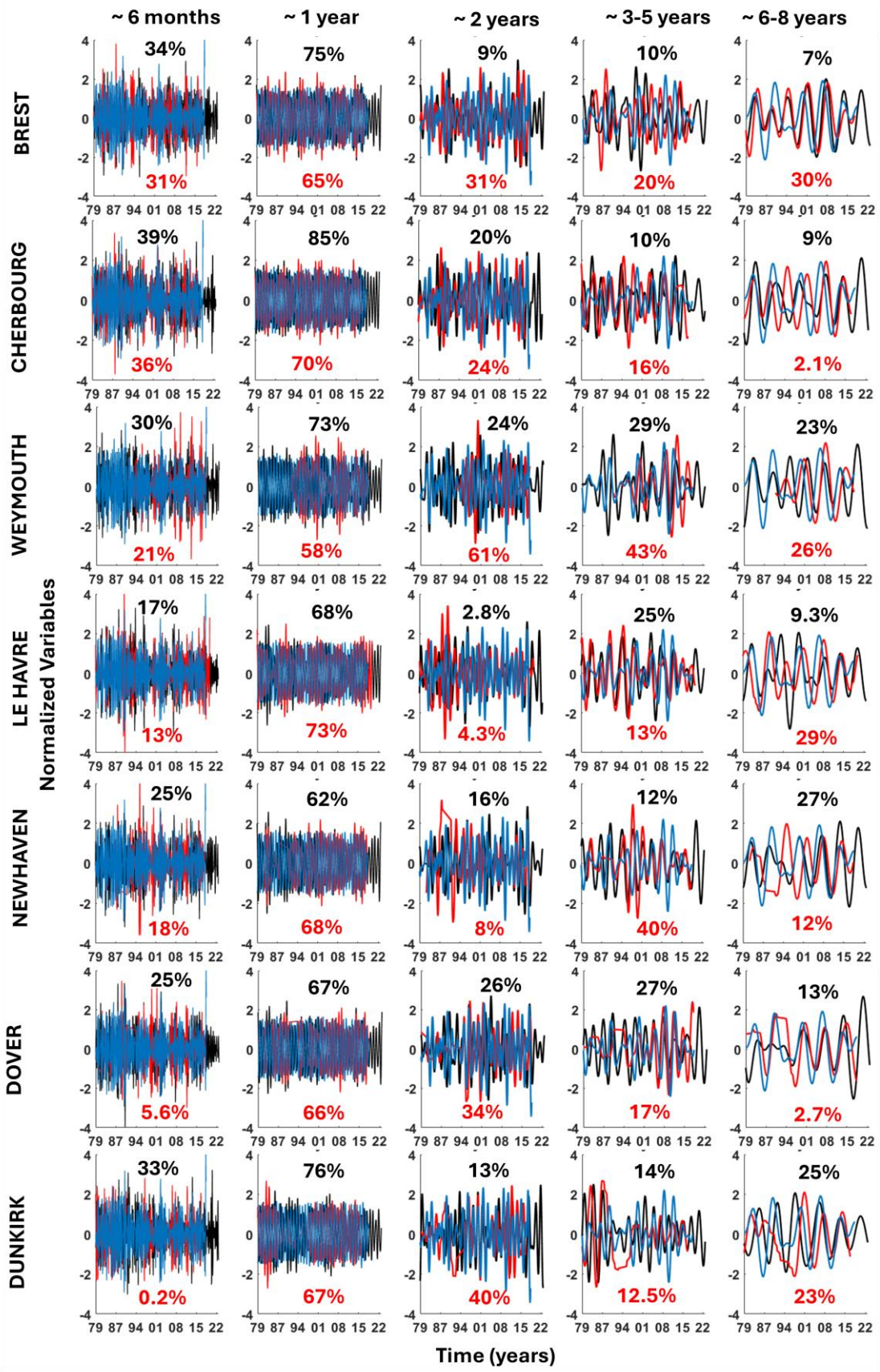

Figure 32. *Correlation of spectral components resulting from the MODWT of normalized variables (in black waves and in red surges) and normalized SST in blue at the intermonthly (~6 months) and interannual (~1 year, ~2 years, ~3-5 years and ~6-8 years) timescales for the 7 stations*

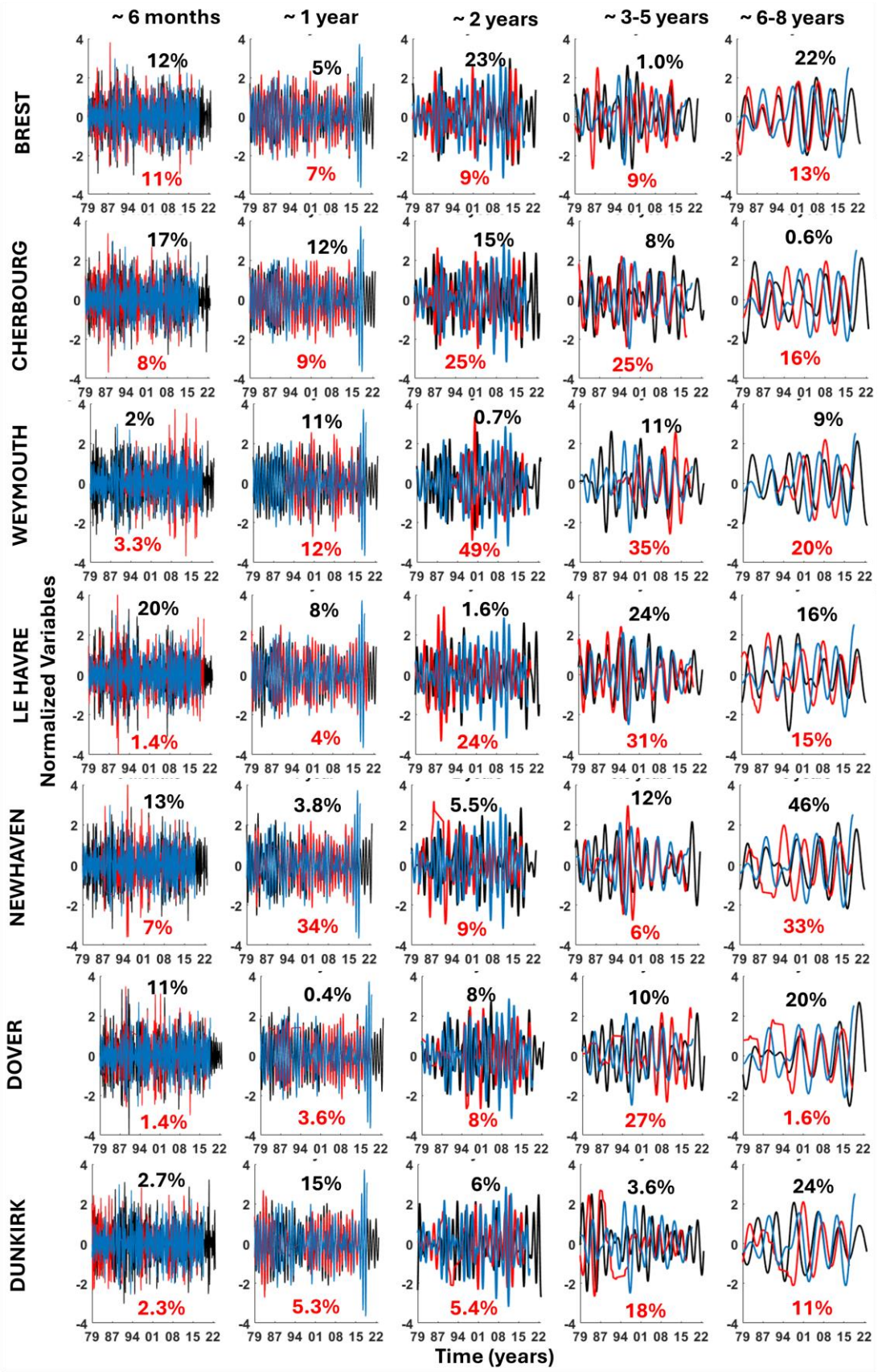

Figure 33. *Correlation of spectral components resulting from the MODWT of normalized variables (in black waves and in red surges) and normalized AMO in blue at the intermonthly (~6 months) and interannual (~1 year, ~2 years, ~3-5 years and ~6-8 years) timescales for the 7 stations*

3.4.1. Non-stationary extreme value analysis

The GEV distribution function is extensively used for estimating variables in extreme value analyses, commonly applied to yearly or monthly maxima selected from the time series of different variables. The cumulative distribution function or CDF of the GEV is illustrated in Eq. 4.

$$F(x) = \begin{cases} exp\left(-\left(1+\xi\left(\frac{x-\mu}{\sigma}\right)\right)^{-1/\xi}\right) & if\ \xi \neq 0 \\ exp\left(-exp\left(-\frac{x-\mu}{\sigma}\right)\right) & if\ \xi = 0 \end{cases} \quad (4)$$

where $\sigma > 0$ and $-\infty < (\mu, \xi) < \infty$, and μ, σ and ξ are the location, the scale, and the shape parameters, respectively. The shape parameter ξ governs the tail behavior of the distribution and defines the sub-families Gumbel, Fréchet and Weibull, corresponding to $\xi = 0$, $\xi > 0$ and $\xi < 0$, respectively. In Eq. 4, the variable x represents the surge or the significant wave height when the fit is applied.

The parameters of the GEV are calculated in a non-stationary way, making them dependent on some selected indexes used as covariables, as defined by Chapon & Hamdi (2022) in the GEV distribution of their non-stationary analysis. These indexes are eight covariates with a monthly time-step, which are five climate indexes and two temporal time series. The climate indexes are the sea surface temperature (SST), the sea level pressure (SLP), two indexes for the North Atlantic Oscillation ($NAO_{Hurrell}$ and NAO_{NOAA}) and the Atlantic Multi-decadal Oscillation (AMO). Two NAO indexes are used because Hurrell's index is defined by station measurements, which cannot track the displacement of the NAO action centers during the annual cycle (J. Hurrell & Phillips, 2023), whereas the NOAA's index is defined by projection of a loading pattern able to track the shifting action centers to the anomaly 500 millibar height field (NOAA, 2021; Pokorná & Huth, 2015). Nonetheless the $NAO_{Hurrell}$ index is also used because it could be more appropriate as a covariate for extreme values of H_s and S, which have higher maxima during winter, when the NAO center of actions is at the defining station's locations.

The first temporal covariate is a linear time variable, named t, with $t = \{1, \dots, m\}$ for m monthly maxima. The second one is a sine wave of period one year modelling the seasonal effect of the annual cycle (Katz et al., 2002), named *s* for *sine* or *season*, given by Eq. 5.

$$s_t = \sin\left(\pi\frac{M_t+1}{6}\right) + \cos\left(\pi\frac{M_t+1}{6}\right) \quad (5)$$

with $M_t \in \{1, \dots, 12\}$ being the month numbers. The term +1 centers the two maximal *s* values in December and January, and the two minimal values in June and July, which is appropriate considering the annual distribution of H_s and S monthly maxima.

For both the surge and the wave height all the 7 indexes are tested in a power of first and second degree for each of the GEV parameters, obtaining in the end an estimator for the three parameters that can go from a lonely value up to 12 coefficients in case the best fit would need all the indexes with a linear or a quadratic dependence, assuming only one NAO index would be incorporated in the model.

3.4.2. Dependence structure of wave height and surge extreme values

After obtaining the estimators for the non-stationary parameters, a bivariate copula is obtained with the aim of getting to know the joint distribution of the storm surge and the wave height. Copulas are multivariate distributions with uniform margins in the interval (0,1), used to model the dependence structure between several variables (Yan, 2007). The simple case of a bivariate distribution with random variables X and Y, and a two-dimensional copula C is shown in Eq. 6.

$$F_{X,Y}(x, y) = C\{F_X(x), F_Y(y)\} \tag{6}$$

where F_X and F_Y are the margins and $F_{X,Y}$ is the bivariate distribution.

In this study five bivariate copulas are tested: the Clayton, Gumbel, Frank, Joe, and Gaussian (also called normal) copulas. These copulas have a unique parameter θ, which is calculated from Kendall's τ with a specific equation per copula. Yan (2007) presents a quick introduction to copulas, and also provides a tutorial on using the R package *copula* (Hofert et al., 2020). The equations linking τ and θ for each copula can be found in the documentation of the R package *VineCopula* (Nagler et al., 2020), which has a function for this. An iterative process is used to find the best fit amongst the five copulas to later proceed to the addition of the non-stationarity, making out of it a dynamic copula.

To account for the non-stationarity, a dynamic copula has a parameter τ dependent on covariates, resulting in a non-stationary dependence structure similarly to the GEV procedure, with the same time covariate t tested and added to τ, with a linear or quadratic dependence. The quadratically time-varying τ, with the maximum number of 3 coefficients for the dynamic copula, would be what is shown in Eq. 7.

$$\tau = \Lambda(\psi_0 + \psi_1 \mathrm{t} + \psi_2 t^2) \quad (7)$$

where the logistic transformation $\Lambda(\mathrm{x}) = (1 + e^{-x})^{-1}$ keeps $\tau \in [0,1]$. In a similar way as for the non-stationary GEV with all the covariates, the coefficients could go up to 3 if τ had a quadratic dependence on the time covariate t.

The dynamic copula is fitted to the same monthly maxima of H_s and S whose margins have been modelled by the non-stationary GEV models.

Finally, the effective return levels are obtained. In a bivariate context, the concept of return period can have different definitions (Shiau, 2003). This study considers $Pr\{X \geq x, Y \geq y\}$, with the corresponding joint return period defined as the expected interval $X \geq x$ and $Y \geq y$ (Sarhadi et al., 2016), given by Eq.8.

$$JRP(x,y) = \frac{E[L]}{1 - F_X(x) - F_Y(y) + C(x,y)} \quad (8)$$

with L being the mean interarrival time between events. Here $L = 1$ due to the block maxima approach.

The concept of return period can also have different definitions in a non-stationary context. This study uses an *effective* return level, dependent on the covariates, with a corresponding static return period (Katz et al., 2002).

3.4.3. Results of the non-stationary extreme value approach of significant wave height and surges

The results for the fitting of the non-stationary GEV model for significant wave height and surge in each of the 7 studied locations are detailed in **Table 4**.

The automated process tends to, firstly add covariates to the location parameter (μ), then to the scale parameter (σ, transformed to the $\log(\sigma)$ for the fit), and lastly in the shape parameter (ξ). It can be noticed how, for most of the locations, H_s is dependent on the SST and SLP, especially on the μ parameter. This can be expected because the correlation between H_s and the variables measured on the surface of water is really strong. In the same way, the NAO index has also a strong influence, with linear and quadratic dependence for 5 of the 7 stations.

Brest	H_s	$\mu = 0.748 - 0.102\ SST - 0.068\ SLP + 0.065\ NAO_{Hurrell} - 0.024\ {NAO_{Hurrell}}^2$, $\sigma = -1.553 - 0.198\ SLP$, and $\xi = -0.1 + 0.095\ SLP$
	S	$\mu = 0.231 - 0.03\ SST - 0.029\ SLP + 0.016\ t$, $\sigma = -2.095 - 0.164\ SST - 0.16\ SST^2 - 0.099\ SLP$, and $\xi = -0.184 + 0.112\ SLP + 0.07\ SLP^2$
Cherbourg	H_s	$\mu = 2.047 - 0.239\ SST - 0.164\ SLP + 0.056\ NAO_{Hurrell} + 0.055\ {NAO_{Hurrell}}^2$ $\sigma = -0.679 - 0.139\ SLP - 0.15\ SLP^2$, and $\xi = -0.19 - 0.044\ AMO + 0.052\ AMO^2$
	S	$\mu = 0.223 - 0.047\ SST$, $\sigma = -2.287 - 0.272\ SLP + 0.099\ NAO_{Hurrell}$, and $\xi = -0.105 - 0.061\ t$
Weymouth	H_s	$\mu = 0.976 - 0.068\ SST - 0.095\ SLP$, $\sigma = -1.382 - 0.12\ SST - 0.131\ t$, and $\xi = -0.129$
	S	$\mu = 0.345 - 0.078\ SST$, $\sigma = -1.799 - 0.43\ SST$, and $\xi = 0.157 + 0.128\ SST + 0.137\ t$
Le Havre	H_s	$\mu = 1.123 - 0.129\ SST + 0.089\ SST^2 - 0.033\ NAO_{Hurrell} + 0.02\ {NAO_{Hurrell}}^2$, $\sigma = -1.041 - 0.246\ SLP - 0.095\ SLP^2 - 0.073\ t$, and $\xi = -0.216 + 0.094\ SLP$
	S	$\mu = 0.335 - 0.056\ SST - 0.059\ SLP + 0.026\ SLP^2 - 0.008\ NAO_{Hurrell} + 0.03\ t + 0.022\ t^2$, $\sigma = -1.728 - 0.17\ SST - 0.216\ SLP + 0.193\ NAO_{Hurrell}$, and $\xi = 0.104 + 0.185\ SST - 0.117\ SST^2$
Newhaven	H_s	$\mu = 2.211 - 0.199\ SST - 0.042\ SST^2 + 0.242\ SLP - 0.093\ SLP^2 + 0.078\ NAO_{Hurrell} + 0.054\ {NAO_{Hurrell}}^2$, $\sigma = -0487 - 0.098\ SLP - 0.094\ SLP^2 - 0.067\ t$, and $\xi = -0.206$
	S	$\mu = 0.361 - 0.039\ SST - 0.029\ SLP + 0.027\ NAO_{Hurrell} + 0.012\ {NAO_{Hurrell}}^2$, $\sigma = -1.898 - 0.267\ SLP + 0.085\ SLP^2 - 0.041\ NAO_{Hurrell} - 0.062\ {NAO_{Hurrell}}^2$, and $\xi = -0.038 + 0.093\ SST$
Dover	H_s	$\mu = 2.269 - 0.213\ SST - 0.099\ SLP + 0.001\ SLP^2 + 0.232\ AMO + 0.051\ AMO^2 + 0.05\ NAO_{Hurrell} + 0.054\ {NAO_{Hurrell}}^2$, $\sigma = -0.682 - 0.118\ SLP + 0.0164\ NAO_{Hurrell}$, and $\xi = 0.039 + 0.086SST - 0.089\ SST - 0.078\ NAO_{Hurrell} - 0.14\ t$
	S	$\mu = 0.533 - 0.083\ SLP + 0.038\ NAO_{Hurrell}$, $\sigma = -1.635 - 0.143\ SLP - 0.131\ SLP^2$, and $\xi = 0.027 - 0.006\ SLP + 0.065\ SLP^2 - 0.062\ AMO$
Dunkirk	H_s	$\mu = 1.414 - 0.178\ SST$, $\sigma = -1.043$, and $\xi = -0.124$
	S	$\mu = 0.35 - 0.056\ SLP - 0.022\ t$, $\sigma = -1.943 - 0.115\ SLP - 0.122\ SLP^2 - 0.071\ t + 0.114\ t^2$, and $\xi = -0.24 - 0.209\ SST + 0.12\ SST^2 + 0.172\ SLP + 0.015\ AMO + 0.011\ NAO_{NOAA} + 0.054\ {NAO_{NOAA}}^2$

Table 4. *Results of the fitting of the GEV with the non-stationary parameters dependent the climate and time indexes for significant wave height and surge in the 7 studied locations*

For S, the results are variable, with the parameters of the GEV sometimes dependent on a lot of covariates and sometimes almost constant (as in Cherbourg or Weymouth). The AMO and the temporal variable t appear more frequently in these non-stationary fits, particularly on the tide gauges located on the East English Channel. In fact, an aggrupation can be observed between the tide gauges of Brest, Cherbourg and Weymouth, with simpler dependencies mostly on SST and SLP, and Le Havre, Newhaven, Dover and Dunkirk, that have also the NAO and the AMO indexes as linear and quadratic covariates.

For limiting the NAO index to $NAO_{Hurrell}$ or to NAO_{NOAA}, both indexes were tested as a first attempt to observe the correlation between the parameters and these indexes, and the one with a stronger dependency, marked by a more frequent appearance as covariate or with a quadratic dependency, is kept, repeating the automated fitting process but eliminating the NAO index that had the weaker dependency. For Brest and Cherbourg, the index NAO_{NOAA} is removed for both H_s and S, for Dover, Le Havre and Newhaven, the same NAO_{NOAA} index is removed, but just from H_s, and for Dunkirk, it is the $NAO_{Hurrell}$ index the one removed from S. In Weymouth, none of the variables is dependent on the NAO index.

3.4.4. Results of the dependence structure between significant wave height and surges

Once the non-stationary GEVs are adjusted independently for H_s and S for the 7 locations, the fitting for the joint distribution of each of them is explored.

For the bivariate distribution, the results of the fitting of the dynamic copula are shown in **Table 5**. In the table, the copula with the equation that presents the best fit to the distribution is also specified, among the five tested (Clayton, Gumbel, Frank, Joe, and Gaussian). As previously mentioned, the five copulas have also been tested constantly, or with a linear or quadratical time-dependency.

For all the stations, the best copula amongst the five tested is the Frank copula. The Frank copula has an absence of tail dependence (Chebana & Ouarda, 2021; Manner & Reznikova, 2012), which means that even though the H_s and S extremes are dependent, this dependence fades away for the lower and upper extreme extremes. This property is important for risk assessment, as it indicates that the chance of compound hazards (an event with extreme H_s and S happening simultaneously) diminishes for the upper tail of the bivariate distribution.

Station	Copula	Parameters
Brest	Frank constant	$\tau = \Lambda(-0.0637)$
Cherbourg	Frank linear	$\tau = \Lambda(-0.479 + 0.096\ t)$
Weymouth	Frank linear	$\tau = \Lambda(-0.500 - 0.186\ t)$
Le Havre	Frank linear	$\tau = \Lambda(0.213 + 0.203\ t)$
Newhaven	Frank linear	$\tau = \Lambda(-0.0908 + 0.1845\ t)$
Dover	Frank constant	$\tau = \Lambda(-0.4993)$
Dunkirk	Frank linear	$\tau = \Lambda(-0.738 + 0.197\ t)$

Table 5. *Results of the fitting of the copulas between significant wave height and surge with the non-stationary time-dependent parameter in the 7 studied locations*

The best fitting copula is dynamic in Cherbourg, Weymouth, Le Havre, Newhaven and Dunkirk, but it is stationary for Brest and Dover. This means that, for the five stations with a linear dependency, the risk of compound hazards is higher, while it is lower for the two locations with a constant copula.

To complete the bivariate distribution analysis, **Figure 34** shows the effective joint return level for the 7 locations. Each graph of the figure also shows the bivariate density of H_s and S monthly maxima and the effective GEV and copula parameters used to calculate both density and return levels.

In a bivariate context the return level is a curve of infinite combinations resulting in the same return period, but not every part of this curve holds the same probability. The most probable combinations are those in the high-density part, towards the middle of the curve, whereas the density falls rapidly in the horizontal and vertical parts of the curve. The fact that the high-density part of the curves stretches with the increasing return period illustrates the fading dependence on the upper tail of the Frank copula.

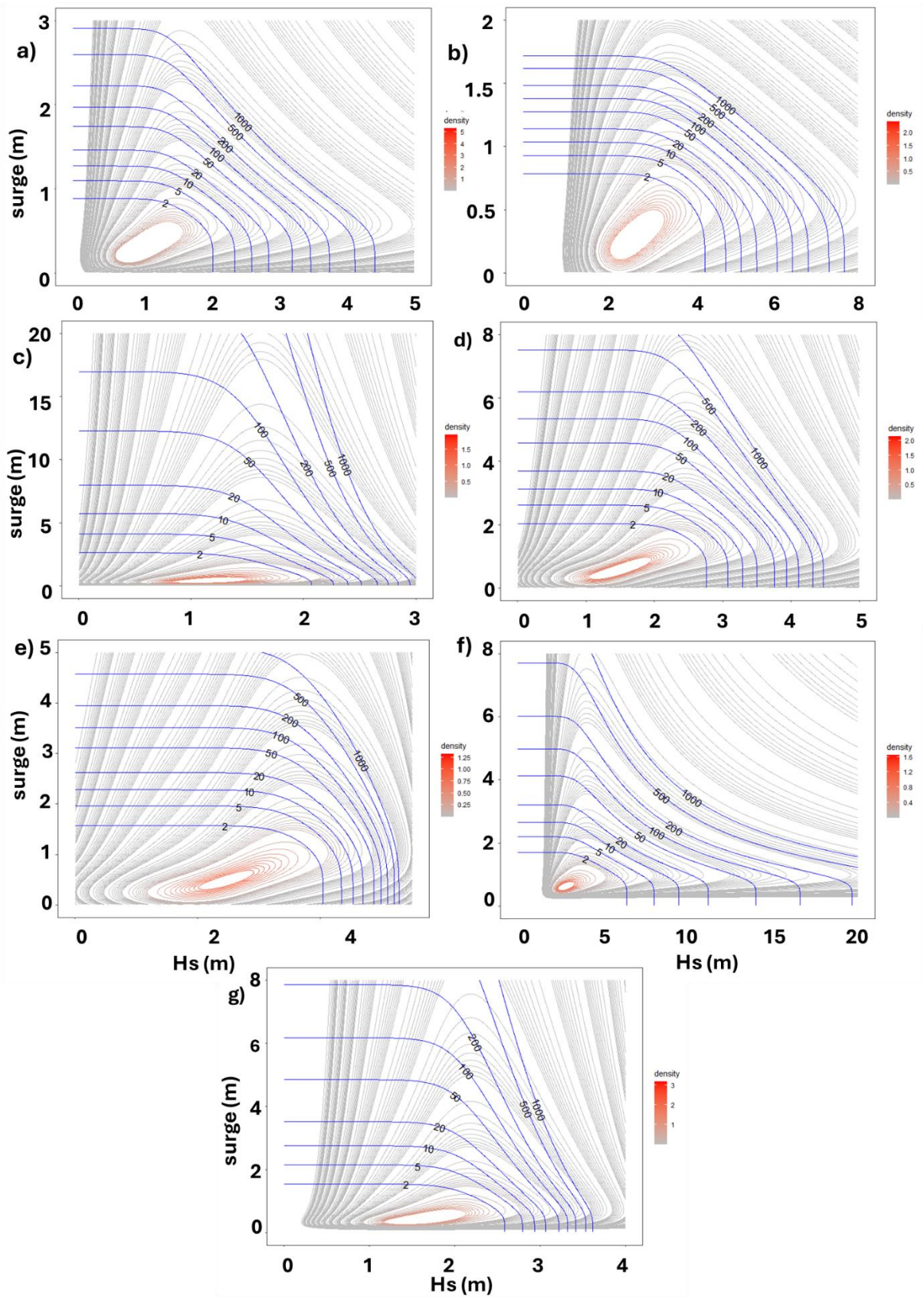

Figure 34. Bivariate density of monthly maxima of significant wave height from reanalysis and measured surge with effective joint return levels for several return periods for a) Brest, b) Cherbourg, c) Weymouth, d) Le Havre, e) Newhaven, f) Dover and g) Dunkirk

As mentioned with the best fitting copulas for each location, for Brest and for Dover, the results are stationary copulas, meaning a lower risk of compound extreme events. This can be observed on the figures of the joint return periods of these locations (**Figure 34**a and **Figure 34**f), with the central part of the return levels decreasing towards the origin of the graphic, while for the other locations they are either more lineal or curved opposing to the origin.

For the case of Weymouth, the surge axis is much higher than for the other sites because of the most common extreme values presented in the time series (**Figure 23**e), producing that the fitting of these values generates higher surges associated to the return periods studied. The same happens with the extreme waves in Dover (**Figure 23**l).

3.4.5. Dynamic copula between frequencies obtained from the spectral analysis

It is possible to combine the spectral analysis and the non-stationary extreme value analysis, applying the same methodology of fitting the best combination of parameters with covariables of the GEV with extreme values of waves and surges, and obtaining the dependence structure of both variables with the joint return levels, but instead of doing it with the monthly maxima, applying it to the spectral components obtained from the MODWT multiresolution analysis.

The non-stationary GEV distributions and the dependence structures of the different frequencies must be calculated using spectral components of H_S and S with similar time scales, i.e., the ~1-year spectral component of H_S has to be calculated with the ~1-year spectral component of surges. In total, according to **Table 1** and **Table 2**, there are 6 common timescales, from intermonthly to interannual.

Since the possible combinations of spectral components and study sites gives 84 GEV distributions with 42 copulas, as an example, in **Table 6** the estimated parameters of the GEV fitting with the covariates, in **Table 7** the fitting copulas, and in **Figure 35** the bivariate density plots of the 6 timescales of Le Havre, are presented. The other tables and figures of the 6 remaining sites can be seen in **Appendix B**.

It can be observed how the ranges of values in the graphics of **Figure 35** correspond to the ranges of the different timescales of the spectral components of **Figure 33** and **Figure 30**.

~3 months	H_s	$\mu = -0.081 + 0.041\, NAO_{Hurrell}$, $\sigma = -1.478 - 0.162\, SLP$, and $\xi = -0.192 - 0.018\, SST - 0.052\, SST^2$
	S	$\mu = -0.053 + 0.025\, NAO_{Hurrell}$, $\sigma = -1.934 - 0.141\, SST + 0.017\, SST^2 - 0.082\, t + 0.126\, t^2$, and $\xi = -0.21 - 0.017\, AMO - 0.052\, AMO^2$
~6 months	H_s	$\mu = -0.052 + 0.019\, NAO_{Hurrell}$, $\sigma = -1.684 - 0.123\, SLP - 0.154\, SLP^2 + 0.0004\, AMO - 0.084\, t - 0.105\ t^2$, and $\xi = -0.299$
	S	$\mu = -0.038$, $\sigma = -2.351 - 0.097 AMO + 0.126\, AMO^2 + 0.075\, NAO_{Hurrell} + 0.067\, {NAO_{Hurrell}}^2$, and $\xi = -0.304$
~1 year	H_s	$\mu = -0.039 - 0.024\, SST - 0.121\, SST^2 + 0.042\, SLP - 0.032\, SLP^2 + 0.027\, NAO_{Hurrell}$, $\sigma = -1.829 + 0.022\, SLP - 0.166\, SLP^2 - 0.187\, t + 0.157\, t^2$, and $\xi = -0.328 - 0.074\, NAO_{Hurrell}$
	S	$\mu = -0.039 - 0.133\, SLP + 0.022\, NAO_{Hurrell}$, $\sigma = -2.133$, and $\xi = -0.388 + 0.04\, AMO + 0.046\, AMO^2$
~2 years	H_s	$\mu = -0.017 + 0.003\, SST + 0.008\, SST^2 - 0.009\, NAO_{Hurrell} + 0.006\, {NAO_{Hurrell}}^2$, $\sigma = -2.671 - 0.119\, AMO$, and $\xi = -0.28 + 0.095\, t$
	S	$\mu = -0.019 + 0.006\, t$, $\sigma = -2.899 - 0.223\, t$, and $\xi = -0.273 - 0.019\, SST - 0.091\, SST^2 - 0.071\, AMO$
3-5 years	H_s	$\mu = -0.009$ $\sigma = -2.62 + 0.129\, AMO - 0.275\, AMO^2 + 0.047\, t - 0.351\, t^2$, and $\xi = -0.504$
	S	$\mu = -0.011 + 0.006\, AMO$, $\sigma = -3.326 - 0.21\, t - 0.081\, t^2$, and $\xi = -0.386 - 0.161\, AMO + 0.02\, AMO^2$
6-8 years	H_s	$\mu = -0.002 - 0.0004\, AMO + 0.002\, AMO^2 - 0.002\, NAO_{Hurrell} + 0.003\, t - 0.008\ t^2$, $\sigma = -3.395 - 0.227\, t - 0.35\, t^2$, and $\xi = -0.54 + 0.101\, t + 0.285\, t^2$
	S	$\mu = -0.014$, $\sigma = -3.245 - 0.075\, t + 0.159\, t^2$, and $\xi = -0.04 - 0.012\, t - 0.388\, t^2$

Table 6. *Results of the fitting of the GEV with the non-stationary parameters dependent the climate and time indexes for the spectral components of significant wave height and surge in Le Havre*

Frequencies	Copula	Parameters
~3 months	Gaussian linear	$\tau = \Lambda(-0.0795 + 0.1937t)$
~6 months	Gaussian linear	$\tau = \Lambda(-0.469 + 0.3834\ t)$
~1 year	Frank linear	$\tau = \Lambda(0.9864 + 0.2992\ t)$
~2 years	Clayton linear	$\tau = \Lambda(-1.6071 + 1.0193\ t)$
3-5 years	Gaussian linear	$\tau = \Lambda(0.1738 + 0.1475\ t)$
6-8 years	Gaussian linear	$\tau = \Lambda(-1.558 + 1.5238\ t)$

Table 7. *Results of the fitting of the copulas between spectral components of significant wave height and surge with the non-stationary time-dependent parameters in Le Havre with the 6 timescales*

3.5. HOW IS AN EXTREME EVENT DEFINED?

Although in the previous sections a stochastic and a spectral analysis of extreme values of H_s and S is performed using the monthly maxima, extreme values can be obtained from time series applying other methodologies that give more characteristics rather than just the seasonal or interannual variation. The extreme value is, therefore, an extreme event or storm, including the duration of these events identified on the time series and other variables associated with H_s or S, especially in the case of waves, where T_p or θ_m can play an important role too.

In the following section, a technique for defining an extreme event is presented: firstly, identifying the persistence of the characteristic variables over a specific threshold, and secondly, characterizing the intensity of the storm from the previously calculated energy.

3.5.1. Definition from a threshold

An extreme event on the ocean is usually defined by high waves, either in deep water or arriving at the coast. Taking into account that the consequences of the storms are essential Mendoza & Jiménez. (2006), and later Mendoza et al. (2011, 2013), introduced a way for including the persistence of a storm in the definition of it from the severity obtained from the time series of significant wave height. Three criteria have to be fulfilled by an extreme event to be considered as such: one of severity and two of persistence.

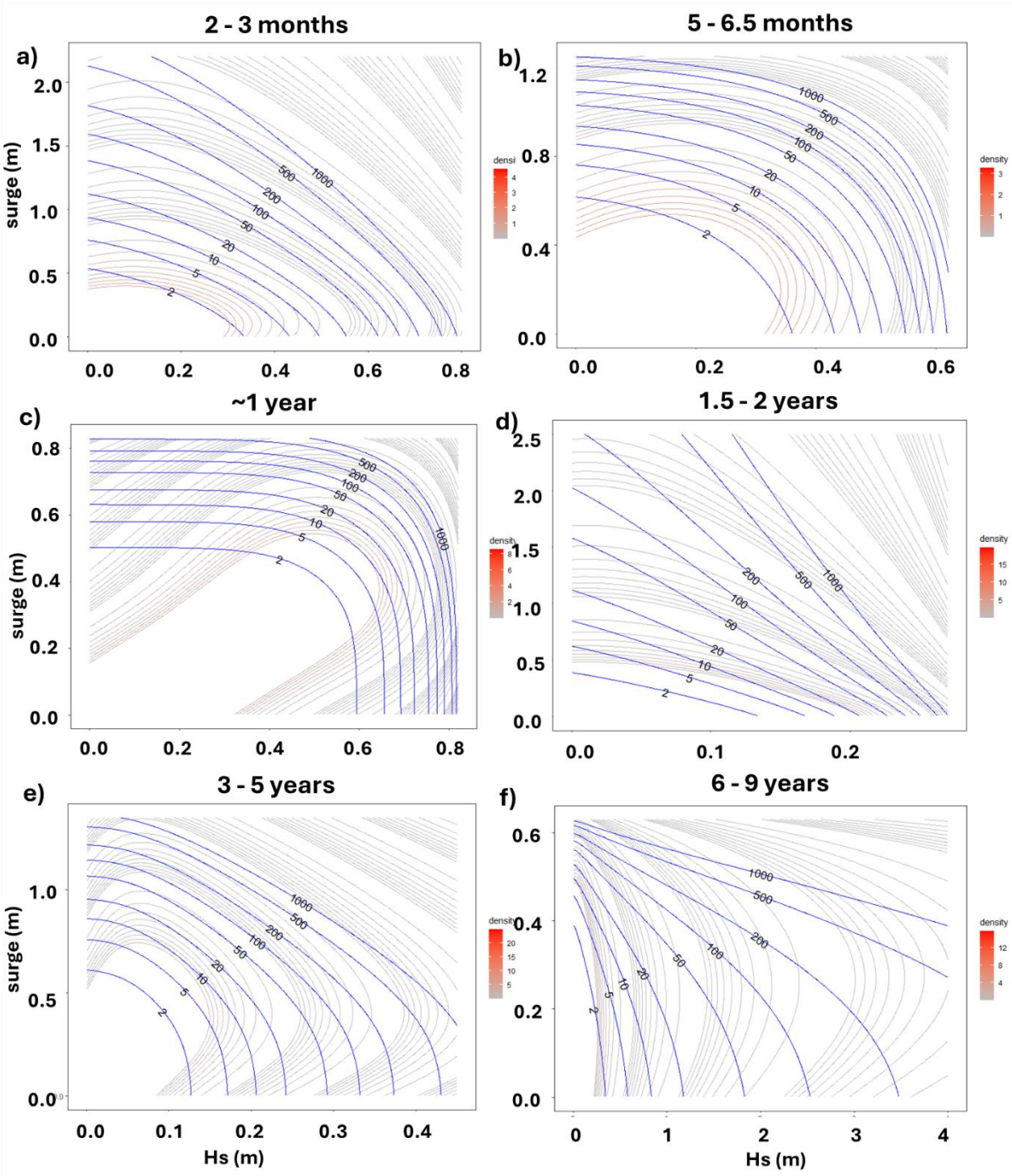

Figure 35. Bivariate density of spectral components of significant wave height from and surge in Le Havre with effective joint return levels for several return periods for the time scales of a) 2-3 months, b) 5-6.5 months, c) ~1 year, d) 1.5-2 years, e) 3-5 years, and f) 6-9 years

Following the most recent studies that apply this method (Molina et al., 2019; Soloy et al., 2024), a marine storm is defined as an event during which the significant wave height (H_s) exceeds a threshold ($H_{s,threshold}$) and lasts for at least 24 hours. The threshold of wave height $H_{s,threshold}$ is selected as the mean of the time series of H_s plus two standard deviations (Eq. 9).

$$H_{s,threshold} = \mu H_s + 2\sigma^2 H_s \quad (9)$$

which usually corresponds to the quantile 95 of the distribution.

The wave height H_s must remain over this threshold for 24 hours or more to be identified as a storm in the time series. Nevertheless, it is allowed to take values under $H_{s,threshold}$ if it happens less than 12 hours during the 24 hours taken as minimum duration. This way, the fluctuations that sometimes occur in the evolution of an extreme event are also taken into account. At this point, the duration of a storm is added to the H_s as a main characteristic.

Other interesting characteristics of the storms are the maximum wave height $H_{s,peak}$ reached during the extreme event, the so-called peak of the storm, and the associated $T_{p,peak}$ and $\theta_{m,peak}$ that corresponds to the sea state of this peak. Also, considering the duration of the storm, the average of H_s during this period $H_{s,mean}$ can be obtained as an additional characteristic.

This methodology can be applied also to the time series of surges, considering the severity criterium for selecting a threshold, defined as in Eq. 9, similarly to wave height. The methodology also includes the two criteria of persistence, with a duration of the extreme event of, at least, 24 hours, allowing a maximum of 12 hours under the threshold.

3.5.1.1. Extreme events of significant wave height

Continuing with the analysis of wave height and surges previously performed with monthly maxima, once the definition of an extreme event from a threshold is presented, it can be performed with the data of H_s obtained from reanalysis and the measurements of surges acquired from the tide gauges in the same 7 locations across the English Channel.

In Brest, a total number of 268 storms are identified in the time series of H_s over a threshold of 0.658 m from 1980 to 2022, with a mean of 6.23 events per year. The averaged $H_{s,mean}$ for all the events is 0.82 m during the storms, with a minimum of 0.6 m and a maximum of 1.24 m. The other characteristics can be found in **Table 8**, including the statistics for the peak of the storms $H_{s,peak}$, the associated $T_{p,peak}$ and $\theta_{m,peak}$, and the duration of the extreme events. The minimum duration is not considered because it is constant, taken as 24 hours.

For Cherbourg, there are 287 storms in the time series of H_s, with a threshold of 1.905 m for the same period as in Brest since the wave data comes from reanalysis for all the locations. This makes an average of 6.67 storms per year, with an average $H_{s,mean}$ of 2.31 m, ranging from 1.87 m to 3.27 m. The additional characteristics are included in **Table 8**.

The time series of H_s in Weymouth has 268 storms, with a $H_{s,threshold}$ of 0.811 m, also with 6.23 events per year as an average, with a mean $H_{s,mean}$ for all the storms of 1.02 m and a minimum and a maximum $H_{s,mean}$ of 0.62 m and 1.61 m, respectively. **Table 8** has the information of the other characteristics, and for all the remaining locations as well.

Le Havre presents 278 stormy events in the time series of wave height, with a threshold of 0.958 m, making 6.46 storms per year. The averaged $H_{s,mean}$ is 1.20 m, with a range from 0.98 to 1.68 m.

In Newhaven, 289 storms are identified in the time series of H_s over a threshold of 2.046 m, with a mean of 6.72 extreme events per year. The mean of $H_{s,mean}$ of all the extreme events is 2.459 m, a minimum of 2.01 m and a maximum of 3.29 m.

For Dover, the time series of H_s presents 281 extreme events, with a $H_{s,threshold}$ of 2.11 m, obtaining an average of 6.535 storms per year, a mean of $H_{s,mean}$ of 2.574 m and a range from 1.94 m to 3.44 m.

Finally, in the time series of wave height in Dunkirk 304 storms can be identified over a threshold of 1.194 m, with an average of 7.070 per year. The mean of $H_{s,mean}$ of all the storms is 1.519 m, with a minimum of 1.19 m and a maximum of 2.22 m.

	$H_{s,peak}$ (m)			$T_{p,peak}$ (s)			$\theta_{m,peak}$ (°)			Duration (hours)	
	Min	**Max**	**Mean**	**Min**	**Max**	**Mean**	**Min**	**Max**	**Mean**	**Max**	**Mean**
Brest	0.71	1.91	1.10	3.26	4.88	3.88	160.3	277	220.4	119	43.5
Cherbourg	1.99	4.44	2.77	6.38	14.89	8.87	275.2	64.3	337.6	109	40.9
Weymouth	0.79	2.11	1.27	3.46	19.59	6.76	93.2	277	135.23	177	43.8
Le Havre	1.09	2.52	1.56	4.69	12.30	8.12	244.8	300.1	284.32	160	43.9
Newhaven	2.17	5.03	3.03	6.75	12.02	8.60	189.2	238.6	224.6	125	43.4
Dover	2.27	5.88	3.21	6.23	10.16	8.13	201.7	58.9	237.72	128	39.9
Dunkirk	1.21	3.23	1.83	5.78	11.36	8.03	272.4	28.1	351.10	143	39.4

Table 8. *Statistics of the main characteristics of the extreme events identified over a threshold in the time series of significant wave height*

3.5.1.2. Extreme events of surges

In an equivalent way, the identification of extreme values technique is also applied to the time series of surges, obtaining in this case the average of surges during the different extreme events identified, the peak of the storms and the duration of the events, since there are no more characteristics in the case of surges. The duration for the extreme events of surges is given in days because the storms are longer when they are identified in the time series of surges than when they are identified in the time series of wave height.

For Brest, there are 207 extreme events identified on the time series of surges from 1980 to 2017 over a threshold of 0.242 m, obtaining 5.447 storms per year, with an averaged surge during all the storms of 0.340 m, with a minimum mean surge during one of the storms of 0.25 m and a maximum of 0.6 m. The statistics of the peak of the storm of surges and the duration are presented in **Table 9**.

In Cherbourg, 190 storms are identified in the time series of surges, from 1980 to 2017, with 5 storms per year and with a threshold of 0.219 m. The mean surge is 0.309 m during all the extreme events, ranging this average from 0.23 m in the lowest value of mean surge to 0.46 m in the highest. **Table 9** presents the rest of values, as for the rest of the following locations.

In Weymouth, there are 156 extreme events obtained over a threshold of 0.263 m, with 6 storms per year from 1991 to 2018. The average of the mean surge is 0.333 m, with a range from a mean surge of 0.21 m to a mean surge of 0.7 m.

The time series of surges in Le Havre allows identifying 311 storms from 1980 to 2020, making 7.974 storms per year, over a threshold of 0.229 m, giving an averaged mean surge for all the storms of 0.290 m, with a minimum mean of 0.08 m and a maximum mean of 0.56 m.

For Newhaven there are 273 extreme events from 1982 to 2018, with a threshold of 0.239 m and an average of 7.8 storms per year. The mean of surges for all the storms is 0.279 m, ranging from 0.16 m as average for one of the storms to 0.47 m as average for another one.

In Dover, a total number of 214 storms with a mean of 5.784 storms per year over threshold of 0.321 m are identified from 1980 to 2018. The averaged mean surge is 0.393 m, with a minimum of 0.13 m and a maximum of 1.02 m.

Lastly, in Dunkirk, 167 extreme events of surges from 1980 to 2016 are identified with a threshold of 0.258 m and an average of 4.771 storms per year. The mean surge for all the storms is 0.425 m, with a range from 0.26 m to 0.88 m as averaged surge during each individual storm.

	Surge peak (m)			Duration (days)	
	Min	**Max**	**Mean**	**Max**	**Mean**
Brest	0.26	1.29	0.430	9.250	2.218
Cherbourg	0.24	0.82	0.402	9.167	2.185
Weymouth	0.29	1.27	0.523	9.667	2.360
Le Havre	0.25	1.74	0.591	10.458	1.933
Newhaven	0.27	0.94	0.481	10.042	2.042
Dover	0.35	1.5	0.682	5.708	1.570
Dunkirk	0.28	1.29	0.563	3.875	1.657

Table 9. *Statistics of the main characteristics of the extreme events identified over a threshold in the time series of measured surges*

Comparing the number of extreme events obtained for significant wave height and for S, almost the same number of storms can be identified when applying the methodology to H_s, than to S, averaging 6.56 storms per year for the 7 locations, when for S, even if for some of the locations less storms are identified, it is because the records are shorter, averaging 6.11 storms per year. The durations of the storms of S over the respective thresholds are longer, with a mean for all the sites of 1.995 days (47.88 hours) over the 42.1 hours for the extreme events of wave height. But the difference comes with the maximum duration of the events, and that is because the threshold is lower for S in relation to the range of values, allowing the time series to remain over the threshold for more time, generating longer durations of storms, up to 10 days for most of the sites, especially in the central-East English Channel (Le Havre and Newhaven).

For the storms identified with H_s, it can be noticed that the direction associated with the peaks $\theta_{m,peak}$ is totally dependent on the location, following the orientation of each study site, since waves tend to arrive perpendicularly to the coast. The peak period associated with the peak $T_{p,peak}$ is approximately the same for every place, except for Brest and Weymouth, the first one because it is a protected location inside an estuary, and the second one because the storms suffer from great refraction till, they arrive at this place. Comparing the statistics of the peaks of the storms, the highest storms in terms of wave height arrive to Dover, Newhaven and Cherbourg, followed by Dunkirk and Le Havre, with the smallest in Weymouth and Brest. This order is correlated to the exposure to the sea of each location, from more to less protected. It is noticeable that for Dunkirk, the place where more storms per year are identified, with an average of 7.07 storms per year, almost one more storm than in Brest and Weymouth, both with 6.23 storms per year. Based on this data, Newhaven presents the worst combination, with the highest minimum $H_{s,peak}$, 2.17 m, the second highest $H_{s,peak}$ with 3.03 m, and the second highest mean number of storms per year, 6.72. Le Havre, the only study site located in Normandy, the combination of characteristics is not among the worst, with 6.46 storms per year, but with a low mean $H_{s,peak}$ of just 1.56 m.

Regarding the extreme events identified in the time series of S, the number of storms per year is strongly variable from some stations to others, with a minimum of 5.87 storms per year in Cherbourg and Dunkirk and a maximum of 8.5 storms per year in Weymouth up to 8.74 in Dover. It is remarkable that Cherbourg presents the lowest threshold with less storms per year than any other location when the opposite situation could be expected. Dunkirk, with the lowest frequency too, has a threshold in the median of all the 7 sites. Also, Weymouth and Dover have the highest thresholds in combination with the highest frequency of storms per year. This fact confirms that there is a correlation between the number of events per year and the threshold for the studied locations: more extreme events can be expected if a threshold is higher in a specific place and vice versa. With respect to the duration of the storm, Cherbourg, Brest, and Weymouth present the longer duration of storms as an average, with the lowest values for Dunkirk and Dover, following a path of decreasing from West to East. A similar trend can be observed for the longest duration of a unique storm identified on each location.

3.5.2. Characterization from wave energy

Once the durations of the storms are obtained, the wave energy of each individual event can be calculated from the wave data. Firstly, the energy flux has to be calculated as in Eq. 10.

$$E_{flux}(t) = \frac{\varrho g^2}{64\pi} {H_s}^2 T \tag{10}$$

where ϱ is the sea water density (1025 kg/m^3), g is the acceleration of gravity (9.81 m/s^2), H_s is the wave significant height of each sea state in meters, and T is the wave period in seconds, which in this case corresponds to the peak period T_p.

The energy flux E_{flux} can be integrated for the complete duration of the storm to obtain the accumulated energy or wave energy of a storm (Eq. 11).

$$E_{storm} = \int_{t_{storm\ start}}^{t_{storm\ end}} E_{flux}(t)dt \tag{11}$$

The cumulated wave energy E_{storm}, measured in W/m, is useful to characterize the extreme events in terms of hazard, since the E_{storm} integrates in a single value the wave height, the wave period, and the duration of the storm.

For obtaining some information about the wave energy, the storms can be sorted by decreasing accumulated energy, obtaining for each location the list of extreme events from a higher energy to a lower. Among the 7 locations, Cherbourg, Newhaven and Dover present the highest storm energy, over 3.0 x 10^6 W/m for some of the storms. In Dunkirk and Le Havre, it barely

surpasses 1.2 x 10^6 W/m for a few storms, and in Weymouth and Brest, it is noticeably less, below 8.0 x 10^5 W/m for all of them. In **Figure 36** the graphics with the storm rank for every location sorted by decreasing cumulated wave energy are presented.

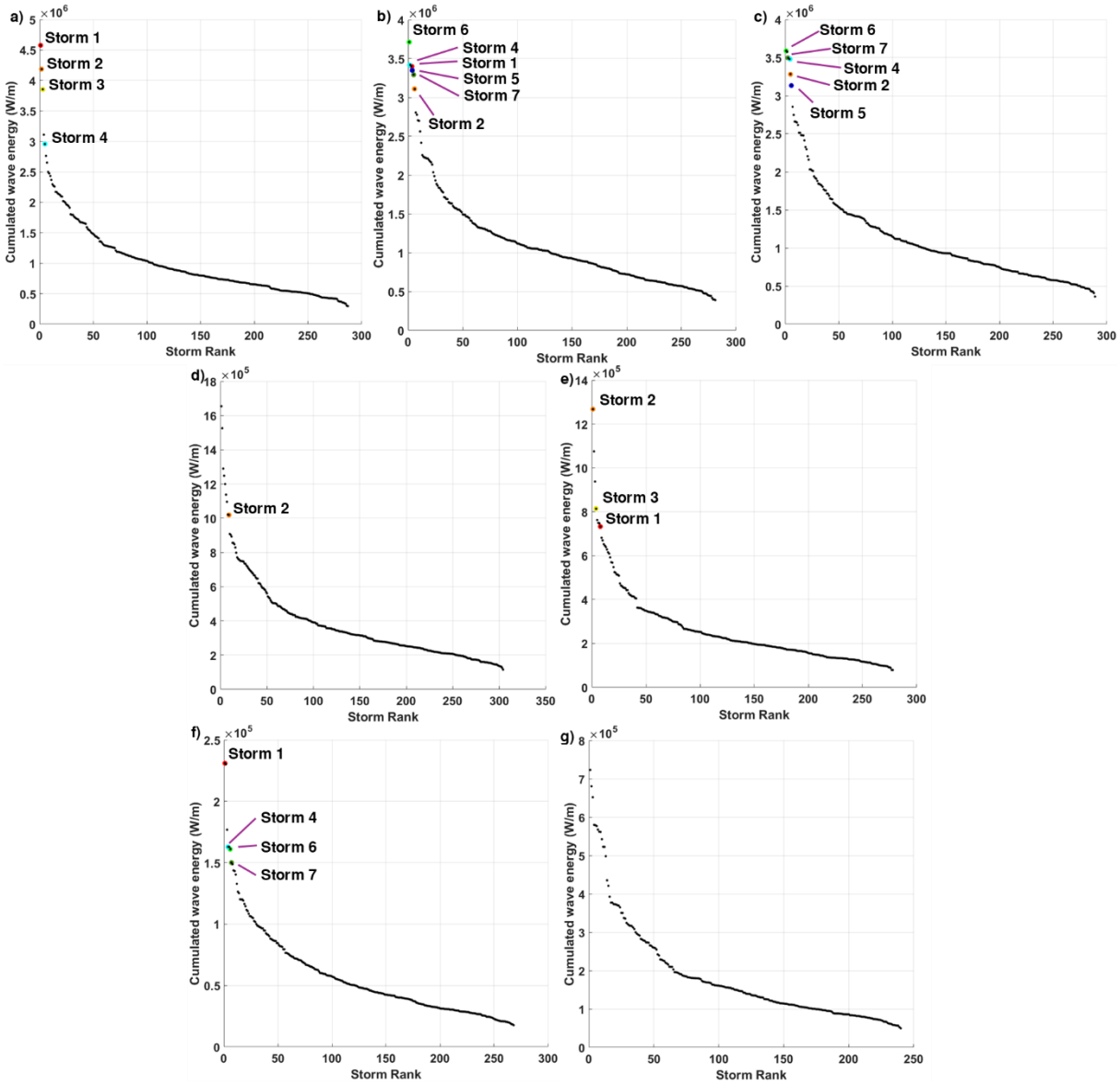

Figure 36. *Storm energy for all the storms identified sorted by accumulated wave energy on a) Cherbourg, b) Dover, c) Newhaven, d) Dunkirk, e) Le Havre, f) Brest, and g) Weymouth*

Taking Cherbourg, Newhaven and Dover as references because they have the highest cumulated energy, the most energetic storms are investigated. In the graphics from **Figure 36**, these storms are indicated. Among all the sites, the top three storms in Cherbourg present the highest wave energy, with more than 3.8 x 10^6 W/m. In **Table 10** and **Table 11** the main characteristics of these 3 storms, named Storms 1, 2 and 3, are presented, with Storm 1 also

located among the most energetic storms in Newhaven, Dover, Le Havre and Brest. Storm 2 can also be identified among the most energeticstorms of Newhaven, Dover, Le Havre and Dunkirk; and Storm 3 just among the most energetic storms of Le Havre, with this coincidence between Cherbourg and Le Havre probably because they are the closest sites with similar characteristics.

To include more information, the other storms that surpass the 3.0×10^6 W/m in Dover and Newhaven, named Storm 4 to Storm 7, are also tracked down in the different sites, being coincident for both places, although in different orders. Out of these 4 more storms, three of them are among the most energetic storms of Brest and one of them in Cherbourg, leaving Le Havre with the same 3 storms coincident with the top 3 of Cherbourg, Dunkirk only with one among the most energetic, and none of them in Weymouth, due to the special configuration of this study site, needing from a big refraction in the storms to arrive there. In **Figure 36** these 4 storms are also indicated for the respective study sites, with the information presented too in **Table 10** and in **Table 11**.

For most recent years, there is one storm that can be identified among the most energetic storms in Cherbourg, Le Havre and Dover, ranking #6, #10 and #8, respectively, and happening between 9th and 12th February 2020, which is storm Ciara, and had a special impact on the coasts of Normandy. An additional column in both tables has been added with the energetic characteristics of this storm for all the sites. In the next sections, storm Ciara and its consequences will be investigated.

	Cherbourg							Dover							Newhaven						
	Start date	End date	Duration	Storm energy (W/m)	Ranking	Start date	End date	Duration	Storm energy (W/m)	Ranking	Start date	End date	Duration	Storm energy (W/m)	Ranking	Start date	End date	Duration	Storm energy (W/m)	Ranking	Ciara
Storm 1	02/01/1998	06/01/1998	96 hours	4.57×10^6	#1	01/01/1998	05/01/1998	101 hours	3.40×10^6	#3	01/01/1998	05/01/1998	102 hours	3.58×10^6	#2	09/02/2020	12/02/2020	65 hours	2.76×10^6	#6	09/02/2020
Storm 2	25/02/1990	02/03/1990	108 hours	4.19×106	#2	25/02/1990	01/03/1990	83 hours	3.11×10^6	#6	25/02/1990	01/03/1990	99 hours	3.28×10^6	#5						
Storm 3	10/02/1990	15/02/1990	109 hours	3.85×10^6	#3																
Storm 4	27/12/1994	31/12/1994	98 hours	2.96×10^6	#5	26/12/1994	31/12/1994	100 hours	3.42×10^6	#2	26/12/1994	31/12/1994	101 hours	3.48×10^6	#4						
Storm 5						28/10/2000	31/10/2000	64 hours	3.35×10^6	#4	28/10/2000	31/10/2000	64 hours	3.13×10^6	#6						
Storm 6						01/01/1988	06/01/1988	128 hours	3.71×10^6	#1	01/01/1988	06/01/1988	125 hours	3.59×10^6	#1						
Storm 7						22/11/2009	26/11/2009	111 hours	3.29×10^6	#5	22/11/2009	26/11/2009	115 hours	3.50×10^6	#3						
Ciara	09/02/2020	12/02/2020	65 hours	2.76×10^6	#6	09/02/2020	12/02/2020	66 hours	2.77×10^6	#8	09/02/2020	11/02/2020	67 hours	2.61×10^6	#12						

Table 10. *Characteristics of the selected storms sorted by the highest cumulated wave energy in Cherbourg, Dover and Newhaven, the sites with the highest energy*

	Storm 1	Storm 2	Storm 3	Storm 4	Storm 5	Storm 6	Storm 7	Ciara
Dunkirk								
Start date		26/02/1990						09/02/2020
End date		02/03/1990						11/02/2020
Duration		114 hours						55 hours
Storm energy		1.02×10^6						3.90×10^5
Ranking		#9						#101
Le Havre								
Start date	02/01/1998	25/02/1990	10/02/1990					09/02/2020
End date	06/01/1998	02/03/1990	15/02/1990					12/02/2020
Duration	91 hours	105 hours	114 hours					72 hours
Storm energy	0.73×10^6	1.27×10^6	0.81×10^6					6.69×10^6
Ranking	#8	#1	#4					#10
Brest								
Start date	02/01/1998			26/12/1994		01/01/1988	22/11/2009	08/02/2020
End date	06/01/1998			31/12/1994		06/01/1988	26/11/2009	11/02/2020
Duration	96 hours			100 hours		109 hours	119 hours	53 hours
Storm energy	2.31×10^5			1.63×10^5		1.61×10^5	1.50×10^5	9.65×10^4
Ranking	#1			#4		#6	#7	#36

Table 11. *Characteristics of the selected storms sorted by the highest cumulated wave energy in Dunkirk, Le Havre and Brest*

3.6. TYPICAL EXTREME EVENTS IN THE ENGLISH CHANNEL

This subsection aims at investigating the distribution of marine storms, induced by extreme waves, extreme surges or the combinations between both of them, using a new approach of Artificial Intelligence (AI). This work has been developed in the framework of the master internship of Pierre Chauris (collaboration M2C-URN and ENPC, from February to July 2024). *This part is a subject of a scientific publication (Lopez Solano, Chauris et al., in preparation for a submission to the journal Oceanologia) in collaboration with M2C and ENPC supervisors*.

Collecting all the information generated about extreme events of waves and surges, a storm database can be obtained from what a classification can be performed. The objective of this classification is categorizing the different storms in terms of similarity, including all possible characteristics in relation to extreme waves and extreme surges.

The first step is adjusting the measurements of the tide gauges to the reanalysis wave data, unifying the time steps of the different stations to obtain data every 3 hours, considering that some of them have hourly data and some others that have semidiurnal data, as explained when the databases were presented. Also, some missing days or periods can be found in the time series. To do this, each station is treated separately, depending on the frequency of data. In the stations with hourly or more frequent data (Weymouth, Le Havre, Newhaven and Dover), one data point every 3 hours is picked in the coincident instant to make them match with the time step of the wave height database. The other three stations have semi diurnal data, needing 4 times more data to match the time steps of waves. At these sites (Brest, Cherbourg and Dunkirk), under-sampled data of surges have been obtained using an upsampling method, in which the spaces between data points are filled with zeros to later use a low pass filter to replace the zeros to smooth the discontinuities created by this addition.

The impact on the existing data is negligible, and it allows having a complete dataset. This process results in a database of surges with 8 daily data for all the stations and both variables, being able to proceed to the different levels of classification.

3.6.1. Classification of individual and compound extreme events

Before the classification of the different extreme events, it is important to understand their occurrence such as: i) individual/single events when extreme waves or surges occur individually and ii) compound events when extreme surges and waves occur simultaneously. Then, it is

important to identify extreme following three different categories. To do this, it is considered that the extreme events occurring in each location are labelled as:

- Class 0 for the non-occurrence of an extreme event,
- Class 1 for the individual extreme event of H_S,
- Class 2 for the individual extreme event of S,
- Class 3 for the compound events.

This type of problem is processed as a supervised classification, for which a neural network, a well-suited and well-known model adapted for multi-class classification, can be applied. It consists of 2 layers, the first one will capture the non-linear interaction of the features thanks to a *Relu* activation, and the second one will perform the classification, thanks to a *Softmax* activation. The output is of size 4, giving each class its probability. The chosen class is then the class with the highest probability.

The model of classification for each study site is trained using a 90/10 ratio for the train/test split. It is then validated using cross-validation, allowing it to reach a mean 95% accuracy among the 10 folds used. Each model is run several times to assure the consistency of the results. Once trained, the model can be used for prediction and analysis. Then, all the possible values among the range are given for the variables H_S and S to generate the graphics of the 7 sites shown in **Figure 37**, asking the model to predict the class for a set of values. H_S and S values are taken in an evenly spaced grid, while keeping T_p and the direction fixed. The varying range of S and H_S from one study site to another is adjusted to the real range of values that the two variables take within their records. In the figure, the percentages represent the fraction of the total number of extreme events identified and classified as each type of event, and not the surface of the colored area.

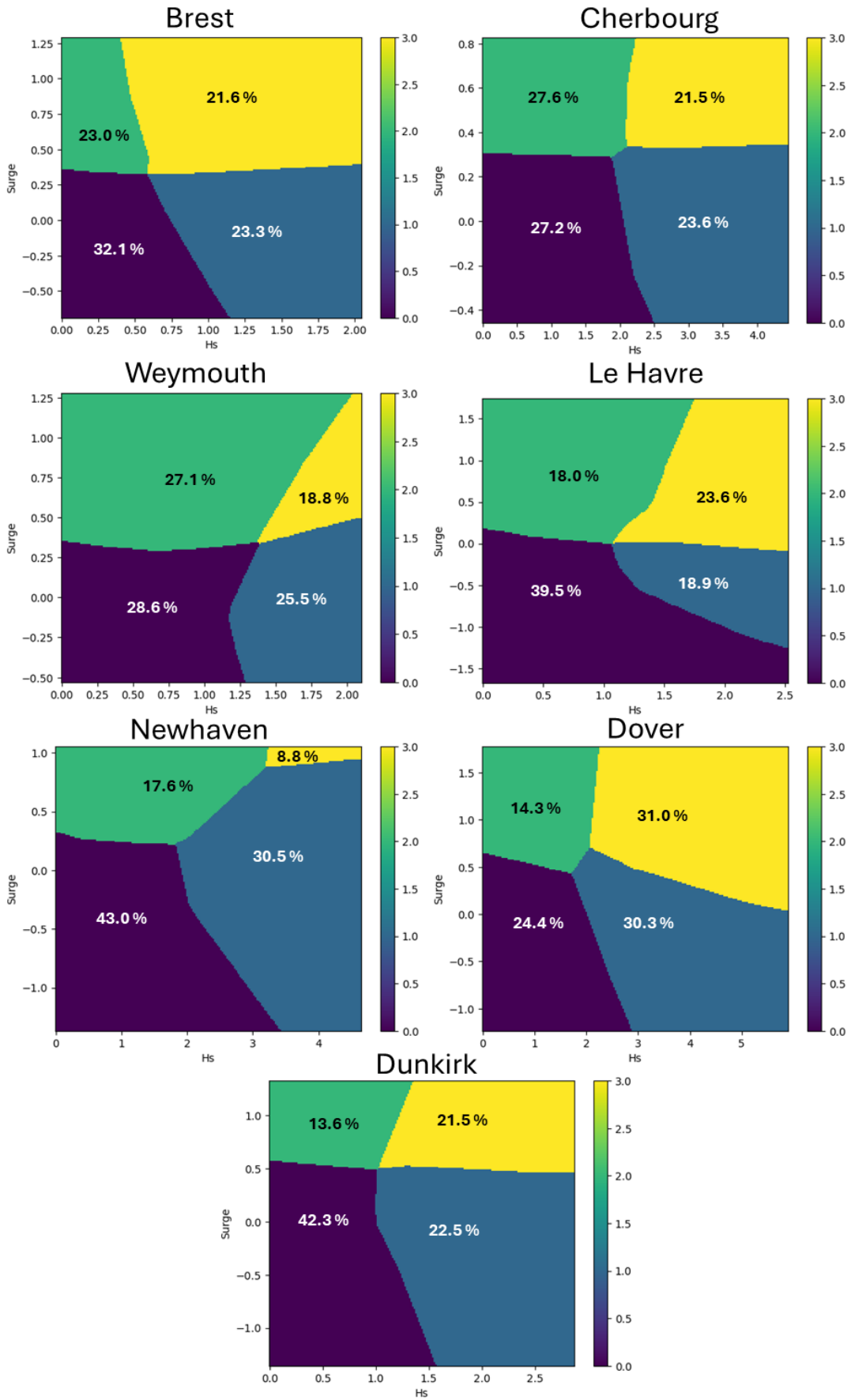

Figure 37. *Percentage of occurrence of compound and individual extreme events at Brest, Cherbourg, Weymouth, Le Havre, Newhaven, Dover, and Dunkirk*

The obtained regions are defined by a combination of H_s and S. As expected, in general, the lowest values of H_s and S correspond to class 0. Class 1 starts when a threshold of H_s is crossed, but also depends on the value of S. Class 2, as it is only events of S, depends only on the value of S. Finally, a compound event seems to correspond to an event with both high values of H_s and S. It can be observed that the biggest area in the graphics for the occurrence of compound events happen for Brest and Dover, while in Newhaven the probability is the lowest. This interpretation gives good confidence in the model. From this plot, the repartition of classes can be obtained by looking at the area of each class (percentages are included in **Figure 37** for each class and site).

To analyze the model further, it is interesting to look at the influence of the other 2 variables, T_p and direction. The class repartition percentages can be generated but varying each time the constant values of T_p or direction. The results are presented as curves in **Figure 38** for the French stations and in **Figure 39** for the British stations.

The distribution of extreme events takes different evolutions in most of stations for wave with direction < 50° and > 200°; events of Class 0 and Class 2 (individual extreme S events) increase while the events of Class 1 (individual extreme wave events) and Class 3 (combined events) decrease. For periods < 8 s, the extreme events of Class 1 and Class 3 are less frequent. These evolutions are not clearly observed at Brest and Dunkirk.

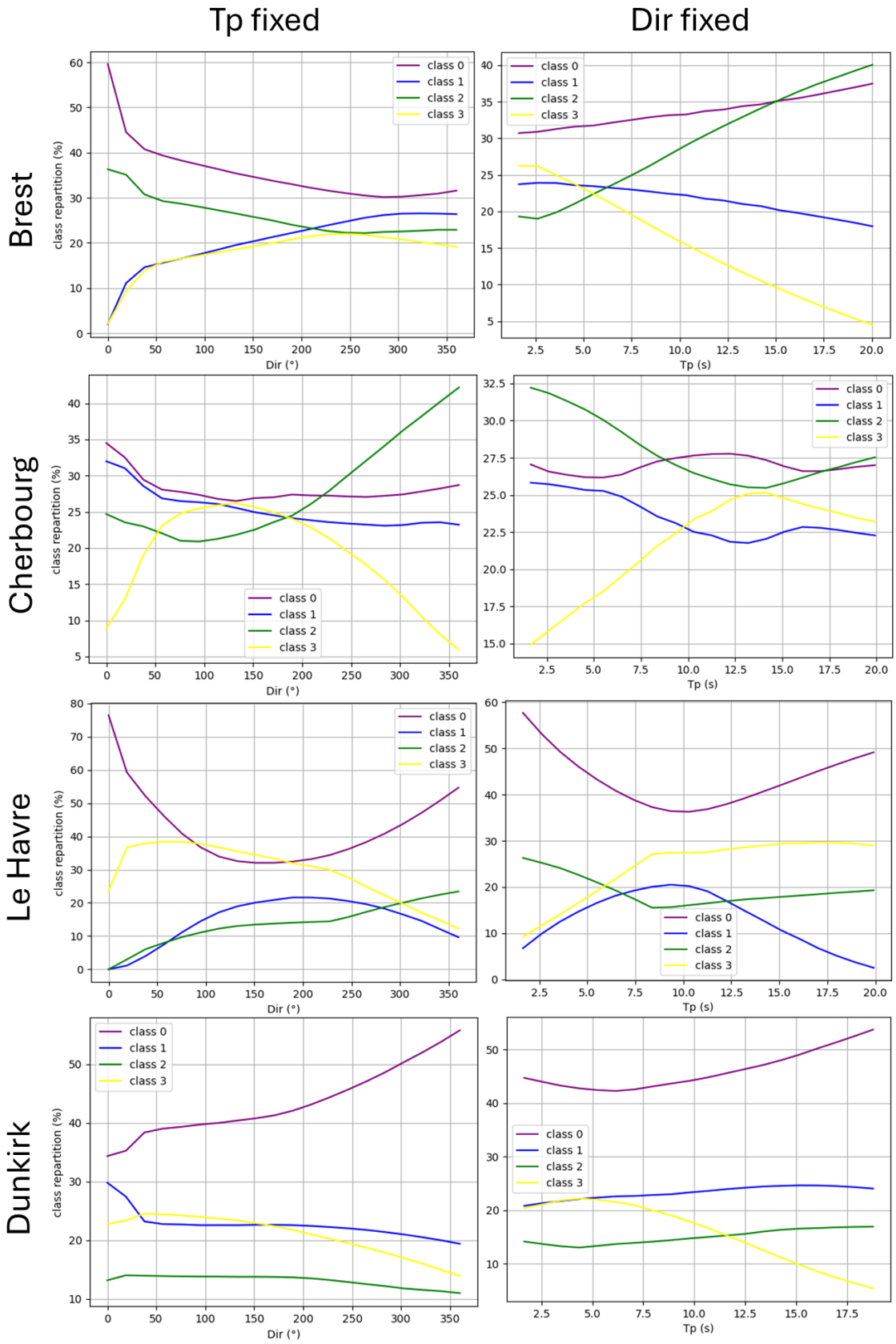

Figure 38. *Classes repartition percentages varying T_p and direction of compound and individual extreme events on the French locations: Brest, Cherbourg, Le Havre and Dunkirk. Purple, blue, green and yellow lines represent respectively the classes 0, 1, 2 and 3*

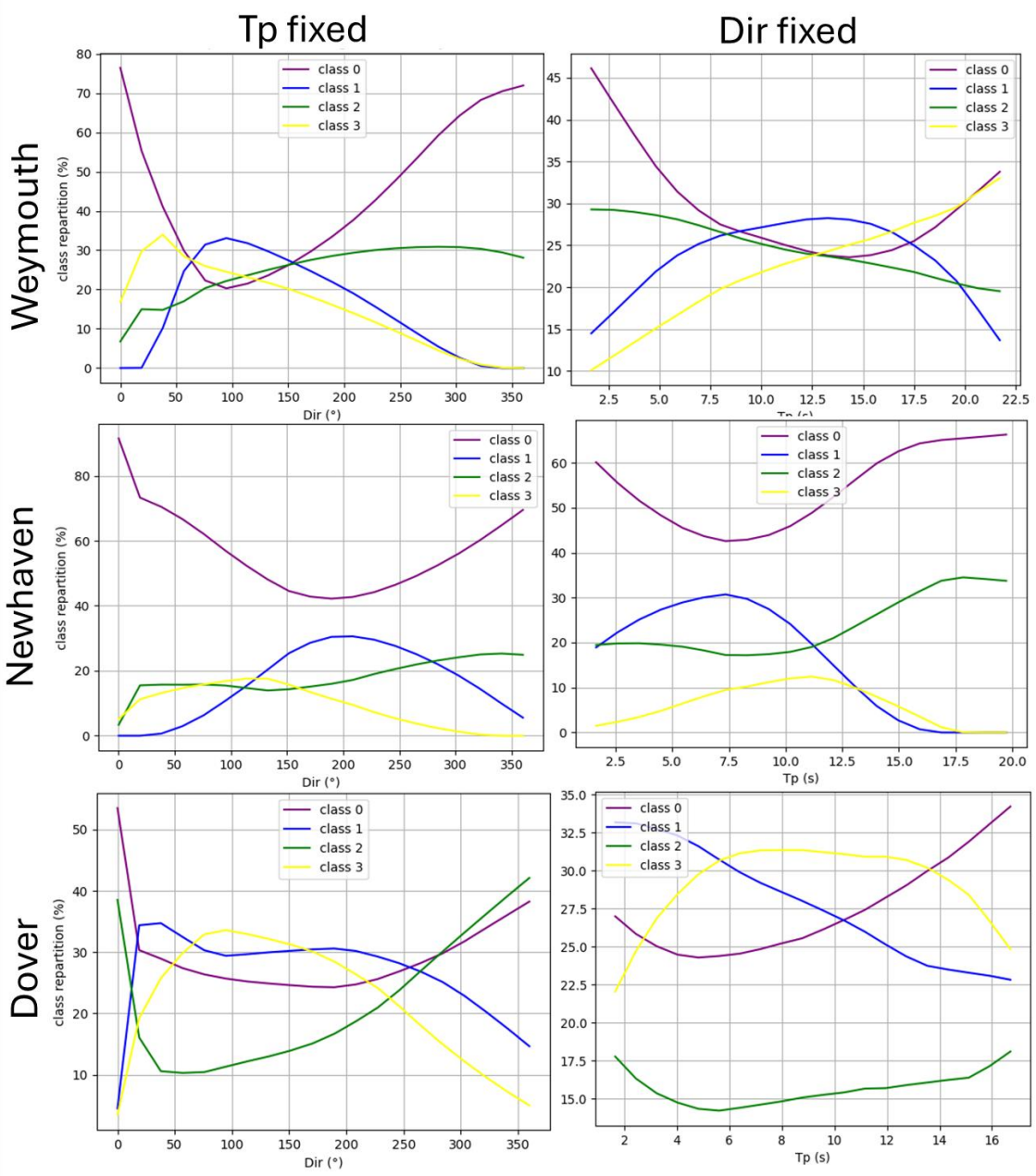

Figure 39. *Classes repartition percentages varying T_p and direction of compound and individual extreme events on the British locations: Weymouth, Newhaven and Dover. Purple, blue, green and yellow lines represent respectively the classes 0, 1, 2 and 3*

3.6.2. Clustering of extreme events

The goal of this section is to showcase the results of a clustering method applied to the storm data. The interest of such method is to divide the data into clusters in which data share similar characteristics. The biggest stake of clustering is to obtain well-defined (well-distinct from each other) and homogenous (data share close characteristics inside the cluster) clusters. It has to be noted that this type of machine-learning method is unsupervised, which means that the method can find an inherent repartition of the data without prior knowledge.

A very popular and well-suited technique to solve this problem is the Gaussian Mixture Model, referred to as GMM. The goal of this method is to model the data as a mixture of Gaussian distribution. Then, a probability distribution is assigned to each cluster. Thus, each point has a probability of belonging to each cluster, allowing dealing with complex cluster shapes and handling clusters overlapping. A toy 1D example with 2 classes can be seen in **Figure 40**.

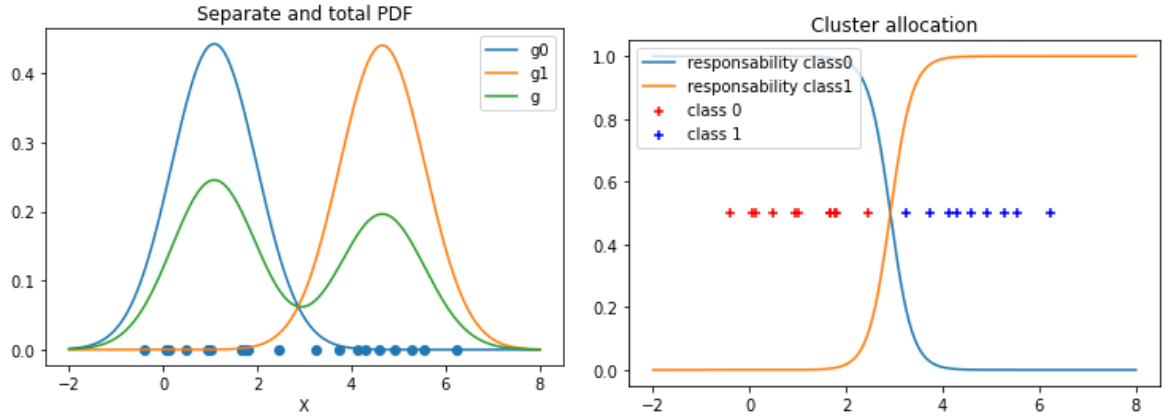

Figure 40. *Gaussian Mixture Model for a one-dimensional problem of 2 classes, with the separate and total PDF and the cluster allocation*

It can first be seen the probability density function of each class and the global density function. Then, each data point is associated with its highest probability cluster. The number of clusters is a hyperparameter of the model and should be previously defined. In this case, it is easy to set it to 2, as it seems to represent the data as simply as possible, whilst having a clear separation of the data. For more complex data, there is an explicit method based on information theory to determine the optimal number of clusters. This method will be investigated in the rest of this section. Following it, each location will be treated separately. This way, a comparison can be made for all the locations.

The clustering is performed with the help of the built-in Python library *Scikit-Learn* and its module *Gaussian Mixture*. For the specification, the covariance type used is “full”, allowing more degrees of freedom for the clusters.

As discussed previously, the number of clusters must be chosen beforehand, and it plays an important role in the reliability of the result. The compromise is to find a balance between an over-complicated and thus good-fitting model (high number of clusters) and a low-complexity but poor-fit model (low number of clusters). This can be achieved by looking at the minimum of the Akaike Information Criterion (AIC). This criterion measures the quality of a statistical model. By computing this criterion for different numbers of clusters, the model with the lowest AIC value can be selected.

For the particular case of Newhaven (**Figure 41**), it can be observed that there are 2 local minima. A general rule is then choosing the model with the lowest complexity. Thus, for Newhaven, 5 clusters will be chosen.

Figure 41. *Model for the selection of the number of clusters with AIC criterion. Example for Newhaven*

For visualization purposes, as the data is 5-dimensional, results can be more easily checked by looking at the 2D-plan formed by combinations of 2 features, the most relevant combinations being (H_s - duration) and (H_s - E_{storm}). A preview of the clustering process is presented in **Figure 42** for Newhaven data.

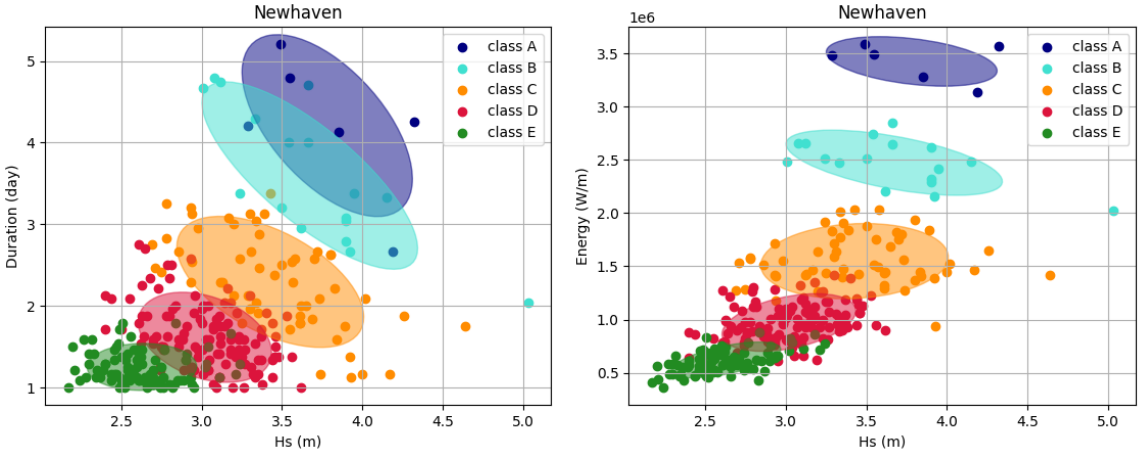

Figure 42. *H_s vs Duration and H_s vs Energy with ellipsoids representing the 95% confidence region of a cluster for the classes obtained from the clustering of extreme events in Newhaven*

Each point is colored depending on its highest belonging probability among the 5 classes. Each class is represented by an ellipse, defined by its center (the mean of the cluster) and the direction and length of its axes (the eigenvectors of the covariance matrix, defining the Gaussian distribution). These ellipsoids represent the 95% confidence region of a cluster. What is

interesting to see is that the clusters are defining levels of energy, with the clusters being horizontal. All the figures of the 7 locations are presented in **Appendix Ca**.

It is then possible to extract the statistics of the classes, namely the mean, minimum, and maximum values. Those values are collected for each location from **Table 12** to **Table 18** for Brest, Cherbourg, Weymouth, Le Havre, Newhaven, Dover and Dunkirk.

	$H_{s,peak}$ (m)	$T_{p,peak}$ (s)	$\theta_{m,peak}$ (°)	Duration (hours)	Energy (W/m)
Class A	1.545 (1.49 | 1.6)	4.455 (4.36 | 4.55)	54.5 (44.8 | 64.2)	4.625 (4.333 | 4.916)	230626 (230259 | 230993)
Class B	1.434 (1.19 | 1.74)	4.332 (4.04 | 4.7)	45.308 (30.2 | 62.7)	3.711 (1.833 | 4.958)	146598 (111581 | 176877)
Class C	1.452 (1.12 | 1.91)	4.33 (3.89 | 4.88)	44.105 (18.7 | 71.2)	2.499 (1.333 | 3.833)	106660 (74567 | 126333)
Class D	1.284 (0.99 | 1.67)	4.158 (3.78 | 4.63)	34.671 (-19.7 | 73.5)	2.441 (1.333 | 3.791)	82939 (59537 | 100050)
Class E	1.176 (0.89 | 1.46)	3.994 (3.55 | 4.37)	43.338 (6.8 | 71.9)	1.817 (1.041 | 2.75)	57769 (41676 | 72313)
Class F	1.03 (0.85 | 1.24)	3.783 (3.34 | 4.21)	43.462 (-13.9 | 97.0)	1.566 (1.0 | 2.375)	42584 (30708 | 55091)
Class G	0.895 (0.75 | 1.04)	3.595 (3.27 | 3.85)	33.684 (-8.4 | 70.0)	1.295 (1.0 | 1.916)	29907 (23363 | 35781)
Class H	0.864 (0.71 | 1.07)	3.514 (3.26 | 3.82)	44.48 (1.9 | 89.8)	1.07 (1.0 | 1.208)	21838 (17650 | 28890)

Table 12. *Statistical characteristics (mean and the range min/max) of the classes of the extreme events identified in the clustering in Brest*

	$H_{s,peak}$ (m)	$T_{p,peak}$ (s)	$\theta_{m,peak}$ (°)	Duration (hours)	Energy (W/m)
Class A	3.883 (3.82 | 3.95)	12.94 (11.2 | 14.1)	114.833 (111.6 | 117.3)	4.347 (4.0 | 4.541)	4204971 (3854947 | 4574519)
Class B	3.62 (3.18 | 4.43)	11.9 (9.1 | 13.1)	113.024 (111.5 | 115.2)	3.364 (2.5 | 4.166)	2869755 (2651064 | 3109920)
Class C	3.296 (2.87 | 3.79)	9.826 (8.1 | 13.1)	31.833 (-142.5 | 119.4)	3.027 (1.95 | 4.375)	2383757 (2257653 | 2498034)
Class D	3.228 (2.58 | 4.44)	11.85 (8.5 | 13.3)	59.0 (-129.2 | 109.8)	2.516 (1.62 | 3.041)	2071706 (1938179 | 2168031)
Class E	2.912 (2.41 | 3.2)	9.447 (7.2 | 14.9)	3.475 (-118.8 | 142.5)	3.156 (1.29 | 4.333)	1677892 (1505169 | 1751065)
Class F	3.087 (2.26 | 4.09)	9.848 (6.6 | 14.5)	117.287 (102.1 | 168.6)	2.057 (1.0 | 3.458)	1456016 (517807 | 2295512)
Class G	2.606 (1.99 | 3.66)	7.444 (6.6 | 8.4)	-130.462 (-171.0 | -115.7)	1.619 (1.0 | 3.708)	756816 (305089 | 1768720)
Class H	2.629 (2.05 | 3.53)	9.544 (6.7 | 13.8)	110.894 (95.2 | 126.6)	1.335 (1.0 | 2.083)	742999 (353825 | 1272058)
Class I	2.58 (2.12 | 3.17)	6.919 (6.4 | 7.6)	50.023 (-174.0 | 175.1)	1.112 (1.0 | 1.333)	472633 (295694 | 629328)

Table 13. *Statistical characteristics (mean and the range min/max) of the classes of the extreme events identified in the clustering in Cherbourg*

	$H_{s,peak}$ (m)	$T_{p,peak}$ (s)	$\theta_{m,peak}$ (°)	Duration (hours)	Energy (W/m)
Class A	1.946 (1.62 | 2.11)	8.026 (7.62 | 8.47)	-64.433 (-70.9 | -55.2)	5.027 (3.58 | 5.875)	685435 (652028 | 723479)
Class B	1.629 (1.29 | 2.0)	8.495 (6.78 | 16.79)	-62.6 (-73.2 | -8.9)	4.441 (1.5 | 7.375)	551581 (498438 | 580156)
Class C	1.371 (1.15 | 1.51)	8.181 (5.98 | 14.8)	-37.333 (-70.3 | -10.9)	3.52 (2.08 | 5.583)	370909 (318311 | 421237)
Class D	1.662 (1.07 | 2.1)	10.947 (7.03 | 19.59)	-35.44 (-69.0 | -6.2)	2.133 (1.16 | 3.375)	337692 (291787 | 377342)
Class E	1.47 (1.08 | 1.99)	6.845 (5.9 | 7.66)	-57.142 (-72.0 | -22.1)	2.492 (1.41 | 3.958)	270608 (115211 | 435623)
Class F	1.638 (1.32 | 2.04)	1.638 (1.32 | 2.04)	-18.58 (-57.6 | 14.1)	1.5 (1.041 | 2.0)	188439 (142536 | 210306)
Class G	1.147 (0.98 | 1.35)	11.721 (6.31 | 17.7)	-1.862 (-18.6 | 18.8)	1.25 (1.0 | 1.75)	151024 (111031 | 181173)
Class H	1.3 (0.93 | 1.86)	6.478 (5.21 | 8.32)	-37.853 (-74.3 | -9.7)	1.3 (1.0 | 2.125)	125507 (57615 | 317197)
Class I	1.153 (0.89 | 1.46)	6.685 (5.11 | 8.23)	-68.479 (-86.8 | -53.4)	1.537 (1.0 | 2.791)	118467 (50089 | 209979)

Table 14. *Statistical characteristics (mean and the range min/max) of the classes of the extreme events identified in the clustering in Weymouth*

	$H_{s,peak}$ (m)	$T_{p,peak}$ (s)	$\theta_{m,peak}$ (°)	Duration (hours)	Energy (W/m)
Class A	2.43 (2.43 | 2.43)	10.11 (10.11 | 10.11)	106.3 (106.3 | 106.3)	4.375 (4.35 | 4.38)	1267280 (1267280 | 1267280)
Class B	1.95 (1.88 | 2.02)	8.92 (7.9 | 9.89)	106.7 (105.0 | 108.8)	5.694 (4.75 | 6.33)	942338 (813953 | 1075459)
Class C	1.864 (1.37 | 2.27)	8.918 (7.75 | 10.14)	107.666 (97.1 | 113.8)	3.462 (2.25 | 6.67)	561679 (344693 | 762602)
Class D	1.722 (1.17 | 2.52)	8.576 (5.72 | 10.28)	105.313 (83.8 | 114.3)	2.046 (1.0 | 4.041)	306823 (136820 | 473496)
Class E	1.496 (1.1 | 1.93)	7.813 (5.18 | 9.82)	105.128 (81.8 | 120.1)	1.463 (1.0 | 2.291)	187726 (106476 | 266568)
Class F	1.248 (1.09 | 1.47)	7.668 (4.69 | 12.3)	99.073 (64.8 | 120.1)	1.176 (1.0 | 1.541)	120296 (78637 | 172001)

Table 15. *Statistical characteristics (mean and the range min/max) of the classes of the extreme events identified in the clustering in Le Havre*

	$H_{s,peak}$ (m)	$T_{p,peak}$ (s)	$\theta_{m,peak}$ (°)	Duration (hours)	Energy (W/m)
Class A	3.781 (3.29 | 4.32)	9.858 (9.12 | 10.89)	44.733 (31.6 | 49.8)	4.208 (2.66 | 5.208)	3426748 (3134165 | 3590508)
Class B	3.677 (3.01 | 5.03)	9.41 (7.91 | 12.02)	41.882 (24.8 | 49.0)	3.593 (2.04 | 4.791)	2474976 (2019143 | 2854599)
Class C	3.444 (2.69 | 4.64)	9.175 (8.18 | 10.46)	44.215 (14.6 | 54.2)	2.307 (1.12 | 3.375)	1564450 (941084 | 2032191)
Class D	3.027 (2.4 | 3.62)	8.623 (7.43 | 9.96)	45.466 (26.0 | 57.0)	1.622 (1.0 | 2.75)	978299 (609847 | 1417201)
Class E	2.613 (2.17 | 3.24)	7.963 (6.75 | 9.35)	44.169 (9.2 | 58.6)	1.238 (1.0 | 1.791)	607554 (361784 | 883614)

Table 16. *Statistical characteristics (mean and the range min/max) of the classes of the extreme events identified in the clustering in Newhaven*

	$H_{s,peak}$ (m)	$T_{p,peak}$ (s)	$\theta_{m,peak}$ (°)	Duration (hours)	Energy (W/m)
Class A	4.118 (3.42 | 4.64)	8.993 (8.45 | 9.3)	39.116 (31.1 | 43.2)	4.076 (2.66 | 5.33)	3381860 (3108347 | 3714830)
Class B	3.934 (3.5 | 4.5)	8.898 (8.3 | 9.7)	39.544 (34.6 | 42.7)	3.203 (2.583 | 4.0)	2507693 (2164602 | 2805370)
Class C	3.99 (2.94 | 5.88)	8.793 (7.96 | 10.1)	-7.949 (-142.4 | 39.4)	2.921 (2.0 | 3.833)	2185097 (2035999 | 2257201)
Class D	3.739 (2.81 | 5.57)	8.651 (7.52 | 10.0)	38.004 (30.5 | 43.3)	2.337 (1.58 | 3.083)	1720063 (1467431 | 1986305)
Class E	3.731 (3.4 | 4.4)	8.665 (7.42 | 10.2)	38.375 (25.7 | 44.9)	1.857 (1.08 | 2.625)	1485359 (1318938 | 1571458)
Class F	2.868 (2.68 | 3.1)	8.052 (7.43 | 8.7)	-68.639 (-144.1 | 42.4)	2.316 (2.04 | 2.541)	1324264 (1251709 | 1408179)
Class G	3.004 (2.59 | 3.42)	8.014 (7.47 | 8.5)	-124.469 (-146.7 | 22.6)	1.358 (1.0 | 1.791)	903389 (765182 | 1065620)
Class H	3.1 (2.27 | 4.29)	8.008 (6.97 | 9.2)	40.934 (28.9 | 49.5)	1.412 (1.0 | 2.625)	875088 (390409 | 1494250)
Class I	2.464 (2.27 | 2.77)	7.454 (6.23 | 8.4)	-93.935 (-169.9 | 158.7)	1.176 (1.0 | 1.458)	549896 (444480 | 679337)

Table 17. *Statistical characteristics (mean and the range min/max) of the classes of the extreme events identified in the clustering in Dover*

	$H_{s,peak}$ (m)	$T_{p,peak}$ (s)	$\theta_{m,peak}$ (°)	Duration (hours)	Energy (W/m)
Class A	2.517 (1.9 | 2.86)	9.315 (7.64 | 10.41)	79.737 (-173.1 | 176.0)	3.692 (2.708 | 5.96)	1246078 (892690 | 1654555)
Class B	2.107 (1.47 | 3.23)	8.806 (6.17 | 11.36)	63.977 (-179.8 | 179.5)	2.194 (1.0 | 3.958)	598823 (155157 | 1096154)
Class C	1.798 (1.21 | 2.57)	7.897 (5.78 | 9.9)	164.85 (105.7 | 179.9)	1.392 (1.0 | 2.333)	305490 (115275 | 647049)
Class D	1.597 (1.28 | 2.11)	7.563 (6.4 | 9.01)	-168.512 (-179.5 | -151.9)	1.514 (1.0 | 2.625)	266620 (133070 | 494024)

Table 18. *Statistical characteristics (mean and the range min/max) of the classes of the extreme events identified in the clustering in Dunkirk*

The choice made is sorting classes by decreasing energy, A being the class with the highest mean energy, and E the lowest. This way, the other variables correlated to the energy are shown for the 7 locations in **Figure 43**. It can be noticed that H_s, T_p, and duration are monotonically increasing with the energy, which is coherent with how the energy of the storm is defined. It can also be observed in **Figure 115** how the clusters are horizontal when comparing H_s to the energy. This means that these clusters represent levels of energy, with the sorted classes being located on subsequent increasing steps. The direction being more random, there is no particular pattern to recognize. This plot gives us confidence in the results.

In the same way, the clustering can be applied to the classes of extreme events of waves obtained in Section 3.6.1., the extreme events of just waves (Class 1), and the compound extreme events of waves and S (Class 3). Reproducing the same methodology, the equivalents tables and

figures to **Table 12** to **Table 18** and **Figure 42** and **Figure 43** are shown in **Appendix Cb** for Class 1 and **Appendix Cc** for Class 3.

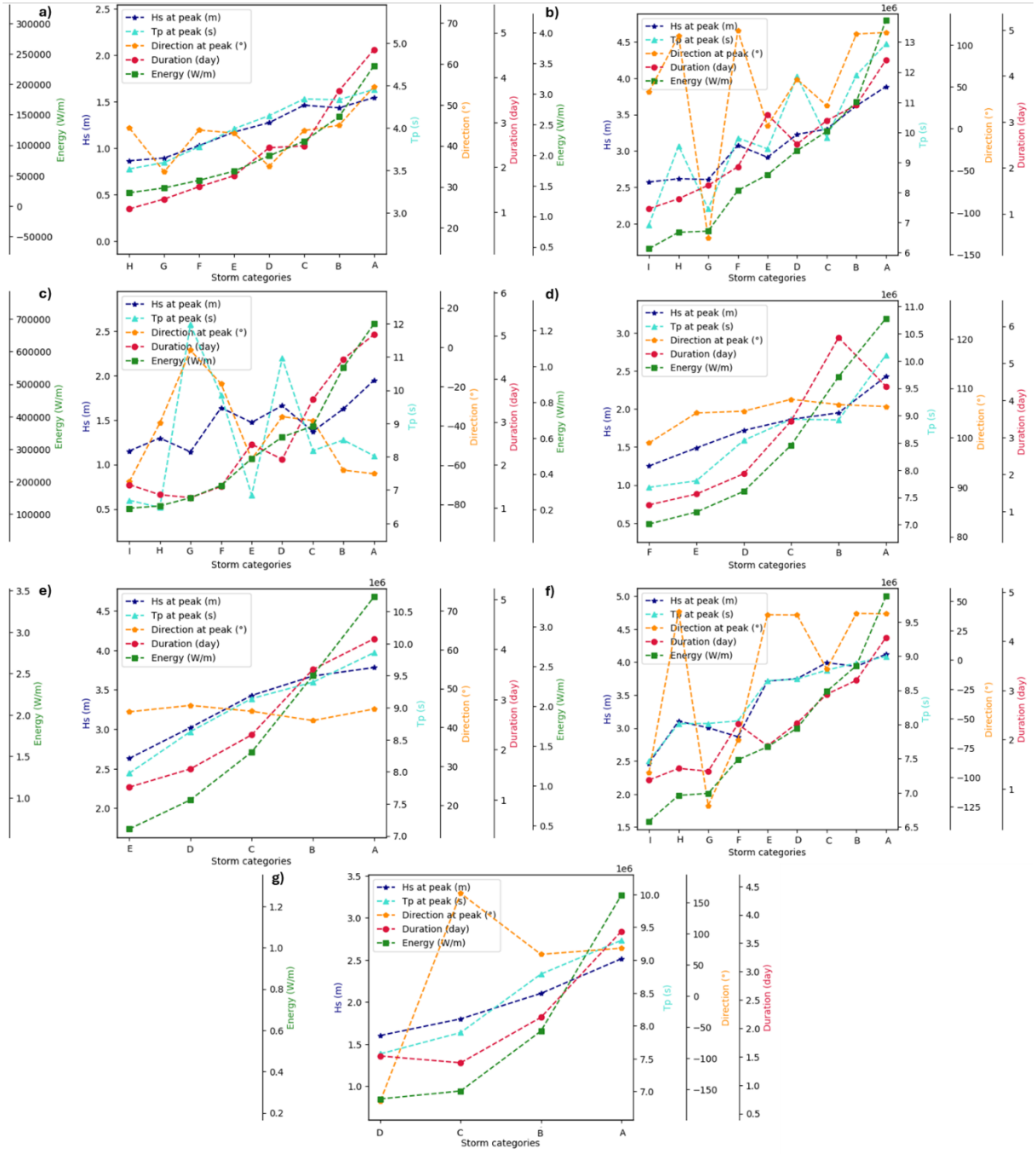

Figure 43. *Class-averaged values of extreme events on a) Brest, b) Cherbourg, c) Weymouth, d) Le Havre, e) Newhaven, f) Dover, and g) Dunkirk for the complete dataset of identified storms*

For the 7 locations, most of the storms fall into the weaker classes of each site. For Brest, classes D to G have the most frequent probability, over 10 and even 20% of the storms. In the strongest category, class A, there are only 2 storms, with an associated probability of 0.74%. Following the same criteria, in Cherbourg, classes G and H have over 30%, and classes A to E less

than 2%. In Dover, 68% of the storms belong to class H, and classes A to G vary from 2 to 4%, with class D presenting almost 8%, similarly to Dunkirk, with 52% of the storms in class C and 2.6% in class A. In Le Havre, the strongest classes have only 1 and 3 storms, with less than 1% probability. The most frequent class is E with more than 40%, as in Newhaven for class D, where class A has around 2%. Finally, in Weymouth, classes H and I have more than 25%, and classes A to G from 1 to 4%, except from class E, with 15%.

It is interesting to notice that, for all the sites except for Weymouth, the weakest class do not present the highest probability, below 25% and even just 4.5% in Cherbourg. It could be anticipated that most of the storms will fall into this weakest class, but the slight overlapping between the two weakest classes on these sites produces this effect. The unsupervised classification and the study of the reliability of the number of classes previously done determined that these classes are different enough. By considering jointly the two weakest classes in each site, the probability grows to be the most frequent as expected. Also, by sorting the classes from weakest to strongest, the probability decreases from class to class without peaks, with the exception of class D in Dover and class E in Weymouth as stated before. This is caused by a different combination of H_s, T_p and duration, and, therefore, energy, in these sites. While in the rest of locations the wave characteristics seem to be more correlated, in Dover and Weymouth the dataset is more spread out.

The frequencies or probabilities of occurrence can also be expressed in terms of return periods by associating the wave height and the energy of every class of each site to one specific return period. Considering it, in Brest the classes would be (A) >40 years, (B), ~20 years, (C), ~10 years, (D) <10 years, and (E) to (H) <5 years. In Cherbourg and Weymouth, the Rp are the same, with (A) ~10 years, (B) <10 years, and (C) to (I) <5 years. For Le Havre, (A) >40 years, (B) <10 years, and (C) to (F) <5 years, just differentiating from Newhaven in the strongest class, with (A) <10 years and (B) to (E) <5 years. In Dover and Dunkirk, (A) ~10 years, (B) < 10 years, and from (C) to (I) and (D), respectively, <5 years. These findings show parallels between sites closely located, even if the number of classes is different, which was also previously observed with the probabilities.

3.7. DISCUSSION AND CONCLUSIONS

In this study, the extreme events are identified as coastal storms, produced by abnormally high values of the most commonly studied variables of the hydrodynamics in the sea, which are the waves and the sea level. The stochastic drivers used to measure the extreme values of these

processes are the significant wave height and the storm surges. These are the variables usually analyzed to study coastal and oceanic storms (Mendoza et al., 2011, 2013; Turki et al., 2019, 2020b), with different temporal and spatial coverage. Nevertheless, other wave variables such as the peak period or the mean direction or the interaction of the storm surge with the astronomical tide could have been considered to understand the extreme sea states arriving to the shore.

The atmospheric indexes taken as reference for the correlation to the extreme values analyzed, the monthly maxima in the spectral and the non-stationary approaches, have been the North Atlantic Oscillation, the Sea Level Pressure, the Sea Surface Temperature, and the Atmospheric Multidecadal Oscillation. Numerous studies have used these indexes to correlate them with the behavior of storms, some of them analyzing the time variability of the indexes, which has not been considered in the current study. Studies like Hurrell et al. (2003) have found that the NAO mainly explains the climate patterns by its inner mechanisms. Deng et al. (2021) analyzed the trends of SST to introduce the affection of climate change on the index, finding a positive trend directly correlated with climate change. Nevertheless, although it could be a limitation, the analysis of the time series of climate patterns is not the goal of this study. A deeper approach could find the possible explanation of certain trends in the evolution of the extreme events of waves or surges by studying these atmospheric indexes.

Other indexes are available in the region and could also explain a part of the variability of the extrema, like the Gulf Stream (GS) or the Near-surface Wind Speed (NWS). Frankignoul et al. (2001) found a correlation between the GS and the NAO, revealing a southward displacement of the GS when the NAO reaches its negative extrema. Also, the NCEP analysis proved the GS path is also related to the SLP.

The consideration of a compound hazard with the bivariate risk assessment addressed in this study could be improved by transforming it into a multivariate analysis including not just the variables that cause the coastal flooding, but also the continental water sources, such as river discharge or precipitation. However, the overall compound hazard analysis of littoral flooding, including the non-stationarity added in the models led to more accurate results than what could have been obtained from an independent and stationary study. The GEV models fitted to the monthly maxima of significant wave height and surge demonstrated that it is crucial to introduce the non-stationarity, finding strong connections between the analyzed variables and the atmospheric patterns for most of the stations. The bivariate approach provided an added value, especially by including the dynamic copulas used in the study instead of the static ones. For two of the stations, the results were a constant Frank copula, showing a weaker dependence between

Hs and surge for the higher return levels, which leads to a decrease in the risk of the compound hazard. If this non-stationarity has not been taken into account, these results would have been foundfor all the sites, which is shown to be incorrect in the current study.

Still, other methods and extreme value distributions could have been applied, obtaining, for example, the extreme values that will be modeled by the POT method, selecting a threshold equivalent to the quantile 0.99 as in Hamdi et al. (2018). These extrema could, then, be fitted to a Generalized Pareto (GP) or to a Non-Homogeneous Poisson Process (NHPP). The first option only presents two parameters in comparison to the GEV distribution, one shape parameter and a scale parameter dependent on the threshold. The NHPP has the same three as the GEV but has also the problem of the threshold. Because this approach requires an appropriate selection of this threshold, probably including the seasonal variability of it. This step needs more hypotheses to continue the non-stationary analysis, introducing, then, more uncertainties that could be reduced by a more detailed study. But this deep look with a probabilistic approach exceeds the objectives of this study, more limited to presenting an understanding of the correlation between extreme waves and surges and climate patterns.

In order to extend the information about storms, a definition of extreme event has been assessed, obtaining the duration of a storm as an extra variable. The duration is taken as the time of exceedance of one event over a threshold, either for wave height or for surges. This time was set as 24 hours, clustering as a same storm if the value drops under the threshold less than 12 hours. For allowing it, the threshold has been taken as the percentile 95 to get a database of storms big enough for the analysis. For the English Channel, these values are appropriate, since the storms arriving to this location are expected to be severe, lasting in time and expanding in space, worse than the storms occurring in the Mediterranean Sea in a similar longitude (Mendoza et al., 2011), where a shorter duration can be considered.

Including the duration of a storm allows studying the characteristics of the different extreme events, such as the wave energy, that integrates severity and persistence. In the present study, a short analysis of the wave energy is carried out, obtaining a ranking of the most energetic storms for the different study sites, which permits to track down throughout the English Channel some of them. Nevertheless, to be able to properly perform this analysis, some observation points located in deep waters would be necessary, placing them along the basin and following the evolution in the main characteristics to observe the affection of propagation phenomena like refraction.

Finally, the time series of significant wave height and storm surge are analyzed considering all the previous characteristics obtained, applying a first classification that gives information about the type of extreme events that happen in each location.

3.8. CONCLUSIONS OF THE CHAPTER

This chapter answers the first scientific questions presented in Chapter 2, which are:

- *How can we characterize the non-stationary connections between the global climate oscillations and the multi-timescale extreme hydrodynamics in the English Channel?*
- *How is this non-stationarity considered for developing the stochastic downscaling and estimating extremes?*
- *What are the main storm classes, representative of multi-timescale extreme hydrodynamics in the English Channel during the last decades?*

The relationship between local dynamics of extreme events, represented by the extreme values of wave height and surges in 7 chosen locations in the French and the British coasts of the English Channel, and global atmospheric circulation, expressed by some specific climate indexes used in this study, is studied performing, first, a spectral analysis, and second, a non-stationary probabilistic approach. Both analyses found a strong correlation between local extrema of significant wave height or storm surge and atmospheric patterns like the North Atlantic Oscillation or the Sea Level Pressure. This study is complemented by a bivariate approach that integrates the risk of compound hazard of extreme waves and extreme sea level. For addressing the definition of the typical extreme scenarios, firstly a definition of extreme event based on a threshold and a duration is necessary. Then, collecting all the information obtained in the different parts of the study, a classification is performed to highlight the typical extreme events in the English Channel, clustering the storms according to their characteristics.

This finding presents a handful of new approaches that are useful as an excellent step forward for understanding the physical relations of downscaling from the global climate mechanisms to the local storms, induced by extreme surge-wave hydrodynamics. This provides an overview for inferring the future projections of sea level change combined with the effects of extreme events.

CHAPTER 4

INTEGRATED MODELING FRAMEWORK FOR MONITORING EXTREME EVENTS FROM THE ENGLISH CHANNEL TO THE NORMANDY COASTS

Coastal storms are characterized by high waves or surges arriving to the shore. The duration and intensity of a storm are conditioned by the characteristics of the extreme event when it is generated in the deep ocean. When storms are propagating through the sea they are modulated, amplifying or softening every attribute. As described before, the English Channel presents some specificities that directly affect storms and increases the necessity of expanding the current studies related to the topic. That is the reason also why the Normandy coasts are exposed to the actions of these extreme events and make it essential to describe and classify the storms arriving to the shores. In this chapter, firstly, a database of 40 years of waves and sea level has been generated expanding from the Atlantic Ocean and the North Sea into the English Channel. This database has been used to find the main features of oceanic storms in the open boundaries of the Channel to later track them throughout the basin and when they approach the coasts of Normandy. In second place, extreme events have been analyzed comparing the characteristics in the English Channel and on the Normandy coasts, focusing on a local scale in Etretat and Hautot-sur-Mer, describing the modulation of storms in terms of the main wave statistics and wave frequency spectrum.

The main results of this chapter have been subject of two scientific publications in Natural Hazards (2024) and Water (2022): *C. López Solano, E. I. Turki, E. T. Mendoza et al., Hydrodynamic Modelling for Simulating Nearshore Waves and Sea Levels: Classification of Extreme Events from the English Channel to the Normandy Coasts*; and *C. López Solano, E. I. Turki et al., Dynamics of Nearshore Waves during Storms: Case of the English Channel and the Normandy Coasts*.

4.1. EVOLUTION AND CLASSIFICATION OF EXTREME EVENTS OF WAVES AND SEA LEVELS FROM THE ENGLISH CHANNEL TO THE NORMANDY COASTS

This section describes the generation of a database of waves and sea level covering the surface of the English Channel, and the identification of extreme events and their evolution throughout the basin, to finally apply a classification and take some storms as example. The text has been published in the journal Natural Hazards: *López Solano, C.; Turki, E. I.; Mendoza, E.T.; Gutiérrez Barceló, A. D.; Migaud, A.; Hamdi, Y.; Laignel, B.; and Lafite, R. (2024)* Hydrodynamic Modelling for Simulating Nearshore Waves and Sea Levels: Classification of Extreme Events from the English Channel to the Normandy Coasts. *https://doi.org/10.1007/s11069-024-06699-7*

4.1.1. Introduction

Storms are one of the most powerful natural phenomena on Earth. They are controlled by strong meteorological and physical drivers induced by a violent atmospheric disturbance, with low barometric pressure, severe winds, and precipitation. From an ocean perspective they are described by high waves (Corbella & Stretch, 2013) and when they have impact on the coasts they are known as coastal storms (Harley, 2017). However, the definition of a storm has proven complicated given the dynamic and complex nature of oceanic systems. The intensity and duration of these phenomena can vary widely, making it difficult to establish clear criteria for what constitutes a storm (Harley, 2017). Additionally, the specific conditions that give rise to storms are influenced by a range of factors, including atmospheric pressure, sea surface temperature, and ocean currents, all of which can be highly variable across different regions and time scales. Moreover, storms can occur in various forms, such as tropical storms, extra-tropical storms, and hurricanes, each with their own distinct characteristics that vary at different spatial and temporal scales over which they take place.

Nonetheless, coastal storms can have significant effects on coastal environments, including erosion of beaches (Jiménez et al., 2012; Mendoza & Jiménez., 2006), coastal infrastructure damage (Bacopoulos & Clark, 2021; Jiménez et al., 2011), flooding (Rouhaud & Vanderlinden, 2022) among other impacts. These impacts will likely increase with climate change (IPCC, 2022; Switzer et al., 2015) and the increasing human pressure due to the overexpansion of urbanization and infrastructure that takes place in these areas.

Accurate wave data is crucial for the design of coastal structure development and the planning and management of coastal areas. This includes protecting vulnerable ecosystems and

assessing coastal hazards to make well-informed decisions regarding coastal management and engineering design. Wave databases play a vital role in this process, as they provide various information, including the identification of storms and storm trends, and also serve as an essential element in validating numerical models. However, there are situations where in situ wave data is unavailable. In this situation, numerical models have proven to be a valuable tool for obtaining wave data (Appendini et al., 2014; Dee et al., 2011; Hersbach et al., 2020).

In the context of the English Channel, previous works have been focused on the dynamics of some energetic storms and their effects close to coastal zones, including marine submersion and coastal erosion. Wells et al. (2001) examined the extreme storm surges, produced during the events of 14th-18th December 1989 within the English Channel, by the use of a shallow water hydrodynamic model to calculate the surge-tide interaction which reduces the peak heights of surges; their accurate estimation requires an adequate use of the wind stress parameter that improves the sea level modeling. The seiche oscillations induced by storms and their effects on the sea level changes have been investigated by Wells et al. (2005), they have shown the variation of such oscillations from their minimum in the central Channel and to their maximum in the Baie de Seine and the Golfe de St Malo.

Ozsoy et al. (2016) studied the high-frequency sea level variations and their coastal impacts during the extreme events of 28th October 2013 in the Solent, UK, a mesotidal estuarine strait located in the central English Channel. Recently, Bennis et al. (2022) used a 3D model to demonstrate that the flooding effects produced by storm Eleanor in early January 2018 are strongly related to the angle between the wave-current direction leading to an acceleration or a reduction of the velocity.

The morphodynamic effects of storms on shoreline changes in the northern coast of France have been extensively studied in previous works by Anthony (2013) and Soloy et al. (2020, 2021, 2022). Anthony (2013) investigated the impacts of storms on coastal dune morphodynamics and erosion in the southern North Sea. His study demonstrated that changes in the shoreline are influenced by various storm characteristics, such as wind speed, angle of incidence relative to the shore, and direct human intervention through beach management. In their recent works, Soloy et al. (2022) analyzed the temporal clustering of storms Ciara (December 1, 2019 - April 1, 2020) and Gareth (February 24 - April 1, 2019) along the Normandy coasts. Their research involved a combination of numerical models and remote sensing measurements to provide a comprehensive understanding of these storm events.

The non-stationary behavior and dynamics of historical storms over the past four decades in the South English Channel have been extensively studied by Turki, et al. (2019, 2020a., 2020b) using tide-gauge measurements. In their research, they employed stochastic approaches to develop novel probabilistic models that rely on global climate oscillations. These models were specifically designed to estimate extreme values and determine their corresponding return periods.

The aforementioned works have examined the behavior of individual storms and their impacts on coastal zones. The multi-timescale variation of storms and their evolution in the global context of climate change is still an issue under debate and is partly addressed in this research.

This research was carried out in the framework of the Surface Water and Ocean Topography (SWOT) program of the French National Centre of Space Studies (CNES) and focuses on gaining insight into the dynamics of storms and their hydrodynamic impacts on Normandy coasts under the time-varying climate and hydrometeorological drivers.

In this study, we examine the hydrodynamics of individual extreme events and analyze the temporal clustering of storms over a 40-year period in the English Channel and the Normandy Coasts. Here, we use a numerical approach to achieve the following objectives: i) generating a comprehensive hindcast dataset of nearshore wave behavior in response to storms by integrating both temporal and spatial scales, ii) classifying and identifying storm characteristics that have a significant impact on coastal zones, thereby identifying the most hazardous hydrodynamic scenarios, and iii) assessing the effects of storms on flooding along the Normandy coasts, thus highlighting their impact on coastal areas.

4.1.2. The English Channel and the Normandy coasts

The English Channel is a sea basin located in Northwest Europe between the coasts of France and England. The Channel is one of the most impacted marine areas by human activities worldwide (Halpern et al., 2008). On the Eastern boundary, it is connected to the North Sea through the Strait of Dover, and in the Western limit, it is open to the Atlantic Ocean. The Channel lies far from the continental slope, considered as a shallow area with a decreasing depth from around 100 m on the West side to less than 30 m on the East.

The Channel, stretching approximately 560 km in length, boasts a varying width that gives rise to captivating hydrodynamic phenomena unique to this region. In the Strait of Dover, the French and English coasts stand a mere 20 km apart, gradually parting ways until reaching a separation of around 240 km near the Atlantic Ocean.

The shallowness of the English Channel along with the narrowing of the two sides eastwards and the intricate coastal morphology, defined by a complex system of capes and bays, generate the intense hydrodynamics of the basin (**Figure 44**). In the same way, the surrounding areas aggravate the situation due to the long fetches presented on the North Sea and, especially on the Atlantic Ocean, with high exposure to storms and extreme events.

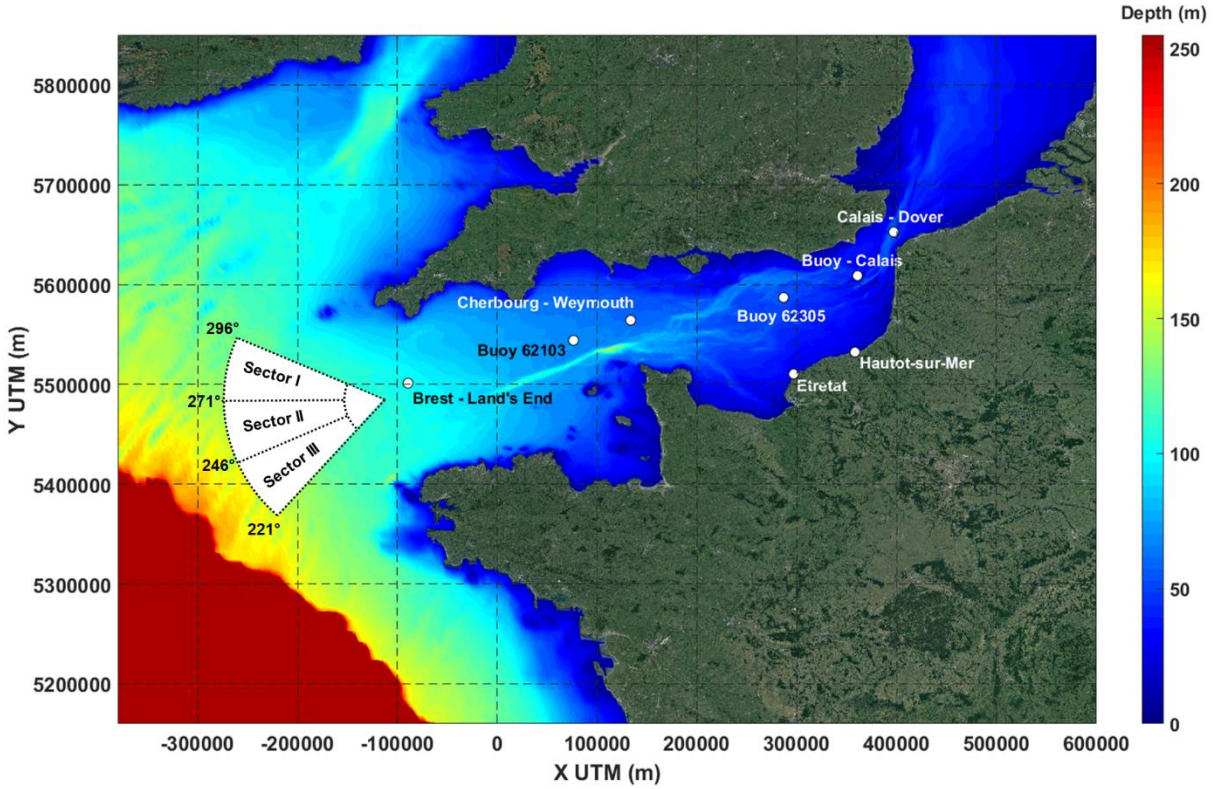

Figure 44. *Bathymetry map of the English Channel with the observation points used in the study, five in deep waters, located along the basin (Brest - Land's End, Cherbourg - Weymouth, Buoy 62305, Buoy - Calais and Calais - Dover), and two nearshore in two representative sites on the Normandy coasts (Etretat and Hautot-sur-Mer). Buoy 62103 was used for validation and the three sectors considered for the study. Extracted from López Solano et al. (2024)*

The Normandy coastal areas are very dynamic environments offering different services including wildlife habitat, erosion and flooding protection, tourism, economic and recreational activities. In the last decade, these areas have received additional interest for their high vulnerability to extreme climate drivers and anthropogenic activities inducing risks of flooding and erosion.

The study sites chosen for this research are situated North of the Seine estuary, in a region characterized by their pebble and gravel beaches, generated by the impact of the sea on the chalk cliffs that get eroded and produce this configuration on the coast. The selected sites were considered as the one of the most hazardous regions, historically exposed to marine submersion

(Turki et al., 2020a, 2020b; Soloy et al. 2021). Additionally, this area is strongly influenced by tides, which are semidiurnal and macro to mega tidal ranges, with up to 10 m at spring tides.

4.1.3. Data and methods

4.1.3.1. Description of the databases: in-situ measurements and model forcings

Different databases have been used in this study with two central objectives: the main purpose has been the forcing of the numerical model, and the following point has been the validation of the results obtained after the simulations. The forcings used in the set-up include the wave parameters and the harmonic components of the astronomical tide defined on the open boundaries of the computational grid employed for the numerical simulations, and the wind and air pressure variables uniformly distributed over a grid defined in geographical coordinates. The bathymetry and topography information have been also specified for all the nodes on the computational grid.

Wave variables have been obtained from the Atlantic-European North-West Shelf – Wave Physics Reanalysis database of the Copernicus Marine Service, with 3-hourly hindcast outputs, with a temporal extent since January 1980. The wave model has already been presented in Chapter 3 for the analysis of extreme values. The variables selected for the simulations from this database include the spectral significant wave height, wave period at spectral peak, and mean wave direction.

The astronomical tide, used for the model set-up, has been generated from the simulation of the harmonic components, provided FES2014 database. This model has been developed, implemented, and validated by LEGOS, NOVELTIS and CLS, within a CNES funded project. The tide elevations, the tide currents and the tide loading grids were available for 34 tidal constituents distributed on 1/16° grids – amplitude and phase – for each tidal product (Carrere et al., 2016).

Wind and air pressure data has been extracted from the ERA5 on single levels database. The atmospheric variables used in this study have been the 10m u- and v-components of wind, which correspond to the eastward and northward components of the speed of air at a height of ten meters above the surface, respectively, and the surface pressure, the force per unit area of the atmosphere at the surface of the planet.

With the aim of defining the digital elevation model (DEM) in the computational grid of the numerical model, the bathymetry information has been obtained from the European Marine

Observation and Data Network (EMODnet) Bathymetry Portal (EMODnet Bathymetry Portal, 2023). A detailed description of the EMODnet project, the digital terrain model (DTM), and the latest release can be found on the website.

In order to validate the accuracy of the water level predictions, sea level measurements from various tide gauges positioned along the coastlines of England and France were compared to the model's outputs in corresponding locations. The tide gauge records from Weymouth, Newhaven, Dover, Calais, Dieppe, Le Havre, and Cherbourg were utilized for the validation process. The model performance is evaluated by calculating the Root Mean Square Error (RMSE, Eq. 12) and the Pearson's correlation coefficient (R, Eq. 13) with the observed and the predicted values of water level. The RMSE is useful to obtain an evaluation of the average distance between the observed data and the data obtained from the simulations.

$$\mathrm{RMSE} = \sqrt{\frac{1}{n}\sum_{i=1}^{n}(y_i - x_i)^2} \tag{12}$$

where n is the total number of coincident data and xi and yi represent the two sets of measured data and model estimation.

The Pearson's correlation coefficient can be used as an indicator of the trends of the measured and the modeled datasets. If the datasets analyzed tend to increase or decrease together it is closer to 1, and if they disagree in their trends it is closer to 0.

$$\mathrm{R} = \frac{\sum_{\mathrm{i}=1}^{\mathrm{n}}[(\mathrm{x_i} - \bar{\mathrm{x}})(\mathrm{y_i} - \bar{\mathrm{y}})]}{\left[\sqrt{\frac{1}{\mathrm{n}}\sum_{\mathrm{i}=1}^{\mathrm{n}}(\mathrm{x_i} - \bar{\mathrm{x}})^2}\sqrt{\frac{1}{\mathrm{n}}\sum_{\mathrm{i}=1}^{\mathrm{n}}(\mathrm{y_i} - \bar{\mathrm{y}})^2}\right]} \tag{13}$$

where $\bar{\mathrm{x}}$ and $\bar{\mathrm{y}}$ are the mean values of coincident observed and simulated data, respectively.

The wave measurements employed in the validation of the wave outputs of the simulations have been obtained from stations 62103 – Channel Lightship and 62305 – Greenwich Lightship, in central locations on the English Channel (49° 54.00' N – 2° 54.00' W and 50° 24.00' N – 0° 0.00' E, respectively), owned and maintained by the UK MetOffice from June 1989 and June 1998. The data provided by the buoy is updated every 60 minutes, supplying wave height and wave period.

The performance of the model is evaluated by calculating the correlation coefficient, alongside the Scatter Index (SI, Eq. 14) and the normalized bias (NBIAS, Eq. 15). The scatter index (SI) is a normalized RMSE, and it provides information on the precision of the results of simulations with respect to the observations in percentage.

$$\mathrm{SI} = \sqrt{\frac{1}{n}\sum_{i=1}^{n}[(y_i - \bar{y}) - (x_i - \bar{x})]^2} \Big/ \bar{x} \tag{14}$$

The normalized bias (NBIAS) contributes to the validation giving information on the bias of the simulated data in relation to the measured data.

$$\mathrm{NBIAS} = (\bar{y} - \bar{x}) \sqrt{\frac{1}{n}\sum_{i=1}^{n} {x_i}^2} \tag{15}$$

4.1.3.2. Numerical approach

Simulations of waves and sea level have been made using the computer software suite Delft3D developed by Deltares, with the modules Delft3D-WAVE and Delft3D-FLOW, respectively. Delft3D is an integrated modelling suite, which simulates two-dimensional (in either the horizontal or a vertical plane) and three-dimensional flow, sediment transport and morphology, waves, water quality, and ecology and is capable of handling the interactions between these processes (Deltares, 2020). **Appendix D** presents a full description of Delft3D, including Delft3D-WAVE and Delft3D-FLOW. In the current study, a two-dimensional hydrodynamics model on a Cartesian curvilinear grid has been used.

The computational mesh employed for simulating the propagation of waves and water levels from the Atlantic Ocean and the North Sea into the English Channel was constructed with spatial resolution that varies across the region. In deep waters along the western boundary, the resolution was set at approximately 4 km, gradually increasing to 1200 m near the Normandy coast. The mesh was comprised of quadrangles, forming a curvilinear grid consisting of 194 cells in one direction and 441 cells in the other, resulting in a total of 85,554 elements. The spatial reference utilized was the EPSG:32631 WGS84/UTM zone 31N projection system.

With respect to the forcings, 63 nodes for the astronomical tide generated by harmonic components and 76 nodes for the wave variables, distributed along the open boundaries on the North Sea, the Irish Sea, and the West and South limits of the grid on the Atlantic Ocean have been defined. For the atmospheric forcings, a rectangle covering the computational area has been extracted from the regular spherical grid, maintaining the spatial distribution of the ERA5 dataset. This spherical grid was converted into a curvilinear grid once the geographical coordinates were transformed into UTM coordinates.

By including the atmospheric forcing, the model is able to generate the storm surge if the extension of the computational grid is wide enough, which was considered when the grid was delimited. Likewise, the model is also able to include the interaction between the astronomical tide and the storm surge.

The generation of a wave database in the central part of the English Channel and nearshore on the Normandy coasts is presumably necessary due to the lack of precision on this area of the currently available datasets, either for the bulk and the extreme conditions. In **Figure 45** the QQplots of significant wave height comparing the results obtained from a node of the reanalysis databases of ERA5 and NWSHELF in comparison to the measurements of the Buoy 62305, placed on the Greenwich meridian, are shown. As can be appreciated, the bulk conditions of both databases overestimate the real records of the buoy, and they slightly approach to the real values when taking higher values, finishing in a small underestimation of the extreme values. When the database obtained from the numerical model of the current study was originally generated, the same problem was found. Carrying an exhaustive analysis about the origin of this problem, the cause was found in the atmospheric conditions, more specifically, on the wind speed with which the model is forced, obtained from ERA5. Potisomporn et al. (2023) analyzed the wind speed of ERA5 onshore and offshore the UK, comparing the database with measurements. They determined that, generally, the wind data is accurate enough, but with the main discrepancies originate from short-term low speed episodes. However, they argue that ERA5 underestimates these events compared to the measurements, contrary to what seems to happen in this study. Thus, the problem is not on the wind data, but in an excessive transmission of the wind energy to the waves inside the model. This issue becomes more important when the waves are lower and with less impact on the higher waves as these propagate through the English Channel.

To avoid overestimation in bulk wave height conditions, a calibration is performed based on the wind speed taking as a reference the measurements of wind intensity of the same buoy 62305. By considering the relationship between wave height and wind speed, it has been observed that the model can more accurately reproduce extreme wave events, typically produced by wind speeds exceeding 20 m/s. However, with intensities lower than that value, the model exhibits this excessive energy transmission. Therefore, it has been found that the most suitable way to calibrate the simulations is by decreasing the wind speed forcing in the model using a reduction factor proportional to the value measured by the buoy. This calibration method has not been previously documented in literature, however, its effectiveness becomes clear when considering the relationship between wind speed and wave height. In **Figure 45** the QQplots of the results of wave height of the simulations of the model before and after calibration are presented in

comparison to the measurements of the buoy. A constant overestimation, especially for the mean conditions, can be observed in the comparison of the outputs of the model and the measurements when the calibration is not applied. After calibration, this situation is generally fixed except for the lowest values, which are not relevant for this study. When it comes to the extreme values, the underestimation of ~1 m shown before the calibration is reduced to less than 0.5 m after the calibration, coherent with the results obtained from the ERA5 and NWSHELF databases for this location. Therefore, the bulk conditions are ameliorated in comparison to the available datasets in a central part of the English Channel, with a similar or lesser error for the lowest and the most extreme values. The best performance among the four databases illustrated in **Figure 45** is the QQplot of the calibrated results of the numerical model of the present study.

Once the grid and the forcings were defined, 40 years of data were simulated, from January 1983 to December 2022, with a time step of 10 minutes in terms of water level propagation, 20 minutes for the outputs of the model, and 3 hours in terms of waves for the propagation and the outputs.

The location of buoy 62305 has been used as a control point for this study. The validation of waves has been assessed on this spot in the same way as a comparison to the outputs obtained in four more points equally distributed along the Channel (**Figure 44**). One point has been designated between Calais, on the French coast, and Dover on the English coast for evaluating the influence of the storms coming from the North Sea, designated as "Calais – Dover" point. With the aim of estimating the evolution from the North Sea to the location of the buoy, a third point situated between the buoy itself, and the second chosen point has been placed in a middle distance from these two other points, named as "Buoy – Calais" observation point. On the Atlantic Ocean, and due to the expectancy of a soft modification between the outer part of the Western English Channel and the central part, where the buoy is located, two additional control points were considered as enough, and have been defined. One of them on the most external part of the Channel, between Cornwall in England and Finistère in France, named as "Brest – Land's End" point, and an additional one on the North of the Cotentin Peninsula, between the cities of Weymouth and Cherbourg, situated on United Kingdom and France's shores respectively, designated as "Cherbourg – Weymouth" point.

Finally, and with the aim of defining the transformation of the extreme events when they approach the High Normandy coasts, two locations considered as representative of the morphology and composition of pebble beaches in this area have been studied too: Etretat and Hautot-sur-Mer.

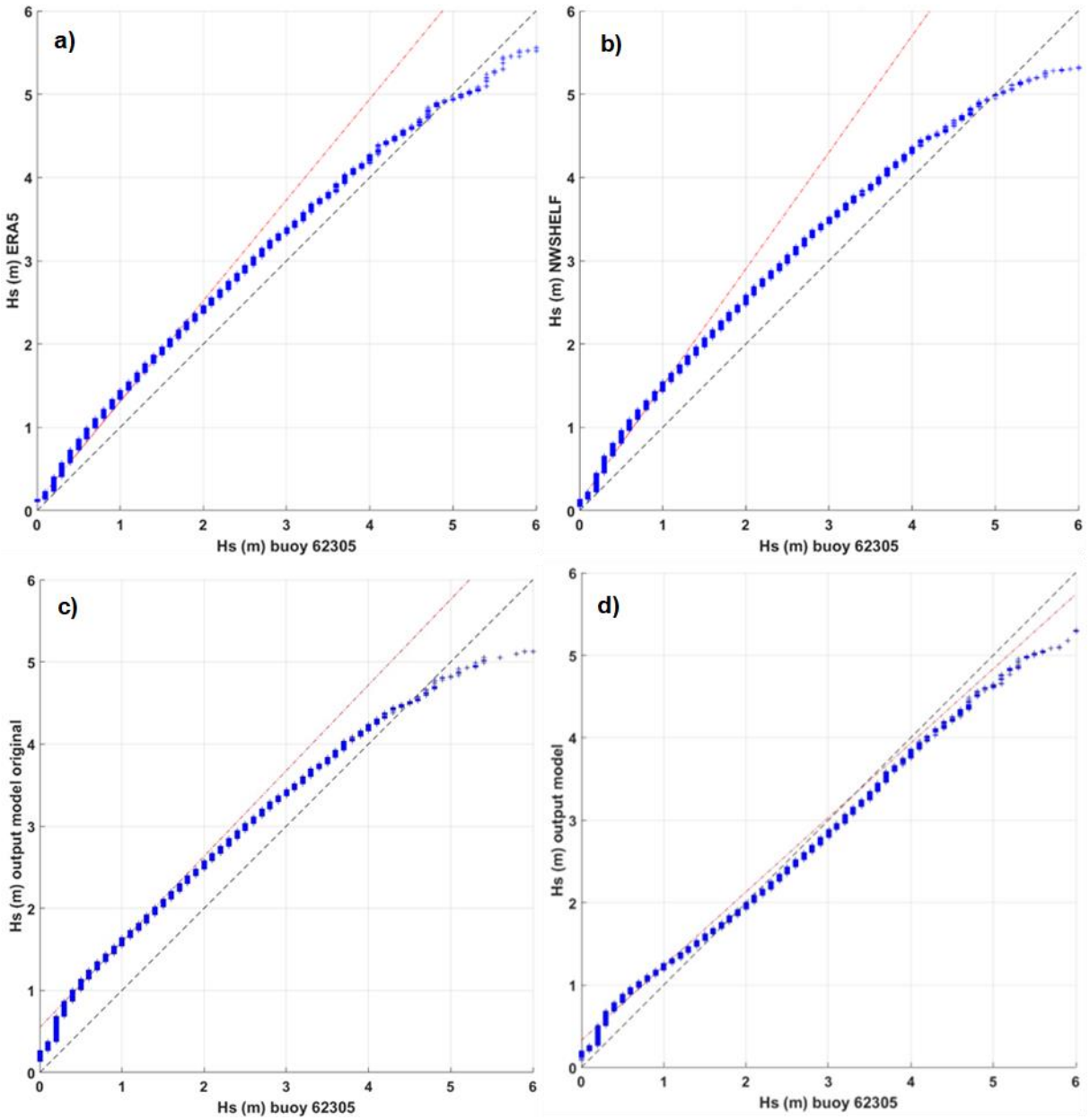

Figure 45. *QQplots of significant wave height (Hs) comparison of reanalysis or results of modelling versus observations measured by buoy 62305: a) reanalysis of ERA5, b) reanalysis of NWSHELF, c) results of the simulations from the Delft3D model forced with the original values of wind, and d) results with the calibrated values of wind speed. Extracted from López Solano et al. (2024)*

4.1.3.3. Study of bottom roughness in Delft3D

This section presents a short study to investigate the parametrization of bottom roughness for carrying out the numerical simulations of waves and sea level propagations in Delft3D.

4.1.3.3.1. Formulations of bottom roughness in Delft3D

In the module Delft3D-FLOW from the suite Delft3D, the bottom roughness can be computed with several formulations and parameters. The easiest parametrization is by setting a uniform value covering the whole numerical grid for one of the possible formulations (**Figure 46**).

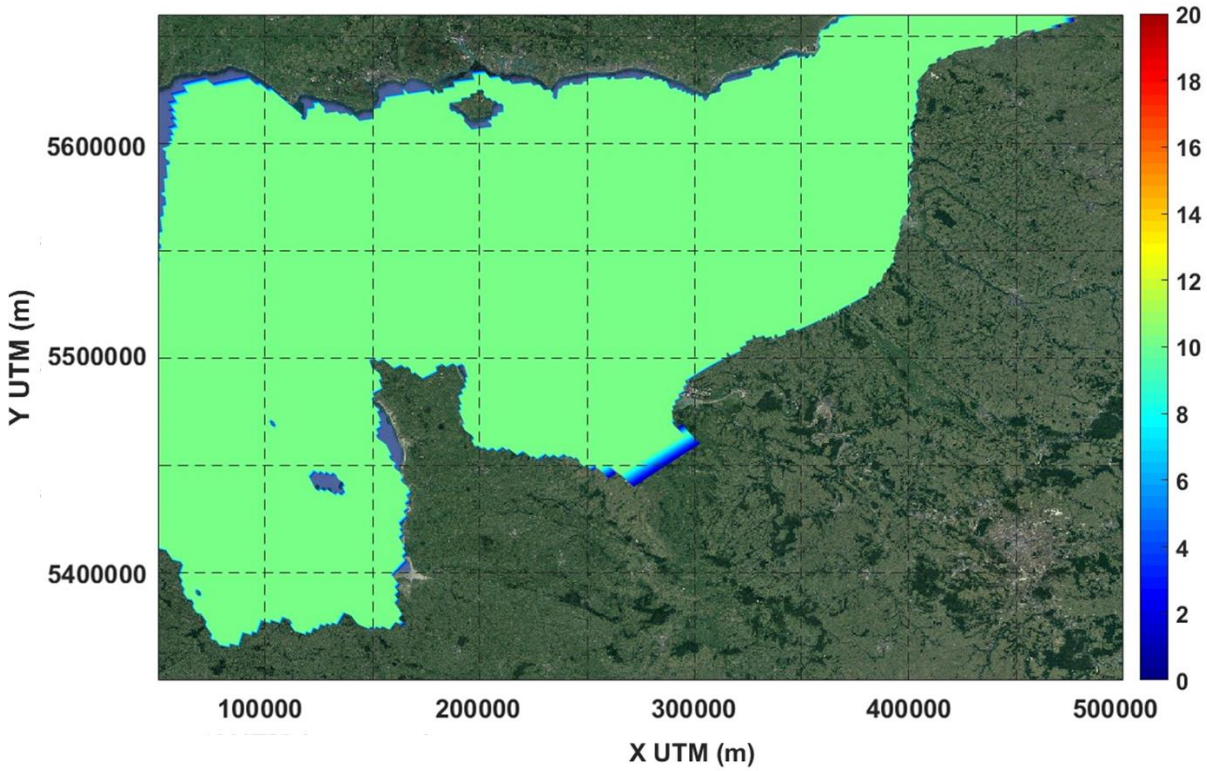

Figure 46. *Bottom roughness in the model set-up as a constant value over the whole study area. Heterogeneous bottom roughness length-scale k_n in m*

Three different friction formulations are given in the numerical model: Manning, White-Colebrook and Chézy.

If the Manning formulation is used, the Manning coefficient, n, must be specified. A typical Manning value is 0.02 s/m$^{1/3}$, ranging from $n = 0.0\ s/m^{1/3}$ up to $n = 0.04\ s/m^{1/3}$. In this formulation, the Chézy friction coefficient is calculated from Eq. 16.

$$C = \frac{h^{1/6}}{n} \tag{16}$$

where h is the water depth.

In the White-Colebrook formulation the equivalent geometrical roughness of Nikuradse, k_s must be specified, ranging from $k_s = 0\ m$ up to $k_s = 10\ m$. For this case, the Chézy friction coefficient is calculated from Eq. 17.

$$C = 18\ log_{10}\left(\frac{12h}{k_s}\right) \tag{17}$$

A first estimate of the bed roughness length z_0 in 3D computations can be derived from the equivalent geometrical roughness of Nikuradse, k_s, in Eq. 18.

$$z_0 = \frac{k_s}{30} \tag{18}$$

Typical values of k_s range from 0.15 m for riverbeds with sediment transport down to 0.01 m or less for very smooth surfaces. A first estimate of the Chézy friction coefficient is given by Eq 19.

$$C = 25 + h \tag{19}$$

A typical Chézy value is 65 $m^{1/2}/s$ but ranging from $C = 1\ m^{1/2}/s$ up to $C = 1000\ m^{1/2}/s$.

The values of bottom roughness can be obtained from the maps of distribution of heterogeneous bottom roughness length-scale k_n shown in Guillou (2013), where it is calculated according to the spatial distribution of the median diameter d_{50}, the bedrock and the bedforms, divided into ripples, mega-ripples and dunes. The bottom roughness length-scale k_n, presented in Madsen et al. (1988) can be expressed as a function of the depth h and the Manning coefficient according to the relation shown in Eq. 20.

$$k_n = h\ exp\left[-\left(1 + \frac{0.4\ h^{1/6}}{n\sqrt{g}}\right)\right] \tag{20}$$

Then, combining Eq. 16 with Eq. 17 and Eq. 20, the relation between the equivalent geometrical roughness of Nikuradse, k_s and the bottom roughness length-scale k_n lead to the bottom friction set up in the model.

4.1.3.3.2. Sensitivity of modelling results to roughness

The bottom roughness has been tested using the different formulations available in the suite Delft3D, taking the default values and comparing the results between the set-ups. In the first try the formulation of Manning has been used with a Manning coefficient n of 0.02 $s/m^{1/3}$, followed by a test with the Chézy formulation with a Chézy value of 65 $m^{1/2}/s$.

With the unsatisfactory results obtained, it was evident that in these simulations the White-Colebrook formulation should be used in order to introduce the equivalent geometrical roughness of Nikuradse, k_s, for which there was available information. Following the recommendations of the SWAN manual, different tests have been carried out, from the minimum value of 0.01 m to the maximum value of 0.15 m.

Although the results improved, they continued to be far from the objective, so a spatial variation of bottom roughness was implemented, taking the values of the bottom roughness length-scale k_n of Guilou (2013) in m (**Figure 47**), later transformed into the equivalent geometrical roughness of Nikuradse k_s for the formulation of White-Colebrook.

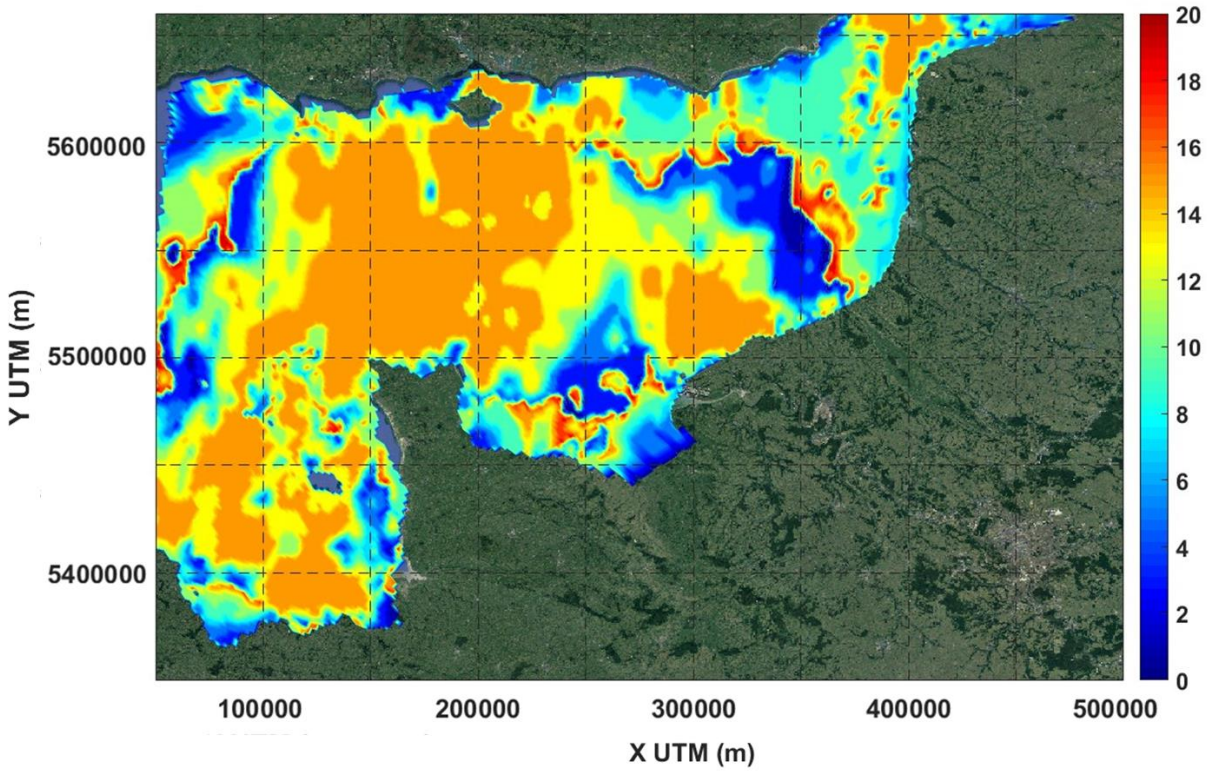

Figure 47. *Bottom roughness in the model set-up as varying values according to the maps of sediment distribution of Guillou (2013). Heterogeneous bottom roughness length-scale k_n in m*

The distribution of the equivalent geometrical roughness of Nikuradse improved notably the results, but several simulations were interrupted due to the complexity of the distribution of bottom roughness, so a simplification of this map was implemented with the objective of obtaining smoother transitions in the bottom friction on the model. For doing that, the heterogeneous bottom roughness length-scale k_n was taken accordingly only to the kind of sediment but ignoring the shapes of the seabed (**Figure 48**), i.e., the ripples, mega-ripples and dunes were assimilated just as sand.

The external part of the English Channel, outside of what is shown in **Figure 48**, receives a value of 0.05 m, as explained in Guillou (2013). This has been the final set-up used in the simulations of the 40 years to generate the database of waves and sea level.

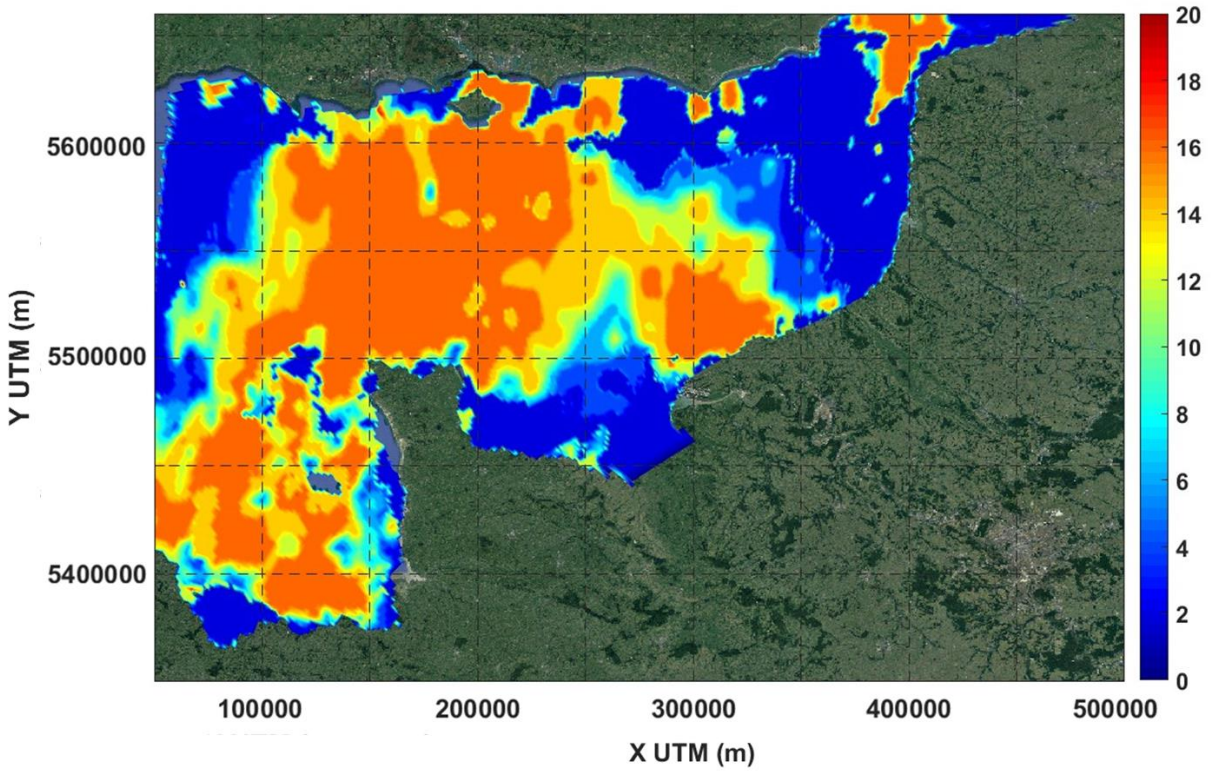

Figure 48. *Bottom roughness in the model set-up as varying values according to the maps of sediment distribution of Guillou (2013), simplified. Heterogeneous bottom roughness length-scale k_n in m*

4.1.3.4. Storm characterization

Coastal storms have been characterized following the methodology proposed by Mendoza et al. (2011) using the 40-year hourly wave height time-series mentioned above, considering three main variables: a wave height threshold, a duration threshold, and an independence criterion, as explained in Section 3.3. The wave height threshold was obtained using the 95th percentile of the significant wave height datasets (Castelle et al., 2015; Masselink et al., 2014; Walker & Basco, 2011).

From West to East, various wave height thresholds were established for specific coastal locations. The Brest – Land's End node had a threshold of 5.13 meters, while the Cherbourg – Weymouth point had a threshold of 3.60 meters. At the location of the buoy, the threshold was set at 2.54 meters, while for Buoy – Calais, it stood at 2.25 meters, and for Calais – Dover, it was 1.93 meters. Moving closer to the shore, the thresholds at the Etretat and Hautot-sur-Mer nodes were 1.70 meters and 1.15 meters, respectively. To determine the storm's duration threshold, factors such as local flooding, erosion processes, and tidal patterns in the area were considered. This involved analyzing a time-series of wave heights, with the storm duration defined as lasting at least 24 hours where the values remained above the designated threshold for each specific point.

For each observation point, considering the different thresholds associated to each one of them, a variable number of stormy events can be identified in the timeseries. For the Brest – Land's End point, 262 extreme events are determined, for Cherbourg – Weymouth, 254 storms, for the location of the buoy, 231 events, for Buoy – Calais, 236 and for Calais – Dover, 252. Nearshore, 252 and 258 storms have been identified in Etretat and Hautot-sur-Mer. As an example, the time-series of wave height alongside the threshold and the 262 storms identified for the Brest – Land's End point is shown in **Figure 49**. Each storm is characterized by the significant wave height and the mean direction at the instant of the peak of the storm, the duration of the whole event and the random wave energy density since the objective of this study is also to focus on the impacts of the events on the coast. The wave energy is defined for the storm energy as the integral in time when the significant wave height surpasses a specified storm threshold for a minimum duration, i.e., the area limited by the line of the time-series of wave height and by the threshold throughout the duration of the storm, multiplied by the sea water density and the gravitational acceleration.

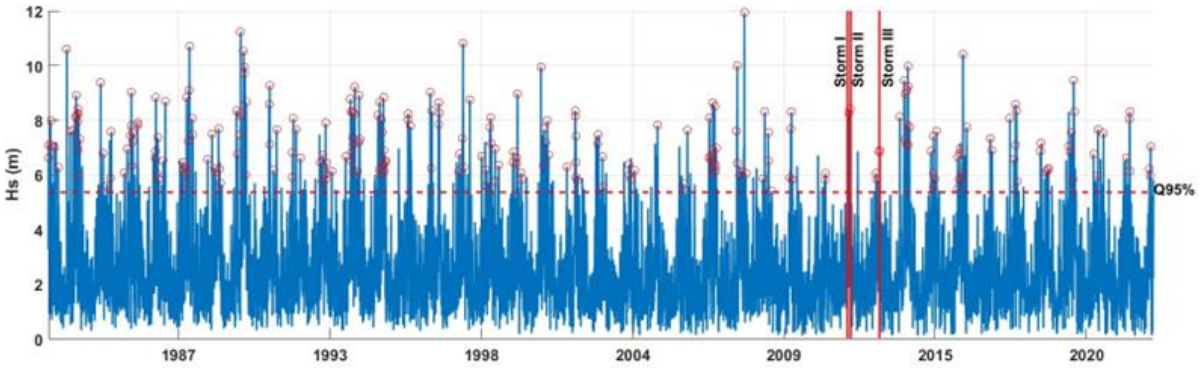

Figure 49. *Time-series of wave height in the Brest – Land's End observation point during the 40 years analyzed with the 262 storms identified over the threshold equivalent to the quantile 95. Storms selected as examples are indicated: Storm Sector I (Joachim), storm Sector II (Andrea) and storm Sector III (designated as Storm 19). Extracted from López Solano et al. (2024)*

Following these characteristics, a storm classification has been carried out based on the offshore direction in the open sea, mainly focusing on the Atlantic Ocean, and the energy density of the extreme events on this point. This classification is explained alongside the evolution of the storms as they propagate through the English Channel and when they approach the Normandy coasts.

4.1.4. Results

The dynamics of nearshore waves have been calculated during a period of 40 years, between 1983 and 2022. Results are presented in four parts: (1) the numerical simulations of waves by

Delft3D and their validation with in-situ measurements; (2) the classification of the 262 stormy events and their physical evolution from regional to local scales; (3) the impacts of highly energetic storms close to Normandy coasts; and (4) implications for coastal flooding.

4.1.4.1. Validation of results: sea level and waves

The results of sea level obtained from the simulations during the 40 years have been validated with in-situ measurements provided by different tide gauges, located along the coasts of England and France. A special focus has been given to the coasts of Normandy using the tide gauges of Le Havre, Dieppe, and Cherbourg.

The comparison between the three tide gauges with the numerical simulations in the coincident period gave, as a result, a RMSE of ~34 cm in Cherbourg, considering that there is a tidal range of around 7 m, an error of ~50 cm in Dieppe with a tidal range of more than 10 m and a RMSE of ~32 cm in Le Havre over a tidal range of slightly less than 9 m. Regarding the correlation coefficient, for Cherbourg a value of 0.9809 was obtained, for Dieppe it was 0.9803, and for Le Havre, 0.9901. These errors of some centimeters were mainly explained by the location of the observation points taken as close as possible to the coast in the computational grid, but still not in the exact same location as they are located in reality due to the limited spatial resolution of the model.

In **Figure 50** the time-series of the three tide gauges along with the output of the model in the closest location to each of them are shown in different short periods taken from the 40 years as an example.

Regarding waves, the simulated wave height has been compared to in-situ measurements, provided by buoy 62103 and buoy 62305, within the English Channel. The comparison between datasets highlighted that the correlation coefficient is 0.869 and 0.845 for the coincident years of buoy 62103 and buoy 62305, respectively, showing a good agreement in the results, having also a high precision proved by a scatter index of 37.1% and 45.2% and a normalized bias of 20.6% and 17.4%.

In **Figure 51** the scatter plot of significant wave height (Hs) for both the measurements of the buoys 62130 and 62305, and the results obtained from the simulations with Delft3D in the same output location are shown for the 40 years.

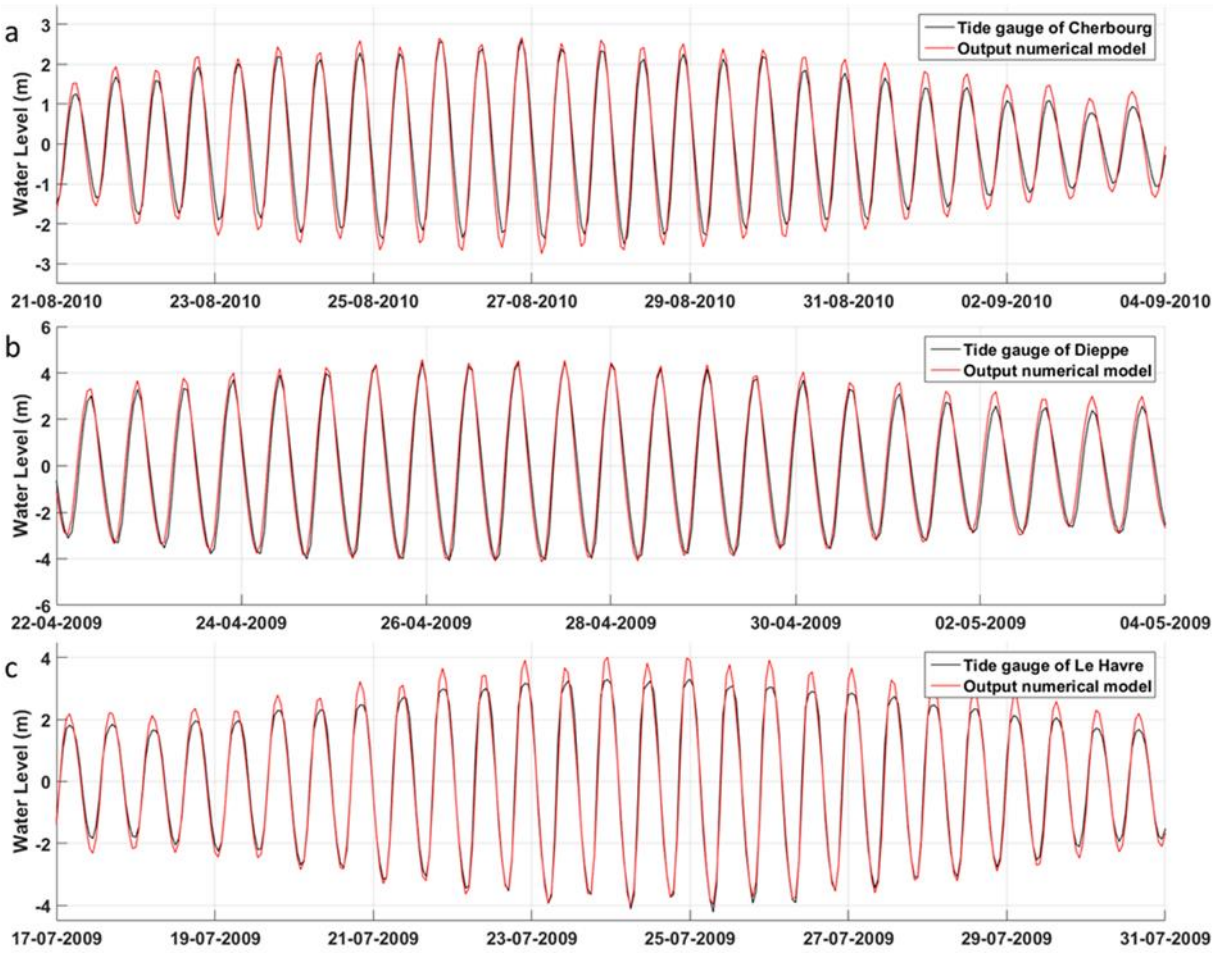

Figure 50.*(a) Water level measured by the tide gauge of Cherbourg in black and the output of the numerical simulations in the closest location in red for the period 21-08-2010 to 04-09-2010; (b) water level measured by the tide gauge of Dieppe in black and the output of the numerical simulations in the closest location in red for the period 22-04-2009 to 04-05-2009; and (c) water level measured by the tide gauge of Le Havre in black and the output of the numerical simulations in the closest location in red for the period 17-07-2009 to 31-07-2009. Extracted from López Solano et al. (2024)*

4.1.4.2. Classification and evolution of storms

The methodology for identifying and characterizing storms has been applied to all 7 observation points: Brest – Land's End, Cherbourg – Weymouth, the location of the buoy, Buoy – Calais, Calais – Dover, Etretat, and Hautot-sur-Mer. The different characteristics of storms selected and tracked down throughout the English Channel have conformed to a database that allows one to follow the evolution conditioned by the location of each node in the basin.

Looking at the main characteristics of the storms at first glance, two origins were highlighted: extreme events formed in the North Sea entering to the English Channel through the Strait of Dover in the Northeast, and storms produced in the Atlantic Ocean entering through the West.

Considering the North Sea as a node of origin of storms, only a few events were identified in comparison to the extreme events coming from the Atlantic Ocean. Moreover, these storms can

only be found in the Calais – Dover observation point. By looking at the second point starting from the West, the Buoy - Calais node, these storms were not distinguished anymore.

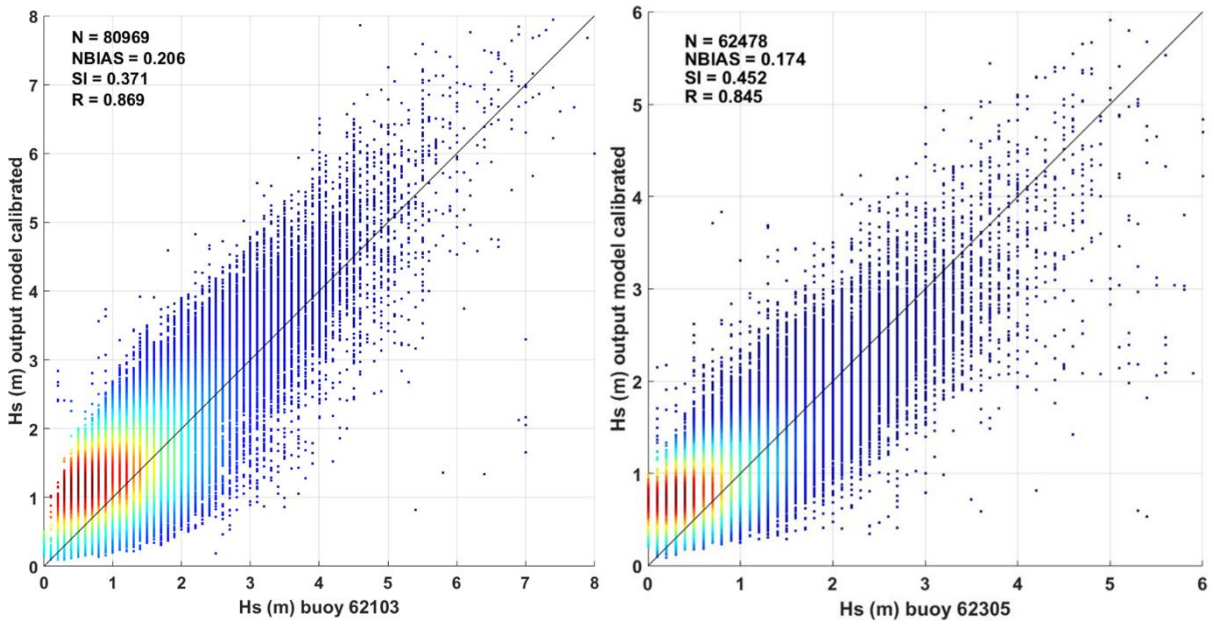

Figure 51. *Significant wave height (Hs) comparison of results of simulations from the Delft3D model versus observations measured by buoy 62103 and buoy 62305. Extracted from López Solano et al. (2024)*

Out of the 252 extreme events cataloged in the Strait of Dover, merely 10 had their origins in the North Sea, characterized by wave heights hovering around ~2.5 meters and a duration spanning 26 to 37 hours. In contrast, the 262 storms that emanated from the Atlantic Ocean, impacting the Brest – Land's End node, exhibited varying characteristics in terms of wave height and duration. These storms, with directions ranging from 221° to 296°, were divided into three distinct sectors, each spanning 25°: Sector I, spanning from 221° to 246°; Sector II, encompassing the range of 246° to 271°; and Sector III, extending from 271° to 296°. This division facilitated a comprehensive study of the storms' behavior within the region. The characteristics of these three sectors are shown in **Table 19**.

Brest – Land's End	Hs (m)		Dir (°)		Duration (hours)		Energy density (J/m²)	
	Min	Max	Min	Max	Min	Max	Min	Max
I	5.415	11.927	271.078	296.07	24	94	448,590	2,902,879
II	5.143	10.811	246.052	270.576	24	273	408,664	4,752,552
III	5.505	9.952	221.932	245.977	26	189	604,156	4,224,517

Table 19. *Main characteristics in terms of wave height at the peak of the storms (Hs), direction at the peak, duration of the storms and random wave energy density of the storms identified divided in the three sectors used in the study: I (271° to 296°), II (246° to 271°) and III (221° to 246°). Extracted from López Solano et al. (2024)*

Out of the 262 storms analyzed, which exhibited an average directional bearing of 258 degrees, nearly half originated from the central sector. Approximately 17% of these storms were closely confined within the range of 258 degrees plus or minus 3 degrees, while 50% fell within the broader span of 258 degrees plus or minus 10 degrees. The storms that emanated from the central sector displayed the longest duration as an average, around 63 hours, but Sector II boasted the highest energy density, surpassing 4,700,000 J/m^2. Conversely, the most substantial wave heights, exceeding 11 meters, were observed in storms approaching from Sector I.

The relationships between energy density and wave height and duration are shown **Figure 52**. It can be observed that the energy content is more sensitive to the duration of the storms, presenting an almost linear evolution between the two variables. The correlation with the wave height is apparently much more scattered.

One can observe a significant correlation between higher energy content and longer storm durations. This connection remarks the fact that storms, regardless of their wave height, can exhibit a substantial energy content, which is not solely contingent on the specific wave height value.

By applying the same analysis in the subsequent points along the English Channel, more specifically, the Cherbourg – Weymouth point, the location of buoy 62305, and the two points studied nearshore, Etretat and Hautot-sur-Mer, it is possible to study how these 138 storms evolve when they propagate through the basin, getting refracted, reflected, or dissipated.

In terms of wave height and duration, 88% of the storms identified nearshore are contained in the range of 25-105 hours of duration and 6-9 m of Hs. But this distribution is different for each sector: 64% of the storms coming from Sector I arrive on the Normandy coasts, with 39% of the ones from the Sector II, and only 7% of the storms from the III. For Sectors II and III, storms with longer durations, over 120 hours, are dissipated when they approach the coast.

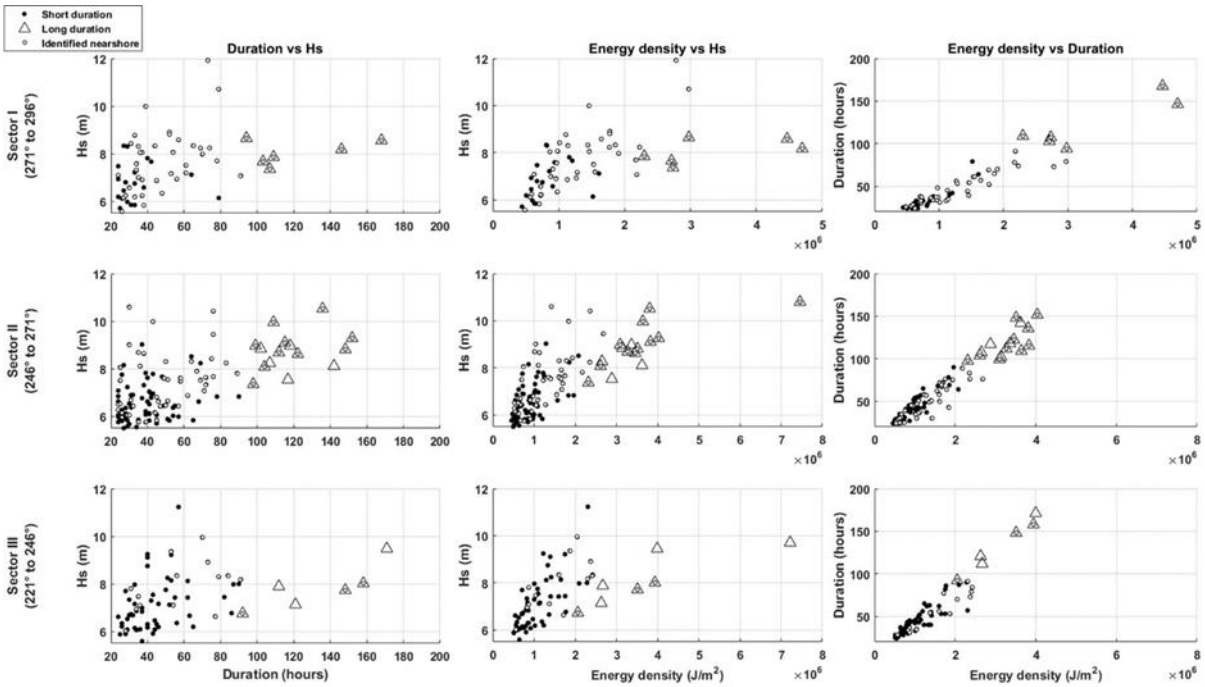

Figure 52. *Energy content versus wave height at the peak of the storms and every content versus duration of the storms for the three sectors used in the study: I, II and III. Extracted from López Solano et al. (2024)*

Analyzing the decrease in the wave height through the different points along the English Channel, in the Cherbourg - Weymouth node there is a 30% decrease with respect to the first point, the same as in the third point in comparison to the second one. Once they have arrived at the location of the buoy, the decrease is reduced to less than 15% in the fourth with respect to the buoy and in the Strait of Dover in comparison to the previous. The distribution among the three sectors is equivalent throughout the points, except for the Calais - Dover node, where the Sector I suffer from a decrease in Hs of 30%, while Sector II stays at the average of 13% and the storms coming from the III only 5%.

The modification of the storms coming from Sector III is the lowest among all the directions, between 1° and 3° from point to point. In Sector II, on average, it is higher, from 1° to 10° and up to 16° in the point of Calais. For Sector I, the refraction ranges from 1° to 20°, notably higher, especially in the second and the last points.

In terms of modifications of the duration of the events, storms with lower wave energy density, independently of the sector, suffer from lower variation in their duration, from 30 to 60% lower than the storms with a higher wave energy density by comparing the storms with higher and lower energy of each sector.

4.1.4.3. Storms tracked throughout the English Channel

For each one of the three sectors corresponding to the Atlantic Ocean origin, a representative storm was chosen in order to track them along the English Channel and when they approach to the shore in the two main locations studied (Etretat and Hautot-sur-Mer):

- For Sector I, with a range of directions from 271° to 296°, the storm Joachim was chosen because it had the highest energy density in most recent years. The date of the peak passing by the location of the Brest – Land's End point occurred on 15 December 2011 at 6h.
- For Sector II, from 246° to 271°, the storm Andrea was chosen because it had the highest wave height nearshore in the most recent years. The date of the peak at Brest – Land's End was registered 3 January 2012 at 9h.
- For Sector III, from 221° to 246°, a storm not identified by a name, simply called "Storm 19", chosen because it was the only storm from the SW that can be identified nearshore after 2008. The date of the peak at Brest – Land's End occurred on 29 January 2013 at 15h.

Table 20 presents a summary of the characteristics of the point near the Atlantic Ocean and the two points nearshore.

Storm Joachim	**Hs (m)**	**Dir (°)**	**Duration (hours)**	**Energy density (J/m²)**
Brest – Land's End	8.26	271.4	115	2,785,795
Etretat	2.51	271.3	74	167,315
Hautot-sur-Mer	1.54	298.6	100	89,274

Storm Andrea	**Hs (m)**	**Dir (°)**	**Duration (hours)**	**Energy density (J/m²)**
Brest – Land's End	8.42	246.7	89	2,148,186
Etretat	3.82	288.6	74	293,313
Hautot-sur-Mer	2.78	305.0	78	149,317

Storm 19	**Hs (m)**	**Dir (°)**	**Duration (hours)**	**Energy density (J/m²)**
Brest – Land's End	6.83	239.4	82	1,898,785
Etretat	1.61	268.2	73	110,678
Hautot-sur-Mer	1.08	294.4	73	51,902

Table 20. *Wave height at the peak (Hs), direction at the peak, duration and random wave energy density of the storms selected as example for the three sectors used in the study: Joachim for the I, Andrea for the II and the storm 19, identified from the III, in the Brest - Land's End observation point and the two points nearshore, Etretat and Hautot-sur-Mer. Extracted from López Solano et al. (2024)*

As mentioned before, the highest energy density in the storm Joachim is explained by the duration of the extreme event, with a total time of 115 hours over the threshold defined in the point of Brest – Land's End. This duration evolves and it is kept throughout the English Channel until it

reached the nearshore, where the storm lasts for 89 and 82 hours in Etretat and in Hautot-sur-Mer.

The time-series of wave height of these three storms in this point alongside the second and third nodes, and the two points nearshore can be seen in **Figure 53**.

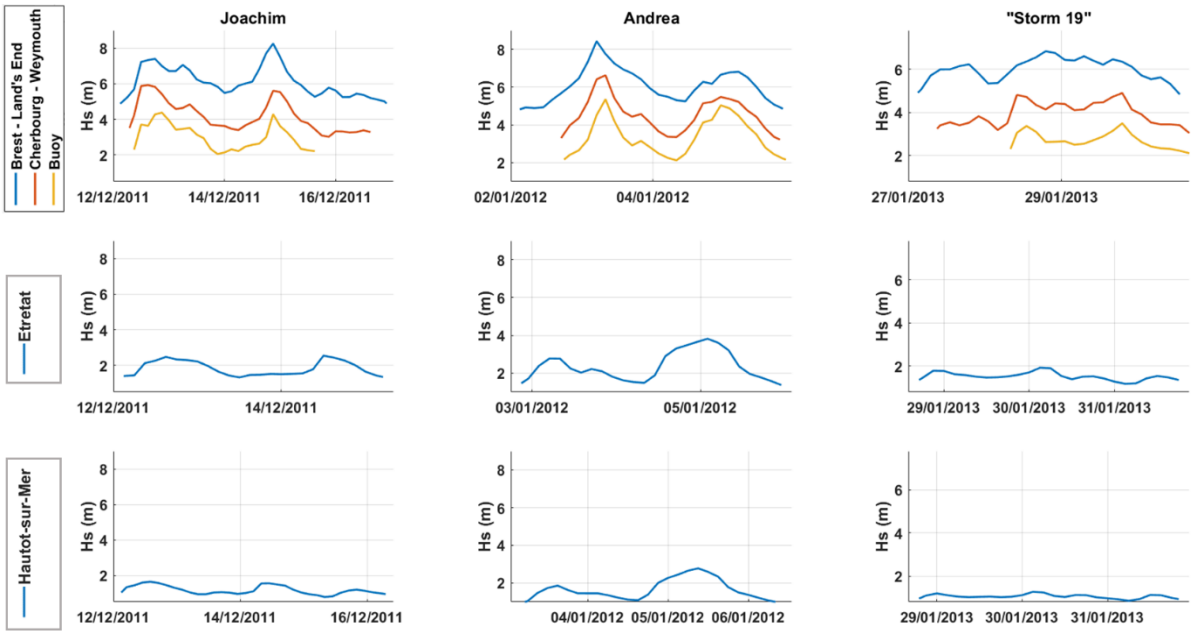

Figure 53. *Time-series of wave height for the three storms selected as example (Joachim, Andrea and Storm 19) in the Brest - Land's End, Cherbourg - Weymouth and Buoy observation points, and in the two nodes located nearshore. Extracted from López Solano et al. (2024)*

It can be noticed how the storms are modulated when they propagate through the English Channel. As an example, Storm Andrea presented a conspicuous peak, especially when the storm is passing by the location of the buoy. Nevertheless, when the three storms arrive to the coast they are completely modified, being more extended in time and with a less noticeable peak.

To track the storms through the English Channel, the contour maps of significant wave height (Hs) of 3 and 6 meters associated to these three storms are shown in **Figure 54**.

Storm Joachim approached from Sector I with a peak wave direction of 271°. A refraction around a node defined by Land's End in the western limit of England can be appreciated in the 6 m (H_s) contour line, where the storm is entering the Channel approximately with this direction of 270° and arriving to the central part of the basin with a direction of ~250°. It is also remarkable that the wave height remains lower in the shoreline of England in the central part of the English Channel due to the direction in origin of the storm and the resulting refraction. When the storm approaches the coasts of Normandy, it takes a direction of 270° and 300° in Etretat and Hautot-

sur-Mer, respectively. It arrives with a high energy to the initial control point, but its energy is quickly dissipated in less than 9 hours.

Since the English Channel basin is oriented at an angle of about 70 degrees to the North, the direction of storm Andrea closely aligned with the basin's orientation, resulting in minimal wave refraction. Consequently, wave height experiences only subtle alterations. In the central regions of the Channel, where observation points are situated, Storm Andrea emerges as one of the strongest storms, although its strength may not rank as high when it initially enters the basin. This storm's arrival can be better understood by examining the contour lines of 3 meters of significant wave height (Hs), which extend even into the North Sea. The storm originates in a direction that causes it to refract only after passing by the Cotentin Peninsula, resulting in a direction of approximately 290° at Etretat and 300° at Hautot-sur-Mer. This orientation is nearly perpendicular to the shoreline at both locations, and it elucidates the significant wave height's substantial impact on the coast. Storm 19 enters into the English Channel with a direction of 239°at the peak of the storm, a notable difference as this extreme event impacts straight into the British shoreline. Unlike the previous storms, it does not extend as far due to the refraction in the western edge of France in Brittany. Consequently, it largely dissipates, resulting in lower wave heights at the subsequent observation points. Originating from Sector III, the storm has suffered from a strong refraction already when approaching to the Normandy coasts, causing it to arrive with a direction of 290° in Hautot-sur-Mer and just 260° in Etretat, impacting these locations more longitudinally than the previous storms analyzed. This difference is evident on the maps, with wave heights measuring below 3 meters upon arrival.

Furthermore, the maximum significant wave height has been tracked down throughout the channel in **Figure 55** to precisely trace the path of the three selected storms. At each time point, the maximum value of wave height has been identified within the limits of the English Channel following the x-coordinate. The figure clearly illustrates the refraction of the three storms: storm Joachim and Andrea proceed from Sectors I and II and impact on the Southern side of the basin and, in a parallel way, Storm 19 proceeds from the Sector III and impacts on the Northern side of the Channel.

4.1.5. Discussion

The validation of the numerical set-up carried out highlights a RMSE for the three tide gauges between ~32 cm and ~50 cm in tidal ranges between 7 m and 10 m, with correlation coefficients of 0.98 and 0.99. In terms of wave height, for the higher values measured by the buoy, over 4 m, there is an underestimation of ~20 cm, but with a SI of 18.5% and a correlation coefficient of 0.96.

for similar configurations, the same statistical parameters for measuring the error are usually calculated in literature. For example, Ardhuin et al. (2012) obtained a SI for the wave height of 13.1% with a correlation coefficient of 0.96 using a model set up with no tides and a SI of 9.5% and a R = 0.98 with tides. Boudière et al. (2013) generated a database and compared the outputs of their numerical modelling to numerous buoys along the coast, achieving an error ranging in the SI from 0.17 m to 0.37 m, not normalized in their study, and a correlation coefficient ranging from 0.89 to 0.97.

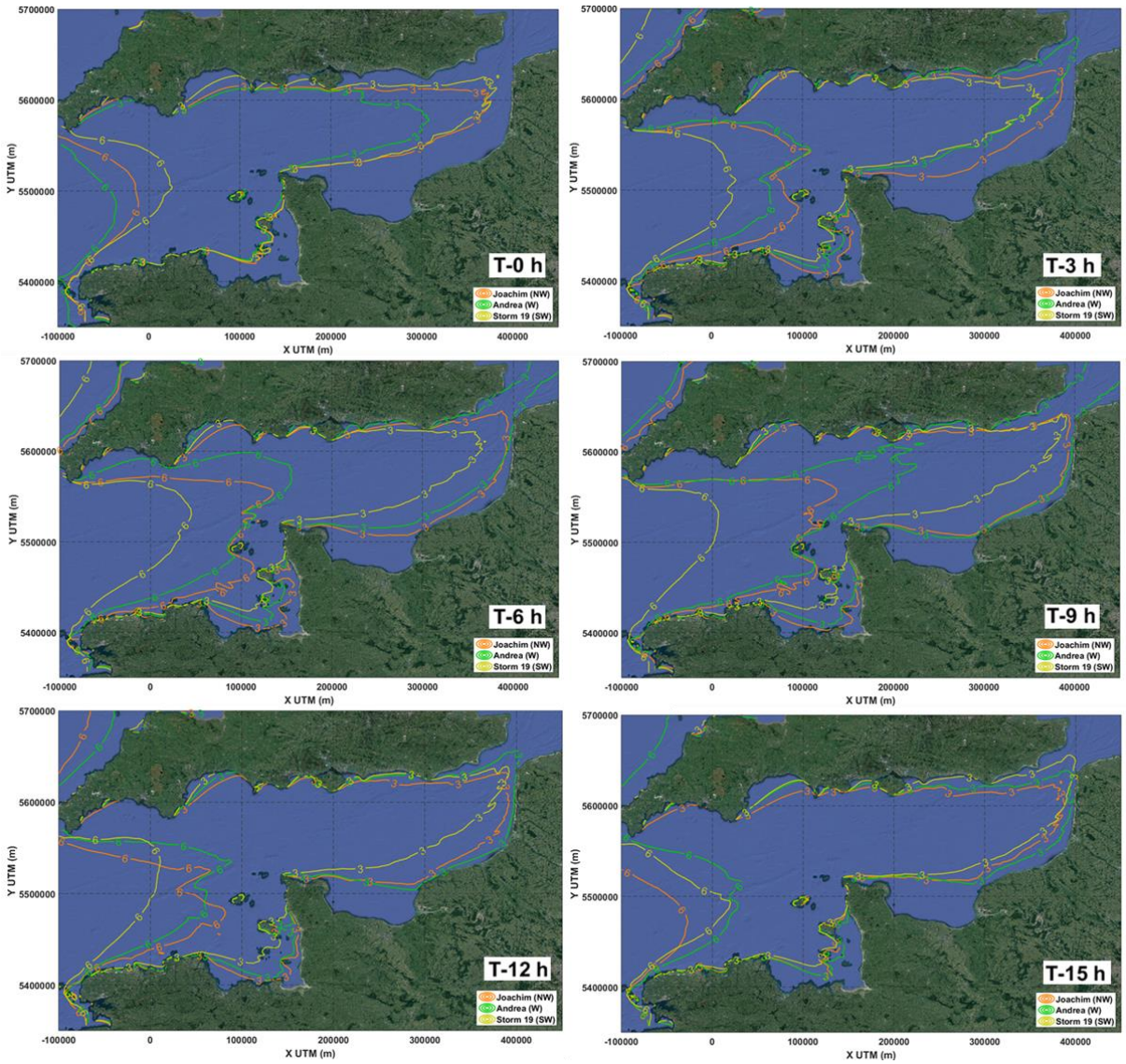

Figure 54. *Significant wave height contour map of Hs = 3 m and Hs = 6 m of three storms in consecutive instants propagating in the English Channel. The three storms (Joachim, Andrea and "Storm 19") correspond to each one of the three sectors in which the coming waves have been classified according to the direction of origin. Extracted from López Solano et al. (2024)*

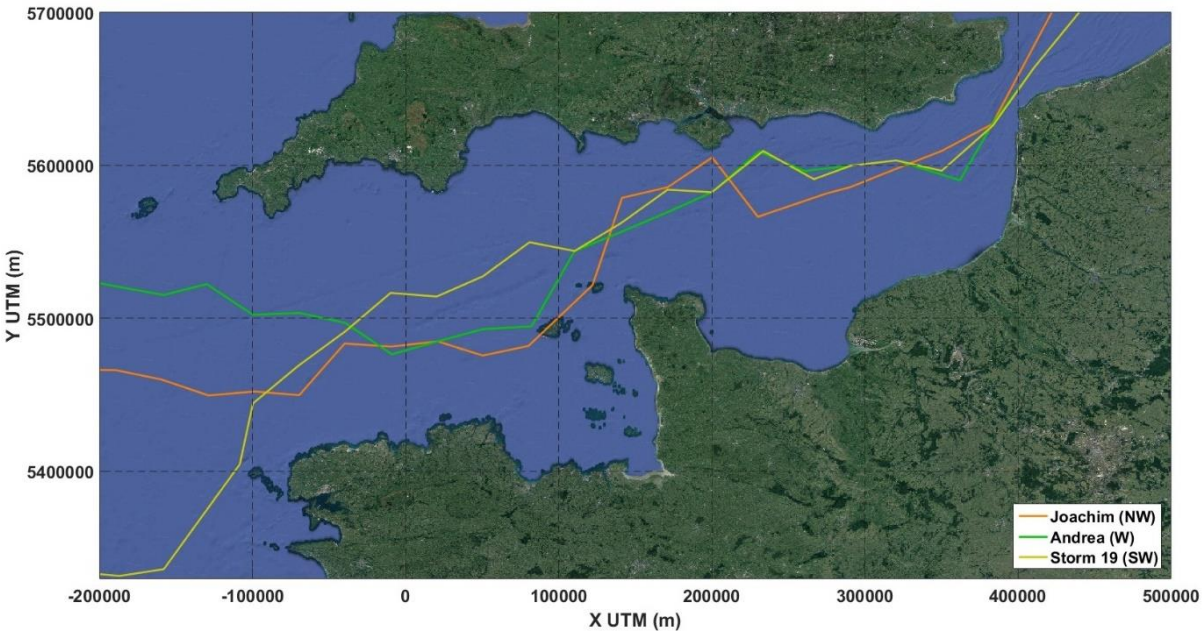

Figure 55. *Maximum significant wave height of the three selected storms, Joachim, Andrea and "Storm 19", tracked throughout the English Channel. Extracted from López Solano et al. (2024)*

Such comparison confirms that the set-up of the numerical model considering the different maritime and atmospheric forcings is accurate enough to obtain reliable results and being able to use the outputs for this analysis and future studies.

For this study, storms have been defined in terms of wave height, duration and energy content, considering a threshold in wave height time-series fixed on the percentile 95%, a minimum time of exceedance of this threshold of 24 hours, and allowing the wave height to drop below this limit no more than 12 hours in order to quantify the independence of the extreme events. Although it is possible to identify storms in terms of other variables, such as the Beaufort scale (WMO, 2018), However, focusing on coastal areas, this study is interested in the potential impacts of storms. Therefore, we have used the two main statistical approaches to identify storms which are wave height and water level analysis as described in Harley (2017), as a function of the local conditions. If they are wave-dominated coastlines, then it is appropriate to identify the storms in terms of wave height. If the presence of meteorologically driven increases in the water level beyond the usual tidal range has a bigger impact, then an analysis of sea level measurements is required. This latter approach also implies the consideration of which variable should be used to define a threshold, since areas where the main objective is establishing a limit on the total sea level beyond which an inundation can be expected, it is indeed the total sea level the variable that should be used, as in Massalin et al. (2007). Instead, if the main interest is the meteorological effects of the increase of the sea level alongside the variability of storms over time, the non-tidal residual is the variable analyzed, eliminating the tidal signal from the measured total

sea level. Studying this variable is analogous to examining wave height. In the work of Bromirski & Flick (2008), they established a threshold based on the 98th percentile with a minimum duration of 6 hours. However, in the context of the English Channel, the major impacts primarily stem from wave height rather than occasional sea level increases. This reinforces the rationale behind defining storms as peaks in the wave height time-series that surpass a specific threshold, along with a minimum duration above the threshold and a maximum allowable time below it, before considering it as a distinct storm event.

Storm characteristics are site dependent, therefore other studies have applied a similar description but taking different values instead. Shand et al. (2011) considered a threshold of either 5% of exceedance wave height or 10% exceedance wave height with minimum exceedance duration of three days, also including a minimum interval between storms of one day and applying it to different measurements of buoys on the Australian coast. This led to identify a range of between 12 and 27 storms per year, in contrast to the 6 storms identified as an average in the nodes of this study on the English Channel. In terms of thresholds, they take values between 2.43 and 4.56 m for the 10% exceedance and between 2.85 and 5.22 m for the 5% exceedance, similar values to the present analysis, with thresholds ranging from 2.03 and 5.37 m in deep waters. In a similar way, the average duration of storms defined in the Australian coast has been ~46 hours, close to the mean of ~50 hours in the English Channel. Biausque & Senechal (2019) also considered the percentile 95% for the definition of storms in SW of France, but, instead, they limited the duration to exceed just one tidal cycle, meaning 12 hours. However, for their study they have also contemplated the succession of storms, considering different storms as part of the same cluster when the period of 'calm' between events has been below 5 days. This is justified because they focused on the morphological response of a beach, while in this study, the main goal has been the characterization and the classification of storms in deep waters. In Jenkins et al. (2022), they considered the 99th percentile as the threshold and studied the succession of events over different points of the British coast, including the English Channel. They found several exceedances over that threshold that happened within 1 or 2 days, meaning that a duration of a storm of minimum 24 hours is necessary for identifying extreme events in this area.

As mentioned earlier, two origins can be identified in terms of classification of storms, the Atlantic Ocean, and the North Sea. Anthony (2013) analyzed the morphodynamics of the shoreface in response to storms in the southern North Sea. He described winds and waves in this region, also taking Calais as one of the study sites. Coinciding with the results obtained in the present study, he described dominant waves in that area as the ones originating from the English Channel, followed by waves generated in the North Sea.

In this work, the three storms mentioned above have been selected as examples, but other studies have tracked down different storms throughout the Channel. Dhoop & Thompson (2021) have followed two exceptional swell events that took place between 30 January and 1 February 2021 along the southern British coast by analyzing the wave and sea level records of tide gauges and buoys located nearshore. They gave a special focus to wave height and peak period, calculating the return periods associated to these events on the coastal locations, in contrast with the focus on direction and energy content used in the present study, due to the interest of their study on the footprint of the swell events rather than the modification when the extreme events enter into the English Channel. Muller et al. (2014) followed different storm surge events on the Western and Northern coasts of France, validating the numerical set-up with the measurements of the tide gauges of La Rochelle, Le Coquet, Saint-Malo, and Dunkirk. Within the different storms tracked down in this work, two were precisely Joachim and Andrea in the present work. Agreeing with the characteristics detailed in this section, in their study they described how Joachim presents a strong behavior in terms of surge when propagating from the Atlantic Ocean and when entering the English Channel but being almost negligible in the tide gauge of Dunkirk. Instead, they described how Andrea is barely recognizable in the time-series of the tide gauges of Le Conquet and Saint-Malo but grows in intensity when propagating within the English Channel, reaching almost 2 m of storm surge in the tide gauge of Dunkirk. These behaviors of the two storms are coincident in terms of wave height, as shown in **Figure 54**, in the current study, arriving at an equivalent characterization of the extreme events.

4.1.6. Conclusions

This work offers a practical approach for the identification and characterization of the different storm events from the English Channel to the Normandy coasts. A 40-year wave database (from January 1983 to December 2022) has been simulated by the use of a numerical model, increasing the resolution of available reanalysis datasets, to be able to follow the behavior of storms from the regional scale of the basin to the local scale of the Normandy coasts. The characterization of the storms at 5 different observation points along the English Channel brings to light two origins of storms: the North Sea and, especially, the Atlantic Ocean. The direction of origin conditions the behavior of the storms when they propagate inside the Channel more than any other variable. Duration and wave height were used to obtain the energy content. These three variables were examined and tracked along the English Channel, revealing modulation when they approached the Normandy coasts. This modulation was especially pronounced when the storms originated from either the Southern or Northern directions in the Atlantic Ocean.

The modeled nearshore wave and sea level data with the English Channel basin provide a relevant monitoring of hydrodynamics in response to various scenarios of extreme events driven by Atlantic and North Sea energetic conditions.

These findings present a handful of an integrative work highly useful as a the most relevant approach forward for understanding the dynamics of storms with a regional scale, case of the English Channel, and their physical mechanisms in nearshore areas.

Monitoring storms and understanding their behavior is relevant to investigating coastal flood risks that should be shaped by a series of adaptation strategies with the aim to reduce the coastal exposure and vulnerability at some cost.

A comprehensive analysis of extreme dynamics and their effects close to coastal areas is required, including additional works at local scales. Further investigations will explore this work of long-term hydrodynamic dataset to examine the multi-time variability to coastal storms in relation with global climate oscillations and their impacts close to Normandy beaches.

4.2. DYNAMICS OF NEARSHORE WAVES ALONG THE NORMANDY COASTS

This section describes the behavior of nearshore waves in the study sites of Etretat and Hautot-sur-Mer, identifying 10 representative storms in the common period of video cameras records and characterizing their evolution when the extreme events approach to the coast. This study has been published in the journal Water: *López Solano, C.; Turki, E. I.; Hamdi, Y.; Soloy, A.; Costa, S.; Laignel, B.; Gutiérrez Barceló, A. D.; Abcha, N.; Jacono, D.; and Lafite, R. (2022)* Dynamics of Nearshore Waves during Storms: Case of the English Channel and the Normandy Coasts*, Water, 14, 321. https:// doi.org/10.3390/w14030321*

4.2.1. Introduction

Extreme storm-related coastal inundation, one of the most destructive natural disasters, is considered a highly challenging issue in the global context of climate change and requires coastal adaptation measures that should be fitted to the changing climates (Liu et al., 2021). Severe flooding cases are constantly increasing in number which, in turn, brings the issue of accurate mapping of inundation zones and designing criteria for adaptive methods to augment flood resiliency. The inundation phenomenon can be observed arising concomitantly with the

combining driving forces of extreme waves, surges during high tides and an ongoing sea-level rise component. The need to increase coastal resilience in the near future is an important aspect since nearly 40% of the global population is living in coastal regions. Indeed, the number of people living in low-lying coastal zones (~625 million in 2000) is expected to increase by a factor of 1.5 to 2 between 2030 and 2060 (Neumann et al., 2015), which makes the need to model coastal wave climate even more important to protect those regions.

Changes in wave climate together with the sea-level rise component have increased the frequency and have reinforced the negative effects of storms and hurricanes world- wide (Liu et al., 2020; McInnes et al., 2003; O'Donnell, 2016). For example, Liu et al. (2020) have found by analyzing 68 years of data that with a sea-level rise of 0.5 m, storms with 1% annual exceedance probability (AEP) can occur up to 5% AEP along with the Connecticut coastal towns. In European water areas, the largest waves are identified at the Atlantic boundaries, where waves are to propagate over large fetches from the Atlantic Ocean. Here the persistence and strength of westerly winds are particularly important (Wolf & Woolf, 2006), as well as the intensity and frequency of storms. Wind-induced waves are generally affected by many factors including the water depth, which is locally modified by the coastal geometry and artificial structures. In shallow water areas, the decrease in height is the result of energy dissipation through bottom friction and wave breaking; this reduction of wave energy at a particular location may decrease over time if the sea level rises unless the coastal morphology in areas of mobile sediment can adapt at a similar rate (Wolf & Woolf, 2006). The wave transformation is also important in semi-enclosed environments such as bays and estuaries, where the spatial variability of water depth is considerable, and the water–land contours are highly reflective and thus responsible for the modification of wave characteristics. This is the case of the English Channel and studying the transformation of waves when they are approaching from the English Channel to Normandy coasts is the focus of this research, including simulation nearshore, with a special interest in stormy events.

Simulating the behavior of wind-induced waves requires the use of third-generation wave models (Komen et al., 1994), which are the most advanced state-of-the-art numerical tools for this matter. Third-generation models differ from first- and second-generation models in that the wave spectrum is computed alone, by integration of the basic spectral transport equation, without any prior restriction of the spectral shape, fixing the numerical limitations of the previous generations' models. In the case of open wave simulation, the most popular wave models are WAM (WAve Modelling) (Hasselmann et al., 1988) and WaveWatch III (denoted as WW3 in the following) (Tolman, 2002a, 2002b, 2009). Applying these models is not always possible in coastal

and shallow waters where non-linear and wave-bottom interactions play an important role. More details about models focused on coastal and shallow waters conditions are given by Booij et al. (1999) or Camus, Mendez, et al. (2011). The wind–wave model, WW3, was applied to the case of the English Channel by Lewis et al. (2019), Saulter et al. (2020) and Skliris et al. (2021) using a main spatial resolution of 7 km, 3 km and 1.5 km depending on the depth or proximity to the coast in different studies to reproduce the wave field and obtain spatially homogeneous long time-series of wave climate parameters, i.e., Wave Reanalysis Databases (WRD). However, the WRD accuracy presents several deficiencies compared to instrumental measurements (Caires et al., 2004; Cavaleri & Sclavo, 2006). Despite such limitations, reanalysis models are useful as they are considered to provide the optimal way to interpolate data in time and space for some locations for which no instrumental measurements work (Weisse et von Storch, 2010). Nevertheless, numerical models allow the simulation of nearshore hydrodynamics while increasing the accuracy and resolution, thus providing an accurate approximation of instrumental measurements.

SWAN is the most extended model for reproducing numerically nearshore conditions in relation to wave transformation. SWAN is a phase-averaging third-generation spectral wind–wave model, and it allows us to increase the resolution of data obtained from models with a wider grid, such as WW3. With this aim, Guillou & Chapalain (2015) have implemented the SWAN model in the Sea of Iroise (western Europe) to assess the amount of a wave energy resource at high spatial resolutions in coastal areas. Their results were validated using eight-year wave measurements at different timescales. They have estimated wave power production variability according to the interseasonal and inter-annual evolutions of the resource mentioned, particularly during the winter period. For the Sea of Iroise, monthly variations of the wave energy flux are distributed in the opposite way during the most energetic periods.

The objective of the present work is to analyze and model wave transformation in coastal areas by investigating their dynamics at two different scales: the English Channel and close to the Normandy coasts. Different datasets will be obtained at the two entrances of the Channel, the Atlantic Ocean and the North Sea, on a point offshore of Normandy and on two points nearshore after a simulation of the propagation of waves using the SWAN model. A special focus will be devoted to two pilot coastal systems, Hautot-sur-Mer and Etretat, monitored by video systems and suffering from hazardous problems of marine submersion and erosion particularly during the last two years 2018-2020 (Soloy et al., 2020, 2021).

The selection of the SWAN model over other models, such as the phase-resolving Boussinesq-type models (Ning et al., 2019; Shi et al., 2012), is motivated by a compromise between the computational cost and the quality of the results obtained. This work aims to study the modification in the energy spectrum and the physical transformation of waves in the English Channel, especially during stormy events, when they are approaching Normandy coasts, but obtaining results only before waves start to break. For this purpose, SWAN is the most appropriate model, since more developed models resolve the dispersive effects of waves in deep water and other physical processes from the breaking zone till the shore, requiring a higher computational cost. SWAN has been extensively proven as the most effective and efficient model for propagating and studying the transformation of waves.

4.2.2. Data

4.2.2.1. Study sites: The English Channel and Normandy Coasts

The English Channel is a basin connecting the Atlantic Ocean and the North Sea and separating both the French and the British coasts. A complex system of capes and bays, alongside multiple islands, characterizes the coastal morphology from the Peninsula of Brittany in the western end of the French coast, to the Cotentin Peninsula (also known as Cherbourg Peninsula) in the middle of the Channel. The Channel Islands lie on the West side of this Peninsula. From that area till the Strait of Dover, the coastline gets smoother, with some notable spots such as the Seine Estuary. Likewise, the British coastline is smoother in the eastern part and more intricate in the western part, defined mainly by the presence of the Isle of Wight in the central part of the British coast.

The Channel represents a shallow area on the continental shelf with an average depth of 60 m in the central part and less than 20 m on the sides of the basin. The depth is increasing westward up to over 100 m, but still far from the continental margin (see bathymetry map in **Figure 56**).

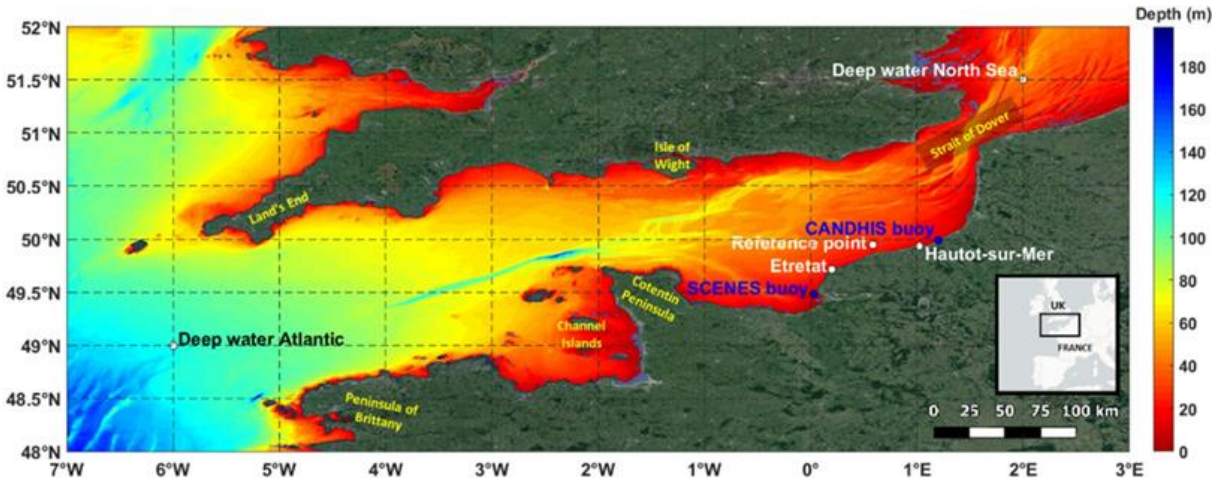

Figure 56. *Bathymetry map of the English Channel with the locations of the study sites (Etretat and Hautot-sur-Mer) the two buoys used for validation (in blue), the two points located in deep waters (North Sea and Atlantic Ocean) and the Reference point in intermediate waters. The latter three were used for studying the transformation of waves when getting inside the Channel and when approaching the study sites. Main geographical features are highlighted in yellow. Extracted from López Solano et al. (2022)*

The areas taken as the study object are located along the northern coast of France, in the eastern part of the Channel. This work is focused on examining the areas surrounding Etretat and Hautot-sur-Mer, which belong to the Normandy region (**Figure 56**). This area is strongly influenced by tides which are semidiurnal and have macro to mega tidal ranges (Levoy et al., 2000), from around 3 m at the neap tides up to 10 m at the spring tides. The Norman beaches located at the North of the mouth of the Seine River are defined by their morphology, mostly constituted by pebbles and gravel (D_{50} of 5.99 cm and 7.44 cm in Etretat and Hautot-sur-Mer, respectively (Jennings & Shulmeister, 2002). This is explained by the configuration of the coast, formed by chalk cliffs with flint strata that get eroded by the impact of the sea.

The beach of Etretat is located between two of these cliff systems, the *Falaise d'Aval* is in the West, and the *Falaise d'Amont* is in the East. It is about 1 km long with the width varying in the tidal range. The shoreline is oriented to the Northeast with an inclination of North 47°. The beach has a steep slope of up to 12% and can be described as a pure gravel beach according to Jennings & Shulmeister (2002).

The Hautot-sur-Mer beach is located in the West of the city of Dieppe, being semi-enclosed by chalk cliffs. This beach is 1.1 km long, with width varying in the tidal range, being a composite beach, which includes a sandy low tide terrace and a pebble ridge, with a slope of 10% for the latter. The shoreline of Hautot-sur-Mer is oriented to the ENE, with an inclination of North 71°.

4.2.2.2. Wind and wave field measurements

For the analysis of the transformation of waves, including the forcing of the model, data were extracted from the MARC project (*Modélisation et Analyse pour la Recherche Côtière*, Modelling and Analysis for Coastal Research (MARC, 2021)). Models implemented in MARC include MARS3D (Model for Applications at Regional Scales (Lazure & Dumas, 2008), circulation, biogeochemistry and sediment dynamics) from Ifremer and WW3 wave model delivered by an international consortium coordinated by NOAA. The implementation used - called NORGAS-2MIN database (Dumas et al., 2021) - offers wave, wind and sea level data alongside the French Atlantic coast with the spatial resolution of 2 min at an hourly frequency starting from 2012, more specifically, along the Normandy and Gascony coasts, in the English Channel and the Bay of Biscay, respectively.

Hourly wave and wind data were obtained from external nodes of the reanalysis model WW3. WW3 (Tolman, 1997, 1999, 2009) is a wave model developed at NOAA/NCEP (National Centers for Environmental Prediction) in the spirit of the WAM model (Hasselmann et al., 1988; Komen et al., 1994). It represents the attempt to sophisticate both models WaveWatch as developed at Delft University of Technology (Dumas et al., 2021; Tolman, 1989) and WaveWatch II, developed at NASA (National Aeronautics and Space Administration), Goddard Space Flight Center (Tolman, 1992). WW3, however, differs from its predecessors in terms of numerous important points such as governing equations, model structure, numerical methods and physical parameterization. Furthermore, along with version 3.14, WW3 evolved from a wave model into a wave modeling framework, which allows the development of additional physical and numerical approaches to wave modeling in an easier way.

WW3 solves the random phase spectral action density balance equation for wavenumber–direction spectra. The implicit assumption of this equation is that the properties of medium (water depth and current), as well as the wave field itself, vary with time and space scales, being much larger than the single wave variance scales, considering wetting and drying of grid points. However, the surf-zone physics implemented so far are still fairly rudimentary and imply that the wave model can be applied for the case of arbitrary shallow waters (WW3, 2019). The data of the sea surface height above sea level were obtained from the MARS3D model. MARS is a community model developed by Ifremer (*Institut Français de Recherche pour l'Exploitation de la Mer*, French Institute for the Research and the Exploitation of the Sea) and shared by the DYNECO/DHYSED team (*Dynamique HYdro-SEDimentaire du département DYNamiques des Ecosystèmes COtier*, Hydro-Sedimentary Dynamics of the Dynamics of Coastal Ecosystems Department). The MARS

model is a three-dimensional (3D) model based on a set of fluid mechanics equations (the so-called primitive equations) solved under some classic approximations for the hypotheses: (1) the Boussinesq assumption (Boussinesq, 1903), for which density in the medium slightly deviates from a reference density and therefore can be replaced by a reference density except within the gravity term; and (2) the hydrostatic approximation resulting from scaling the equations, for which the horizontal movement scale is assumed to be an order of magnitude larger than the vertical one. These equations are transformed under the sigma framework in order to make free surface processing easier.

The MARS model is used to provide some realistic description of the coastal phenomena and is implemented for research and for operational interests over the three metropolitan basins: the Channel itself, the Bay of Biscay and the North-Western Mediterranean Sea. The main original aspect of the MARS model is the coupling between barotropic and baroclinic modes specifically. The base resolution of the free surface is 5 km (Lazure & Dumas, 2008), increased to 500 m along the French Atlantic coast in the MARC project (MARC, 2021).

Validation of the propagated data is proposed with the objective of confirming that the setup of the SWAN model is correctly defined and that the datasets used for forcing the model are also appropriate since the results of these propagations are potentially usable in further studies. For validating the results obtained from the simulations, wave measurements of two buoys were compared to the time series extracted at the same locations of these two stations (one for each of the study areas).

For Etretat, the wave measurement data were extracted from SCENES buoy (*Station Côtière pour l'observation de l'Environnement en Estuaire de Seine*, Coastal Station for the Observation and the Environment in the Seine Estuary) at the Seine Estuary mouth at a depth of 10 m (49° 28.844' N–0° 1.932' E, **Figure 56**), operated by Ifremer from October 2017. An ADCP (Acoustic Doppler Durrent Profiler) provides current velocity profiling every 30 min (the same goes for the wave parameters being provided every hour).

Regarding Hautot-sur-Mer, data were obtained by the campaign 07608 carried out by Cerema and EDF (*Electricité de France*, France Electricity Company, Paris, France) close to Penly (49° 59.36' N–01° 12.06' E, **Figure 56**), at 11 m of depth with more than three years of wave data measurements every 30 min (7 November 2017–31 May 2021).

4.2.2.3. Storm events identification

A 26-month time series of significant wave height was used to identify extreme events. It was obtained from the WW3 model output at intermediate waters in the node located between both study sites (49◦58.728' N–0◦32.01' E, at 29 m of depth, **Figure 56**), marked as a Reference point. The extreme events in the wave height time series were identified using a Peak Over Threshold (POT) method. Extreme events were selected with a threshold equal to the quantile Q95% following the hypothesis that, at least 5 days separate two consecutive peaks (**Figure 57**) for ensuring the independence of storms. A storm's duration was defined as the time elapsed during the increase before the peak and decrease after the peak of the wave height time series. This aims to cover the whole development and fading processes during a storm. More than 30 extreme events were identified applying this definition. In the literature, it is worth noting that in some of them several values for the elapsed time between storms were used, from 1.25 days in Morton et al. (1997) up to 20 days in Guedes Soares & Scotto (2004). In this study, choosing 5 days is motivated by the will to get a short enough elapsed time for obtaining a higher number of extreme events, while remaining long enough so that the definition of duration allows obtaining the growth and decay of every storm independently.

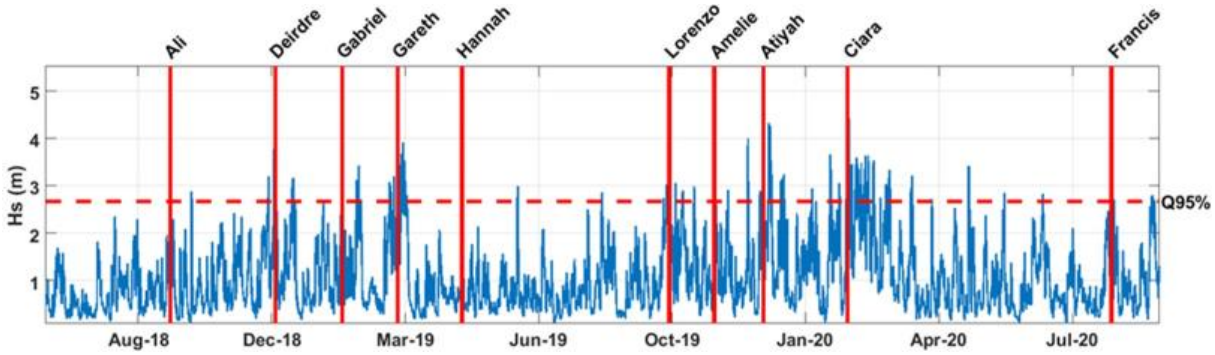

Figure 57. *Time series of significant wave height (Hs) from June 2018 to September 2020. The red dotted line represents the quantile 95, used as threshold for the identification of extreme events. The vertical red still lines locate in the time series the 10 storms used for the analysis of transformation of waves in this study. Extracted from López Solano et al. (2022)*

Among these 30 extreme events, 10 were selected to be analyzed considering variability in their characteristics (seasonal occurrence, wave magnitude, wave direction, sea level, storm duration) with the aim to classify the different events and identify their similarities and their differences, including their common hydrodynamic response close to the shoreline. Three storms, among the 10 ones analyzed, have happened at summer–autumn time each year: that is the case of Ali (starting 20 September 2018), Lorenzo (29 September 2019) and Francis (25 August 2020). The seven remaining storms took place during winter-spring time: Deirdre (5 December 2018), Gabriel (25 January 2019), Gareth (10 March 2019), Hannah (26 April 2019), Amelie (31

November 2019), Atiyah (7 December 2019) and Ciara (8 February 2020). The 10 storms are identified in **Figure 57**.

4.2.3. Methodology

4.2.3.1. Wave model

Wave propagation and evolution were simulated using the SWAN model. SWAN was developed at Delft University of Technology, and computes random, short-rested wind-generated waves in coastal regions and inland waters swells. The model simulates the growth, decay and transformation of wind-generated surface gravity waves and swells (SWAN, 2021).

SWAN solves the spectral action balance equation without any a priori restrictions on the spectrum for the evolution of wave growth. SWAN wave propagation is calculated from deep water to the surf zone.

The discretization of the wave action balance equation in both geographical and spectral space is performed using a finite difference approach based on the so-called method of lines, while the geographical domain is discretized by structured rectangular meshes in the set-up used in this study.

SWAN accounts for the following physics: (a) wave transformation processes (shoaling, refraction due to current and depth, frequency shifting due to currents and non-stationary depth) (b) energy source/dissipation processes (wave generation by wind, white capping/bottom friction/depth-induced breaking, dissipation due to aquatic vegetation/turbulent flow/viscous fluid mud, wave-induced set-up, transmission through and reflection (specular and diffuse) against obstacles), and (c) non-linear energy transfer conservative processes (three- and four-wave interactions).

4.2.3.2. Model set-up

The boundary conditions of the SWAN model are defined by nine variables, including waves, wind and sea level, that need to be set up into the model in the coarse grids for both Etretat and Hautot-sur-Mer.

Wave data extracted from the MARC's WRD applying the WW3 model consists in the significant height of wind and swell waves (H_s), the peak period of the energy spectrum (T_p) calculated from the wave peak frequency, the mean wave direction (θ_m) and the coefficient of directional spreading. The breaking constant (γ_b) is calculated from the wavelength and the

Iribarren number, considering the averaged slope at each study site. The peak enhancement parameter of the Jonswap spectrum is obtained from the energy of the waves.

Wind was also obtained from the MARC database applying WW3 (WW3, 2019), and a middle node in the center of each study site was chosen to force the model considering velocity (W_{speed}) and direction ($W_{direction}$) at 10 m of elevation, calculated from the horizontal Northward and Eastward components.

Sea surface height above sea level, taken from MARC database through the use of MARS3D model (WW3, 2019) is also set as an hourly constant value considering the same coordinates of the node chosen for wind input data.

An output nested grid, i.e., an additional grid located inside the coarse grid with a higher resolution, is defined at each location. To reduce the scale, the ratio of the size of the cells from the coarse grid to the nested grid must be up to 1:5. When nesting, SWAN searches for the boundary conditions of the internal grid in the output files of the previous coarse runs to take the boundary conditions at the start time of the nested run.

Hourly data from June 2018 to September 2020 were extracted from WW3 and MARS3D through MARC database to force the model. The model was run in a non-stationary mode with white capping, quadruplets and dissipation by bottom friction processes activated.

The meshes used for the simulations were created defining two density zones. The first grids (coarse meshgrids, **Figure 58**) are extended on the deep-water boundaries from 43 m of maximum depth in Etretat (spatial domain of 20.23 × 26.73 km) and from 31 m of maximum depth in Hautot-sur-Mer (19.54 × 20 km) to the shoreline with a cell size resolution of about 100 m. The second grids (nested meshgrids, **Figure 58**) are extended from 24 m of maximum depth in Etretat (3.6 × 3 km) and 21 m in Hautot-sur-Mer (3.9 × 4 km) on the boundaries to the shoreline of the Normandy coasts with a constant cell size resolution of 20 m.

This results in a coarse grid of 203 × 268 nodes in Etretat and a coarse grid of 196 × 201 nodes in Hautot-sur-Mer, and nested grids of 181 × 151 nodes and 201 × 231 nodes in each of the locations.

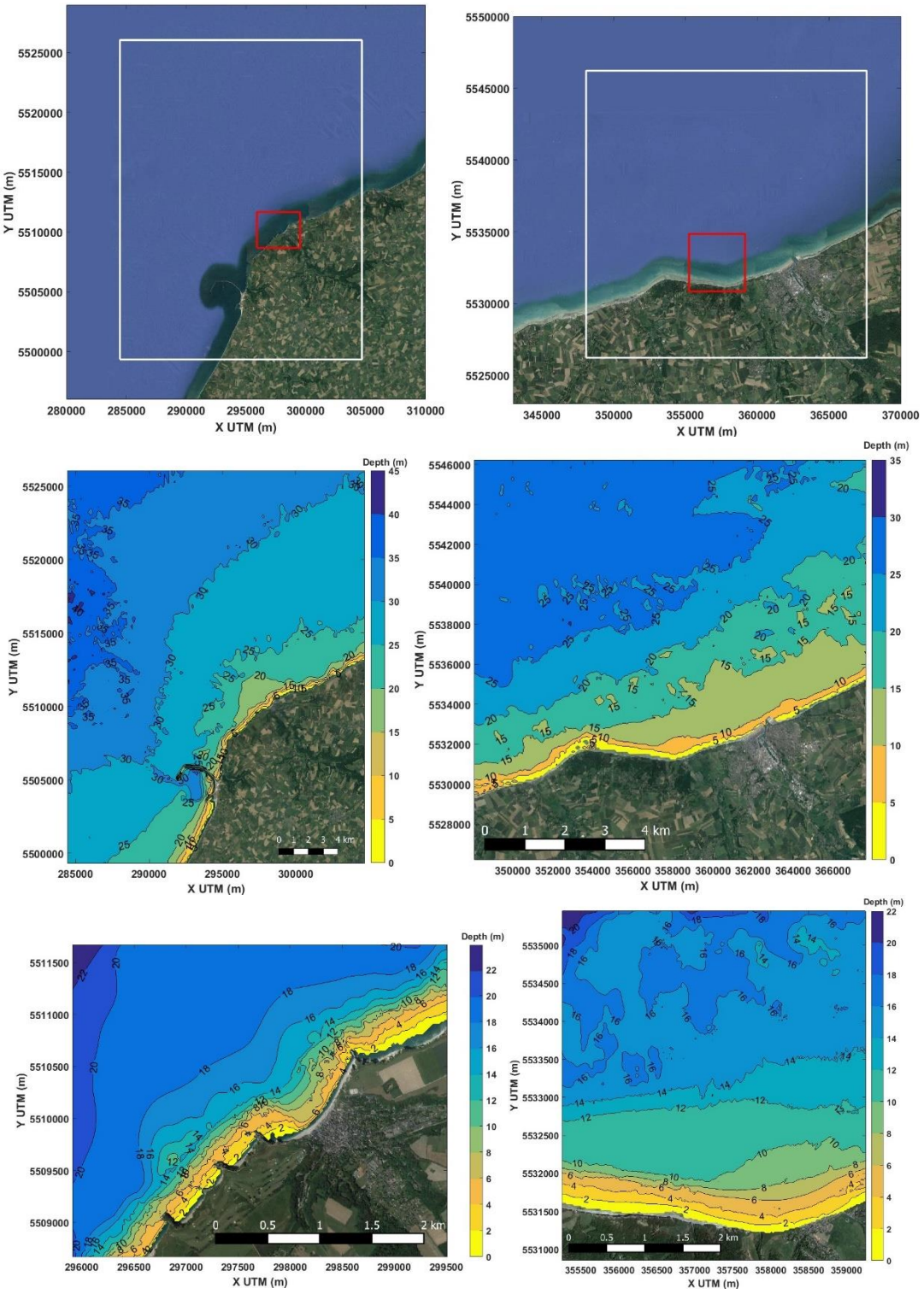

Figure 58. *Coarse and nested grids, in white and red colors, respectively, for (a) Etretat and (b) Hautot- sur-Mer. DEMs of coarse grids in (c) Etretat and (d) Hautot-sur-Mer, and DEMs of nested grids in (e) Etretat and (f) Hautot-sur-Mer. Bathymetry data obtained from a merged DEM of EMODnet dataset and LiDAR campaign datasets. Satellite images from Google Earth. Extracted from López Solano et al. (2022)*

Increasing the resolution nearshore through the use of nested grids is necessary to obtain more reliable datasets that can be used in following studies, such as sediment transport near engineering works or coastal modeling focused on the beaches of Etretat and Hautot-sur- Mer.

Raw datasets with the 100 m resolution defined in coarse grids would not be fine enough for the studies mentioned. At the same time, the computational cost of adding nested grids in the propagations is not noticeable for the 2 years simulated and the spatial domains considered.

The model's computational DEM is a composition and merging of regional bathymetry from the EMODnet Bathymetry portal (EMODnet, 2021) and high-resolution images from LiDAR campaigns. The vertical datum was the Lowest Astronomical Tide (LAT) for both sources and both locations. The spatial reference was the projection system EPSG:32631 WGS84/UTM zone 31N.

Bathymetry of the external area was extracted from the EMODnet portal. The nearshore bathymetry of the LiDAR campaigns was provided by the ROL (*Réseau d'Observation du Littoral de Normandie et des Hauts-de- France*, Observation Network of the Coast of Normandy and Hauts-de-France). ROL is a monitoring strategy for coordinating a homogeneous coastline, which provides the information used in this study (ROL, 2020). This dataset provides information of water depth every 1 m along the beaches and in all the surrounding area, seawards and landwards, for both locations.

4.2.3.1. Wave statistics

Firstly, validation of the results of the numerical model was evaluated by calculating classical statistical parameters in comparison to buoy measurements. In the second place, the Continuous Wavelet Transform (CWT) was calculated with the datasets to perform the frequency analysis in the transformation of waves from the English Channel to the Normandy coasts.

Model performances are assessed using standard statistical parameters, as in Stopa et al. (2016), including the Root Mean Square Error ($RMSE$, Eq. 12), the Pearson's correlation coefficient (R, Eq. 13) and the scatter index (SI, Eq. 14).

$RMSE$ is useful to obtain an evaluation of the average distance between the observed data and the data obtained from the simulations. The Pearson's correlation coefficient R can be used as an indicator of the trends of the measured and the modeled datasets. If the datasets analyzed tend to increase or decrease together, R is closer to 1, and if they disagree in their trends, R is closer to 0. And the scatter index (SI) is a normalized $RMSE$, and it provides information on the precision of the results of simulations with respect to the observations in percentage.

A spectral approach of continuous wavelet was used to investigate the non-stationary behavior of waves and changes in their spectrum and their direction at different timescales. The CWT has been largely used in meteorological applications to investigate the time–frequency evolution of climate patterns (Labat, 2005; Massei et al., 2017; Turki et al., 2019). The technique

of wavelet consists of decomposing a signal into scaled and translated versions (i.e., daughter wavelets) of a reference wave function (i.e., mother wavelet). The correlation between the undecomposed signal and the larger daughter wavelets allows the identification of different scales of variability. For example, the existence of a correlation between the undecomposed signal and the smaller wavelets emphasizes the presence of the smaller (shorter wavelength) variations in the undecomposed signal. Scanning the undecomposed signal with the set of daughter wavelets (i.e., convolving the signal with the wavelets) produces a diagram of space (X direction) versus space frequency of the variability.

The diagrams of CWT contain: (1) the contour diagram with space on the x-axis; (2) the frequency (spatial scale) or equivalent wavelength on the y-axis; and (3) the power or variance, which quantifies the correlation between the signal and the wavelet basis, on the z-axis.

4.2.4. Results

4.2.4.1. Model validation

The wave measurements were compared to the SWAN wave simulations during the 26-month period propagated (from June 2018 to September 2020) to quantify the accuracy of the numerical approach in shallow water areas where the wave buoys are available (for Etretat, the SCENES buoy operated by Ifremer, and, for Hautot-sur-Mer, the buoy of the campaign 07608 carried out by Cerema and EDF). The comparison between both datasets highlights that RMSE is about ~20 cm in Etretat and about ~15 cm in Hatout-sur-Mer, agreeing with previous values obtained extensively in the literature for WRD obtained from the WW3 model (Ardhuin et al., 2012; Boudière et al., 2013; Dodet et al., 2019), with less than 20 cm for the whole set of validation points.

For the site of Etretat, larger errors are caused by the Seine River discharge, which is not considered in our simulations since SWAN is not able to consider river flow inputs without coupling it with an external hydrodynamical model, and which affects wave buoymeasurements. Nevertheless, the datasets of observations and simulations show good agreement with a correlation coefficient higher than 0.92 in both locations, reaching R = 0.96 in Hautot-sur-Mer (**Figure 59**). In the literature, these values for databases obtained from WW3 are also around 0.94. Precision is also better in Hatout-sur-Mer than in Etretat, with a scatter index of around 33% in the second site and around 22% in the first location, which includes goof precision.

For example, the significant wave height of 2.5 m in Etretat is overestimated by the model with a bias of 0.3 m (**Figure 59**a). In Hautot-sur-Mer, these errors appear when wave height takes values superior to 3 m and the simulations underestimate the observations also by around 0.2 m (**Figure**

59b). For an extreme event of 4 m, this explained variance is around ~0.30 m in Etretat and ~0.28 m in Hautot-sur-Mer.

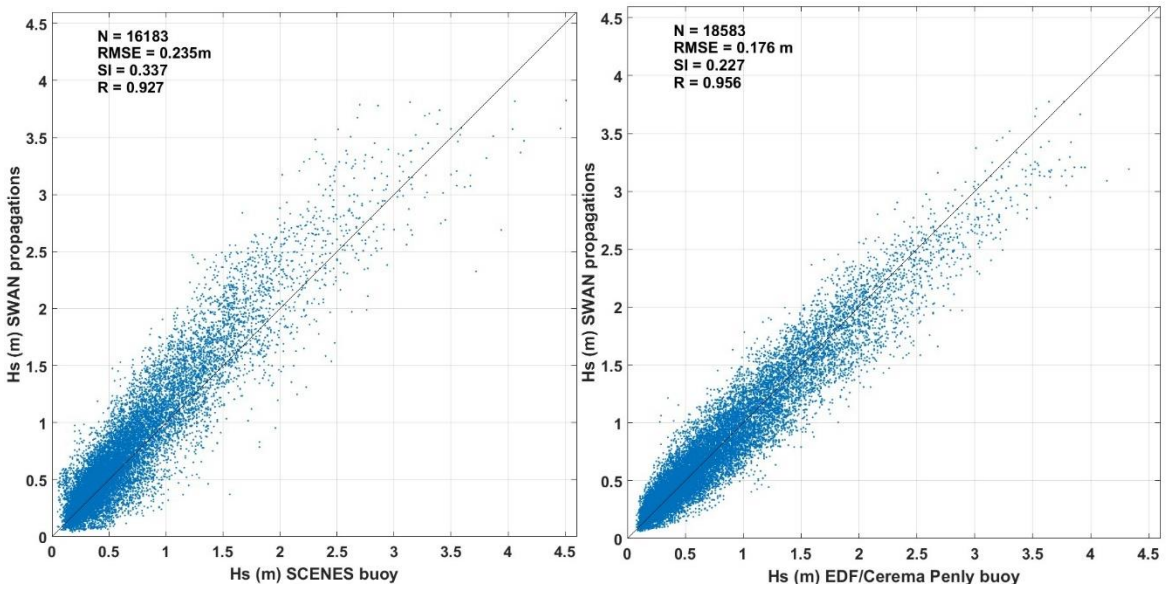

Figure 59. *Significant wave height (Hs) comparison of results of simulations from the SWAN model versus observations measured by (a) SCENES buoy for Etretat and (b) campaign 07608 for Hautot- sur-Mer. Extracted from López Solano et al. (2022)*

Such comparison highlights the accuracy of wave propagations with the SWAN model and the set-up of this study considering wind, waves and sea level, with positive biases in Etretat and negative ones in Hautot-sur-Mer for higher values. The validation of the results obtained from the model with the observations of the two buoys avoids the necessity of a calibration of the set-up of the model before propagation and provides support for the use of the datasets obtained as results in further studies.

4.2.4.2. Changes in directional wave spectrum

In this section, five time series of simulated waves, extracted at different depths, from deep waters to nearshore, were studied. The signal of the wave height and the direction during the whole record of the dataset during the 26 months period was analyzed to investigate the variability of each parameter. They were calculated for five different points: two external points in deep water from WW3 on the North Sea (1) and the Atlantic Ocean (2); the Reference point in intermediate water between the two study sites (3); and two points extracted from nested grids and located at the closure depth of Etretat (4) and Hautot-sur-Mer (5) (**Figure 56**). The closure depth is situated in shallow water most of the time, but with the possibility of being in intermediate water for some combinations of sea level and wave height, and it represents the shallowest depth where there is no significant change in the bottom elevation. The selection of this point as the representative

point is motivated because it is the last permanent depth that can be used landward, where waves are still not broken and where SWAN can reproduce their behavior accurately.

The wave climate regime in deep water is mainly controlled by the waves coming from the North Sea and from the Atlantic Ocean where waves present directional distributions with two modes, 40° and 225°, exhibiting both sea and swell waves, respectively (**Figure 60**). The frequency of sea waves is higher in the North Sea while swell waves are more important on the Atlantic side. At the Reference point, the distribution is composed of 30% sea waves and 70% swell waves. In the shallower water areas of Hautot-sur-Mer and Etretat, the swell waves are dominant for the period of time studied. Regarding the distribution of H_s, the gaussian behavior is fully conserved from deep water to shallow water with decreasing height induced by changes in water depth. The maximum Atlantic waves reach 10 m and are limited to 5 m at the North Sea. The average H_s is reduced to around 50% from the Atlantic to the Reference point where wave energy is also dissipated with 25% to reach Etretat and Hautot-sur-Mer.

Indeed, the maximum wave height is reduced by 15% and by 35%, close to Etretat and Hautot-sur-Mer, respectively. Changes in wave direction take an average of 18° clockwise for most of the storms close to Etretat at the peak of the storm; and they increase to 38° close to Hautot-sur-Mer, varying their directions from the sectors W-WNW to the sectors WNW-NW. The overall changes in wave height and direction are mainly induced by the refraction and energy dissipation processes, respectively, due to the bathymetry variation and the bottom friction, still too deep to start the breaking process (**Figure 60**).

In the frequency domain, the Continuous Wavelet Transform (CWT) of H_s and θ were calculated for different locations (**Figure 61**). In these spectra, the color scale represents an increasing power (variance) from blue to yellow and red. The CWT diagrams highlight the existence of several scales of variability for depths with different ranges of frequencies: the inter-monthly scales of ~3-6 months and ~1-2 months and the inter-daily scales of ~0.5 months.

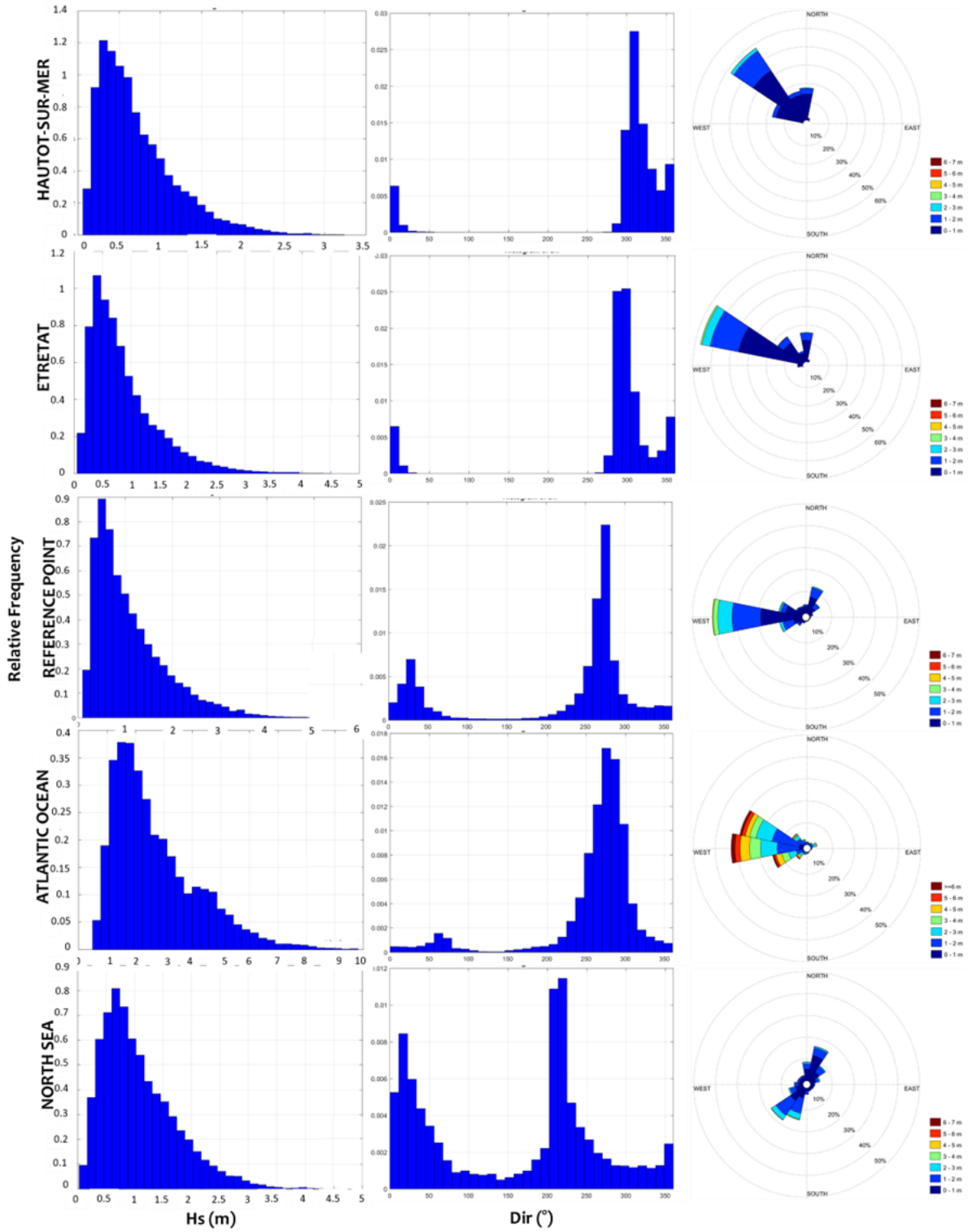

Figure 60. *Probability Density Functions (PDF) of Hs (a) and of θ (b) and wave roses (c) at deep waters in the North Sea (depth = 44 m), the Atlantic Ocean (depth = 116 m), the Reference point (depth = 28 m), close to Etretat (depth = 13.4 m) and to Hautot-sur-Mer (depth = 13 m). Extracted from López Solano et al. (2022)*

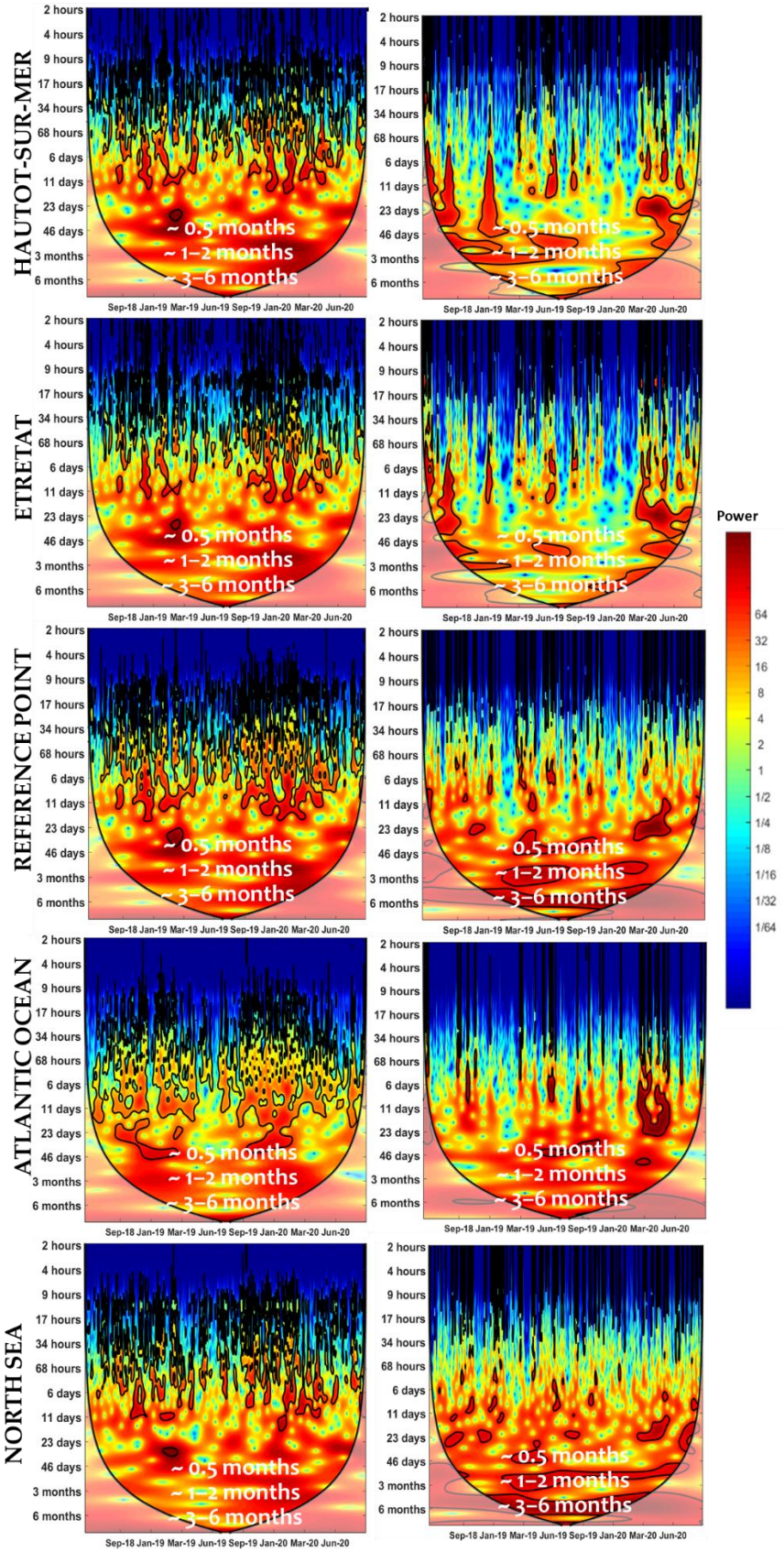

Figure 61. *Continuous Wavelet Transform (CWT) of Hs (a) and θ (b) at deep waters in the North Sea, the Atlantic Ocean, the Reference point (depth = 28 m), close to Etretat (depth = 13.4 m) and Hautot-sur-Mer (depth = 13 m). Extracted from López Solano et al. (2022)*

For high frequencies less than 0.5 months, the H_s spectrum is relatively important at the North Sea, varying hourly scales, compared to the Atlantic where the low frequencies of 1-2 months and ~3-6 months are more structured. The full spectrum decreases from deep water to the Reference point and then to Etretat and Hautot-sur-Mer. Accordingly, waves do not exhibit significant changes in their height but should be modulated in their spectrum resulting from wind sea and swell waves. Such modulation seems to be related to an energy transfer between the wave frequencies induced by their physical transformation in shallow water areas.

Regarding the θ, significant changes are outlined at the different locations. Contrary to H_s, high frequencies are less structured for the wave direction that varies at scales of days. The full spectrum from high to low frequencies is clearly observed at the North Sea and decreases slightly at the Reference point; it is reduced at Etretat and Hautot-sur-Mer. This variation should be mainly explained by the wave refraction induced by changes in sea bottom within the English Channel; it seems to be similarly produced for all waves coming from different directions in deep water.

4.2.4.1. Storms Evolution within the English Channel

The hydrodynamics related to waves were investigated for the selected storms within the English Channel, more specifically, the time series of the variables Hs and θ at the Reference point. The value of the maximum wave height ($H_{s,max}$) was identified in the Hs timeseries, named hereafter as the peak of the storm. In the same way, $\theta_{Hs,peak}$ was identified in the time series of θ as the value associated with the instant of this peak. $H_{s,max}$ gives us the information of the most hazardous scenario, when Hs is reaching the highest value during the storm. If $\theta_{Hs,peak}$ turns perpendicular to the shoreline at this instant, the extreme event comes with an associated risk that requires to be deemed.

The definition of the duration of a storm between the instants of the two minima located before and after the peak was also applied at the Reference point. We defined the new variables $H_{s,storm}$ and θ_{storm} as the timeseries of Hs and θ for the duration of each storm.

Finally, in order to know the occurrence of the values $H_{s,max}$ and $\theta_{Hs,peak}$, we analyzed the distribution of the variables $H_{s,storm}$ and θ_{storm}. We sorted the time series of $H_{s,storm}$ and θ_{storm} and divided the records into 10 equally spaced bins between the minimum and the maximum values of the two variables, with each bin containing 10% of the record. Calculating the relative frequencies of those bins, we figured out the occurrences of the 10% of the record of $H_{s,storm}$ and θ_{storm} within which $H_{s,max}$ and $\theta_{Hs,peak}$ are contained. This information is important to realize the real impact of each storm. A more elevated value of the occurrence of $H_{s,max}$ implies

a longer time with the coast exposed to the impact of these extreme events, whereas a lower value results in faster growth and decay of the storm.

A confluence of a high value of $H_{s,max}$ with a high value of its associated occurrence brings the worst scenario, with a strong impact due to the elevated wave height at the peak and persistent in time because of the high relative frequency of the 10% of the sorted distribution of the variable $H_{s,storm}$ within which $H_{s,max}$ is included. If this happens to be with a $\theta_{Hs,peak}$ perpendicular to the shoreline and with an elevated associated occurrence of the bin containing it, the combination is the most hazardous.

Table 21 summarizes the main variables: the duration, the values of the wave height $H_{s,max}$ and the associated mean direction $\theta_{Hs,peak}$, the percentage of occurrence of the bins containing $H_{s,max}$ and $\theta_{Hs,peak}$, and the standard deviation of $H_{s,storm}$ and θ_{storm}.

Storm	Duration (Days)	$H_{s,max}$ (m)	$\theta_{Hs,peak}$ (°)	Occurrence $H_{s,max}$ (%)	Occurrence $\theta_{Hs,peak}$ (%)	Standard Deviation $H_{s,storm}$ (m)	Standard Deviation θ_{storm} (°)
Ali	2.1	3.25	274.6	9	29	0.8	9.3
Deirdre	6.6	4.43	276.2	7	48	1.24	18.26
Gabriel	4.5	3.5	293.3	3	17	0.88	24.68
Gareth	2.1	4.02	274.4	6	15	0.9	8.83
Hannah	3.3	3.55	274.3	8	32	1.1	6.89
Lorenzo	1.8	3.94	271.8	4	14	0.83	13.39
Amelie	2.7	3.81	259.3	7	32	1.11	39.68
Atiyah	2.7	4.46	280.6	6	12	1.11	17.16
Ciara	4.4	5.33	276	3	43	1.26	12.11
Francis	2.5	3.93	268.1	9	37	1.12	13.56

Table 21. *Summary of characteristics of the 10 storms in the Reference point selected from June 2018 to September 2020 with the duration, the wave height $H_{s,max}$, the mean direction $\theta_{Hs,peak}$, the occurrences of $H_{s,max}$ and $\theta_{Hs,peak}$, and the standard deviation of $H_{s,storm}$ and θ_{storm}. Extracted from López Solano et al. (2022)*

Among the different storms investigated, we distinguish: (1) Three storms were produced in summer–autumn (Ali, Lorenzo and Francis) with values of $H_{s,max}$ and $\theta_{Hs,peak}$ of 3.2-3.9 m and 277-279°, respectively; (2) Seven winter–spring storms (Deirdre, Gabriel, Gareth, Hannah, Amelie, Atiyah and Ciara) with a maximum wave height of 3.25-5.3 m and a mean direction of 259-293°, respectively. On the European coast of the North Atlantic Ocean, the season of low pressures or depressions starts traditionally in September–October. The events with the strongest impacts receive a name given by one of the coordinated European groups formed by the meteorological services of the different countries. Coinciding with the initial time of this work, the Southwest Group names the storms since the 2017-2018 season. Accounting for all the storms named by this Group since 2017, 12% were produced in summer-autumn and 88% of them were produced

in winter-spring time, agreeing with this work in a bigger proportion of winter storms and with the strongest impact.

Storms with a shorter duration usually take place during the summer–autumn period and storms with longer durations in the winter–spring period. However, duration is not directly related to $H_{s,max}$, since Lorenzo, being the shortest storm with a duration of 1.8 days, ranks fifth in the $H_{s,max}$ classification, and Deirdre, being the longest storm with a duration of 6.6 days, has just the third-highest $H_{s,max}$.

As described before, investigating the occurrence of $H_{s,max}$ and $\theta_{Hs,peak}$ is important for learning about the behavior of the storms, especially at their peak. The occurrence of the highest 10% of the time series $H_{s,storm}$ appears to be high during Ali, Deirdre, Hannah Amelie and Francis. Nevertheless, for these five storms, just Deirdre takes an elevated value of $H_{s,max}$, which results in a risky situation, with a strong wave height that is also persistent in time. If we complete this information with the fact that Deirdre had the longest duration of all, we can declare that Deirdre is one of the most hazardous storms. In the case of Ciara, with the highest $H_{s,max}$, the occurrence remains low, but this is conditioned probably by a high value of a standard deviation, as shown in **Table 21**. For this storm, the most elevated value of the standard deviation shows a wide range in the $H_{s,storm}$, leading to the assumption that it is one of the most hazardous storms too.

For this analysis, we assume that a high occurrence or a large wave height are considered when the percentage of occurrence or the value of Hs at the peak are above the average value obtained from the storms studied, that is, 6.2% for the occurrence and 4.02 m for $H_{s,max}$.

In the case of the occurrence of $\theta_{Hs,peak}$, it becomes less important since a real affection to our study sites is conditioned by the value of $\theta_{Hs,peak}$ itself. In Etretat, the worst $\theta_{Hs,peak}$ of a storm would be the perpendicular direction to the shoreline, which is 317°. For Hautot-sur-Mer, this direction would be 341°. Considering that the storm with a stronger northern component is Gabriel, and the value of $\theta_{Hs,peak}$ is just 293.3°, we can accept that the storms studied are not as hazardous as they could be in relation to $\theta_{Hs,peak}$ and the associated occurrence.

It can be observed that, for some of the storms, the standard deviation of θ_{storm} is elevated. This is conditioned by the evolution of the mean direction during the storms, showing some variabilities, generally a shift to sectors with a W-SW component during the development phase of $H_{s,storm}$, taking an almost constant value during the fading phase. The storms with a bigger shift, before or after the peak, can be easily recognized by these high values in the standard deviation of θ_{storm}, especially Amelie.

These four storms pointed out for their different characteristics, Ciara, Amelie, Deirdre and Gabriel, are shown at their own peaks in **Figure 62** and **Figure 63** for the coarse and nested grids used during the simulations. The color maps represent the significant wave height, and the arrows represent the field of mean directions.

4.2.4.2. Storm Evolution in Normandy Coasts: Case of Etretat and Hautot-sur-Mer

In shallow water, the energy of nearshore waves is dissipated close to the Normandy coasts. More than 50% is reduced at Hautot-sur-Mer and Etretat with a mean of 70% and 85%, respectively. This amount of dissipation is higher than 90% for storms produced at spring tides. The wave dissipation seems to be not homogenous along the coastal zones with an Hs gradient strongly influenced by changes in the morphology of sea bottom and the coastal geometry.

Indeed, the wave gradients at Hautot-sur-Mer (**Figure 63**) take different distributions between the western and the eastern side with an increasing and decreasing wave height, respectively. Such changes are mainly controlled by the presence of sandbanks and irregularities of the bathymetric responsible for wave refraction.

A clear example is observed for the line of 10 m of depth (see **Figure 58**), which is approximately 1.5 km and 3 km away from the shoreline in the western and the eastern side, respectively. Similar irregularities between both sides are also observed for the 20 m bathymetric contour which is far from the shoreline with a distance varying between 5 km and 7 km. Such a configuration exhibits changes in the morphological slope which are limited to 0.2% between 10 m and 20 m of depth and increases to 0.45% between the shoreline and 10 m of depth. Then, waves are bigger close to the soft slope while they break when the slope is steeper, which is the case for storms occurring during high tides. Here, the breaking depth ranges from 4.5 m for the biggest waves to less than 1 m for the smallest. For the storms studied, this depth is 3-4 m.

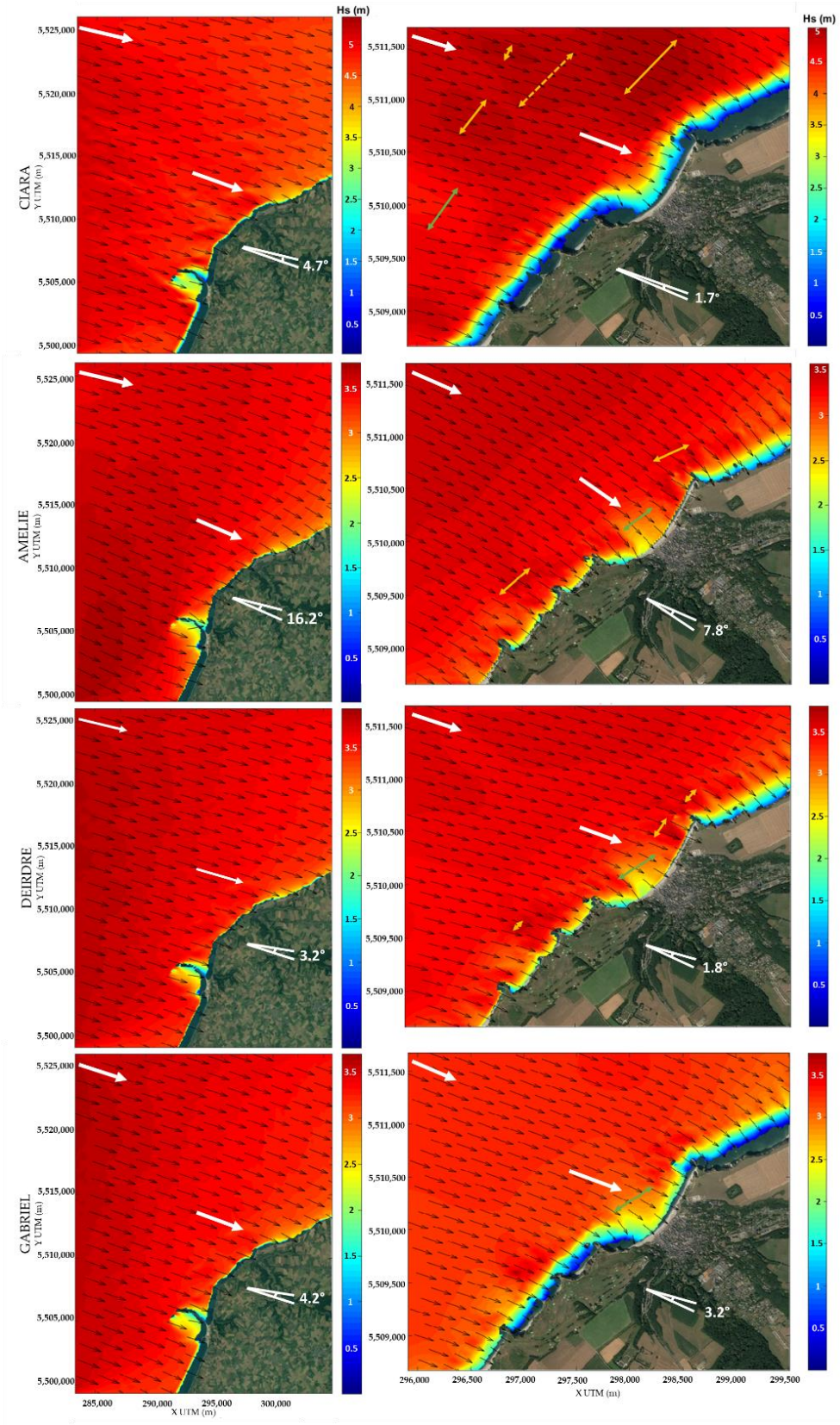

Figure 62. *Distribution maps at the peak of the storm of Hs and θ in the coarse grid (a,c,e,g) and nested grid (b,d,f,h) in Hautot-sur-Mer for Ciara (February 2020) (a,b), Amelie (November 2019) (c,d), Deirdre (December 2018) (e,f) and Gabriel (January 2019) (g,h) storms. White arrows show the refraction of waves when approaching to coast. Extracted from López Solano et al. (2022)*

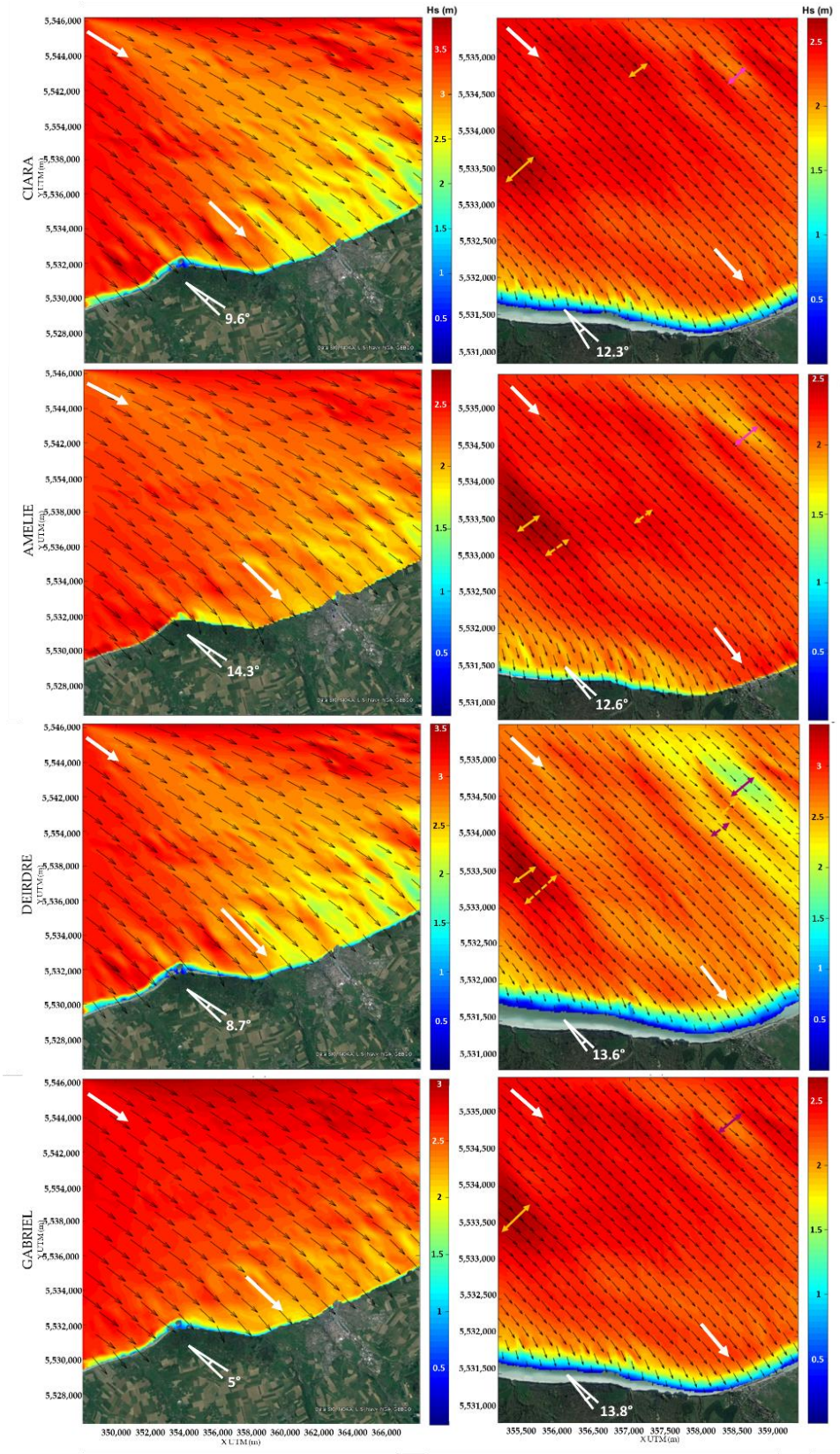

Figure 63. *Distribution maps at the peak of the storm of Hs and θ in the coarse grid (a,c,e,g) and nested grid (b,d,f,h) in Etretat for Ciara (February 2020) (a,b), Amelie (November 2019) (c,d), Deirdre (December 2018) (e,f) and Gabriel (January 2019) (g,h) storms. White arrows show the refraction of waves when approaching to coast. Extracted from López Solano et al. (2022)*

Some changes in $\theta_{Hs,peak}$ from deep water to shallow water are observed. Waves, coming from deep water, are refracted twice at the intermediate and the shallow areas, respectively. The first refraction, with an average value of 10° for the storms studied, is less pronounced than the second one, given that the second refraction reaches a mean value of 13°. This is due to the configuration of the bathymetry at the bottom of the sea (**Figure 58**). The first refraction makes all the waves turn into the SE direction, increasing this shift inside the same sector by strengthening the southern component with the second refraction.

The wave dissipation is differently manifested at Etretat beach, considered as a pocket beach, where nearshore waves are refracted close to rocky structures limiting the beach cell (**Figure 62**). Such geometry is mainly responsible for the reduction of the Hs and a regular bathymetric configuration parallel to the shoreline. Contrary to Hautot-sur-Mer, no sandbanks or bathymetric irregularities are highlighted. For this zone, changes in morphological slope are mainly observed between the center of Etretat bay and the East and West boundary areas with 1.5% and 0.3%, respectively.

This almost flat zone produces waves going unaltered over it, lacking any increasing or decreasing on the $H_{s,max}$, especially since these depths are the ones causing the shoaling process.

$\theta_{Hs,peak}$ also changes in Etretat with two different refractions in intermediate and in shallow water. The first refraction, with an average of 7°, is more pronounced than the second one, since this second one is half of it, with a mean of 3.5°.

For this location, no matter where the storms come from, during the first refraction, $\theta_{Hs,peak}$ tends towards the E-ESE sectors and, during the second, almost exclusively to the ESE sector. The presence of the Cotentin Peninsula limits the range of directions where storms can come from in Etretat, being more to the South and closer to the Peninsula with respect to Hautot-sur-Mer. Hence, the change in direction can be explained considering this fact alongside the bathymetry.

In the light of these results, the configuration of the bottom morphology has a key role in generating variability in the wave height, which is largely observed in Hautot-sur-Mer beach where the wave gradient is significant. Energy dissipation is significant while Etretat is more exposed to storms coming from the Atlantic Ocean. In Hautot-sur-Mer, further from the ocean, storms were losing strength due to bottom friction and other processes, and they arrived with a smaller wave height. The bedrock, the enclosed beach and the presence of the cliffs play an important role in the dissipation of energy and wave gradient when they approach the coast.

Considering changes in $\theta_{Hs,peak}$, refractions produced on both sites are manifestly different because of some characteristics in the morphology of the beaches. The main reason is the orientation of the shoreline with respect to the North as described above. The shoreline in Etretat presents an inclination of 47° clockwise. However, the shoreline in Hautot-sur-Mer is more oriented towards the East, with an inclination of 71°. This difference produces bigger refraction of the waves when approaching Hautot-sur-Mer, especially offshore, since waves tend to acquire the orthogonal direction to the bathymetric lines and when they are close to the coast, they have already obtained it, considering also that all the storms studied and most of the storms arriving at these coasts come from the Atlantic Ocean. These characteristics condition the range of $\theta_{Hs,peak}$. In Hautot-sur-Mer, it is in the range of 15°, and in Etretat only 8°.

4.2.5. Discussion

This work uses wave datasets and a simulation with SWAN numerical model to investigate the dynamics of waves transformation during a period of 26 months. An analysis of the evolution of these different datasets was carried out in the spectral domain investigating the frequencies of wave height and mean direction and in relation to the spatial distribution of hydrodynamics. The main focus is devoted to different storm events at two spatial scales: a regional scale, the English Channel, and a local scale close to Normandy coasts, on the sites of Etretat and Hautot-sur-Mer.

Simulated data were validated with buoy measurements employed at shallow areas (depth of 10–11 m) to corroborate that the databases generated are utilizable both in this work and for further studies. Error metrics were estimated for the significant wave height. The comparison of modeling results with the buoy measurements for each location showed that waves are accurately reproduced for the simulated period, with a good correlation coefficient of 92% and 96% for Etretat and Hautot-sur-mer, respectively.

This correlation is limited in the validation for the grid of Etretat, where the hydrodynamics and the measurements of the buoy are partly influenced by the hydrological effects of the Seine River. The measured waves, extracted from the SCENES buoy, should be modulated by marine surges and hydrological discharge. The variability of the stochastic component of water level in Seine Bay was investigated by Turki et al. (2019). They have demonstrated that its variability is induced by the combining effects of local-driven forces with meteorological, oceanographic and hydrological origins. This activity is largely observed during flooding periods.

In this work, the directional wave spectrum was investigated in the different scales mentioned, from the English Channel to the Normandy coasts, using frequency analyses. Results

exhibit that waves are modulated and change in their spectrum at shallow water areas evolving a possible energy transfer between the wave frequencies induced by their physical transformation. Regarding the wave direction, its mainly controlled by sea and swell waves at the North Sea, with a large spectral width from high to low frequencies. This width does not show significant changes in intermediate water depths in the Channel while it is deeply modified close to Etretat and Hautot-sur-Mer after the physical transformation of waves. Their refraction is similarly produced and modified for all waves coming from different directions in deep water.

The energy transfer between the frequencies of wave height was also investigated in previous works (Abroug et al., 2020). Abroug et al. have studied in the laboratory the non-linear wave–wave interactions in the littoral zone using the bispectral analysis. They demonstrated that the phase coupling increases gradually and approaches one just prior to breaking, accordingly with the spectrum broadening and the energy increase in high-frequency components. They analyzed waves downstream of breaking, however the breaking zone is the limit of the present study when waves are approaching the coast.

In contexts with strong tidal dynamics, such as the coasts of Normandy, the wave climate is generally modulated by the wave–tide interaction exhibiting changes in its spectrum; a very important process that should be considered in flood risk assessments. An example of wave–tide interaction effects on coastal hazards was outlined in the works of Lewis et al. (2019) where the risk of coastal flooding by extreme waves in the Irish Sea is investigated. They have highlighted that the tidal dynamics have a key role in the nearshore wave climate at shallow areas of around 10 m of depth and water wave heights with 20% larger in some regions, which proves to have a clear implication in coastal hazards. They have also shown that the sea-level rise influences the extreme wave height, i.e., during stormy events as the 10 events analyzed, with a 5% increase in hazardous areas.

In the present work, the evolutions of wave height and direction during each storm were considered to study the different characteristics of coastal extreme events. The characteristics highlighted were defined from a 26-month period of waves, which is useful and distinctive enough for an overview of the storm events in the English Channel, and particularly on the Normandy coasts, but not fully representative of the different hydro-dynamic conditions of the zone. In a longer period, more variations will show up and provide other information to be able to identify some additional patterns in the behavior of extreme events.

For the 10 storms identified, the distribution and the persistence of the high values in the time series of wave height and mean direction were investigated. A joint analysis of the frequencies of

occurrence of the maxima, alongside the maximum values themselves and the deviation from the mean, allowed us to appreciate the possible risk associated with the different storms. A combination of a high peak in wave height that is persistent in time implies a greater impact on the coast, as happened during the storm Deirdre. In the same way, Ciara showed a low occurrence of its maximum values, but it was explained because of an elevated deviation, producing a hazardous scenario too.

Other parameters could have been highlighted and deeply analyzed such as the duration (Martzikos et al., 2018) of the event and also the associated extreme surges (Bertin et al., 2014; Turki et al., 2020a).

Martzikos et al. (2018) defined a storm in a different way to the present study, as the event exceeding a minimum significant wave height with a certain minimum duration. They have considered that the thresholds for the wave height, the duration and the calm period between two successive storms vary depending on the area of interest. Applying their definition to the period of time studied in this work in the English Channel, a similar number of storms can be identified. Their classification was achieved with cluster analysis based on the storm energy and the storm period and validated via appropriate indices related to their impacts on the coastal area.

Then, Turki et al. (2020a) used the extreme surges in the English Channel and along the Normandy coasts to identify the historical storms, their impacts and their physical relationship with the large climate oscillations.

In this context, and in a nearby area, the West coast of France, Bertin et al. (2014) investigated the storm-induced coastal flooding associated with Xynthia that severely damaged the central part of the Bay of Biscay in February 2010 using a numerical approach of a 2DH fully coupled modeling applied to the North-East Atlantic Ocean. They demonstrated the impact of Xynthia on coastal areas with anthropogenic activities, including a simulation increasing the height of the dikes and barriers in the study area responsible for disabling floods.

After an analysis of the evolution and transformation of waves from the English Channel to the Normandy coasts, a numerical simulation with SWAN allowed for obtaining a database nearshore to complete the study. Wave height gradients and wave direction refraction are clearly observed when the storms analyzed reach their maximum, modified by the sea bottom morphology and by the characteristic geometry of Normandy coasts, defined in this area by the presence of cliffs that enclose beaches along the shore.

The numerical approach used in the research is based on the structured version of SWAN, but it is also possible to use the unstructured grids for studies of wave propagations. In this case, we used structured grids, which implies the use of nested grids for obtaining a higher resolution in coastal areas. When using unstructured grids, mainly built on triangles, this becomes unnecessary, because the triangles, or any other kind of polygon used, are decreasing in size when approaching the coast so that they can provide a higher resolution and adapt to land boundaries. The use of coarse and nested grids in this study was the alternative chosen due to the available bathymetry data, with a low density of information outside of the study areas and really dense bathymetry data obtained from LiDAR campaigns nearshore. The ratio when reducing the scale is linked to this increase in information on the available data, being appropriate for this study. Using an unstructured grid requires a higher computational cost, and propagating hour by hour during 26 months would have demanded a too long time.

As an example of this alternative, Guillou & Chapalain (2015) have implemented an unstructured version of SWAN in the Sea of Iroise to assess the wave energy resource along coastal zones for an eight-year period (2004–2011). They have used numerical modeling to estimate the variability of wave power production conducted over the European shelf seas significant inter-seasonal and inter-annual evolutions of the resource in the Sea of Iroise.

4.2.6. Conclusions

The analysis of the directional wave spectrum in the different scales defined provides information on the behavior of waves in relation to their frequencies when they are propagated inside the English Channel and when they approach Normandy coasts. There is a modulation in the significant wave height spectrum resulting from wind sea and swell waves, related to an energy transfer between the wave frequencies induced by their physical transformation at shallow water areas. The variation in the mean direction spectrum is mainly explained by the wave refraction induced by changes in the sea bottom within the English Channel.

Considering the 10 storms analyzed, which are representative of the 26-month period simulated, in the scale of the Channel, the hazard is increased by a confluence of an elevated maximum wave height with a lasting persistence of high values in time, as was confirmed with the Deirdre or Ciara storms. On the scale of Normandy coasts, wave height is reduced by more than 50%. Both of the sites studied, Etretat and Hautot-sur-Mer, present beaches enclosed by cliffs, typical of the Normandy region. The wave height gradient is remarkably influenced by changes in the morphology of the sea bottom and the coastal geometry, also forcing refraction of waves that

cannot occur as quickly as necessary in these locations to impact perpendicularly to the shoreline, this way avoiding the worst scenario.

The implementation of a structured version of SWAN gives promising results for the quantification of the nearshore wave contribution in coastal flooding. However, this approach is not enough to fully resolve the physical processes close to the shoreline in response to storms, the case of the long-crested waves and their influence on the marine submersion, although that was not the aim of this research. Different models can deal with these limitations and provide more information from the breaking zone to the coast. Future work will be focused on the hydrodynamics at regional and local scales of the English Channel and the Normandy coasts by considering the interaction between waves and sea level, constituted by tide and surges. Resolving the infragravity waves and their impacts on the overwash at the shoreline and the overtopping close to maritime structures requires the use of new probabilistic and empirical approaches to avoid the overestimated coastal safety obtained using the statistical and numerical methods in current practice.

This finding is a first step to deeply understanding the modification of energy within the English Channel basin from deep water till nearshore using a phase-averaging model. It is also considered a key phase for coastal management strategies as well as engineering topics relying on one-way nesting. The impact close to the shoreline and over maritime structures, including the impact of infragravity waves, will be carried out by coupling these results, using high-computational phase-resolving models.

4.3. CONCLUSIONS OF THE CHAPTER

This chapter answers the second scientific questions presented in Chapter 2, which are:

- *How can we characterize the hydrodynamic evolution of storms from the English Channel towards the Normandy coasts during the last 40 years, and to what extent can numerical modelling accurately reproduce the extreme event hydrodynamics?*
- *What are the main physical transformations of extreme energy scenarios within the basin and close to the coast?*
- *How is the severity of extreme storms (magnitude, duration) controlling the evolution of storms within the Channel?*

By modeling 40 years of data in the English Channel, we are able to find the main characteristics of extreme events arriving to the basin. The Atlantic Ocean as the principal origin

node is the main finding. The direction of origin conditions the behavior of the storms when they propagate inside the Channel more than any other variable. This variable, alongside duration and wave height, were examined and tracked along the English Channel, revealing modulation when they approached the Normandy coasts. This modulation was especially pronounced when the storms are originated with a Southern or Northern component in their directions. There is also a modulation in the significant wave height spectrum resulting from wind sea and swell waves, related to an energy transfer between the wave frequencies induced by their physical transformation at shallow water areas. Nearshore, the hazard is increased by a confluence of an elevated maximum wave height with a lasting persistence of high values in time. The wave height gradient is remarkably influenced by changes in the morphology of the sea bottom and the coastal geometry on the Normandy coasts, taking into account the situation of Etretat as an enclosed beach and Hautot-sur-Mer as a mixed gravel-sand beach.

CHAPTER 5

ASSESSING THE IMPACTS OF EXTREME STORMS ON THE COASTS OF NORMANDY

Storms, from the English Channel to Normandy coasts, suffer from a series of modulations including the physical processes of wave transformation and bottom friction, and induce flooding on the coast. Normandy beaches exhibit diverse morphological contexts from sandy to mixed and gravel/pebble beaches, which control the response of the beach to the hydrodynamics drivers and the water extension during flooding, including wave run-up. In this chapter, wave run-up height during four extreme events at three Normandy sites is analyzed, simulating the storms with the SWASH numerical model and validating the results with video monitoring systems (VMS). The chapter highlights the complex calculation of flooding and its validation for gravel and pebble beaches where the internal characteristics of permeability and porosity, as well as beach slopes, are changing during the storms.

The main results of this chapter are subject of a new publication submitted to the journal Results in Engineering in August 2024: C. López Solano, E. I. Turki, Á. D. Gutiérrez Barceló, et al., An integrative approach of numerical modelling for assessing coastal flooding driven by extreme storms: case of Normandy.

5.1. INTRODUCTION

In coastal areas, storms reaching the shore from the ocean can be characterized, among other possibilities, by their wave height. This wave height is modified from the nearshore to the coastline, amplified due to processes such as shoaling, a result of interaction with the seabed, but also dissipated due to energy loss caused by bottom friction or wave breaking. If, as will likely happen (IPCC, 2022), sea level rises, this energy reduction could decrease over time unless coastal morphology adapts accordingly (Wolf & Woolf, 2006). Wave transformation is more significant in semi-enclosed environments such as bays, where water depth varies spatially, and land contours modify wave characteristics. Understanding this transformation and its impact on coastal systems is crucial to prevent risks such as flooding.

Coastal flooding, caused by complex atmospheric and oceanographic dynamics interacting with coastal topography, is expected to increase in frequency and severity due to rising sea levels and storm intensity. The English Channel exemplifies this phenomenon, especially when waves approach Normandy coasts. Previous studies in the English Channel have mainly focused on the dynamics of energetic storms and their coastal effects, including flooding and beach erosion. Bennis et al. (2022) demonstrated the relationship between the flooding effects of storm Eleanor in January 2018 and wave-current angles using a 3D model. The morphodynamic impacts of storms on changes in the coastline have also been extensively studied (Anthony, 2013; Soloy et al., 2020, 2021). Soloy et al. (2022) analyzed storm clustering along Normandy coasts, using numerical models and remote sensing to comprehensively understand storm events.

Normandy coasts, especially north of the Seine Estuary, have the main characteristic of being gravel and pebble beaches, providing significant natural protection against sediment loss and contributing to energy dissipation during extreme wave storms (Almeida et al., 2015; Buscombe & Masselink, 2009). The morphodynamic evolution of these beaches is complex due to variable distribution of grain sizes, influenced by energetic swash movements generated by breaking waves, and their reflective beach faces, which increases the risks of flooding and erosion. Numerous studies over decades have aimed to understand and predict the behavior of these coastal systems under extreme hydrodynamic conditions. However, these approaches often overlook characteristics such as sediment grain size, permeability, or porosity, crucial aspects for understanding swash dynamics. Research on gravel beach morphodynamics usually relies on field observations, numerical modeling, and physical experiments. These studies collectively contribute to understanding the intricate dynamics of coarse-grained coastal systems. Although numerical wave models effectively simulate nearshore hydrodynamics, their computational cost limits widespread use. Hybrid models, integrating statistical methods, measurement

technologies, and numerical models, offer a more resource-efficient alternative (Ricondo et al., 2024).

This study focuses on the analysis of the wave run-up height that can cause flooding from four extreme events at three sites located on the Normandy coasts, where observations on hydro-morphodynamics are constantly collected by video monitoring systems (VMS). Remote sensing methods such as coastal video imaging have proven to be effective solutions in monitoring temporal beach changes during extreme storm events (Rodríguez-Padilla et al., 2019; Arriaga et al., 2022). Additionally, accurate prediction of wave run-up height is essential for designing coastal protection works, beach nourishment projects, and planning coastal management schemes. Coastal engineers typically estimate run-up using empirical formulations based on offshore wave parameters and beach slope, but recently, coastal VMS have facilitated long-term measurements of wave run-up, with studies by Stockdon et al. (2006) providing extensive analyses.

Generating wave run-up measurements from images obtained from VMS can be challenging due to the need for manual supervision, leading to increased processing times. The study by Vousdoukas et al. (2012) presents a semi-automatic procedure for generating wave run-up data from image timestacks, applied to images from a reflective beach on the Portuguese coast.

For the three Norman study sites of this project, Villers-sur-Mer, Etretat and Hautot-sur-Mer, a combination of these methodologies has been applied, especially focusing on the use of numerical model SWASH, developed for the interaction of nearshore hydrodynamics with coastal morphologies, including reflective and porous beaches as the ones selected. The run-up over some selected representative profiles is calculated, validating the results with those obtained from statistical methods and measurements from VMS. Finally, the analysis of the results is carried out, contrasting the characteristics of the different extreme events numerically simulated and the morphologies of the three study sites. Section 2 describes the methodology with the description of the study sites and Section 3 the validation, Sections 4 and 5, the analysis of the results, and Section 6 the discussion and conclusions of the study.

5.2. METHODOLOGY

This section describes the numerical modelling of the three study sites with the different forcings and the set-up of the model.

The dataset used for the simulations as forcing of the numerical model is the output of the database generated and described in Section 4.1.

5.2.1. Description of the model

The simulations of stormy waves arriving to the coast have been carried out using the numerical model SWASH (an acronym of Simulating WAves till SHore), developed at Delft University of Technology. SWASH is a non-hydrostatic wave-flow model, intended to be used for predicting transformation of dispersive surface waves from offshore to the beach for studying the surf zone and swash zone dynamics, wave propagation and agitation in ports and harbors (Zijlema et al., 2011).

The governing equations are the Non-Linear Shallow Water (NLSW) equations including non-hydrostatic pressure correction term. Not being a Boussinesq-type wave model, SWASH can be run in depth-averaged mode or multi-layered mode in which the computational domain is divided into a fixed number of vertical terrain-following layers. SWASH improves its frequency dispersion by increasing this number of layers rather than increasing the order of derivatives of the dependent variables like Boussinesq-type wave models do. SWASH is close in spirit to SWAN model used in Section 4.2 with respect to the pragmatism employed in the development of the code in the sense that comprises are sometimes necessary for reasons of efficiency and robustness.

SWASH accounts for the following physical phenomena: (a) wave propagation, frequency dispersion, shoaling, refraction and refraction, (b) nonlinear wave-wave interactions, (c) depth-limited wave growth by wind, (d) wave breaking, (e) wave runup and rundown, (f) moving shoreline, (g) bottom friction, (h) partial reflection and transmission, (i) wave-current interaction, (j) wave-induced currents, and (k) tidal waves among others.

SWASH can provide the following output quantities (among others): surface elevation, discharges, significant wave height, wave-induced setup, maximum horizontal runup or inundation depth or vertical runup height, as desired for the present study.

5.2.2. Forcings and set-ups of the model

The boundary conditions of the model are defined by the wave spectrum aggregated parameters and the water level. The outputs of the numerical simulation of Section 4.1 are taken as inputs for the simulations using SWASH. Firstly, some storms have been selected from the time series of significant wave height in the 3 study sites following the criteria of simulating storm Ciara as the strongest event that took place over the past few years, and then the 3 storms selected as an example because of their inner characteristics in Section 4.1.4.2, making the 4 extreme events simulated out of it.

Considering the limitation in the outputs of the numerical modeling in the English Channel that can only provide reliable information on waves every 3 hours due to the limitation at the same time in the forcing used, the simulations of SWASH have been divided in 3-hour periods throughout the storms. With the aim of keeping a comparable time between storms and study sites, every event is simulated during 3 days, which produces 25 simulations per storm and location. Wave parameters used to force the model are significant wave height (H_s) and peak period (T_p), alongside the water level. Since SWASH can only be forced with either variable waves and constant sea level or the opposite, and resolution in time of wave parameters of very sea state cannot be reduced, a constant water level had to be set for each 3-hour simulation. As the main objective of this study is analyzing the differences in run-up between the different storms and locations, the water level chosen for each simulation has been then maximum registered over every 3-hour period in order to obtain the worst scenario of every sea state.

Before simulating all the 4 storms in the 3 study sites, a correction to the output of water level is applied, since it is expected that, due to the resolution of the computational grid of the English Channel when the cells are located nearshore, the results do not have the total amplitude in the tidal waves as reflected in Section 4.1.4.1. For doing this, the records of sea level of the buoy SCENES located in the Seine estuary (49° 28.844' N–0° 1.932' E) are used, because of the location in a central part of the study area between Villers-sur-Mer and Etretat, being representative of the tidal conditions of the study sites.

The buoy has measurements from October 2017 to October 2020, only including storm Ciara, so the full time series has been used to correct the equivalent time series in the 3 study sites. The calibration method consists in applying an amplification factor for the values different from 0 of the tidal ranges of every tidal cycle of the time series output of the model so that the amplitude of the tidal range of each cycle matches the measurements of the buoy. Out of the dates of the records, the amplification factor is applied according to the similarity of the tidal range of each

tidal cycle to the tidal ranges of the data already calibrated. Then, these factors obtained for every value of every tidal cycle during the 3 days of simulation are extrapolated to the 3 study sites for each of the 4 storms, obtaining the corresponding water levels. As an example, in **Figure 64** the correction applied to Ciara storm in Villers-sur-Mer is shown, with the original output of the coarse model and the time series of water level from which the maximum every 3 hours is obtained to force the simulation with SWASH.

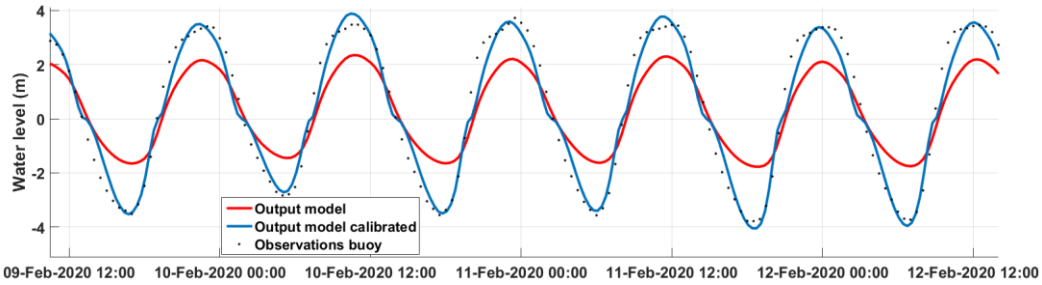

Figure 64. *Time series of water level with the output of the English Channel model in Villers-sur-Mer during the 3 days of simulation of Ciara storm and time series of water level corrected according to the corrections in amplitude obtained from SCENES buoy*

Then, for the 3 sites, different profiles along the beach are selected as representative of the different conditions and morphologies of each location. The simulations are repeated for every profile of every study site and, as output, the surface elevation of water is obtained to calculate the run-up height.

According to the EurOtop manual (EurOtop, 2018), the wave run-up height is represented by $R_{u2\%}$, which is the wave run-up level, measured vertically from the still water line, which is exceeded by 2% of the individual incident waves. From this calculation, a run-up time series associated to the number of incoming waves is obtained for all the waves within a 3-hour sea state, giving a value of $R_{u2\%}$ for every sea state of every profile for all the storms and study sites.

Villers-sur-Mer is a sandy beach, while Hautot-sur-Mer and Etretat are mixed and gravel beaches, respectively. For this reason and considering the grain size of the pebbles of both locations, a porosity parameter has to be introduced in the model. The pebbles in Hautot-sur-Mer present a d_{50} = 7.1 cm, and in Etretat, a d_{50} = 5.2 cm. According to Wu & Wang (2006) the initial porosity of sediment deposit p'_m can be calculated from Eq. 21.

$$\mathrm{p}'_m = 0.13 + \frac{0.21}{(d_{50} + 0.002)^{0.21}} \tag{21}$$

where d_{50} is in millimeters.

Applying the formulation to the pebbles at both sites, the porosity obtained is 0.216 and 0.222 for Hautot-sur-Mer and Etretat, respectively. For introducing in the set-up of SWASH the presence of pebbles, a porous structure equivalent to a breakwater must be defined. The height of this structure is measured from the sandy layer in both locations, and the separation between these layers can be identified following the inflexion point of the slope, smoother for sand and steeper for gravels. For the structure layer, the grain size and the porosity are set. The sand below this sediment and the complete sandy beach in Villers-sur-Mer are considered impermeable layers, defined in the model as the bottom layer from which the depth is measured.

To illustrate the different profiles used in the simulations, each location is explained independently with the particular set-ups and configurations in the next sections (**Figure 66**, **Figure 68** and **Figure 70**).

5.2.2.1. Villers-sur-Mer

The bathymetry used in the numerical model is extracted from a high-resolution LiDAR campaign carried out in October 2019 (**Figure 65**) with an extension of 9000 x 7000 m and interpolated in the working domain. The obtained DEM allows defining the profiles selected for the simulations, equally spaced along the beach separated 200 meters each avoiding being placed over the groins located in some parts of the coast of Villers-sur-Mer. The 7 chosen profiles are named P7, P9, P11, P13, P15, P17 and P19 from East to West (**Figure 65**).

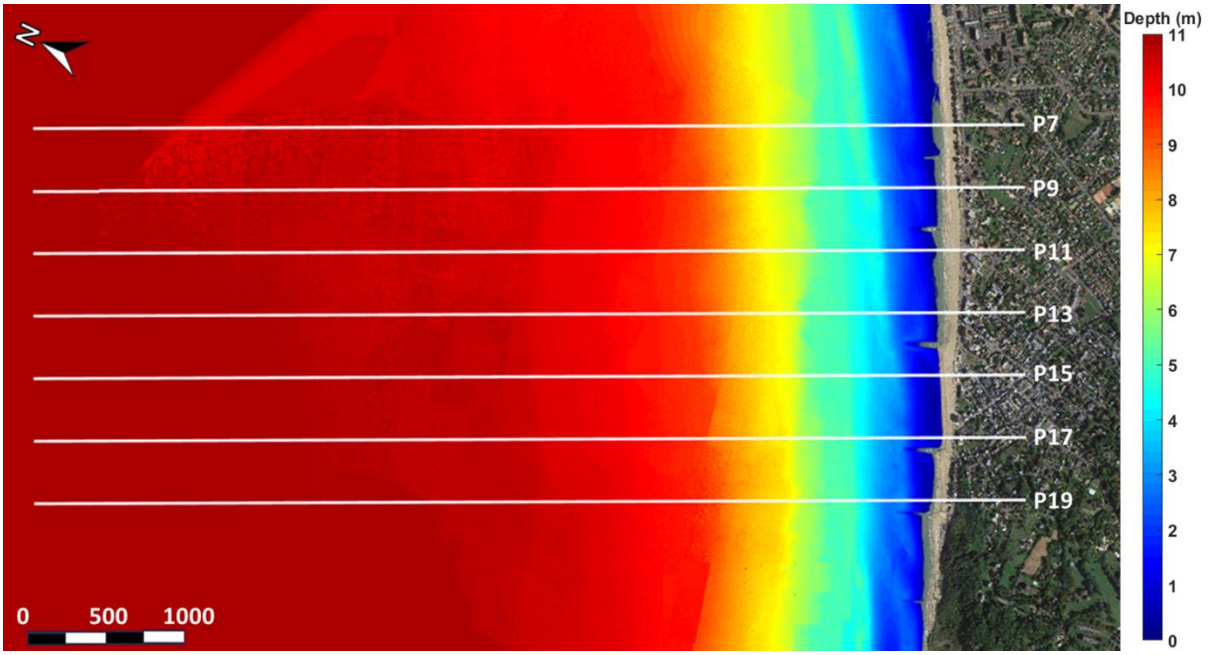

Figure 65. *Bathymetry from the LiDAR campaign used for the set-up of the numerical model, and profiles selected for the simulations in Villers-sur-Mer*

The total length of the simulated profiles is 3000 meters, limited to 1000 meters for the set-up of the model in order to have similar lengths in the three locations. It has to be considered that beyond those 1000 meters the depth is barely augmented seawards even by taking longer profiles. At the same time, extending the profiles would increase proportionally the computational cost. These 1000 m profiles are artificially extended 200 m in the deeper boundary to produce a "conditioning area" with a flat bottom that facilitates the simulation of waves at the beginning of the computational domain to stabilize the propagation before the interaction with the real profile.

This way, the 7 profiles have an extension of 1200 m. The computational grid is defined over this length with 1200 cells of 1 m width, and for each node between cells the bathymetry is set (the depth profiles are shown in **Figure 66**). The vertical domain is divided in 10 vertical sigma layers, equally distributed with a 10% of the depth of water following the bottom layer from the open boundary on the seaside to the coast side. A sponge layer of 50 m is also set on the shore side of the computational grid to absorb the flux of water propagating in the model when simulating the surface of water.

For the 7 profiles, the 25 simulations corresponding to each 3-hour sea state of each of the 4 storms are defined by the significant wave height (H_s), peak period (T_p) and the water level (WL). In **Table 22** the variables and dates (UTC) of the 4 storms used for the simulations are shown.

5.2.2.2. Hautot-sur-Mer

The bathymetry used for Hautot-sur-Mer in the numerical model is also extracted from a high-resolution LiDAR campaign carried out in January 2019 (**Figure 67**). The extension is 6000 x 6000 m and is also interpolated in the working domain. The profiles for the simulations, defined from the DEM obtained, are selected following the criteria for taking one profile between each pair of groins in the central part of the beach in front of the population and two more profiles on the sides of the beach. The profiles are named PA, PB, PC, PD, PE and PF from East to West for the 6 profiles between groins and P5 and P18 for the 2 profiles on Eastern and Western sides (**Figure 67**).

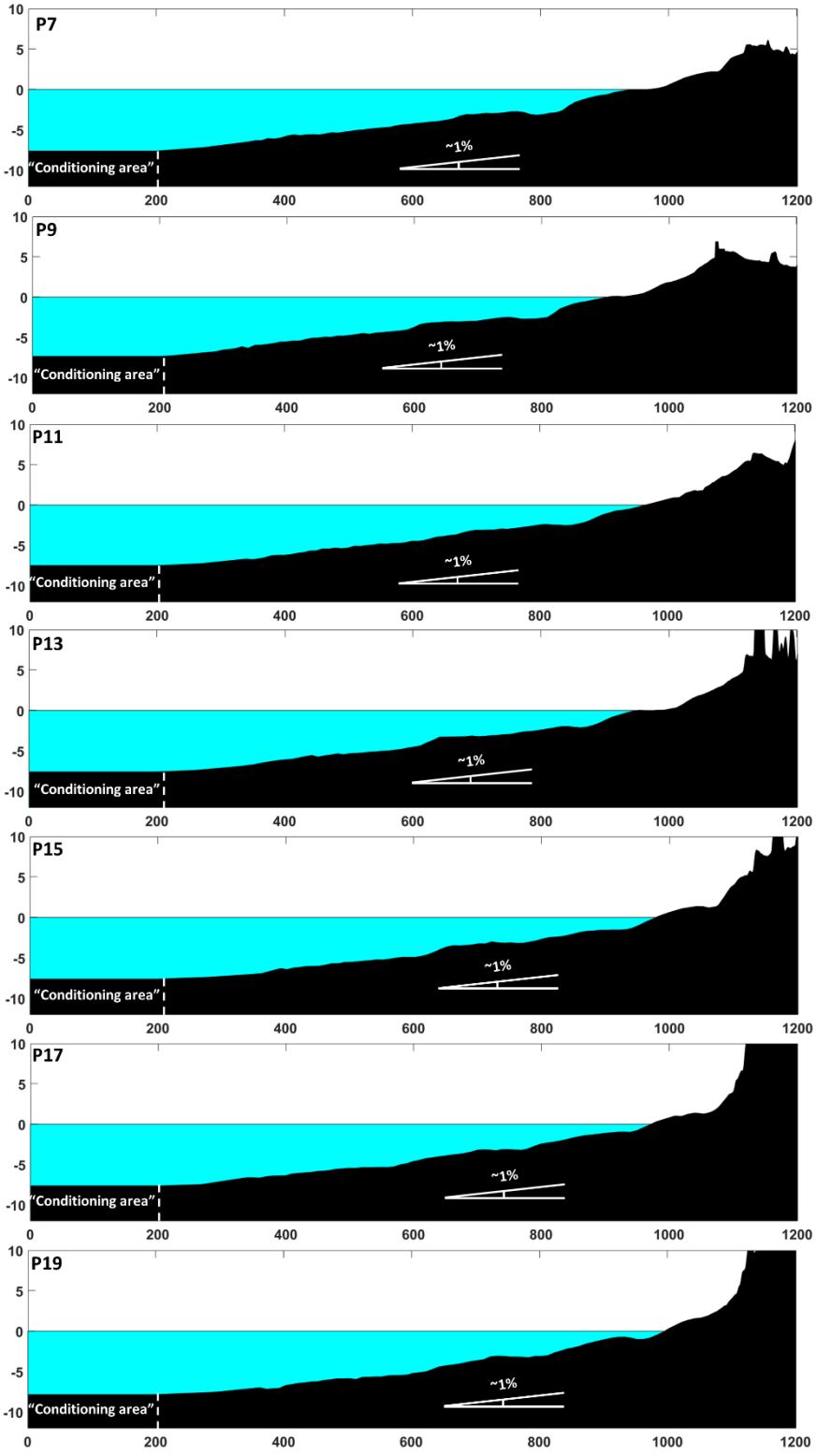

Figure 66. *Geometry of the 7 profiles used for the simulations in Villers-sur-Mer relative to the MSL*

Storm Ciara (09/02/2020 12h – 12/02/2020 12h)			Storm Joachim (12/12/2011 21h – 15/12/2011 21h)			Storm Andrea (03/01/2012 06h – 06/01/2012 06h)			"Storm 19" (28/01/2013 18h – 31/01/2013 18h)		
H_s (m)	T_p (s)	WL (m)	H_s (m)	T_p (s)	WL (m)	H_s (m)	T_p (s)	WL (m)	H_s (m)	T_p (s)	WL (m)
0.91	3.48	2.999	0.64	2.71	2.490	0.73	3.08	1.678	0.64	2.71	-0.562
0.94	3.48	-0.273	0.67	3.08	2.641	0.98	3.48	0.142	0.77	3.48	0.358
1.17	3.95	0.221	0.84	3.48	0.581	1.16	3.95	-0.077	0.77	3.95	2.938
1.54	5.07	3.497	0.84	3.48	-0.708	1.25	4.47	1.788	0.70	3.48	2.692
1.57	5.74	3.416	1.04	5.74	2.932	1.07	5.74	1.920	0.69	3.48	-0.24
1.93	6.50	0.000	1.15	5.74	3.257	1.00	5.74	0.635	0.69	4.47	0.311
1.75	6.50	0.074	1.09	5.74	1.275	1.11	6.50	-0.692	0.67	4.47	3.230
1.50	6.50	3.88	1.01	6.50	-1.927	1.15	6.50	1.378	0.67	4.47	3.097
1.26	6.50	3.858	0.94	5.74	2.174	1.02	5.74	1.835	0.69	3.08	-0.048
1.45	5.74	0.165	0.79	5.74	2.848	0.88	5.74	1.207	0.74	3.95	-0.045
1.51	6.50	-0.825	0.66	5.74	1.349	0.82	5.74	-0.907	0.81	3.48	3.013
1.55	6.50	3.402	0.62	5.74	-1.705	0.81	5.74	0.855	0.85	3.48	2.985
1.51	6.50	3.589	0.72	5.07	2.068	0.90	5.07	1.782	0.80	3.48	0.003
1.45	6.50	0.688	0.71	5.07	3.014	1.36	5.74	1.392	0.68	5.07	-0.107
1.34	6.50	-1.308	0.71	5.07	1.957	1.55	6.50	-0.527	0.67	4.47	3.208
1.29	6.50	3.383	0.67	5.07	-1.356	1.69	6.50	0.759	0.78	4.47	3.245
1.22	5.74	3.767	0.69	5.07	1.170	1.81	6.50	2.298	0.79	5.07	0.194
1.16	5.74	1.450	0.68	4.47	2.686	2.08	6.50	2.152	0.76	5.07	-1.222
1.01	6.50	-2.418	0.75	4.47	1.949	2.13	7.37	-0.036	0.67	5.07	2.749
0.98	5.74	2.492	1.11	5.07	-0.816	1.93	7.37	0.108	0.60	5.07	2.946
0.90	5.74	3.382	1.14	5.74	1.224	1.50	7.37	2.117	0.62	5.07	0.448
0.84	5.74	1.825	1.10	5.74	3.070	1.21	6.50	2.062	0.69	3.95	-1.460
0.79	5.74	-1.897	1.02	6.50	2.658	1.05	5.74	-0.002	0.76	3.95	2.766
0.78	5.74	2.301	0.86	6.50	-0.406	0.96	5.74	-0.068	0.73	4.47	3.133
0.71	5.74	3.555	0.76	5.74	0.127	0.88	5.74	2.250	0.69	5.07	1.089

Table 22. *Forcings of significant wave height (Hs), peak period (Tp) and water level (WL) for the set-up of the numerical model of every 3-hour sea state of the 4 storms in Villers-sur-Mer*

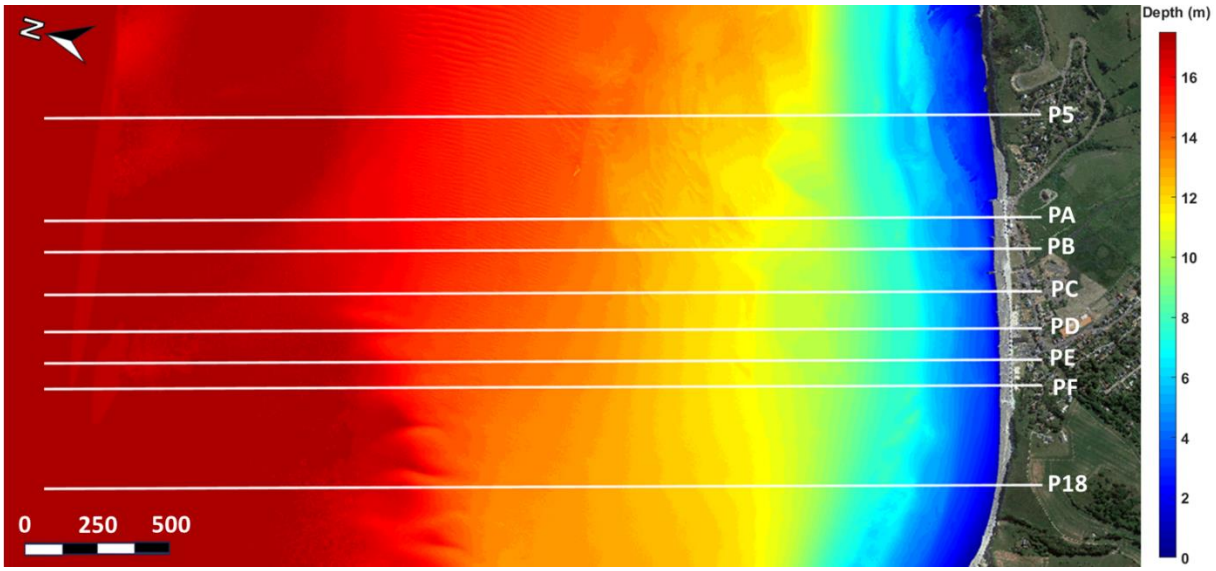

Figure 67. *Bathymetry from the LiDAR campaign used for the set-up of the numerical model, and profiles selected for the simulations in Hautot-sur-Mer*

The total length of the profiles is, as in Villers-sur-Mer, 3000 meters, limited to 1000 meters for the set-up of the model too. These 1000 m profiles are artificially extended 200 m in the deeper boundary to produce the same conditioning area with a flat bottom before the real profile.

The 8 profiles have an extension of 1200 m, with a computational grid defined by 1200 cells of 1 m width, and the bathymetry set for each node between cells (the depth profiles are shown in **Figure 68**). The vertical domain is divided in 20 vertical sigma layers, equally distributed with a 5% of the depth of water following t,he bottom layer. More vertical layers are considered for this location because of the inclusion of porosity in the modeling. In the case of Hautot-sur-Mer, an extra layer containing a porous structure equivalent to the pebbles is defined as explained before. The structure layer starts at the inflexion point where the slope changes on each profile and finishes where the beach ends, with the presence of a vertical wall on the profiles in front of the populated area and the cliffs on the other profiles, where the bottom layer defines the profile again. To specify the structure layer, three input grids are set: a structure height grid with the height of this layer measured from the bottom layer (set as 0 in the parts of the profile where there is sand or after the vertical wall), a grain size grid with the size of pebbles set for this part of the profile (d_{50} = 7.1 cm), and a porosity layer also set for this part of the profile (p = 0.2). A sponge layer of 50 m is also set on the beach side of the computational grid to absorb the flux of water propagating in the model when simulating the surface of water.

For the 8 profiles, the 25 simulations corresponding to each 3-hour sea state of each of the 4 storms are defined by the significant wave height (H_s), peak period (T_p)and the water level (WL). In **Table 23** the variables and dates of the 4 storms used for the simulations are shown.

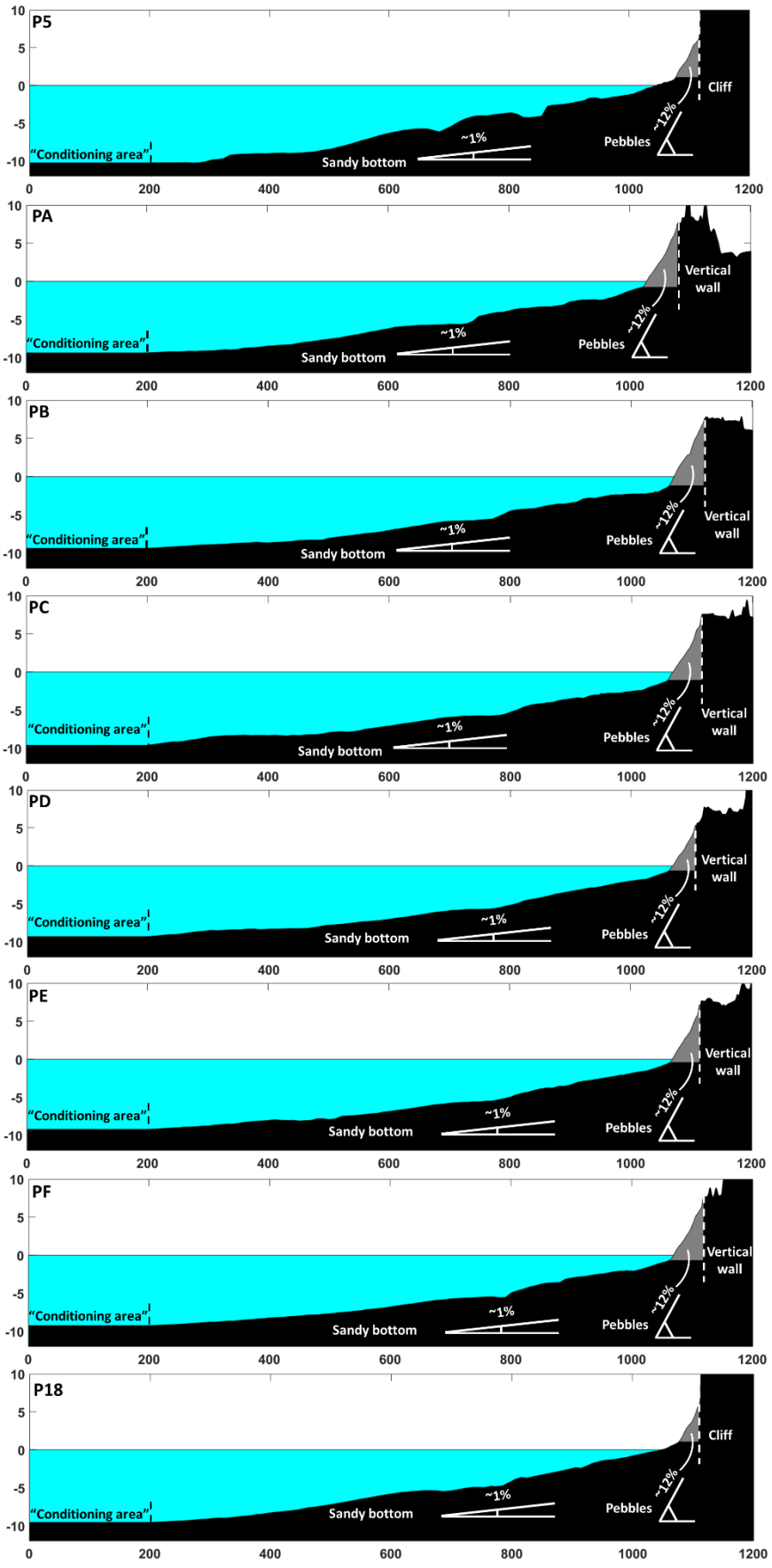

Figure 68. *Geometry of the 8 profiles used for the simulations in Hautot-sur-Mer relative to the MSL*

Storm Ciara (09/02/2020 09h – 12/02/2020 09h)			Storm Joachim (12/12/2011 21h – 15/12/2011 21h)			Storm Andrea (03/01/2012 06h – 06/01/2012 06h)			"Storm 19" (28/01/2013 18h – 31/01/2013 18h)		
H_s (m)	T_p (s)	WL (m)	H_s (m)	T_p (s)	WL (m)	H_s (m)	T_p (s)	WL (m)	H_s (m)	T_p (s)	WL (m)
0.99	3.08	3.316	0.86	2.71	1.534	1.03	6.50	2.125	0.88	5.74	-1.057
1.28	7.37	3.583	0.87	2.71	3.162	1.48	7.37	0.587	1.09	7.37	0.999
1.51	8.35	0.236	1.33	6.50	1.712	1.73	9.46	-0.494	1.19	7.37	3.300
1.87	9.46	-0.186	1.43	8.35	-1.007	1.86	9.46	1.338	1.11	7.37	2.550
2.30	9.46	3.080	1.59	8.35	1.759	1.63	7.37	2.156	1.04	7.37	-0.646
2.24	8.35	3.725	1.63	7.37	3.443	1.45	7.37	1.284	1.02	6.50	0.867
2.8	9.46	0.842	1.56	7.37	2.405	1.45	7.37	-0.680	1.03	6.50	3.403
2.43	9.46	-0.384	1.44	8.35	-0.686	1.45	7.37	0.754	1.04	6.50	2.96
2.24	8.35	3.004	1.30	8.35	0.939	1.35	6.50	2.201	1.01	6.50	-0.343
1.80	8.35	4.014	1.18	7.37	3.145	1.22	5.74	1.803	1.04	7.37	0.310
2.01	8.35	1.418	1.03	7.37	2.467	1.12	5.74	-0.299	1.11	7.37	3.343
2.08	8.35	-1.688	0.93	7.37	-0.593	1.08	5.74	0.192	1.26	7.37	3.170
2.15	8.35	2.179	0.93	5.74	0.654	1.38	6.50	2.141	1.24	8.35	-0.117
2.17	8.35	3.857	1.03	5.74	3.203	2.00	7.37	2.061	1.07	7.37	0.174
2.13	8.35	2.051	1.04	6.50	2.849	2.27	8.35	-0.041	1.03	6.50	3.395
1.91	8.35	-1.202	1.02	6.50	-0.266	2.44	8.35	0.083	1.12	5.74	3.345
1.64	8.35	1.834	0.94	6.50	0.093	2.65	9.46	2.520	1.11	6.50	-0.016
1.62	7.37	3.906	1.00	6.50	3.019	2.78	8.35	2.608	1.01	6.50	-0.011
1.59	7.37	2.683	1.09	7.37	2.962	2.59	8.35	0.189	0.96	6.50	3.040
1.43	7.37	-0.829	1.54	8.35	-0.062	2.33	8.35	-0.062	0.92	5.74	3.236
1.27	6.50	0.958	1.54	8.35	0.078	1.77	7.37	1.991	0.85	5.74	0.004
1.24	6.50	3.668	1.48	7.37	3.139	1.50	5.74	2.447	0.93	5.74	-0.063
1.20	6.50	3.004	1.41	7.37	3.195	1.37	5.74	0.257	1.12	6.50	2.944
1.08	6.50	-0.531	1.19	7.37	0.015	1.22	5.74	-0.589	1.11	6.50	3.313
1.00	5.74	0.565	1.03	6.50	-0.162	1.07	5.07	1.693	0.98	6.50	0.187

Table 23. *Forcings of significant wave height (Hs), peak period (Tp) and water level (WL) for the set-up of the numerical model of every 3-hour sea state of the 4 storms in Hautot-sur-Mer*

5.2.2.3. Etretat

Finally, in Etretat the bathymetry is also extracted from a high-resolution LiDAR campaign carried out in August 2019 (**Figure 69**) with an extension of 6000 x 4000 m and interpolated in the working domain. The profiles selected for the simulations, obtained from the DEM, are also equally spaced along the shore separated 200 meters each avoiding being placed over the groins located in some parts of the beach. The 5 chosen profiles are named P2, P4, P6, P8, and P10 from East to West (**Figure 69**), with P6 and P8 in front of the populated area.

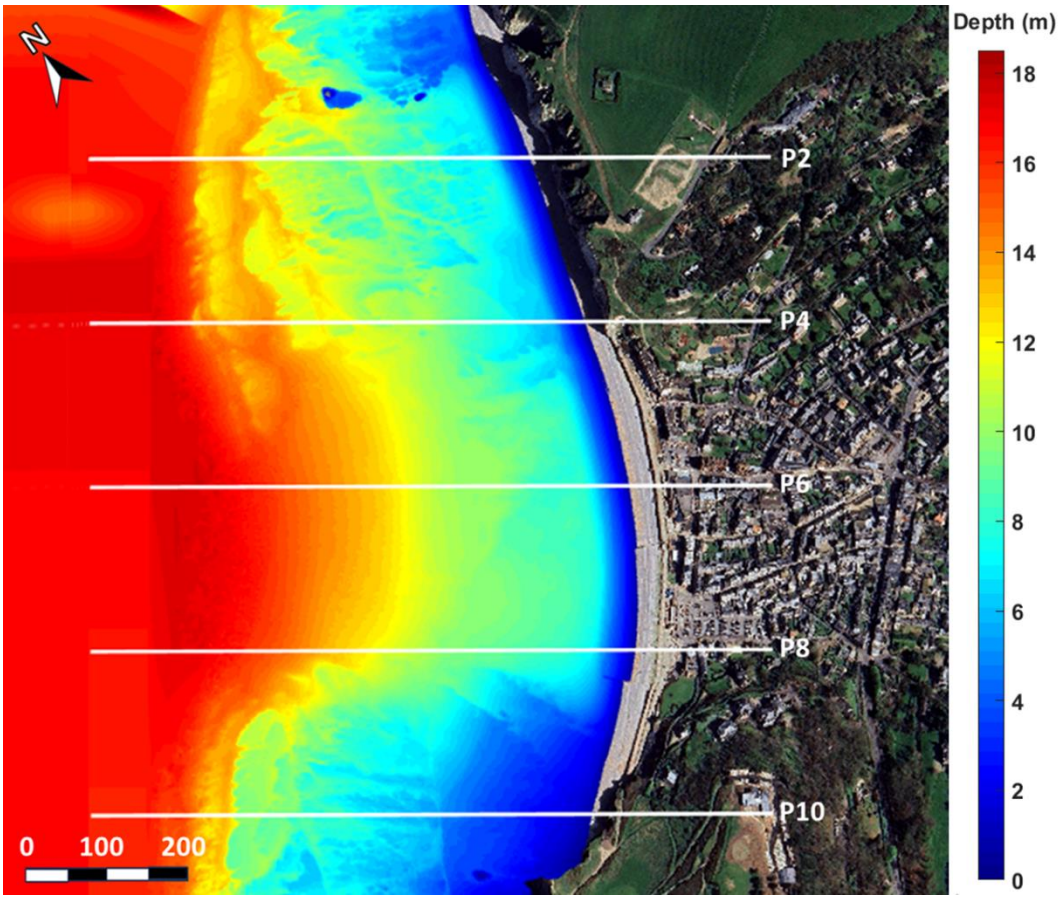

Figure 69. *Bathymetry from the LiDAR campaign used for the set-up of the numerical model, and profiles selected for the simulations in Etretat*

The total length of the profiles is just 750 meters in Etretat because of the limits of the LiDAR due to the steep slope of the bathymetry. These 750 m profiles are artificially extended 250 m in the deeper boundary to produce the same "conditioning area" with a flat bottom before the real profile.

The 5 profiles have a computational grid defined by 1000 cells of 1 m width, and the bathymetry set for each node between cells (the depth profiles are shown in **Figure 70**). The vertical domain is divided in 20 vertical sigma layers, equally distributed with a 5% of the depth of water following the bottom layer. As in Hautot-sur-Mer, more vertical layers are also required for the accurate simulation of a porous model. In the case of Etretat there is also an extra layer representing the pebbles as a porous structure with the three input grids that must be set: a structure height grid with the height of this layer (between the inflexion point and the vertical wall in P6 and P8 or the cliffs in P2, P4 and P10), a grain size grid with the size of pebbles set for this part of the profile (d_{50} = 5.2 cm), and a porosity layer also set for this part of the profile (p = 0.2). A sponge layer of 50 m is also set on the shore side of the computational grid.

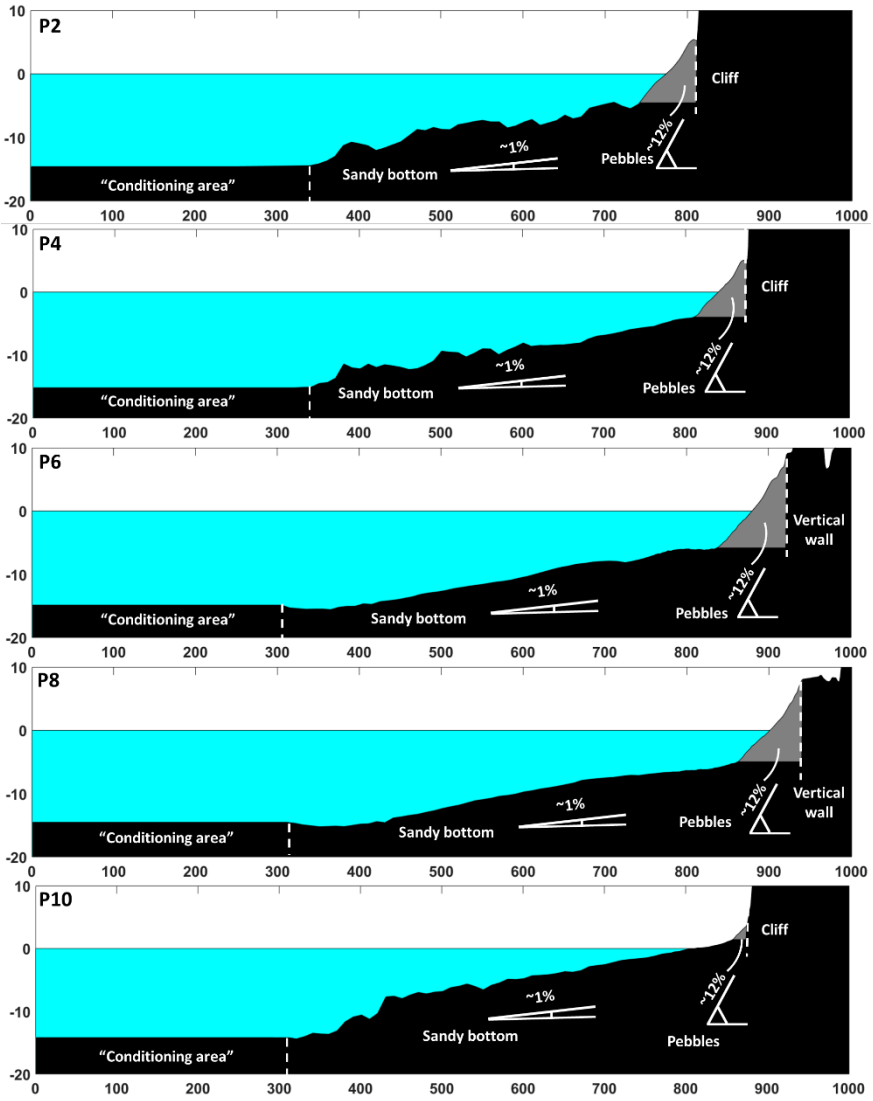

Figure 70. *Geometry of the 8 profiles used for the simulations in Etretat relative to the MSL*

For the 5 profiles, the 25 simulations corresponding to each 3-hour sea state of each of the 4 storms are defined by the significant wave height (H_s), peak period (T_p) and the water level (WL). In **Table 24** are shown the variables and dates of the 4 storms used for the simulations.

Storm Ciara (09/02/2020 09h – 12/02/2020 09h)			Storm Joachim (12/12/2011 21h – 15/12/2011 21h)			Storm Andrea (03/01/2012 06h – 06/01/2012 06h)			"Storm 19" (28/01/2013 18h – 31/01/2013 18h)		
H_s (m)	T_p (s)	WL (m)	H_s (m)	T_p (s)	WL (m)	H_s (m)	T_p (s)	WL (m)	H_s (m)	T_p (s)	WL (m)
1.74	5.74	3.316	1.41	5.07	1.983	1.71	5.07	1.604	1.46	5.07	-0.207
2.15	5.74	3.583	1.44	5.07	2.473	2.39	6.50	0.240	1.79	5.74	0.063
2.46	6.50	0.236	2.12	5.74	0.834	2.77	7.37	-0.135	1.78	5.74	2.652
2.99	7.37	-0.186	2.27	6.50	-0.722	2.77	7.37	1.461	1.63	5.74	2.637
3.33	7.37	3.080	2.48	7.37	2.369	2.25	7.37	1.825	1.59	5.74	-0.041
3.24	7.37	3.725	2.33	6.50	3.000	2.03	6.50	0.735	1.51	5.74	0.049
3.98	8.35	0.842	2.30	6.50	1.482	2.22	6.50	-0.832	1.47	5.07	2.896
3.58	9.46	-0.384	2.22	7.37	-1.271	2.10	7.37	0.981	1.48	5.74	2.929
3.01	8.35	3.004	1.97	7.37	1.562	1.81	6.50	1.753	1.53	5.74	0.005
2.45	7.37	4.014	1.65	7.37	2.554	1.62	6.50	1.318	1.60	5.74	-0.117
3.02	7.37	1.418	1.43	7.37	1.597	1.53	5.74	-0.529	1.71	5.74	2.584
3.20	8.35	-1.688	1.32	7.37	-1.084	1.49	5.74	0.468	1.93	5.74	2.706
3.13	8.35	2.179	1.46	5.07	1.435	1.89	5.74	1.672	1.90	5.74	0.130
3.16	8.35	3.857	1.47	5.07	2.725	2.90	7.37	1.525	1.55	5.74	-0.174
2.98	8.35	2.051	1.52	5.74	2.120	3.30	8.35	-0.236	1.39	5.07	2.685
2.81	8.35	-1.202	1.51	5.74	-0.757	3.47	8.35	0.377	1.51	5.74	2.917
2.46	7.37	1.834	1.52	5.74	0.592	3.65	8.35	2.177	1.53	5.74	0.419
2.35	6.50	3.906	1.55	5.74	2.385	3.82	8.35	2.180	1.43	6.50	-1.101
2.28	6.50	2.683	1.78	5.74	2.115	3.61	8.35	0.000	1.28	5.74	2.152
2.00	7.37	-0.829	2.55	7.37	-0.400	3.21	8.35	0.010	1.18	5.74	2.601
1.87	6.50	0.958	2.43	7.37	0.632	2.36	7.37	1.905	1.21	5.07	0.703
1.74	6.50	3.668	2.27	6.50	2.788	1.96	6.50	1.950	1.44	5.07	-1.371
1.66	5.74	3.004	2.02	7.37	2.676	1.79	5.74	0.014	1.55	5.07	2.147
1.53	5.74	-0.531	1.65	7.37	-0.122	1.59	5.74	-0.123	1.48	5.74	2.821
1.42	6.50	0.565	1.44	7.37	0.001	1.37	5.74	1.908	1.36	5.74	1.302

Table 24. *Forcings of significant wave height (Hs), peak period (Tp) and water level (WL) for the set-up of the numerical model of every 3-hour sea state of the 4 storms in Etretat*

5.3. VALIDATION OF THE MODEL

The validation is performed by evaluating three different aspects of the simulations: the inputs used for the simulations, the outputs of run-up 2% in comparison to theoretical formulations, and the outputs of run-up 2% in comparison to the results extracted from VMS.

5.3.1. Validation of the forcing inputs

The first validation is applied to the inputs used for the simulations with SWASH of significant wave height (H_s) and peak period (T_p) with the existing buoys located on the study area. The buoys used are SCENES buoy mentioned before between Villers-sur-Mer and Etretat, and the buoy from the Penly campaign of Cerema and EDF west of Hautot-sur-Mer (49° 59.36' N–01° 12.06' E), with

measurements available for one of the extreme events simulated, the storm Ciara. The comparison is performed between the records of the buoys and the outputs of the numerical simulation performed in the English Channel obtained on the same exact locations of these two buoys (**Figure 71**).

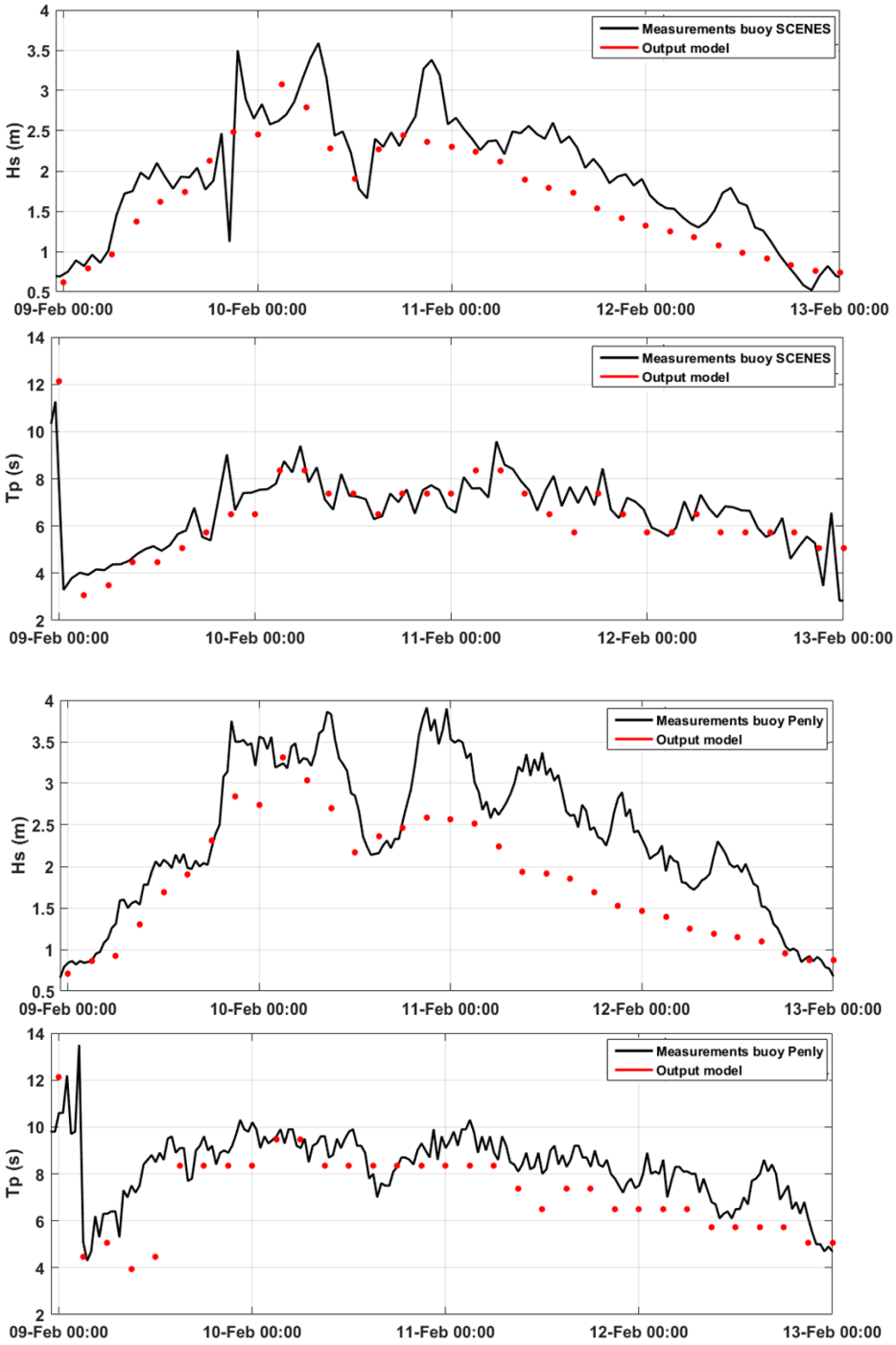

Figure 71. *Time series comparing the outputs of the numerical simulations in the English Channel with the measurements of the buoy SCENES of (a) significant wave height (Hs) and (b) peak period (Tp), and with the measurements of the buoy of Penly of (c) Hs and (d) Tp during the 3 days simulated of storm Ciara*

As can be seen, both variables on both locations show good agreement, despite the differences on the time step on the two sources, to consider the inputs of the simulations with SWASH correct on the three study sites. The other variable with which the model is forced is the water level, already corrected as previously explained.

5.3.2. Validation with theoretical formulations

The second validation is applied to the outputs of Run-Up 2% obtained on the simulations of the 4 storms in Villers-sur-Mer, comparing the outputs of SWASH to the results that can be calculated using theoretical formulations. Two formulations are used to carry out this comparison. The first formulation is taken from the EurOtop Manual (EurOtop, 2018), where they express a mean value approach for the wave run-up as in Eq. 22.

$$\frac{R_{u2\%}}{H_{m0}} = 1.65 \cdot \gamma_b \cdot \gamma_f \cdot \gamma_\beta \cdot \xi_{m-1,0} \tag{22}$$

where $R_{u2\%}$ is the wave run-up height exceeded by 2% of the incoming waves, γ_b is the influence factor for a berm, γ_f is the influence factor for roughness elements on a slope, γ_β is the influence factor for oblique wave attack and $\xi_{m-1,0}$ is the breaker parameter, surf similarity parameter or Iribarren number, which is defined by Eq. 23.

$$\xi_{m-1,0} = \frac{\tan\alpha}{\sqrt{H_{m0}/L_{m-1,0}}} \tag{23}$$

where $\tan\alpha$ is the slope in the front face of the structure, and H_{m0} and $L_{m-1,0}$ are the significant wave height and wavelength in deep waters, in this study, the forcings of the simulations on the boundary.

$L_{m-1,0}$ is calculated as $g{T_{m-1,0}}^2/(2\pi)$, being $T_{m-1,0}$ the spectral wave period. According to the manual, there is a clear relationship between this spectral wave period $T_{m-1,0}$ and the peak period T_p for conventional single peak wave spectra and can be calculated as $T_p = 1.1\ T_{m-1,0}$.

Since there are no berms or bars on the beach of Villers-sur-Mer, the berm factor γ_b is set as 1. The roughness factor γ_f is also set as 1 to approach the formulation to the smoothness of the bottom level of the numerical model. Finally, the wave attack factor γ_β is also set as 1 because the 4 storms simulated arrive perpendicularly to the shoreline in this study. Considering these values and making the substitutions, Eq. 17 can be transformed into Eq. 24.

$$R_{u2\%} = 1.5 \cdot \tan\alpha \cdot \sqrt{H_{m0}/L_p} \tag{24}$$

only dependent on the slope of the beach $\tan\alpha$, and the forcings H_s and T_p.

The second formulation compared is the one proposed by Stockdon et al. (2006), where the Run-Up 2% is parametrized as in Eq. 25.

$$R_{u2\%} = 1.1 \cdot \left[< \eta > + \frac{S}{2} \right] \tag{25}$$

where $< \eta >$ is the setup of the surface of water due to the presence of waves and S is the swash, calculated as in Eq. 26 and Eq. 27, respectively.

$$< \eta >= 0.35 \cdot \tan\alpha \cdot \sqrt{H_{m0} L_p} \tag{26}$$

$$S = \sqrt{(S_{inc})^2 + (S_{IG})^2} \tag{27}$$

where S_{inc} is the swash uprush related to incident waves and S_{IG} is the additional uprush related to infragravity waves, obtained from Eq. 28 and Eq. 29.

$$S_{inc} = 0.75 \cdot \tan\alpha \cdot \sqrt{H_{m0} L_p} \tag{28}$$

$$S_{IG} = 0.06 \cdot \sqrt{H_{m0} L_p} \tag{29}$$

Then, this second formulation of $R_{u2\%}$ would be as in Eq. 30.

$$R_{u2\%} = 1.1 \cdot \left(0.35 \cdot \tan\alpha \cdot \sqrt{H_{m0} L_p} + \frac{\sqrt{H_{m0} L_p (0.563 \tan^2\alpha + 0.004)}}{2} \right) \tag{30}$$

also, only dependent on the slope of the beach $\tan\alpha$, and the forcings H_s and T_p.

Out of the 7 profiles simulated, 2 are selected as representative: P11 and P15. Both of them have a similar slope, an approximative value of $\tan\alpha$ that can be set as 0.0264 to obtain the value of $R_{u2\%}$ with the formulations of the EurOtop manual and of Stockdon et al. (2006). The results obtained from the formulations will be compared to the results of the simulations of the 4 storms with the numerical model SWASH. In **Table 25** the results of the simulations for these 2 profiles are presented alongside the results from theoretical formulations. To be able to compare the relative changes, for each storm the cells are colored independently for the numerical results and for the theoretical results conditioning the ranges from green to red. The results are also visually presented in **Figure 72** for each storm in one graphic, showing the values of $R_{u2\%}$ every 3 hours obtained from the numerical simulations and the analytical formulations.

Storm Ciara (09/02/2020 09h – 12/02/2020 09h)				Storm Joachim (12/12/2011 21h – 15/12/2011 21h)				Storm Andrea (03/01/2012 06h – 06/01/2012 06h)				"Storm 19" (28/01/2013 18h – 31/01/2013 18h)			
P11	P15	EurOtop	Stockdon	P11	P15	EurOtop	Stockdon	P11	P15	EurOtop	Stockdon	P11	P15	EurOtop	Stockdon
0.34	0.38	0.52	0.59	0.08	0.15	0.34	0.38	0.14	0.18	0.41	0.46	0.11	0.1	0.34	0.38
0.28	0.27	0.53	0.6	0.15	0.17	0.39	0.45	0.31	0.32	0.54	0.61	0.24	0.29	0.48	0.54
0.49	0.5	0.66	0.75	0.21	0.24	0.5	0.56	0.52	0.49	0.66	0.75	0.45	0.44	0.54	0.61
0.99	1	0.98	1.11	0.15	0.19	0.5	0.56	0.58	0.63	0.78	0.88	0.27	0.29	0.45	0.51
1.23	1.27	1.12	1.27	0.68	0.89	0.91	1.03	0.7	0.76	0.93	1.05	0.23	0.24	0.45	0.51
1.56	1.38	1.41	1.59	0.82	0.66	0.96	1.08	0.66	0.74	0.89	1.01	0.38	0.41	0.58	0.65
1.22	1.3	1.34	1.52	0.7	0.73	0.93	1.06	0.89	0.8	1.06	1.21	0.48	0.57	0.57	0.65
1.66	1.76	1.24	1.4	0.74	0.67	1.01	1.15	0.9	0.83	1.08	1.23	0.47	0.45	0.57	0.65
1.56	1.61	1.14	1.29	0.68	0.71	0.87	0.98	0.73	0.7	0.9	1.02	0.16	0.16	0.4	0.45
0.88	0.89	1.08	1.22	0.7	0.62	0.8	0.9	0.59	0.65	0.84	0.95	0.32	0.34	0.53	0.6
0.88	0.97	1.24	1.41	0.46	0.51	0.73	0.82	0.53	0.58	0.81	0.91	0.32	0.36	0.49	0.55
1.29	1.43	1.26	1.43	0.44	0.44	0.71	0.8	0.55	0.53	0.8	0.91	0.35	0.39	0.5	0.57
1.24	1.24	1.24	1.41	0.49	0.46	0.67	0.76	0.54	0.52	0.75	0.85	0.27	0.23	0.48	0.55
0.97	1.05	1.22	1.38	0.55	0.57	0.66	0.75	0.81	0.91	1.04	1.18	0.46	0.49	0.65	0.74
1.05	0.82	1.17	1.33	0.49	0.46	0.66	0.75	1.02	1.07	1.26	1.43	0.44	0.56	0.57	0.64
1.1	1.19	1.15	1.31	0.55	0.47	0.65	0.73	1.11	1.22	1.32	1.49	0.55	0.65	0.61	0.7
0.88	1.06	0.99	1.12	0.42	0.46	0.65	0.74	1.25	1.39	1.36	1.54	0.52	0.55	0.7	0.79
0.74	0.75	0.96	1.09	0.46	0.57	0.57	0.65	1.4	1.62	1.46	1.66	0.6	0.64	0.69	0.78
0.77	0.89	1.02	1.15	0.45	0.47	0.6	0.68	1.52	1.7	1.67	1.9	0.54	0.63	0.64	0.73
0.79	0.76	0.88	1	0.77	0.67	0.83	0.94	1.39	1.41	1.59	1.81	0.51	0.51	0.61	0.69
0.86	0.69	0.85	0.96	0.57	0.63	0.95	1.08	1.23	1.26	1.4	1.59	0.4	0.44	0.62	0.7
0.63	0.59	0.82	0.93	0.89	0.89	0.94	1.06	0.85	0.94	1.11	1.26	0.41	0.39	0.51	0.58
0.59	0.48	0.8	0.9	0.69	0.72	1.02	1.16	0.77	0.72	0.92	1.04	0.42	0.4	0.53	0.61
0.59	0.59	0.79	0.89	0.72	0.67	0.94	1.06	0.68	0.69	0.87	0.99	0.48	0.56	0.6	0.68
0.78	0.92	0.75	0.85	0.56	0.61	0.78	0.88	0.65	0.64	0.84	0.95	0.43	0.45	0.66	0.74

Table 25. *Results of Run-Up 2% (m) from the numerical simulations in P11 and P15 in Villers-sur-Mer and results obtained from the theoretical formulations of the EurOtop manual (EurOtop, 2018) and Stockdon et al. (2006). The scales of colors are conditioned by the results of the simulations of both profiles and for both formulations independently for each storm (with color scales corresponding to range of values)*

From these values, the RMSE (Eq. 1) is obtained for all the possible combinations of simulations against formulations, having 4 values of RMSE for each storm. In **Table 26** all the results and means are presented. This gives a mean RMSE of 0.213 m 0.277 m for the EurOtop and Stockdon formulations, respectively, for storm Ciara, a mean RMSE of 0.22 m 0.314 m for Storm Joachim, a mean RMSE of 0.196 m and 0.322 m for Storm Andrea and a mean RMSE of 0.16 m and 0.226 m for "Storm 19". A total averaged RMSE of 0.197 m for the EurOtop (2018) for all the storms and an averaged RMSE of 0.285 m for the Stockdon et al. (2006) formulations in comparison to the results of $R_{u2\%}$ for the simulations on these profiles is obtained.

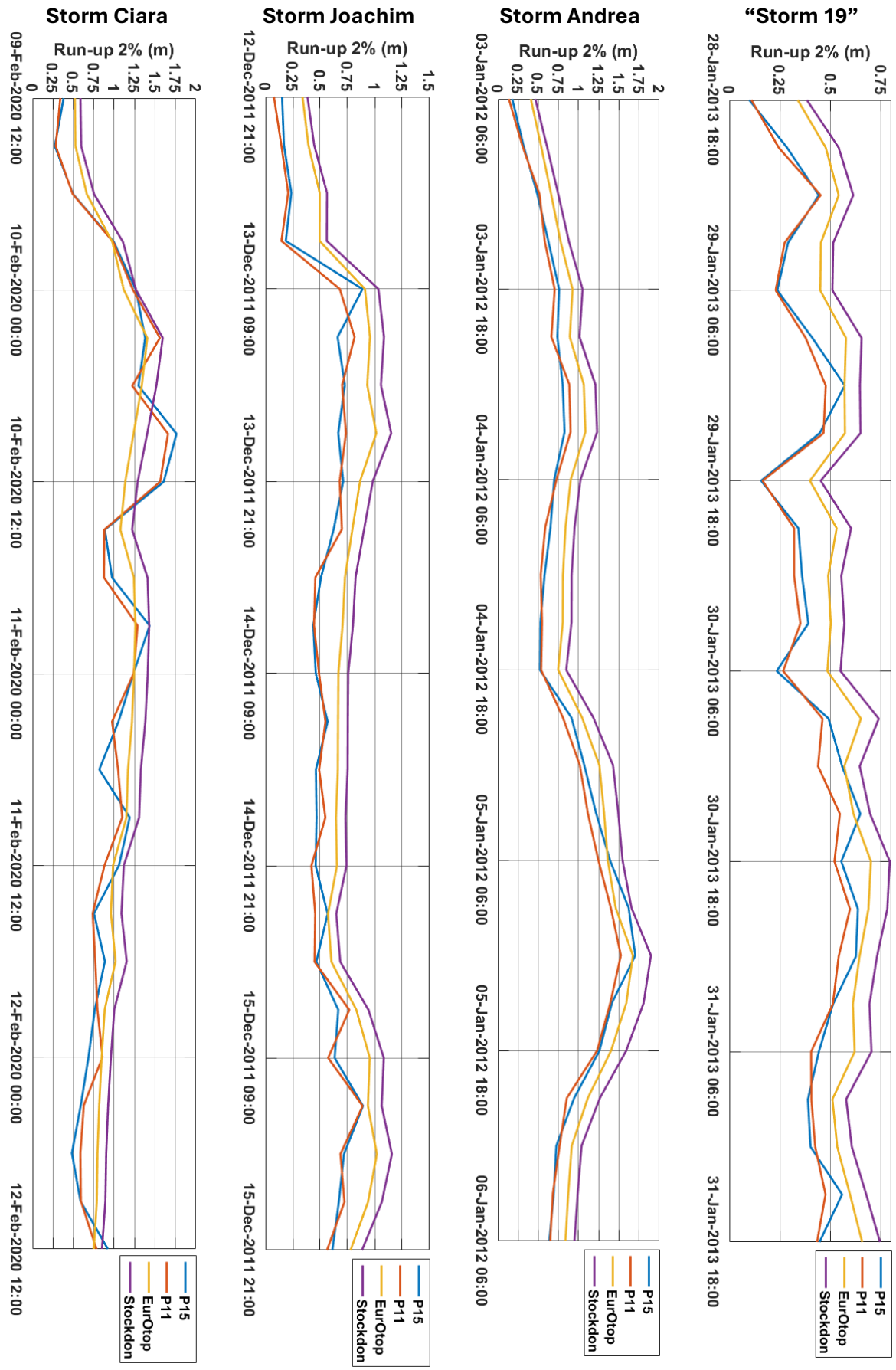

Figure 72. *Results of Run-Up 2% from the numerical simulations and for the formulations of EurOtop and Stockdon for the four simulated storms in Villers-sur-Mer*

	Ciara			Joachim			Andrea			Storm 19			Mean
	P11	P15	Mean	P11	P15	Mean	P11	P15	Mean	P11	P15	Mean	
EurOtop	0.20	0.22	0.21	0.22	0.22	0.22	0.21	0.19	0.20	0.17	0.15	0.16	**0.197**
Stockdon	0.27	0.28	0.28	0.32	0.31	0.31	0.34	0.31	0.32	0.24	0.22	0.23	**0.285**

Table 26. *Results of RMSE (m) calculated with the Run-Up 2% from the numerical simulations in P11 and P15 in Villers-sur-Mer and results obtained from the theoretical formulations of the EurOtop manual (EurOtop, 2018) and Stockdon et al. (2006)*

The maximum differences happen when the water level set for each sea state is too low or too high in respect to the Mean Sea Level (MSL), producing that the variations of the free surface of water varies over some parts of the profiles where the slope changes rapidly and does not keep a constant value as it must be defined on the theoretical formulations. On the other hand, when the SWL is set on a part of the profile with an almost constant slope close to the given value of 0.0264, the results for both formulations show a high accuracy with just some millimeters of difference, even with high values of H_s for some sea states. Then, the results of the numerical model can be considered accurate enough in contrast with theoretical formulations.

5.3.3. Validation with timestacks from VMS

Finally, the third, and most important validation is done by comparing some specific variables of the simulations to the records of video cameras located in the three study sites. This comparison is performed by understanding the limitations of both datasets used. The outputs of the numerical simulations are obtained with a constant water level set for each 3-hour sea state but chosen as the maximum within the 3 hours to be able to compare to the worst scenario record by the video cameras.

The video monitoring systems (VMS) installed at the three locations (**Figure 11**) provide different products useful for the validation of the results. The validation is performed using the timestacks, images formed by stacking side-by-side transects obtained from snap images at different instants. Each column of a timestack corresponds to a transect at a given instant, so they record wave by wave the run-up on one specific profile of the beach during the 10 minutes of exposure of each image. By considering the angle of the camera in respect to the transect that composes the timestacks, and the tidal range of the different water levels during a storm, the real-world coordinates of each pixel of the timestack can be calculated, which allows to obtain the horizontal run-up for each instant of the timestack.

From the horizontal run-ups of the timestacks and including the elevation of the surface on the vertical profile, the $R_{u2\%}$ can be extracted every 10 minutes during daylight of the 3 days simulated for the 4 storms. This methodology can be carried out with the timestacks when there

is not any other inconvenience for obtaining the images like rain drops, absence of enough sunlight, foggy weather, or malfunctions of the video cameras

Considering the central camera of the three study sites as the most useful for validation, the closest profiles to the hypothetical perpendicular profile of each camera among the simulated are the ones that are used for this purpose. In the case of Hautot-sur-Mer the closest profile is PD, in Villers-sur-Mer the profile is P11 and in Etretat, P6.

Among the three study sites, Etretat and Hautot-sur-Mer present certain difficulties due to the presence of the vertical wall at the end of the profiles. Instead, Villers-sur-Mer, with the smooth slope of the sandy beach and the smaller waves that arrive at this location, facilitates the validation with video.

The VMS of Villers-sur-Mer started the record on March 2019, so, among the four extreme events simulated, only Ciara has available images to perform the validation. And, from the 3 days simulated, only 2 of them have processed images, the so-called timestacks, 10^{th,} and 11th February 2020. At this point there are some limitations to consider associated with the simulations and with the VMS. The timestacks are only available during daylight, approximately from 7:30 in the morning to 18:20 in Villers-sur-Mer at this time of the year, and these images are not always usable, only when there are no drops or fog covering the cameras, and when the water level is not too far from the point of record of the VMS. Regarding the simulations, the main limitation is the time, since each simulation covers 3 hours, with each sea state defined by the wave height, the period and the water level, this latter taken as the maximum water level within the 3 hours. This fact provides the ideal instant for performing the comparison between the timestacks and the outputs of the simulation. To be able to compare, the timestack that should be taken is the 10-minute timestack, within the 3 hours corresponding to each simulation, that has the highest water level. By doing this, it is sure that the waves are varying over the same part of the profile and then, the slope is the same. This way, and since the $R_{u2\%}$ is just relative to the number of incoming waves and not the time during which it is calculated, the values can be compared.

After considering all these limitations and looking for the maximum number of available comparisons, 6 sea states among the 25 simulations are the ones that can be validated with timestacks: for the 10th February, the sea stated of 9h, 12h and 15h, and for the 11th February, the same sea states of 9h, 12h and 15h, each of them with the timestack that has the highest water level. The timestacks are treated using the software developed by Vousdoukas et al. (2012), who provide an open-access GUI to extract and process the time series of the cross-shore position of

the swash extrema. The cross-shore positions are transformed into elevations using the topographic information provided, which, in this case, corresponds to the profile P11 on which the simulations are performed, located only a few meters away from the profile on which the timestacks are obtained. The swash time series are manually corrected using the GUI interface from the automatically identified time series when necessary. Finally, the two percent exceedance values, the $R_{u2\%}$, are estimated from the swash time series after extracting the local maxima.

An example for one of the six timestacks is shown in **Figure 73**. It corresponds to the timestack associated with the sea state of 11/02/2020 at 9h, which is the timestack of 11/02/2020 at 10:20. As can be seen, all the waves on the timestack are identified with the red dotted line and the local maxima with the yellow dots, through which the $R_{u2\%}$ is obtained.

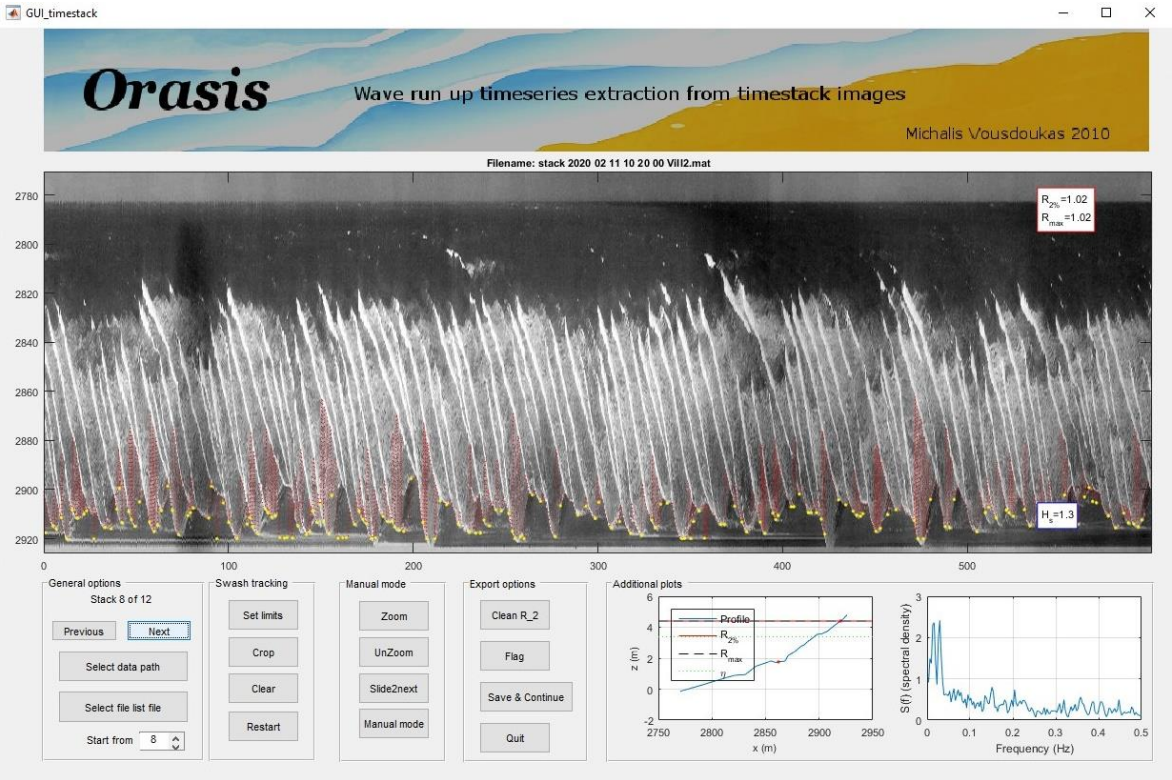

Figure 73. *Snapshot of the GUI timestack processing software used (Vousdoukas et al., 2012). Red lines indicate the swash front motions, and yellow dots the discrete maxima considered for the estimation of 2% exceedance values. The timestack corresponds to 11/02/2020 10:20*

In **Table 27** there is a summary of the characteristics with the H_s, the T_p, the water level set for the simulation and the water level corresponding to the 10-minute timestack. The $R_{u2\%}$ calculated from the output of water level of the simulations with SWASH on P11 and the $R_{u2\%}$ calculated from the processed timestacks are also presented.

The results converge into a good agreement, with only a few centimeters of difference, a maximum of 0.43 cm for the worst sea state and a minimum of 1 cm for the best fit. The water level generally remains on a high value on the sea states used for the validation, with two of them with lower values, which provides a wider range for the comparison. The average is less than 5 cm of difference not accounting for the worst sea state, which proves a good accuracy for the $R_{u2\%}$ obtained from the simulations of SWASH in Villers-sur-Mer.

Date	Simulation					Timestack		
	Hour	H_s (m)	T_p (s)	WL (m)	$R_{u2\%}$ (m)	Hour	WL (m)	$R_{u2\%}$ (m)
10/02/2020	09h	1.49	6.50	3.88	1.659	10 :10	3.8	1.6613
10/02/2020	12h	1.26	6.50	3.86	1.562	10 :40	3.88	1.5881
10/02/2020	15h	1.45	5.74	0.16	0.879	13 :40	0.67	0.9097
11/02/2020	09h	1.29	6.50	3.38	1.098	10 :20	3.1	1.0178
11/02/2020	12h	1.22	5.74	3.77	0.881	12 :40	3.83	0.7807
11/02/2020	15h	1.16	5.74	1.45	0.736	14 :00	1.45	0.3584

Table 27. *Summary of characteristics of the 6 sea states of Villers-sur-Mer for which the validation of run-up 2% with timestacks obtained from VMS has been performed*

For Etretat and Hautot-sur-Mer, the VMS have available records from January 2019 and December 2018, respectively. On these sites, the validation is performed in a different way, considering that, for most of the worst sea states, the run-up during storm Ciara, the only extreme event happening within the records, reaches the vertical wall located at the end of the profiles. Those sea states happen to be the ones with timestacks available for validation, obtained during daylight and for the corresponding sea states, i.e., the surface of water touches the wall and overtops it approximately from 9:30 in the morning during those days until 14:00 when there is enough daylight only from 8:30 to 16:00. So, since in these study sites the 3 days of simulation have records of timestacks, the sea states to compare would be 9th, 10^{th,} and 11th February at 9h and 12h for Etretat, and also 15h for Hautot-sur-Mer.

In both locations, a control point is chosen located on the vertical wall on the position of the profile of the timestack, close to the profiles simulated, P8 in Etretat and PD in Hautot-sur-Mer. On these points, the overtopping is obtained from the timestacks by counting the number of times the waves have passed through them. This number cannot be compared straightly because the hydrodynamic conditions are different for the simulations and for the timestacks, instead, the overtopping can be treated independently, accounting just for the occurrence in the simulations. This way, for each sea state, it can be established if the overtopping is happening or not in comparison to the timestacks.

It must be considered that the numerical model SWASH is set including the porosity of the gravel part of the beaches, set as 0.2 and not as an impermeable slope over which the waves can

uprush. This configuration reduces the run-up on the results and highlights the limitations of the numerical models when an abnormal size of sediment is included.

In the same way, when a storm arrives at a gravel or pebble beach, the changes in the morphology can be abrupt due to highly active morphodynamics, altering the profile of the beach. In the numerical model, the profile is just taken as a non-modifiable, so it can be close to reality, but modifications could exist, explaining the differences in the results of overtopping.

In **Table 28**, a summary of the characteristics of the coincident sea states of the simulations in Etretat is presented alongside the results of overtopping, considering for the outputs of the numerical model if the overtopping is happening or not, and checking for the timestacks if the waves overtop the vertical wall located at the end of the profile.

Date	Simulation					Timestack
	Hour	H_s (m)	T_p (s)	WL (m)	OT (Y/N)	OT (Y/N)
09/02/2020	09h	1.74	5.74	3.32	N	Y
09/02/2020	12h	2.15	5.74	3.58	Y	Y
10/02/2020	09h	3.01	8.35	3.00	N	Y
10/02/2020	12h	2.45	7.37	4.02	Y	Y
11/02/2020	09h	2.46	7.37	1.83	N	Y
11/02/2020	12h	2.35	6.50	3.91	Y	Y

Table 28. *Summary of characteristics of the 6 sea states of Etretat for which the validation of overtopping (OT) with timestacks obtained from VMS has been performed*

In **Table 29**, in an equivalent way, a summary of the characteristics of the sea states and the results of validation of Hautot-sur-Mer are presented.

Date	Simulation					Timestack
	Hour	H_s (m)	T_p (s)	WL (m)	OT (Y/N)	OT (Y/N)
09/02/2020	09h	0.99	3.08	3.32	N	Y
09/02/2020	12h	1.28	7.37	3.58	Y	Y
09/02/2020	15h	1.51	8.35	0.24	N	Y
10/02/2020	09h	2.24	8.35	3.00	Y	Y
10/02/2020	12h	1.80	8.35	4.01	Y	Y
10/02/2020	15h	2.01	8.35	1.42	N	Y
11/02/2020	09h	1.64	8.35	1.83	N	Y
11/02/2020	12h	1.62	7.37	3.91	Y	Y
11/02/2020	15h	1.59	7.37	2.68	N	Y

Table 29. *Summary of characteristics of the 9 sea states of Hautot-sur-Mer for which the validation of overtopping (OT) with timestacks obtained from VMS has been performed*

Even if the results are apparently satisfactory, the numerous limitations throughout the process add uncertainties that have to be addressed in future developments. Nevertheless, the overall methodology and results accomplished the aim of the validation.

5.4. IMPACTS OF PHYSICAL DRIVERS: DIFFERENT EVENTS IN ONE SITE

The results of run-up 2% $R_{u2\%}$ are presented independently for the three study sites in order to compare and analyze the transformation of each storm from waves on the boundary of the numerical model to the run-up over the profile of the beach.

5.4.1. Villers-sur-Mer

For the 7 profiles simulated, P7 to P19 taking odd numbers from East to West, the $R_{u2\%}$ is obtained for each storm. The results are presented in **Table 30** with the scale of colors conditioned to the range of values of the $R_{u2\%}$ and in **Figure 74** including the comparison to the water level set for each simulation and the H_s of each sea state during the 3 days.

Time		P19	P17	P15	P13	P11	P9	P7
09/02/2020	12h	0.446	0.365	0.381	0.327	0.34	0.298	0.354
09/02/2020	15h	0.179	0.276	0.273	0.198	0.284	0.19	0.205
09/02/2020	18h	0.438	0.48	0.496	0.315	0.492	0.35	0.344
09/02/2020	21h	0.885	0.963	0.996	0.878	0.988	0.918	0.9
10/02/2020	00h	1.135	1.131	1.266	1.068	1.23	1.188	1.075
10/02/2020	03h	1.316	1.311	1.379	1.366	1.559	1.504	1.374
10/02/2020	06h	1.167	1.179	1.297	1.227	1.221	1.278	1.227
10/02/2020	09h	1.72	1.737	1.763	1.668	1.659	1.737	1.667
10/02/2020	12h	1.567	1.635	1.606	1.57	1.562	1.582	1.569
10/02/2020	15h	0.905	0.858	0.886	0.884	0.879	0.914	0.854
10/02/2020	18h	1.066	0.943	0.974	0.879	0.875	1.076	1.045
10/02/2020	21h	1.271	1.388	1.433	1.349	1.286	1.453	1.411
11/02/2020	00h	1.222	1.223	1.235	1.188	1.237	1.252	1.243
11/02/2020	03h	0.957	0.957	1.053	1.024	0.974	1.019	1.011
11/02/2020	06h	0.756	0.904	0.817	0.966	1.048	1.014	1.058
11/02/2020	09h	1.089	1.19	1.19	1.104	1.098	0.942	0.983
11/02/2020	12h	0.875	1.091	1.059	0.983	0.881	0.977	1.049
11/02/2020	15h	0.732	0.775	0.752	0.712	0.736	0.707	0.745
11/02/2020	18h	0.801	0.848	0.886	0.671	0.768	0.78	0.742
11/02/2020	21h	0.726	0.676	0.763	0.836	0.794	0.806	0.772
12/02/2020	00h	0.856	0.672	0.685	0.7	0.856	0.799	0.693
12/02/2020	03h	0.682	0.579	0.591	0.723	0.628	0.657	0.621
12/02/2020	06h	0.606	0.592	0.482	0.552	0.586	0.537	0.586
12/02/2020	09h	0.598	0.578	0.587	0.649	0.592	0.593	0.594
12/02/2020	12h	0.833	1.036	0.922	0.76	0.783	0.785	0.811

Table 30. *Results of Run-Up 2% (m) from the numerical simulations for storm Ciara for all the profiles in Villers-sur-Mer. Scale of colors are conditioned by the results of the simulations on all the profiles*

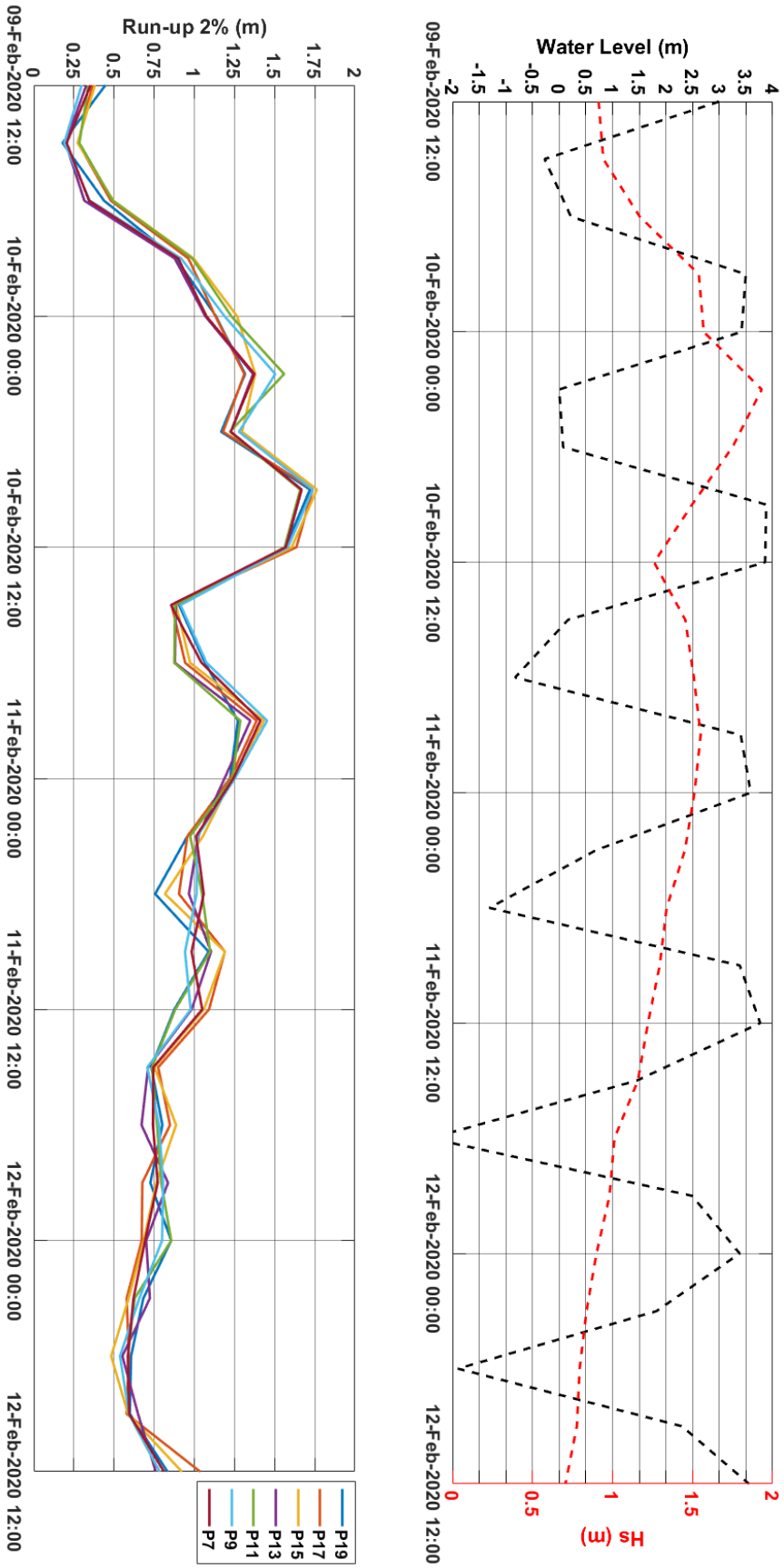

Figure 74. *Results of Run-Up 2% from the numerical simulations for storm Ciara for all the profiles in Villers-sur-Mer. Black dotted line on the left y-axis corresponds to the water level set for each simulation and red dotted line on the right y-axis corresponds to the significant wave height of every sea state*

At first sight, it is remarkable that the greatest value of H_s does not produce the maximum value of $R_{u2\%}$, for storm Ciara in Villers-sur-Mer, it is the highest value of water level, but in combination with a high enough value of H_s what gives the greatest $R_{u2\%}$, surpassing the 1.65 m for every profile. This is explained by the transversal shape of the beach, facilitating the uprush of the water on the upper part and generating the opposite on the down part of the profiles. After the two sea states with the highest water level, the peak of the storm, defined by the maximum H_s, produces a run-up of more than 1.3 m on every profile, reaching a value of 1.55 m on P11. The first two instants, with low values of H_s and T_p barely produce any $R_{u2\%}$. In general, the water level apparently presents a bigger influence on the values of $R_{u2\%}$ obtained than the H_s. It can be noticed too that all the profiles vary approximately in the same way, growing and decreasing harmonically all along the beach.

In the same way, for storm Joachim, the results of $R_{u2\%}$ can be seen in **Table 31** and **Figure 75** including the scale of colors relative to the run-up of this storm in the table and the time series of water level and significant wave height in the figure.

Time		P19	P17	P15	P13	P11	P9	P7
12/12/2011	21h	0.126	0.093	0.152	0.095	0.077	0.076	0.112
13/12/2011	00h	0.194	0.141	0.169	0.152	0.145	0.159	0.155
13/12/2011	03h	0.262	0.201	0.237	0.214	0.208	0.154	0.23
13/12/2011	06h	0.133	0.212	0.186	0.158	0.146	0.178	0.147
13/12/2011	09h	0.825	0.803	0.887	0.795	0.68	0.824	0.806
13/12/2011	12h	0.838	0.656	0.66	0.659	0.815	0.697	0.658
13/12/2011	15h	0.721	0.722	0.726	0.668	0.701	0.62	0.666
13/12/2011	18h	0.67	0.792	0.666	0.654	0.736	0.672	0.709
13/12/2011	21h	0.727	0.704	0.711	0.742	0.679	0.729	0.718
14/12/2011	00h	0.732	0.68	0.624	0.688	0.699	0.676	0.619
14/12/2011	03h	0.594	0.461	0.508	0.466	0.456	0.453	0.504
14/12/2011	06h	0.54	0.466	0.437	0.471	0.444	0.529	0.531
14/12/2011	09h	0.492	0.515	0.46	0.525	0.49	0.532	0.535
14/12/2011	12h	0.575	0.651	0.569	0.586	0.549	0.579	0.527
14/12/2011	15h	0.466	0.439	0.461	0.52	0.491	0.533	0.562
14/12/2011	18h	0.472	0.445	0.467	0.519	0.548	0.558	0.567
14/12/2011	21h	0.504	0.412	0.459	0.425	0.42	0.41	0.416
15/12/2011	00h	0.471	0.483	0.569	0.457	0.455	0.518	0.395
15/12/2011	03h	0.434	0.447	0.465	0.489	0.449	0.504	0.492
15/12/2011	06h	0.603	0.605	0.666	0.659	0.767	0.749	0.715
15/12/2011	09h	0.612	0.614	0.633	0.561	0.573	0.526	0.555
15/12/2011	12h	0.852	0.88	0.892	0.87	0.889	0.833	0.84
15/12/2011	15h	0.643	0.709	0.718	0.657	0.686	0.718	0.696
15/12/2011	18h	0.608	0.636	0.671	0.814	0.722	0.62	0.612
15/12/2011	21h	0.491	0.548	0.612	0.493	0.563	0.538	0.542

Table 31. *Results of Run-Up 2% (m) from the numerical simulations for storm Joachim for all the profiles in Villers-sur-Mer. Scale of colors are conditioned by the results of the simulations on all the profiles*

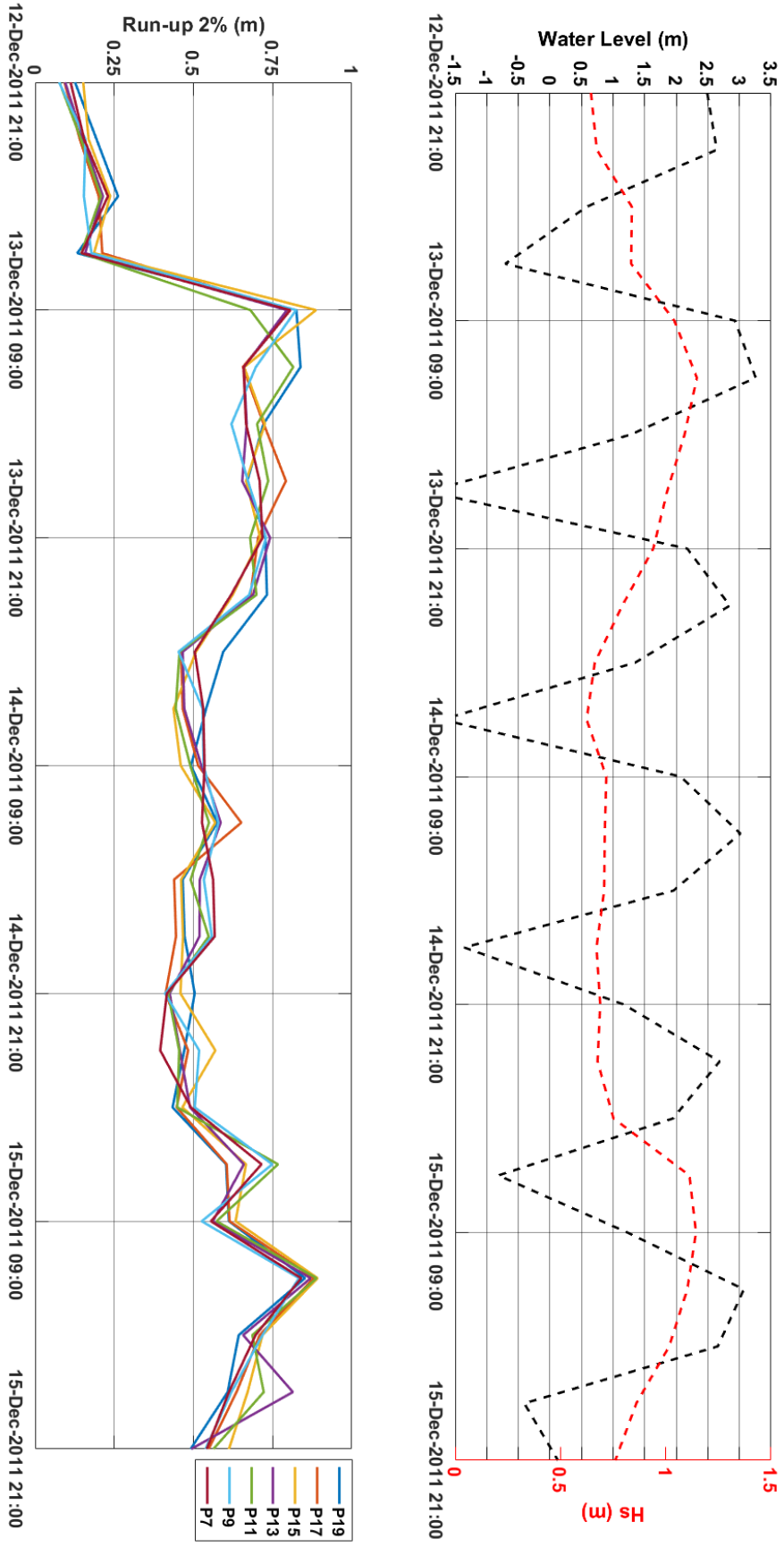

Figure 75. *Results of Run-Up 2% from the numerical simulations for storm Joachim for all the profiles in Villers-sur-Mer. Black dotted line on the left y-axis corresponds to the water level set for each simulation and red dotted line on the right y-axis corresponds to the significant wave height of every sea state*

After the fourth sea state, the $R_{u2\%}$ remains in a range between 0.3 m and 0.9 m because the H_s of storm Joachim takes values of ~0.7 m for most of the sea states of the storm, producing a $R_{u2\%}$ of 0.4-0.5 m whatever the water level set for each simulation is. The maximum $R_{u2\%}$ is reached from 13th December at 9:00 to 13th December at 21:00, and in the last sea states, because the time series of H_s takes its peak and grows again with a second peak, respectively, but still no values higher than 0.9 m, since H_s does not exceed 1.15 m. For the four first instants, the T_p is too low to produce barely any run-up, in combination too with an H_s lower than 0.83 m.

The third storm, Andrea, gives the results of $R_{u2\%}$ shown in **Table 32** and **Figure 76**.

Time		P19	P17	P15	P13	P11	P9	P7
03/01/2012	06h	0.163	0.185	0.179	0.155	0.137	0.146	0.168
03/01/2012	09h	0.259	0.315	0.321	0.187	0.307	0.217	0.202
03/01/2012	12h	0.459	0.425	0.489	0.306	0.516	0.295	0.32
03/01/2012	15h	0.716	0.699	0.627	0.654	0.582	0.637	0.657
03/01/2012	18h	0.818	0.761	0.759	0.791	0.704	0.755	0.776
03/01/2012	21h	0.681	0.739	0.737	0.667	0.663	0.649	0.592
04/01/2012	00h	0.746	0.774	0.803	0.766	0.885	0.825	0.756
04/01/2012	03h	0.812	0.844	0.826	0.8	0.9	0.755	0.82
04/01/2012	06h	0.721	0.749	0.698	0.728	0.726	0.727	0.689
04/01/2012	09h	0.584	0.607	0.652	0.571	0.587	0.54	0.558
04/01/2012	12h	0.529	0.549	0.579	0.631	0.531	0.597	0.617
04/01/2012	15h	0.619	0.537	0.527	0.5	0.547	0.516	0.524
04/01/2012	18h	0.636	0.614	0.522	0.655	0.536	0.605	0.658
04/01/2012	21h	0.962	0.914	0.911	0.835	0.806	0.774	0.807
05/01/2012	00h	0.989	1.11	1.07	0.954	1.015	1.136	1.016
05/01/2012	03h	1.185	1.109	1.215	1.152	1.113	1.145	1.115
05/01/2012	06h	1.381	1.278	1.389	1.303	1.245	1.295	1.246
05/01/2012	09h	1.611	1.514	1.62	1.503	1.399	1.439	1.401
05/01/2012	12h	1.692	1.539	1.702	1.636	1.523	1.566	1.525
05/01/2012	15h	1.496	1.408	1.412	1.453	1.392	1.432	1.394
05/01/2012	18h	1.337	1.254	1.258	1.283	1.229	1.264	1.237
05/01/2012	21h	1.026	0.917	0.944	0.961	0.853	0.975	0.927
06/01/2012	00h	0.655	0.681	0.724	0.667	0.765	0.736	0.677
06/01/2012	03h	0.647	0.63	0.692	0.646	0.681	0.705	0.629
06/01/2012	06h	0.713	0.631	0.637	0.699	0.648	0.649	0.65

Table 32. *Results of Run-Up 2% (m) from the numerical simulations for storm Andrea for all the profiles in Villers-sur-Mer. Scale of colors are conditioned by the results of the simulations on all the profiles*

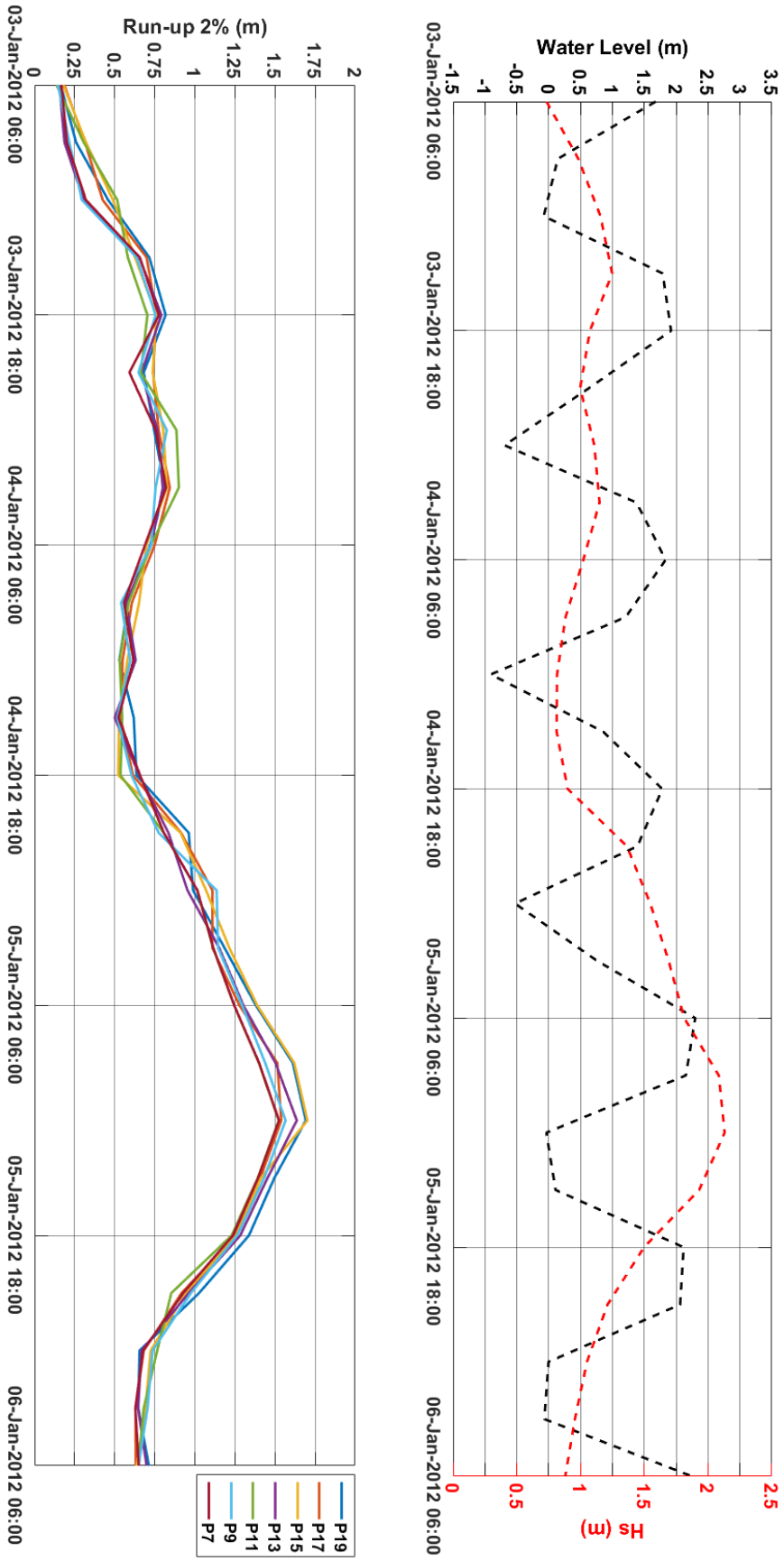

Figure 76. *Results of Run-Up 2% from the numerical simulations for storm Andrea for all the profiles in Villers-sur-Mer. Black dotted line on the left y-axis corresponds to the water level set for each simulation and red dotted line on the right y-axis corresponds to the significant wave height of every sea state*

Storm Andrea arrives to the nearshore with the highest H_s among the four storms. The water level varies within a range of -0.5 m to 2 m during the 3 days of this storm, so, by staying around this part of the profile, the results of $R_{u2\%}$ seem to follow much more the trends of the time series of H_s than in the previous storms analyzed. After the sea state in which the storm starts to increase stronger, 4th January at 18:00, the $R_{u2\%}$ takes values greater than 1 m in every profile and during the next 7 sea states, reaching values of 1.6 – 1.7 m. The maximum water level is also reached during the instants around the peak of the storm, generating the worst scenarios in terms of combination of a high water level with a high $R_{u2\%}$. The profiles seem to differ more in their behavior during the 3 days of simulation of Andrea, probably due to the smaller range in the variation of the water level.

Finally, the results of "Storm 19" in Villers-sur-Mer of $R_{u2\%}$ are the values presented in **Table 33** and **Figure 77**.

Time		P19	P17	P15	P13	P11	P9	P7
28/01/2013	**18h**	0.057	0.104	0.099	0.085	0.109	0.076	0.076
28/01/2013	**21h**	0.295	0.303	0.285	0.178	0.244	0.184	0.176
29/01/2013	**00h**	0.511	0.433	0.442	0.393	0.451	0.434	0.329
29/01/2013	**03h**	0.293	0.284	0.29	0.255	0.273	0.261	0.293
29/01/2013	**06h**	0.24	0.212	0.237	0.183	0.229	0.172	0.19
29/01/2013	**09h**	0.383	0.414	0.41	0.31	0.377	0.327	0.326
29/01/2013	**12h**	0.533	0.576	0.57	0.454	0.476	0.477	0.5
29/01/2013	**15h**	0.489	0.566	0.446	0.503	0.465	0.428	0.444
29/01/2013	**18h**	0.193	0.199	0.157	0.088	0.164	0.122	0.083
29/01/2013	**21h**	0.292	0.318	0.341	0.228	0.32	0.21	0.248
30/01/2013	**00h**	0.432	0.351	0.359	0.313	0.32	0.289	0.34
30/01/2013	**03h**	0.46	0.38	0.39	0.342	0.351	0.31	0.367
30/01/2013	**06h**	0.243	0.266	0.234	0.149	0.266	0.133	0.169
30/01/2013	**09h**	0.404	0.43	0.49	0.387	0.46	0.352	0.414
30/01/2013	**12h**	0.555	0.525	0.557	0.471	0.438	0.44	0.431
30/01/2013	**15h**	0.595	0.56	0.647	0.543	0.546	0.51	0.486
30/01/2013	**18h**	0.467	0.505	0.553	0.516	0.519	0.47	0.447
30/01/2013	**21h**	0.615	0.58	0.635	0.636	0.596	0.619	0.639
31/01/2013	**00h**	0.475	0.641	0.625	0.576	0.54	0.544	0.51
31/01/2013	**03h**	0.505	0.525	0.512	0.515	0.511	0.526	0.492
31/01/2013	**06h**	0.436	0.454	0.442	0.398	0.404	0.389	0.359
31/01/2013	**09h**	0.383	0.399	0.388	0.35	0.405	0.395	0.404
31/01/2013	**12h**	0.393	0.412	0.401	0.404	0.424	0.438	0.402
31/01/2013	**15h**	0.491	0.599	0.557	0.516	0.475	0.462	0.503
31/01/2013	**18h**	0.517	0.374	0.445	0.435	0.433	0.402	0.42

Table 33. *Results of Run-Up 2% (m) from the numerical simulations for "Storm 19" for all the profiles in Villers-sur-Mer. Scale of colors are conditioned by the results of the simulations on all the profiles*

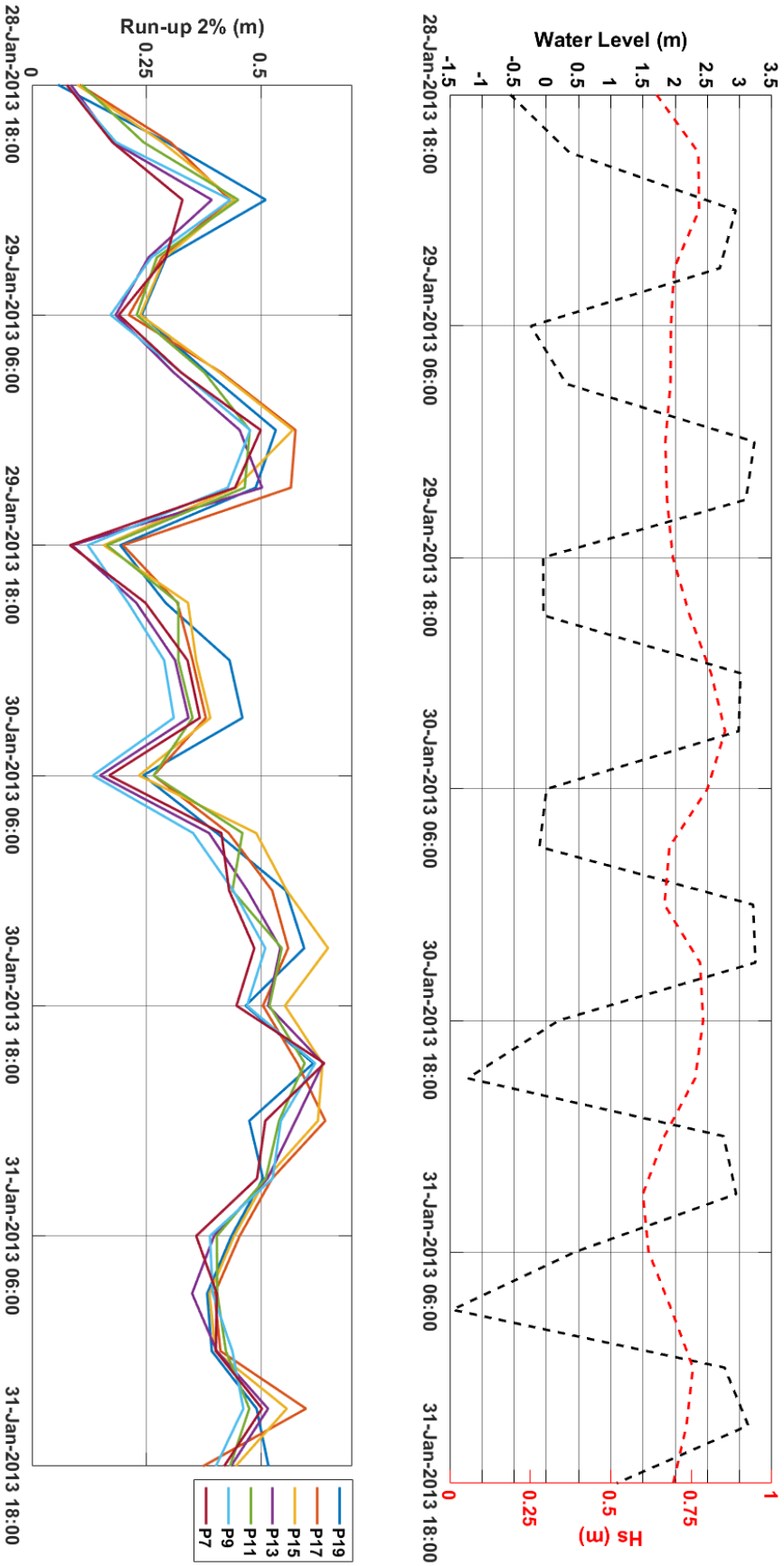

Figure 77. *Results of Run-Up 2% from the numerical simulations for "Storm 19" for all the profiles in Villers-sur-Mer. Black dotted line on the left y-axis corresponds to the water level set for each simulation and red dotted line on the right y-axis corresponds to the significant wave height of every sea state*

The behavior of $R_{u2\%}$ presents an almost flat evolution in time, with barely any variation around ~0.4 or ~0.5 m, since "Storm 19" never reaches 1 m of height.

Analyzing the four events together, some straight conclusions are obtained. Firstly, low values of T_p, especially in combination with low values of H_s, barely produce any $R_{u2\%}$. It is necessary for the T_p to remain over 4 s, and for the H_s to reach 0.8 or 0.9 m to be able to generate run-up. Secondly, it is the combination of high values of water level and high values of H_s what produces the greatest $R_{u2\%}$, but the H_s has a bigger effect on the run-up than the water level. This effect seems to be increased when the range of water level is smaller, taking the H_s almost the complete control over the $R_{u2\%}$. The worst scenario, highest $R_{u2\%}$, is produced when the time series of H_s grows and the water level reaches the high tide, even if this sea state is not the peak of the storm. And finally, no difference can be appreciated along the beach, as all the profiles seem to vary in the same manner independently of their location in front of Villers-sur-Mer.

5.4.2. Hautot-sur-Mer

The analysis of the simulations on the different profiles in Hautot-sur-Mer is divided in two main features: the analysis of the profiles located on the beach between groins in front of the populated area and the two profiles located on the sides of the beach in front of the cliffs. Taking into account that the beach is considered as a composite beach with pebbles on top and sand at the bottom, it is interesting looking at the differences between sea states depending on the water level set for each simulation, since for some cases, waves are arriving to the shoreline on the gravel part and some cases waves can arrive either on the sandy part or moving around the inflexion point where the sediment changes. On the 8 profiles simulated, being PA to PF from East to West the profiles between groins and P5 and P18 the profiles on the sides, the $R_{u2\%}$ is obtained for each storm.

The results for storm Ciara are presented in **Table 34** with the scale of colors conditioned to the variation of the $R_{u2\%}$ and in **Figure 78** including the comparison to the water level set for each simulation and the H_s of each sea state during the 3 days.

Time		P18	PF	PE	PD	PC	PB	PA	P5
09/02/2020	09h	0.032	0.035	0.024	0.033	0.029	0.04	0.03	0.033
09/02/2020	12h	0.654	0.594	0.609	0.583	0.464	0.591	0.544	0.654
09/02/2020	15h	1.213	0.881	0.953	0.963	0.901	0.9	0.927	1.201
09/02/2020	18h	1.604	1.312	1.36	1.391	1.292	1.298	1.261	1.589
09/02/2020	21h	1.891	1.506	1.531	1.718	1.612	1.547	1.594	1.872
10/02/2020	00h	1.405	1.333	1.336	1.402	1.356	1.262	1.323	1.479
10/02/2020	03h	1.803	1.711	1.715	1.795	1.69	1.571	1.597	1.785
10/02/2020	06h	1.872	1.494	1.545	1.603	1.52	1.505	1.444	1.853
10/02/2020	09h	1.559	1.372	1.404	1.382	1.327	1.378	1.323	1.544
10/02/2020	12h	1.163	1.023	1.024	1.079	1.045	0.943	0.975	1.138
10/02/2020	15h	1.258	1.185	1.261	1.295	1.193	1.098	1.21	1.238
10/02/2020	18h	1.762	1.66	1.768	1.666	1.519	1.408	1.613	1.736
11/02/2020	21h	1.367	1.287	1.278	1.275	1.28	1.288	1.298	1.397
10/02/2020	00h	1.269	1.234	1.225	1.349	1.26	1.15	1.231	1.276
11/02/2020	03h	1.29	1.257	1.277	1.204	1.247	1.213	1.301	1.318
11/02/2020	06h	1.552	1.375	1.397	1.376	1.242	1.241	1.309	1.511
11/02/2020	09h	1.051	0.957	0.966	1.026	0.956	0.911	1.001	1.012
11/02/2020	12h	0.876	0.777	0.773	0.883	0.731	0.74	0.758	0.876
11/02/2020	15h	0.839	0.802	0.824	0.838	0.771	0.78	0.785	0.867
11/02/2020	18h	0.973	0.862	0.886	0.879	0.805	0.835	0.82	0.946
11/02/2020	21h	0.709	0.639	0.698	0.644	0.645	0.674	0.664	0.733
12/02/2020	00h	0.547	0.511	0.516	0.494	0.459	0.507	0.458	0.562
12/02/2020	03h	0.565	0.473	0.452	0.485	0.449	0.445	0.423	0.549
12/02/2020	06h	1	0.573	0.605	0.591	0.567	0.573	0.626	0.963
12/02/2020	09h	0.635	0.516	0.513	0.528	0.466	0.518	0.494	0.612

Table 34. *Results of Run-Up 2% (m) from the numerical simulations for storm Ciara for all the profiles in Hautot-sur-Mer. Scale of colors are conditioned by the results of the simulations on all the profiles*

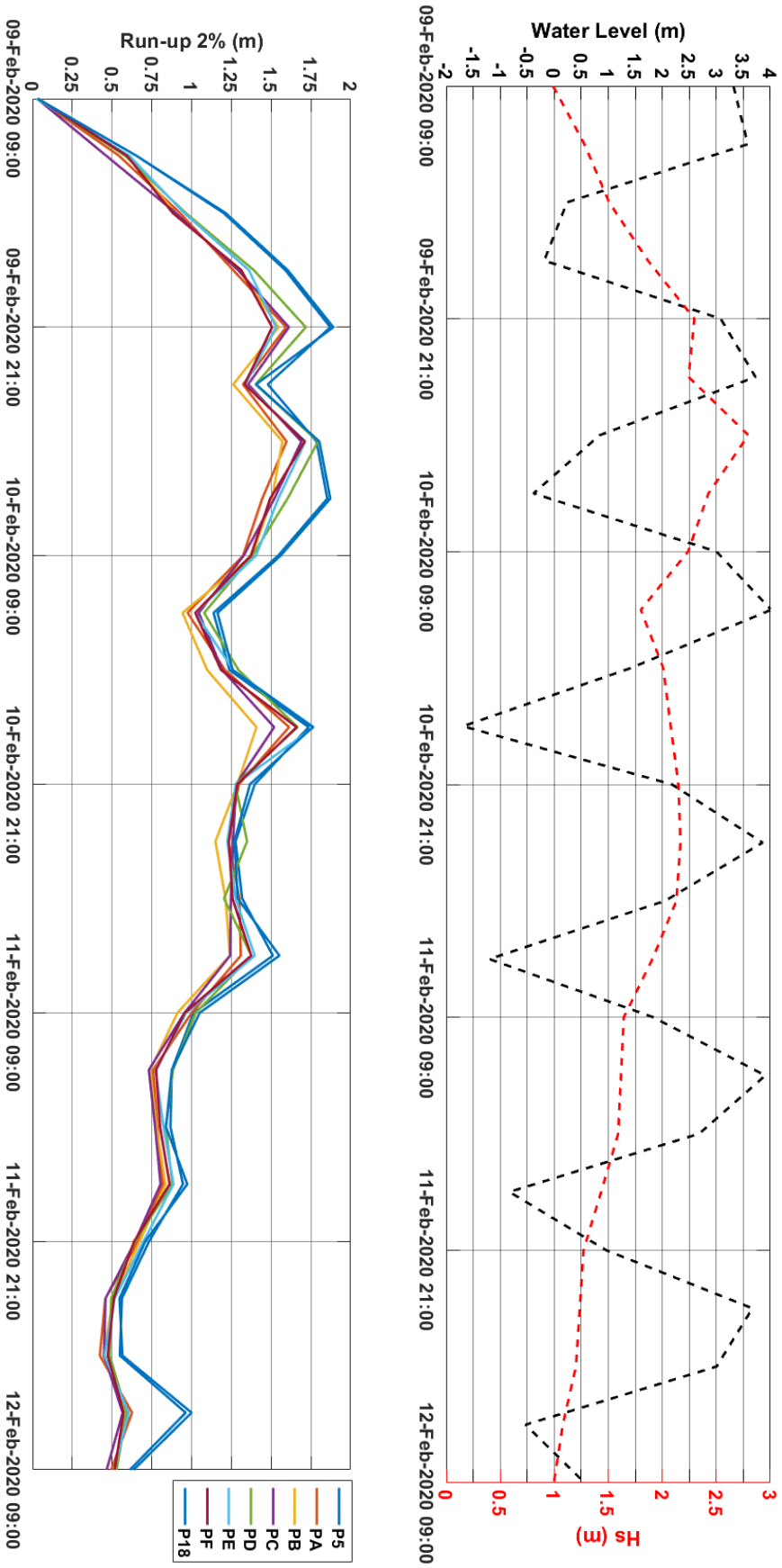

Figure 78. *Results of Run-Up 2% from the numerical simulations for storm Ciara for all the profiles in Hautot-sur-Mer. Black dotted line on the left y-axis corresponds to the water level set for each simulation and red dotted line on the right y-axis corresponds to the significant wave height of every sea state*

As in Villers-sur-Mer, the highest value of H_s does not produce the maximum value of $R_{u2\%}$ for storm Ciara, it is a combination of a low values of water level with high values of H_s what gives the greatest $R_{u2\%}$. For Hautot-sur-Mer, the time series of water level has the opposite effect on the $R_{u2\%}$, so when the water level decreases, the $R_{u2\%}$ is bigger and vice versa. It is noticeable that the $R_{u2\%}$ is higher at every sea state on the profiles located on the sides of the beach, P5 and P18, being 10 to 30 cm higher. There is barely any difference in the $R_{u2\%}$ on the profiles located between the groins, behaving almost in the same way, and always less than the results of $R_{u2\%}$ on the sides. This means that the groins indeed hold the pebbles creating a natural barrier against the waves preventing the $R_{u2\%}$ to reach greater values as it could have. The maximum $R_{u2\%}$ is almost 1.9 m on the profiles on the sides and almost 1.8 m between groins. For the first sea state, the waves do not produce any $R_{u2\%}$ because the H_s and the T_p are too low.

The results of $R_{u2\%}$ for storm Joachim can be seen in **Table 35** and **Figure 79** including the scale of colors relative to the run-up of this storm independently.

Time		P18	PF	PE	PD	PC	PB	PA	P5
12/12/2011	**21h**	0.101	0.059	0.065	0.046	0.06	0.045	0.049	0.116
13/12/2011	**00h**	0.066	0.04	0.043	0.041	0.034	0.047	0.045	0.049
13/12/2011	**03h**	0.716	0.679	0.697	0.683	0.619	0.618	0.631	0.73
13/12/2011	**06h**	1.566	1.029	1.12	1.002	0.945	0.906	0.965	1.518
13/12/2011	**09h**	1.017	0.932	0.968	0.982	0.944	0.888	0.977	0.986
13/12/2011	**12h**	0.91	0.774	0.792	0.857	0.712	0.761	0.757	0.929
13/12/2011	**15h**	0.852	0.851	0.823	0.85	0.732	0.761	0.798	0.852
13/12/2011	**18h**	1.434	0.968	1.026	0.959	0.895	0.887	0.94	1.434
13/12/2011	**21h**	0.885	0.771	0.845	0.766	0.774	0.808	0.817	0.885
14/12/2011	**00h**	0.662	0.513	0.535	0.533	0.486	0.542	0.48	0.661
14/12/2011	**03h**	0.59	0.436	0.477	0.46	0.396	0.36	0.412	0.579
14/12/2011	**06h**	1.116	0.516	0.653	0.543	0.553	0.552	0.572	1.009
14/12/2011	**09h**	0.611	0.452	0.493	0.454	0.402	0.455	0.434	0.552
14/12/2011	**12h**	0.392	0.319	0.317	0.341	0.287	0.287	0.289	0.404
14/12/2011	**15h**	0.502	0.43	0.4	0.43	0.338	0.358	0.366	0.504
14/12/2011	**18h**	1.201	0.57	0.548	0.557	0.56	0.565	0.583	1.215
14/12/2011	**21h**	0.958	0.526	0.538	0.489	0.498	0.558	0.56	0.969
15/12/2011	**00h**	0.459	0.367	0.356	0.396	0.319	0.345	0.335	0.463
15/12/2011	**03h**	0.596	0.496	0.474	0.477	0.451	0.471	0.424	0.575
15/12/2011	**06h**	1.212	0.948	0.984	1.01	0.941	0.909	0.93	1.206
15/12/2011	**09h**	1.177	0.932	0.982	0.994	0.937	0.918	0.948	1.091
15/12/2011	**12h**	0.834	0.696	0.716	0.695	0.645	0.638	0.654	0.853
15/12/2011	**15h**	0.797	0.647	0.664	0.65	0.599	0.596	0.606	0.807
15/12/2011	**18h**	1.034	0.696	0.719	0.682	0.666	0.672	0.685	1.048
15/12/2011	**21h**	1.209	0.581	0.575	0.565	0.563	0.544	0.578	1.224

Table 35. *Results of Run-Up 2% (m) from the numerical simulations for storm Joachim for all the profiles in Hautot-sur-Mer. Scale of colors are conditioned by the results of the simulations on all the profiles*

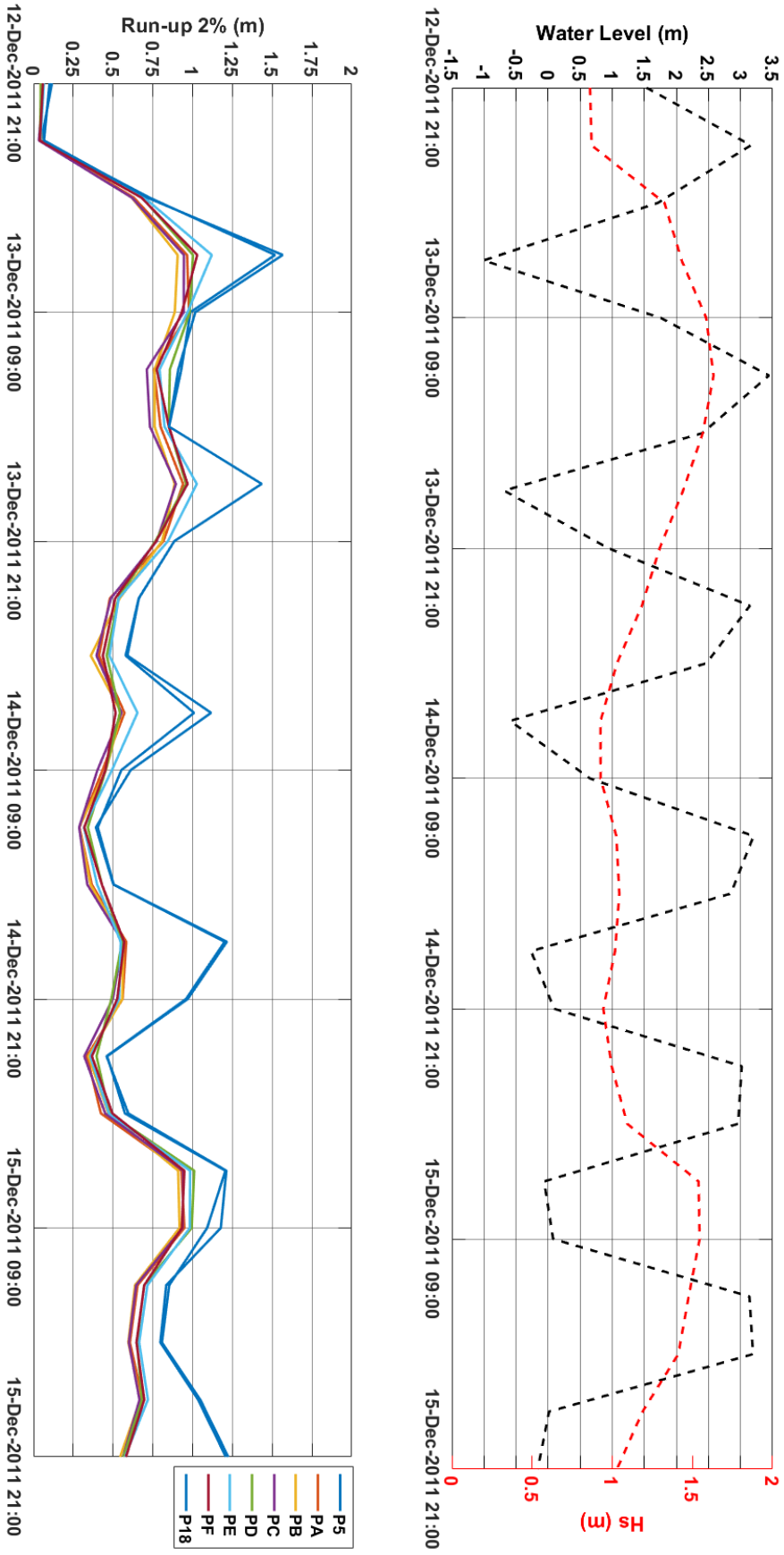

Figure 79. *Results of Run-Up 2% from the numerical simulations for storm Joachim for all the profiles in Hautot-sur-Mer. Black dotted line on the left y-axis corresponds to the water level set for each simulation and red dotted line on the right y-axis corresponds to the significant wave height of every sea state*

For storm Joachim the behavior of $R_{u2\%}$ follows the same patterns as for storm Ciara, but the effects are more remarkable in this case. The $R_{u2\%}$ on the sides is also 10 cm to even half a meter higher than on the profiles between groins, also producing the accumulation of pebbles a reducing effect on the waves. Similarly, the $R_{u2\%}$ is greater when the water level drops and lower when it grows, especially on profiles P5 and P18. The maximum $R_{u2\%}$ is barely 1 m between groins since the H_s is not higher than 1.6 m in the peak.

Storm Andrea, in Hautot-sur-Mer, gives the results of $R_{u2\%}$ shown in **Table 36** and **Figure 80**.

Time		P18	PF	PE	PD	PC	PB	PA	P5
03/01/2012	**06h**	0.548	0.433	0.477	0.462	0.371	0.396	0.416	0.537
03/01/2012	**09h**	0.972	0.776	0.838	0.805	0.809	0.816	0.829	0.949
03/01/2012	**12h**	1.583	1.254	1.256	1.298	1.188	1.184	1.173	1.558
03/01/2012	**15h**	1.309	1.175	1.205	1.271	1.25	1.186	1.209	1.277
03/01/2012	**18h**	0.886	0.845	0.843	0.866	0.789	0.697	0.815	0.897
03/01/2012	**21h**	0.857	0.776	0.845	0.821	0.797	0.786	0.832	0.842
04/01/2012	**00h**	1.728	0.861	0.918	0.856	0.818	0.846	0.892	1.742
04/01/2012	**03h**	0.927	0.748	0.804	0.777	0.834	0.788	0.788	0.915
04/01/2012	**06h**	0.712	0.595	0.614	0.657	0.542	0.532	0.566	0.675
04/01/2012	**09h**	0.573	0.484	0.545	0.478	0.426	0.445	0.455	0.596
04/01/2012	**12h**	1.346	0.568	0.542	0.548	0.558	0.529	0.57	1.361
04/01/2012	**15h**	0.856	0.552	0.564	0.493	0.507	0.525	0.555	0.871
04/01/2012	**18h**	0.742	0.63	0.657	0.628	0.581	0.575	0.604	0.709
04/01/2012	**21h**	1.073	1.065	1.045	1.075	1.019	0.946	1.071	1.099
05/01/2012	**00h**	1.721	1.401	1.48	1.469	1.407	1.297	1.314	1.764
05/01/2012	**03h**	1.785	1.389	1.47	1.439	1.412	1.342	1.4	1.829
05/01/2012	**06h**	1.684	1.656	1.689	1.648	1.608	1.668	1.61	1.658
05/01/2012	**09h**	1.565	1.537	1.579	1.528	1.495	1.556	1.501	1.558
05/01/2012	**12h**	1.941	1.505	1.545	1.485	1.49	1.431	1.444	1.932
05/01/2012	**15h**	1.745	1.353	1.396	1.501	1.319	1.424	1.345	1.737
05/01/2012	**18h**	0.961	0.906	0.918	0.947	0.908	0.839	0.924	0.996
05/01/2012	**21h**	0.687	0.563	0.585	0.582	0.502	0.406	0.52	0.678
06/01/2012	**00h**	0.854	0.632	0.663	0.682	0.651	0.677	0.64	0.805
06/01/2012	**03h**	0.787	0.583	0.652	0.582	0.571	0.603	0.648	0.816
06/01/2012	**06h**	0.463	0.339	0.382	0.336	0.301	0.301	0.333	0.446

Table 36. *Results of Run-Up 2% (m) from the numerical simulations for storm Andrea for all the profiles in Hautot-sur-Mer. Scale of colors are conditioned by the results of the simulations on all the profiles*

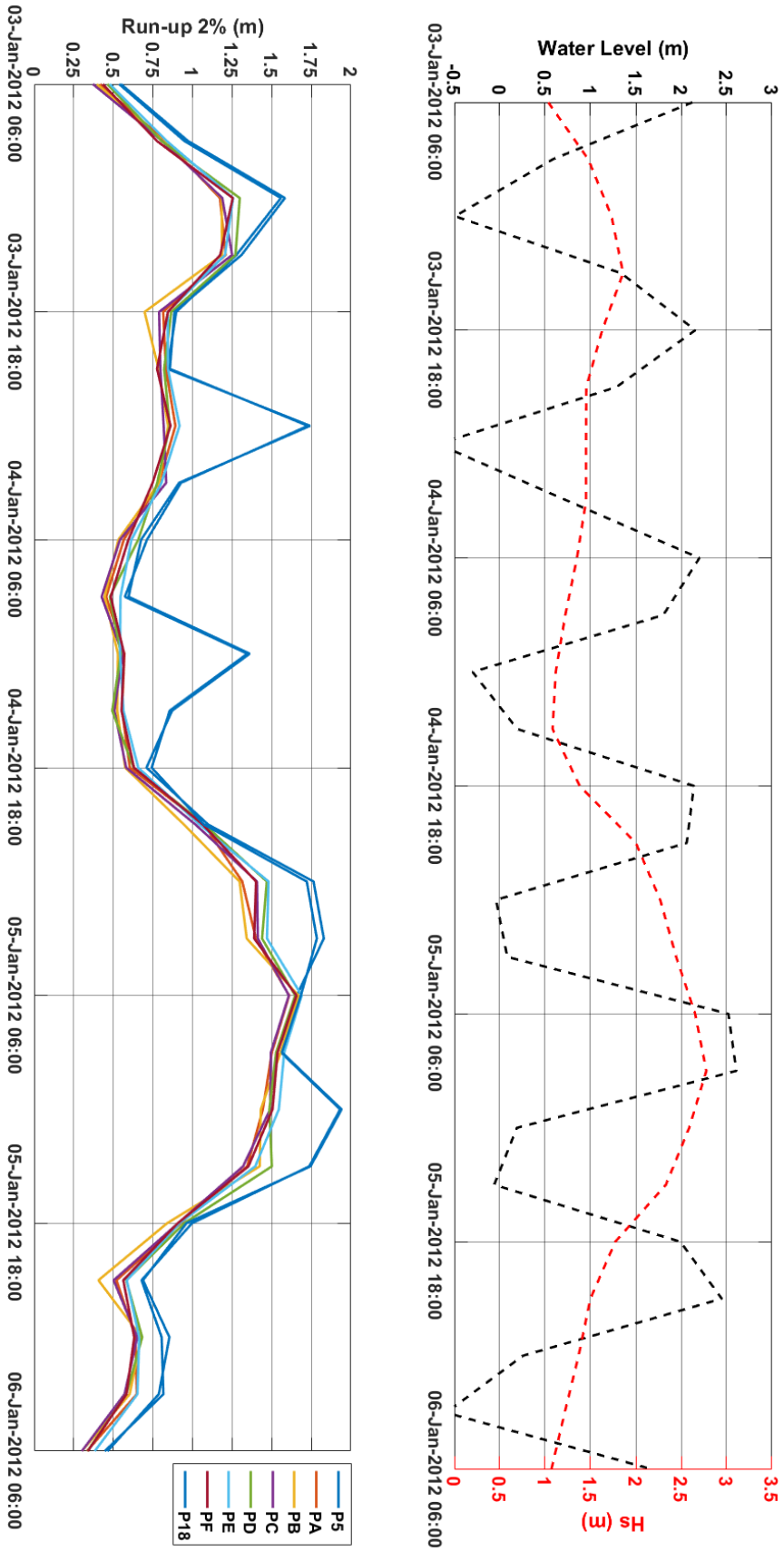

Figure 80. *Results of Run-Up 2% from the numerical simulations for storm Andrea for all the profiles in Hautot-sur-Mer. Black dotted line on the left y-axis corresponds to the water level set for each simulation and red dotted line on the right y-axis corresponds to the significant wave height of every sea state*

For storm Andrea, the water level has a smaller range, varying from -0.5 m to 2.5 m during the 3 days, so, in contrast to the previous storms analyzed, the results on the profiles between groins of $R_{u2\%}$ seem to follow much more the trends of the time series of H_s. For profiles P5 and P18 the same happens too, but there still a strong affection of the water level time series, reaching the maximum $R_{u2\%}$ of almost 2 m around the H_s only when the water level drops. But the worst scenario is 5th January at 6:00 or 9:00 with a $R_{u2\%}$ of 1.5 – 1.6 m, but with a water level reaching the 2.5 m above the MWL, but still under the the 1 m to 1.5 m of $R_{u2\%}$ reached in storm Ciara, but with a SWL of 3 and even 4 m, which, in combination, increases the risk of flooding.

The results of $R_{u2\%}$ for the last event, "Storm 19", are presented in **Table 37** and **Figure 81**.

Time		P18	PF	PE	PD	PC	PB	PA	P5
28/01/2013	**18h**	0.7	0.51	0.649	0.59	0.494	0.451	0.533	0.759
28/01/2013	**21h**	0.654	0.6	0.666	0.577	0.604	0.629	0.618	0.695
29/01/2013	**00h**	0.65	0.526	0.538	0.489	0.484	0.472	0.482	0.629
29/01/2013	**03h**	0.639	0.48	0.538	0.472	0.426	0.352	0.458	0.603
29/01/2013	**06h**	1.126	0.571	0.679	0.599	0.605	0.616	0.629	1.062
29/01/2013	**09h**	0.659	0.512	0.565	0.516	0.512	0.533	0.534	0.637
29/01/2013	**12h**	0.446	0.405	0.365	0.318	0.337	0.346	0.359	0.458
29/01/2013	**15h**	0.477	0.383	0.379	0.359	0.355	0.33	0.362	0.463
29/01/2013	**18h**	1.39	0.542	0.573	0.533	0.537	0.545	0.592	1.404
29/01/2013	**21h**	0.738	0.582	0.608	0.613	0.606	0.643	0.578	0.774
30/01/2013	**00h**	0.575	0.484	0.494	0.448	0.444	0.431	0.438	0.556
30/01/2013	**03h**	0.679	0.588	0.55	0.515	0.494	0.549	0.525	0.69
30/01/2013	**06h**	1.167	0.748	0.786	0.79	0.777	0.778	0.784	1.18
30/01/2013	**09h**	0.875	0.6	0.627	0.627	0.623	0.65	0.618	0.889
30/01/2013	**12h**	0.448	0.409	0.354	0.315	0.329	0.348	0.358	0.46
30/01/2013	**15h**	0.443	0.339	0.35	0.316	0.304	0.366	0.303	0.454
30/01/2013	**18h**	1.063	0.611	0.624	0.578	0.586	0.622	0.645	1.078
30/01/2013	**21h**	1.058	0.57	0.563	0.548	0.548	0.543	0.563	1.073
31/01/2013	**00h**	0.436	0.348	0.335	0.323	0.302	0.338	0.316	0.449
31/01/2013	**03h**	0.318	0.259	0.24	0.226	0.243	0.244	0.243	0.318
31/01/2013	**06h**	1.043	0.441	0.461	0.401	0.389	0.438	0.407	1.057
31/01/2013	**09h**	1.11	0.481	0.479	0.445	0.439	0.444	0.456	1.125
31/01/2013	**12h**	0.535	0.449	0.433	0.41	0.383	0.395	0.403	0.546
31/01/2013	**15h**	0.519	0.426	0.399	0.371	0.35	0.408	0.377	0.522
31/01/2013	**18h**	0.863	0.555	0.569	0.521	0.518	0.565	0.568	0.877

Table 37. *Results of Run-Up 2% (m) from the numerical simulations for "Storm 19" for all the profiles in Hautot-sur-Mer. Scale of colors are conditioned by the results of the simulations on all the profiles*

The $R_{u2\%}$ on the profiles between groins in Hautot-su-Mer presents an almost flat evolution in time, varying in a range from 0.3 to almost 0.8 m, but still on the sides, $R_{u2\%}$ grows to reach 1.4 m even if the H_s never gets higher than 1.3 m.

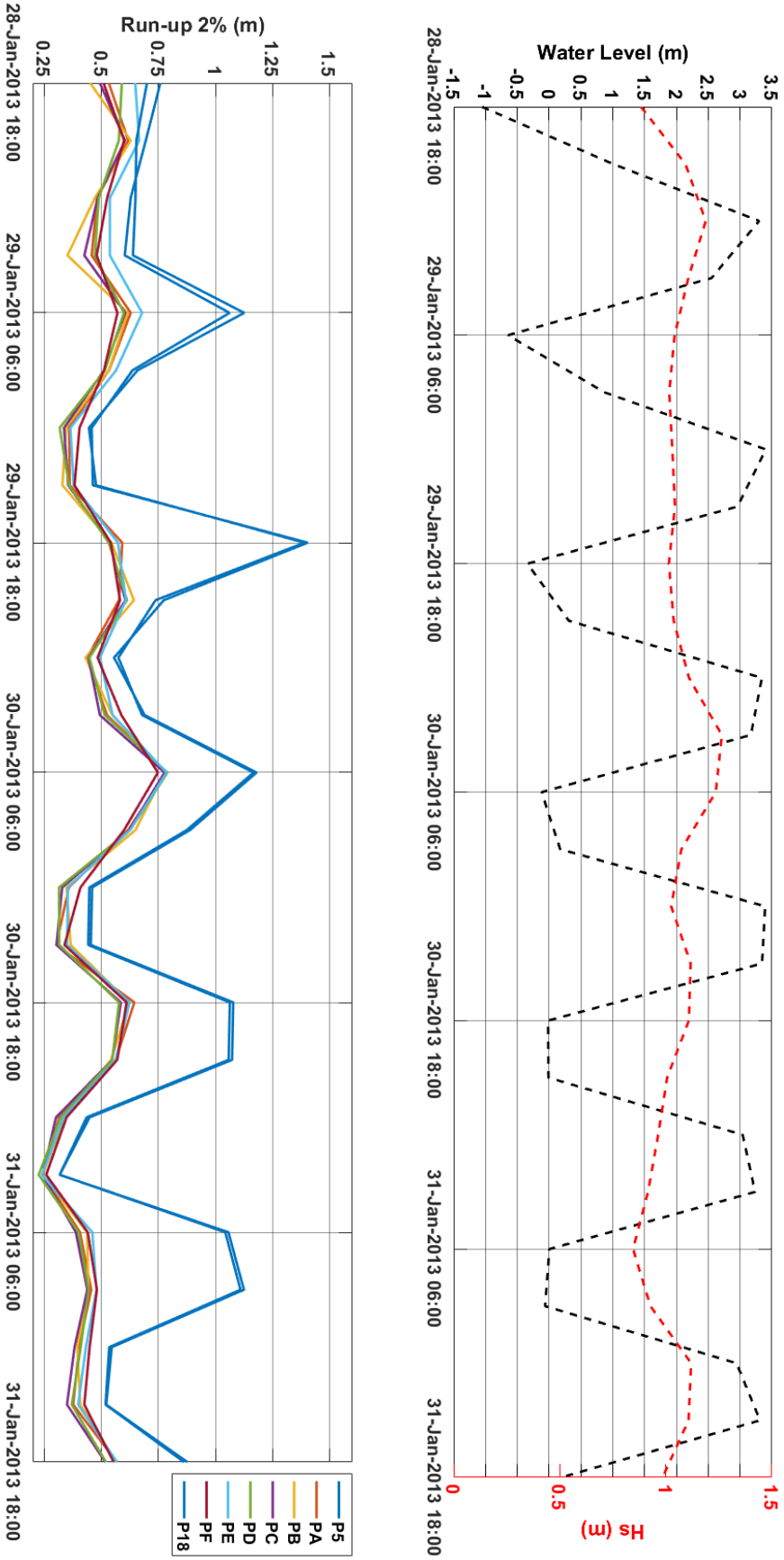

Figure 81. *Results of Run-Up 2% from the numerical simulations for "Storm 19" for all the profiles in Hautot-sur-Mer. Black dotted line on the left y-axis corresponds to the water level set for each simulation and red dotted line on the right y-axis corresponds to the significant wave height of every sea state*

5.4.3. Etretat

In Etretat just 5 profiles are studied because it is an enclosed beach and choosing profiles every 200 m gives enough information about the different characteristics about the storms arriving at the coast. The waves in Etretat arrive at the shoreline on the gravel part of the profiles whatever is the water level set for each simulation, since the inflexion point of change of sediment is too far underwater, behaving in the end as a gravel beach on this case. The $R_{u2\%}$ is obtained for each storm on the profiles, named from East to West P2 to P10 taking even numbers.

As in the previous study sites, the results for storm Ciara are presented in **Table 38** with the scale of colors conditioned to the variation of the $R_{u2\%}$ and in **Figure 82** including the comparison to the water level set for each simulation and the H_s of each sea state during the 3 days.

Time		P10	P8	P6	P4	P2
09/02/2020	**09h**	1.102	0.502	0.564	0.589	0.576
09/02/2020	**12h**	1.346	0.614	0.722	0.781	0.703
09/02/2020	**15h**	1.583	0.936	0.934	0.979	0.938
09/02/2020	**18h**	1.812	1.332	1.299	1.399	1.377
09/02/2020	**21h**	2.758	1.311	1.458	1.537	1.478
10/02/2020	**00h**	2.489	1.464	1.264	1.312	1.333
10/02/2020	**03h**	2.286	2.003	1.983	2.121	2.099
10/02/2020	**06h**	2.572	2.131	2.002	2.194	2.362
10/02/2020	**09h**	2.88	1.37	1.506	1.597	1.543
10/02/2020	**12h**	2.52	1.06	0.945	0.989	0.947
10/02/2020	**15h**	1.574	1.314	1.378	1.434	1.338
10/02/2020	**18h**	2.202	1.839	1.669	1.777	1.619
11/02/2020	**21h**	2.239	1.555	1.609	1.669	1.553
10/02/2020	**00h**	2.323	1.613	1.332	1.241	1.473
11/02/2020	**03h**	1.834	1.464	1.509	1.565	1.494
11/02/2020	**06h**	1.829	1.429	1.433	1.558	1.491
11/02/2020	**09h**	1.303	1.013	1.025	1.117	1.092
11/02/2020	**12h**	1.048	0.815	0.838	0.906	0.86
11/02/2020	**15h**	1.201	0.826	0.878	0.919	0.8
11/02/2020	**18h**	1.347	0.926	0.884	0.987	0.905
11/02/2020	**21h**	1.145	0.59	0.64	0.703	0.655
12/02/2020	**00h**	1.098	0.566	0.68	0.717	0.671
12/02/2020	**03h**	0.88	0.516	0.569	0.56	0.49
12/02/2020	**06h**	1.163	0.446	0.44	0.564	0.489
12/02/2020	**09h**	0.826	0.434	0.448	0.523	0.478

Table 38. *Results of Run-Up 2% (m) from the numerical simulations for storm Ciara for all the profiles in Etretat. Scale of colors are conditioned by the results of the simulations on all the profiles*

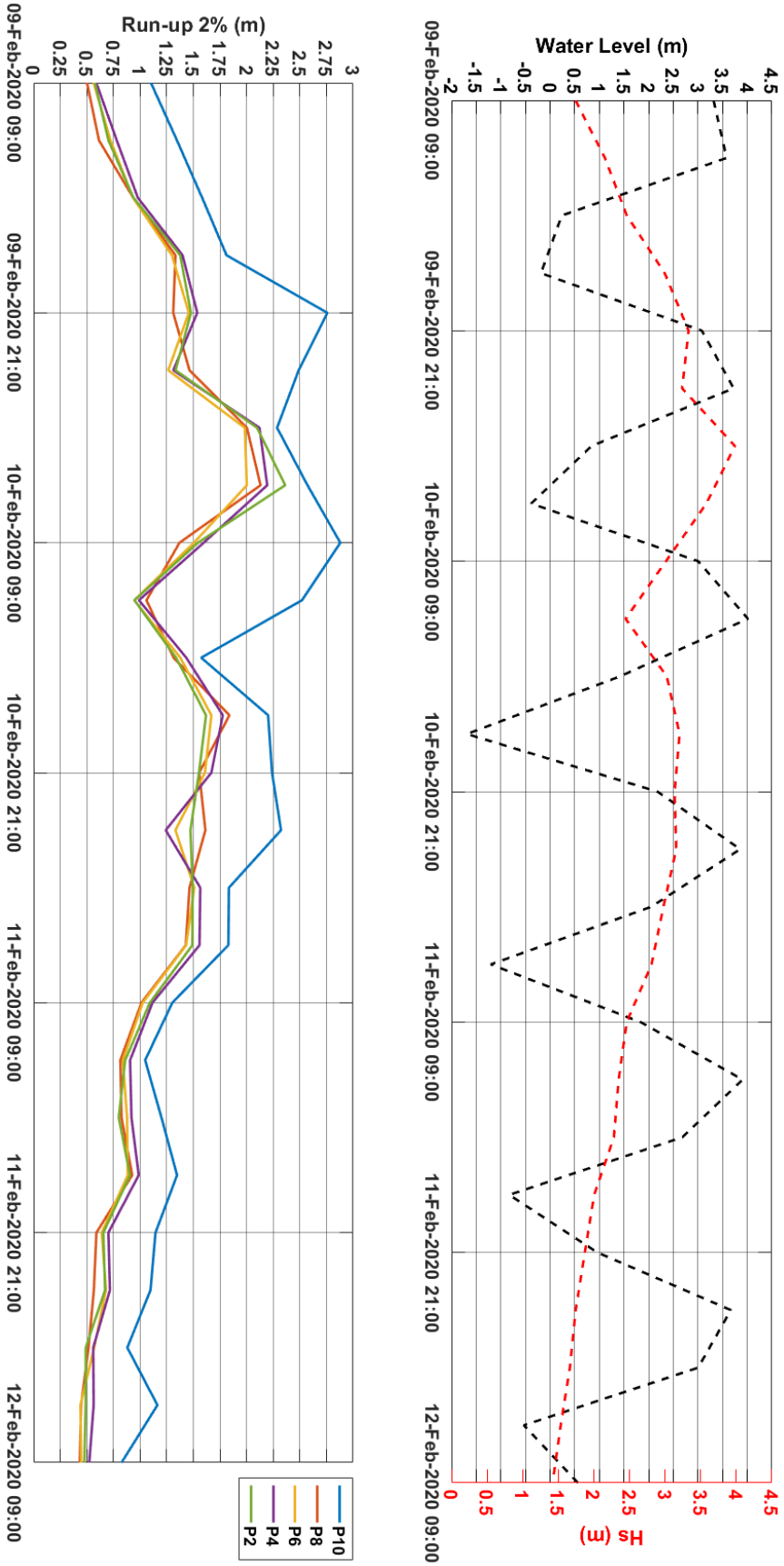

Figure 82. *Results of Run-Up 2% from the numerical simulations for storm Ciara for all the profiles in Etretat. Black dotted line on the left y-axis corresponds to the water level set for each simulation and red dotted line on the right y-axis corresponds to the significant wave height of every sea state*

It is noticeable that the trends of $R_{u2\%}$ for storm Ciara in Etretat follow much more the patterns of increasing and decreasing of the water level than the H_s, especially for the profile P10. The other profiles, P2 to P8, have a similar behavior in the results of $R_{u2\%}$. The H_s for this storm reaches a really high value of almost 4 m, and it remains over 2.5 m or even 3 m for most of the sea states of the storm, so, in combination with a high water level, the $R_{u2\%}$ reaches greater values in Etretat, probably due to the steep slope of the beach profile. Below the results of $R_{u2\%}$ of P10, the highest values are reached on profiles P4 and P2, and the lowest on profiles P6 and P8, being these two the ones taken in front of the populated area.

The results of $R_{u2\%}$ for storm Joachim can be seen in **Table 39** and **Figure 83** including, respectively, the scale of colors relative to the run-up and the time series of water level and significant wave height.

Time		P10	P8	P6	P4	P2
12/12/2011	**21h**	0.608	0.275	0.327	0.307	0.322
13/12/2011	**00h**	0.598	0.327	0.373	0.379	0.331
13/12/2011	**03h**	1.183	0.584	0.61	0.677	0.649
13/12/2011	**06h**	1.634	0.938	0.891	0.964	0.904
13/12/2011	**09h**	1.515	0.976	1.019	1.093	1.074
13/12/2011	**12h**	1.256	0.817	0.876	0.914	0.89
13/12/2011	**15h**	1.19	0.778	0.858	0.906	0.854
13/12/2011	**18h**	1.677	1.079	1.001	1.108	1.053
13/12/2011	**21h**	1.15	0.732	0.798	0.867	0.802
14/12/2011	**00h**	0.947	0.617	0.684	0.706	0.653
14/12/2011	**03h**	0.865	0.482	0.546	0.541	0.537
14/12/2011	**06h**	1.21	0.569	0.573	0.678	0.592
14/12/2011	**09h**	0.683	0.29	0.324	0.356	0.308
14/12/2011	**12h**	0.614	0.352	0.381	0.403	0.344
14/12/2011	**15h**	0.731	0.396	0.462	0.421	0.437
14/12/2011	**18h**	1.173	0.462	0.462	0.59	0.487
14/12/2011	**21h**	1.058	0.383	0.388	0.481	0.408
15/12/2011	**00h**	0.73	0.438	0.464	0.489	0.42
15/12/2011	**03h**	0.828	0.501	0.511	0.538	0.487
15/12/2011	**06h**	1.643	1.175	1.136	1.19	1.141
15/12/2011	**09h**	1.502	1.008	1.05	1.125	1.043
15/12/2011	**12h**	1.63	0.781	0.833	0.871	0.866
15/12/2011	**15h**	1.209	0.836	0.883	0.921	0.807
15/12/2011	**18h**	1.46	0.658	0.691	0.777	0.685
15/12/2011	**21h**	1.277	0.555	0.585	0.659	0.584

Table 39. *Results of Run-Up 2% (m) from the numerical simulations for storm Joachim for all the profiles in Etretat. Scale of colors are conditioned by the results of the simulations on all the profiles*

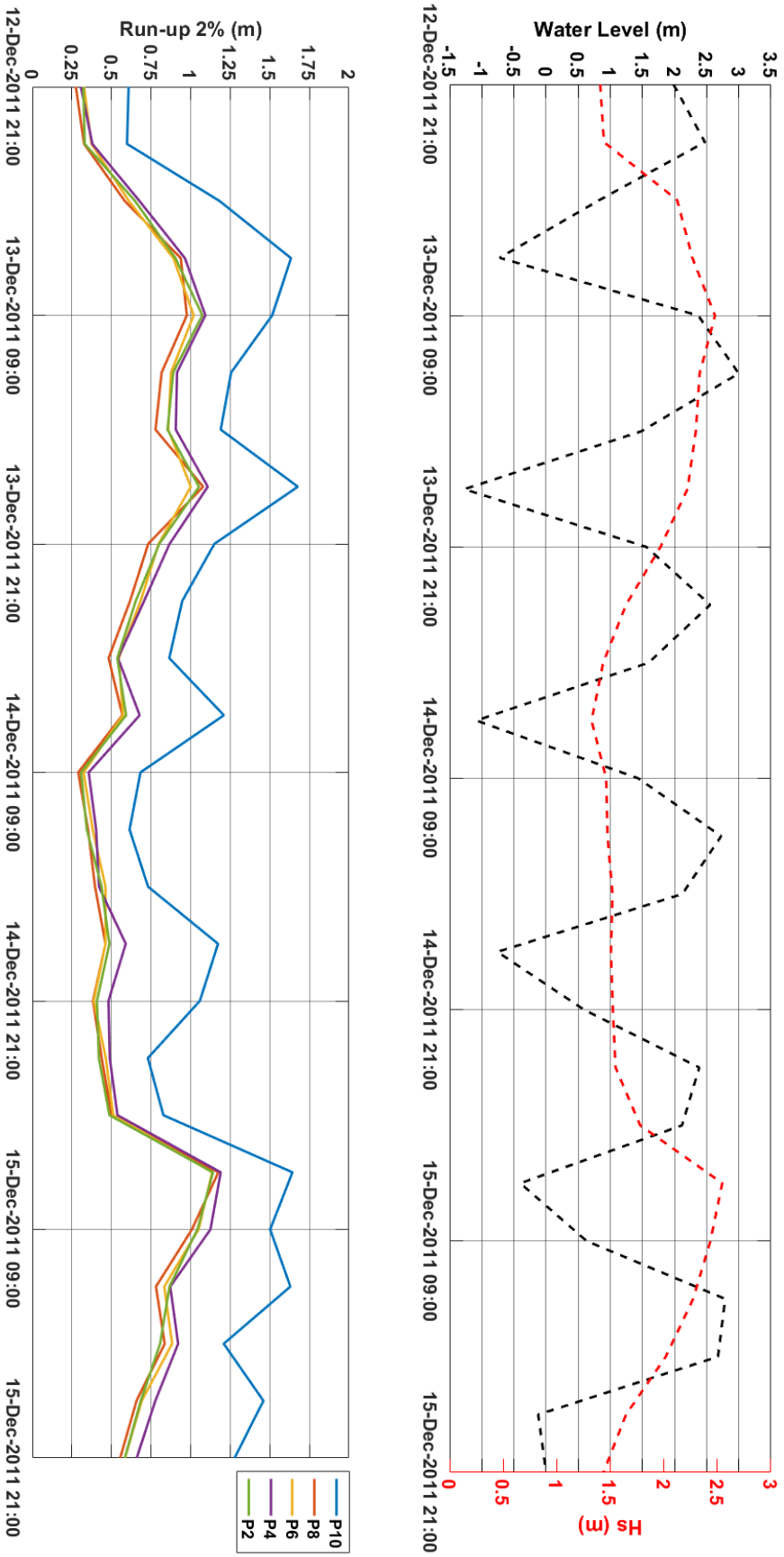

Figure 83. *Results of Run-Up 2% from the numerical simulations for storm Joachim for all the profiles in Etretat. Black dotted line on the left y-axis corresponds to the water level set for each simulation and red dotted line on the right y-axis corresponds to the significant wave height of every sea state*

For storm Joachim, the difference in the results of $R_{u2\%}$ between P10 and the other profiles is bigger than for storm Ciara, with the greatest values around the two possible peaks of the storm. The time series of all the profiles follow clearly the trends of water level, not having, apparently, a big influence the values of H_s on the $R_{u2\%}$. Again, the results obtained from highest to lowest seem to be P4, P2, P8 and P6 below the $R_{u2\%}$ obtained on P10.

The third storm, Andrea, gives the results of $R_{u2\%}$ shown in **Table 40** and **Figure 84**.

Time		P10	P8	P6	P4	P2
03/01/2012	**06h**	0.674	0.18	0.162	0.271	0.217
03/01/2012	**09h**	1.609	0.962	0.952	1.046	0.992
03/01/2012	**12h**	1.85	1.055	1.026	1.149	1.084
03/01/2012	**15h**	1.328	0.903	0.87	0.998	0.925
03/01/2012	**18h**	1.158	0.656	0.594	0.79	0.696
03/01/2012	**21h**	1.238	0.644	0.632	0.75	0.694
04/01/2012	**00h**	1.659	0.928	0.888	1.005	0.933
04/01/2012	**03h**	1.252	0.729	0.721	0.878	0.791
04/01/2012	**06h**	0.85	0.358	0.326	0.466	0.389
04/01/2012	**09h**	0.842	0.314	0.305	0.423	0.346
04/01/2012	**12h**	1.197	0.36	0.341	0.483	0.416
04/01/2012	**15h**	0.93	0.371	0.378	0.464	0.377
04/01/2012	**18h**	0.828	0.312	0.28	0.419	0.343
04/01/2012	**21h**	1.334	0.962	0.949	1.061	0.983
05/01/2012	**00h**	2.243	1.425	1.573	1.576	1.49
05/01/2012	**03h**	1.956	1.644	1.666	1.669	1.578
05/01/2012	**06h**	1.674	1.354	1.292	1.491	1.406
05/01/2012	**09h**	1.725	1.419	1.373	1.537	1.449
05/01/2012	**12h**	2.059	1.743	1.659	1.834	1.728
05/01/2012	**15h**	2.037	1.521	1.518	1.602	1.601
05/01/2012	**18h**	1.246	0.706	0.643	0.85	0.758
05/01/2012	**21h**	0.941	0.413	0.367	0.515	0.439
06/01/2012	**00h**	1.37	0.521	0.514	0.633	0.56
06/01/2012	**03h**	1.735	0.336	0.318	0.454	0.387
06/01/2012	**06h**	0.531	0.132	0.114	0.205	0.152

Table 40. *Results of Run-Up 2% (m) from the numerical simulations for storm Andrea for all the profiles in Etretat. Scale of colors are conditioned by the results of the simulations on all the profiles*

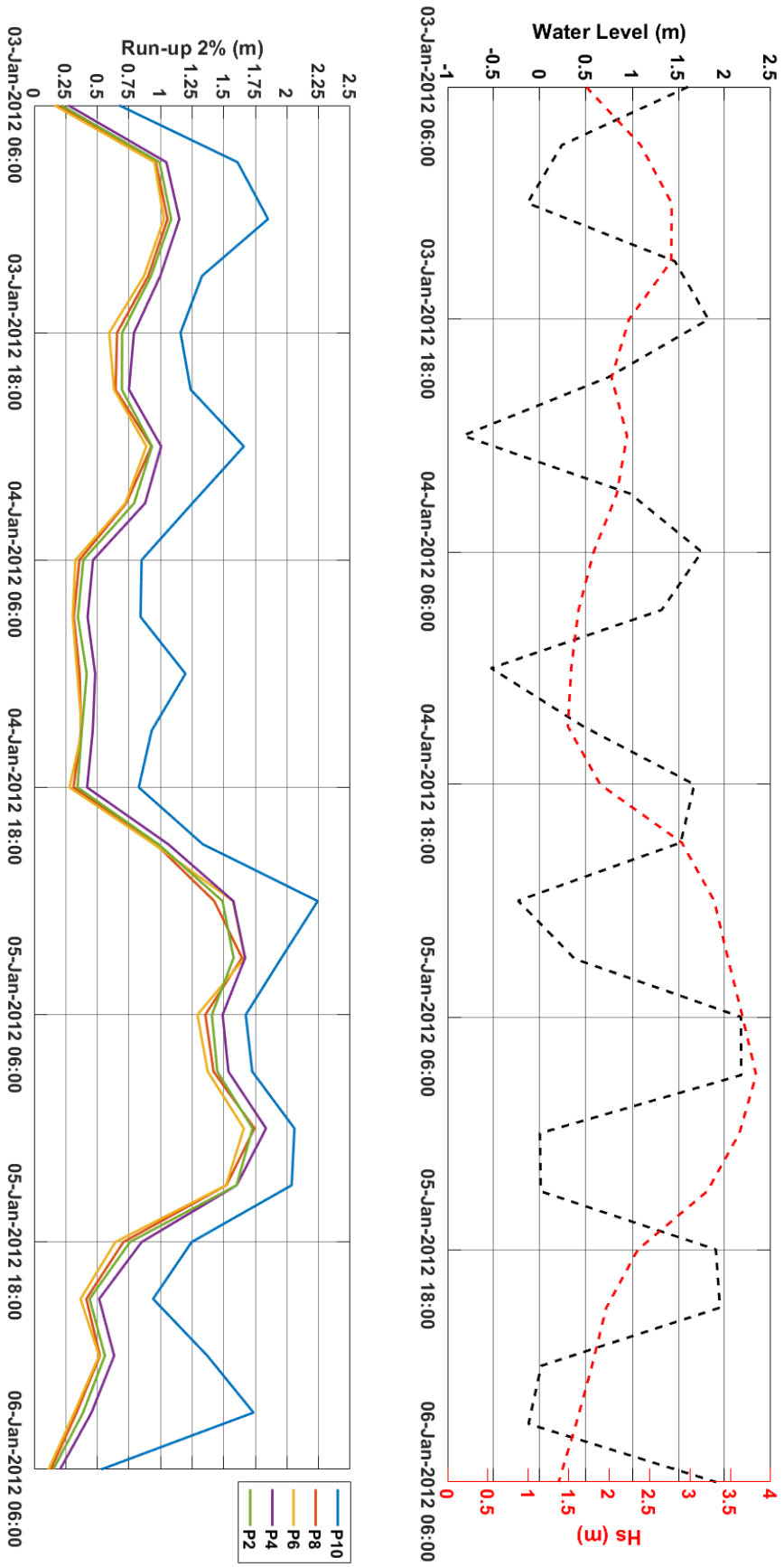

Figure 84. *Results of Run-Up 2% from the numerical simulations for storm Andrea for all the profiles in Etretat. Black dotted line on the left y-axis corresponds to the water level set for each simulation and red dotted line on the right y-axis corresponds to the significant wave height of every sea state*

Keeping the difference on the results of $R_{u2\%}$ between P10 and the other profiles, the results of storm Andrea coincide more with the time series of H_s than in storms Ciara and Joachim, due to the short range of values in the forcing of water level. The peak of H_s for this event almost reaches 4 m, coincident with a high water level, but the sea states around the peak, with lower water levels give greater values of $R_{u2\%}$. Nevertheless, considering that it is the combination of those factors what produces the risk of flooding, it is remarkable that the $R_{u2\%}$ remains at ~1.3 m for the profiles P6 and P8, the ones that measure the hazard for the population.

Finally, the results of "Storm 19" in Etretat of $R_{u2\%}$ are the values presented in **Table 41** and **Figure 85**.

Time		P10	P8	P6	P4	P2
28/01/2013	**18h**	1.074	0.326	0.362	0.435	0.361
28/01/2013	**21h**	1.355	0.566	0.564	0.661	0.586
29/01/2013	**00h**	0.85	0.539	0.6	0.56	0.564
29/01/2013	**03h**	0.736	0.452	0.482	0.505	0.479
29/01/2013	**06h**	1.214	0.429	0.466	0.53	0.467
29/01/2013	**09h**	1.137	0.423	0.432	0.516	0.427
29/01/2013	**12h**	0.623	0.38	0.425	0.415	0.362
29/01/2013	**15h**	0.956	0.409	0.446	0.469	0.469
29/01/2013	**18h**	1.41	0.415	0.449	0.509	0.431
29/01/2013	**21h**	1.24	0.445	0.459	0.576	0.477
30/01/2013	**00h**	0.784	0.493	0.522	0.553	0.498
30/01/2013	**03h**	0.841	0.581	0.619	0.631	0.55
30/01/2013	**06h**	1.329	0.531	0.537	0.645	0.564
30/01/2013	**09h**	0.994	0.425	0.466	0.536	0.473
30/01/2013	**12h**	0.575	0.334	0.383	0.379	0.329
30/01/2013	**15h**	0.967	0.418	0.455	0.479	0.477
30/01/2013	**18h**	0.763	0.396	0.399	0.489	0.407
30/01/2013	**21h**	1.185	0.555	0.522	0.667	0.579
31/01/2013	**00h**	0.6	0.306	0.371	0.329	0.355
31/01/2013	**03h**	0.57	0.295	0.34	0.334	0.347
31/01/2013	**06h**	0.789	0.238	0.252	0.326	0.236
31/01/2013	**09h**	1.101	0.373	0.397	0.536	0.441
31/01/2013	**12h**	0.646	0.324	0.405	0.367	0.397
31/01/2013	**15h**	0.699	0.444	0.497	0.484	0.425
31/01/2013	**18h**	0.716	0.326	0.339	0.374	0.361

Table 41. *Results of Run-Up 2% (m) from the numerical simulations for "Storm 19" for all the profiles in Etretat. Scale of colors are conditioned by the results of the simulations on all the profiles*

The results of $R_{u2\%}$ are coherent with what is exposed in the previous storms, with a big difference between P10 and the rest of the profiles. Taking into account only the profiles from P2 to P8, the $R_{u2\%}$ only varies between 0.1 m to a maximum of no more than 0.7 m, since neither the H_s takes values over 2 m.

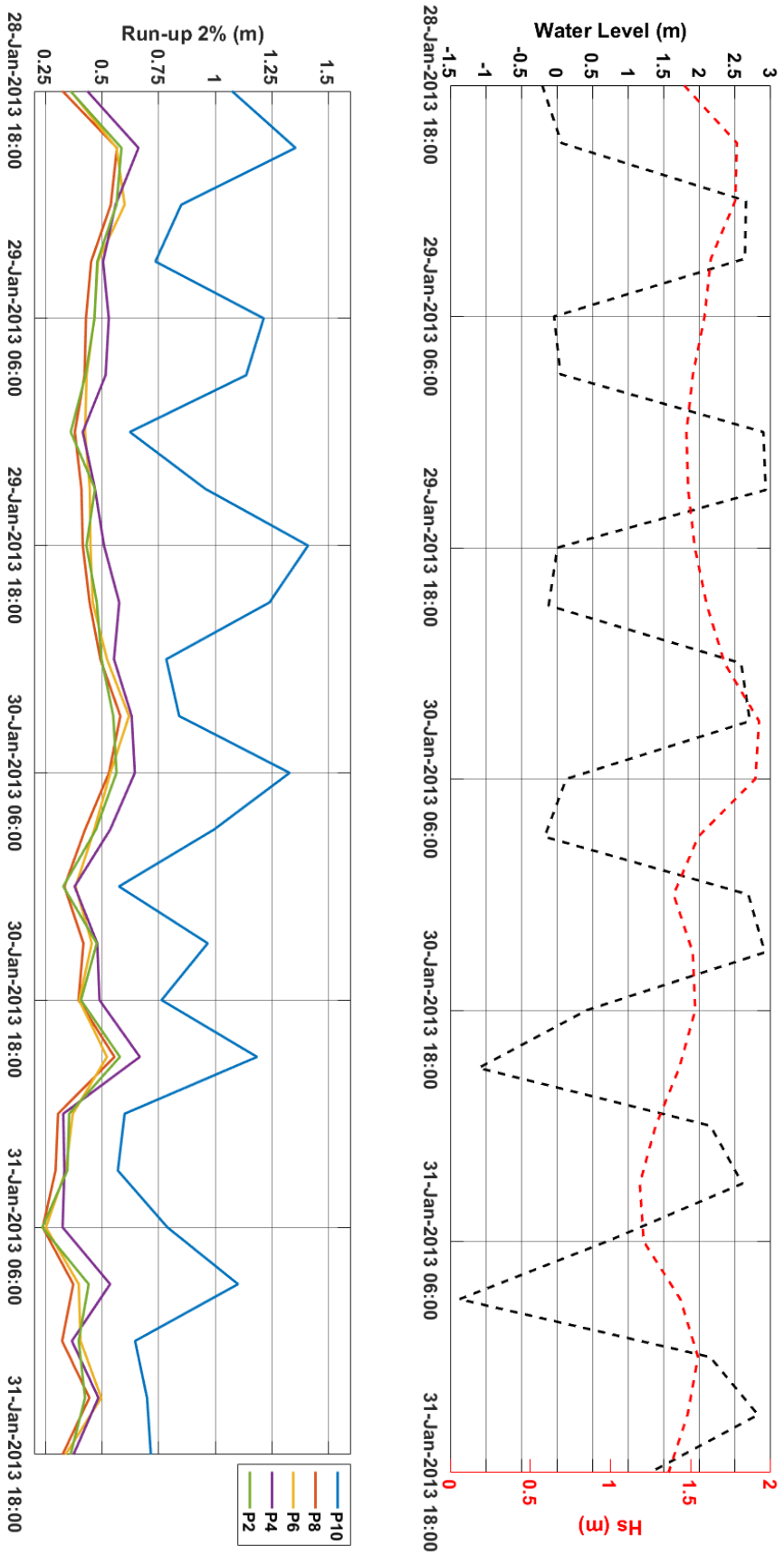

Figure 85. *Results of Run-Up 2% from the numerical simulations for "Storm 19" for all the profiles in Etretat. Black dotted line on the left y-axis corresponds to the water level set for each simulation and red dotted line on the right y-axis corresponds to the significant wave height of every sea state*

5.5. VARIATION IN DIFFERENT SYSTEMS: FROM SANDY TO MIXED AND GRAVEL BEACHES

As demonstrated in this chapter dealing with the response of different morphological contexts to a series of marine storms, the $R_{u2\%}$ is more influenced by the effects of water level of each state rather than those of H_s. Indeed, the combination of medium to high values of both variables could produce the highest value of $R_{u2\%}$. For Villers-sur-Mer, the sandy beach, the $R_{u2\%}$ seems to grow in concordance with the increase of water level and decreases also accordingly, but not with a strong connection. However, Hautot-sur-Mer and Etretat present a clear relationship between the results of $R_{u2\%}$ and the forcing of water level. At both sites, the $R_{u2\%}$ is always higher when the water level drops and the opposite, it is reduced when the water level is greater. The difference between Villers-sur-Mer and the two sites of Etretat and Hautot-sur-Mer is mainly explained by the slope of the beach profile, much smoother for the sandy beach and steeper for the gravel beaches. Although Hautot-sur-Mer is considered as a mixed beach, with presence of pebbles and sand, a high water level leaves the inflexion point, point of change from gravel to sand on the profile, further underwater behaving as a gravel beach like Etretat.

Nonetheless, Storm Andrea gives an exception compared to the aforementioned results. For the three study sites, the results of $R_{u2\%}$ during the 3 days simulated on the model follow the patterns of the forcing of H_s much more than for the other events. Even if it is still influenced by the forcing of water level, the trends match with the wave height, especially for Villers-sur-Mer. This is justified by the smaller range of water level in comparison to the other storms. For the rest, the water level set for the 25 simulations varies more than 4 meters, and even almost 6 meters during storm Ciara, but for storm Andrea the range stays under 3 meters, such that the waves propagate only around a limited part of the profile. Considering that the beach profiles do not have a constant slope, keeping the interaction between the surface of water and the topography on a restricted part of the profile produces that the slope remains similar. Then, the water level has less effect on the results, and the H_s has a stronger influence on the $R_{u2\%}$.

A few sea states among all the storms, mainly the initial sea states of most of the simulated events, barely produce any $R_{u2\%}$, being even 0 meters for some of them. This circumstance has a clear explanation, because all these sea states have a common characteristic: the forcings of H_s and T_p have very low values, particularly the peak period. When the T_p is around ~3 seconds, the waves cannot reach the shore with a wave length long enough to uprush the beach, especially in combination with a low value of H_s. The steeper slope of Etretat in comparison to the other study sites seems to reduce this effect, letting the $R_{u2\%}$ reach 0.2 or 0.3 meters.

But, in general, the $R_{u2\%}$ tends to take higher values in Etretat, not only for the situation described, but for all the sea states. Then, it is in Hautot-sur-Mer where the $R_{u2\%}$ is greater, being the smallest in Villers-sur-Mer. The location and bathymetry of the three study sites conditions this situation, because, among the three, Etretat is more exposed to the open sea and presents a steeper slope on the bathymetry, growing rapidly in depth, which allows the waves to arrive stronger. In Etretat, the 10 meters of depth are reached in just 500 meters from the shoreline at the LAT. Reaching the same depth in Hautot-sur-Mer needs almost 2 kilometers and more than 6 kilometers in Villers-sur-Mer. This configuration of the bathymetry protects the two beaches and makes the waves arrive weaker in Villers-sur-Mer than in Hautot-sur-Mer, and there than in Etretat. This is straightly reflected on the forcings of the model, with a smaller H_s and then, a smaller $R_{u2\%}$ too in Villers-sur-Mer and Hautot-sur-Mer.

Taking a look at all the profiles of the three study sites, it is noticeable that the modulations of the results of the $R_{u2\%}$ in profile P10 of Etretat and in the profiles on the sides P5 and P18 of Hautot-sur-Mer have a strong similitude. All the three profiles have a similar configuration, with a smoother slope on P10 in Etretat in comparison to the rest of the profiles of the same beach, and on P5 and P18 than on the rest of the profiles of Hautot-sur-Mer, and the cliffs at the end of the profiles limiting the $R_{u2\%}$ to grow in height.

The same happens with the profiles between groins in Hautot-sur-Mer, PA to PF, and the profiles in front of the populated area in Etretat, P6 to P8, all of them with a vertical wall at the end of the profiles. The beach in Hautot-sur-Mer is sustained by the groins with a steeper slope because of the presence of pebbles, and something similar happens in Etretat, with the groins partially holding the pebbles, although the situation is different since Etretat is an enclosed beach. The steep slopes and the presence of pebbles seem to reduce the effect of waves, attenuating the H_s when it arrives to the shoreline and producing less $R_{u2\%}$. Then, holding the pebbles with groins on the sides of the beach and a vertical wall at the end of the profiles happens to be an effective action to reduce the $R_{u2\%}$, protecting, this way, the population located nearshore.

5.6. STUDY OF WAVE BREAKING IN SWASH

This section presents a summary of a study to investigate the interest in using multiple vertical layers for numerically simulating wave-breaking in SWASH. The full study is presented in

Appendix E. This work has been carried out in the framework of the master internship of Pierre Chauris under the supervision of M2C (Imen Turki) and ENPC (Marisa Yates).

For this study, the simulations have been carried out in profile P13 of Villers-sur-Mer, previously presented (**Figure 65** and **Figure 66**). In SWASH, wave breaking is considered as a discontinuity of the free surface, that can be detected with a sufficient vertical resolution of more than $k = 10$ layers. Otherwise, SWASH still offers a way to manually control the initiation and termination of wave breaking, that can be expressed in terms of the temporal variation of the free surface ζ and the depth h, with formulations dependent on α and β, which are user-defined parameters.

The interest relays on investigating the effects of α and β on the breaking zone estimation. By varying one parameter while keeping the others fixed, it is possible to see the effect of this isolated parameter on the model. When β is fixed (**Figure 86**a), it can be seen that as α increases, the initiation of wave breaking is identified closer to the coast. As β is fixed, the end of wave breaking is identical. When α is constant (**Figure 86**b), increasing β will trigger the breaker to stop earlier, which is consistent again with the definition. Since the position and width of the breaking area are strongly dependent on the parameters α and β, a validation process is required to find out which configuration actually corresponds to the real breaking zone. The simulated breaking zone is then compared with real measurements obtained from the VMS.

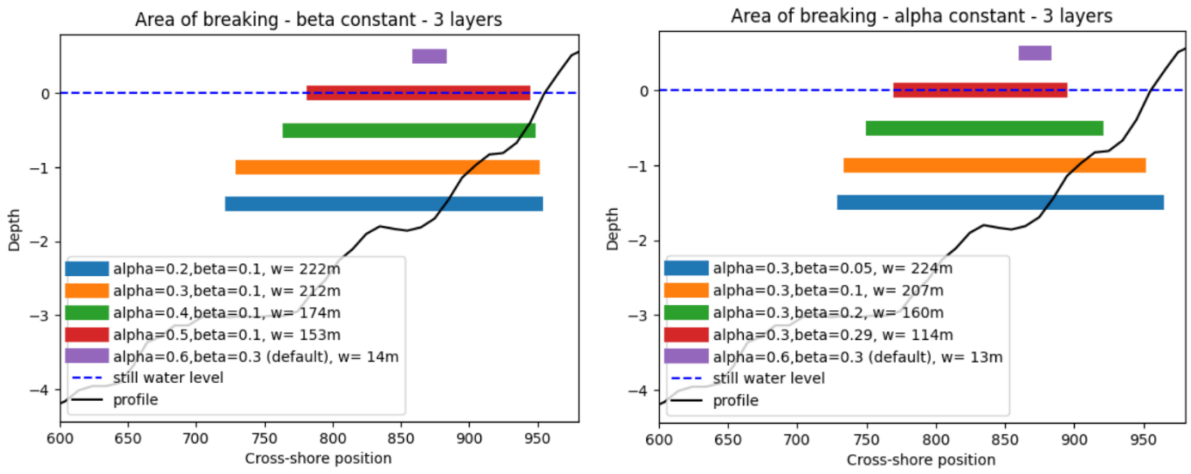

Figure 86. *Sensitivity of the breaking area to α and β for a fixed number of layers (k = 3): a) Influence of α with β constant, and b) Influence of β with α constant. Internship of Pierre Chauris (2024)*

The significant wave height at breaking H_b is extracted from timestacks as described in Almar et al. (2012), based on the fact that breaking waves produce foam. The method consists first in extracting the breaking position from a timestack and then extracting the breaker height. The results are presented in **Figure 87**.

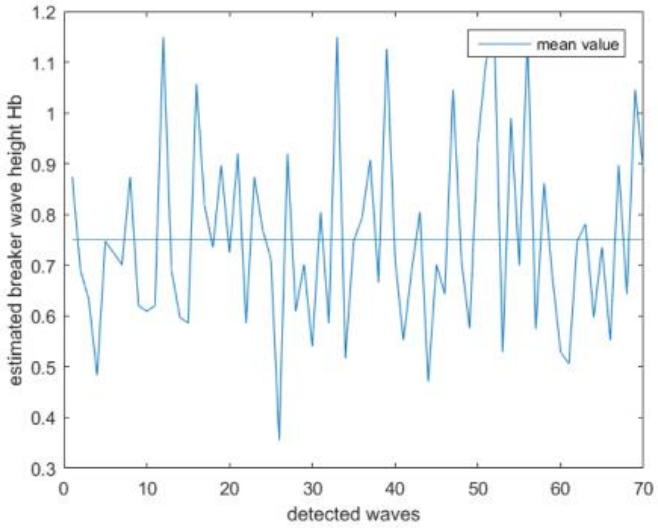

Figure 87. *Estimated breaking position across the timestack. Internship of Pierre Chauris (2024)*

To test the methodology, the H_b obtained from timestacks is compared with the values obtained by the SWASH simulation during February 2020, with multiple storms hitting the Normandy coast, including Ciara storm. A SWASH simulation is performed every day for the sea state corresponding to the highest energy conditions for the comparisons between the SWASH simulations and the VMS observations. The obtained values for H_b are compared in **Figure 88**, noticing an overall agreement between the two methods.

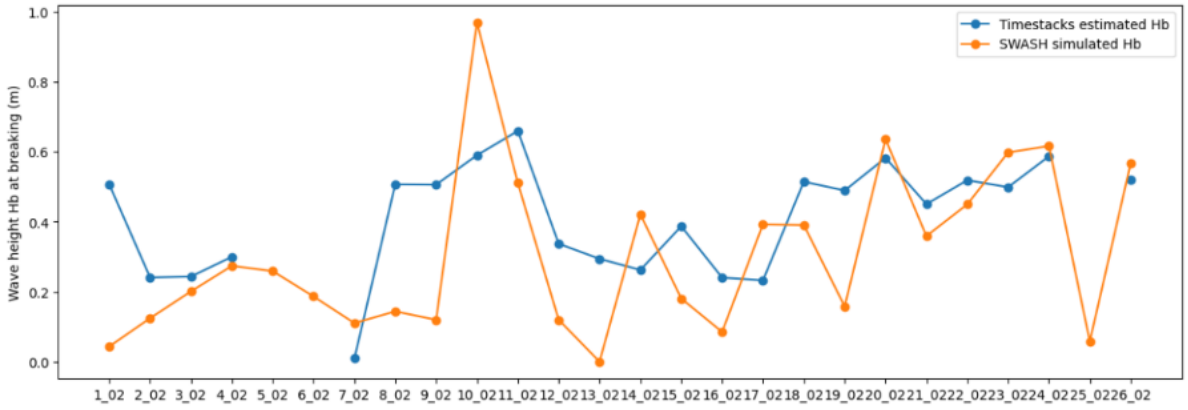

Figure 88. *Comparison between the wave height at breaking simulated with SWASH and extracted from timestacks. Internship of Pierre Chauris (2024)*

Finally, a comparison between breaking distribution simulated in SWASH and breaking obtained from the observed timestacks is conducted, for the same scenario presented. It is possible to extract the breaking area from the timestacks, since breaking is characterized by foam corresponding to a high-intensity variation in the timestack. The process with SWASH and with the observed timestacks is compared in **Figure 89**.

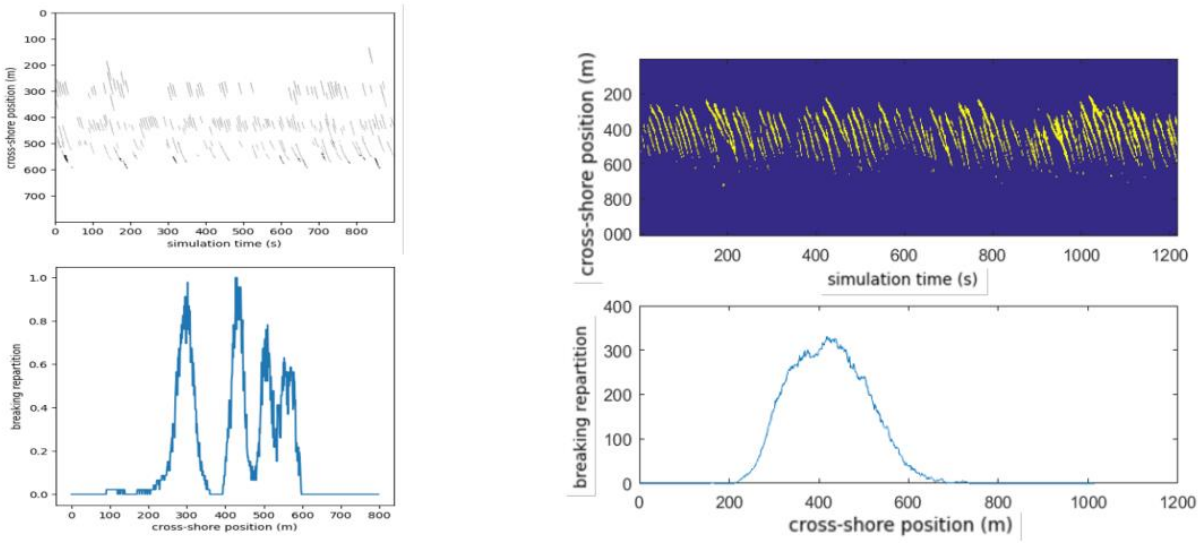

Figure 89. *Comparison between simulation and image extraction of wave breaking repartition: a) Binary map and associated distribution over a 10-minute duration from SWASH and b) Binary map and associated repartition over a 10-minute duration from timestack. Internship of Pierre Chauris (2024)*

Finally, the comparison is conducted over February 2020, with the same scenario presented for wave height comparisons. Many SWASH simulations were performed, with different combinations of k, α and β, and the results giving the best comparison between SWASH simulations and timestacks extraction are presented in **Figure 90**.

The breaking configuration of SWASH giving the best results is the combination of a number of layers of $k = 3$, and, for controlling the position and width of the breaking area, $\alpha = 0.3$ and $\beta = 0.1$. The position and the width of the breaking zone obtained from simulations and image processing are overall accurate.

5.7. DISCUSSION AND CONCLUSIONS

This work highlights the difficulty of simulating the hydrodynamics of gravel beaches with numerical modelling. The gravel beaches are conformed by pebbles in Etretat and Hautot-sur-Mer and are defined by characteristics that differentiate them from the sandy beaches like the permeability or the porosity. In this study the gravels are considered as a porous media and have been set up on the SWASH model as porous structures located on the impermeable layers equivalent to the sand that can be found under the pebbles on these beaches. This fact has allowed to increase the number of vertical layers to 20 in comparison to the 10 used in Villers-sur-Mer, the other beach simulated totally conformed by sand, but they were also necessary to accurately reproduce the hydrodynamics through the porous layers, including the information of the sediment size (d_{50} = 7.1 cm for Hautot-sur-Mer and d_{50} = 5.2 for Etretat).

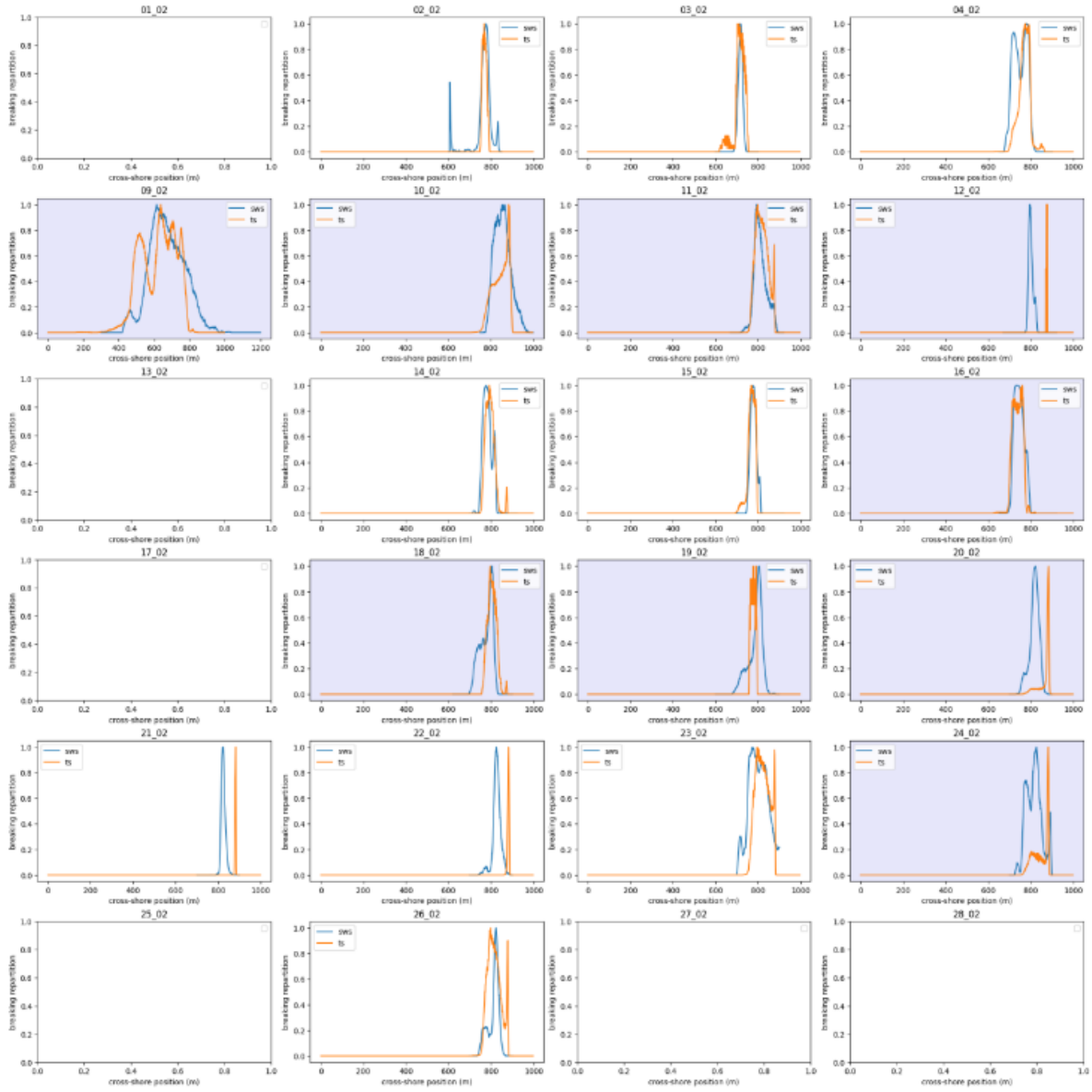

Figure 90. *Comparison of the breaking repartition obtained from SWASH and from timestack images. Plots with a colored background correspond to days during a storm. Internship of Pierre Chauris (2024)*

Including more than 20 layers in the gravel beaches and more than 10 in the sandy beach complicates the calculations during the simulations and causes that some of them become unstable before the 3 hours set for every simulation, not giving appropriate results. Other studies (Mellink, 2012) have found the same problems when setting up the porosity in SWASH, determining that, according to his study, SWASH tends to underestimate reflection while overestimates transmission, which justifies the underestimation on the results of run-up obtained for the two gravel beaches. Moreover, Alabart Llinàs et al. (2013), after several tests in one and two dimensions, prove that, by including a porous structure in the model, the instability is notably increased, leading to a sudden end of some simulations.

Nevertheless, SWASH is a preferable option when a high number of simulations have to be carried out. In SWASH, a minimum number of 10 vertical layers should be included for accurately computing the phase velocity and the breaking wave front. Furthermore, the "conditioning area" added at the beginning of the profile of more than 2 wave lengths for the highest periods (in this case, ~200 m), allows the waves to propagate on the real profile with the desired shape. Also, being SWASH a phase-resolving model, the cross-shore grid spacing Δx of 1 m on the cells is also appropriate, typically keeping the relation $L_0/\Delta x$ between 50 and 100 for this kind of models. Increasing the resolution by reducing Δx led to a higher number of instabilities after some tests already caried out for these study sites.

XBeach was also considered for this study. The model presents two main modes, the XBeach Nonhydrostatic (XB-NH), which also resolves the NLSW equations with a non-hydrostatic pressure correction term, and the XBeach Surfbeat (XB-SB), that solves the wave-action equation, being a phase-averaged model, the reason why this mode of XBeach was straightly discarded. In comparison to XB-NH, SWASH allows including a varying number of vertical layers not averaging the results in depth, while the maximum number of vertical layers in XB-NH is two. Using XB-NH with no definition of the vertical distribution is equivalent to one-layer modelling with SWASH. The use of depth averaging models as XB-NH could decrease considerably the computational time, but previous studies (Lashley et al., 2018; Zhang et al., 2019) found that depth-averaged models were unable to accurately estimate the evolution of the surface of water due to their lack of vertical resolution. In the opposite side, there are the Boussinesq-type models and the depth-resolving models that solves the Navier-Stokes equations, but which require a much higher computational demand, not always leading to more accurate results (a full comparison of the use of the different numerical models and their application on the simulation of waves and their interaction with coastal structures can be found in Lashley et al. (2021), which was used as a base for the election of the most appropriate model in this study).

The validation of the results of run-up obtained from the numerical simulations also highlights the difficulty of finding the most satisfactory formulation that accurately parametrizes the run-up, especially when it happens over gravel beaches. The two formulations applied in this study (EurOtop, 2018; Stockdon et al., 2006) show similar trends to the results obtained from the numerical simulations in Villers-sur-Mer, the sandy beach where the waves propagate over an impermeable layer, particularly the formulation of Stockdon et al. (2006). The main problem on the parametrization of wave run-up comes from the way the energy is calculated, relying entirely on the offshore wave spectrum using wave statistical and spectral parameters, as stated by Vousdoukas et al. (2012), which is a simplification and possible source of errors. Additionally, the

present study highlights the obstacle on the formulations produced by the introduction of a constant value of the Iribarren number, with just one value of slope, when, on real profiles, this slope is variable with larger differences in the case of mixed beaches, especially on the inflexion point, change from the sandy layer to the pebbles.

For these reasons, the validation of the results of the numerical simulations can be performed using images obtained from VMS. Even considering the numerous limitations from both the numerical modelling and the records from videocameras, the results seem to be satisfactory enough. For this study, the images used for the validation have been the timestacks, presenting wave by wave the run-up on the beach for every interval of 10 minutes. Since the sea states propagated on the model cover a period of 3 hours with the highest water level set for each simulation, the timestack of 10 minutes with the highest water level within the 3 hours of every sea state has been taken for validation. With every pair of results of outputs of the model and timestacks, the 2% exceedance of the time series of run-up can be compared, because this variable just depends on the number of incoming waves and not on the time during which it is calculated.

For Villers-sur-Mer, with the images allowing to measure the $R_{u2\%}$ because of the smoother slope of the beach in comparison to the other two study sites, the GUI interface developed by Vousdoukas et al. (2012) gives similar results to those obtained from SWASH, being the validation limited to the daylight and the availability of records during the days of the storms selected. For Etretat and Hautot-sur-Mer, this validation had to be performed considering the presence of a vertical wall at the end of the two beaches, reached by the run-up of waves during the storms and occasionally overtopped, precisely the circumstance used for validating the results. Even if the results show similar trends, again, the complication of numerically reproducing the presence of pebbles in gravel and mixed beaches is of great importance. Soloy et al. (2024) have demonstrated that parametrizing this kind of sediment through the permeability, instead of through porosity as in the present study, using the numerical model XBeach leads to more difficulties when realizing the morphodynamics also plays an important role.

The simulation of flooding during extreme storms and its validation using VMS in the complex coastal systems of Normandy with different morphologies has been investigated for the first time in this area by coupling numerical, analytical and imagery approaches, which is a first step for further works on coastal flooding in Normandy systems.

The role of VMS is very important in complex coastal systems with complex internal parameters such as morphology and the presence of anthropogenic activities, as in Normandy.

Such systems could be highly useful for extracting: 1) the intertidal bathymetry that is changing in time during the storm and should be considered in the numerical model, 2) the water extension, including the run-up and the infragravity waves IGW. The quality of snap images and the timestacks, including during winter periods, is the other limitation for the use of VMS.

5.8. CONCLUSIONS OF THE CHAPTER

This chapter answers the third scientific questions presented in Chapter 2, which are:

- *By integrating the scales from the regional basin to the local Normandy beaches, how can we characterize and model the coastal flooding, in response to extreme scenarios at this scale close to the coastline?*
- *To what extent can phase-resolving models integrating the sub-resolution of depth accurately reproduce the flooded water extent?*
- *How varies coastal flooding in different Norman coastal contexts, from sandy to mixed and gravel beaches?*

The extreme events seem to present a heavier influence of the bathymetries and morphologies of the study sites rather than the hydrodynamic conditions. Smoother slopes and beaches completely conformed by sand make waves to be weaker, generating less run-up and, therefore, less impact on the coast. Mixed and gravel beaches, with steeper slopes, produce fewer modifications of the waves, which makes them arrive with a higher amplitude leading to a worse scenario. Regardless, the presence of groins that sustain the coarse sediment in front of the nearshore population seem to reduce the waves because, even by being less reflective, they are more transmissive, decreasing the uprush of the water level over the beach profile. Then, the impact of extreme scenarios on the different morphologies present on the Norman coasts is directly related to the bathymetric conditions and the coastal structures that are necessary to ameliorate the protection of the population.

CHAPTER 6

APPLICATIONS OF THE METHODOLOGIES TO COASTAL RISK ASSESSMENT: FROM FLOODING TO BEACH EROSION

Coastal systems are facing severe extreme events inducing a series of risks such as flooding and beach erosion with high social and economic impacts. Managing these risks requires solutions considering climate change impacts, and understanding natural drivers like tidal regimes, extreme wave climates or beach dynamics, and their interaction with estuarine morphology. This chapter introduces different applications of the different approaches developed previously in Chapters 3, 4 and 5 through the use of numerical modeling in combination with probabilistic approaches or imagery. These applications demonstrate the use of the PhD research findings for studying coastal systems and their multi-timescale evolution, taking into account the identification and definition of extreme hydrodynamic scenarios and coastal morphodynamics, resulting from complex interactions between internal and external parameters of meteorological drivers and morphological characteristics, respectively.

The main results of this chapter have been subject of three scientific publications, one submitted to Oceanologia (2024) and two published in Marine Geology (2022) as second author and in Journal of Marine Science and Engineering (2024) as co-author: *C. López Solano, Y. Hamdi, et al., Effects of extreme river discharge and storm surge on the compound coastal flooding in the Seine Bay*; *A. Soloy, C. López Solano, et al., Rapid Changes in Permeability: Numerical Investigation into Storm-Driven Pebble Beach Morphodynamics with XBeach-G*; and *A. Soloy, E. I. Turki, N. Lecoq, C. López Solano and B. Laignel, Spatio-temporal variability of the morpho-sedimentary dynamics observed on two gravel beaches in response to hydrodynamic forcing*.

6.1. COMPOUND FLOODING

This section describes the analysis of the compound flooding produced by extreme storm surge and extreme river discharge applied to the case of the Seine Bay by carrying out a probabilistic approach followed by a numerical simulation. The text has been submitted to the journal Oceanologia: *López Solano, C.; Hamdi, Y.; Turki, E. I.; Gutiérrez Barceló, A. D.; Migaud, A.; Gilbert, R.; Laignel, B.; and Lafite, R. (2024)* Effects of extreme river discharge and storm surge on the compound coastal flooding in the Seine Bay.

6.1.1. Introduction

In recent decades, flooding in coastal and low-lying environments, such as estuaries and deltas, is considered one of the major hazards that humanity must face (Arns et al., 2017; Church et al., 2013; IPCC, 2022; Wahl et al., 2017). These events are highly modulated under the sea-level rise and the increasing of extreme floods driven by the interaction of oceanographic, hydrological, and meteorological phenomena. Intense rain produced in the atmosphere, fluvial events of heavy discharges or increases of the sea level generated by storm surges are examples of these inundations. When these events co-occur in space and time, they can exacerbate the flood extent, depth, and duration, resulting in a so-called compound flood event (Zscheischler et al., 2018). These events have the potential to cause large social and economic impacts and can directly or indirectly impact on the emergency response and the infrastructure against flooding (Leonard et al., 2014; Zscheischler et al., 2018).

Then, the coastal management of flood risks is a crucial aspect of the adaptation to these challenging developments for coastal communities (Vousdoukas et al., 2016; Wadey et al., 2015) with the aim of obtaining sustainable solutions based on the consideration of the climate change impacts and the socio-economic developments.

Investigating coastal flooding and its impact on deltaic and estuarine systems requires the consideration of the different natural drivers induced by fluvial and marine forces with their specific return period (Stewart & Melchers, 1997; Turki et al., 2023a). The probability of occurrence of such simultaneous drivers increases in estuaries, potentially modulating the severity of the flood hazard both spatially and temporally, and the induced impacts (Klerk et al., 2015; Maskell et al., 2014; Orton et al., 2020). Flooding hazards in the estuarine environments are strongly sensitive to the variation in tidal regimes (Guo et al., 2019; Turki et al., 2023b), surges (Turki et al., 2023a) and wave climates combined with estuarine morphology. However, the risk also changes spatially for each estuary depending on the internal characteristics of the system (sediment texture, porosity, ...) and the population demographics (Mansur et al., 2016).

This investigation is commonly performed by means of inundation modelling of the coastal area. The numerical scheme has been also developed for reliable predictions of future inundations using an accurate evaluation of future extreme sea levels. Harrison et al. (2021) investigated the intra-estuary sensitivities to fluvial and surge tide extreme values, for two contrasting UK estuaries; they demonstrated that the impact of the relative timing of the fluvial and surge-tide drivers increases in small estuaries and the use of coast-impact models for assessing compound flooding hazards is crucial to enhance the prediction of flooding risks.

Lopes et al. (2022) have developed a methodology integrating the estimation of local extreme sea levels with high-resolution numerical modeling for assessing the future inundation extent in five Portuguese estuarine systems. They highlighted that the uncertainties resulting from numerical approaches, related to the physical drivers (e.g. sea level rise) and estuarine morphology changes, are complex to be resolved and post major challenges to the efficient and sustainable management of estuaries.

However, the complex behavior of the physical processes driving these systems should be resolved by developing a probabilistic approach to consider different flooding hazards in a non-stationary context, combining a series of climate drivers and integrating the regional and the local scales, which is the main objective of this research. Such is the case of the Seine Estuary (Northwest France), where the coastal hydrodynamics present this complexity in a river-tidal environment.

Indeed, some techniques are accurately used for flood risk assessments depending on the scientific focus and the scale of interest. The water waves propagation in complex systems, as is the case of semi-enclosed basins and estuaries, is examined by 2D hydrodynamic models with high input data and computational requirements that are generally applied at local scales. The regional scales, from which physical drivers are originating, should also be considered to simulate the water level dynamics in such local systems. This interaction between regional to local scales is a key for an accurate determination of the flood hazards in complex environments as well as the flooding mechanisms resulting from the compound flood events induced by riverine and marine drivers.

This study follows the aforementioned physical context to investigate the coastal flooding in the Seine Bay, the down part of the Seine Estuary (NW France), by identifying the potential hotspot areas impacted by the compound floods from riverine and coastal floods.

The dynamics of the Seine Bay are highly controlled by the North-Western European shelf environment which is considered as one of the most active and energetic marine systems with a

mean estimated wave power of 60 kW m^{-1} (Guillou & Chapalain, 2015). Thus, the wave height should be considered to quantify the marine water levels controlling the coastal flooding in the bay. This work takes advantage of the recent developments on nonstationary methods of riverine and marine drivers, calculated by accurate numerical approaches close to the Seine Bay and based on spatial scale interaction (Chapon & Hamdi, 2022), to provide a first assessment of the potential compound flood scenarios in the global context of climate change.

6.1.2. Materials and methods

6.1.2.1. Datasets

6.1.2.1.1. Study site: The English Channel and the Seine Estuary

The English Channel is a basin lying between France and Great Britain, connecting the Atlantic Ocean and the North Sea. It is a shallow area on the continental shelf with an average depth of 60 m in the central part and less than 20 m on the coastal boundaries. The Channel extends over about 560 km with a varying width between the French and the British shores, from around 240 km in the Atlantic Ocean to less than 35 km in the Strait of Dover (**Figure 91**).

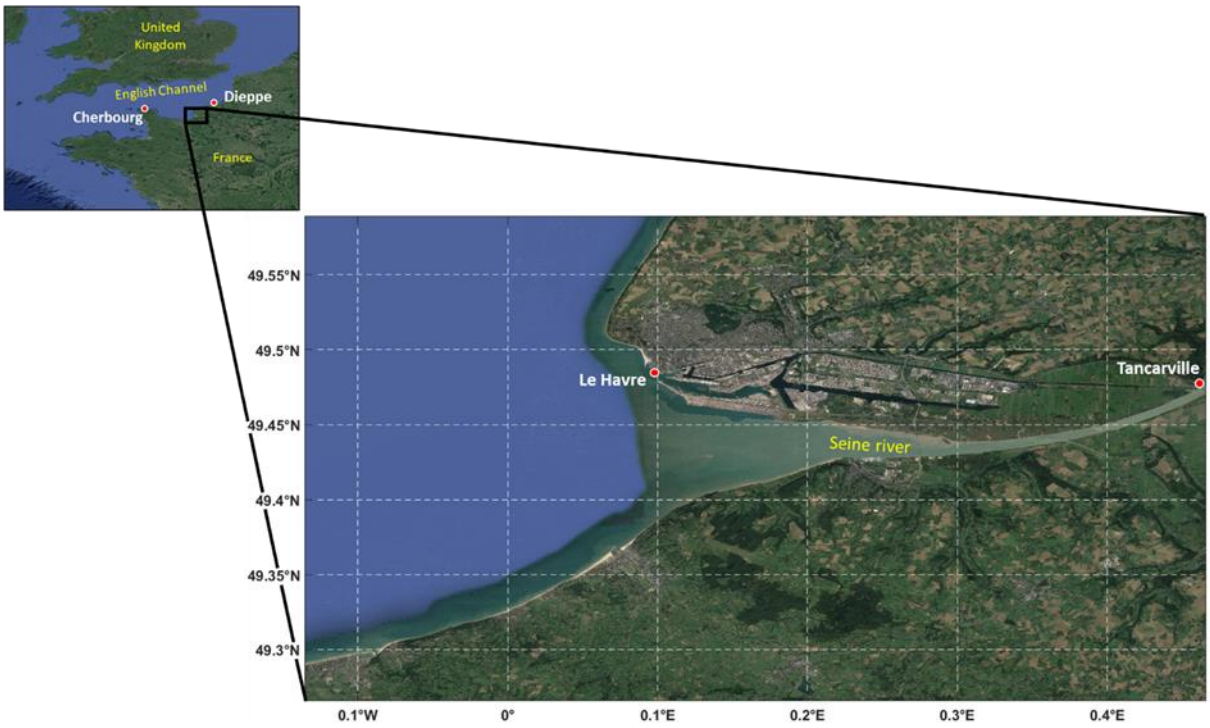

Figure 91. *Study sites: (a) English Channel between the coasts of France and the United Kingdom, and the locations of the tide gauges of Cherbourg and Dieppe; and (b) the Seine Estuary with the locations of the tide gauges of Le Havre and Tancarville. Extracted from López Solano et al. (2024)*

This work is focused on studying the hydrodynamics of the Seine Estuary, located in Normandy. This area is strongly influenced by tides which are semidiurnal and have macro to mega tidal ranges (Levoy et al., 2000), from around 3 m at the neap tides up to 10 m at the spring tides in the downstream part of the river. The Seine Estuary is a river-tide system with high spatial variations of fluvial and tidal energy. The mean river discharge is 435 m^3/s and reaches a maximum of 1000 m^3/s during events of floods. The 170-km-long Seine estuary, from the upper to the lower zones, is intensively monitored with a series of tide gauges, which is useful for the understanding of the estuarine dynamics as well as the calibrations of the numerical models.

6.1.2.1.2. Model forcings and measurements

The large scale set-up of the numerical model is forced by different databases. The forcings comprises the wave parameters set on the lateral boundaries of the grid obtained from the Atlantic-European North-West Shelf – Wave Physics Reanalysis of the Copernicus Marine Service, the wind speed and air pressure uniformly distributed over the grid from the ERA5 on single levels database, and the harmonic components of the astronomical tide specified also on the open boundaries from FES2014, as described in Section 4.1.

To define the digital elevation model (DEM) in the external computational grid, the bathymetry information is extracted from the European Marine Observation and Data Network (EMODnet) Bathymetry portal (EMODnet Bathymetry Portal, 2023). The bathymetry information is defined for all the nodes over the computational grid.

Concerning the forcings in the configuration of the model for the Seine Estuary mouth at a regional scale, the astronomical tide is generated on the boundaries with the same FES2014 database as the coarse grid, with an additional amplitude on the sea level identified with the surge obtained as an output of the large-scale model. A second forcing, corresponding to the river discharge, is defined on the open boundary located in the downstream part of the river. The river discharge information is obtained from the Port of Rouen (*Grand Port Maritime de Rouen*).

The model's computational DEM in the Seine River mouth is a composition of regional bathymetry from the EMODnet Bathymetry portal and high-resolution bathymetry obtained from Lidar Campaigns (carried out by the Université de Rouen Normandie, GIPSA) and measurements provided by the Port of Rouen.

In order to validate the results, both for the coarse and the detailed set-ups, sea level measurements of different tide gauges located along the coast are compared to the outputs of these models in the same locations. The timeseries of sea level in the tide gauges from Le Havre,

Dieppe, Cherbourg and Tancarville are the focus of the validation, considering that these are the available measurements close to the area of interest.

The tide gauges of Le Havre (**Figure 91**b) and Cherbourg (**Figure 91**a) are presented in Section 3.2.1.

Adding the remaining information in the same way, the tide gauge of Dieppe is also operated by SHOM in collaboration with the Joint Association of the Port of Dieppe. The Dieppe tidal observatory is located at the eastern end of the *Quai Henri IV* in the port of Dieppe (49.92917°N, 1.08449°E, **Figure 91**a). Various tide gauges are fitted over the years, providing an hourly series from May 1993 to January 2018.

Finally, the hydrometric station of Tancarville is also used, located in the Seine close to the river mouth (49.4769°N, 0.4672°E, **Figure 91**b), and managed by *EauFrance*. Hourly series of water level in the river is available from 1960 to 2016.

6.1.2.2. Methodology

6.1.2.2.1. Description of the model

In this study, the model used is Delft3D, more specifically, the modules Delft3D-FLOW and Delft3D-WAVE of the Delft3D software suite. Delft3D can carry out simulations of flows, sediment transports, waves, water quality, morphological developments and ecology, for coastal, river and estuarine areas (Deltares, 2020).

The Delft3D-FLOW module is a multi-dimensional hydrodynamic program which can be used for 3D- or 2D-simulations (depth averaged) which calculates non-steady flow and transport phenomena that result from tidal and meteorological forcing on a rectilinear or a curvilinear, boundary fitted grid.

The Delft3D-WAVE module is based on the SWAN model (Booij et al., 1999). This third-generation model simulates the evolution of random, short-crested wind-generated waves in estuaries, tidal inlets, lakes etc. SWAN solves the spectral action balance equation without any a priori restrictions on the spectrum for the evolution of wave growth. The discretization of the wave action balance equation in both geographical and spectral space is performed using a finite difference approach based on the so-called method of lines.

For the coarse set-up defined in the current work, a 2D-model of waves and flow on a Cartesian curvilinear grid is used. In the case of the Seine Estuary mouth, a 2D-model of only flow on another Cartesian curvilinear grid is the chosen configuration. The increase in the water level

due to the presence of waves is generated by the run of the coarse model, as long as the storm surge, which is produced by the effects of the atmospheric forcings on the sea surface and the interaction between this atmospheric forcing and the astronomical tide. These three processes are transmitted from the English Channel simulation to the Seine River run by adding to the forcing of sea level on the boundaries the total increase.

6.1.2.2.2. Set-ups and forcings of the model

The coarse computational domain used for simulating waves and water level propagation from the Atlantic Ocean and the North Sea till the English Channel is constructed with spatially varying resolution ranging from around 4 km in deep water on the West boundary up to 1200 m close to the shore on the Normandy coasts (computational grid of the coarse grid is in **Figure 92**). It was formed by quadrangles constituting a curvilinear grid of 194 and 441 cells in both directions with a total number of 85,554 elements. The spatial reference was the projection system EPSG:32631 WGS84/UTM zone 31N.

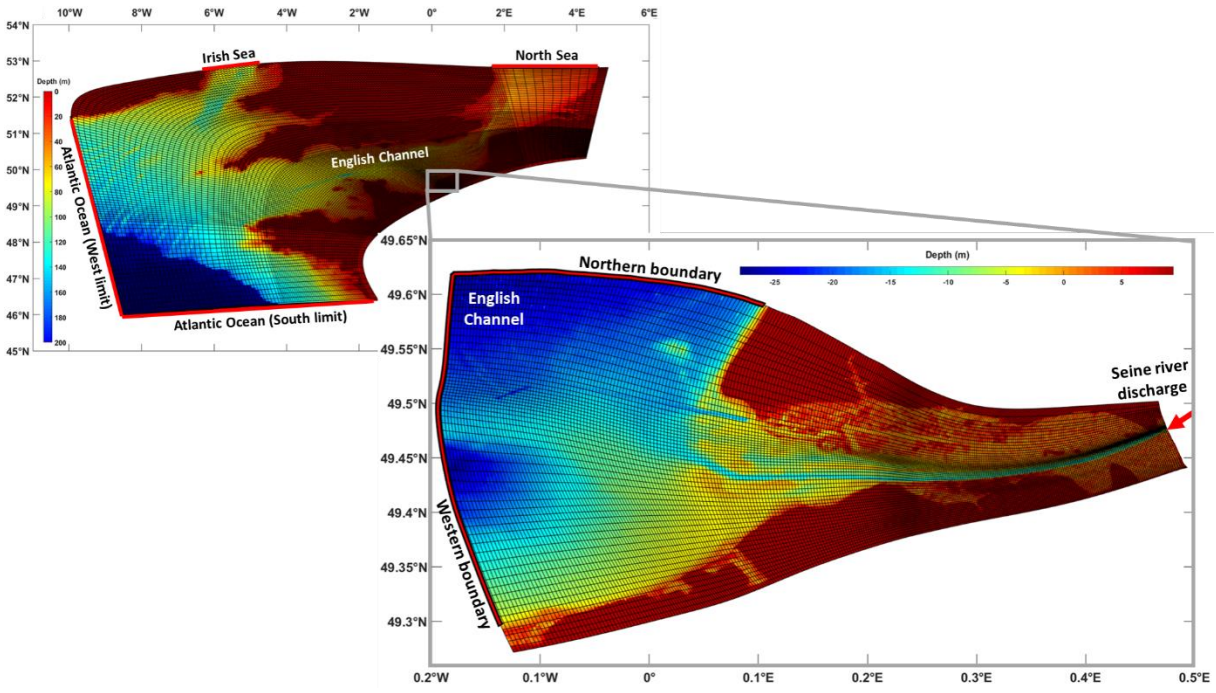

Figure 92. *Computational grids used for the numerical model set-ups in the English Channel and in the Seine Estuary. Waves, sea level and river discharge forcings on the open boundaries are marked for each computational grid in red color. Color scale represents the topobathymetry interpolated in each cell. Extracted from López Solano et al. (2024)*

To generate the astronomical tide, the harmonic components have been defined in 54 nodes distributed along the open boundaries on the North Sea, the Irish Sea, and the West and South limits of the grid on the Atlantic Ocean. In the same way, 76 nodes of wave parameters have

been defined on the same boundaries (**Figure 92**). For the atmospheric forcings, a rectangular spherical grid covering the computational area defined the nodes, maintaining the spatial distribution available on the ERA5 dataset. This spherical grid was converted into a curvilinear grid once the geographical coordinates were transformed into UTM coordinates.

The aim of simulating waves is obtaining the set-up of the sea level due to the presence of waves and their interaction with the tidal propagation. By including the atmospheric forcing, the model is able to generate the storm surge if the extension of the computational grid is wide enough, which was considered when the grid was delimited.

Once the grid and the forcings are defined, 40 years of data are simulated, from January 1983 to December 2022, with a time step of 10 minutes in terms of water level propagation and 20 minutes for the outputs of the model. The sea level obtained on the area of the second computational grid considered allows to define an additional amplitude included in the forcings of sea level of this second grid.

The Seine Estuary grid is used for simulating the flooding process in the compound events due to the action of the sea level and of the river discharge. The computational grid is formed by 1298 per 233 nodes in the two directions of the curvilinear grid, respectively, with a total number of 300,904 elements (computational grid of the detailed grid is in **Figure 92**). The spatial reference was the projection system EPSG:32631 WGS84/UTM zone 31N too.

For this second computational grid, the forcings of sea level are defined in a similar way to the coarser grid. The astronomical tide is generated by the harmonic components specified at 10 nodes along the Northern and Western open boundaries in the English Channel. At these points, an extra amplitude associated with the storm surge and the set-up produced by the waves, obtained from the outputs of the external grid simulations, are added. This residual is calculated as the remaining part of the sea level signal extracting the astronomical tide. Firstly, a tidal fit is applied to the sea level time series extracted in this area as a result of the 40 years simulated, and then, this fit is subtracted from the total series obtaining the residual, assimilated as the storm surge. Once the residual is obtained, a joint extreme analysis is applied to both the timeseries of this residual or storm surge, and to wave height timeseries, since both variables are correlated and cannot be studied separately. Finally, the extreme values associated with certain return periods are estimated for calculating the total amplitude added to the forcings of the numerical simulations. Waves are computed as wave set-up instead of directly forcing the model with the extreme wave heights because it would not be realistic simulating a wave height of several meters impacting the coast during all the simulation time.

These variables are the extra amplitude added to the harmonic components in order to simulate the astronomical tide with the extreme values of waves and surges, assimilated to the extreme values of sea level due to the affection of storm surge and the wave set-up.

The additional forcing of this model is the river discharge. Since the interest of this study is the flooding related to the combined actions of the sea level and the river, an extreme value analysis is also applied to the time series of discharge. The extreme values obtained are the values of river discharge used as forcings for the set-up of the model, which are associated to the same return periods as the ones calculated for the storm surge. The cells in which the river discharge is applied, on the boundaries of the computational grid, are located 30 km upstream the river mouth, approximately 1 km upstream of Tancarville (**Figure 91**). This boundary is chosen as a compromise between the place where the river discharge measurements are available and a limit for the affection of the same cycle of astronomical tide close enough to the sea.

With a sea level defined by the astronomical tide plus the extreme values associated to the storm surge and the waves obtained for the area of interest in the coarser grid simulations, and the extreme values calculated for the river discharge, a simulation of 2 days for average tide conditions is carried out for every combination of return periods of the two fits for which the extreme value analysis is done. Considering the extension of the computational grid, 3 to 6 hours are enough for the model to work accurately so that, after this time, there are more than 36 hours of results with 3 cycles of astronomical tide to evaluate the flooding in the extreme situations.

Before the analysis of the extreme values, it is necessary to know how these variables, the three related to waves, i.e., significant wave height, peak period and mean direction, and the storm surge alongside the river discharge, look like. For this purpose, the histograms of all the variables are calculated.

The significant wave height has a mean of 0.67 m on the study area, with a standard deviation of 0.46 m (**Figure 93**a), the peak period has a mean and a standard deviation of 2.65 s (**Figure 93**b), and the mean direction has a mean of 217.65° with a standard deviation of 111.32° (Fi**Figure 93**c). The histograms of wave height and period take the usual distribution, weighted to the left because of the most common presence of lower values and extremes rarely occurring. The direction is distributed in relation to the orientation of the coast, that produces waves taking the perpendicular direction to it and influenced by the directions from where the wind usually blows. These three variables are used for calculating the set-up of the sea level due to the presence of waves.

The distribution of the storm surge is centered on the ordinate axis, with an average slightly over 0 m and a standard deviation of 0.14 m, following a normal distribution as expected (**Figure 93**d). This is explained because of the effect of the processes involved in the generation of this variable, since sometimes the storm surge can take positive values and sometimes negative.

In the case of the river discharge, it is weighted to the left part of the histogram, taking mostly smaller values, with the tail of this distribution getting the lowest relative frequencies because of the rarely occurrence of the extreme values (**Figure 93**e). This is a common distribution for a variable that moves only on a positive range. The river discharge has an average of ~350 m^3/s, with a standard deviation of ~200 m^3/s.

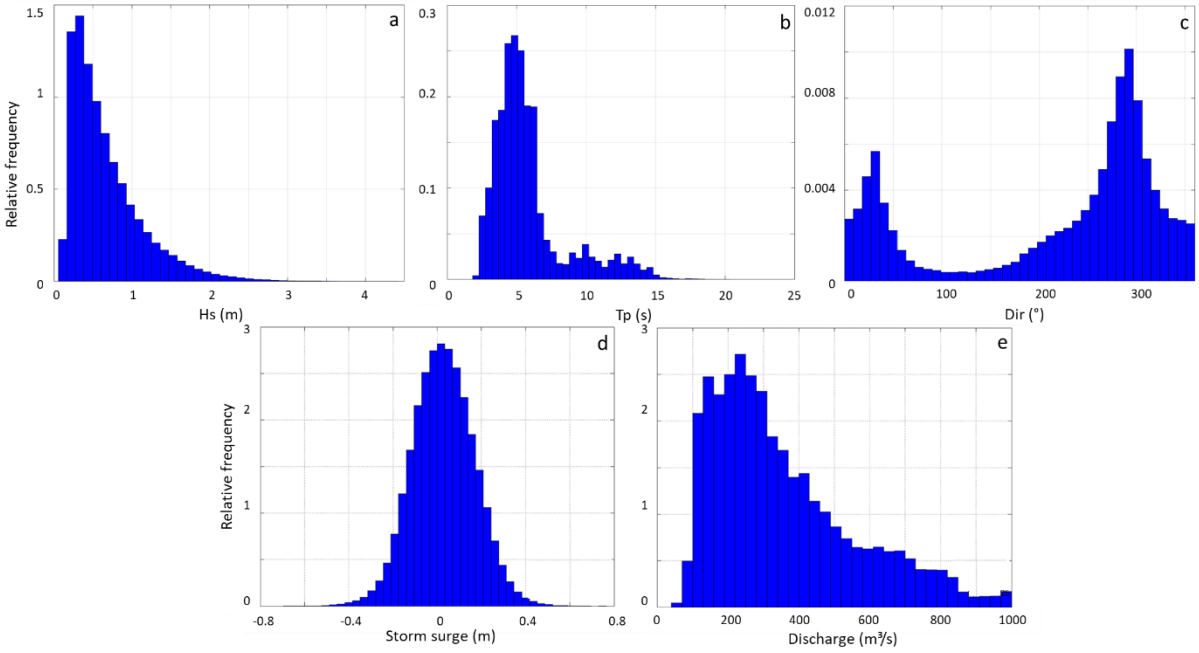

Figure 93. *Histograms with the relative frequency of the (a) significant wave height Hs; (b) peak period Tp; (c) mean direction; (d) storm surge and (e) river discharge. Extracted from López Solano et al. (2024)*

The results of the 40 years simulated of sea level are compared to the measurements of tide gauges available in the area, focusing on the ones closest to the Seine Estuary grid, which are the tide gauges of Dieppe, Le Havre and Cherbourg. To determine the performance of the model, observed and predicted water levels are used to calculate the Root Mean Square Error (RMSE, Eq. 12) and the Pearson's correlation coefficient (R, Eq. 13). RMSE is useful to obtain an evaluation of the average distance between the observed data and the data obtained from the coarse model simulations. The Pearson's correlation coefficient can be used as an indicator of the trends of the measured and the modeled datasets. If the datasets analyzed tend to increase or decrease together, it is closer to 1, and if they disagree in their trends, it is closer to zero.

6.1.2.2.3. Extreme value analysis

The numerical approach is coupled with a probabilistic approach, defined by the extreme value analysis applied to the variables in order to obtain the values with which the model will be forced. The extreme value analysis carried out for the storm surge, the wave height and the river discharge are done in three steps: first, extraction of extreme values from the complete timeseries, then, a fit of a distribution function to these extremes, and finally, the obtention of the extreme quantiles associated with the return periods chosen for the compound flooding events. These return periods correspond to 5, 10, 20, 50, 100 and 200 years for the two variables.

In the time series of the storm surge and the wave height obtained as outputs of the coarser grid model, the extreme values corresponding to the monthly maxima are identified along the 30 years of data. The distribution of 360 data of both variables is fitted to a Generalized Extreme Value (GEV) distribution function, already explained in Section 3.2.2. The non-stationarity is introduced on the parameters of the GEV, correlating them with the climate and temporal indexes also presented in the same section.

This results in the next estimators for the non-stationary parameters for the GEV distribution fitted to wave height maxima:

$$\mu = 1.612 - 0.22\,SST + 0.124\,NAO$$

$$\sigma = -0.880 - 0.247\,SLP - 0.052\,SLP^2, \text{ and}$$

$$\xi = -0.183 + 0.102\,SST - 0.011\,SST^2 - 0.107\,AMO + 0.072\,AMO^2$$

In the same way, for surge, the estimators of the parameters of the non-stationary GEV are:

$$\mu = 0.350 - 0.004\,SLP + 0.011\,SLP^2 - 0.02\,NAO + 0.007\,t$$

$$\sigma = -2.835 - 0.092\,SST - 0.022\,SLP^2 + 0.1235\,t - 0.176\,t^2, \text{ and}$$

$$\xi = -0.105$$

After obtaining the estimators for the non-stationary parameters, a bivariate copula is obtained with the aim of determining the joint distribution of the storm surge and the wave height. The effective joint return periods for the extreme storm surge and the extreme wave height associated to the return periods selected can be calculated from the copula, obtaining a range of values that goes from lower values of H_s occurring at the same time as higher values of surge to the opposite case, higher values of H_s with lower values of surge (**Figure 94**a).

Regarding the river discharge, the maxima are selected by annual maxima since the availability of data is over 60 years of daily measurements. The extreme events of volume of water selected is fitted also to a GEV distribution model, but stationary in this case. Adjusting the parameters to the best fit, the estimators obtained are:

$$\mu = 1260.84, \sigma = 483.37, \text{and } \xi = -0.41$$

In the same way as for the storm surge and the wave height, the river discharge associated to the return periods chosen can be calculated (**Figure 94**b).

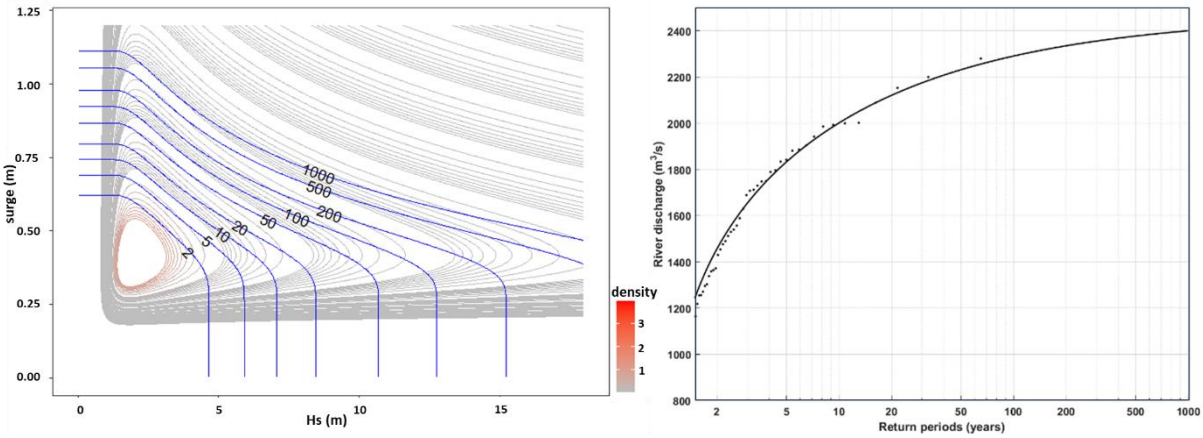

Figure 94. *(a) Joint return period of the storm surge and the wave height in the Seine mouth; and (b) Generalized Extreme Value distribution function fitted to the annual maxima for the 62 years timeseries of river discharge. Extracted from López Solano et al. (2024)*

Once the variables are adjusted to extreme values distribution functions, **Table 42** shows the values associated to the chosen return periods obtained for the three variables studied. Extreme values of river discharge are taken from the fit of the GEV function. In the case of the significant wave height and the storm surge, two possibilities are considered, taken arbitrarily from the joint return period distribution. One possibility is considering a high value of H_s and a low value of storm surge, and the other possibility is the opposite, a high value of storm surge and a low value of H_s, chosen carefully as an agreement of a high enough value of one of the variables but avoiding the other variable to remain in a low constant value.

		Return periods (years)					
		5	**10**	**20**	**50**	**100**	**200**
River discharge (m^3/s)		1832.32	1984.47	2090.96	2209.25	2269.10	2314.29
Low surge, high wave height	**Storm surge (m)**	0.479	0.494	0.513	0.539	0.559	0.582
	Wave height (m)	4.48	5.10	5.79	6.78	7.55	8.40
High surge, low wave heigh	**Storm surge (m)**	0.622	0.664	0.706	0.764	0.806	0.851
	Wave height (m)	2.56	2.73	2.85	3.01	3.13	3.27

Table 42. *Extreme values of river discharge, storm surge and wave height obtained from the distribution functions adjusted to the extreme data of the three variables and associated with the return periods of 5, 10, 20, 50, 100 and 200 years. Extracted from López Solano et al. (2024)*

Considering that the waves are computed as wave set-up added to the storm surge, there are 36 possible combinations of return periods of river discharge and sea variables. The sea variables are accounted as low surge and high wave height or low wave height and high storm surge, which results in a total number of 72 simulations of 2 days.

A synthesis of the methodological approach used in the study is illustrated in **Figure 95**.

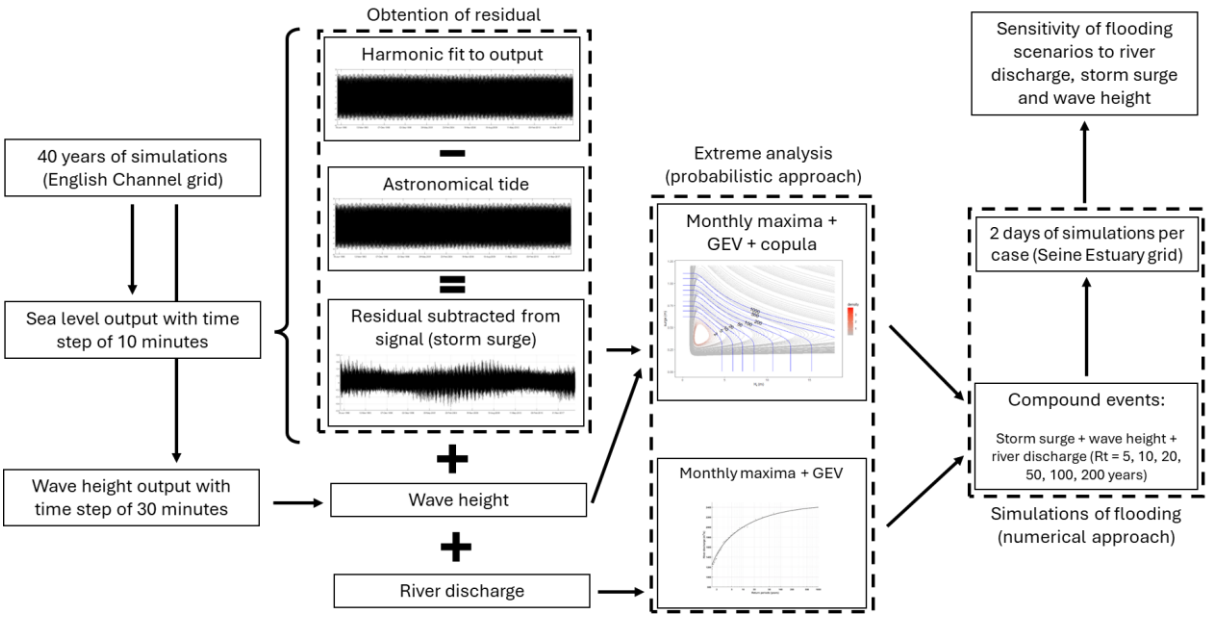

Figure 95. *Synthesis of the methodological approach used to study the compound scenarios of flooding produced by extremes of storm surge, wave height and river discharge on the Seine Bay. Extracted from López Solano et al. (2024)*

6.1.3. Results

6.1.3.1. Validation of the results in the coarse grid

In **Figure 50** the timeseries of the three tide gauges along with the output of the model in the closest location to each of them are shown in different short periods taken from the 40 years as an example. As mentioned in Chapter 4, the comparison of the three tide gauges in the coincident period leads to a RMSE of ~34 cm in Cherbourg over a tidal range of around 7 m, an error of ~50 cm in Dieppe with a tidal range of more than 10 m and a RMSE of ~32 cm in Le Havre over a tidal range of slightly less than 9 m. In terms of the correlation coefficient, for Cherbourg it takes a value of 0.9809, for Dieppe it is 0.9803, and for Le Havre, 0.9901.

6.1.3.2. Validation of the results in the Seine grid

For the Seine Estuary mouth, the same tide gauge of Le Havre is considered for validating the results obtained. For this case, the tide gauge of Tancarville upstream the river is used too. An additional simulation is carried out for the purpose of this validation, forcing the model with no added amplitude on the maritime boundaries and with a real river discharge measured during the specific time simulated with the intention of obtaining realistic outputs that can be compared to the measurements of the two tide gauges.

The two tide gauges are compared in the coincident period, obtaining a RMSE of ~29 cm in Tancarville over a tidal range of around 6 m, and an error of ~32 cm in Le Havre with a tidal range of slightly less than 9 m. The correlation coefficient takes a value of 0.9929 for Tancarville and 0.9953 for Le Havre.

The timeseries of the two tide gauges along with the output of the Seine Bay model in the closest location to each of them are shown in **Figure 96** in the simulation period run with realistic data as an example.

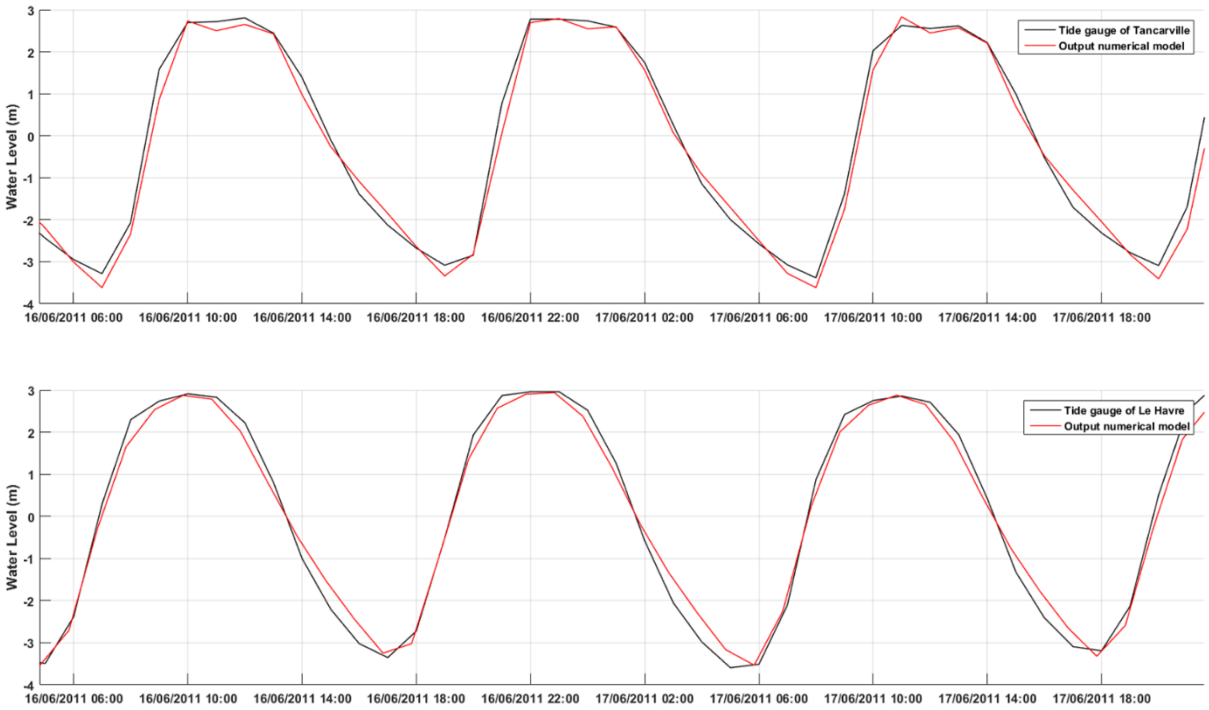

Figure 96. *(a) Timeseries of water level measured by the tide gauge of Tancarville in black and the output of the numerical simulations in the closest location in red for the period from 16-06-2011 at 04:00 to 18-06-2011 at 20:00; and (b) timeseries of water level measured by the tide gauge of Le Havre in black and the output of the numerical simulations in the closest location in red for the period from 16-06-2011 at 04:00 to 18-06-2011 at 20:00. Extracted from López Solano et al. (2024)*

6.1.3.3. Analysis of compound events

In order to identify the sensitivity of the coast and the riverbanks to flooding produced by storm surge or by fluvial discharge, two areas of control along the shoreline on the North and the South of the Seine are selected (a map containing both areas is shown in **Figure 97**). Each control area is selected according to environmental criteria and with the aim of appreciating the contribution of each flood source within them. Area 1 is located on the northern bank of the Seine River before its mouth, between the Tancarville Bridge and below the Normandy Bridge. This area is a protected zone, the *Réserve Naturelle de l'Estuaire de la Seine*. It is an intertidal floodplain limited on its northern perimeter by the road *Route de l'Estuaire*, which is built as a containment dike. This area is one of the largest areas of reed cultivation for use in construction, and due to its exposure in the event of a river or coastal flood, it presents a high vulnerability. The southern bank at the mouth of the Seine is protected by an equivalent dike downstream from a tributary of the Seine, the Risle River. Therefore, this area is not studied because it does not present vulnerability in the same scale. Area 2 is located in a coastal area south of Villerville, at the end of the Seine River mouth facing the English Channel. Villerville beach, located in this study area, is a sandy beach exposed to the action of the river and to the coastal dynamics. No control areas are selected further South

of Area 2 or North of Le Havre because they would be just suffering from coastal flooding, not fulfilling the compound flooding condition that this study is meant to identify.

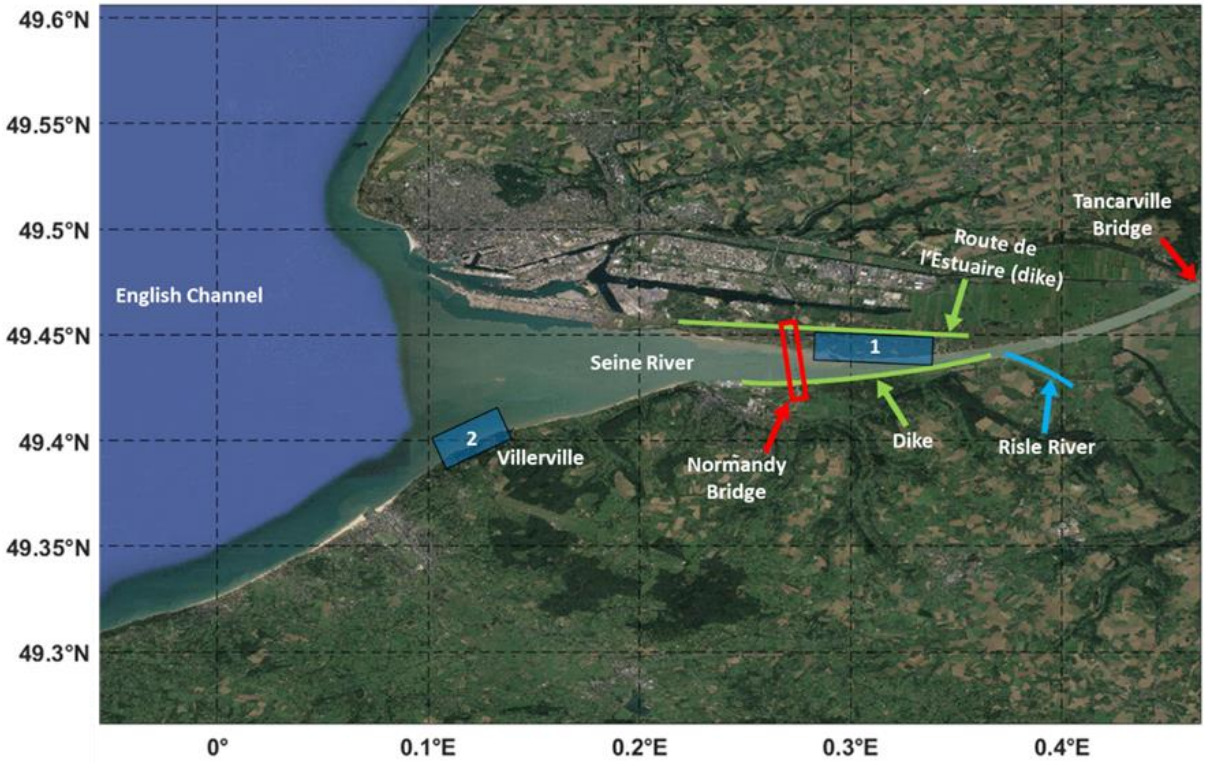

Figure 97. *Distribution of the control areas where the outputs of the simulation have been extracted to evaluate the flooding of the compound events. Main features of the study area are also specified. Extracted from López Solano et al. (2024)*

For the 72 cases simulated, and with the aim of obtaining the contribution of each forcing of the model to the compound event of flooding, the hazard curves at different cells of the computational grid contained in these control areas, are obtained for the combinations of the return periods of 5, 10, 20, 50, 100, and 200 years (In **Table 42** are shown the extreme values of the two variables associated with these 6 return periods). The hazard curves represent the maximum depth reached at a specific location during the simulation as a result of the combination of the extreme values of storm surge and river discharge associated with the specified return periods. **Figure 98** and **Figure 99** contain the hazard curves associated with one return level fixed of one of the variables and varying the other forcing with the values associated to all the return periods, i.e., a constant river discharge with a variable storm surge in **Figure 98** and a constant storm surge and a variable river discharge in **Figure 99**. In both figures, the left panels represent the forcing of storm surge calculated with a high value of wave height and a low value of storm surge and the right panels the opposite, the storm surge forcing calculated with a low value of wave height and a high value of storm surge.

At first glance, it can be observed that the depth reached is directly proportional to the extreme value distribution functions of storm surge and river discharge. Keeping a constant value of river discharge associated with a specific return period and varying the storm surge associated with different return periods, it is observed that all maximum depths obtained in the simulations follow a linear growth on a logarithmic scale, equivalent to the fit obtained in **Figure 94**a, in the joint return period of Hs and storm surge. In parallel, by keeping a constant value of storm surge associated with a specific return period and varying the values of river discharge associated with different return periods, it can be seen that the maximum depth reached during the simulations follows a growth equivalent to that of the GEV fitted to the annual maxima of river discharge in **Figure 94**b. As expected, the maximum depth reached in the control area increases when the forcing of storm surge also increases, reaching the highest value when the forcing corresponds to the storm surge associated with the return period of 200 years.

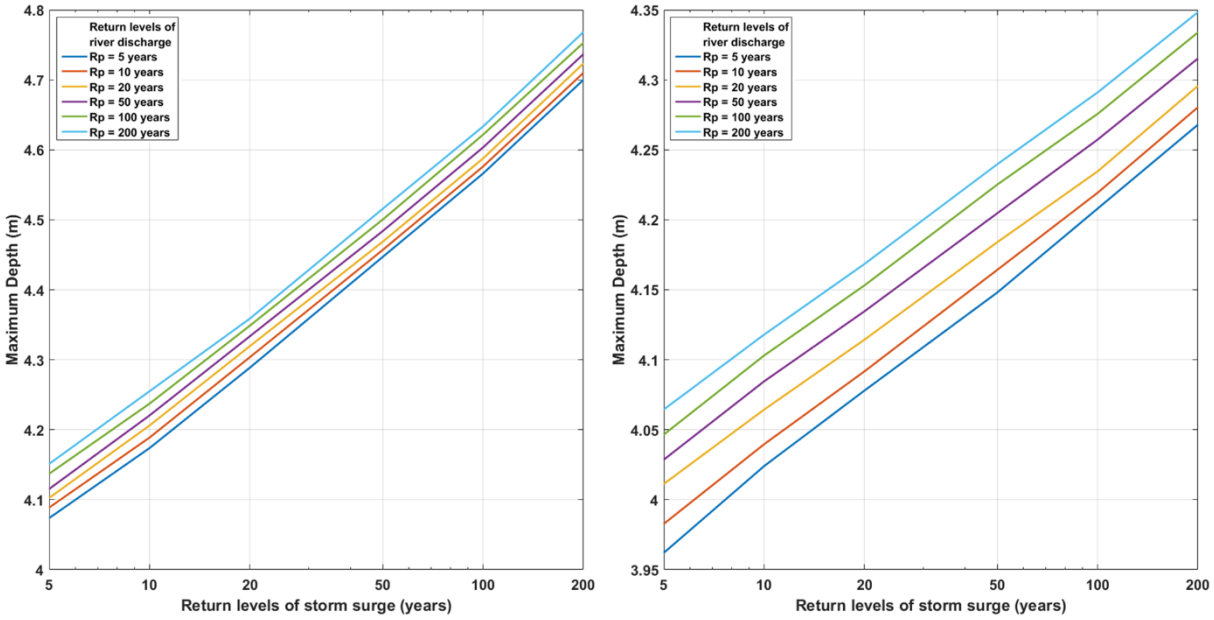

Figure 98. *Hazard curves showing the maximum depth reached in representative cells produced by compound events of flooding. Left panel represents the forcing of storm surge calculated with a high value of wave height and a low value of storm surge and right panel the forcing with a high value of storm surge and a low value of wave height. Each hazard curve represents one return period fixed associated with river discharge and the storm surge varying for 5, 10, 20, 50, 100 and 200 years. Extracted from López Solano et al. (2024)*

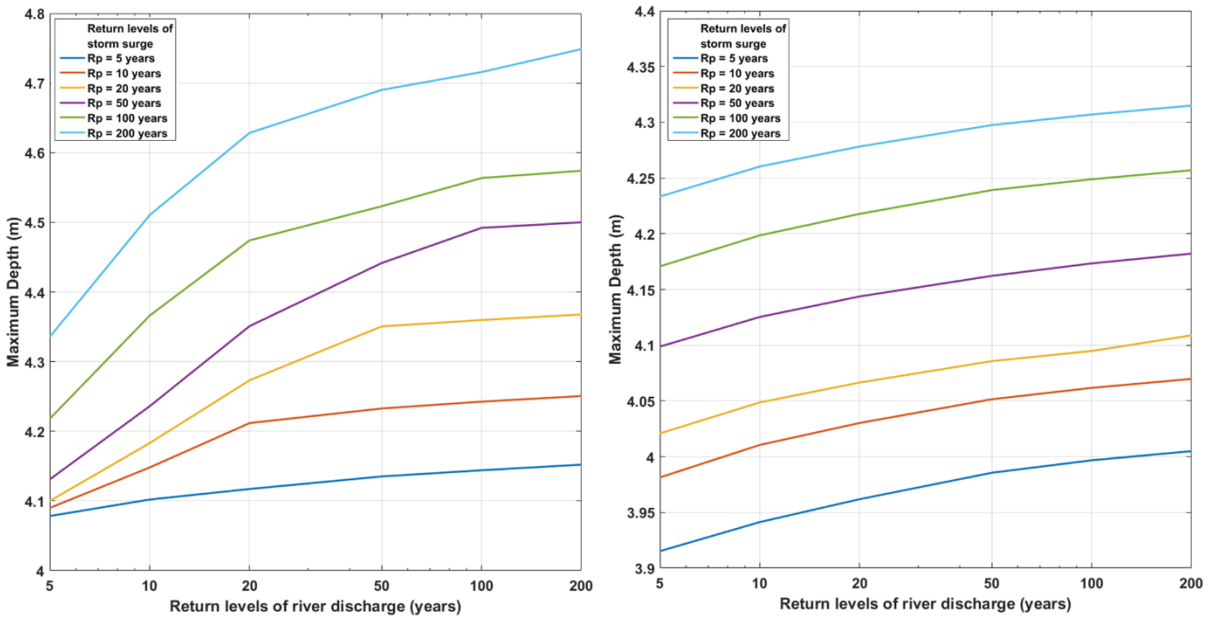

Figure 99. *Hazard curves showing the maximum depth reached in representative cells produced by compound events of flooding. Left panel represents the forcing of storm surge calculated with a high value of wave height and a low value of storm surge and right panel the forcing with a high value of storm surge and a low value of wave height. Each hazard curve represents one return period fixed associated with storm surge and the river discharge varying for 5, 10, 20, 50, 100 and 200 years. Extracted from López Solano et al. (2024)*

By comparing the storm surge forcings calculated in the two possible ways, with high wave height and low storm surge values (on the left panels in **Figure 98** and **Figure 99**) and with low wave height and high storm surge values (on the right panels in **Figure 98** and **Figure 99**), it is evident that higher maximum depth values are obtained when the wave height is higher. In the case of storm surge hazard curves, for lower return levels, a maximum depth between 10 and 15 cm higher is obtained with higher wave height, and for higher return levels, the maximum depth reached is up to 50 cm higher, which represents up to a 10% increase in relative terms compared to when the storm surge forcing is calculated with lower wave height and higher storm surge. The range of maximum depths reached in the case of lower wave height is less than 30 cm between return periods of 5 years and 200 years. However, when the storm surge forcing is calculated with higher wave height, it is almost 70 cm, more than double. In the case of the river discharge hazard curves, equivalently, the maximum depth obtained in the simulations with the lowest return levels is between 10 and 15 cm higher when the storm surge forcing is calculated with a higher value of wave height. For the higher return levels, the depth is between 15 and up to 45 cm higher, almost half a meter. The ranges in which the maximum depths vary are very variable in this case, ranging from only 10 cm between the lowest and highest return levels to ranges of half a meter.

The comparison of lower return levels with higher ones for both cases highlights that the variation of storm surge while keeping the river discharge value fixed is approximately equivalent

in the control area, with only a few centimeters of variation for all return periods, always within a range of 30 or 70 cm. The difference is established in that the linear variation on a logarithmic scale is about 15 cm less when the river discharge is kept constant at the value associated with 5 years compared to the value associated with 200 years. When the value of storm surge is kept fixed and the value of river discharge associated with the different studied return periods is varied, the range in which the maximum depths reached fluctuates within ~9 cm when the storm surge forcing is calculated with a low value of wave height. However, it increases to 30 cm between the value associated with a 5-year return period and the value associated with a 200-year return period. For the situation where the storm surge is calculated with a higher value of wave height, both the range of maximum depths reached and the minimum value obtained increase, expanding the range from ~8 cm to ~40 cm, and also increasing the difference between the value associated with a 5-year return period and the value associated with a 200-year return period by 30 cm.

Finally, it is evident that storm surge forcings produce greater flooding than river discharge forcings, even if the control area is located in an apparently more exposed zone to the action of extreme river events. Furthermore, the greatest flooding occurs when the storm surge is generated by storms with higher wave heights than those purely produced by a higher storm surge. Of all possible combinations, as expected, the greatest compound event of flooding occurs when a storm surge is given as a combination of a high 200-year return period wave height with its associated storm surge calculated from the joint return period in **Figure 94**a, along with a 200-year return period river discharge, reaching almost 4.8 m of maximum depth in the simulations. In comparison to the lowest value obtained, which corresponds to a storm surge obtained with a 5-year return period calculated with a high storm surge event occurring simultaneously with a 5-year wave height but with a low value, and in turn a 5-year return period river discharge, barely reaching ~3.9 m. This represents almost 1 m of difference, more than 20% in terms of total depth, which in a flat floodplain with high exposure like the chosen control area, poses a significant risk that will have a very high impact.

When comparing these results to the values of maximum depth obtained in Area 2, the hazard curves of a fixed value of river discharge with a variable value of storm surge are almost equal to the hazard curves obtained in **Figure 98**, but with a different starting value of depth taken as the depth corresponding to the study area. This fact means that the impact of extreme storm surge in a coastal area is equivalent to the impact in the downstream part of the Seine, i.e., the flooding produced by coastal forcings is always the main factor that needs to be considered. When it comes to the river discharge, the hazard curves obtained are flat, constant on the value of the fixed storm surge that produces the compound event. This could be expected, but it is supported

by these results, meaning that the impact of a fluvial extreme event in a selected area out of the Seine mouth is negligible, even if Area 2 is selected in the limit of the estuary when still some actions produced by the river can be noticed. It can be also expected, then, that study areas taken further from this point will present similar results, showing just hazard curves as the ones presented in **Figure 98** but adapted to the depth of each area.

6.1.4. Discussion

Validation in this study is performed by calculating the RMSE and the correlation coefficient for the outputs of water level in comparison to the measurements of tide gauges both in the coarse grid covering the English Channel and in the Seine Estuary grid. Considering the second grid as the main one in which the simulations are carried out, the RMSE obtained in the tide gauge of Le Havre is ~32 cm, and the RMSE in the tide gauge of Tancarville is ~29 cm in tidal ranges between 6 and 9 m, which represents 3 to 5% of error. Lopes et al. (2022) have also used the numerical model Delft3D in their simulations and have calculated the RMSE in different stations along five estuarine systems in the Portuguese coast, obtaining a range of values from 5 to 23 cm in tidal ranges of less than 4 m, representing 2 to 5% of error, equivalent to the metrics obtained in this study. Orton et al. (2020) calculated the RMSE for some storms simulated in terms of water level, obtaining values from 0.14 m to 0.54 m, averaging 20 cm for most of the storms in the Hudson River in the US. These similar results show a good performance of the numerical modelling of this study, proving it is reliable.

Return periods used in this study cover the variability of extreme events of storm surge and river discharge associated with 5, 10, 20, 50, 100 and 200 years. This temporal coverage is appropriate for a compound event analysis in an estuarine system, since this kind of environment is highly dynamic, suffering from changes due to the exposure to different factors such as the fluvial dynamics, coastal factor or anthropogenic actions and activities. In the 62-year time series of river discharge analyzed, no extreme event associated with a return period higher than 200 years is found. For the simulations, the combination of extreme events of storm surge and river discharge are considered as the main conductor, other studies have proved the possibility of these events occurring at the same time by analyzing the time series (Klerk et al., 2015; Orton et al., 2020). Nevertheless, in this study we consider a joint return period for wave height and storm surge for obtaining the storm surge with which we force the numerical model and a separated extreme analysis of river discharge. This assumption of independence between coastal and fluvial forcings has also been considered in other studies (Kew et al., 2013) when calculating the extreme

events of storm surge and river discharge, and the hypothesis of independence of these two variables has been proofed by van den Brink et al. (2005).

Moreover, this study is focused on the Seine Estuary, analyzing the extreme events of storm surge simulated in the English Channel computational grid extracting the results on the Normandy coasts, and the river discharge from the Seine itself measured by the Tancarville tide gauge. Different studies (Massei et al., 2017; Turki et al., 2019) have analyzed timeseries of both variables, finding statistically significant cycles of more than 20 years. This effect justifies the necessity of considering return periods of 100 years and even 200 years when obtaining the extreme events to cover the possible variations generated by these cycles.

The importance of assessing compound events of flooding using numerical models is sustained by several studies (Khojasteh et al., 2021; Lopes et al., 2022; Passeri et al., 2015), strengthening the idea of facing this problematic in estuarine systems. However, the limitation of the present study in comparison to other equivalent analyses does not consider hydrodynamic alterations produced by climate change. This may have or not have impact on the results, since other studies that consider these modifications state that there will be an overall sea level rise happening in all the coastal areas, whereas a decrease in river discharge is expected in this part of the planet due to warming that will likely produce more aridity reducing the mean precipitations (IPCC, 2022). The assumption of not accounting for climate change modifications may lead to accurate results in terms of inundation considering the findings of Pickering et al. (2017), where they consider a global fixed sea level rise of 2 m and find the modifications in mean high water level for every region of the world. Results in the central part of the English Channel in the area of the Seine Estuary suggest a decrease of 0.02 m in the maximum tidal range. Nevertheless, the present study focuses on the comparison of the different scenarios simulated rather than the absolute values of flooding obtained.

6.1.5. Conclusions

In this study, the numerical simulation of 40 years of water level and waves with atmospheric forcings is carried out with the objective of obtaining the residual of the sea level constituted by the set-up due to the presence of waves, the storm surge produced by the interaction of the sea with the atmosphere, and the interaction between the astronomical tide with the storm surge. This residual, or storm surge, is used for obtaining the extreme events associated with sea level and, alongside the extreme events obtained from the river discharge of the Seine in its estuary, an additional simulation in the Seine Bay is performed for the compound events of both variables.

The results of this second simulation allow studying the effects of the compound flooding produced by fluvial and coastal extreme scenarios.

For the case of the Seine Bay, the extreme events of river discharge are delimited by an asymptotic margin, so the flooding produced by this variable is not strongly increased by the highest return periods, keeping it under an upper limit of 2500 m^3/s. Nevertheless, with a mean value of 350 m^3/s, the flooding produced by the river discharge is not negligible, especially in the areas close to the Seine mouth, where wide extensions present a nearly flat surface vulnerable to every extreme flooding occurring on this area.

The storm surge produces a stronger impact on the study area, especially when the extreme events occur during a storm with higher waves arriving to the coast. The major impact is produced by compound events of river discharge and storm surge taking place at the same time, that may happen simultaneously by demonstrated in other studies. The effect of extreme events of river discharge in this estuary mostly disappear when the area of interest is located further from the Seine mouth.

6.2. MORPHODYNAMIC RESPONSE OF BEACHES TO EXTREME HYDRODYNAMICS

In this section, two cases are presented in relation to the action of hydrodynamics on different study sites, focusing on the morphodynamic response of beaches. One of them explores the use of video monitoring systems to understand the main morphodynamics of gravel beaches as a consequence of hydrodynamics. The second one is centered in the action of extreme events to study the evolution of the beach profile in Etretat to estimate the efficacy of the numerical model XBeach-G when simulating storms. The cases are presented as the summaries of the corresponding publications in two scientific journals.

6.2.1. Variability of the morpho-sedimentary dynamics on two gravel beaches in response to hydrodynamics

The following section corresponds to the summary of the publication: *Soloy, A.; Turki, E. I.; Lecoq, N.; López Solano, C.; and Laignel, B. (2022)* Spatio-temporal variability of the morpho-sedimentary dynamics observed on two gravel beaches in response to hydrodynamic forcing. *Marine Geology, 447, 106796, https://doi.org/10.1016/j.margeo.2022.106796*.

6.2.1.1. Introduction

Coastal engineering faces significant challenges in monitoring, understanding, and predicting coastal dynamics, particularly in the context of climate change and rising sea levels. Coastal morphodynamics result from complex interactions between hydrodynamic forces (such as currents, waves, and tides) and local characteristics (including sediment size, embayment, and intertidal zone structuration). Advances in monitoring technologies over recent decades have enabled progress in studying coasts at various scales, from global and regional perspectives using satellite imagery to local scales through ground surveys and VMS.

Satellite techniques rely on optical or radar sensors to identify coastal features regionally or globally, with measurements constrained by orbital parameters. Ground surveys, including methods like lidar, or photogrammetry, provide in situ measurement of topography. VMS, a popular methodology, offers high-resolution monitoring of shorelines at specific study sites over the long term, allowing for detailed analysis of morphological changes. However, challenges such as image variability and vertical biases in digital elevation models exist.

VMS data often involves techniques like Empirical Orthogonal Function (EOF) analysis to identify shoreline variability mechanisms. Despite advancements benefiting sandy coastal systems, knowledge of gravel beaches remains relatively limited due to the challenges in measuring sediment characteristics. Gravel beach dynamics are influenced by spatial and temporal variations in sediment size and shape, impacting sediment transport and morphological changes.

6.2.1.2. Methodological approach

The present study aims to investigate the geomorphodynamics and gravel size variability of two coastal systems in Normandy, France (Etretat and Hautot-sur-Mer) using VMS data (as explained in Section 5.2 and shown in **Figure 11**) and recently developed methodologies. Questions addressed include shoreline shape changes, mechanisms of change, physical phenomena driving morphological changes, and the link between morphological and sedimentary variability.

Hydrodynamic parameters are used to estimate beaches' 3D morphology and compare morphodynamics with hydrodynamics. Water level data is obtained from a tide gauge and a hindcast model, for Hautot-sur-Mer and Etretat, respectively, while wave data comes from the implementation of WaveWatch 3 model in the English Channel by Ifremer.

To monitor shoreline variability, VMS is used. VMS were installed in June and December of 2018 respectively in Etretat and Hautot-sur-Mer, with video cameras recording images every 10 minutes during daylight. Morphological indices like Beach Width (BW), Beach Slope (BS), and Beach Orientation Angle (BOA) are analyzed. Statistical approaches including EOF and wavelet analysis are employed to analyze beaches' morphology and sediment variability.

6.2.1.3. Results and discussions

This section describes the results and discussions of the study investigating the morphological changes in shoreline position at Etretat and Hautot-sur-Mer beaches over a period of two years but focusing in the most relevant results in relation to the action of hydrodynamics, which is the main objective of the overall project. EOF are calculated using time series of average beach width at the various selected elevations (**Figure 100**) with the aim of extracting principal components (PC) of morphological variability to characterize the beaches' spatiotemporal morphodynamics. Each PC describes a percentage of the shoreline's total variability through space and time between -2 m and +3 m in Etretat, and from +1 m to +3 m in Hautot-sur-Mer and captures various mechanisms such as cross-shore translation, beach rollover, breathing, and large-scale rotation, revealing the complexity of beach dynamics (**Figure 101**).

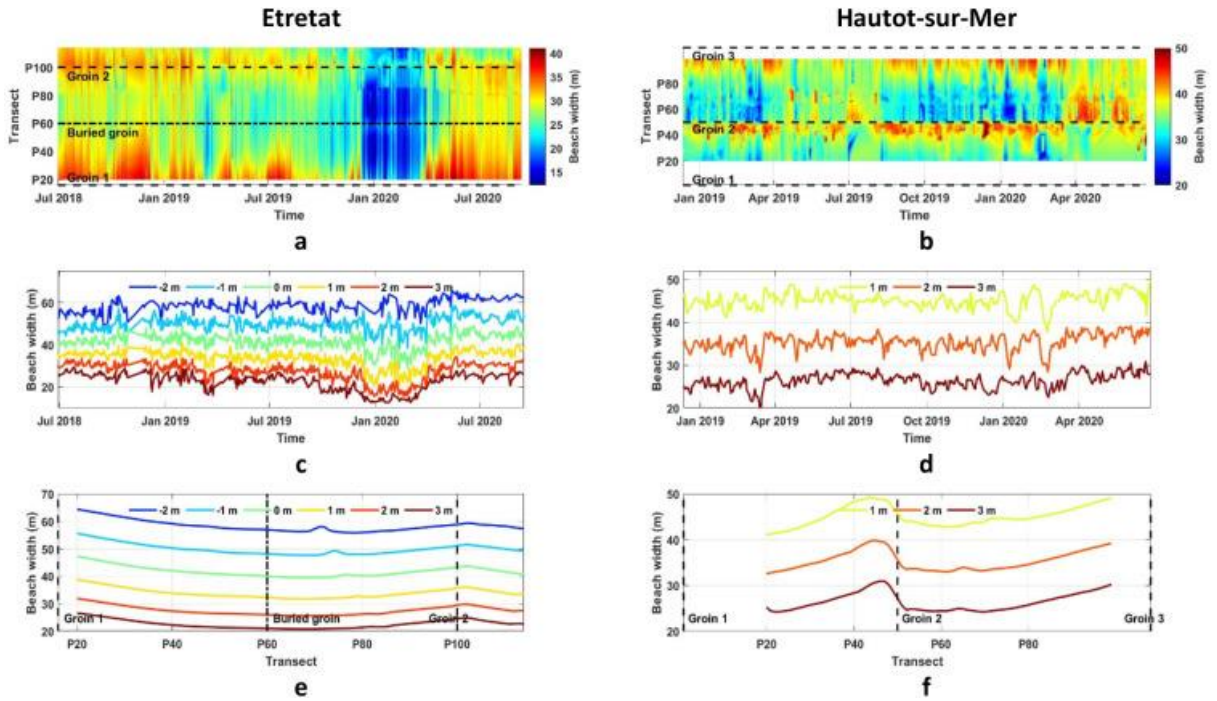

Figure 100. *Planform evolution of the +2 m elevation shoreline position in Etretat (a) and Hautot-sur-Mer (b), from July 2018 to November 2020. Time series of average beach width between elevations −2 m and + 3 m in Etretat (c), and from +1 and + 3 m in Hautot-sur-Mer (d), with 1 m of span. Average planform shape of the shoreline at the same elevations in Etretat (e) and Hautot-sur-Mer (f). The position of groin structures is indicated with black dashed lines. Extracted from Soloy et al. (2022)*

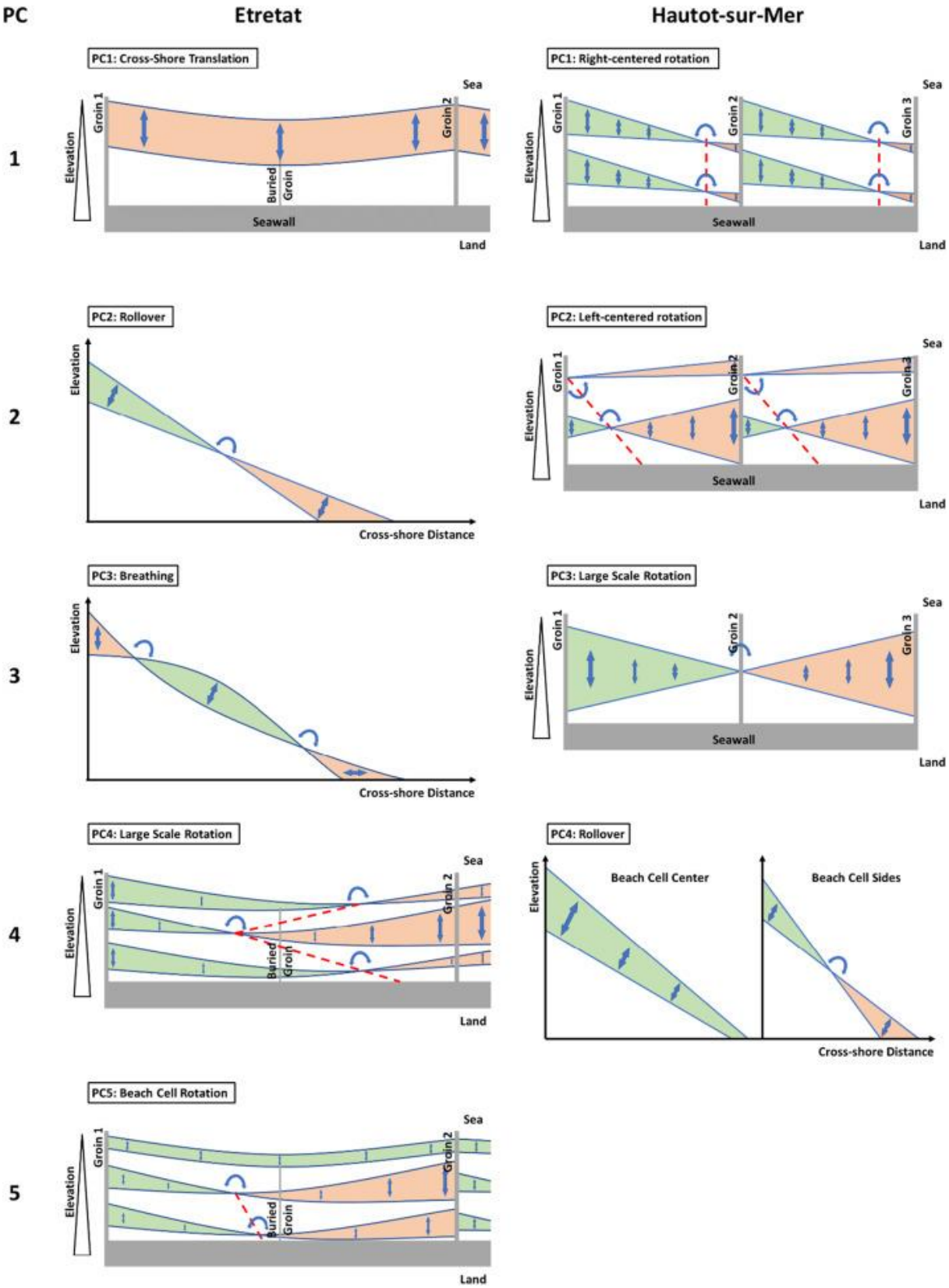

Figure 101. *Conceptual model of the isolated mechanisms of beach morphological variability in Etretat (left) and Hautot-sur-Mer (right), associated with their corresponding principal component (PC). Extracted from Soloy et al. (2022)*

The study reveals differences in shoreline planform shapes between Etretat and Hautot-sur-Mer. Etretat exhibits a parabolic shape, while Hautot-sur-Mer has a more linear shape, attributed to differences in beach openness and the presence of groin structures affecting sediment distribution. Cross-shore slopes vary with elevation, showing increasing slopes in Etretat and lower slopes in Hautot-sur-Mer. Groin structures influence shoreline planform shapes, with accumulative and erosive sides affecting sediment distribution. Seasonal patterns in shoreline changes are observed, particularly in Hautot-sur-Mer, where beach orientations alternate between wider sides facing different directions throughout the year.

In terms of hydrodynamics, Etretat experiences more significant retreat during clustered storm events compared to Hautot-sur-Mer, attributed to differences in beach composition and the protective effect of dissipative low tide terraces. Correlation analysis between PCs and morphological parameters (BW, BS and BOA) as well as hydrodynamic parameters (wave energy, current velocity and tidal range) provides insights into the influence of hydrodynamic processes on shoreline changes (**Figure 102**).

Wavelet analysis identifies periods of morphological variability, highlighting the importance of medium-term processes such as wave exposure and storm events in driving beach changes. Overall, the study sheds light on the complex interactions between morphological processes and hydrodynamic conditions shaping the shoreline evolution at Etretat and Hautot-sur-Mer beaches over the studied period.

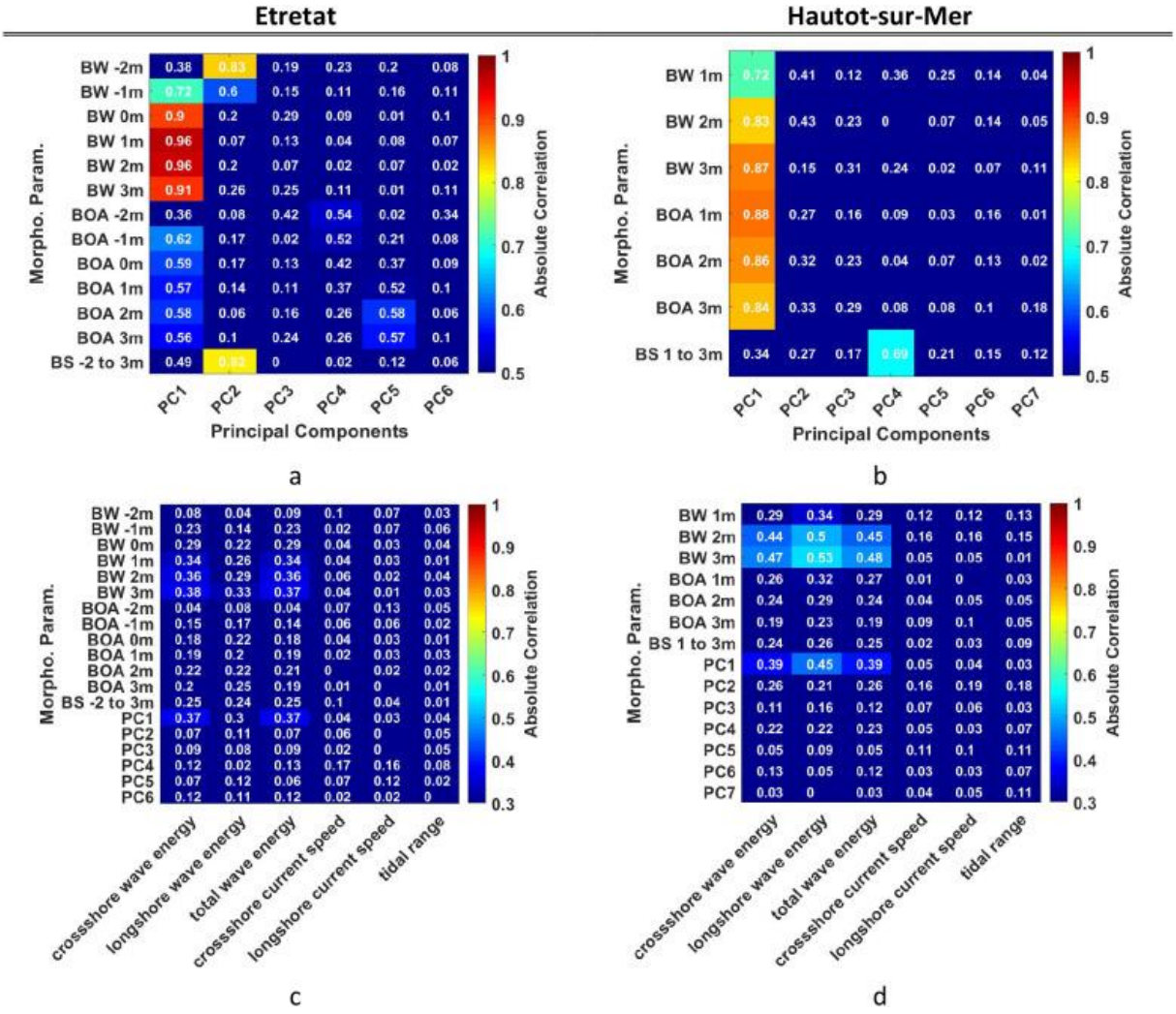

Figure 102. *Correlation matrix between morphodynamical parameters including Beach Width (BW), Beach Orientation Angle (BOA) and Beach Slope (BS) and the temporal eigenfunction of the principal components (PC) resulting from the EOF analysis applied to Etretat's shoreline position from elevations −2 m to +3 m (a), and to Hautot-sur-Mer from elevations +1 m to +3 m (b). c and d present the same operation calculated with hydrodynamic parameters including wave energy, current velocity and tidal range. Extracted from Soloy et al. (2022)*

6.2.1.4. Conclusion

The morphological evolution of two pebble beaches, including a purely gravel one in Etretat and a composite one in Hautot-sur-Mer, was investigated using an EOF analysis applied to a 2-year time series of shoreline positions at different elevations obtained from VMS. The EOF's PC highlighted the existence of at least four mechanisms of shoreline change including rotation, cross-shore translation, rollover and breathing. Despite their relative proximity, the two beaches present different sets of modes. The interpretation of most of the PCs was confirmed when calculating correlation coefficient between PCs and morphological parameters including BW, BOA and BS.

Moreover, the analysis showed that elevation plays a significant role in all mechanisms of shoreline position change, and that the influence of groin structures is more important in Hautot-sur-Mer, where it plays a role in every single PC, than in Etretat, where it is only visible in PC5.

A wavelet analysis highlighted common temporal periods of variability at a mid-term scale including 2, 3, 5, 6 and 8+ months. Periods of 2, 6 and 8+ months also identified in signals of wave energy, however tidal range and current velocity did not share any common period of variability with the considered morphodynamical parameters.

6.2.2. Numerical investigation into storm-driven pebble beach morphodynamics

The following section corresponds to the summary of the publication: *Soloy, A.; López Solano, C.; Turki, E. I.; Mendoza, E. T.; and Lecoq, N. (2024)* Rapid Changes in Permeability: Numerical Investigation into Storm-Driven Pebble Beach Morphodynamics with XBeach-G. *Journal of Marine Science and Engineering, 12, 237, https://doi.org/10.3390/jmse12020327*.

6.2.2.1. Introduction

Coarse-grained coastal systems, particularly gravel and pebble beaches, represent a substantial portion of shorelines in mid- to high-latitude regions globally, serving as vital natural buffers against sediment loss and energy dissipation during high-energy wave conditions and extreme storm events. These beaches, characterized by their steep faces and varying coarse-grain distribution influenced by energetic swash motions, play a crucial role in coastal protection. Despite extensive research spanning several decades, understanding and predicting the behavior of these coastal systems remain challenging, primarily due to limitations in accounting for sediment grain size and permeability, essential factors in swash dynamics on coarse-grained beaches. This study seeks to address these limitations by focusing on pebble beach morphodynamics using the XBeach-G numerical model.

The research site is the pebble beach of Etretat in Normandy, France, which is approximately 1000 m long and composed mainly of pebbles ranging from 2 to 10 cm. The beach experiences significant hydrodynamic conditions due to its location in the southern part of the English Channel, characterized by large tidal ranges and high energy waves during winter months. A video monitoring system deployed on the beach provides high-resolution images (**Figure 11**), essential for estimating pre- and post-storm cross-shore morphological profiles.

6.2.2.2. Methodological approach

The methodological approach integrates morphological data from various sources, including offshore data from SHOM, aerial lidar surveys by ROL, and daily observations from the Video Monitoring System (**Figure 103**). Hydrodynamic conditions are assessed using numerical model SWAN to generate the wave database described in Section 4.2, from June 2018 to September 2020.

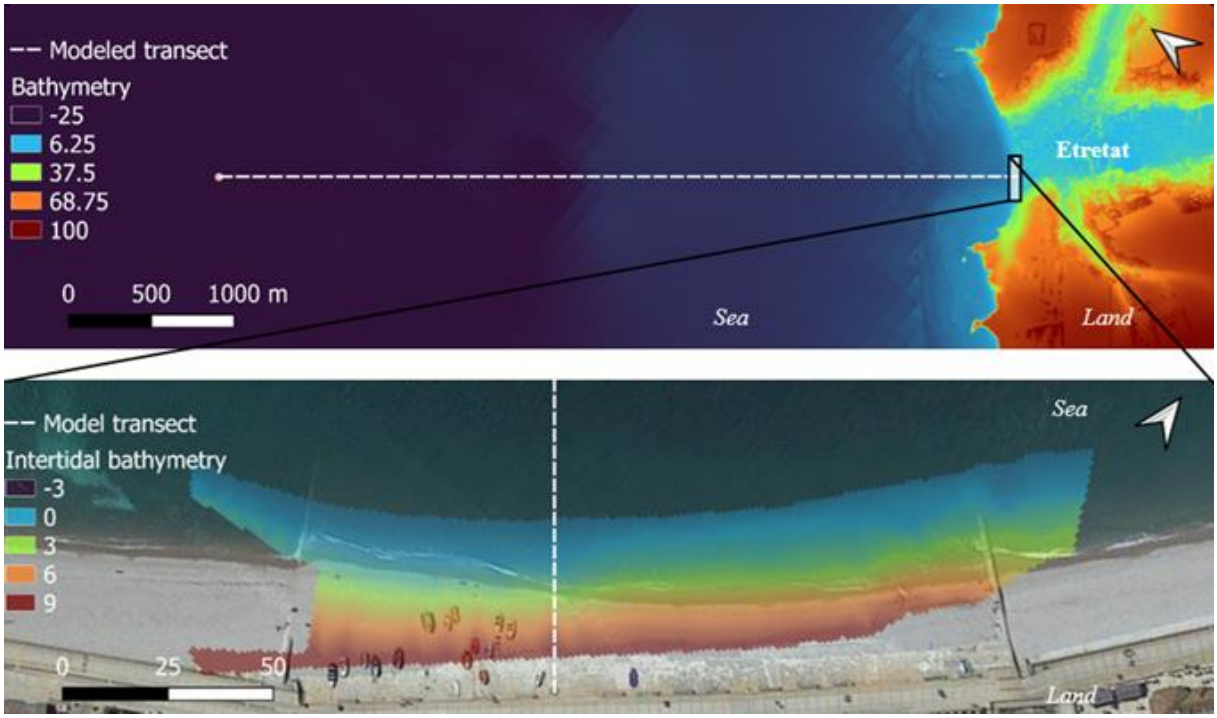

Figure 103. *Digital elevation model (DEM) of the subtidal along the offshore to nearshore transect from SHOM and ROL (a) and of the intertidal area observed using coastal Video Monitoring Systems (VMS, b). All datasets were merged, and elevations were extracted along the transect in order to provide profiles for each modeled day. Extracted from Soloy et al. (2024)*

Storm events are identified based on excessive wave heights. A marine storm is defined in this study as an event during which the significant wave height (H_s) exceeds a threshold ($H_{s,threshold}$) and lasts for at least 12 h. $H_{s,threshold}$ is set as the mean value of H_s plus two standard deviations. In addition, consecutive events separated by an interval of less than 48 h are merged and considered as one longer event. The list of storm events identified includes 30 storms, and, sorting them by decreasing accumulated energy, three major storms (A, B, and C) are selected for detailed investigation, considering their severity and duration (**Figure 104**).

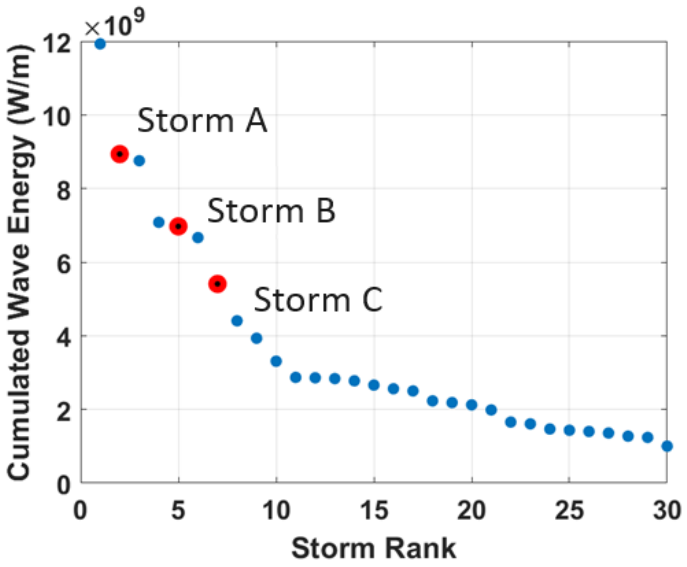

Figure 104. *Storm energy of the 30 most intense storms sorted by cumulated wave energy. Extracted from Soloy et al. (2024)*

The aim of the present numerical investigation is to assess beach permeability evolution by modeling storms with varying permeability (k) within the range of 0 to 0.6 m/s. This range aligns with the expected permeability for the measured surficial grain size in Etretat. Storms are segmented and modeled in 24 h intervals, approximately matching the daily frequency of intertidal bathymetry estimation from VMS observations. **Figure 105** shows the evolution of E_{flux} during the 3 selected storm events, as well as the dates on which the intertidal bathymetry data could be measured by the VMS (i.e., start, transition and end dates of the simulations). Only the dates where VMS-derived DEMs are wider than 35 m (an empirically chosen threshold) are considered usable to minimize the potential temporal decorrelation between the modeled profile and the real bathymetry.

6.2.2.3. Results

The XBeach-G numerical model is employed to simulate the morphological response of the beach profile to varying permeability values, ranging from 0 to 0.6, during the selected storm events. The simulations are conducted every 24 hours following the availability of DEMs derived from the VMS, covering the progression of each storm. To evaluate model performance, error calculations are performed. Results indicate that the morphological response of the beach is influenced by permeability, with optimal values identified for different storm conditions. However, the model's performance varies among storm events, with storm A showing the most significant agreement between observed and modeled profiles.

Morphological observations reveal changes in beach width, slope, and orientation in response to the different storm events. Accurate reproduction of accretion phenomena at the top of the beach is observed, but simulations underestimate movements in the lower part of the beach, especially with lower permeability values. The study highlights the importance of considering pebble permeability in numerical models to improve the understanding of pebble beach morphodynamics and inform coastal management decisions.

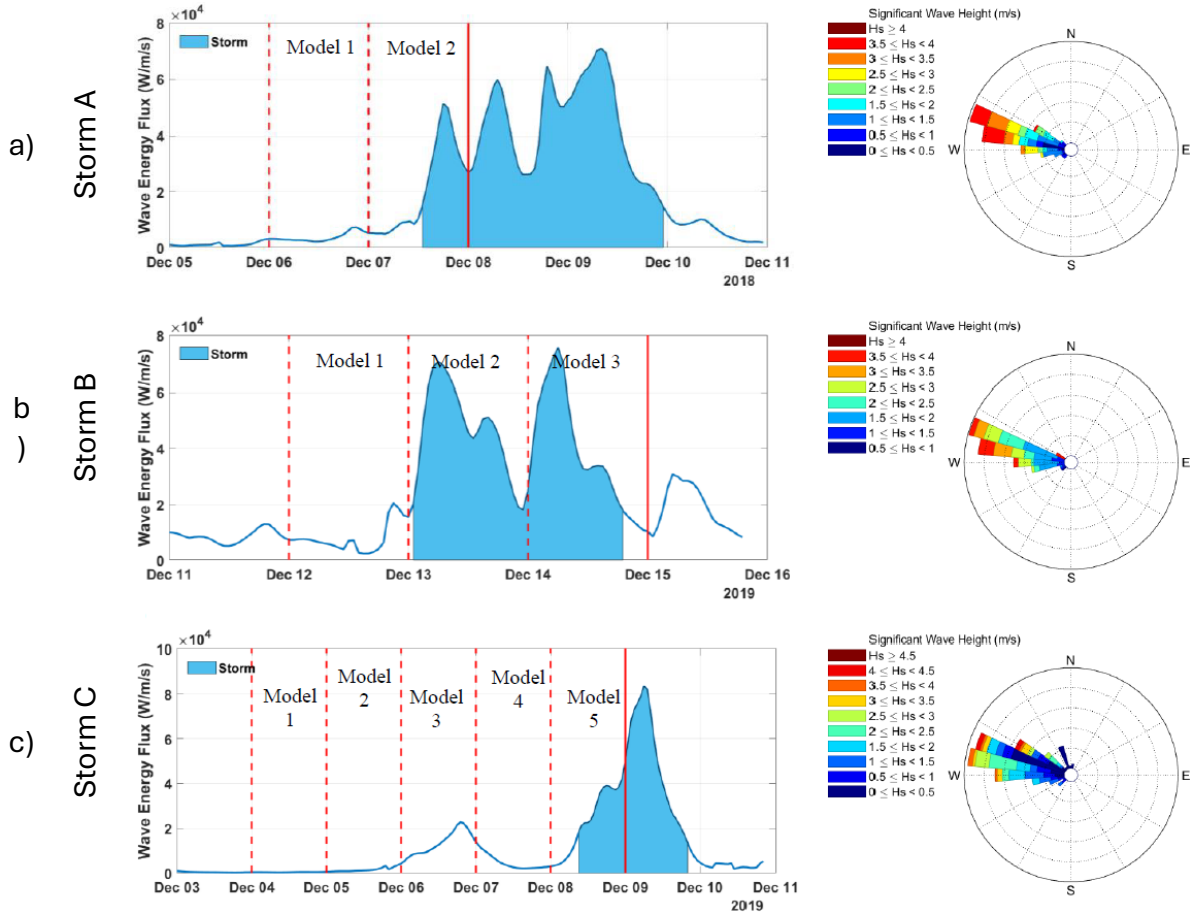

Figure 105. *Energy conditions associated to the different storm event, A (a), B (b) and C (c). Time series of wave energy flux during the three storms modeled using XBeach-G by intervals of 24 h. Vertical red lines (both dashed and solid) indicate the dates at which VMS-derived intertidal DEMs were available, the dashed ones specifically correspond to model starting dates while the solid lines indicate the last date with data available for model performance assessment. Extracted from Soloy et al. (2024)*

6.2.2.4. Discussion

The most relevant point that the study highlights is the intricate relationship between permeability and the morphodynamics of pebble beaches, particularly during storm events. The model underscores the significant impact of groundwater flow, as demonstrated during storm A, where the absence of flow accentuated sediment erosion and accumulation. This finding aligns with previous research and underscores the necessity of incorporating groundwater flow into morphodynamic estimations. Moreover, the study reveals that permeability plays a critical role in

controlling profile changes, with lower values resulting in smoother profiles and higher values favoring berm buildup. These observations highlight the nuanced influence of permeability on beach morphology under varying hydrodynamic conditions.

A critical aspect is the limitations of the modeling approach employed, particularly regarding data quality and the neglect of subtidal changes and supratidal morphology. Despite these challenges, the model results for storm A exhibit relative accuracy, suggesting a close approximation to reality for that specific date. Furthermore, comparisons with other studies at different sites reveal similar model performances, albeit with varying degrees of success in meeting specific criteria, which underscores the complexity of accurately modeling pebble beach dynamics.

The implications of grain size on modeling pebble beaches are explored, with a focus on observed morphological changes during calm periods and storm events. Notably, the construction of horizontal berms during calm periods and subsequent erosion during storms aligns with previous findings on the rollover mechanism. The study suggests that the morphological characteristics of berms could serve as a proxy for permeability during storms, highlighting the need for further investigation in this area. Moreover, the study emphasizes the temporal variability in permeability, with potential shifts from “pure gravel” to “mixed sand and gravel” systems under certain conditions.

Insights into the complex evolution of pebble beaches are provided, acknowledging the successful modeling of storm A while recognizing the inherent limitations of the dataset and modeling approach. This study underscores the need for advancements in coastal monitoring and grain size mapping techniques to enhance model accuracy, particularly in capturing the spatiotemporal variability in permeability during storm events. Overall, the analysis sheds light on the intricate interplay between storm dynamics, permeability, and morphological changes in pebble beaches, calling for further exploration and refinement in this field to better understand and predict coastal processes.

6.2.2.5. Conclusions

This study employed XBeach-G to simulate the impact of three intense storms occurring between 2018 and 2020 on the Etretat beach in Normandy, France. The modeling aimed to calibrate the permeability value (k) to understand its day-to-day and inter-storm variations. Among the modeled events, satisfactory results were obtained for storm A. These results indicated permeability values of k = 0.20 m/s to 0.35 m/s and k = 0.05 m/s, consistent with expectations for well-sorted coarse and fine gravel sizes, respectively.

However, storms B and C yielded unsatisfactory results, likely due to limitations in the approach, including imprecise subtidal and supratidal topography, lack of updating in the subtidal area, and the neglect of longshore sediment transport. Indeed, the time series of beach orientation angle suggested significant longshore transport, which the model could not capture due to the one-dimensional nature of XBeach-G.

This study emphasized the sensitivity of the beach profile to permeability, where high values led to berm formation, and low values resulted in erosion. The intensity of wave conditions influenced the amplitude of topographic changes. The storm A results indicated a potential fourfold decrease in permeability within 24 h, emphasizing the dynamic nature of pebble beaches during storm events, especially regarding their ability to dissipate wave energy through infiltration/exfiltration processes.

The findings challenged the strict characterization of Etretat beach as “purely gravel”, suggesting occasional transitions to a “mixed sand and gravel” system, possibly seasonal. The spatial and temporal uniformity of k, grain size, and porosity were identified as limitations in the XBeach-G model.

6.3. CONCLUSIONS OF THE CHAPTER

This chapter explores the potential hydro-macrodynamic coastal applications of the different methodologies and generated databases developed in Chapters 3 and 4 and presents the connections of the studies of hydrodynamics to other studies centered in morphodynamics of beaches in response to the extreme scenarios found in this PhD research.

The first application presented integrates the non-stationary stochastic approach described in Chapter 3 for identifying and defining extreme scenarios of waves and sea level with the database generated in the English Channel by numerical modeling described in Chapter 4. This study focuses on the compound flooding produced in the Seine estuary by fluvial and coastal extreme events. The key findings show that, for the case of the Seine Bay, the extreme events of river discharge are delimited by an asymptotic margin, so the flooding produced by this variable is not strongly increased by the highest return periods. The storm surge produces a stronger impact on the study area, especially when the extreme events occur during a storm with higher waves arriving to the coast. The major impact is produced by compound events of river discharge and storm surge taking place at the same time, that may happen simultaneously by demonstrated

in other studies. The effect of extreme events of river discharge in this estuary mostly disappear when the area of interest is located further from the Seine mouth.

Second and third applications are more related to the morphodynamic response of pebble beaches to extreme hydrodynamic scenarios. The first of them presents the analysis of the morphological evolution of the pebbles beaches of Etretat and Hautot-sur-Mer through time series of shoreline positions recorded by Video Monitoring Systems. The PCs obtained from EOF analysis highlighted the existence of at least four mechanisms of shoreline change, in which elevation plays a significant role, and that the influence of groin structures is more important in Hautot-sur-Mer than in Etretat, coherent with what is presented in Chapter 5. A final wavelet analysis highlighted common temporal periods of variability at a mid-term scale, with some of them also identified in signals of wave energy but not with tidal range.

The last application uses the nearshore database described in Chapter 4 in combination with VMS records to simulate storms with numerical model XBeach-G, aiming to calibrate the permeability value. This study emphasized the sensitivity of the beach profile to permeability, where high values led to berm formation, and low values resulted in erosion. The intensity of wave conditions influenced the amplitude of topographic changes, highlighting the dynamic nature of pebble beaches during storm events, especially regarding their ability to dissipate wave energy through infiltration/exfiltration processes, also coherent with the results of Chapter 5.

CHAPTER 7

CONCLUSIONS AND PERSPECTIVES OF THE DISSERTATION

7.1. MAIN CONCLUSIONS OF THE DISSERTATION

The PhD research is mainly focused on the dynamics of extreme events in coastal systems from the regional scale to the local scales of Normandy, taking into account the effects of climate mechanisms on the extreme hydrodynamics. This work has been carried out by coupling stochastic and numerical approaches and exploring the coupling of both to obtain the dynamics of these events at different spatial and time scales. Although the English Channel has been extensively studied previously, the perspectives and combination of methodologies developed in the present project is innovative and sheds light on the influence of large-scale parameters on local extreme events of waves and sea level, represented by the wave height and the storm surge, followed by the study of the evolution and transformation of storms from deep waters towards the coasts of Normandy, including the impact on the shoreline.

However, coastal systems are often subject to different complexities, induced by the diversity of regimes and interacting processes in the nearshore zone, especially in zones controlled by different forcings (waves, tides, surges) including the effects of river discharge, case of the Normandy beaches, in the proximity of the Seine Bay, that are influenced by the Seine River. Such complexities are significantly important during extreme events of storms, river floods and the concomitant events when the modulation of sea level, induced by the hydrodynamics forcings, is highly observed.

These challenges should be addressed by integrating the different timescales, from the scale of the event to climate change, and spatial scales from the large-scales to the regional and the local dynamics. In the course of the research activities carried out, the key research questions are centered on different stochastic and numerical approaches to identify and characterize extreme events arriving from the ocean to the coast, studying particularly their behavior in the English Channel and on the Normandy coasts.

The first group of questions were focused on the non-stationary connections between the global climate oscillations and the extreme hydrodynamics, considering them for developing diverse stochastic downscalings and estimating the extreme events in the English Channel during the last decades.

The stochastic approaches performed involve the spectral and the probabilistic analyses of extreme values of coastal waves and surges in different locations along the English Channel, from Brest on the West to Dover and Dunkirk on the East, including Le Havre on the coasts of Normandy. The spectral analysis includes the frequential decomposition of extreme values to obtain the spectral components that present a significant explained variance. The spectral

components obtained from the decomposition of the signal of the extreme values of waves and surges have allowed finding direct correlations with some of the main atmospheric patterns and climate indexes, particularly noticeable for lower frequencies. In the same way, the non-stationary fitting of the sample of extreme values of waves and surges reinforces these correlations, by accounting for the non-stationarity with the atmospheric patterns taken as covariates in the parameters of the adjusted distribution functions.

This has led to a further characterization of the joint return levels of both variables for each study site, represented in an additional bivariate adjusted distribution. It was possible to combine both analyses by performing a supplementary extreme value fitting of the different timescales taken from the spectral decomposition. Common explained variances of the different timescales between the atmospheric circulation and the local extreme events were found, from monthly to interannual and, when possible, interdecadal.

A definition of extreme event is also given by including the duration, identifying the severity and the persistence of a storm, which enables the obtention of the storm energy. The energy has been used to perform a classification of single and compound extreme events of waves and surges for the studied locations. A clustering of storms has been performed lastly, determining the typical hydroclimatic extreme scenarios on the coasts of the English Channel.

In a parallel way, the second group of questions assessed the hydrodynamic evolution of storms from the English Channel towards the Normandy coasts to extend the study of the dynamics of extreme events to all the basin in a regional scale, highlighting their physical transformations and addressing their severity as one of their main drivers.

The numerical approach is represented by modelling 40 years of waves and sea level covering the whole English Channel. The forcings of the numerical model, which included harmonic components for the astronomical tides, wave parameters and wind speed and atmospheric pressure, have been taken from different reanalysis databases and calibrated aiming more accuracy in the results. From this modelling, representative points throughout the Channel were chosen to analyze the evolution and modification of storms.

The databases obtained at each point allowed recognizing the Atlantic Ocean as the main source of origin of the extreme events arriving, although some could come from the North Sea arriving to Normandy but dissipated if they propagate in the English Channel. Among the extreme events generated in the Atlantic Ocean, storms can be grouped into three main directional sectors of origin that present different evolutions when they propagate towards the Normandy coasts. The most important impact seems to come from the ones entering the Channel with a direction close

to the orientation of the basin, of about 70 degrees to the North, since they suffer from minimal wave refraction. Other storms, even if they are bigger when incoming, are more dissipated, generating less impact on the coasts of Normandy.

On a more local scale, focusing on Etretat and Hautot-sur-Mer, some known storms were taken as an example to examine the last modifications of extreme events before reaching the Norman shore. The characteristics analyzed were refraction and wave height gradient of the extreme events from deep waters to shallow waters. Supporting the previous findings, out of the 10 studied storms, storms arriving with the most hazardous conditions seem to be those propagating in a longitudinal direction of the English Channel, which allows a refraction that makes them reach the shoreline perpendicularly and with a higher wave height.

Continuing the downscaling and tracing the extreme events from outside of the English Channel to the Normandy coasts, the subsequent group of questions aimed to model coastal flooding in response to extreme scenarios. Considering the particularities of the different Norman coastal contexts, from sandy to mixed and gravel beaches, the limitations in accurately reproducing the process of flooding by the use of numerical models were addressed, with the solving of depth as a key point.

The impacts of the extreme events on the coasts of Normandy have been studied by the analysis of 4 representative storms on the same two previous locations, Etretat and Hautot-sur-Mer, characterized by their coarse grain size, considered as a purely gravel and a composite beach, respectively. Villers-sur-Mer, a sandy beach, is also included to exemplify the typical morphologies of beaches on the south of the Seine estuary.

Different beach profiles were chosen at these sites according to the local morphologies and conditions in order to compare the simulated storms on each location between them and, additionally, allowing the comparison of the same storm between sites. On these profiles, run-up of waves was measured to figure out these differences or find out some possible similarities. The run-up model was modelled and also validated comparing the output of the simulations with the results of traditional formulations, but, innovatively, the measurements obtained from records of the Video Monitoring Systems (VMS) installed on these beaches were also used for this purpose.

Pebbles and gravel, retained between groins on the beaches north of the Seine Estuary play an important role in the dissipation of extreme events impacting the shoreline, making it difficult for the run-up to reach the coast and cause flooding. Nevertheless, the dynamism of this kind of sediment limits the extent of the study, needing the model from updated data of the elevation of the beach and the distribution of the sediment that agrees with the time of the simulation carried

out. The absence or a sudden reduced quantity of pebbles may lead to less protected shorelines that are more vulnerable to flooding. On the other hand, on sandy beaches with a gentler slope, waves uprush easily, but the impact is less significant due to the dissipation of important storms when they reach these systems.

Finally, exploring the different findings of the whole PhD research, and combining them, some hydro-macrodynamic coastal applications were developed. The stochastic and numerical approaches developed can be merged and this combination can be used for other types of studies.

Taking the probabilistic analysis of extreme values of waves and surges, extracted from the generated database in the English Channel, and their bivariate distribution, in the Seine estuary, the typical extreme levels of these two variables were obtained. Merging it with extreme fluvial discharge of the Seine River, an application of these methodologies was carried out to study the compound flooding in the Seine Estuary.

Out of all the possible combinations of extreme coastal and fluvial conditions, the main finding was proving that storm surge plays a more important role than river discharge when it comes to the compound flooding, even in areas located on the riverbanks before the transitional part where the river joins the sea.

Other phenomena can also be included in the studies of coastal applications, like the morphodynamics of beaches, combining the numerical approach to study hydrodynamics and obtaining the response of beaches to typical extreme scenario impacting on them.

All these findings are linked to applied actions coordinated by coastal managers of public and private environmental organisms (Agence de l'Eau and IRSN), including stakeholders, as well as different societal issues.

7.2. RESEARCH PERSPECTIVES

In continuation of the presented achievements, the major challenge is related to the vulnerability of coastal and estuarine systems as well as their resilience by the use of coupling approaches, including multi-sensor, numerical stochastic and physical approaches.

A special focus will be given to the response of coastal systems to extreme events of storms and fluvial floods as well as their multi-timescale evolution. To do this, integrating the different spatial and temporal scales is key for assessing the coastal risks of erosion and flooding. This

requires the development of new approaches based on deep learning techniques to improve the accuracy of coupling between numerical modelling and remote sensing dataset, including the data assimilation. In the context of SWOT mission, the acquired water level data will be explored to improve the full coverage of the different coastal and estuarine processes. The data will also be used for assimilating water levels in hydrodynamic models.

At large scales of climate change, the future projections of the shoreline position require the use of hybrid models, especially for coastal systems with a series of data-driven parametrization as gravel and mixed sand-gravel beaches. Additionally, I would like to improve my understanding of the nonlinear interaction between the coastal processes and the morphological changes as well as the sensitivity of these changes to the hydrodynamics forcings. In particular, the depth and wave resolved models will be coupled with laboratory experiments for quantifying the storm-induced overwash and beach erosion.

Overall, such ongoing works are uniquely positioned to help us for (1) understanding the physical interrelationships of parameters, (2) improving the numerical models use on a large scale in conjunction with observed surveys, (3) proposing the mitigation measures to reduce the hazard impacts in the interface zones.

These ongoing works could be addressed through a series of scientific challenges:

1. Nearshore sea-level variability resulting from the nonlinear interaction between the different processes (wave-tide-surges). The modulation of tides, waves and the wave-induced set-up should be taken into account as well as the interaction between surges, tides and waves.

In this part, we try to resolve the following points: (a) the evolution of the high and the low frequencies of sea level variability, frequently under-represented in sea level analyses, and their contribution on the extreme sea levels (ESL) which are of great research interest and importance to coastal managers, (b) the shorter- and longer term effects of atmospheric forcing on the SLR as a main driver of coastal sea level change, (c) the physical dependence between the shelf properties (width, slope, topography) and the frequencies of sea level when ocean waves are traveling to the nearshore, (d) the extent of the use of high-resolution numerical models and satellites to improve our understanding of this dependence.

2. Coastal changes and wave driven processes (IGW, seiches, swash, ...) on beaches (sandy and gravel systems) and estuaries (in their lower part - downstream).

In this part and with the aim to resolve the wave-driven processes and their effects on sea level variability, a special focus will be given to the effects of high-frequency waves on the flooding

assessment close to the coasts and the lower estuaries. Understanding the processes of the tidal deformation, wave-induced set up and the river run-off as well as their effects on the sea level variability, in particular during extreme events of storms and flooding, are also the objectives of this part. Moreover, laboratory experimentation has a key role on the improvement of our understanding of some physical processes; this approach is strongly recommended for the validation of the numerical models.

3. The response hydro-morphodynamics of coastal and Estuarine (river-tidal systems) to extreme events of storms and high river discharge. A special focus is given to the risks related to flooding through the processes of wave run-up/swash, overwash and overtopping close to beaches and breakwaters, as well as the resonance induced by the standing waves of seiches.

The impact of such processes on the beach changes and their recovery after storm events will be investigated with the aim of assessing coastal vulnerability.

Finally, and in the framework of the new mission SWOT, the assimilation of data in ocean and coastal models will be instrumental to control smaller scales (< 100 km) that are not well constrained by conventional altimeters. Most impacted fields will be surface and intermediate horizontal velocities. This will directly impact onkey applications such as marine safety, pollution monitoring, ship routing, offshore industry. A better constraint of vertical velocities will also directly impact biogeochemical applications. Our main objective is to prepare the assimilation of SWOT high resolution ocean and coastal models. Assimilation of SWOT data together with conventional altimeter missions into ocean analysis and forecasting models is an essential and (most likely) mandatory step to develop a wide use of SWOT data for ocean applications. This is also required to better address many coastal research issues. SWOT will provide very high and unique resolution observations along its swaths (effective wavelength resolution of 15 km as stated in the mission science requirement document) but will not be able to observe high frequency signals (periods < 20 days). In addition, at large scales (> 1000 km), SWOT data will have to be adjusted and merged with conventional altimeter data.

REFERENCES

Abroug, I., Abcha, N., Jarno, A., & Marin, F. (2020). Laboratory study of non-linear wave-wave interactions of extreme focused waves in the nearshore zone. *Natural Hazards and Earth System Sciences*, *20*(12), 3279–3291. https://doi.org/10.5194/nhess-20-3279-2020

Alabart Llinàs, J., Sánchez-Arcilla, A., Gerbrant, C., & Vledder, V. (2013). *Analysis of the performance of SWASH in harbour domains*.

Almar, R., Cienfuegos, R., Catalán, P. A., Michallet, H., Castelle, B., Bonneton, P., Marieu, V. (2012). A new breaking wave height direct estimator from video imagery. *Coastal Engineering*, 61, 42-48. https://doi.org/10.1016/j.coastaleng.2011.12.004

Almar, R., Ranasinghe, R., Bergsma, E. W. J., Diaz, H., Melet, A., Papa, F., Vousdoukas, M., Athanasiou, P., Dada, O., Almeida, L. P., & Kestenare, E. (2021). A global analysis of extreme coastal water levels with implications for potential coastal overtopping. *Nature Communications*, *12*(1), 3775. https://doi.org/10.1038/s41467-021-24008-9

Almeida, L. P., Masselink, G., Russell, P. E., & Davidson, M. A. (2015). Observations of gravel beach dynamics during high energy wave conditions using a laser scanner. *Geomorphology*, *228*, 15–27. https://doi.org/10.1016/j.geomorph.2014.08.019

Anthony, E. J. (2013). Storms, shoreface morphodynamics, sand supply, and the accretion and erosion of coastal dune barriers in the southern North Sea. *Geomorphology*, *199*, 8–21. https://doi.org/10.1016/j.geomorph.2012.06.007

Antolínez, J. A. A., Méndez, F. J., Anderson, D., Ruggiero, P., & Kaminsky, G. M. (2019). Predicting Climate-Driven Coastlines With a Simple and Efficient Multiscale Model. *Journal of Geophysical Research: Earth Surface*, *124*(6), 1596–1624. https://doi.org/10.1029/2018JF004790

Appendini, C. M., Torres-Freyermuth, A., Salles, P., López-González, J., & Mendoza, E. T. (2014). Wave climate and trends for the Gulf of Mexico: A 30-yr wave hindcast. *Journal of Climate*, *27*(4), 1619–1632. https://doi.org/10.1175/JCLI-D-13-00206.1

Ardhuin, F., Roland, A., Dumas, F., Bennis, A. C., Sentchev, A., Forget, P., Wolf, J., Girard, F., Osuna, P., & Benoit, M. (2012). Numerical wave modeling in conditions with strong currents: Dissipation,refraction, and relative wind. *Journal of Physical Oceanography*, *42*(12), 2101–2120. https://doi.org/10.1175/JPO-D-11-0220.1

Arns, A., Dangendorf, S., Jensen, J., Talke, S., Bender, J., & Pattiaratchi, C. (2017). Sea-level rise induced amplification of coastal protection design heights. *Scientific Reports*, *7*. https://doi.org/10.1038/srep40171

Arriaga, J., Medellin, G., Ojeda, E. & Salles, P. (2022) Shoreline Detection Accuracy from Video Monitoring Systems. *Journal of Marine Science and Engineering*, *10(1):95*. https://doi.org/10.3390/jmse10010095

Bacopoulos, R. G., & Perry, A. H. (1973). Synoptic climatology: methods and applications. *Methuen & Co Ltd*, 555

Barry, P., & Clark, R. R. (2021). Coastal erosion and structural damage due to four consecutive-year major hurricanes: Beach projects afford resilience and coastal protection. *Ocean & Coastal Management*, *209*, 105643. https://doi.org/10.1016/j.ocecoaman.2021.105643

Bennis, A. C., Furgerot, L., Bailly Du Bois, P., Poizot, E., Méar, Y., & Dumas, F. (2022). A winter storm in Alderney Race: Impacts of 3D wave–current interactions on the hydrodynamic and tidal stream energy. *Applied Ocean Research*, *120*. https://doi.org/10.1016/j.apor.2021.103009

Bertin, X., Li, K., Roland, A., Zhang, Y. J., Breilh, J. F., & Chaumillon, E. (2014). A modeling-based analysis of the flooding associated with Xynthia, central Bay of Biscay. *Coastal Engineering*, *94*(212), 80–89. https://doi.org/10.1016/j.coastaleng.2014.08.013

Biausque, M., & Senechal, N. (2019). Seasonal morphological response of an open sandy beach to winter wave conditions: The example of Biscarrosse beach, SW France. *Geomorphology*, *332*, 157–169. https://doi.org/10.1016/j.geomorph.2019.02.009

Booij, N., Ris, R. C., & Holthuijsen, L. H. (1999). A third-generation wave model for coastal regions 1. Model description and validation. *Journal of Geophysical Research: Oceans*, *104*(C4), 7649–7666. https://doi.org/10.1029/98JC02622

Boudière, E., Maisondieu, C., Ardhuin, F., Accensi, M., Pineau-Guillou, L., & Lepesqueur, J. (2013). A suitable metocean hindcast database for the design of Marine energy converters. *International Journal of Marine Energy*, *3–4*. https://doi.org/10.1016/j.ijome.2013.11.010

Boussinesq, J. (1903). *Théorie Analytique de la Chaleur: Vol. II* (Gauthier-Villars).

Bromirski, P. D., & Flick, R. E. (2008). Storm surge in the San Francisco Bay/Delta and nearby coastal locations. *Shore & Beach*, *76*(3), 29–37.

BUSCOMBE, D., & MASSELINK, G. (2009). Grain-size information from the statistical properties of digital images of sediment. *Sedimentology*, *56*(2), 421–438. https://doi.org/10.1111/j.1365-3091.2008.00977.x

Caires, S., Sterl, A., Bidlot, J.-R., Graham, N., & Swail, V. (2004). *Intercomparison of Different Wind-Wave Reanalyses* (Vol. 17, Issue 10).

Camus, P., Cofiño, A. S., Mendez, F. J., & Medina, R. (2011). Multivariate wave climate using self-organizing maps. *Journal of Atmospheric and Oceanic Technology*, *28*(11), 1554–1568. https://doi.org/10.1175/JTECH-D-11-00027.1

Camus, P., Mendez, F. J., & Medina, R. (2011). A hybrid efficient method to downscale wave climate to coastal areas. *Coastal Engineering*, *58*(9), 851–862. https://doi.org/10.1016/j.coastaleng.2011.05.007

Camus, P., Menéndez, M., Méndez, F. J., Izaguirre, C., Espejo, A., Cánovas, V., Pérez, J., Rueda, A., Losada, I. J., & Medina, R. (2014). A weather-type statistical downscaling framework for ocean wave climate. *Journal of Geophysical Research: Oceans*, *119*(11), 7389–7405. https://doi.org/10.1002/2014JC010141

Carrere, L., Lyard, F., Guillot, A., & Picot, N. (2016). FES2014, a new tidal model: Validation results and perspectives for improvements. *ESA Living Planet Conference*.

Castelle, B., Marieu, V., Bujan, S., Splinter, K. D., Robinet, A., Sénéchal, N., & Ferreira, S. (2015). Impact of the winter 2013-2014 series of severe Western Europe storms on a double-barred sandy coast: Beach and dune erosion and megacusp embayments. *Geomorphology*, *238*, 135–148. https://doi.org/10.1016/j.geomorph.2015.03.006

Cavaleri, L., & Sclavo, M. (2006). The calibration of wind and wave model data in the Mediterranean Sea. *Coastal Engineering*, *53*(7), 613–627. https://doi.org/10.1016/j.coastaleng.2005.12.006

Chapon, A., & Hamdi, Y. (2022). A Bivariate Nonstationary Extreme Values Analysis of Skew Surge and Significant Wave Height in the English Channel. *Atmosphere*, *13*(11). https://doi.org/10.3390/atmos13111795

Chau, K. W. (2010). *Modelling for Coastal Hydraulics and Engineering*. Spon Press.

Chebana, F., & Ouarda, T. B. M. J. (2011). Multivariate quantiles in hydrological frequency analysis. *Environmetrics*, *22*(1), 63–78. https://doi.org/10.1002/env.1027

Chebana, F., & Ouarda, T. B. M. J. (2021). Multivariate non-stationary hydrological frequency analysis. *Journal of Hydrology*, *593*, 125907. https://doi.org/10.1016/j.jhydrol.2020.125907

Church, J., Clark, P. U., Cazenave, A., Gregory, J. M., Jevrejeva, S., Levermann, A., Merrifield, M. A., Milne, G., Nerem, R. S., Nunn, P. D., Payne, A. J., Pfeffer, W. T., Stammer, D., & Unnikrishnan, A. (2013). *Climate Change 2013: The Physical Science Basis. Contribution of Working Group I to the Fifth Assessment Report of the Intergovernmental Panel on Climate Change*. https://www.researchgate.net/publication/284695835

Coles, S. (2001). *An Introduction to Statistical Modeling of Extreme Values*. Springer London. https://doi.org/10.1007/978-1-4471-3675-0

Corbella, S., & Stretch, D. D. (2013). Simulating a multivariate sea storm using Archimedean copulas. *Coastal Engineering*, *76*, 68–78. https://doi.org/10.1016/j.coastaleng.2013.01.011

Dangendorf, S., Wahl, T., Hein, H., Jensen, J., Mai, S., & Mudersbach, C. (2012). Mean Sea Level Variability and Influence of the North Atlantic Oscillation on Long-Term Trends in the German Bight. *Water*, *4*(1), 170–195. https://doi.org/10.3390/w4010170

Dee, D. P., Uppala, S. M., Simmons, A. J., Berrisford, P., Poli, P., Kobayashi, S., Andrae, U., Balmaseda, M. A., Balsamo, G., Bauer, P., Bechtold, P., Beljaars, A. C. M., van de Berg, L., Bidlot, J., Bormann, N., Delsol, C., Dragani, R., Fuentes, M., Geer, A. J., … Vitart, F. (2011). The ERA-Interim reanalysis: Configuration and performance of the data assimilation system. *Quarterly Journal of the Royal Meteorological Society*, *137*(656), 553–597. https://doi.org/10.1002/qj.828

Deltares. (2020). *Delft3D-FLOW User Manual Version 3.15*.

Deng, W., Cohen, J. B., Wang, S., & Lin, C. (2021). Improving the understanding between climate variability and observed extremes of global NO_2 over the past 15 years. *Environmental Research Letters*, *16*(5), 054020. https://doi.org/10.1088/1748-9326/abd502

Dhoop, T., & Thompson, C. (2021). Swell wave progression in the English Channel: implications for coastal monitoring. *Anthropocene Coasts*, *4*(1), 281–305. https://doi.org/10.1139/anc-2021-0008

Dodet, G., Castelle, B., Masselink, G., Scott, T., Davidson, M., Floc'h, F., Jackson, D., & Suanez, S. (2019). Beach recovery from extreme storm activity during the 2013–14 winter along the Atlantic coast of Europe. *Earth Surface Processes and Landforms*, *44*(1), 393–401. https://doi.org/10.1002/esp.4500

Dumas, F., Pineau-Guillou, L., Lecornu, F., le Roux, J.-F., & le Squère, B. (2021). *General Introduction: PREVIMER, a French pre-operational coastal ocean forecasting capability*. https://archimer.ifremer.fr/doc/00189/30037

Egbert, G. D., & Erofeeva, S. Y. (2002). Efficient Inverse Modeling of Barotropic Ocean Tides. *Journal of Atmospheric and Oceanic Technology*, *19*(2), 183–204. https://doi.org/10.1175/1520-0426(2002)019<0183:EIMOBO>2.0.CO;2

Elsevier Ocean Engineering Series. (1999). *Ocean Wave Measurement* (pp. 227–254). https://doi.org/10.1016/S1571-9952(99)80011-7

EMODnet Bathymetry Portal. (2023).

E.U. Copernicus Marine Service Information (CMEMS) (2024a). *Atlantic- European North West Shelf- Wave Physics Reanalysis*. Marine Data Store (MDS). https://doi.org/https://doi.org/10.48670/moi-00060

E.U. Copernicus Marine Service Information (CMEMS) (2024b). *Global Ocean Waves Reanalysis*. Marine Data Store (MDS). Retrieved May 30, 2024, from https://data.marine.copernicus.eu/product/GLOBAL_MULTIYEAR_WAV_001_032/description

EurOtop. (2018). *EurOtop Manual on wave overtopping of sea defences and related structures An overtopping manual largely based on European research, but for worldwide application Second Edition 2018*. www.overtopping-manual.com

Frankignoul, C., de Coëtlogon, G., Joyce, T. M., & Dong, S. (2001). Gulf Stream Variability and Ocean–Atmosphere Interactions*. *Journal of Physical Oceanography*, *31*(12), 3516–3529. https://doi.org/10.1175/1520-0485(2002)031<3516:GSVAOA>2.0.CO;2

Goda, Y. (1985). *Random Seas and Design of Maritime Structures* (Vol. 33). WORLD SCIENTIFIC. https://doi.org/10.1142/7425

Gouldby, B., & Samuels, P. (2005). *Language of Risk - Project definitions*. FLOODsite.

Guedes Soares, C., & Scotto, M. G. (2004). Application of the r largest-order statistics for long-term predictions of significant wave height. *Coastal Engineering*, *51*(5–6), 387–394. https://doi.org/10.1016/j.coastaleng.2004.04.003

Guillou, N. (2013) Effects of bed-sediment grain-size distribution on wave height predictions in the English Channel *Conference: Coastal Dynamics 2013*

Guillou, N., & Chapalain, G. (2015). Numerical modelling of nearshore wave energy resource in the SeaofIroise. *Renewable Energy*, *83*, 942–953. https://doi.org/10.1016/j.renene.2015.05.021

Guo, L., Wang, Z. B., Townend, I., & He, Q. (2019). Quantification of Tidal Asymmetry and Its Nonstationary Variations. *Journal of Geophysical Research: Oceans*, *124*(1), 773–787. https://doi.org/10.1029/2018JC014372

Halpern, B. S., Walbridge, S., Selkoe, K. A., Kappel, C. V., Micheli, F., D'Agrosa, C., Bruno, J. F., Casey, K. S., Ebert, C., Fox, H. E., Fujita, R., Heinemann, D., Lenihan, H. S., Madin, E. M. P., Perry, M. T., Selig, E. R., Spalding, M., Steneck, R., & Watson, R. (2008). A Global Map of Human Impact on Marine Ecosystems. *Science*, *319*(5865), 948–952. https://doi.org/10.1126/science.1149345

Hamdi, Y., Duluc, C.M., Bardet, L. & Rebour, V. (2019) Development of a target-site-based regional frequency model using historical information. *Natural Hazards* 98, 895–913 (2019). https://doi.org/10.1007/s11069-018-3237-8

Hamdi, Y., Duluc, C. M., & Rebour, V. (2018). Temperature extremes: Estimation of non-stationary return levels and associated uncertainties. *Atmosphere*, *9*(4). https://doi.org/10.3390/atmos9040129

Hanson, S., Nicholls, R., Ranger, N., Hallegatte, S., Corfee-Morlot, J., Herweijer, C., & Chateau, J. (2011). A global ranking of port cities with high exposure to climate extremes. *Climatic Change*, *104*(1), 89–111. https://doi.org/10.1007/s10584-010-9977-4

Harley, M. (2017). Coastal Storm Definition. In *Coastal Storms: Processes and Impacts* (pp. 1–21). Wiley Blackwell. https://doi.org/10.1002/9781118937099.ch1

Harrison, L. M., Coulthard, T. J., Robins, P. E., & Lewis, M. J. (2021). Sensitivity of Estuaries to Compound Flooding. *Estuaries and Coasts*, *45*(5), 1250–1269. https://doi.org/10.1007/s12237-021-00996-1

Hasselmann, K., Barnett, T. P., Bouws, E., Carlson, H., Cartwright, D. E., Enke, K., Ewing, J. A., Gienapp, H., Hasselmann, D. E., Kruseman, P., Meerburg, A., Müller, P., Olbers, D. J., Richter, K., Sell, W., & Walden, H. (1973). *Measurements of wind-wave growth and swell decay during the Joint North Sea Wave Project (JONSWAP)*. Deutches Hydrographisches Institut.

Hasselmann, K., Bauer, E., & Janssen, P. A. E. M. (1988). The WAM model-a third generation ocean wave prediction model. Acoustic monitoring of Ocean Climate in the Arctic Ocean (AMOC) View project. In *Article in Journal of Physical Oceanography*. https://www.researchgate.net/publication/215722039

Hegermiller, C. A., Antolinez, J. A. A., Rueda, A., Camus, P., Perez, J., Erikson, L. H., Barnard, P. L., & Mendez, F. J. (2017). A Multimodal Wave Spectrum–Based Approach for Statistical Downscaling of Local Wave Climate. *Journal of Physical Oceanography*, *47*(2), 375–386. https://doi.org/10.1175/JPO-D-16-0191.1

Hersbach, H., Bell, B., Berrisford, P., Hirahara, S., Horányi, A., Muñoz-Sabater, J., Nicolas, J., Peubey, C., Radu, R., Schepers, D., Simmons, A., Soci, C., Abdalla, S., Abellan, X., Balsamo, G., Bechtold, P., Biavati, G., Bidlot, J., Bonavita, M., … Thépaut, J. N. (2020). The ERA5 global reanalysis. *Quarterly Journal of the Royal Meteorological Society*, *146*(730), 1999–2049. https://doi.org/10.1002/qj.3803

Hersbach, H., Bell, B., Berrisford, P., Biavati, G., Horányi, A., Muñoz Sabater, J., Nicolas, J., Peubey, C., Radu, R., Rozum, I., Schepers, D., Simmons, A., Soci, C., Dee, D., & Thépaut, J.-N. (2023). *ERA5 hourly data on single levels from 1940 to present*. Copernicus Climate Change Service (C3S) Climate Data Store (CDS). 10.24381/cds.adbb2d47

Hofert, M., Kojadinovic, I., Maechler, M., & Yan, J. (2020). *copula: Multivariate Dependence with Copulas*. https://CRAN.R-project. org/package=copula

Holthuijsen, L. (2007). *Waves in Oceanic and Coastal Waters*. https://doi.org/10.2277/0521860288

Horikawa, K. (1988). *Nearshore Dynamics and Coastal Processes: Theory, Management, and Predictive Models*. University of Tokyo Press.

Hurrell, J., & Phillips, A. (2023). *The Climate Data Guide: Hurrell North Atlantic Oscillation (NAO) Index (station-based)*. National Center for Atmospheric Research Staff. https://climatedataguide.ucar.edu/climate-data/hurrell-north-atlantic-oscillation-nao-index-station-based

Hurrell, J., & Phillips, A. (2024). *The Climate Data Guide: Hurrell North Atlantic Oscillation (NAO) Index (PC-based)*. National Center for Atmospheric Research Staff . https://climatedataguide.ucar.edu/climate-data/hurrell-north-atlantic-oscillation-nao-index-pc-based

Hurrell, J., & Trenberth, K. (2022). *The Climate Data Guide: NCAR Sea Level Pressure*. National Center for Atmospheric Research Staff. https://climatedataguide.ucar.edu/climate-data/ncar-sea-level-pressure

Hurrell, J. W., Kushnir, Y., Ottersen, G., & Visbeck, M. (2003). *An overview of the North Atlantic Oscillation* (pp. 1–35). https://doi.org/10.1029/134GM01

Idier, D., Dumas, F., & Muller, H. (2012). Tide-surge interaction in the English Channel. *Natural Hazards and Earth System Science*, *12*(12), 3709–3718. https://doi.org/10.5194/nhess-12-3709-2012

Idier, D., Paris, F., Le Cozannet, G., Boulahya, F. & Dumas, F. (2017) Sea-level rise impacts on the tides of the European Shelf. *Continental Shelf Research,* 137, 56-71. https://doi.org/10.1016/j.csr.2017.01.007

IPCC. (2022). *Climate Change 2022: Impacts, Adaptation, and Vulnerability. Contribution of Working Group II to the Sixth Assessment Report of the Intergovernmental Panel on Climate Change*.

Jasak, H., Jemcov, A., & Tukovi, Z. (2007). OpenFOAM: A C++ library for complex physics simulations. *International Workshop on Coupled Methods in Numerical Dynamics*.

Jenkins, L. J., Haigh, I., Camus, P., Pender, D., Lamb, R., Trust, J., & Kassem, H. (2022). *The Temporal Clustering of Storm Surge, Wave Height, and High Sea Level Exceedances Around the UK Coastline*.

Jennings, R., & Shulmeister, J. (2002). A field based classification scheme for gravel beaches. *Marine Geology*, *186*(3–4), 211–228. https://doi.org/10.1016/S0025-3227(02)00314-6

Jiménez, J. A., Gracia, V., Valdemoro, H. I., Mendoza, E. T., & Sánchez-Arcilla, A. (2011). Managing erosion-induced problems in NW Mediterranean urban beaches. *Ocean and Coastal Management*, *54*(12), 907–918. https://doi.org/10.1016/j.ocecoaman.2011.05.003

Jiménez, J. A., Sancho-García, A., Bosom, E., Valdemoro, H. I., & Guillén, J. (2012). Storm-induced damages along the Catalan coast (NW Mediterranean) during the period 1958-2008. *Geomorphology*, *143–144*, 24–33. https://doi.org/10.1016/j.geomorph.2011.07.034

Karpytchev, M., Ballu, V., Krien, Y., Becker, M., Goodbred, S., Spada, G., Calmant, S., Shum, C. K., & Khan, Z. (2018). Contributions of a Strengthened Early Holocene Monsoon and Sediment Loading to Present-Day Subsidence of the Ganges-Brahmaputra Delta. *Geophysical Research Letters*, *45*(3), 1433–1442. https://doi.org/10.1002/2017GL076388

Katz, R. W., Parlange, M. B., & Naveau, P. (2002). Statistics of extremes in hydrology. *Advances in Water Resources*, *25*(8–12), 1287–1304. https://doi.org/10.1016/S0309-1708(02)00056-8

Kew, S. F., Selten, F. M., Lenderink, G., & Hazeleger, W. (2013). The simultaneous occurrence of surge and discharge extremes for the Rhine delta. *Natural Hazards and Earth System Sciences*, *13*(8), 2017–2029. https://doi.org/10.5194/nhess-13-2017-2013

Khojasteh, D., Glamore, W., Heimhuber, V., & Felder, S. (2021). Sea level rise impacts on estuarine dynamics: A review. In *Science of the Total Environment* (Vol. 780). Elsevier B.V. https://doi.org/10.1016/j.scitotenv.2021.146470

King, R. R., While, J., Martin, M. J., Lea, D. J., Lemieux-Dudon, B., Waters, J., & O'Dea, E. (2018). Improving the initialisation of the Met Office operational shelf-seas model. *Ocean Modelling*, *130*, 1–14. https://doi.org/10.1016/j.ocemod.2018.07.004

Klerk, W. J., Winsemius, H. C., Van Verseveld, W. J., Bakker, A. M. R., & Diermanse, F. L. M. (2015). The co-incidence of storm surges and extreme discharges within the Rhine-Meuse Delta. *Environmental Research Letters*, *10*(3). https://doi.org/10.1088/1748-9326/10/3/035005

Komen, G. J., Cavaleri, L., Donelan, M., Hasselmann, K., Hasselmann, S., & Janssen, P. A. E. M. (1994). *Dynamics and Modelling of Ocean Waves*. Cambridge University Press. https://doi.org/10.1017/CBO9780511628955

Labat, D. (2005). Recent advances in wavelet analyses: Part 1. A review of concepts. *Journal of Hydrology*, *314*(1–4), 275–288. https://doi.org/10.1016/j.jhydrol.2005.04.003

Lashley, C. H., Roelvink, D., van Dongeren, A., Buckley, M. L., & Lowe, R. J. (2018). Nonhydrostatic and surfbeat model predictions of extreme wave run-up in fringing reef environments. *Coastal Engineering*, *137*, 11–27. https://doi.org/10.1016/j.coastaleng.2018.03.007

Lashley, C. H., van der Meer, J., Bricker, J. D., Altomare, C., Suzuki, T., & Hirayama, K. (2021). Formulating Wave Overtopping at Vertical and Sloping Structures with Shallow Foreshores Using Deep-Water Wave Characteristics. *Journal of Waterway, Port, Coastal, and Ocean Engineering*, *147*(6). https://doi.org/10.1061/(ASCE)WW.1943-5460.0000675

Lavers, D., Prudhomme, C., & Hannah, D. M. (2010). Large-scale climate, precipitation and British river flows: Identifying hydroclimatological connections and dynamics. *Journal of Hydrology*, *395*(3–4), 242–255. https://doi.org/10.1016/j.jhydrol.2010.10.036

Lazure, P., & Dumas, F. (2008). An external-internal mode coupling for a 3D hydrodynamical model for applications at regional scale (MARS). *Advances in Water Resources*, *31*(2), 233–250. https://doi.org/10.1016/j.advwatres.2007.06.010

Leonard, M., Westra, S., Phatak, A., Lambert, M., van den Hurk, B., Mcinnes, K., Risbey, J., Schuster, S., Jakob, D., & Stafford-Smith, M. (2014). A compound event framework for understanding extreme impacts. In *Wiley Interdisciplinary Reviews: Climate Change* (Vol. 5, Issue 1, pp. 113–128). Wiley-Blackwell. https://doi.org/10.1002/wcc.252

Letetrel, C., Karpytchev, M., Bouin, M.-N., Marcos, M., Santamaría-Gómez, A., & Wöppelmann, G. (2015). Estimation of vertical land movement rates along the coasts of the Gulf of Mexico over the past decades. *Continental Shelf Research*, *111*, 42–51. https://doi.org/10.1016/j.csr.2015.10.018

Levoy, F., Anthony, E. J., Monfort, O., & Larsonneur, C. (2000). The morphodynamics of megatidal beaches in Normandy, France. *Marine Geology*, *171*(1–4), 39–59. https://doi.org/10.1016/S0025-3227(00)00110-9

Lewis, M. J., Palmer, T., Hashemi, R., Robins, P., Saulter, A., Brown, J., Lewis, H., & Neill, S. (2019). Wave-tide interaction modulates nearshore wave height. *Ocean Dynamics*, *69*(3), 367–384. https://doi.org/10.1007/s10236-018-01245-z

Liu, C., Jia, Y., Onat, Y., Cifuentes-Lorenzen, A., Ilia, A., McCardell, G., Fake, T., & O'Donnell, J. (2020). Estimating the annual exceedance probability of water levels and wave heights from high resolution coupled wave-circulation models in long island sound. *Journal of Marine Science and Engineering*, *8*(8). https://doi.org/10.3390/JMSE8070475

Liu, M., Smith, J. A., Yang, L., & Vecchi, G. A. (2021). Tropical cyclone flooding in the Carolinas. *Journal of Hydrometeorology*. https://doi.org/10.1175/JHM-D-21-0113.1

Lopes, C. L., Sousa, M. C., Ribeiro, A., Pereira, H., Pinheiro, J. P., Vaz, L., & Dias, J. M. (2022). Evaluation of future estuarine floods in a sea level rise context. *Scientific Reports*, *12*(1). https://doi.org/10.1038/s41598-022-12122-7

López Solano, C., Turki, E.I., Hamdi, Y., Soloy, A., Costa, S., Laignel, B., Gutiérrez Barceló, Á.D., Abcha, N., Jacono, D. & Lafite, R. (2022) Dynamics of Nearshore Waves during Storms: Case of the English Channel and the Normandy Coasts. *Water, 14*(3), 321. https://doi.org/10.3390/w14030321

López Solano, C., Turki, E.I., Mendoza, E.T., Gutiérrez Barceló, A. D., Migaud, A., Hamdi, Y., Laignel, B. & Lafite R (2024). Hydrodynamic modelling for simulating nearshore waves and sea levels: classification of extreme events from the English Channel to the Normandy coasts. *Natural Hazards*. https://doi.org/10.1007/s11069-024-06699-7

Madsen, O. S., Poon, Y. K., & Graber, H. C. (1988) *Spectral wave attenuation by bottom friction: theory, Coastal Engineering Proceedings, 1*(21), 34. https://doi.org/10.9753/icce.v21.34

Mangor, K., Drønen, N. K., Kaergaard, K. H., & Kristensen, S. E. (2017). *SHORELINE MANAGEMENT GUIDELINES*. www.dhigroup.com

Manner, H., & Reznikova, O. (2012). A Survey on Time-Varying Copulas: Specification, Simulations, and Application. *Econometric Reviews*, *31*(6), 654–687. https://doi.org/10.1080/07474938.2011.608042

Mansur, A. V., Brondízio, E. S., Roy, S., Hetrick, S., Vogt, N. D., & Newton, A. (2016). An assessment of urban vulnerability in the Amazon Delta and Estuary: a multi-criterion index of flood exposure, socio-economic conditions and infrastructure. *Sustainability Science*, *11*(4), 625–643. https://doi.org/10.1007/s11625-016-0355-7

Martin, J. L., McCutcheon, S. C., & Schottman, R. W. (1999). *Hydrodynamics and Transport for Water Quality Modeling*. CRC Press. https://doi.org/10.1201/9780203751510

Martzikos, N., Afentoulis, V., Tsoukala, V. K., Martzikos, N., Afentoulis, V., & Tsoukala, V. (2018). Storm clustering and classification for the port of Rethymno in Greece Analysis of Coastal Storms for their Application in Harbours and Coastal Structures Design View project Storm clustering and classification for the port of Rethymno in Greece. In *Water Utility Journal* (Vol. 20). https://www.researchgate.net/publication/330739052

Masina, M., Lamberti, A., & Archetti, R. (2015). Coastal flooding: A copula based approach for estimating the joint probability of water levels and waves. *Coastal Engineering*, *97*, 37–52. https://doi.org/10.1016/j.coastaleng.2014.12.010

Maskell, J., Horsburgh, K., Lewis, M., & Bates, P. (2014). Investigating river-surge interaction in idealised estuaries. *Journal of Coastal Research*, *30*(2), 248–259. https://doi.org/10.2112/JCOASTRES-D-12-00221.1

Massalin, A., Zampato L, Papa A, & Canestrelli P. (2007). Data monitoring and sea level forecasting in the Venice Lagoon: the ICPSM's activity. *Bolletino Di Geofisica Teorica Ed Applicata*, *48*, 241–257.

Massei, N., Dieppois, B., Hannah, D. M., Lavers, D. A., Fossa, M., Laignel, B., & Debret, M. (2017). Multi-time-scale hydroclimate dynamics of a regional watershed and links to large-scale atmospheric circulation: Application to the Seine river catchment, France. *Journal of Hydrology*, *546*, 262–275. https://doi.org/10.1016/j.jhydrol.2017.01.008

Massel, S. R. (1996). *Ocean Surface Waves: Their Physics and Prediction* (Vol. 11). WORLD SCIENTIFIC. https://doi.org/10.1142/2285

Masselink, G., Austin, M., Scott, T., Poate, T., & Russell, P. (2014). Role of wave forcing, storms and NAO in outer bar dynamics on a high-energy, macro-tidal beach. *Geomorphology*, *226*, 76–93. https://doi.org/10.1016/j.geomorph.2014.07.025

McInnes, K. L., Walsh, K. J. E., Hubbert, G. D., & Beer, T. (2003). Impact of sea-level rise and storm surges in a coastal community. *Natural Hazards*, *30*(2), 187–207. https://doi.org/10.1023/A:1026118417752

Mellink, B. A. (2012). *Numerical and experimental research of wave interaction with a porous breakwater*.

Mendoza, E. T., Jiménez, J. A., & Mendoza, E. T. (2006). Storm-Induced Beach Erosion Potential on the Catalonian Coast MICORE View project Extreme ocean waves and climate change in the Gulf of Mexico View project Storm-Induced Beach Erosion Potential on the Catalonian Coast. *Proceedings) Spain Journal of Coastal Research*, *48*, 81–88. https://www.researchgate.net/publication/228943996

Mendoza, E. T., Jimenez, J. A., & Mateo, J. (2011). A coastal storms intensity scale for the Catalan sea (NW Mediterranean). *Natural Hazards and Earth System Science*, *11*(9), 2453–2462. https://doi.org/10.5194/nhess-11-2453-2011

Mendoza, E. T., Trejo-Rangel, M. A., Salles, P., Appendini, C. M., Lopez-Gonzalez, J., & Torres-Freyermuth, A. (2013). Storm characterization and coastal hazards in the Yucatan Peninsula. *Journal of Coastal Research*, *65*, 790–795. https://doi.org/10.2112/si65-134.1

Menéndez, M., & Woodworth, P. L. (2010). Changes in extreme high water levels based on a quasi-global tide-gauge data set. *Journal of Geophysical Research: Oceans*, *115*(10). https://doi.org/10.1029/2009JC005997

Mínguez, E., Florido, R., Rodríguez, R., Gil, J. M., Rubiano, J. G., Mendoza, M. A., Espinosa, G., & Martel, P. (2012). Modelling of spectral properties and population kinetics studies of inertial

fusion and laboratory-astrophysical plasmas. *Plasma Physics and Controlled Fusion*, *54*(12), 124004. https://doi.org/10.1088/0741-3335/54/12/124004

Modélisation et Analyse pour la Recherche Côtière (MARC). (2021). *MARC*. https://marc.ifremer.fr

Molina, R., Manno, G., Re, C. Lo, Anfuso, G., & Ciraolo, G. (2019). Storm energy flux characterization along the mediterranean coast of Andalusia (Spain). *Water (Switzerland)*, *11*(3). https://doi.org/10.3390/w11030509

Morton, I. D., Bowers, J., & Mould, G. (1997). Estimating return period wave heights and wind speeds using a seasonal point process model. *Coastal Engineering*, *31*(1–4), 305–326. https://doi.org/10.1016/S0378-3839(97)00016-1

Morton, R. A., & Sallenger, A. H. (2003). Morphological Impacts of Extreme Storms on Sandy Beaches and Barriers. *Journal of Coastal Research*, *19*(3), 560–573.

Muis, S., Verlaan, M., Winsemius, H. C., Aerts, J. C. J. H., & Ward, P. J. (2016). A global reanalysis of storm surges and extreme sea levels. *Nature Communications*, *7*(1), 11969. https://doi.org/10.1038/ncomms11969

Muller, H., Pineau-Guillou, L., Idier, D., & Ardhuin, F. (2014). Atmospheric storm surge modeling methodology along the French (Atlantic and English Channel) coast. *Ocean Dynamics*, *64*(11), 1671–1692. https://doi.org/10.1007/s10236-014-0771-0

Nagler, T., Schepsmeier, U., Stoeber, J., Brechmann, E. C., Graeler, B., & Erhardt, T. (2020). *VineCopula: Statistical Inference of Vine Copulas*. https://CRAN.R-project.org/package=VineCopula

National Oceanic and Atmospheric Administration (NOAA). (2021). *North Atlantic Oscillation (NAO)*. National Centers for Environmental Information. https://www.ncei.noaa.gov/access/monitoring/nao/

Neumann, B., Vafeidis, A. T., Zimmermann, J., & Nicholls, R. J. (2015). Future coastal population growth and exposure to sea-level rise and coastal flooding - A global assessment. *PLoS ONE*, *10*(3). https://doi.org/10.1371/journal.pone.0118571

Nicholls, R. J., Marinova, N., Lowe, J. A., Brown, S., Vellinga, P., de Gusmão, D., Hinkel, J., & Tol, R. S. J. (2011). Sea-level rise and its possible impacts given a 'beyond 4°C world' in the twenty-first century. *Philosophical Transactions of the Royal Society A: Mathematical,*

Physical and Engineering Sciences, *369*(1934), 161–181. https://doi.org/10.1098/rsta.2010.0291

Nielsen, P. (2009). *Coastal And Estuarine Processes*. World Scientific Publishing Company.

Ning, Y., Liu, W., Zhao, X., Zhang, Y., & Sun, Z. (2019). Study of irregular wave run-up over fringing reefs based on a shock-capturing Boussinesq model. *Applied Ocean Research*, *84*, 216–224. https://doi.org/10.1016/j.apor.2019.01.013

O'Dea, E. J., Arnold, A. K., Edwards, K. P., Furner, R., Hyder, P., Martin, M. J., Siddorn, J. R., Storkey, D., While, J., Holt, J. T., & Liu, H. (2012). An operational ocean forecast system incorporating NEMO and SST data assimilation for the tidally driven European North-West shelf. *Journal of Operational Oceanography*, *5*(1), 3–17. https://doi.org/10.1080/1755876X.2012.11020128

O'Dea, E., Furner, R., Wakelin, S., Siddorn, J., While, J., Sykes, P., King, R., Holt, J., & Hewitt, H. (2017). The CO5 configuration of the 7km Atlantic Margin Model: Large-scale biases and sensitivity to forcing, physics options and vertical resolution. *Geoscientific Model Development*, *10*(8), 2947–2969. https://doi.org/10.5194/gmd-10-2947-2017

O'Donnell, J. (2016). *A Study of Coastal Flooding at Jarvis Creek, Connecticut LIS PO review View project Sea Level Rise View project*. https://doi.org/10.13140/RG.2.2.22747.98089

Orton, P. M., Conticello, F. R., Cioffi, F., Hall, T. M., Georgas, N., Lall, U., Blumberg, A. F., & MacManus, K. (2020). Flood hazard assessment from storm tides, rain and sea level rise for a tidal river estuary. *Natural Hazards*, *102*(2), 729–757. https://doi.org/10.1007/s11069-018-3251-x

Ozsoy, O., Haigh, I. D., Wadey, M. P., Nicholls, R. J., & Wells, N. C. (2016). High-frequency sea level variations and implications for coastal flooding: A case study of the Solent, UK. *Continental Shelf Research*, *122*, 1–13. https://doi.org/10.1016/j.csr.2016.03.021

Pasquini, A. I., Lecomte, K. L., & Depetris, P. J. (2008). Climate change and recent water level variability in Patagonian proglacial lakes, Argentina. *Global and Planetary Change*, *63*(4), 290–298. https://doi.org/10.1016/j.gloplacha.2008.07.001

Passeri, D. L., Hagen, S. C., Medeiros, S. C., Bilskie, M. V., Alizad, K., & Wang, D. (2015). The dynamic effects of sea level rise on low-gradient coastal landscapes: A review. In *Earth's Future* (Vol. 3, Issue 6, pp. 159–181). John Wiley and Sons Inc. https://doi.org/10.1002/2015EF000298

Phillips, N. A. (1957). A COORDINATE SYSTEM HAVING SOME SPECIAL ADVANTAGES FOR NUMERICAL FORECASTING. *Journal of Meteorology*, *14*(2), 184–185. https://doi.org/10.1175/1520-0469(1957)014<0184:ACSHSS>2.0.CO;2

Pickering, M. D., Horsburgh, K. J., Blundell, J. R., Hirschi, J. J. M., Nicholls, R. J., Verlaan, M., & Wells, N. C. (2017). The impact of future sea-level rise on the global tides. *Continental Shelf Research*, *142*, 50–68. https://doi.org/10.1016/j.csr.2017.02.004

Pierson, W. J., & Moskowitz, L. (1964). A proposed spectral form for fully developed wind seas based on the similarity theory of S. A. Kitaigorodskii. *Journal of Geophysical Research*, *69*(24), 5181–5190. https://doi.org/10.1029/JZ069i024p05181

Pokorná, L., & Huth, R. (2015). Climate impacts of the NAO are sensitive to how the NAO is defined. *Theoretical and Applied Climatology*, *119*(3–4), 639–652. https://doi.org/10.1007/s00704-014-1116-0

Potisomporn, P., Adcock, T. A. A., & Vogel, C. R. (2023). Evaluating ERA5 reanalysis predictions of low wind speed events around the UK. *Energy Reports*, *10*, 4781–4790. https://doi.org/10.1016/j.egyr.2023.11.035

Pugh, D. (2004). *Changing Sea Levels Effects of Tides, Weather and Climate*. Cambridge University Press.

Rahman, M. S., Islam, R., Rana, M. M., Spitzhorn, L.-S., Rahman, M. S., Adjaye, J., & Asaduzzaman, S. M. (2019). Characterization of burn wound healing gel prepared from human amniotic membrane and Aloe vera extract. *BMC Complementary and Alternative Medicine*, *19*(1), 115. https://doi.org/10.1186/s12906-019-2525-5

Ranasinghe, R., & Stive, M. J. F. (2009). Rising seas and retreating coastlines. *Climatic Change*, *97*(3–4), 465–468. https://doi.org/10.1007/s10584-009-9593-3

Ranjan, P., Kazama, S., Sawamoto, M., & Sana, A. (2009). Global scale evaluation of coastal fresh groundwater resources. *Ocean & Coastal Management*, *52*(3–4), 197–206. https://doi.org/10.1016/j.ocecoaman.2008.09.006

Ricondo, A., Cagigal, L., Pérez-Díaz, B., & Méndez, F. J. (2024). HySwash: A hybrid model for nearshore wave processes. *Ocean Engineering*, *291*. https://doi.org/10.1016/j.oceaneng.2023.116419

Rodríguez-Padilla, I., Castelle, B., Marieu, V. & Morichon, D. (2019). A Simple and Efficient Image Stabilization Method for Coastal Monitoring Video Systems. *Remote Sensing*. *12(1):70*. https://doi.org/10.3390/rs12010070.

Roeber, V., & Cheung, K. (2012). BOSZ (Boussinesq Ocean and Surf Zone model). *2011 NTHMP Model Benchmarking Workshop*.

Roelvink, D., Reniers, A., van Dongeren, A., van Thiel de Vries, J., McCall, R., & Lescinski, J. (2009). Modelling storm impacts on beaches, dunes and barrier islands. *Coastal Engineering*, *56*(11–12), 1133–1152. https://doi.org/10.1016/j.coastaleng.2009.08.006

Roelvink, D., & Costas, S. (2019). Coupling nearshore and aeolian processes: XBeach and duna process-based models. *Environmental Modelling & Software*, *115*, 98–112. https://doi.org/10.1016/j.envsoft.2019.02.010

Rouhaud, E., & Vanderlinden, J. P. (2022). 10 years and going strong? Coastal flood risk management in the wake of a major coastal event (the 2010 Xynthia storm, Charente Maritime, France). *Climate Risk Management*, *35*. https://doi.org/10.1016/j.crm.2022.100413

Rueda, A., Camus, P., Tomás, A., Vitousek, S., & Méndez, F. J. (2016). A multivariate extreme wave and storm surge climate emulator based on weather patterns. *Ocean Modelling*, *104*, 242–251. https://doi.org/10.1016/j.ocemod.2016.06.008

Rueda, A., Vitousek, S., Camus, P., Tomás, A., Espejo, A., Losada, I. J., Barnard, P. L., Erikson, L. H., Ruggiero, P., Reguero, B. G., & Mendez, F. J. (2017). A global classification of coastal flood hazard climates associated with large-scale oceanographic forcing. *Scientific Reports*, *7*(1), 5038. https://doi.org/10.1038/s41598-017-05090-w

Sarhadi, A., Burn, D. H., Concepción Ausín, M., & Wiper, M. P. (2016). Time-varying nonstationary multivariate risk analysis using a dynamic Bayesian copula. *Water Resources Research*, *52*(3), 2327–2349. https://doi.org/10.1002/2015WR018525

Saulter, A. N., Bunney, C., King, R. R., & Waters, J. (2020). An Application of NEMOVAR for Regional Wave Model Data Assimilation. *Frontiers in Marine Science*, *7*. https://doi.org/10.3389/fmars.2020.579834

Schuerch, M., Spencer, T., Temmerman, S., Kirwan, M. L., Wolff, C., Lincke, D., McOwen, C. J., Pickering, M. D., Reef, R., Vafeidis, A. T., Hinkel, J., Nicholls, R. J., & Brown, S. (2018). Future

response of global coastal wetlands to sea-level rise. *Nature*, *561*(7722), 231–234. https://doi.org/10.1038/s41586-018-0476-5

Shand, T. D., Cox, R. J., Mole, M. A., Carley, J. T., & Peirson, W. L. (2011). *Coastal Storm Data Analysis: Provision of Extreme Wave Data for Adaptation Planning*.

Shi, F., Kirby, J. T., Harris, J. C., Geiman, J. D., & Grilli, S. T. (2012). A high-order adaptive time-stepping TVD solver for Boussinesq modeling of breaking waves and coastal inundation. *Ocean Modelling*, *43–44*, 36–51. https://doi.org/10.1016/j.ocemod.2011.12.004

Shiau, J. T. (2003). Return period of bivariate distributed extreme hydrological events. *Stochastic Environmental Research and Risk Assessment (SERRA)*, *17*(1–2), 42–57. https://doi.org/10.1007/s00477-003-0125-9

Skliris, N., Marsh, R., Srokosz, M., Aksenov, Y., Rynders, S., & Fournier, N. (2021). Assessing extreme environmental loads on offshore structures in the north sea from high-resolution ocean currents, waves and wind forecasting. *Journal of Marine Science and Engineering*, *9*(10). https://doi.org/10.3390/jmse9101052

Smit, P., Stelling, G., Roelvink, J., Van Thiel de Vries, J., McCall, R., Van Dongeren, A., Zwinkels, C., & Jacobs, R. (2010). XBeach: Non-hydrostatic model: Validation, verification and model description. *Delft Univ. Technol*.

Soloy, A., Turki, I., Fournier, M., Costa, S., Peuziat, B., & Lecoq, N. (2020). A deep learning-based method for quantifying and mapping the grain size on pebble beaches. *Remote Sensing*, *12*(21), 1–23. https://doi.org/10.3390/rs12213659

Soloy, A., Turki, I., Lecoq, N., Gutiérrez Barceló, Á. D., Costa, S., Laignel, B., Bazin, B., Soufflet, Y., Le Louargant, L., & Maquaire, O. (2021). A fully automated method for monitoring the intertidal topography using Video Monitoring Systems. *Coastal Engineering*, *167*. https://doi.org/10.1016/j.coastaleng.2021.103894

Soloy, A., Turki, I., Lecoq, N., Solano, C. L., & Laignel, B. (2022). Spatio-temporal variability of the morpho-sedimentary dynamics observed on two gravel beaches in response to hydrodynamic forcing. *Marine Geology*, *447*. https://doi.org/10.1016/j.margeo.2022.106796

Soloy, A., Lopez Solano, C., Turki, E. I., Mendoza, E. T., & Lecoq, N. (2024). Rapid Changes in Permeability: Numerical Investigation into Storm-Driven Pebble Beach Morphodynamics with XBeach-G. *Journal of Marine Science and Engineering*, *12*(2). https://doi.org/10.3390/jmse12020327

Stewart, M., & Melchers, R. E. (1997). *Probabilistic Risk Assessment of Engineering Systems*.

Stockdon, H. F., Holman, R. A., Howd, P. A., & Sallenger, A. H. (2006). Empirical parameterization of setup, swash, and runup. *Coastal Engineering*, *53*(7), 573–588. https://doi.org/10.1016/j.coastaleng.2005.12.005

Switzer, S., Gerber, L., & Sindico, F. (2015). Access to Minerals: WTO Export Restrictions and Climate Change Considerations. *Laws*, *4*(3), 617–637. https://doi.org/10.3390/laws4030617

Toffoli, A., & Bitner-Gregersen, E. M. (2017). Types of Ocean Surface Waves, Wave Classification. In *Encyclopedia of Maritime and Offshore Engineering* (pp. 1–8). Wiley. https://doi.org/10.1002/9781118476406.emoe077

Tolman, H. L. (1989). The numerical model WAVEWATCH: a third generation model for the hindcasting of wind waves on tides in shelf seas. *Communications on Hydraulic and Geotechnical Engineering*, *89*(2), 72-pp.

Tolman, H. L. (1992). Effects of numerics on the physics in a third-generation wind-wave model. *J. Phys. Oceanogr.*, 1095–1111.

Tolman, H. L. (1997). User manual and system documentation of WAVEWATCH III version 1.15. *NOAA / NWS / NCEP / OMB Technical Note*, *151*, 97-pp.

Tolman, H. L. (1999). User manual and system documentation of WAVEWATCH-III version 1.18. *NOAA / NWS / NCEP / OMB Technical Note*, *166*, 110-pp.

Tolman, H. L. (2002a). Distributed-memory concepts in the wave model WAVEWATCH III. *Parallel Computing*, *28*(1), 35–52.

Tolman, H. L. (2002b). Validation of WAVEWATCH III version 1.15 for a global domain. In *Environmental Modeling Center*.

Tolman, H. L. (2009). *User manual and system documentation of WAVEWATCH III TM version 3.14 †*.

Tomasin, A. & Pirazzoli, P. A. (2008) *Extreme Sea Levels in the English Channel: Calibration of the Joint Probability Method*, 24(sp3), 1-13 https://doi.org/10.2112/07-0826.1

Trenberth, K. E., & Paolino, D. A. (1980). The Northern Hemisphere Sea-Level Pressure Data Set: Trends, Errors and Discontinuities. *Monthly Weather Review*, *108*(7), 855–872. https://doi.org/10.1175/1520-0493(1980)108<0855:TNHSLP>2.0.CO;2

Trenberth, K., & Zhang, R. (2023). *The Climate Data Guide: Atlantic Multi-decadal Oscillation (AMO) and Atlantic Multidecadal Variability (AMV)*. National Center for Atmospheric Research Staff. https://climatedataguide.ucar.edu/climate-data/atlantic-multi-decadal-oscillation-amo

Turki, I., Laignel, B., Kakeh, N., Chevalier, L., & Costa, S. (2015). A new hybrid model for filling gaps and forecast in sea level: application to the eastern English Channel and the North Atlantic Sea (western France). *Ocean Dynamics*, *65*(4), 509–521. https://doi.org/10.1007/s10236-015-0824-z

Turki, I., Massei, N., & Laignel, B. (2019). Linking sea level dynamic and exceptional events to large-scale atmospheric circulation variability: A case of the Seine Bay, France. *Oceanologia*, *61*(3), 321–330. https://doi.org/10.1016/j.oceano.2019.01.003

Turki, I., Massei, N., Laignel, B., & Shafiei, H. (2020a). Effects of Global Climate Oscillations on Intermonthly to Interannual Variability of Sea levels along the English Channel Coasts (NW France). *Oceanologia*, *62*(2), 226–242. https://doi.org/10.1016/j.oceano.2020.01.001

Turki, I., Baulon, L., Massei, N., Laignel, B., Costa, S., Fournier, M., & Maquaire, O. (2020b). A nonstationary analysis for investigating the multiscale variability of extreme surges: Case of the English Channel coasts. *Natural Hazards and Earth System Sciences*, *20*(12), 3225–3243. https://doi.org/10.5194/nhess-20-3225-2020

Turki, E. I., Deloffre, J., Gilbert, R., Mendoza, E. T., Salameh, E., Abcha, N., Lecoq, N., & Laignel, B. (2023a). Effects of tidal wave modulation on coastal flooding along a tide-river context: Case of the seine estuary. *Annals of Marine Science*, *7*(1), 051–060. https://doi.org/10.17352/ams.000039

Turki, E. I., Deloffre, J., Lecoq, N., Gilbert, R., Mendoza, E. T., Laignel, B., Salameh, E., Gutierrez Barcelo, A. D., Fournier, M., & Massei, N. (2023b). Multi-timescale dynamics of extreme river flood and storm surge interactions in relation with large-scale atmospheric circulation: Case of the Seine estuary. *Estuarine, Coastal and Shelf Science*, *287*. https://doi.org/10.1016/j.ecss.2023.108349

Unnikrishnan, A., Akiyoshi, B., Biggins, S., & Tsukiyama, T. (2012). *An Efficient Purification System for Native Minichromosome from Saccharomyces cerevisiae* (pp. 115–123). https://doi.org/10.1007/978-1-61779-477-3_8

U.S. Geological Survey (USGS). (2024). *Coastal Change Hazards: Hurricanes and Extreme Storms*. http://coastal.er.usgs.gov/hurricanes/extreme-storms

van den Brink, H. W., Können, G. P., Opsteegh, J. D., van Oldenborgh, G. J., & Burgers, G. (2005). Estimating return periods of extreme events from ECMWF seasonal forecast ensembles. *International Journal of Climatology*, *25*(10), 1345–1354. https://doi.org/10.1002/joc.1155

Vitousek, S., Barnard, P. L., Fletcher, C. H., Frazer, N., Erikson, L., & Storlazzi, C. D. (2017). Doubling of coastal flooding frequency within decades due to sea-level rise. *Scientific Reports*, *7*(1), 1399. https://doi.org/10.1038/s41598-017-01362-7

Vousdoukas, M. I., Voukouvalas, E., Mentaschi, L., Dottori, F., Giardino, A., Bouziotas, D., Bianchi, A., Salamon, P., & Feyen, L. (2016). Developments in large-scale coastal flood hazard mapping. *Natural Hazards and Earth System Sciences*, *16*(8), 1841–1853. https://doi.org/10.5194/nhess-16-1841-2016

Vousdoukas, M. I., Wziatek, D., & Almeida, L. P. (2012). Coastal vulnerability assessment based on video wave run-up observations at a mesotidal, steep-sloped beach. *Ocean Dynamics*, *62*(1), 123–137. https://doi.org/10.1007/s10236-011-0480-x

Wadey, M. P., Brown, J. M., Haigh, I. D., Dolphin, T., & Wisse, P. (2015). Assessment and comparison of extreme sea levels and waves during the 2013/14 storm season in two UK coastal regions. *Natural Hazards and Earth System Sciences*, *15*(10), 2209–2225. https://doi.org/10.5194/nhess-15-2209-2015

Wahl, T., Haigh, I. D., Nicholls, R. J., Arns, A., Dangendorf, S., Hinkel, J., & Slangen, A. B. A. (2017). Understanding extreme sea levels for broad-scale coastal impact and adaptation analysis. *Nature Communications*, *8*. https://doi.org/10.1038/ncomms16075

Walker, R. A., & Basco, D. R. (2011). Application of coastal storm impulse (COSI) parameter to predict coastal erosion. *Coastal Engineering Proceedings*, *32*. http://frf.usace.army.mil/storms.shtml

WAVEWATCH III R Development Group (WW3DG). (2019). *User manual and system documentation of WAVEWATCH III R version 6.07. Tech. Note 333*. Tech. Note 333. https://polar.ncep.noaa.gov/waves/wavewatch/

Wells, N., Baldwin, D., Wang, J., & Collins, M. (2001). Modelling of extreme storm surge events in the English Channel for the period 14–18 December 1989. *The Global Atmosphere and Ocean System*, *7*(4), 275–294.

Wells, N. C., Bladwin, D., & Haigh, I. (2005). Seiches induced by storms in the English Channel. *Journal of Atmospheric and Ocean Science*, *10*, 1–14.

Wolf, J., & Woolf, D. K. (2006). Waves and climate change in the north-east Atlantic. *Geophysical Research Letters*, *33*(6). https://doi.org/10.1029/2005GL025113

Wong, P., Losada, I. J., Gattuso, J.-P., Hinkel, J., Khattabi, A., McInnes, K. L., Saito, Y., Sallenger, A., Nicholls, R. J., Santos, F., Amez, S., Losada, I., Gattuso, J., Hinkel, J., Khattabi, A., McInnes, K., Saito, Y., Sallenger, A., Barros, V., … Levy, A. (2014). *Coastal Systems and Low-Lying Areas Coordinating Lead Authors: Lead Authors: Review Editors*.

Woodworth, P. L., Melet, A., Marcos, M., Ray, R. D., Wöppelmann, G., Sasaki, Y. N., Cirano, M., Hibbert, A., Huthnance, J. M., Monserrat, S., & Merrifield, M. A. (2019). Forcing Factors Affecting Sea Level Changes at the Coast. *Surveys in Geophysics*, *40*(6), 1351–1397. https://doi.org/10.1007/s10712-019-09531-1

World Meteorological Organization (WMO). (2018). *Guide to Instruments and Methods of Observation*.

Wu, W., & Wang, S. S. Y. (2006). Formulas for Sediment Porosity and Settling Velocity. *Journal of Hydraulic Engineering*, *132*(8). https://doi.org/10.1061/ASCE0733-94292006132:8858

Yan, J. (2007). Enjoy the Joy of Copulas: With a Package **copula**. *Journal of Statistical Software*, *21*(4). https://doi.org/10.18637/jss.v021.i04

Zampieri, M., Ceglar, A., Dentener, F., & Toreti, A. (2017). Wheat yield loss attributable to heat waves, drought and water excess at the global, national and subnational scales. *Environmental Research Letters*, *12*(6), 064008. https://doi.org/10.1088/1748-9326/aa723b

Zhang, S. J., Zhu, L. S., & Zou, K. (2019). A Comparative Study of Numerical Models for Wave Propagation and Setup on Steep Coral Reefs. *China Ocean Eng*, *33*(4), 424–435.

Zijlema, M., Stelling, G., & Smit, P. (2011). SWASH: An operational public domain code for simulating wave fields and rapidly varied flows in coastal waters. *Coastal Engineering*, *58*(10), 992–1012. https://doi.org/10.1016/j.coastaleng.2011.05.015

Zscheischler, J., Westra, S., Van Den Hurk, B. J. J. M., Seneviratne, S. I., Ward, P. J., Pitman, A., Aghakouchak, A., Bresch, D. N., Leonard, M., Wahl, T., & Zhang, X. (2018). Future climate risk from compound events. In *Nature Climate Change* (Vol. 8, Issue 6, pp. 469–477). Nature Publishing Group. https://doi.org/10.1038/s41558-018-0156-3

APPENDICES

APPENDIX A

NON-STATIONARY DYNAMICS OF EXTREME MONTHLY WAVES AND SURGES

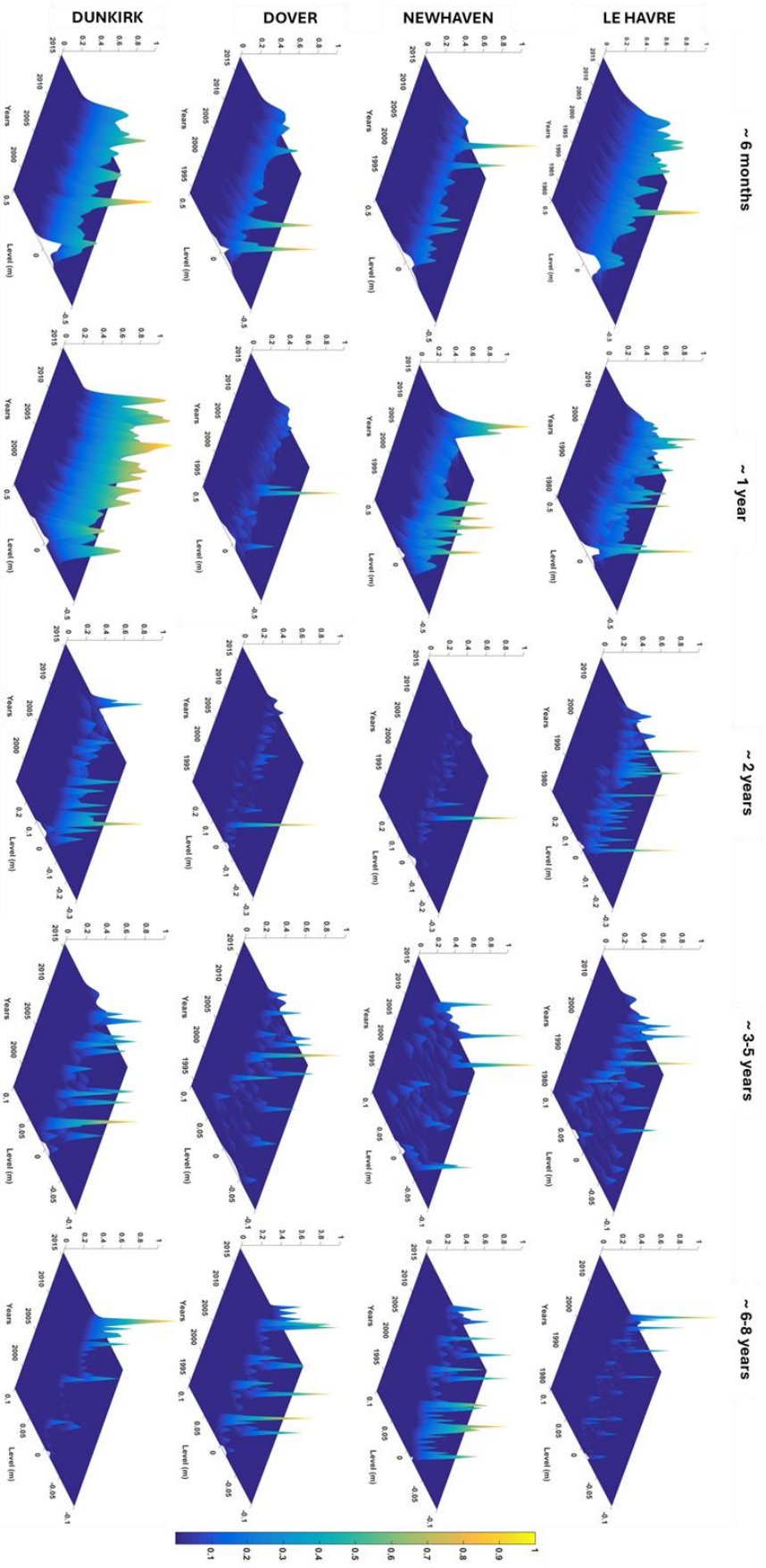

Figure 106. *Time-dependent PDF of monthly extreme surges during the period 1981 – 2018 at the semi-annual and interannual scales in Le Havre, Newhaven, Dover and Dunkirk*

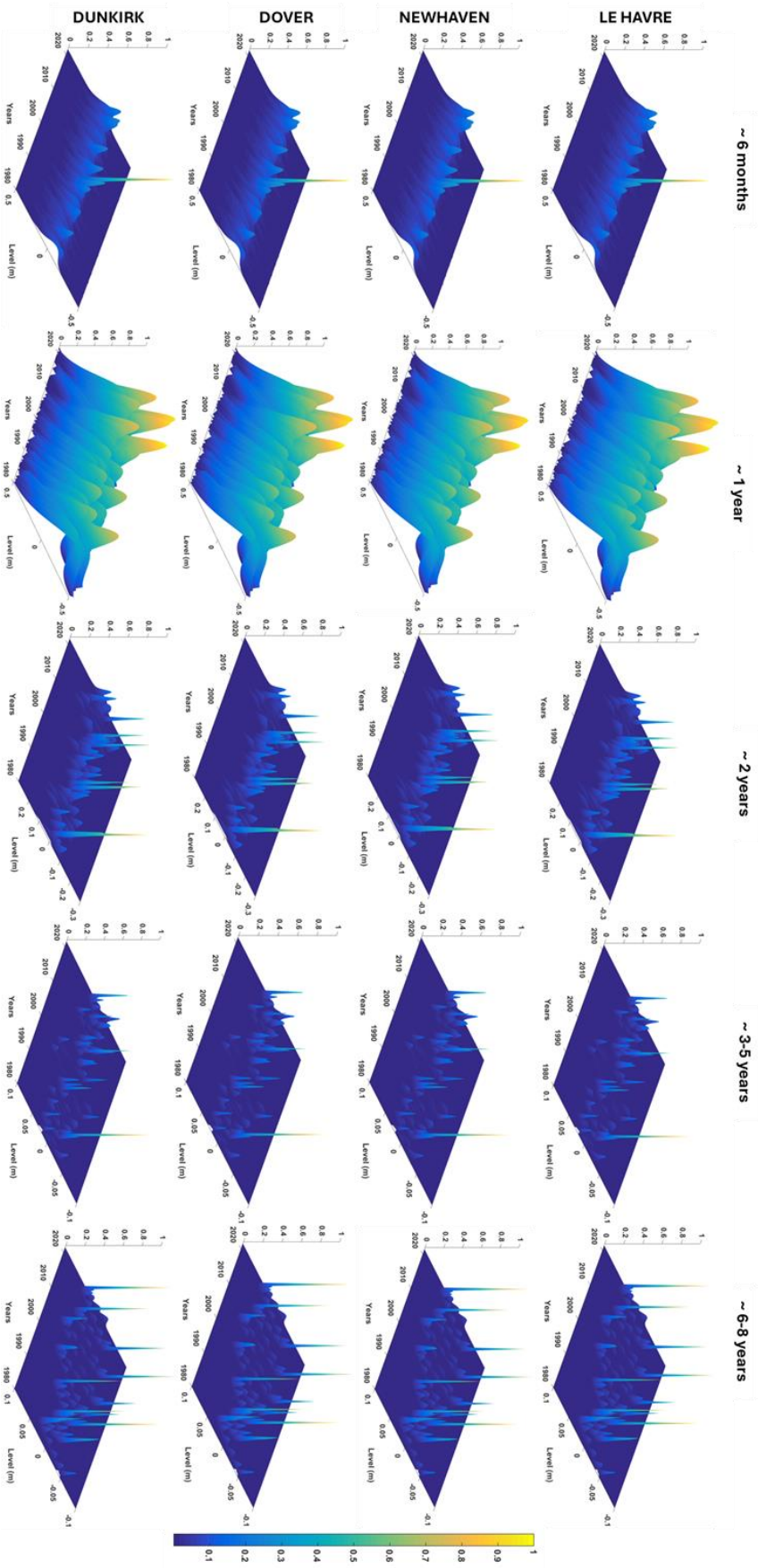

Figure 107. *Time-dependent PDF of monthly extreme waves during the period 1980 – 2022 at the semi-annual and interannual scales in Le Havre, Newhaven, Dover and Dunkirk*

APPENDIX B

RESULTS OF NON-STATIONARY FITTINGS AND DEPENDENCE STRUCTURES OF H_S AND S

a. GEVs distributions of H_s and S

~3 months	H_s	$\mu = -0.062$ $\sigma = -1.77$, and $\xi = -0.229 - 0.071\ SST - 0.058\ SST^2$
	S	$\mu = -0.031 - 0.011\ NAO_{NOAA}$, $\sigma = -2.375 - 0.081\ SLP - 0.052\ t - 0.061\ t^2$, and $\xi = -0.284 - 0.276\ SST + 0.189\ SLP$
~6 months	H_s	$\mu = -0.022 - 0.031\ SST + 0.025\ SLP - 0.016\ SLP^2$, $\sigma = -2.239 - 0.063\ SLP$, and $\xi = -0.271$
	S	$\mu = -0.022$, $\sigma = -2.791 - 0.087\ SLP - 0.069\ AMO + 0.059\ AMO^2$, and $\xi = -0.257 - 0.131\ SST + 0.131\ SST^2 - 0.05\ SLP$
~1 year	H_s	$\mu = -0.049 - 0.155\ SST + 0.039\ NAO_{Hurrell} + 0.011\ NAO_{Hurrell}{}^2$, $\sigma = -1.896 - 0.015\ SST + 0.095\ SST^2 - 0.08\ SLP - 0.103\ SLP^2 - 0.073\ t$, and $\xi = -0.376$
	S	$\mu = -0.026 - 0.056\ SLP + 0.009\ NAO_{Hurrell} + 0.006\ NAO_{Hurrell}{}^2$, $\sigma = -2.6 - 0.056\ SST + 0.135\ SST^2 - 0.067\ SLP - 0.093\ t - 0.145\ t^2$, and $\xi = -0.298$
~2 years	H_s	$\mu = -0.02 - 0.007\ AMO - 0.003\ AMO^2 + 0.004\ NAO_{NOAA}$, $\sigma = -3.203 - 0.17\ SLP + 0.097\ NAO_{NOAA} + 0.086\ t + 0.208\ t^2$, and $\xi = -0.154 + 0.091\ SST + 0.018\ SST^2 - 0.065\ NAO_{NOAA} - 0.092\ NAO_{NOAA}{}^2$
	S	$\mu = -0.018 - 0.003\ AMO + 0.003\ AMO^2$, $\sigma = -3.223 - 0.093\ SLP + 0.13\ t$, and $\xi = -0.265$
3-5 years	H_s	$\mu = -0.01 - 0.00048\ SLP + 0.002\ SLP^2$ $\sigma = -3.466 + 0.095\ AMO - 0.249\ AMO^2 - 0.074\ t - 0.285\ t^2$, and $\xi = -0.369 + 0.133\ t + 0.08\ t^2$
	S	$\mu = -0.008$, $\sigma = -3.818$, and $\xi = -0.289$
6-8 years	H_s	$\mu = -0.007 + 0.004\ NAO_{NOAA} - 0.003\ t - 0.004\ t^2$, $\sigma = -3.506\ AMO - 0.168\ t$, and $\xi = -0.369 - 0.223\ t$
	S	$\mu = -0.011$, $\sigma = -3.972$, and $\xi = 0.147 - 0.198\ t - 0.446\ t^2$

Table 43. *Results of the fitting of the GEV with the non-stationary parameters dependent the climate and time indexes for the spectral components of significant wave height and surge in Brest*

~3 months	H_s	$\mu = -0.117$, $\sigma = -1.075 - 0.091\ SLP - 0.07\ SLP^2$, and $\xi = -0.251$
	S	$\mu = -0.028$, $\sigma = -2.54 - 0.133\ SST$, and $\xi = -0.232 - 0.101\ SST + 0.059\ SST^2 - 0.046\ SLP$
~6 months	H_s	$\mu = -0.077 - 0.092\ SST + 0.073\ SLP$, $\sigma = -1.545$, and $\xi = -0.27$
	S	$\mu = -0.019 - 0.005\ SST - 0.008\ NAO_{NOAA}$, $\sigma = -2.975 - 0.126\ SST - 0.117\ AMO$, and $\xi = -0.268$
~1 year	H_s	$\mu = -0.07 - 0.107\ SST - 0.289\ SLP + 0.051\ NAO_{Hurrell} + 0.023\ NAO_{Hurrell}{}^2 + 0.011\ t$, $\sigma = -1.218 - 0.101\ SST + 0.044\ SST^2 - 0.184\ SLP - 0.073\ SLP^2 - 0.168\ t$, and $\xi = -0.424 + 0.151\ SST$
	S	$\mu = -0.02 - 0.057\ SLP + 0.013\ NAO_{Hurrell} + 0.005\ NAO_{Hurrell}{}^2$, $\sigma = -2.666 - 0.005\ SST + 0.126\ SST^2 + 0.087\ SLP - 0.03\ AMO - 0.157\ t - 0.084\ t^2$, and $\xi = -0.401$
~2 years	H_s	$\mu = -0.045 + 0.01\ NAO_{Hurrell} + 0.011\ NAO_{Hurrell}{}^2$, $\sigma = -2.146 - 0.064\ AMO - 0.063\ AMO^2$, and $\xi = -0.375 + 0.05\ SLP$
	S	$\mu = -0.009$, $\sigma = -3.49 - 0.089\ SLP + 0.158\ t - 0.128\ t^2$, and $\xi = -0.299 - 0.079\ AMO$
3-5 years	H_s	$\mu = -0.022$ $\sigma = -2.805 + 0.05\ AMO + 0.027\ AMO^2 + 0.066\ t + 0.173\ t^2$, and $\xi = -0.379 - 0.106\ AMO$
	S	$\mu = -0.005 + 0.002\ AMO - 0.01\ AMO^2$, $\sigma = -3.813 - 0.069\ AMO + 0.015\ AMO^2 - 0.088\ NAO_{Hurrell} - 0.02\ NAO_{Hurrell}{}^2$, and $\xi = -0.288 + 0.077\ AMO - 0.23\ t - 0.208\ t^2$
6-8 years	H_s	$\mu = -0.016 + 0.004\ AMO + 0.008\ AMO^2 + 0.006\ NAO_{Hurrell}$, $\sigma = -3.323 - 0.157\ t + 0.298\ t^2$, and $\xi = -0.44 + 0.065\ SLP + 0.094\ AMO - 0.088\ AMO^2 - 0.091\ NAO_{Hurrell}$
	S	$\mu = -0.004 - 0.002\ AMO$, $\sigma = -3.682 + 0.079\ t - 0.166\ t^2$, and $\xi = -0.517 + 0.143\ AMO$

Table 44. *Results of the fitting of the GEV with the non-stationary parameters dependent the climate and time indexes for the spectral components of significant wave height and surge in Cherbourg*

~3 months	H_s	$\mu = -0.064$, $\sigma = -1.786$, and $\xi = -0.223 - 0.052\ NAO_{Hurrell}$
	S	$\mu = -0.049$, $\sigma = -1.956 + 0.058\ SLP + 0.084\ SLP^2 + 0.086\ NAO_{Hurrell} + 0.094\ t - 0.104\ t^2$, and $\xi = -0.129 - 0.144\ NAO_{Hurrell} - 0.095\ t - 0.13\ t^2$
~6 months	H_s	$\mu = 0.001 + 0.001\ SLP + 0.001\ SLP^2 - 0.032\ AMO - 0.016\ AMO^2$, $\sigma = -2.242 - 0.147\ SST - 0.118\ AMO + 0.085\ AMO^2$, and $\xi = -0.235$
	S	$\mu = -0.038$, $\sigma = -2.318 - 0.139\ AMO + 0.031\ NAO_{Hurrell} + 0.262\ {NAO_{Hurrell}}^2 + 0.122\ t$, and $\xi = -0.214 - 0.094\ SLP - 0.059\ SLP^2$
~1 year	H_s	$\mu = -0.037 - 0.152\ SLP$, $\sigma = -1.818 + 0.025\ SLP - 0.231\ SLP^2 - 0.114\ t$, and $\xi = -0.393 + 0.077\ NAO_{Hurrell}$
	S	$\mu = -0.042 - 0.101\ SLP$, $\sigma = -2.099 - 0.055\ NAO_{Hurrell} + 0.137\ t$, and $\xi = -0.231 + 0.131\ NAO_{Hurrell} - 0.067\ {NAO_{Hurrell}}^2$
~2 years	H_s	$\mu = -0.029 + 0.003\ AMO - 0.007\ AMO^2 + 0.012\ NAO_{NOAA}$, $\sigma = -2.844 - 0.106\ SLP - 0.149\ t - 0.078\ t^2$, and $\xi = -0.229 - 0.067\ AMO - 0.082\ AMO^2$
	S	$\mu = -0.023 - 0.024\ AMO - 0.007\ AMO^2$ $\sigma = -2.483 + 0.339\ AMO - 0.184\ AMO^2$, and $\xi = -0.262 - 0.094\ AMO + 0.112\ AMO^2 + 0.043\ NAO_{NOAA} + 0.033\ {NAO_{NOAA}}^2$
3-5 years	H_s	$\mu = -0.013 - 0.005\ SST + 0.009\ SLP$ $\sigma = -3.316 + 0.099\ AMO - 0.063\ AMO^2 + 0.087\ t - 0.074\ t^2$, and $\xi = -0.141 - 0.146\ SST - 0.227\ t - 0.197\ t^2$
	S	$\mu = -0.029 - 0.027\ t - 0.012\ t^2$ $\sigma = -2.199 + 0.653\ t - 0.108\ t^2$, and $\xi = -0.117 + 0.137\ t - 0.433\ t^2$
6-8 years	H_s	$\mu = 0.003 - 0.005\ t - 0.012\ t^2$, $\sigma = -2.928 - 0.05\ SST - 0.942\ SST^2 - 0.007\ t - 0.374\ t^2$, and $\xi = -1.179 - 0.097\ t + 0.602\ t^2$
	S	$\mu = 0.016 + 0.018\ t - 0.01\ t^2$, $\sigma = -1.795 + 0.461\ t - 0.664\ t^2$, and $\xi = -0.717 - 0.285\ t$

Table 45. *Results of the fitting of the GEV with the non-stationary parameters dependent the climate and time indexes for the spectral components of significant wave height and surge in Weymouth*

~3 months	H_s	$\mu = -0.154 + 0.103\ NAO_{Hurrell} + 0.022\ {NAO_{Hurrell}}^2$, $\sigma = -0.963 - 0.086\ SST - 0.075\ SST^2 - 0.065\ AMO - 0.071\ NAO_{Hurrell}$, and $\xi = -0.237$
	S	$\mu = -0.033 + 0.017\ SLP - 0.008\ SLP^2$, $\sigma = -2.31 + 0.32\ SST - 0.336\ SST^2 + 0.071\ SLP - 0.05\ AMO = 0.107\ NAO_{Hurrell}$, and $\xi = -0.138 + 0.027\ SST + 0.18\ SST^2 + 0.029\ NAO_{Hurrell}$
~6 months	H_s	$\mu = -0.052 - 0.05\ SST + 0.033\ SLP - 0.038\ SLP^2$, $\sigma = -1.369 - 0.122\ AMO$, and $\xi = -0.285$
	S	$\mu = -0.025 - 0.003\ AMO + 0.005\ AMO^2$, $\sigma = -2.288 + 0.075\ AMO + 0.042\ AMO^2 - 0.119\ t - 0.284\ t^2$, and $\xi = -0.166 + 0.094\ NAO_{NOAA} - 0.064\ {NAO_{NOAA}}^2$
~1 year	H_s	$\mu = -0.088 - 0.285\ SLP + 0.097\ NAO_{Hurrell}$, $\sigma = -1.048 - 0.047\ SST + 0.108\ SST^2 - 0.118\ SLP - 0.11\ SLP^2 - 0.103\ t + 0.133\ t^2$, and $\xi = -0.396 - 0.098\ NAO_{Hurrell}$
	S	$\mu = -0.027 - 0.07\ SLP + 0.012\ AMO + 0.012\ NAO_{Hurrell}$, $\sigma = -2.364 + 0.078\ SST - 0.062\ SST^2$, and $\xi = -0.367 - 0.085\ SST$
~2 years	H_s	$\mu = -0.043$, $\sigma = -1.895 + 0.096\ SST + 0.146\ SST^2 - 0.063\ t$, and $\xi = -0.274 + 0.023\ NAO_{NOAA} - 0.051\ {NAO_{NOAA}}^2$
	S	$\mu = -0.016 + 0.005\ t$, $\sigma = -3.034 - 0.067\ NAO_{NOAA} - 0.207\ {NAO_{NOAA}}^2 - 0.094\ t$, and $\xi = -0.252$
3-5 years	H_s	$\mu = -0.004$ $\sigma = -2.064 - 0.058\ AMO - 0.209\ AMO^2 + 0.035\ t - 0.251\ t^2$, and $\xi = -0.732 - 0.07\ SLP - 0.081\ SLP^2 - 0.028\ t$
	S	$\mu = -0.012 - 0.001\ AMO + 0.002\ AMO^2 - 0.002\ NAO_{Hurrell} - 0.002\ t + 0.006\ t^2$, $\sigma = -3.272 + 0.087\ SLP + 0.085\ AMO - 0.051\ NAO_{Hurrell} + 0.071\ {NAO_{Hurrell}}^2 - 0.017\ t - 0.346\ t^2$, and $\xi = -0.308 - 0.134\ SLP - 0.089\ NAO_{Hurrell} - 0.213\ {NAO_{Hurrell}}^2 - 0.087\ t - 0.044\ t^2$
6-8 years	H_s	$\mu = -0.028 + 0.013\ AMO + 0.006\ AMO^2 - 0.025\ NAO_{Hurrell} + 0.005\ t$, $\sigma = -3.122 + 0.308\ AMO - 0.018\ t + 0.186\ t^2$, and $\xi = -0.267 - 0.256\ AMO - 0.07\ AMO^2 + 0.348\ NAO_{Hurrell} - 0.143\ {NAO_{Hurrell}}^2 + 0.014\ t$
	S	$\mu = -0.017 + 0.0008\ AMO - 0.004\ AMO^2 - 0.003\ t + 0.009t^2$, $\sigma = -3.036 + 0.15\ t - 0.455\ t^2$, and $\xi = -0.374$

Table 46. *Results of the fitting of the GEV with the non-stationary parameters dependent the climate and time indexes for the spectral components of significant wave height and surge in Newhaven*

~3 months	H_s	$\mu = -0.149$, $\sigma = -0.874 - 0.079\,SST - 0.119\,SST^2$, and $\xi = -0.199$
	S	$\mu = -0.061 - 0.01\,t + 0.011\,t^2$, $\sigma = -1.703 - 0.13\,SLP - 0.031\,SLP^2 + 0.132\,AMO + 0.183\,AMO^2 - 0.107\,NAO_{NOAA} + 0.082\,{NAO_{NOAA}}^2 - 0.051\,t - 0.295\,t^2$, and $\xi = -0.228 + 0.056\,SLP - 0.048\,SLP^2 - 0.056\,NAO_{NOAA} + 0.071\,{NAO_{NOAA}}^2$
~6 months	H_s	$\mu = -0.064 - 0.066\,SST + 0.063\,SST^2 + 0.022\,SLP - 0.03\,NAO_{Hurrell}$, $\sigma = -1.321 - 0.129\,AMO + 0.069\,NAO_{Hurrell}$, and $\xi = -0.27$
	S	$\mu = -0.032$, $\sigma = -2.234 + 0.045\,t - 0.153\,t^2$, and $\xi = -0.279 - 0.021\,NAO_{Hurrell} + 0.052\,{NAO_{Hurrell}}^2$
~1 year	H_s	$\mu = -0.113 - 0.306\,SLP + 0.079\,NAO_{Hurrell} + 0.025\,{NAO_{Hurrell}}^2$, $\sigma = -1.006 - 0.039\,SST + 0.096\,SST^2 - 0.088\,SLP - 0.13\,SLP^2 - 0.11\,t + 0.058\,t^2$, and $\xi = -0.418 + 0.012\,AMO + 0.057\,AMO^2$
	S	$\mu = -0.049 - 0.091\,SLP - 0.01\,AMO + 0.018\,AMO^2 + 0.012\,NAO_{Hurrell}$, $\sigma = -2.057 + 0.026\,SLP + 0.103\,SLP^2 - 0.151\,t + 0.05\,t^2$, and $\xi = -0.331$
~2 years	H_s	$\mu = -0.065 + 0.003\,NAO_{NOAA} - 0.017\,{NAO_{NOAA}}^2 + 0.016\,t$, $\sigma = -1.686 - 0.124\,AMO + 0.254\,t - 0.222\,t^2$, and $\xi = -0.264 - 0.023\,SST + 0.048\,AMO - 0.044\,AMO^2 + 0.065\,NAO_{NOAA} - 0.129\,{NAO_{NOAA}}^2$
	S	$\mu = -0.008 - 0.002\,SLP + 0.001\,AMO - 0.003\,AMO^2 - 0.003\,t$, $\sigma = -3.214 + 0.133\,SST + 0.493\,t - 0.396\,t^2$, and $\xi = -0.352 - 0.101\,SLP - 0.034\,AMO + 0.076\,AMO^2$
3-5 years	H_s	$\mu = -0.039 + 0.001\,t + 0.016\,t^2$ $\sigma = -2.122 - 0.032\,AMO - 0.234\,t - 0.16\,t^2$, and $\xi = -0.297 + 0.013\,SST + 0.111\,SST^2 + 0.006\,t - 0.245\,t^2$
	S	$\mu = -0.012 + 0.0006\,AMO + 0.0008\,AMO^2 - 0.002\,NAO_{Hurrell} + 0.002\,{NAO_{Hurrell}}^2 - 0.001\,t + 0.004\,t^2$, $\sigma = -3.84 - 0.041\,AMO + 0.876\,AMO^2 + 0.088\,t - 0.214\,t^2$, and $\xi = -0.187 + 0.081\,SLP - 0.292\,t$
6-8 years	H_s	$\mu = -0.015 + 0.008\,AMO - 0.015\,AMO^2 + 0.004\,t - 0.008\,t^2$, $\sigma = -3.61 + 0.078\,SST + 0.264\,AMO + 0.092\,t + 0.331\,t^2$, and $\xi = -0.245 - 0.082\,t + 0.281\,AMO^2 - 0.2\,t$
	S	$\mu = -0.015 + 0.005\,t - 0.01\,t^2$, $\sigma = -3.361 + 0.019\,AMO + 0.252\,t - 0.227\,t^2$, and $\xi = -0.519 - 0.402\,t$

Table 47. *Results of the fitting of the GEV with the non-stationary parameters dependent the climate and time indexes for the spectral components of significant wave height and surge in Dover*

~3 months	H_s	$\mu = -0.101 - 0.033\ NAO_{Hurrell}$, $\sigma = -1.315 - 0.085\ SST$, and $\xi = -0.25$
	S	$\mu = -0.039 + 0.004\ NAO_{Hurrell} + 0.008\ NAO_{Hurrell}^{2}$, $\sigma = -2.508 + 0.063\ SST - 0.167\ SST^2 + 0.087\ SLP - 0.067\ AMO + 0.008\ NAO_{Hurrell} + 0.069\ NAO_{Hurrell}^{2} - 0.116\ t + 0.194\ t^2$, and $\xi = -0.265 + 0.009\ SLP + 0.028\ SLP^2 - 0.106\ NAO_{Hurrell} + 0.122\ NAO_{Hurrell}^{2}$
~6 months	H_s	$\mu = -0.027 - 0.071\ SST + 0.065\ SST^2 - 0.012\ SLP - 0.015\ SLP^2$, $\sigma = -1.888 - 0.119\ t$, and $\xi = -0.265 - 0.064\ NAO_{NOAA}$
	S	$\mu = -0.019$, $\sigma = -3.077 + 0.148\ AMO - 0.164\ t + 0.253\ t^2$, and $\xi = -0.254 - 0.019\ SST + 0.051\ SST^2 - 0.059\ NAO_{NOAA} + 0.047\ NAO_{NOAA}^{2}$
~1 year	H_s	$\mu = -0.077 - 0.059\ SST - 0.12\ SLP + 0.022\ SLP^2 + 0.025\ NAO_{Hurrell}$, $\sigma = -1.895$, and $\xi = -0.156 + 0.131\ SLP - 0.155\ SLP^2$
	S	$\mu = -0.029 - 0.063\ SLP$, $\sigma = -2.574 + 0.115\ SST + 0.134\ AMO - 0.095\ t + 0.152\ t^2$, and $\xi = -0.33 - 0.123\ SST + 0.085\ NAO_{Hurrell}$
~2 years	H_s	$\mu = -0.026$, $\sigma = -2.585$, and $\xi = -0.294$
	S	$\mu = -0.017 - 0.005\ t$, $\sigma = -2.822 - 0.077 + 0.301\ t - 0.178\ t^2$, and $\xi = -0.292$
3-5 years	H_s	$\mu = -0.013$ $\sigma = -2.975 + 0.025\ AMO - 0.243\ AMO^2 - 0.066\ t + 0.2\ t^2$, and $\xi = -0.226 - 0.11\ t - 0.297\ t^2$
	S	$\mu = -0.005 + 0.008\ t - 0.009\ t^2$, $\sigma = -4.049 - 0.443\ t + 0.366\ t^2$, and $\xi = -0.791 + 0.042\ SST + 0.067\ t + 0.615\ t^2$
6-8 years	H_s	$\mu = -0.012 - 0.001\ SST + 0.003\ SST^2 + 0.002\ AMO + 0.003\ AMO^2$, $\sigma = -3.512 - 0.062\ t - 0.355\ t^2$, and $\xi = -0.319 - 0.078\ AMO - 0.102\ AMO^2$
	S	$\mu = -0.018 - 0.006\ t + 0.013\ t^2$, $\sigma = -3.668 - 0.004\ SST + 0.255\ t - 0.134\ t^2$, and $\xi = -0.257 + 0.124\ t - 0.388\ t^2$

Table 48. *Results of the fitting of the GEV with the non-stationary parameters dependent the climate and time indexes for the spectral components of significant wave height and surge in Dunkirk*

b. Copulas

Frequencies	Copula	Parameters
2-3 months	Gaussian constant	$\tau = \Lambda(-0.3277)$
5-6.5 months	Gaussian constant	$\tau = \Lambda(-0.3008)$
~1 year	Gaussian linear	$\tau = \Lambda(0.7124 + 0.1041\ t)$
1.5-2 years	Gaussian linear	$\tau = \Lambda(0.1227 - 0.1116\ t)$
3-5 years	Frank constant	$\tau = \Lambda(-1.151)$
6-9 years	Frank linear	$\tau = \Lambda(0.1567 - 0.0789\ t)$

Table 49. *Results of the fitting of the copulas between spectral components of significant wave height and surge with the non-stationary time-dependent parameters in Brest with the 6 timescales*

Frequencies	Copula	Parameters
2-3 months	Gumbel constant	$\tau = \Lambda(-1.2746)$
5-6.5 months	Gaussian constant	$\tau = \Lambda(-1.1448)$
~1 year	Frank linear	$\tau = \Lambda(0.7782 - 0.1102\ t)$
1.5-2 years	Gaussian linear	$\tau = \Lambda(-2 + 0.5883\ t)$
3-5 years	Frank linear	$\tau = \Lambda(-1.7233 - 0.3277\ t)$
6-9 years	Gumbel linear	$\tau = \Lambda(-2 + 1.8156\ t)$

Table 50. *Results of the fitting of the copulas between spectral components of significant wave height and surge with the non-stationary time-dependent parameters in Cherbourg with the 6 timescales*

Frequencies	Copula	Parameters
2-3 months	Frank constant	$\tau = \Lambda(-1.1908)$
5-6.5 months	Frank linear	$\tau = \Lambda(-0.7277 - 0.4475\ t)$
~1 year	Frank constant	$\tau = \Lambda(0.0195\ t)$
1.5-2 years	Frank linear	$\tau = \Lambda(-2 - 1.016\ t)$
3-5 years	Frank linear	$\tau = \Lambda(-1.3596 + 0.8169\ t)$
6-9 years	Gaussian constant	$\tau = \Lambda(-1.5305)$

Table 51. *Results of the fitting of the copulas between spectral components of significant wave height and surge with the non-stationary time-dependent parameters in Weymouth with the 6 timescales*

Frequencies	Copula	Parameters
2-3 months	Gaussian linear	$\tau = \Lambda(-0.4235 + 0.1908\ t)$
5-6.5 months	Frank linear	$\tau = \Lambda(-0.8027 + 0.3402\ t)$
~1 year	Frank linear	$\tau = \Lambda(0.474 + 0.4867\ t)$
1.5-2 years	Frank linear	$\tau = \Lambda(-1.3 + 1.2217\ t)$
3-5 years	Gaussian linear	$\tau = \Lambda(0.0233 + 0.5078\ t)$
6-9 years	Frank linear	$\tau = \Lambda(-2 + 0.9712\ t)$

Table 52. *Results of the fitting of the copulas between spectral components of significant wave height and surge with the non-stationary time-dependent parameters in Newhaven with the 6 timescales*

Frequencies	Copula	Parameters
2-3 months	Frank linear	$\tau = \Lambda(-1.2683 - 0.03154\ t)$
5-6.5 months	Frank constant	$\tau = \Lambda(-1.3178)$
~1 year	Frank linear	$\tau = \Lambda(0.2943 + 0.3352\ t)$
1.5-2 years	Gaussian linear	$\tau = \Lambda(-2 - 1.6519\ t)$
3-5 years	Gaussian constant	$\tau = \Lambda(-1.3053)$
6-9 years	Frank linear	$\tau = \Lambda(-0.7075 + 0.3003\ t)$

Table 53. *Results of the fitting of the copulas between spectral components of significant wave height and surge with the non-stationary time-dependent parameters in Dover with the 6 timescales*

Frequencies	Copula	Parameters
2-3 months	Gaussian linear	$\tau = \Lambda(-1.4017 + 0.5086\ t)$
5-6.5 months	Frank constant	$\tau = \Lambda(-2)$
~1 year	Gaussian linear	$\tau = \Lambda(0.2217 + 0.2604\ t)$
1.5-2 years	Gaussian linear	$\tau = \Lambda(-1.508 + 0.9825\ t)$
3-5 years	Clayton linear	$\tau = \Lambda(-2 + 0.9341\ t)$
6-9 years	Frank linear	$\tau = \Lambda(-2 + 1.1711\ t)$

Table 54. *Results of the fitting of the copulas between spectral components of significant wave height and surge with the non-stationary time-dependent parameters in Dunkirk with the 6 timescales*

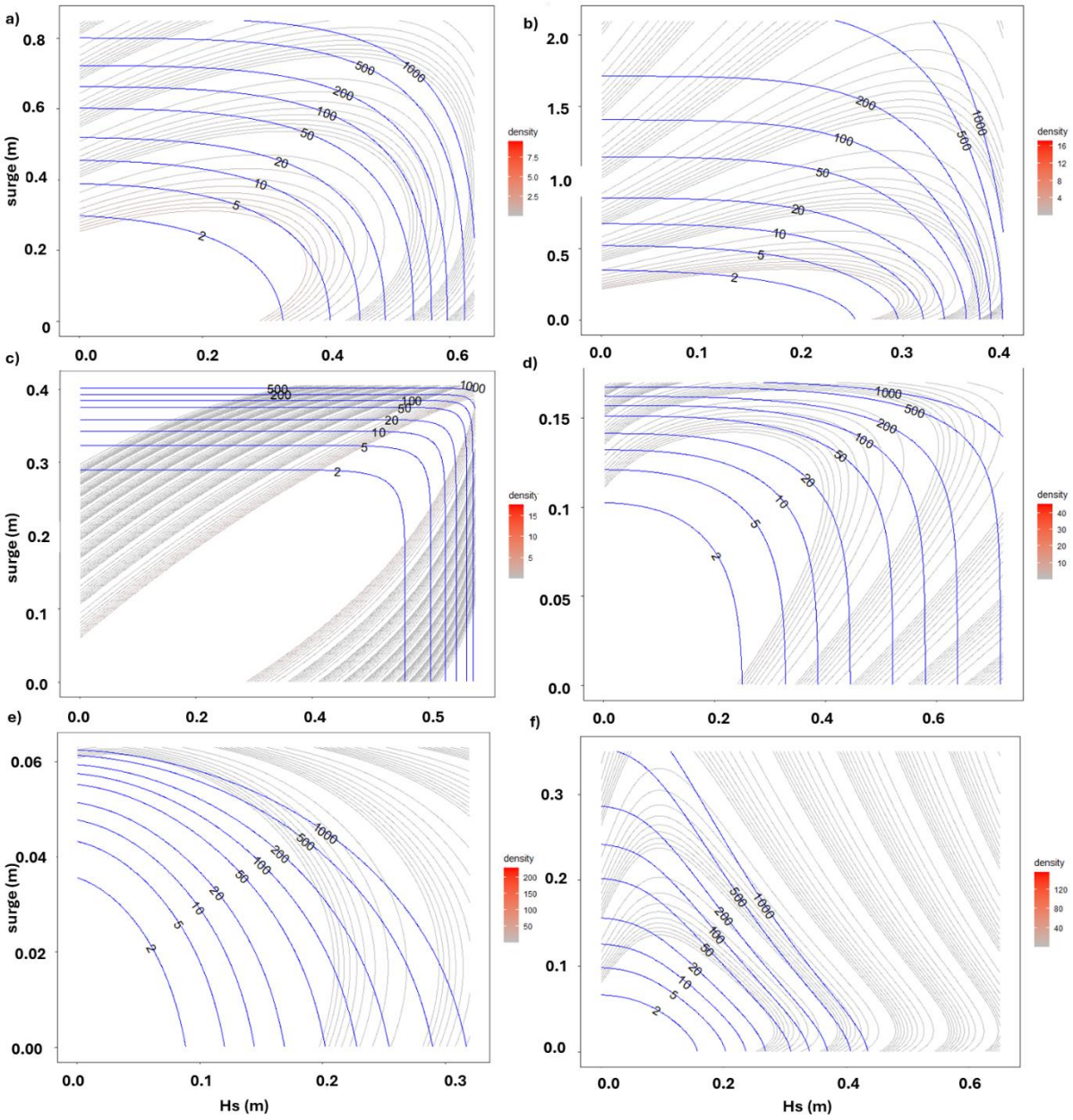

Figure 108. *Bivariate density of spectral components of significant wave height from and surge in Brest with effective joint return levels for several return periods for the time scales of a) 2-3 months, b) 5-6.5 months, c) ~1 year, d) 1.5-2 years, e) 3-5 years, and f) 6-9 years*

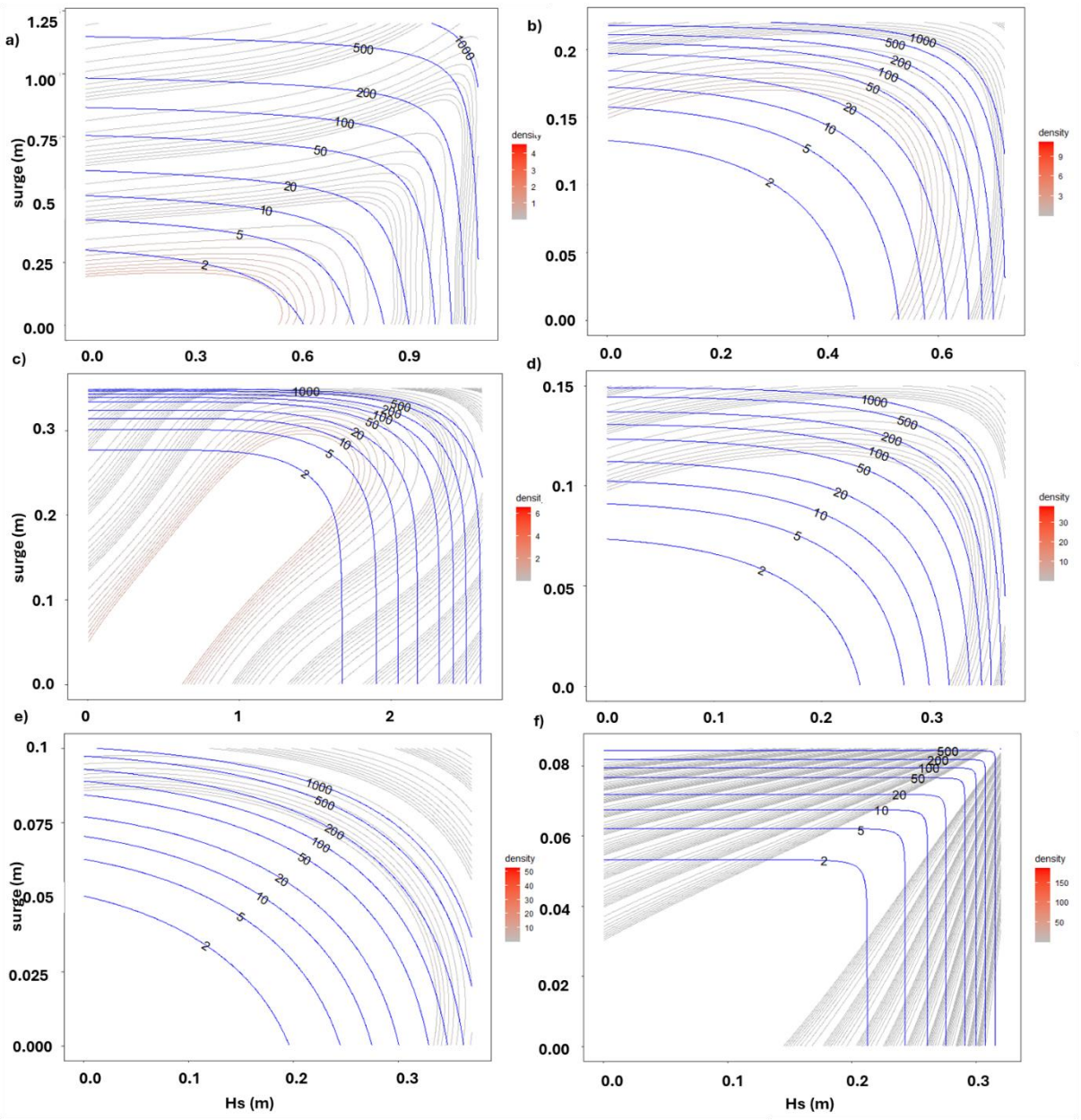

Figure 109. *Bivariate density of spectral components of significant wave height from and surge in Cherbourg with effective joint return levels for several return periods for the time scales of a) 2-3 months, b) 5-6.5 months, c) ~1 year, d) 1.5-2 years, e) 3-5 years, and f) 6-9 years*

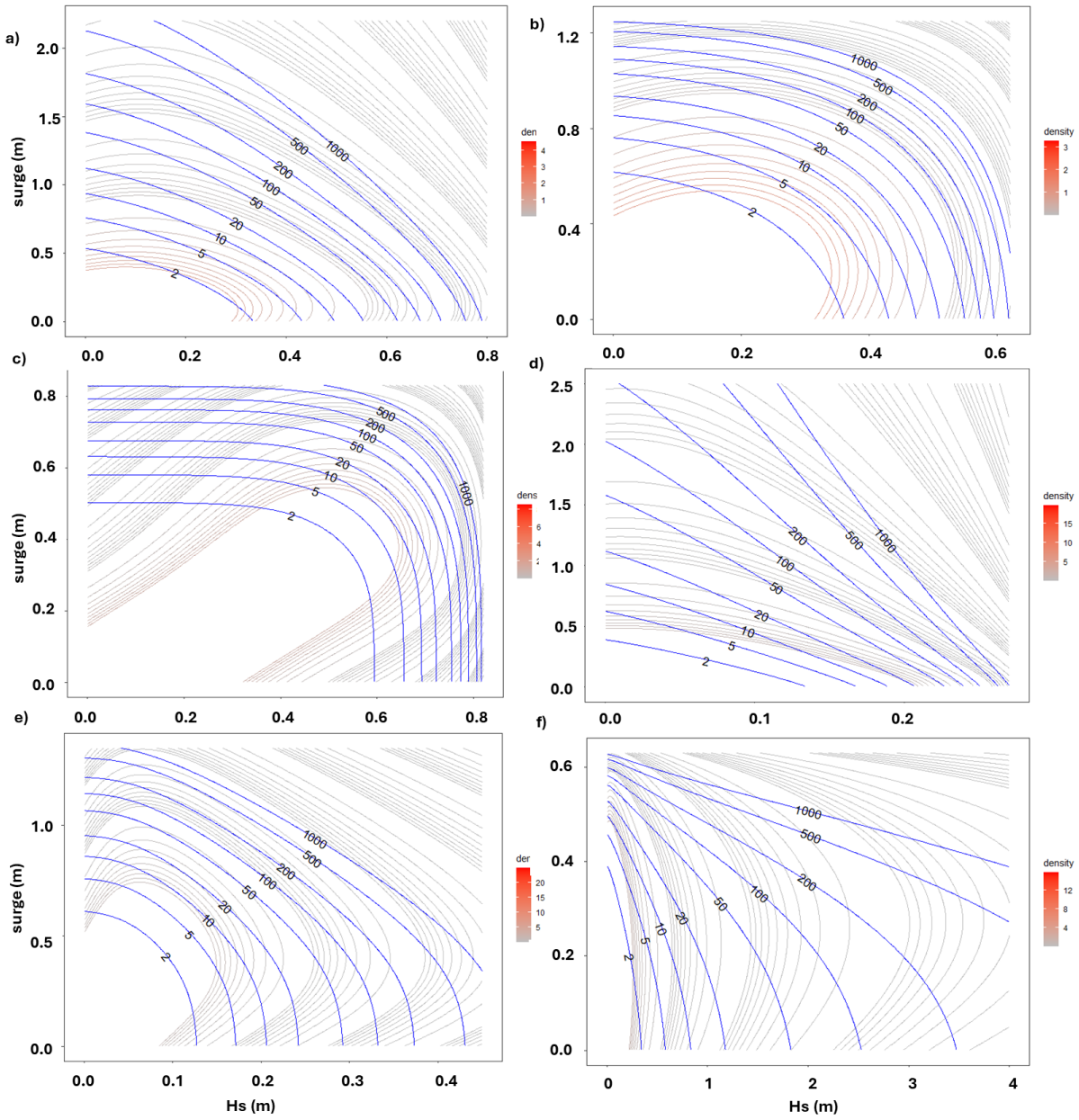

Figure 110. *Bivariate density of spectral components of significant wave height from and surge in Weymouth with effective joint return levels for several return periods for the time scales of a) 2-3 months, b) 5-6.5 months, c) ~1 year, d) 1.5-2 years, e) 3-5 years, and f) 6-9 years*

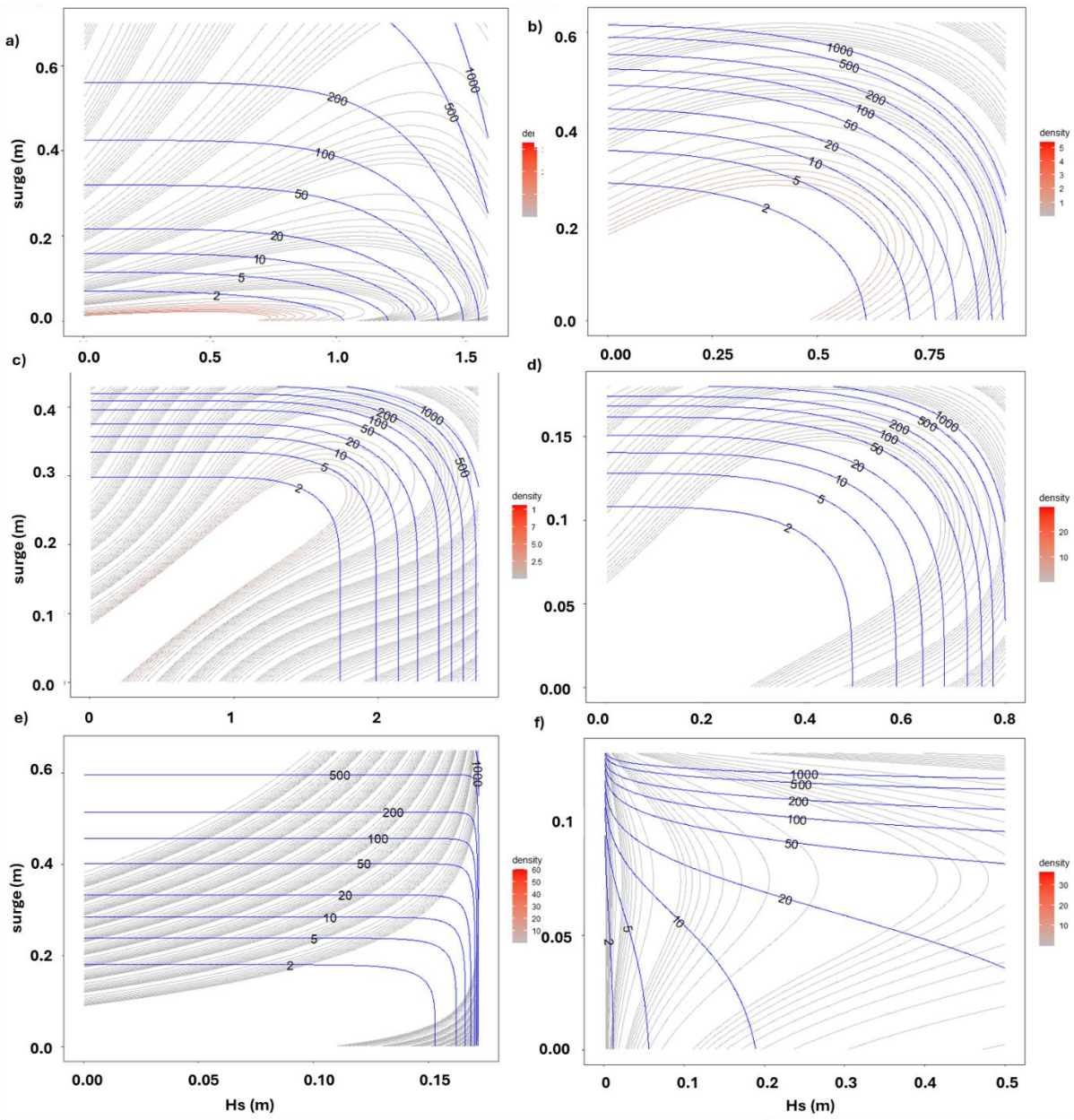

Figure 111. *Bivariate density of spectral components of significant wave height from and surge in Newhaven with effective joint return levels for several return periods for the time scales of a) 2-3 months, b) 5-6.5 months, c) ~1 year, d) 1.5-2 years, e) 3-5 years, and f) 6-9 years*

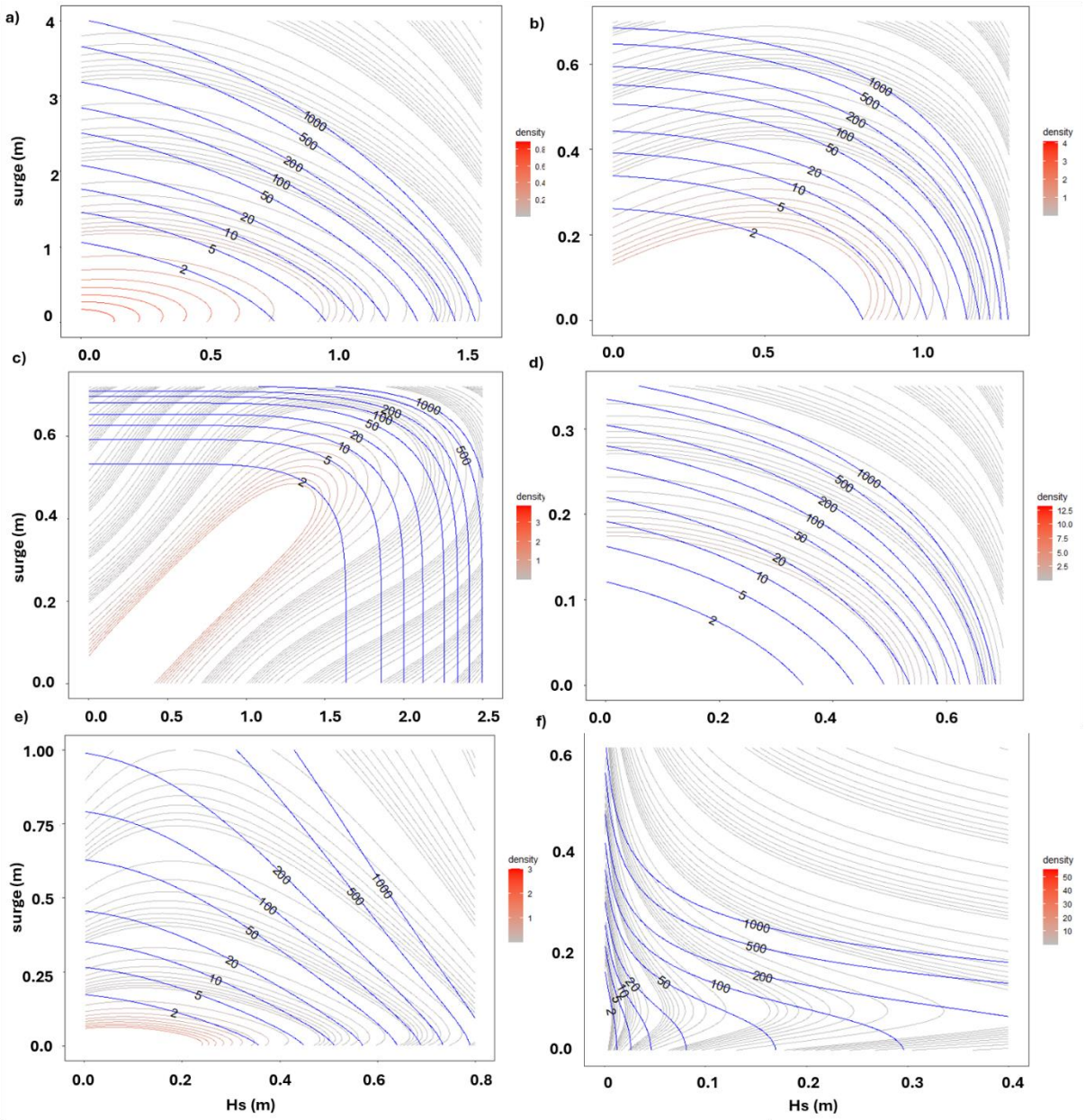

Figure 112. *Bivariate density of spectral components of significant wave height from and surge in Dover with effective joint return levels for several return periods for the time scales of a) 2-3 months, b) 5-6.5 months, c) ~1 year, d) 1.5-2 years, e) 3-5 years, and f) 6-9 years*

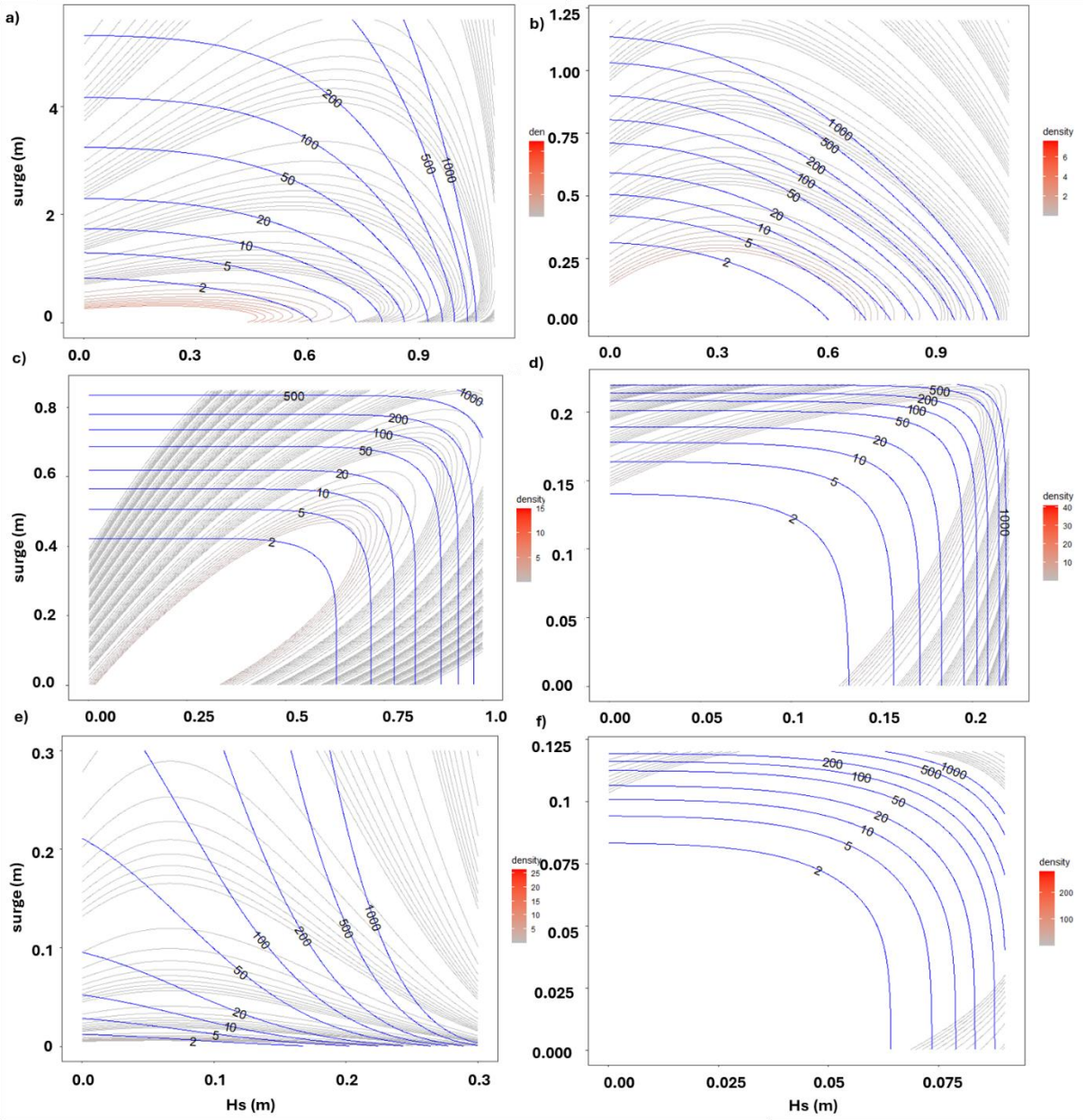

Figure 113. *Bivariate density of spectral components of significant wave height from and surge in Dunkirk with effective joint return levels for several return periods for the time scales of a) 2-3 months, b) 5-6.5 months, c) ~1 year, d) 1.5-2 years, e) 3-5 years, and f) 6-9 years*

APPENDIX C

RESULTS OF CLUSTERING OF EXTREME EVENTS

a. Clustering of extreme events of the complete dataset of extreme events

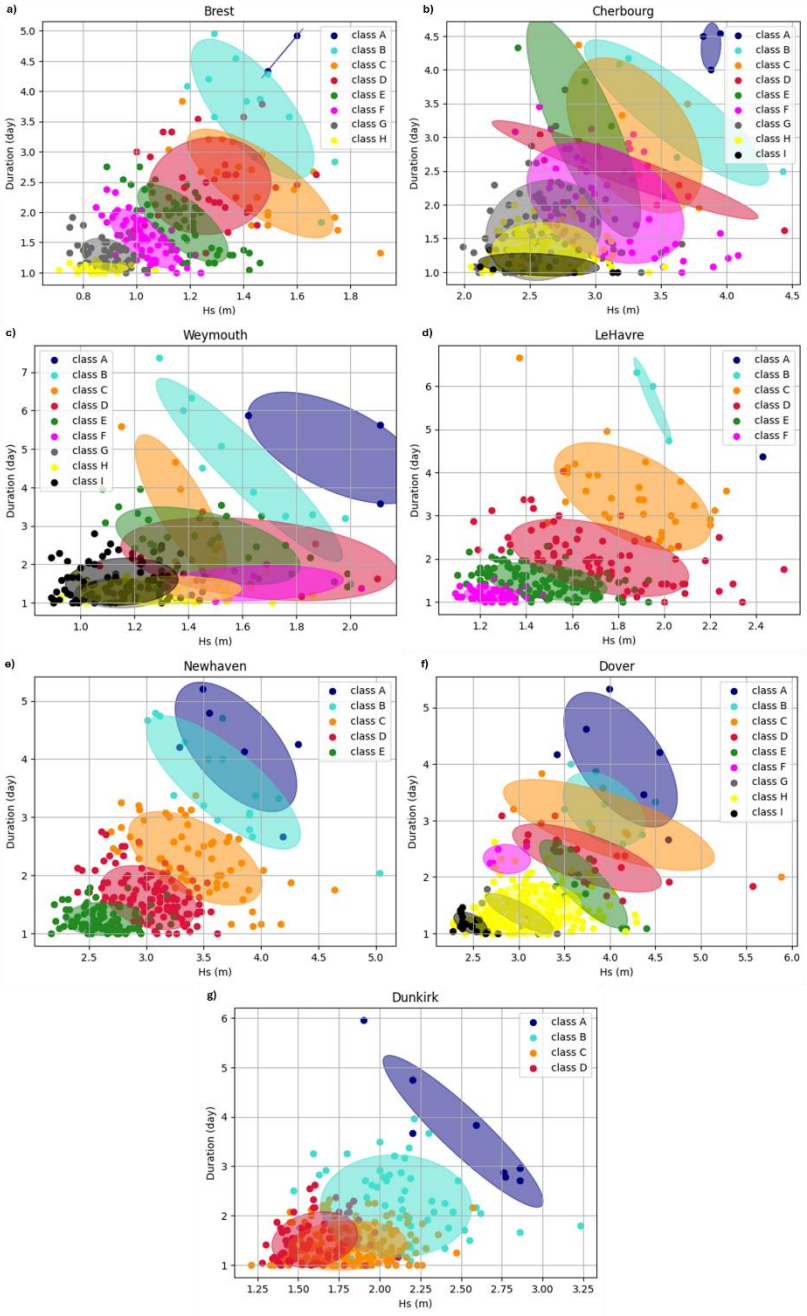

Figure 114. *H_s vs Duration for the classes obtained from the clustering of extreme events on a) Brest, b) Cherbourg, c) Weymouth, d) Le Havre, e) Newhaven, f) Dover, and g) Dunkirk for the complete dataset of identified storms*

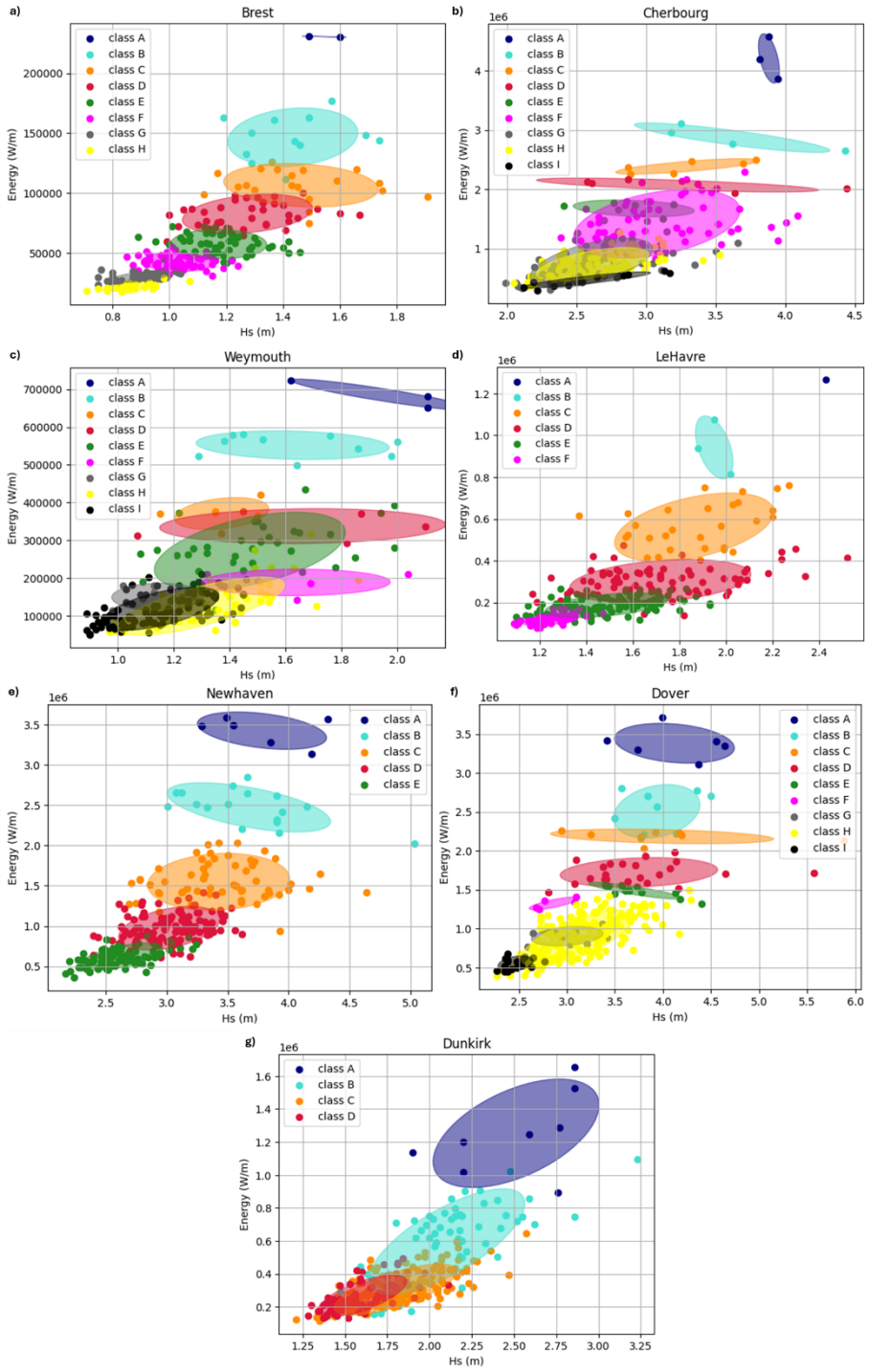

Figure 115. *H_s vs Energy for the classes obtained from the clustering of extreme events on a) Brest, b) Cherbourg, c) Weymouth, d) Le Havre, e) Newhaven, f) Dover, and g) Dunkirk for the complete dataset of identified storms*

b. Clustering of extreme events of class 1 (single events of extreme waves)

	$H_{s,peak}$ (m)	$T_{p,peak}$ (s)	$\theta_{m,peak}$ (°)	Duration (hours)	Energy (W/m)
Class A	1.53 (1.49 | 1.57)	4.43 (4.36 | 4.5)	49.5 (34.8 | 64.2)	3.958 (3.583 | 4.333)	203935 (176877 | 230993)
Class B	1.428 (1.17 | 1.74)	4.317 (3.99 | 4.7)	45.97 (18.7 | 67.5)	3.374 (1.916 | 4.958)	130832 (94891 | 162885)
Class C	1.35 (1.05 | 1.67)	4.216 (3.85 | 4.63)	49.211 (25.9 | 71.2)	2.358 (1.791 | 3.041)	88202 (74567 | 105468)
Class D	1.183 (0.89 | 1.45)	4.006 (3.55 | 4.37)	42.418 (-19.7 | 73.5)	1.953 (1.166 | 3.333)	61191 (41676 | 79501)
Class E	1.033 (0.85 | 1.22)	3.777 (3.34 | 3.99)	51.893 (7.8 | 97.0)	1.571 (1.0 | 2.333)	43228 (28890 | 55091)
Class F	0.891 (0.71 | 1.15)	3.581 (3.26 | 4.01)	36.393 (-8.4 | 86.9)	1.254 (1.0 | 1.916)	28306 (18310 | 44490)

Table 55. *Statistics of the classes of the extreme events identified in the clustering in Brest*

	$H_{s,peak}$ (m)	$T_{p,peak}$ (s)	$\theta_{m,peak}$ (°)	Duration (hours)	Energy (W/m)
Class A	3.82 (3.82 | 3.82)	11.18 (11.2 | 11.2)	115.6 (115.6 | 115.6)	4.5 (4.5 | 4.5)	4185447 (4185447 | 4185447)
Class B	2.976 (2.41 | 3.7)	7.834 (7.15 | 8.51)	-94.649 (-142.5 | 142.5)	3.505 (2.291 | 4.38)	1887886 (1481767 | 2432493)
Class C	3.238 (2.39 | 4.01)	9.456 (6.6 | 13.34)	86.94 (-118.1 | 168.6)	2.274 (1.083 | 3.17)	1339928 (1184759 | 1505169)
Class D	2.887 (2.25 | 3.66)	10.101 (7.45 | 14.5)	110.696 (100.0 | 120.7)	1.823 (1.0 | 4.166)	1208410 (516986 | 3109920)
Class E	3.092 (2.53 | 3.95)	8.545 (7.4 | 10.15)	61.65 (-131.9 | 154.4)	1.895 (1.583 | 2.29)	1101833 (939395 | 1287459)
Class F	2.587 (1.99 | 3.66)	7.401 (6.38 | 8.41)	-131.516 (-174 | -115.7)	1.56 (1.0 | 2.875)	716859 (295694 | 1462800)
Class G	2.55 (2.05 | 3.17)	7.619 (6.57 | 8.86)	122.585 (106.8 | 175.1)	1.242 (1.0 | 2.041)	583344 (353825 | 888681)

Table 56. *Statistics of the classes of the extreme events identified in the clustering in Cherbourg*

	$H_{s,peak}$ (m)	$T_{p,peak}$ (s)	$\theta_{m,peak}$ (°)	Duration (hours)	Energy (W/m)
Class A	1.689 (1.29 | 2.11)	8.423 (6.78 | 16.79)	-62.541 (-73.2 | -8.9)	4.684 (1.5 | 7.375)	585763 (498438 | 723479)
Class B	1.535 (1.15 | 1.99)	7.128 (6.61 | 7.65)	-56.066 (-70.7 | -13.5)	3.024 (1.416 | 5.583)	374801 (324653 | 435623)
Class C	1.297 (0.89 | 1.78)	6.847 (5.22 | 8.32)	-67.457 (-74.7 | -57.0)	2.122 (1.083 | 3.958)	190929 (101798 | 350654)
Class D	1.353 (0.93 | 2.04)	7.154 (5.21 | 13.75)	-27.666 (-57.6 | 14.1)	1.423 (1.0 | 2.0)	146694 (57615 | 291787)
Class E	1.364 (1.09 | 1.54)	7.931 (6.2 | 17.7)	-22.022 (-38.8 | 3.1)	1.06 (1.0 | 1.208)	113729 (83081 | 155481)
Class F	1.096 (0.89 | 1.41)	6.553 (5.11 | 8.23)	-67.407 (-86.8 | -48.1)	1.272 (1.0 | 1.666)	89680 (50089 | 139473)

Table 57. *Statistics of the classes of the extreme events identified in the clustering in Weymouth*

	$H_{s,peak}$ (m)	$T_{p,peak}$ (s)	$\theta_{m,peak}$ (°)	Duration (hours)	Energy (W/m)
Class A	1.915 (1.88 | 1.95)	8.435 (7.9 | 8.97)	105.65 (105.0 | 106.3)	6.166 (6.0 | 6.333)	1006531 (937603 | 1075459)
Class B	1.99 (1.58 | 2.27)	8.905 (7.75 | 9.49)	108.49 (97.1 | 113.8)	3.55 (2.916 | 4.958)	631183 (460368 | 762602)
Class C	1.87 (1.56 | 2.3)	8.969 (5.72 | 10.28)	105.75 (83.8 | 112.2)	2.97 (1.25 | 4.125)	476969 (406746 | 547662)
Class D	1.68 (1.39 | 2.18)	8.252 (6.54 | 9.64)	105.345 (94.5 | 114.3)	2.272 (1.375 | 3.375)	333466 (259134 | 412770)
Class E	1.472 (1.17 | 1.81)	7.591 (5.18 | 9.86)	103.131 (81.8 | 117.8)	1.998 (1.416 | 2.875)	226908 (148273 | 317707)
Class F	1.562 (1.15 | 2.01)	8.229 (7.19 | 9.48)	108.131 (92.9 | 117.9)	1.412 (1.0 | 2.166)	194642 (116784 | 265991)
Class G	1.254 (1.09 | 1.58)	7.477 (4.69 | 11.04)	100.644 (74.0 | 120.1)	1.162 (1.0 | 1.416)	116833 (78637 | 171483)

Table 58. *Statistics of the classes of the extreme events identified in the clustering in Le Havre*

	$H_{s,peak}$ (m)	$T_{p,peak}$ (s)	$\theta_{m,peak}$ (°)	Duration (hours)	Energy (W/m)
Class A	3.67 (3.49 | 3.85)	9.635 (9.12 | 10.15)	46.6 (43.4 | 49.8)	4.666 (4.125 | 5.21)	3437036 (3283563 | 3590508)
Class B	3.532 (3.01 | 4.15)	9.003 (7.91 | 9.89)	41.455 (29.3 | 49.0)	3.782 (2.791 | 4.79)	2537013 (2205637 | 2747318)
Class C	3.365 (2.55 | 5.03)	9.076 (7.58 | 12.02)	44.941 (29.8 | 54.5)	2.21 (1.125 | 3.38)	1496489 (825345 | 2326047)
Class D	2.775 (2.17 | 3.44)	8.355 (7.1 | 9.96)	48.326 (36.8 | 58.6)	1.318 (1.0 | 1.875)	734615 (409153 | 1116838)
Class E	2.743 (2.24 | 3.46)	7.748 (6.75 | 8.79)	33.682 (9.2 | 47.9)	1.485 (1.0 | 2.25)	729623 (361784 | 1097146)

Table 59. *Statistics of the classes of the extreme events identified in the clustering in Newhaven*

	$H_{s,peak}$ (m)	$T_{p,peak}$ (s)	$\theta_{m,peak}$ (°)	Duration (hours)	Energy (W/m)
Class A	4.029 (3.57 | 4.5)	9.042 (8.63 | 9.72)	39.099 (34.6 | 42.7)	4.008 (2.75 | 5.333)	3058435 (2699956 | 3714830)
Class B	3.561 (2.94 | 3.94)	8.488 (7.96 | 9.27)	-5.999 (-142.4 | 43.1)	3.098 (2.33 | 3.833)	2214202 (1885848 | 2562446)
Class C	3.44 (2.68 | 5.57)	8.43 (7.42 | 10.16)	-7.058 (-144.1 | 42.4)	2.263 (1.08 | 3.083)	1452343 (1251709 | 1716898)
Class D	3.123 (2.28 | 4.29)	7.995 (6.89 | 9.3)	40.504 (27.5 | 48.1)	1.445 (1.0 | 2.625)	914209 (395667 | 1931502)
Class E	2.645 (2.27 | 3.37)	7.694 (6.23 | 8.47)	-115.931 (-169.9 | 158.7)	1.26 (1.0 | 1.791)	681987 (444480 | 1065620)

Table 60. *Statistics of the classes of the extreme events identified in the clustering in Dover*

	$H_{s,peak}$ (m)	$T_{p,peak}$ (s)	$\theta_{m,peak}$ (°)	Duration (hours)	Energy (W/m)
Class A	2.655 (2.2 | 2.86)	9.8 (9.17 | 10.4)	102.02 (-171.8 | 176.0)	3.191 (2.71 | 3.833)	1383811 (1199813 | 1654555)
Class B	2.316 (1.9 | 3.23)	8.99 (7.64 | 11.4)	97.486 (-178.1 | 179.3)	2.888 (1.5 | 5.96)	848832 (592307 | 1137877)
Class C	2.261 (1.91 | 2.86)	9.256 (8.73 | 10.2)	-8.747 (-179.8 | 179.5)	2.144 (1.333 | 3.21)	665458 (502943 | 892690)
Class D	1.819 (1.46 | 2.36)	8.02 (6.17 | 9.3)	65.291 (-179.3 | 179.1)	2.044 (1.291 | 3.25)	425454 (291876 | 561111)
Class E	1.706 (1.3 | 2.47)	7.735 (6.12 | 9.0)	-2.693 (-178.6 | 179.8)	1.417 (1.08 | 1.88)	274619 (151101 | 433978)
Class F	1.654 (1.21 | 2.26)	7.69 (5.78 | 9.51)	73.944 (-179.6 | 179.9)	1.05 (1.0 | 1.166)	200979 (115275 | 320606)

Table 61. *Statistics of the classes of the extreme events identified in the clustering in Dunkirk*

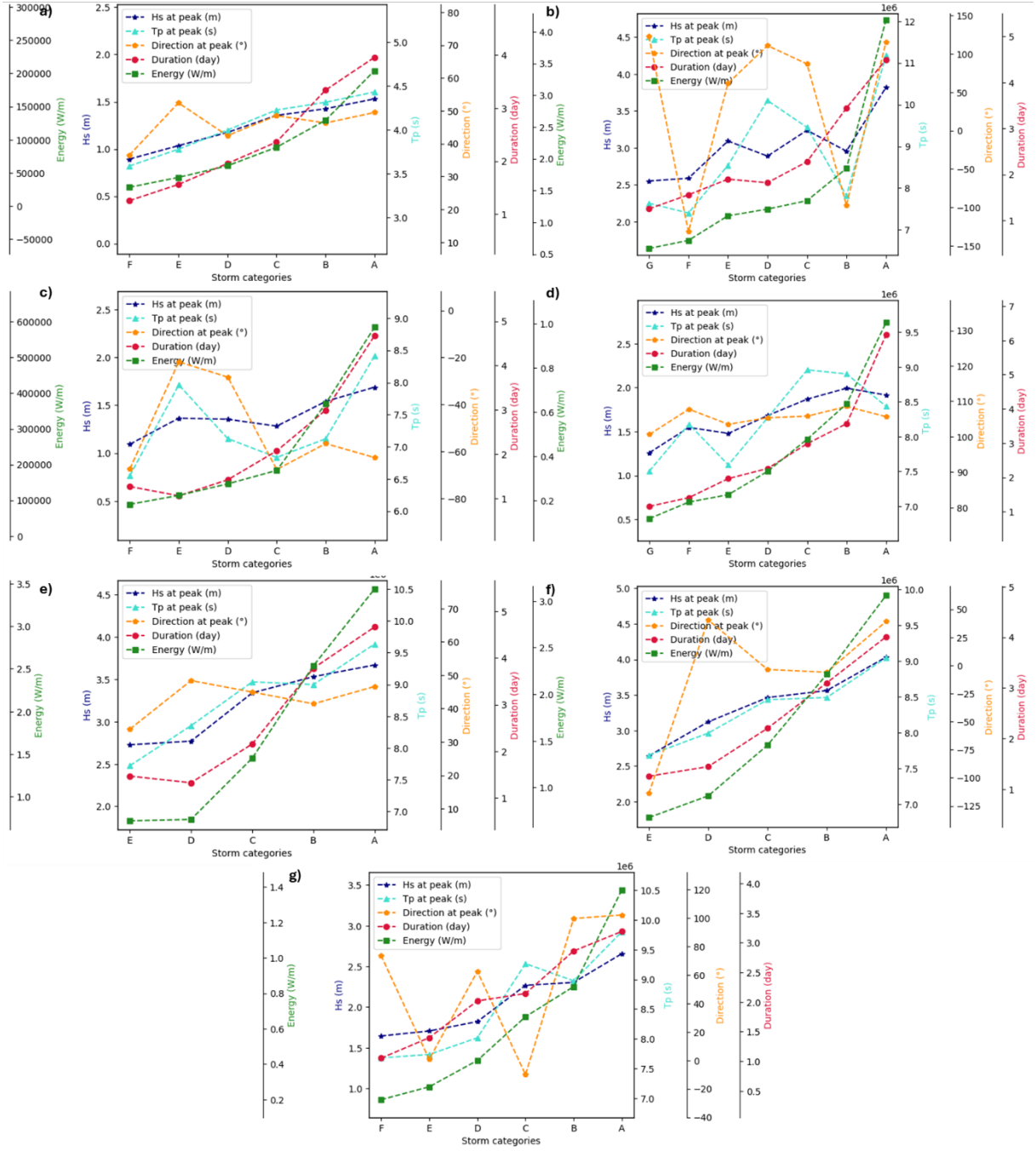

Figure 116. *Class-averaged values of extreme events on a) Brest, b) Cherbourg, c) Weymouth, d) Le Havre, e) Newhaven, f) Dover, and g) Dunkirk for the complete dataset of identified storms*

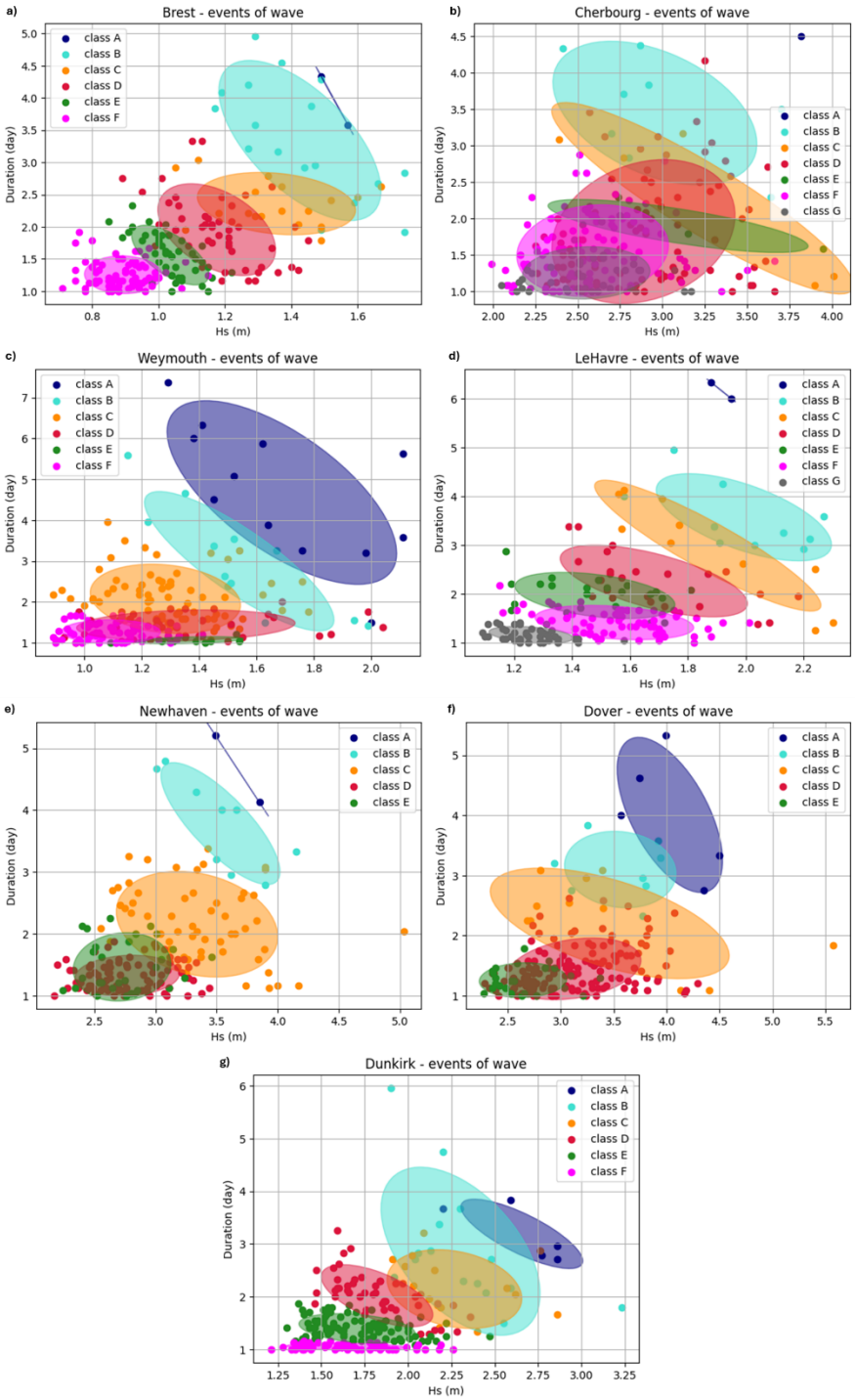

Figure 117. *H_s vs Duration for the classes obtained from the clustering of extreme events on a) Brest, b) Cherbourg, c) Weymouth, d) Le Havre, e) Newhaven, f) Dover, and g) Dunkirk for the complete dataset of identified storms*

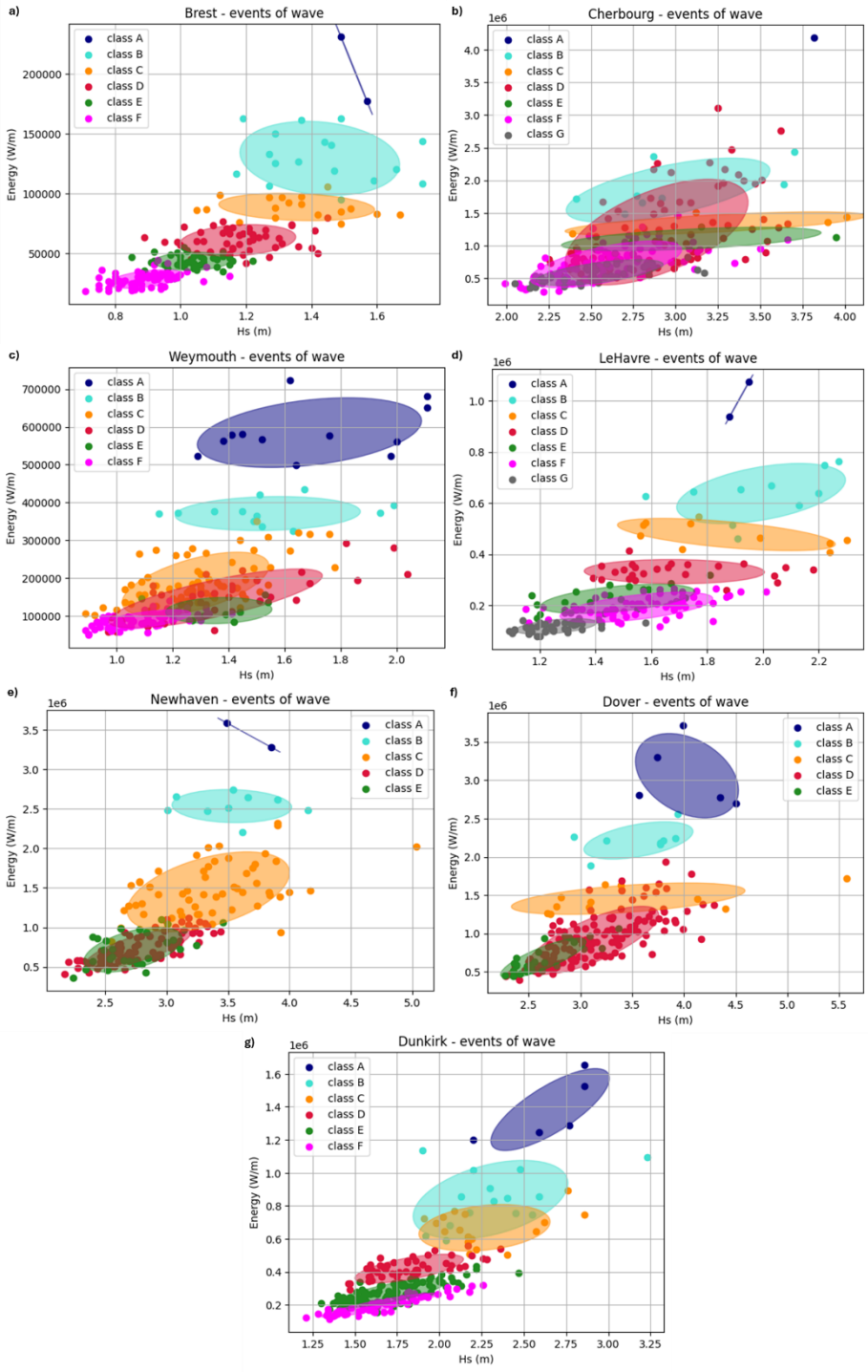

Figure 118. *H_s vs Energy for the classes obtained from the clustering of extreme events on a) Brest, b) Cherbourg, c) Weymouth, d) Le Havre, e) Newhaven, f) Dover, and g) Dunkirk for the complete dataset of identified storms*

c. Clustering of extreme events of class 3 (compound events of extreme waves and surges)

	$H_{s,peak}$ (m)	$T_{p,peak}$ (s)	$\theta_{m,peak}$ (°)	Duration (hours)	Energy (W/m)
Class A	1.6 (1.6 | 1.6)	4.55 (4.55 | 4.55)	44.8 (44.8 | 44.8)	4.916 (4.916 | 4.916)	230259 (230259 | 230259)
Class B	1.462 (1.23 | 1.91)	4.363 (4.06 | 4.88)	39.981 (22.3 | 61.9)	2.549 (1.333 | 3.833)	111480 (97279 | 148678)
Class C	1.23 (1.0 | 1.47)	4.086 (3.78 | 4.36)	26.184 (-9.5 | 48.5)	2.458 (1.75 | 3.791)	83369 (70875 | 100050)
Class D	1.221 (1.04 | 1.46)	4.059 (3.78 | 4.37)	33.036 (10.0 | 57.2)	1.647 (1.041 | 2.541)	56912 (50352 | 64354)
Class E	1.077 (0.87 | 1.29)	3.856 (3.43 | 4.21)	42.769 (15.2 | 88.7)	1.65 (1.0 | 2.458)	42855 (35288 | 48925)
Class F	0.922 (0.8 | 1.09)	3.639 (3.34 | 3.92)	21.317 (-13.9 | 89.8)	1.21 (1.0 | 1.625)	28896 (17650 | 39119)

Table 62. *Statistics of the classes of the extreme events identified in the clustering in Brest*

	$H_{s,peak}$ (m)	$T_{p,peak}$ (s)	$\theta_{m,peak}$ (°)	Duration (hours)	Energy (W/m)
Class A	3.915 (3.88 | 3.95)	13.82 (13.52 | 14.12)	114.45 (111.6 | 117.3)	4.27 (4.0 | 4.54)	4214733 (3854947 | 4574519)
Class B	3.777 (3.18 | 4.43)	12.742 (12.34 | 13.14)	113.175 (111.5 | 115.2)	2.666 (1.96 | 4.08)	2600129 (2295512 | 2955908)
Class C	3.261 (2.58 | 4.44)	12.049 (9.02 | 14.9)	108.916 (99.0 | 118.1)	2.045 (1.17 | 3.04)	1837545 (1560349 | 2144772)
Class D	2.8 (2.62 | 3.26)	9.379 (7.23 | 11.54)	111.989 (102.3 | 130.9)	1.812 (1.46 | 2.3)	1166248 (977213 | 1435574)
Class E	2.673 (2.27 | 3.12)	10.922 (6.59 | 13.8)	110.631 (100.7 | 141.1)	1.197 (1.0 | 1.63)	795398 (510100 | 1064194)
Class F	2.462 (2.24 | 2.87)	8.209 (6.77 | 12.96)	-31.219 (-154.4 | 169)	1.208 (1.08 | 1.33)	556595 (461370 | 700073)

Table 63. *Statistics of the classes of the extreme events identified in the clustering in Cherbourg*

	$H_{s,peak}$ (m)	$T_{p,peak}$ (s)	$\theta_{m,peak}$ (°)	Duration (hours)	Energy (W/m)
Class A	1.86 (1.86 | 1.86)	7.95 (7.95 | 7.95)	-68.8 (-68.8 | -68.8)	3.291 (3.291 | 3.291)	542950 (542950 | 542950)
Class B	1.61 (1.35 | 1.87)	10.915 (7.03 | 14.8)	-33.6 (-56.3 | -10.9)	2.312 (2.083 | 2.541)	372179 (370586 | 373773)
Class C	1.488 (1.07 | 2.1)	8.585 (5.98 | 19.59)	-39.328 (-69.1 | -6.2)	2.315 (1.583 | 3.958)	302695 (278783 | 335900)
Class D	1.595 (1.42 | 1.85)	6.949 (6.06 | 7.66)	-41.0 (-68.4 | -27.7)	2.0 (1.416 | 2.75)	244800 (225464 | 258925)
Class E	1.305 (1.02 | 1.51)	9.307 (6.47 | 16.45)	-41.125 (-69.8 | -18.6)	1.562 (1.458 | 1.708)	178059 (161878 | 186708)
Class F	1.308 (0.98 | 1.71)	8.893 (6.32 | 14.21)	-16.033 (-46.8 | 18.8)	1.097 (1.0 | 1.375)	118834 (111031 | 130421)
Class G	1.168 (1.0 | 1.42)	6.223 (5.84 | 6.82)	-31.724 (-67.7 | -12.6)	1.088 (1.0 | 1.375)	78049 (58485 | 89458)

Table 64. *Statistics of the classes of the extreme events identified in the clustering in Weymouth*

	$H_{s,peak}$ (m)	$T_{p,peak}$ (s)	$\theta_{m,peak}$ (°)	Duration (hours)	Energy (W/m)
Class A	2.43 (2.43 | 2.43)	10.11 (10.11 | 10.11)	106.3 (106.3 | 106.3)	4.375 (4.35 | 4.38)	1267280 (1267280 | 1267280)
Class B	2.012 (1.91 | 2.07)	9.44 (8.97 | 9.89)	109.175 (107.0 | 111.5)	3.697 (2.88 | 4.75)	744410 (681444 | 813953)
Class C	1.766 (1.37 | 2.2)	8.828 (7.95 | 10.14)	105.1 (97.8 | 112.6)	4.008 (2.42 | 6.67)	574361 (509035 | 615474)
Class D	1.742 (1.25 | 2.52)	8.482 (6.54 | 9.84)	104.605 (90.2 | 110.6)	2.613 (1.75 | 3.67)	361549 (239498 | 453286)
Class E	1.615 (1.25 | 2.34)	8.629 (5.98 | 10.17)	103.781 (90.3 | 109.2)	1.601 (1.0 | 2.041)	258362 (175179 | 361128)
Class F	1.528 (1.12 | 1.93)	7.723 (6.25 | 8.63)	103.442 (91.8 | 120.1)	1.284 (1.0 | 1.67)	170363 (114181 | 219891)
Class G	1.268 (1.1 | 1.47)	7.68 (4.87 | 12.3)	95.7 (64.8 | 111.4)	1.355 (1.041 | 2.0)	130929 (97192 | 172001)

Table 65. *Statistics of the classes of the extreme events identified in the clustering in Le Havre*

	$H_{s,peak}$ (m)	$T_{p,peak}$ (s)	$\theta_{m,peak}$ (°)	Duration (hours)	Energy (W/m)
Class A	3.837 (3.29 | 4.32)	9.969 (9.36 | 10.89)	43.799 (31.6 | 49.2)	3.979 (2.666 | 4.791)	3421605 (3134165 | 3575334)
Class B	3.492 (3.12 | 3.95)	9.14 (8.17 | 10.15)	40.4 (24.8 | 47.8)	4.052 (3.375 | 4.75)	2609702 (2413304 | 2854599)
Class C	3.566 (3.29 | 3.92)	9.533 (8.72 | 10.28)	43.666 (34.4 | 49.5)	2.437 (1.833 | 2.875)	1918633 (1755518 | 2160553)
Class D	3.566 (2.94 | 4.64)	9.041 (8.36 | 10.16)	39.2 (14.6 | 50.8)	2.462 (1.75 | 3.125)	1498599 (1373635 | 1649833)
Class E	3.102 (2.61 | 3.61)	8.794 (7.49 | 9.88)	44.862 (26.0 | 54.9)	1.956 (1.333 | 2.75)	1171555 (916534 | 1436870)
Class F	2.984 (2.32 | 3.62)	8.571 (7.43 | 9.81)	45.907 (26.4 | 56.1)	1.404 (1.0 | 1.791)	850004 (614696 | 1125619)
Class G	2.594 (2.21 | 3.19)	8.042 (6.83 | 9.15)	45.731 (12.5 | 53.7)	1.119 (1.0 | 1.416)	541399 (437879 | 658180)

Table 66. *Statistics of the classes of the extreme events identified in the clustering in Newhaven*

	$H_{s,peak}$ (m)	$T_{p,peak}$ (s)	$\theta_{m,peak}$ (°)	Duration (hours)	Energy (W/m)
Class A	4.164 (3.42 | 4.64)	9.017 (8.45 | 9.28)	39.219 (31.1 | 43.2)	3.675 (2.666 | 4.208)	3197462 (2705703 | 3420237)
Class B	4.062 (3.38 | 5.88)	8.983 (8.3 | 10.12)	38.066 (31.9 | 43.3)	2.255 (1.333 | 3.208)	1950061 (1494250 | 2417056)
Class C	3.453 (3.04 | 4.16)	8.399 (7.69 | 8.93)	40.661 (35.6 | 45.1)	1.845 (1.208 | 2.666)	1298757 (1045543 | 1635107)
Class D	3.009 (2.65 | 3.75)	8.091 (7.37 | 8.79)	42.191 (33.8 | 45.7)	1.958 (1.541 | 2.625)	1060300 (766804 | 1280049)
Class E	3.332 (2.9 | 3.85)	8.332 (7.61 | 9.19)	37.127 (22.6 | 44.8)	1.375 (1.0 | 1.875)	893646 (772932 | 1001107)
Class F	2.96 (2.27 | 3.56)	7.862 (7.05 | 8.55)	41.856 (34.2 | 49.5)	1.133 (1.0 | 1.333)	666411 (390409 | 1025072)

Table 67. *Statistics of the classes of the extreme events identified in the clustering in Dover*

	$H_{s,peak}$ (m)	$T_{p,peak}$ (s)	$\theta_{m,peak}$ (°)	Duration (hours)	Energy (W/m)
Class A	2.163 (1.8 | 2.52)	8.793 (8.23 | 10.06)	92.288 (-179.6 | 177.6)	2.726 (1.708 | 3.958)	746577 (666937 | 903497)
Class B	2.148 (1.95 | 2.42)	8.723 (8.38 | 9.19)	106.6 (-178.5 | 167.0)	2.187 (1.75 | 2.916)	618652 (569880 | 676499)
Class C	1.982 (1.68 | 2.14)	7.858 (7.11 | 8.8)	88.5 (-179.0 | 177.7)	1.825 (1.5 | 2.125)	425718 (357913 | 519806)
Class D	1.794 (1.4 | 2.23)	8.026 (6.12 | 9.46)	161.902 (98.2 | 178.1)	1.332 (1.0 | 2.0)	291273 (145364 | 504765)
Class E	1.569 (1.45 | 1.77)	6.786 (6.32 | 8.119)	74.24 (-172.3 | 150.6)	1.708 (1.291 | 2.083)	265612 (245768 | 294824)

Table 68. *Statistics of the classes of the extreme events identified in the clustering in Dunkirk*

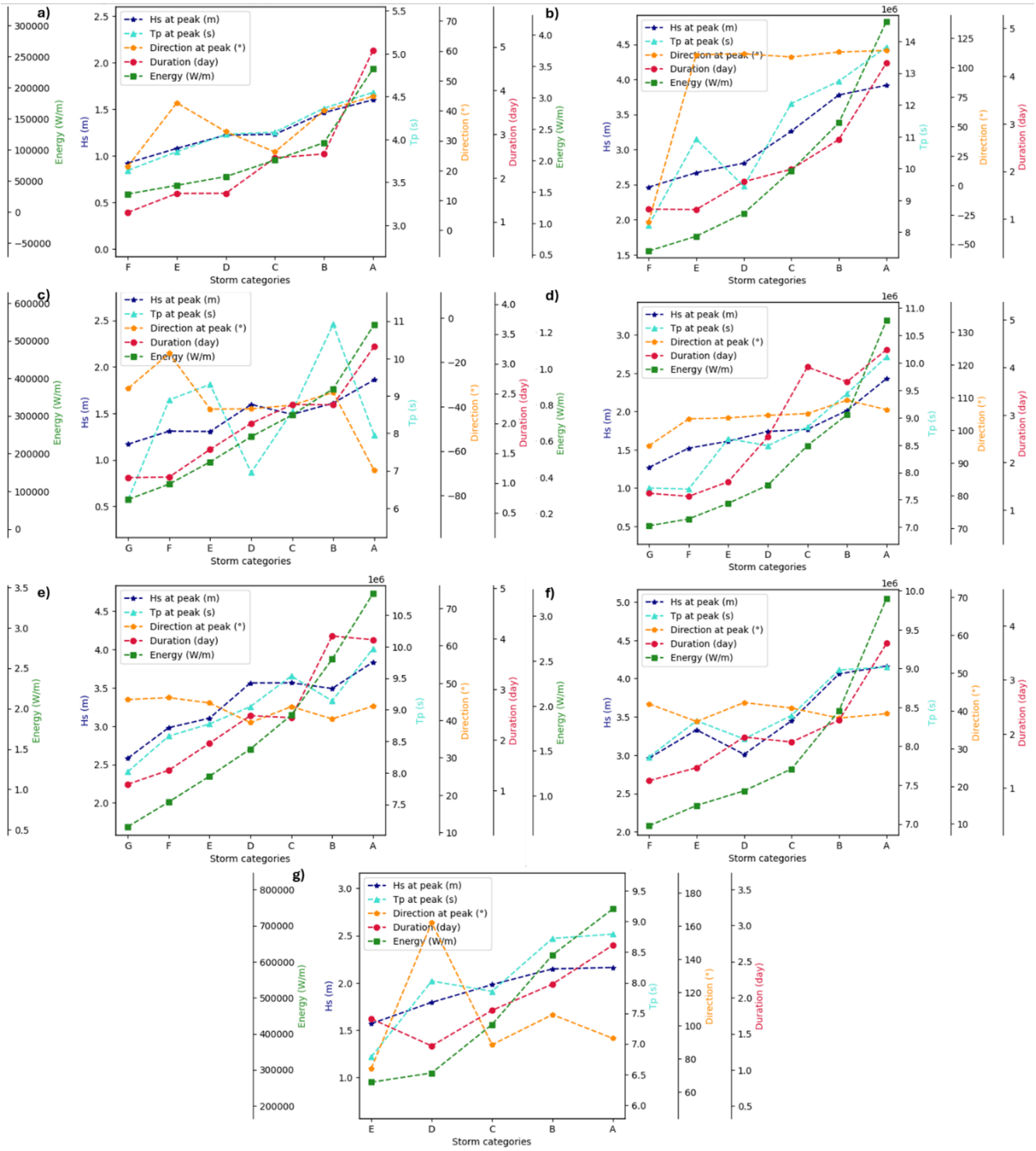

Figure 119. *Class-averaged values of extreme events on a) Brest, b) Cherbourg, c) Weymouth, d) Le Havre, e) Newhaven, f) Dover, and g) Dunkirk for the complete dataset of identified storms*

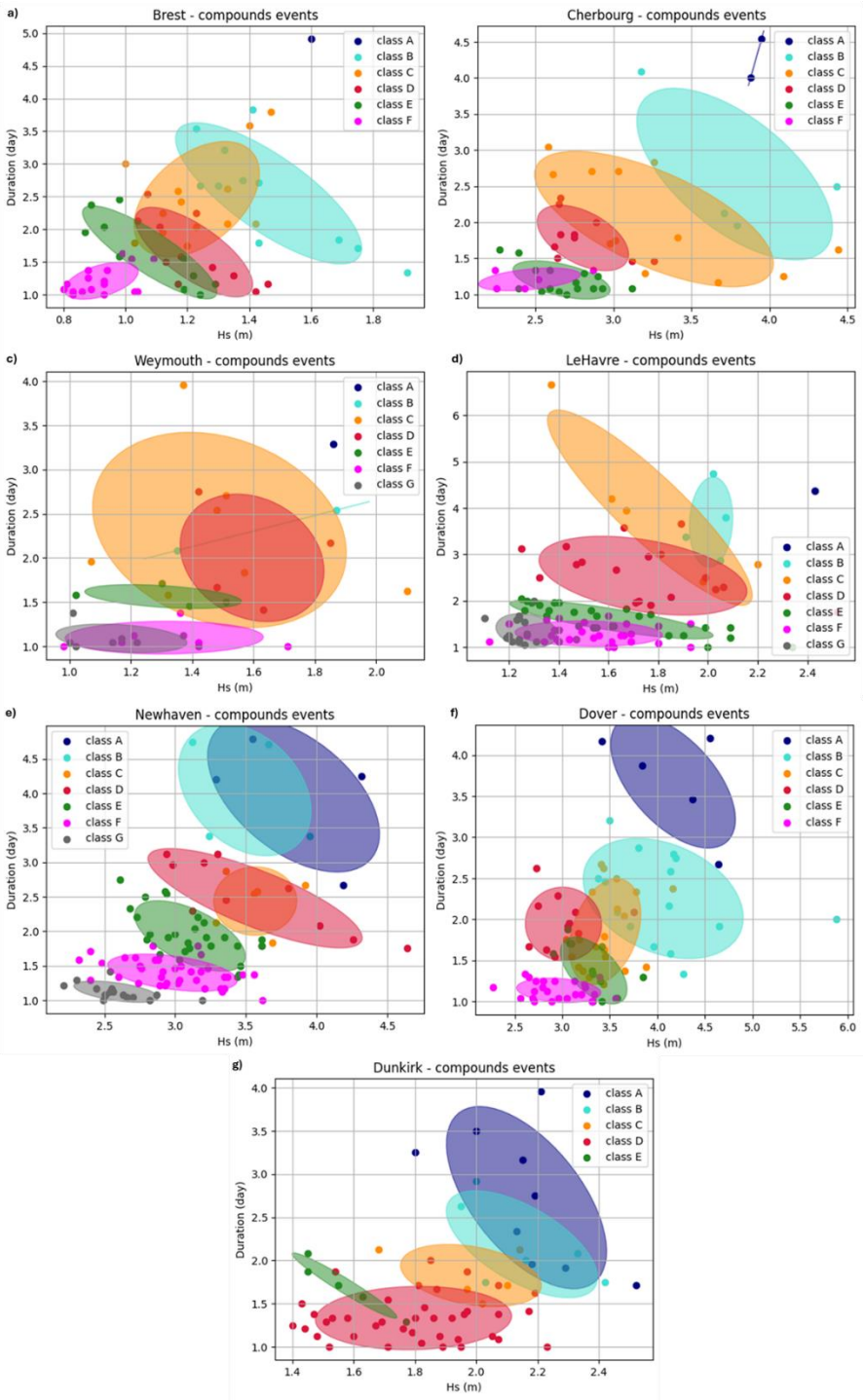

Figure 120. *H_s vs Duration for the classes obtained from the clustering of extreme events on a) Brest, b) Cherbourg, c) Weymouth, d) Le Havre, e) Newhaven, f) Dover, and g) Dunkirk for the complete dataset of identified storms*

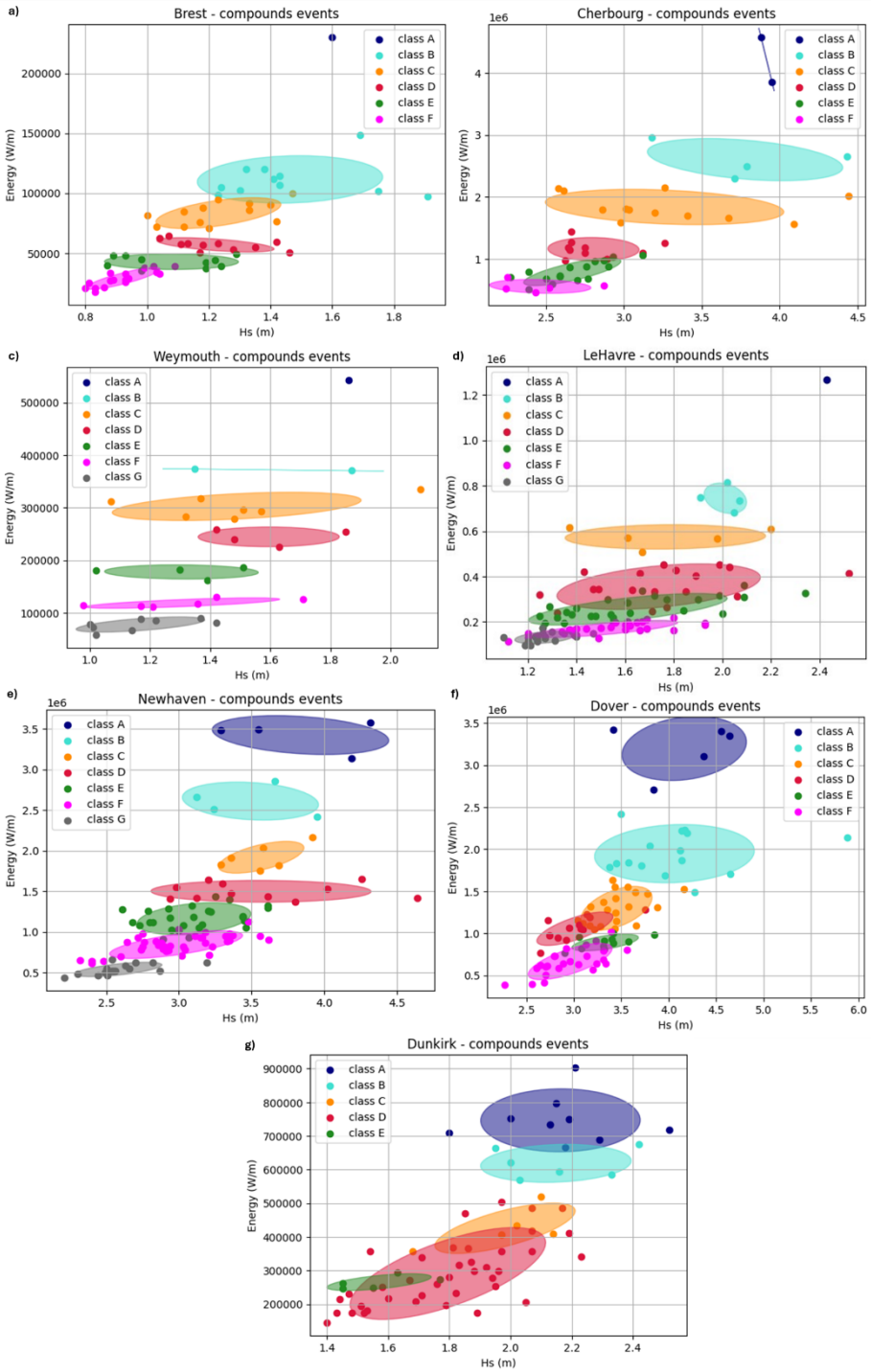

Figure 121. *H_s vs Energy for the classes obtained from the clustering of extreme events on a) Brest, b) Cherbourg, c) Weymouth, d) Le Havre, e) Newhaven, f) Dover, and g) Dunkirk for the complete dataset of identified storms*

APPENDIX D

FORMULATIONS AND NUMERICAL SOLUTIONS OF DELFT3D

This appendix presents a short description of the conceptualizations and the numerical solutions of the suite Delft3D focusing on the modules Delft3D-FLOW and Delft3D-WAVE, taken from the Delft3D-FLOW User Manual and the Delft3D-WAVE User Manual.

a. Formulations and numerical solutions of Delft3D-FLOW

The module Delft3D FLOW simulates multi-dimensional hydrodynamic flows and transport phenomena, including sediments, whose areas of application involves tide and wind-driven flows (i.e. storm surges) and river flow simulations, among others. In the present research, the focus lies on the hydrodynamic flow. The numerical modelling solves the unsteady shallow water equations in two (depth-averaged) or in three dimensions.

The system of equations consists of the horizontal equations of motion and the continuity equation. The equations are formulated in orthogonal curvilinear co-ordinates or in spherical co-ordinates on the globe. In curvilinear co-ordinates, the free surface level and bathymetry are related to a flat horizontal plane of reference.

The flow is forced by tide at the open boundaries, wind stress at the free surface, pressure gradients due to free surface gradients (barotropic) or density gradients (baroclinic). Source and sink terms are included in the equations to model the discharge and withdrawal of water.

The Delft3D-FLOW model includes mathematical formulations that take into account the following physical phenomena:

- Free surface gradients (barotropic effects).
- The effect of the Earth's rotation (Coriolis force).
- Horizontal density gradients in the pressure (baroclinic effects).
- Turbulence induced mass and momentum fluxes (turbulence closure models).
- Tidal forcing at the open boundaries.
- Space and time varying wind shear-stress at the water surface.
- Space varying shear-stress at the bottom.
- Space and time varying atmospheric pressure on the water surface.
- Time varying sources and sinks (e.g. river discharges).
- Drying and flooding of tidal flats.
- Tide generating forces.
- Effect of secondary flow on depth-averaged momentum equations.

- Lateral shear-stress at wall.
- Vertical exchange of momentum due to internal waves.
- Influence of waves on the bed shear-stress (2D and 3D).
- Wave induced stresses (radiation stress) and mass fluxes.
- Wind driven flows including tropical cyclone winds.

Delft3D-FLOW solves the Navier Stokes equations for an incompressible fluid, under the shallow water and the Boussinesq assumptions. In the vertical momentum equation the vertical accelerations are neglected, which leads to the hydrostatic pressure equation. In the horizontal direction Delft3D-FLOW uses orthogonal curvilinear co-ordinates. From the two coordinates systems supported by the model, the cartesian coordinates are used. In the vertical direction, from the two different vertical grid systems, the σ coordinate system is used.

The depth-averaged continuity equation is derived by integration the continuity equation for incompressible fluids over the total depth, taken into account the kinematic boundary conditions at water surface and bed level. Under the shallow water assumption, the vertical momentum equation is reduced to a hydrostatic pressure equation. Vertical accelerations due to buoyancy effects and due to sudden variations in the bottom topography are not taken into account. The discharge of water, when momentum is taken into account, gives an additional term in the momentum equation.

To solve the partial differential equations the equations should be transformed to the discrete space, with the numerical method of Delft3D-FLOW based on finite differences. The primitive variables water level and velocity (u, v, w) describe the flow. To discretize the 3D shallow water equations, the variables are arranged in a special way on the grid, with a pattern called staggered grid, particularly the Arakawa C-grid (**Figure 122**). The water level points (pressure points) are defined in the center of a (continuity) cell. The velocity components are perpendicular to the grid cell faces where they are situated.

Staggered grids have several advantages such as boundary conditions can be implemented in a rather simple way, it is possible to use a smaller number of discrete state variables in comparison with discretizations on non-staggered grids, to obtain the same accuracy, and prevent spatial oscillations in the water levels for shallow water solvers.

For the σ co-ordinate grid, the number of layers over the entire horizontal computational area is constant, irrespective of the local water depth. The distribution of the relative layer thickness is usually non-uniform. This allows for more resolution in the zones of interest such as the near

surface area (important for e.g. wind-driven flows, heat exchange with the atmosphere) and the near bed area (sediment transport).

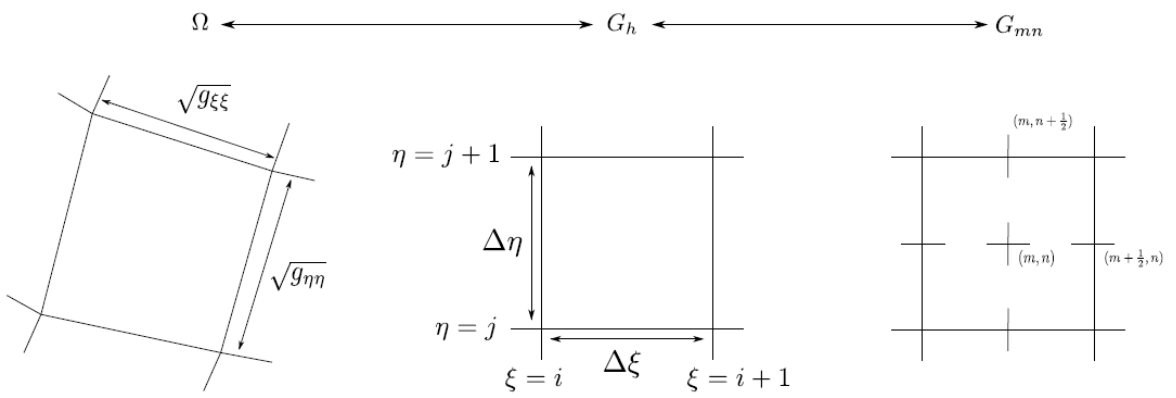

Figure 122. *Mapping of physical space to computational space. Extracted from the User Manual of Delft3D-FLOW*

Regarding the boundary conditions, the horizontal model area is defined by specifying the so-called computational grid enclosure. The computational grid enclosure consists of one or more closed polygons that specify the boundaries of the model area. There are two types of boundaries: closed boundaries along “land-water” lines (coastlines, riverbanks) and open boundaries across the flow field. The open boundaries are artificial and chosen to limit the computational area. The computational cells on the grid enclosure are land points (permanent dry) or open boundary points.

The solution of the discretized equations is just an approximation of the exact solution. The accuracy of the solution depends not only on the numerical scheme, but also on the way in which the bottom topography, the geographical area, and the physical processes (turbulence, wave-current interaction) are modelled.

The time integration method strongly influences the wave propagation when applying a large time step. The assumption is made that, by restricting the computational time step, the free surface waves can be propagated correctly.

When it comes to taking into account the effect of waves on the flow and viceversa (via set-up, current refraction and enhanced bottom friction) and the effect of waves on current (via forcing, enhanced turbulence and enhanced bed shear stress), there are three different types of wave computations within the Delft3D module. In this research, the coupling of WAVE with Delft3D-FLOW is made online: the WAVE model has a dynamic interaction with the FLOWmodule of Delft3D (i.e. two way wave-current interaction). Through this coupling, both the effect of waves on current and the effect of flow on waves are accounted for.

b. Formulations and numerical solutions of Delft3D-WAVE

To simulate the evolution of random, short-crested wind-generated waves in estuaries, barrier islands with tidal inlets, tidal flats, lakes, channels etc., the Delft3D-WAVE module can be used. Delft3D-WAVE is based on the third-generation SWAN calculation model.

The SWAN model is based on the discrete spectral action balance equation and is fully spectral (in all directions and frequencies). The latter implies that short-crested random wave fields propagating simultaneously from widely different directions can be accommodated (e.g. a wind sea with super-imposed swell). SWAN computes the evolution of random, shortcrested waves in coastal regions with deep, intermediate and shallow water and ambient currents. The SWAN model accounts for (refractive) propagation due to current and depth and represents the processes of wave generation by wind, dissipation due to whitecapping, bottom friction and depth-induced wave breaking and non-linear wave-wave interactions (both quadruplets and triads) explicitly with state-of-the-art formulations.

In the input for Delft3D-WAVE the directions of winds and (incident) waves are defined relative to the coordinate system according to a Nautical convention or Cartesian convention. In the Cartesian system, all geographic locations and orientations in SWAN, e.g. for the computational grid or for output points, are defined in one common Cartesian coordinate system with origin (0,0) by definition.

Delft3D-WAVE accepts input and provides output on different grids. Input grids on which the bathymetry, current field and wind field (if present) are given by the user. During the computations (on the computational grid) Delft3D-WAVE obtains bathymetry and current information by bilinear interpolation from the input grid. The output on the output grid is in turn obtained in Delft3D-WAVE by interpolation from the computational grid.

In SWAN the waves are described with the two-dimensional wave action density spectrum, even when non-linear phenomena dominate (e.g., in the surf zone). The evolution of the wave spectrum is described by the spectral action balance equation, with one term representing the local rate of change of action density in time, two terms representing propagation of action in geographical space (with propagation velocities in x- and y-space, respectively), one term representing shifting of the relative frequency due to variations in depths and currents and one term representing depth-induced and current-induced refraction. Those terms are equaled

to the source term in terms of energy density representing the effects of generation, dissipation and non-linear wave-wave interactions

The integration of the action balance equation has been implemented in SWAN with finite difference schemes in all five dimensions (time, geographic space and spectral space). In Delft3D-WAVE, SWAN is applied in a stationary mode so that time has been omitted from the equations. The geographic space is discretized with a rectangular grid with constant resolutions. The numerical schemes in SWAN have been chosen on the basis of robustness, accuracy and economy. The wave components in SWAN are correspondingly propagated in geographic space with the first-order upwind scheme in a sequence of four forward-marching sweeps (one per quadrant). To properly account for the boundary conditions between the four quadrants, the computations are carried out iteratively at each time step.

APPENDIX E

STUDY OF WAVE BREAKING SIMULATION WITH SWASH

This appendix presents a short study to investigate the interest in using multiple vertical layers for numerically simulating wave-breaking in SWASH. This work has been carried out in the framework of the master internship of Pierre Chauris under the supervision of M2C (Imen Turki) and ENPC (Marisa Yates).

a. Set-up of wave breaking parameters in SWASH

In the numerical model, depth plays a major role, improving the precision of the results when adding more layers, but at the expense of an increased computational cost. With SWASH, it is possible to calculate a Boolean mask that determines the presence of wave breaking on each cell over the entire profile (**Figure 123**a). The result is an estimated breaking zone at each timestep to consider, then, the average position of these breaking zones over the entire duration of the event (**Figure 123**b).

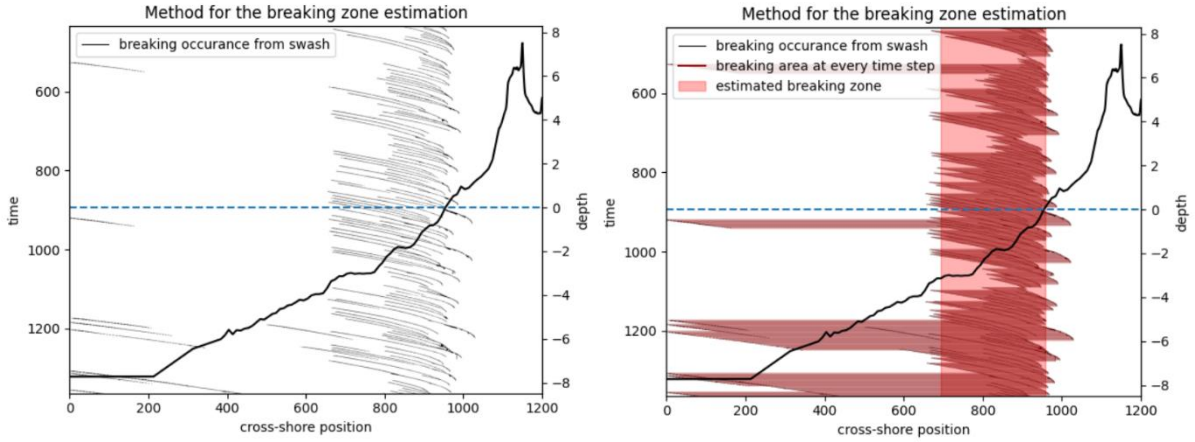

Figure 123. *Breaking zone estimation method: a) Boolean mask over the cross-shore profile between instants 400s and 1200s of simulation, and b) At each time step, the breaking zone is in dark red, and the averaged breaking zone in light red. Internship of Pierre Chauris (2024)*

For this study, the simulations have been carried out in profile P13 of Villers-sur-Mer, previously presented (**Figure 65** and **Figure 66**). The individual breaking areas seem to be concentrated around 800 m, which is the expected surf zone, with only some breaking occurring outside of this region, due to numerical errors. The breaking zone is numerically controlled by different model parameters, so the objective is understanding the effect of these parameters. Then, validating the simulation with VMS, the optimal model configuration to simulate wave breaking can be determined.

In SWASH, wave breaking is considered as a discontinuity of the free surface, that can be detected with a sufficient vertical resolution of more than $k = 10$ layers. Otherwise, SWASH still

offers a way to manually control the initiation and termination of wave breaking, that can be expressed in terms of the temporal variation of the free surface. Wave breaking is initiated when:

$$\frac{\partial \zeta}{\partial t} > \alpha\sqrt{gh} \tag{32}$$

and stopped when:

$$\frac{\partial \zeta}{\partial t} < \beta\sqrt{gh} \tag{33}$$

where α, β are user-defined parameters respecting $0 < \alpha < \beta$, h is the depth and ζ is the free surface elevation.

The interest relays on investigating the effects of α and β on the breaking zone estimation for a small number of layers (k < 10) in order to improve the precision of breaking simulation with a low computational cost. By varying one parameter while keeping the others fixed, it is possible to see the effect of this isolated parameter on the model. In particular, the study focuses on the width (w) and position of the breaking zone.

For the first case (**Figure 86**a), when β is fixed, it can be seen that as α increases, the initiation of wave breaking is identified closer to the coast. As β is fixed, the end of wave breaking is identical. This is physically consistent with what would be expected for the initiation and termination of wave breaking in relation to the values of α and β defined by Eq. 32 and Eq.33, respectively. For the second case (**Figure 86**b), when α is constant, increasing β will trigger the breaker to stop earlier, which is consistent again with the definition Eq.33. Since the position and width of the breaking area are strongly dependent on the parameters α and β, a validation process is required to find out which configuration actually corresponds to the real breaking zone. The simulated breaking zone is then compared with real measurements obtained from the VMS.

b. Validation of the breaker height

The methodology to extract the significant wave height at breaking H_b from timestacks is presented in Almar et al. (2012) as described in **Figure 124**. The methodology is based on the fact that breaking waves produce foam from the beginning to the end of the breaking process, leading to a high-intensity variation along a timestack vertical axe. The method consists first in extracting the breaking position from a timestack and then extracting the breaker height. The breaking position extraction method is illustrated in **Figure 125**.

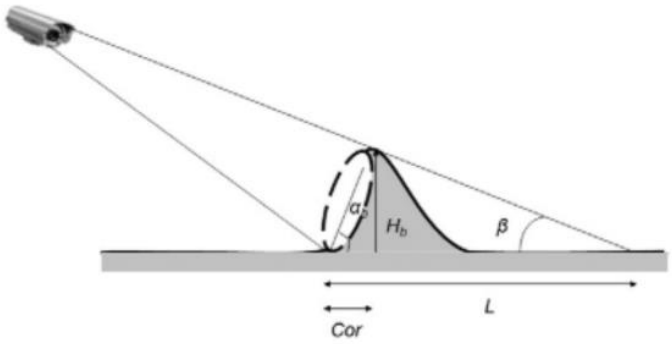

Figure 124. *Schematic of the principal method. The camera view angle is β and α_b is the wavefront face slope. The roller appears as a dashed oval. L is the wave roller horizontal projection, Cor a correction taking into account α_b and H_b is the actual breaker height. Extracted from Almar et al. (2012). Internship of Pierre Chauris (2024)*

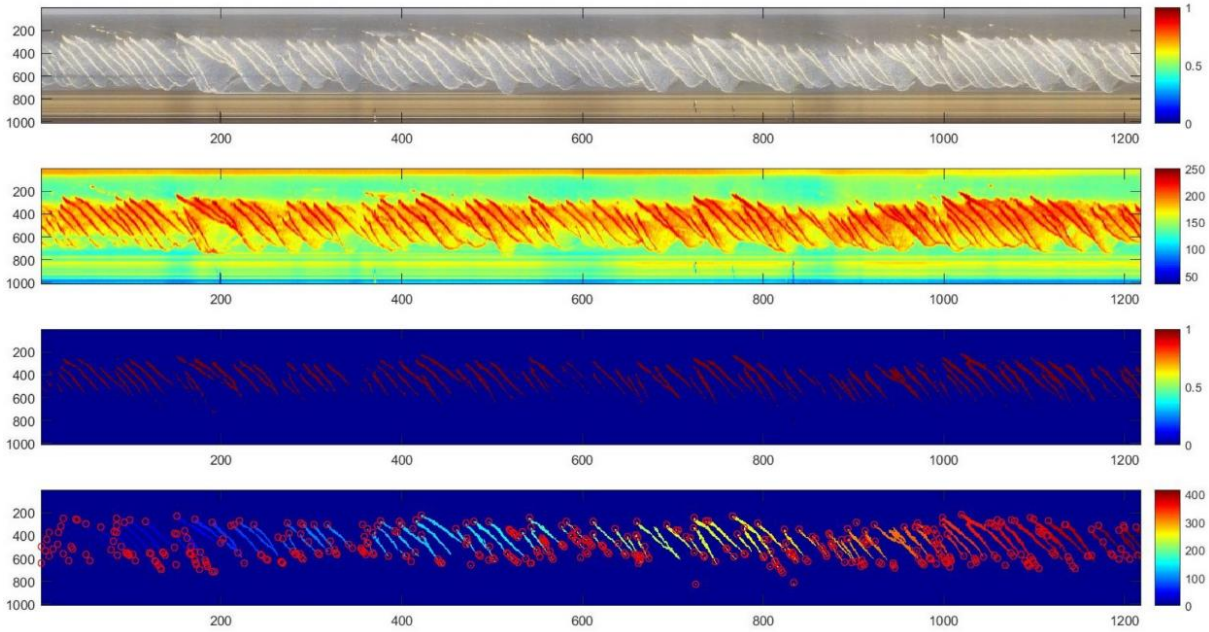

Figure 125. *Step-by-step extraction of the breaking positions in a timestack. Internship of Pierre Chauris (2024)*

From the timestack (**Figure 125**a), the image intensity is determined (**Figure 125**b) and normalized. The area corresponding to the zone of wave breaking can be identified with a clear intensity level. **Figure 125**c is a binary image obtained from the previous representing “breaking” and “non-breaking” pixels, considered “breaking” if their intensity is above a certain threshold, arbitrarily chosen. As the intensity is normalized, this threshold can be kept constant from one image to another. Finally, breaking pixels are grouped by proximity (**Figure 125**d) with each group representing a single wave. Then, the breaking position x_b (and the corresponding instant t_b) is obtained as the most offshore point of each wave, corresponding to the beginning of a breaking wave. The beginning and end of each wave are labeled by a red circle in Figure Dd. The position is

first expressed in terms of pixels but can be converted into real coordinates with the rectification algorithm.

The second step consists of computing the wave height of the waves extracted previously. This is based on the intensity signal evolution. Considering an individual breaking event, Figure E represents the cross-shore intensity profile during breaking. Each curve of **Figure 126**a corresponds to a cross-shore intensity slice of the timestack image, represented by the blue lines, and d_t corresponds to the time interval between 2 columns of the timestack, i.e., $d_t = 0.5\ s$. The blue transects are intersected by multiple waves, represented by the intensity bumps.

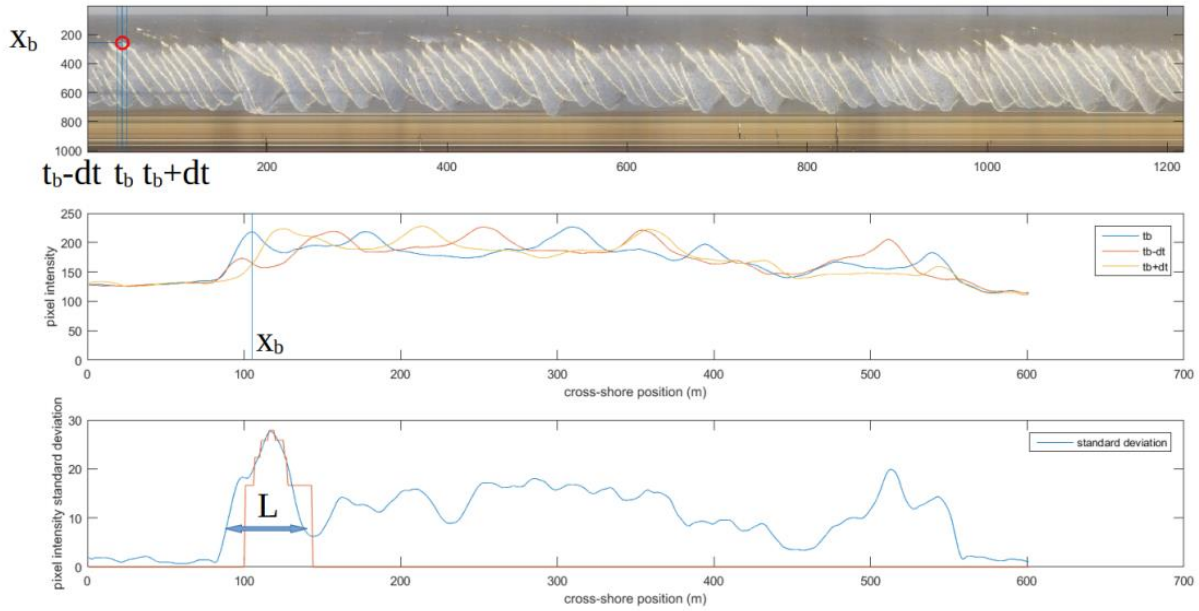

Figure 126. *Breaker height extraction methodology: a) timestack intensity around a breaking event at 3 consecutive time steps; b) intensity standard deviation over the 2dt period; and c) horizontal projection of the wave face covered by the roller. Internship of Pierre Chauris (2024)*

Then, the intensity standard deviation is computed for each cross-shore point. Note that as the waves continue to break, the horizontal extension of the intensity peak is no longer only associated with the wave face but also with roller propagation and the remaining foam. For this reason, the breaker height can only be computed at x_b. The standard deviation allows to capture the location where breaking induces a sudden intensity variation. A peak around the breaking position can be observed. The width of the peak, L, is directly linked to the wave height considering the following relations developed in Almar et al. (2012). The relations are obtained considering the geometric configuration of **Figure 126**. The breaker height extraction process is then repeated for all the detected waves. The results are presented in **Figure 87**.

To test the methodology, the H_b obtained from timestacks is compared with the values obtained by the SWASH simulation. The scenario chosen for validation is February 2020,

particularly rich month in terms of extreme events, with multiple storms hitting the Normandy coast, including Ciara storm. To extend the database of comparisons between the SWASH simulations and the VMS observations, a SWASH simulation is performed every day for the sea state corresponding to the highest energy conditions, as presented in **Figure 127**.

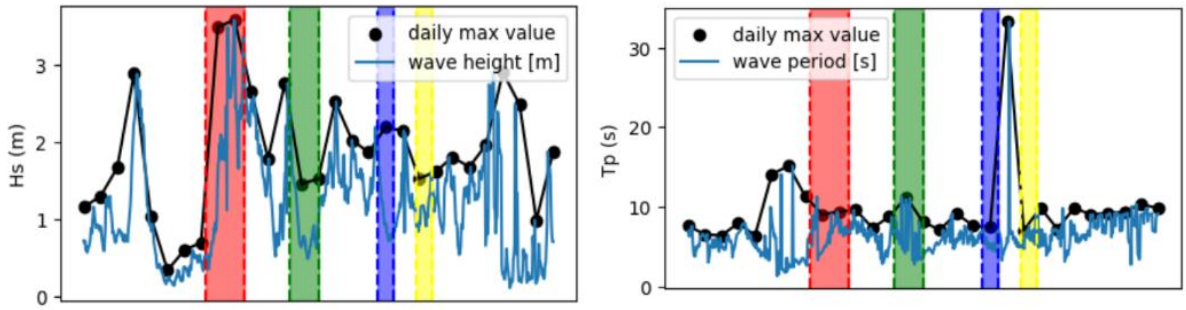

Figure 127. *Daily maximal values of wave height and period measured during February 2020 used for the SWASH simulations. The colored sections represent the duration of energetic storm events, with Ciara storm in red. Internship of Pierre Chauris (2024)*

The obtained values for H_b comparing the values extracted from the timestacks and the values obtained from the simulations of SWASH are compared in **Figure 88**, noticing an overall agreement between the two methods. Some values from timestacks are missing due to poor image quality, leading to low-intensity contrast, making it impossible to detect waves and to extract the H_b.

c. Validation of the breaker zone

Finally, a comparison between breaking distribution simulated in SWASH and breaking obtained from the observed timestacks is conducted, for the same scenario presented. It is possible to extract the breaking area from the timestacks, since breaking is characterized by foam corresponding to a high-intensity variation in the timestack. The methodology is similar to the wave height extraction method and consists of image processing on the timestacks. The individual waves are first extracted from a timestack, with the intensity-based technique and then a binary map, from which the area of wave breaking can be obtained. This corresponds to the same area of wave breaking previously presented but adds information about how the individual breaking waves are distributed over the whole breaking area. The process with SWASH and with the observed timestacks is compared in **Figure 89**.

Finally, the comparison is conducted over February 2020, with the same scenario presented for wave height comparisons. Similarly, some days are missing due to poor image quality, making it impossible to apply the image processing method.

Many SWASH simulations were performed, with different combinations of k, α and β, and the results giving the best comparison between SWASH simulations and timestacks extraction are presented in **Figure 90**. The breaking configuration of SWASH giving the best results is the combination of a number of layers of $k = 3$, and, for controlling the position and width of the breaking area, $\alpha = 0.3$ and $\beta = 0.1$. The position and the width of the breaking zone obtained from simulations and image processing are overall accurate, outside for some days (especially for the 12th, 20th, 21st, and 22nd February), presenting an easy methodology for the calibration of the SWASH model.